

THESIS / THÈSE

DOCTOR OF SCIENCES

Quantum Chemistry Investigations on Nonlinear Optical Materials from Reference to Complex Systems

Beaujean, Pierre

Award date:
2021

Awarding institution:
University of Namur

[Link to publication](#)

General rights

Copyright and moral rights for the publications made accessible in the public portal are retained by the authors and/or other copyright owners and it is a condition of accessing publications that users recognise and abide by the legal requirements associated with these rights.

- Users may download and print one copy of any publication from the public portal for the purpose of private study or research.
- You may not further distribute the material or use it for any profit-making activity or commercial gain
- You may freely distribute the URL identifying the publication in the public portal ?

Take down policy

If you believe that this document breaches copyright please contact us providing details, and we will remove access to the work immediately and investigate your claim.

Namur Institute of Structured Matter (NISM)
Laboratoire de Chimie Théorique (LCT)

Quantum Chemistry Investigations on Nonlinear Optical Materials: from Reference to Complex Systems

October, 7th 2021

Thesis submitted by
Pierre Beaujean

in fulfillment of the requirements for the Degree of
DOCTOR OF SCIENCES

Committee:

- Prof. Benoît Champagne (supervisor)
- Prof. Frédéric Castet
- Prof. Olivier Deparis (president)
- Dr. Marc de Wergifosse
- Dr. Vincent Liégeois
- Dr. Lionel Sanguinet
- Prof. Daniel P. Vercauteren

Graphisme de couverture: © Presses universitaires de Namur

© Presses universitaires de Namur & Pierre Beaujean
Rue Grandgagnage 19
B-5000 Namur (Belgique)

Toute reproduction d'un extrait quelconque de ce livre, hors des limites restrictives prévues par la loi, par quelque procédé que ce soit, et notamment par photocopie ou scanner, est strictement interdite pour tous pays.

Imprimé en Belgique
ISBN : 978-2-39029-150-3
Dépôt légal: D/2021/1881/18

Abstract

The interplay between light and matter gives rise to several phenomena, including nonlinear optical (NLO) effects. This thesis aims at describing and understanding, using quantum chemistry, the NLO properties of molecules. In particular, it focuses on their second (SHS) and third (THS) harmonic scattering responses: β_{SHS} and γ_{THS} , respectively. The goal is to provide insights and to help towards the design of new materials, in a multidisciplinary framework combining theory and experiment.

In the first part, the chapters are dedicated to the accurate description of (gas phase) molecular responses of reference molecules, crucial for experimental measurements. So, a hierarchy of Coupled Cluster methods has been employed with large basis sets and checked against experimental results in order to select an appropriate level of approximation. Then, the first quantum chemical investigation on γ_{THS} is reported, presenting the calculated values and their decomposition into spherical components, at the light of comparisons with β_{SHS} . It shows that γ_{THS} is dominated by its isotropic contribution contrary to β_{SHS} , of which the major contribution is dipolar or octupolar as a function of the molecular structure. Finally, the impact of vibrational contributions has been addressed for the water molecule as a model system, thanks to a homemade implementation of finite-field differentiation techniques. It is shown that the contributions to the dynamic NLO properties are small but non-negligible (10% or less), while much larger in the static limit.

The second part focuses on the study of molecules of increasing complexity, displaying large or remarkable second-order NLO responses. On the one hand, NLO switches have been explored, with a focus on the characterization (structures, linear and nonlinear optical responses) of each of their states as well as the β_{SHS} contrast between them. In particular, two types of compounds have been considered: i) octupolar molecules with 6 ruthenium(II) centers that can be oxidized and ii) multi-state compounds, involving two or three benzazolooxazolidine units, leading up to 4 or 8 different states, respectively. In both cases, quantum chemical calculations have provided precious insights for a better understanding of their behavior and optimization. In particular, the second-order NLO responses have been rationalized using different few-state models to account for their complex architectures. On the other hand, a new methodology to study the NLO response of fluorescent proteins, biotags of interest in second-harmonic imaging microscopy, has been developed. As a proof of concept, two proteins have been considered, with promising results. For instance, for the bacteriorhodopsin, the comparison with experimental data is excellent, providing an avenue for unraveling the origin of these NLO responses.

These different contributions pinpoint the importance of quantum chemistry to deduce structure-activity relationships and help the design of new and improved molecules.

Contents

I	Introduction, objectives and methods	1
1	Introduction and objectives	3
1.1	Nonlinear optics (NLO)	4
1.2	NLO materials	8
1.3	NLO molecular switches	14
1.4	Objectives	18
2	Second and third harmonic scattering	29
2.1	Generation and measurement of harmonics	30
2.2	From the molecular tensor to the macroscopic quantities	33
2.3	Irreducible tensor forms	37
3	Quantum chemistry methods	47
3.1	The wavefunction approaches	48
3.2	The density functional theory (DFT) approach	57
3.3	Molecular properties	65
3.4	Effects of the surroundings	77
II	Accurate description and understanding of the first and second hyperpolarizabilities of reference molecules	89
4	Coupled Cluster evaluation of the frequency dispersion of the first and second hyperpolarizabilities of water, methanol and dimethyl ether	91
4.1	Introduction	92
4.2	Theoretical methods and computational procedures	93
4.3	Results and discussions	96
4.4	Conclusions	108
5	Coupled cluster evaluation of the second and third harmonic scattering responses of small molecules	115
5.1	Introduction	116

5.2	The SHS and THS spectroscopies	117
5.3	Computational methodology	121
5.4	Results and discussions	122
5.5	Conclusions	129
6	Coupled Cluster investigation of the vibrational and electronic second and third harmonic scattering hyperpolarizabilities of the water molecule	137
6.1	Introduction	139
6.2	Theoretical aspects	140
6.3	Computational aspects	144
6.4	Results and discussions	145
6.5	Conclusions	158
III	Study of complex NLO molecules	169
7	Unraveling the Symmetry Effects on the Second-Order Nonlinear Optical Responses of Molecular Switches: the Case of Ruthenium Complexes	171
7.1	Introduction	173
7.2	Methodological and Computational Elements	176
7.3	Results and discussions	180
7.4	Conclusions and outlook	197
8	Multi-state nonlinear optical switches: a quantum chemical investigation of compounds bearing two identical multi-addressable benzazolo-oxazolidine units	205
8.1	Introduction	207
8.2	Methods	210
8.3	Results and Discussion	213
8.4	Further Discussions, Conclusions, and Outlook	226
9	When the π-conjugation of a connector cheats the statistical transformation of an octastate multimodal molecular switch: a theoretical characterization	235
9.1	Introduction	236
9.2	Theoretical and computational aspects	239
9.3	Results and discussion	240
9.4	Conclusions	249
10	All-atom quantum mechanical calculation of the second-harmonic generation of fluorescent proteins	257

11 Few-state description of the first hyperpolarizability	273
11.1 Introduction	274
11.2 Theory	276
11.3 Results and discussion	280
11.4 Conclusions and outlooks	301
 IV Conclusions and perspectives	 305
 12 Summary, conclusions and outlook	 307
 13 List of publications	 315
 V Appendices	 317
 A Supporting information of Chapter 7	 319
A.1 Benchmarks	320
A.2 Electronic transitions	325
 B Supporting information of Chapter 10	 337
B.1 Geometry optimizations	338
B.2 Fine-tuning of the parameters for the sTD-DFT-xTB method	339
B.3 Extrapolating the experimental β_{HRS} frequency dispersion to the static limit for the bacteriorhodopsin	347
 C Supporting information of Chapter 11	 351

Remerciements

C'est avec une certaine appréhension que je m'attelle ici à l'exercice qui est probablement le plus complexe de cette thèse, à savoir rédiger cette partie. Loin des règles (très) complexes qui encadrent l'écriture d'un tel manuscrit, il s'agit d'un petit espace de liberté qui m'est offert afin de m'adresser à toi, lecteur,^a qui souhaite connaître le contexte dans lequel ce document (et tout ce qui le précède !) a été réalisé, ou qui est simplement curieux. La tâche est donc complexe, d'autant qu'il s'agit de n'oublier personne^b !

Pour le contexte, donc, l'histoire de cette thèse commence en fait en décembre 2015, lorsque je finis par me décider pour un mémoire sous la supervision ~~du Professeur B. Champagne~~ de Benoît dans le domaine de la chimie quantique et de l'étude d'interrupteurs moléculaires nommés les oxazines. 7 ans, 15 kilos, plusieurs piscines de café, quelques cheveux blancs et 200 années en temps réel de calcul plus tard,^c vous tenez entre vos mains le résultat. Ce serait peu dire que j'ai changé au cours de ces années, mais j'ai aussi beaucoup appris, et mesuré à quel point je n'avais rien compris ! Entre les coups, j'ai dédié une partie de ma vie à l'assistanat, une très chouette expérience, et j'ai aussi réussi à caser un baccalauréat en informatique, une ... très chouette expérience ! L'histoire nous dira si j'arrive encore à concilier toutes ces passions dans le futur, mais j'espère bien. Quoiqu'une légende raconte que les chimistes ont une certaine tendance à finir en politique,^d donc on verra.

Commençons maintenant, si vous le voulez bien, la liste des personnes que je dois remercier pour une raison ou une autre, et sans qui ce manuscrit, à bien des égards, n'aurait pas pu atterrir dans vos mains. Bien entendu, le premier est adressé à Benoît pour m'avoir permis de réaliser une thèse dans son laboratoire, et m'avoir permis d'obtenir un poste d'assistant pour la financer. Je le remercie aussi pour les trop nombreuses heures qu'il a passé à corriger mes innombrables fautes de grammaire, d'orthographe et de sciences. Merci également à mon comité d'accompagnement, ainsi qu'aux membres de mon jury, qui ont également oeuvré pour la qualité de ce manuscrit. Je retiendrai tout particulièrement le dévouement de D. Vercauteren et la qualité de ses corrections orthographiques (et le reste) !

Je remercie ensuite, une seconde fois, M. de Wergifosse, F. Castet et L. Sanguinet pour les différentes collaborations que nous avons eues au cours de cette thèse, et qui ont donné de

^aOui, toi, là!

^bSi c'était le cas, la règle avec mes étudiants était "un chocolat offert". Et toutes mes excuses, bien entendu.

^cEt c'est sous-estimé !

^dComme démontré par différents exemples: A. Merkel, J. M. Bergoglio (*aka* le pape), E. Di Rupo et O. Louant.

très chouettes travaux. Je tiens également à m'excuser auprès de Lionel pour l'avoir embêté avec mon chapitre 11, que je lui dédicace donc tout particulièrement ;)

Je tiens également à adresser des remerciements tout particuliers à L. Demellenne et F. Wauthelet pour la gestion, respectivement, du matériel informatique et du cluster Hercules. Dieu sait ce que serait devenu ma thèse sans eux ! Et ... Désolé pour le dérangement ;)

Je remercie par ailleurs tous les membres du LCT, passés et présents, pour 7 années de temps de midi, de cafés et de discussions (scientifiques, bien entendu, mais heureusement, pas que). Merci donc à Audrey, Conrad, François, Freddy, Jojo, Julien, Laura, Kornelia, Jean, Maxime, Tárcius, Tom, Tomasz et Vincent. Je n'oublie pas non plus tous mes collègues assistants et en particulier François, Conrad, Frédéric, Jérémy et L. Leherste avec qui j'ai eu l'occasion de collaborer. Sont également à remercier; la cellule didactique, D. Baillieul et I. Ravet, pour avoir toujours été présentes en cas de besoin. Elles y sont également pour beaucoup dans le souvenir que je garderai de ces années de thèse !

Continuons par quelques personnes qui n'ont aucune idée de mon existence, mais qui encore une fois ont été déterminantes pour cette thèse: Linus Thorvald et Ian Murdock, Guido van Rossum, Jimmy Wales et Larry Sanger, ainsi que Aaron Swartz et Alexandra Elbakyan. Ces personnes,^e au même titre que les grands noms qui seront cités dans la suite de ce travail, sont l'exemple que la passion mène très loin en science et que l'argent, s'il est le nerf de la guerre, est loin d'en être le seul moteur (et ça devrait rester ainsi, qu'on se le dise !).

Avant de terminer, je souhaite également dire que je ne remercie pas la corrélation électronique, le COVID-19,^f les transformées de Fourier et les coordonnées sphériques. C'est dit.

Je finirai donc ces remerciements par plusieurs groupes de personnes qui m'ont également aidé et soutenu durant ces 7 longues années, voire même avant. Merci à mes parents, mes grands-parents et mes frères, pour m'avoir soutenu, sans vraiment en comprendre grand-chose. J'essayerai de faire mieux la prochaine fois ! Merci à Anaïs et Éva pour le soutien aussi, on recommence quand vous voulez. Merci à mes collègues des cours du soir (en particulier Maxime et Gauthier), c'était trois très chouettes années ! Merci aux gens de Zeste de Savoir, vous y êtes pour quelque chose aussi ! Et finalement, merci à Marie et Lio, Jean et Charlotte, Orian et Kim et Loïc pour tous ces vendredis (et le reste, d'ailleurs !).

... Mais je n'oublie bien entendu pas Guillaume, la petite surprise de cette fin de thèse qui fait plaisir, alors que je croyais que ça n'arriverait plus jamais. Grawr ! Merci également à ma belle-famille, pour l'accueil et la simplicité. Et bienvenue, petite Batida !

Namur, Le 22 septembre 2021

Cette thèse est également dédiée à Michel Beaujean, Christelle Fairon et Stuff, partis un tout petit peu trop tôt à mon gout.

^eSi vous les reconnaissez tous du premier coup, respect!

^fL'enseignement en distanciel, c'est juste tout nul. Wallah.

I wanna run away tonight
Just leave everything behind
Together we'll make our sweet escape
In the shadows out of sight
Like ghosts in ultraviolet

The Sweet Escape, Poets of the fall

After sleeping through a hundred million centuries
We have finally opened our eyes on a sumptuous planet, sparkling with color, bountiful with life
Within decades we must close our eyes again
Isn't it a noble and enlightened way of spending our brief time in the sun
To work at understanding the universe and how we have come to wake up in it?

The Greatest Show on Earth, Nightwish

Part I

Introduction, objectives and methods

Chapter One

Introduction and objectives

Abstract

This first Chapter is dedicated to lay the foundations of our work. Hence, the first part introduces the interaction between light and matter, which is the source of nonlinear optics (NLO). It is followed, in second and third sections, by the description of NLO materials and NLO molecular switches, which are the main topics of the thesis. Emphasis is put on both the first and second hyperpolarizabilities. Finally, the main objectives of the manuscript are detailed at the end of this chapter.

This thesis lies at the crossroad between three domains of science. The first is chemistry, *study of matter and its transformations*. As such, its realm extends roughly from the atomic to the macromolecular level, with a particular focus on the composition, structure, and properties of substances, together with the examination of the changes they undergo when they interact. It is of primary importance in the work. The second is quantum chemistry, a branch of quantum mechanics, which has seen rapid developments in the last 100 years and provides, since then, unprecedented understanding of the chemical phenomena, thanks to many methodological developments (some of them are reviewed in Chapter 3). The last is modern computing: together with robust algorithms, it provides the ability to translate the theories into computer codes that are applied routinely to systems with hundreds of electrons. These three topics are combined here for the study, at the molecular level, of nonlinear optics.

Section 1.1

Nonlinear optics (NLO)

Interactions between light (or any other electromagnetic field) and matter give rise to several phenomena. It is also the basis of many spectroscopic techniques, which depend on both the range of wavelengths that are used and the intensity of the beam to probe the properties of matter. Indeed, with the invention of the laser, it was discovered that the optical properties of a material may not result from phenomena that are linearly dependent to the intensity of light, hence the term *nonlinear optics* (NLO). An example is the experimental observation of the second harmonic generation (SHG) by Franken *et al.*¹ in 1961^a and of the third harmonic generation (THG) by Terhune and co-workers² in 1962. In such processes, a photon of frequency 2ω (3ω for THG) is generated from the interaction of a NLO material with a laser beam of frequency ω . The amount of generated photons is proportional to the square (cube) of the incident intensity in SHG (THG).

At the macroscopic level

Electromagnetic phenomena at the macroscopic level are well described by Maxwell's equations. Simplifications arise from neglecting the magnetic properties, which are not considered in this work, so that only the interactions between an electric field, \mathbf{F} , and matter are of interest. It is easy to show that this results in a polarization, $\mathbf{P}(\mathbf{F})$, of the material coming from the modification of its charge distribution (electrons and nuclei). In isotropic media and for weak fields, the resulting polarization is linearly dependent to \mathbf{F} :

$$\mathbf{P}(\mathbf{F}) = \varepsilon_0 \chi \mathbf{F}, \quad (1.1)$$

^aNote: the bibliographic references will be given chapter per chapter.

where ε_0 is the dielectric constant of vacuum and χ , the electric susceptibility of the medium. In anisotropic media, which is the case for many crystals, the polarization depends on the direction and so the susceptibility becomes a (rank 2) tensor:

$$\mathbf{P}_i(\mathbf{F}) = \varepsilon_0 \sum_j^{X,Y,Z} \chi_{ij} \mathbf{F}_j = \varepsilon_0 (\chi \cdot \mathbf{F}), \quad (1.2)$$

where i and j are Cartesian coordinates X, Y, Z , in the laboratory frame (denoted with uppercase letters). In strong electric fields, the linear behavior described by previous equations is no longer valid, and a power series is used instead:

$$\frac{\mathbf{P}(\mathbf{F})}{\varepsilon_0} = \chi^{(1)} \cdot \mathbf{F} + \chi^{(2)} : \mathbf{F}^2 + \chi^{(3)} : \mathbf{F}^3 + \dots \quad (1.3)$$

where $\chi^{(1)}$ is the linear susceptibility, and $\chi^{(2)}, \chi^{(3)}$ are the first and second nonlinear susceptibilities.

At the molecular level

The source of the polarization is, at the molecular level, the modification of the dipole moment of the molecule in response to the field, so its phenomenological description is:

$$\mu(\mathbf{F}) = \mu_0 + \Delta\mu(\mathbf{F}), \text{ with } \Delta\mu(\mathbf{F}) = \alpha \cdot \mathbf{F} + \frac{1}{2!} \beta : \mathbf{F}^2 + \frac{1}{3!} \gamma : \mathbf{F}^3 + \dots \quad (1.4)$$

where μ_0 is the intrinsic dipole moment of the molecule and α , the molecular polarizability, while β and γ are the first and second hyperpolarizability tensors, respectively. Note that instead of a Taylor series (which is referred to as the “T” convention), a power series may be used (the “B” convention).³

If, instead of a static electric field, one composed of a static and dynamic part is used, $\mathbf{F}(\omega) = \mathbf{F}^0 + \mathbf{F}^\omega (e^{-i\omega t} + e^{i\omega t})$, different nonlinear optical phenomena appear. Indeed, when plugging this expression in Eq. (1.4) truncated after the third term, one gets:

$$\Delta\mu(\mathbf{F}) = \Delta\mu^{(0)} + \Delta\mu^{(\omega)} (e^{-i\omega t} + e^{i\omega t}) + \Delta\mu^{(2\omega)} (e^{-2i\omega t} + e^{2i\omega t}) + \Delta\mu^{(3\omega)} (e^{-3i\omega t} + e^{3i\omega t}) \quad (1.5)$$

wherein the terms oscillating at the same pulsation were collected:

$$\begin{aligned} \Delta\mu^{(0)} &= \alpha \cdot \mathbf{F}^0 + \frac{1}{2} \beta : \mathbf{F}^0 \mathbf{F}^0 + \beta : \mathbf{F}^\omega \mathbf{F}^\omega + \frac{1}{6} \gamma : \mathbf{F}^0 \mathbf{F}^0 \mathbf{F}^0 + \gamma : \mathbf{F}^0 \mathbf{F}^\omega \mathbf{F}^\omega, \\ \Delta\mu^{(\omega)} &= \alpha \cdot \mathbf{F}^\omega + \beta : \mathbf{F}^0 \mathbf{F}^\omega + \frac{1}{2} \gamma : \mathbf{F}^0 \mathbf{F}^0 \mathbf{F}^\omega + \frac{1}{3} \gamma : \mathbf{F}^\omega \mathbf{F}^\omega \mathbf{F}^\omega, \\ \Delta\mu^{(2\omega)} &= \frac{1}{2} \beta : \mathbf{F}^\omega \mathbf{F}^\omega + \frac{1}{2} \gamma : \mathbf{F}^0 \mathbf{F}^\omega \mathbf{F}^\omega, \end{aligned}$$

$$\Delta\mu^{(3\omega)} = \frac{1}{6} \gamma : \mathbf{F}^\omega \mathbf{F}^\omega \mathbf{F}^\omega. \quad (1.6)$$

Each term identifies a different process, characterized by the combination of static (\mathbf{F}^0) and dynamic (\mathbf{F}^ω) electric fields for the input and output pulsations. For example, the THG process is the only term to contribute to $\mu^{(3\omega)}$ in Eq. (1.6). The γ tensor probed by THG is generally written $\gamma(-3\omega; \omega, \omega, \omega)$ to reflect this combination. The different NLO processes found in the previous equation are detailed in Table 1.1. In all generalities, the tensors are written:

$$\alpha(-\omega_\sigma; \omega_1), \beta(-\omega_\sigma, \omega_1, \omega_2), \text{ and } \gamma(-\omega_\sigma; \omega_1, \omega_2, \omega_3), \quad (1.7)$$

where $\omega_\sigma = \sum_i \omega_i$ is the frequency of the outgoing electric field (conservation of energy), and

$$\begin{aligned} \Delta\mu_i(\mathbf{F}) = & \sum_j^{xyz} \alpha_{ij}(-\omega_\sigma; \omega_1) \mathbf{F}_j(\omega_1) \\ & + \frac{1}{2!} \sum_{jk}^{xyz} \beta_{ijk}(-\omega_\sigma; \omega_1, \omega_2) \mathbf{F}_j(\omega_1) \mathbf{F}_k(\omega_2) \\ & + \frac{1}{3!} \sum_{jkl}^{xyz} \gamma_{ijkl}(-\omega_\sigma; \omega_1, \omega_2, \omega_3) \mathbf{F}_j(\omega_1) \mathbf{F}_k(\omega_2) \mathbf{F}_l(\omega_3) + \dots \end{aligned} \quad (1.8)$$

where i, j, k, l refer to Cartesian coordinates x, y and z , this time in the molecular frame (denoted with lowercase letters). In Chapter 2, one will explore how to relate these molecular tensors (which are the outputs of the calculations) to the macroscopic quantities obtained in experimental measurements (in the cases of SHG and THG).

Permutation and symmetry

The order of the input fields does not matter in Eq. (1.8) (the incident photons are indiscernible and the scalar product is commutative). This translates into an **intrinsic permutation** symmetry: for a rank n NLO tensor, permutation of the $n-1$ last indices gives unchanged quantity. In other word:

$$\beta_{ijk} = \beta_{ikj} = \beta_{i(jk)}, \text{ and } \gamma_{ijkl} = \gamma_{ijlk} = \gamma_{ikjl} = \gamma_{iklj} = \gamma_{ilkj} = \gamma_{ijjk} = \gamma_{i(jkl)}, \quad (1.9)$$

where the parentheses indicate the permutation of the indices. Hence, the first and second hyperpolarizability tensors, which contain 27 and 81 components, only feature 18 and 30 independent ones, respectively (in the case of SHG and THG). Furthermore, in the static case, full permutation symmetry is assumed. In this case:

$$\beta_{i(jk)} = \beta_{j(ik)} = \beta_{k(ij)} = \beta_{(ijk)}, \quad (1.10)$$

and so on for the γ tensor. The number of independent components further reduces to 10 (15) for the first (second) hyperpolarizability tensor. The Kleinman's conditions state that this remains valid if all input/output frequencies are far from any resonance (excitation energies). In such conditions, the components present no imaginary part.

Furthermore, some (independent) components may be zero due to the symmetry of the probed system. The root of this assumption lies in the Neumann-Miningerode-Curie Principle (also called Curie's principle), which states basically that:⁵⁻⁷

$$\mathcal{G}_{\text{object}} \subseteq \mathcal{G}_{\text{property}}, \quad (1.11)$$

where \mathcal{G} is the symmetry group: for a property to exist for an object, it is necessary (but not sufficient) that the group of the object is a subgroup of the physical operation. In other words, if a molecule is invariant with respect to certain symmetry operations, then any of its properties must also be invariant to those operations. An important result is that all components of the β tensor are zero if the system is centrosymmetric (contains an inversion center).

	$\alpha(0; 0)$	Static polarizability
	$\beta(0; 0, 0)$	Static first hyperpolarizability
	$\gamma(0; 0, 0, 0)$	Static second hyperpolarizability
OR	$\beta(0; -\omega, \omega)$	Optical rectification: static electric field from a NLO medium
dc-OR	$\gamma(0; -\omega, \omega, 0)$	dc-optical rectification
Light scattering	$\alpha(-\omega; \omega)$	Dynamic polarizability
dc-Pockels	$\beta(-\omega; \omega, 0)$	Linear change of the birefringence of a medium (linear electrooptic effect, EO)
dc-Kerr	$\gamma(-\omega; \omega, 0, 0)$	Quadratic change of the birefringence of a medium (quadratic EO)
DFWM	$\gamma(-\omega; \omega, -\omega, \omega)$	Degenerate four-wave mixing (intensity dependent refractive index)
SHG	$\beta(-2\omega; \omega, \omega)$	Second Harmonic Generation
ESHG	$\gamma(-2\omega; \omega, \omega, 0)$	Electric field induced SHG (also written EFISHG)
THG	$\gamma(-3\omega; \omega, \omega, \omega)$	Third Harmonic Generation

Table 1.1: List of the different NLO processes that may arise from a combination of static and dynamic electric fields (up to third order).⁴

Section 1.2

NLO materials

Although NLO materials may be inorganic, our thesis focuses on organic compounds. Interestingly, they have been identified to give large NLO responses, while providing many opportunities to design NLO switches, which are one of the topic of this thesis, and of the next section.

Preamble: the sum-over-states (SOS) expression

On the ground of perturbation theory (see Chapter 3), the SOS expression of Orr and Ward⁸ states that any component of any nonlinear optical tensor $\chi(\omega_\sigma; \omega_1, \dots)$ (of order n) is given by:

$$\chi_{ijk\dots(n \text{ times})}(-\omega_\sigma; \omega_1, \dots) = \sum_{\mathcal{P}}^{(i, \omega_\sigma), (j, \omega_1) \dots} \sum_{a_1, a_2 \dots (n-1 \text{ times})} \frac{\mu_{0a_1}^i \bar{\mu}_{a_1 a_2}^j \dots \mu_{a_{n-1} 0}^n}{(\hbar\omega_{a_1} - \hbar\omega_\sigma)(\hbar\omega_{a_2} - \hbar\omega_\sigma - \hbar\omega_1) \dots (\hbar\omega_{a_{n-1}} - \sum_k^{\sigma, 1, \dots} \hbar\omega_k)}, \quad (1.12)$$

where $i, j, k \dots$ are the Cartesian coordinates x, y, z (in the molecular frame), $\omega_1, \omega_2 \dots$, the corresponding pulsations, $a_1, a_2 \dots$, the excited states of the system (with $\hbar\omega_{a_i}$ the excitation energy of the state a_i), $\bar{\mu}_{a_i, a_j}^r = \langle a_i | r | a_j \rangle - \delta_{a_i a_j} \langle 0 | r | 0 \rangle$, the transition dipole moment from excited state a_i to a_j (it corresponds to the excited state dipole moment of state a_i when $i = j$, from which the ground state dipole moment is subtracted), with r the fluctuation operator, and $\sum_{\mathcal{P}}$ is the sum of the different permutations over each pair $(i, \omega_\sigma), \dots$

Organic NLO materials with large first hyperpolarizabilities

For the first hyperpolarizability, a common approximation is to consider a one-dimensional (main axis oriented along z) two-state system, with therefore only one excited state (labeled e , while the ground state is re-labeled g). This is the so-called two-state approximation (TSA).⁹ Taking Eq. (1.12) in the static limit, it yields

$$\beta_{zzz} = 6 \frac{\Delta\mu_{ge}^z (\mu_{ge}^z)^2}{(\hbar\omega_{ge})^2}, \text{ with } \Delta\mu_{ge}^z = \mu_e^z - \mu_g^z. \quad (1.13)$$

From this equation, it is clear that a molecule presents a large first hyperpolarizability provided it combines the following characteristics: i) small excitation energy, ii) large difference between the ground and this excited state dipole moment, and iii) large ground to excited transition dipole moment (or oscillator strength, which is proportional to the area under the

curve in a UV/VIS spectrum). Push-pull molecules check all those requirements: they are constituted of a donor (D) and acceptor (A) group, connected together by a π -conjugated segment and they generally feature a low-energy charge-transfer excited state. Furthermore, one could use the electron-in-a-box approximation, to show that the difference of energy between the ground and excited state decreases with the length of the π -conjugated path, so $\beta \propto L^4$. Nevertheless, Lu and co-workers¹⁰ showed that saturation with the size of the path is, in fact, observed.

A very simple model to understand the property of those systems is the so-called VB-CT model, which assumes that a system can be described by two limiting (orthogonal) states, Ψ_{VB} (valence bond state) and Ψ_{CT} (charge-transfer state, see Fig. 1.1). First studied by Mulliken¹¹ in the 50's, this model was applied to the prediction of hyperpolarizabilities in the 90's.^{10,12-15} The parameters used to describe the first hyperpolarizability differ from one author to another,

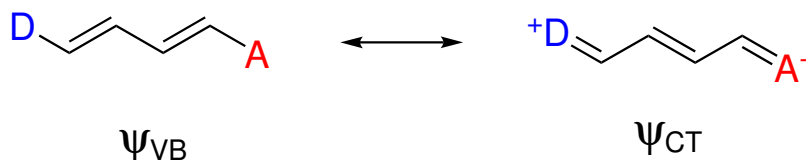


Figure 1.1: Limiting forms of the VB-CT model.

but one combination is composed of:¹⁴

- $m_{CT} \in [-1; 1]$, the mixing between the VB and CT states in the ground state: -1 means that the ground state is dominated by VB, 1 means it is dominated by CT and 0 is the so-called cyanine limit. This parameter is linked to the bond length alternation (BLA, mean difference between single and double bond lengths) ;
- t , a off-diagonal Hamiltonian element related to the difference of energy between Ψ_{VB} and Ψ_{CT} ;
- $\mu_{CT} = \langle \Psi_{CT} | \hat{\mu} | \Psi_{CT} \rangle$, the CT state dipole moment (the one of the ground state is assumed to be zero).

As shown in Chapter 11, Eq. (1.13) gets the form:

$$\beta_{zzz} = -\frac{3}{8} m_{CT} (1 - m_{CT}^2)^2 \frac{\mu_{CT}^3}{t^2}. \quad (1.14)$$

An additional design rule follows: though t lowers (and β increases) if the strength of the donor and acceptor increases, it is obvious from that expression that β is null if $m_{CT} \in \{-1, 0, 1\}$ and maximal if $m_{CT} = \pm\sqrt{5}/5$. The donor/acceptor pair should therefore be well chosen to get into this area.

Variation of this simple “dipolar” architecture is also explored in Chapter 11. For example, the TSA model can’t describe the octupolar compounds (*i.e.*, they belong to the D_{3h} , T or

T_d point groups), proposed by Zyss in the 90's as efficient NLO compounds.^{16,17} Indeed, with group theory arguments, it is easy to show that $\Delta\mu_{ge} = 0$, so one needs to increase the number of states to describe this kind of system.

Finally, instead of purely organic molecules, organometallic compounds can be used, thanks to various low-energy CT processes, including metal-to-ligand CT (MLCT). Ruthenium- and iron-based (e.g., ferrocene moiety) complexes have been the most investigated,^{18,19} but other metals are also found in NLO materials.²⁰⁻²² Different ligands are linked to the metal center, which modulate the NLO properties and provide access to various molecular arrangements¹⁹ (e.g., tetrahedral, square planar or octupolar). Metal-organic frameworks (MOFs) are also part of these organometallic compounds, which can display large NLO properties if well designed.²³

Organic NLO materials with large second hyperpolarizabilities

The second hyperpolarizability is better described using a three-state model (g , e_1 and e_2),

$$\gamma_{zzzz} = \gamma^{(I)} + \gamma^{(II)} + \gamma^{(III-1)} + \gamma^{(III-2)}, \quad (1.15)$$

with

$$\begin{aligned} \gamma^{(I)} &= \sum_n \frac{e_1, e_2 (\mu_{gn}^z)^2 (\Delta\mu_{gn}^z)^2}{\omega_{gn}^3}, \gamma^{(II)} = - \sum_n \frac{e_1, e_2 (\mu_{gn}^z)^4}{\omega_{gn}^3}, \\ \gamma^{(III-1)} &= \sum_{m \neq n} \frac{e_1, e_2 \mu_{gn}^z \Delta\mu_{gn}^z \mu_{nm}^z \mu_{mg}^z}{\omega_{gn}^2 \omega_{gm}}, \text{ and } \gamma^{(III-2)} = \sum_{m \neq n} \frac{e_1, e_2 (\mu_{gn}^z)^2 (\mu_{mn}^z)^2}{\omega_{gn}^2 \omega_{gm}}. \end{aligned} \quad (1.16)$$

Four excitation channels are featured in this formula (Fig. 1.2). Again, a low excited state and large difference of dipole moment between the ground and excited states helps to design molecules with large second hyperpolarizabilities. Furthermore, starting from the electron-in-a-box model, Rustagi and Ducuing²⁴ showed that the chain length dependence in the case of π -conjugated polymers should be $\gamma \propto L^5$ (again, with saturation in practice²⁵).

An additional route to achieve molecules with large γ is provided by Nakano and its co-workers.²⁶⁻³⁰ Focusing on centrosymmetric molecules ($\Delta\mu_{gn} = 0$, so $\gamma^{(I)} = \gamma^{(III-1)} = 0$), they discovered that diradical open-shell compounds present interesting features. They proposed a simple system based on the dissociation of the H_2 molecule. Considering two sites (a and b) and two electrons, 4 possible arrangement are possible, using localized natural orbitals: $|a\bar{b}\rangle$, $|b\bar{a}\rangle$ (neutral, diradical, determinants), $|a\bar{a}\rangle$, and $|b\bar{b}\rangle$ (ionic determinants), where $|\bar{a}\rangle$ indicates an electron of spin β on site a , while $|b\rangle$ indicates an electron of spin α on site b . Diagonalizing the Hamiltonian results in four energy levels (eigenvalues) with corresponding orbitals (eigenstates). In particular, three of them are singlet: two with the g symmetry (including the ground state), and the other with u symmetry. Application of the Laporte rule³¹

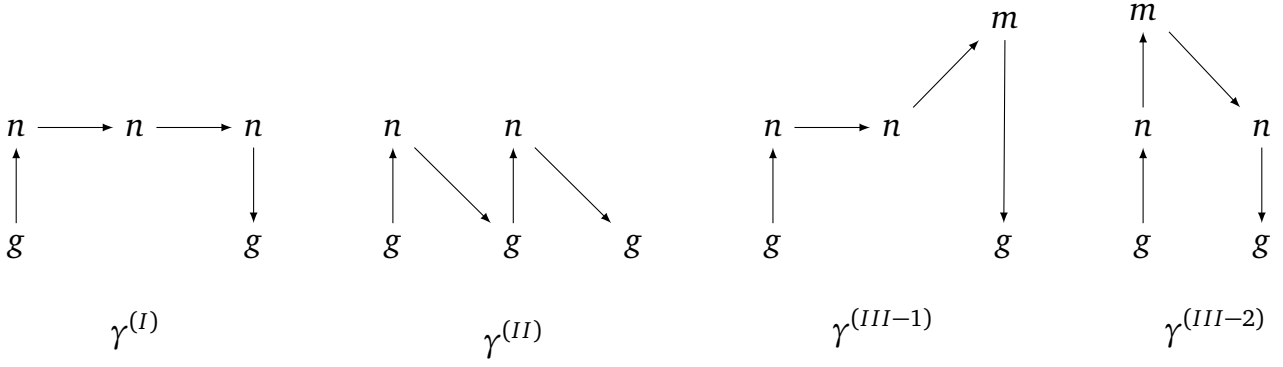


Figure 1.2: Excitation channels of the three-state model given in Eq. (1.16). Vertical and oblique arrows indicate transition dipole moments (e.g., μ_{gn}) while horizontal lines indicate differences between excited and ground state dipole moments (e.g., $\Delta\mu_{gn}$). Adapted from Ref. 26.

results in:

$$\gamma = \gamma^{(II)} + \gamma^{(III-2)} = -\frac{(\mu_{ge_u}^z)^4}{\omega_{ge_u}^3} + \frac{(\mu_{ge_u}^z)^2 (\mu_{e_ue_g}^z)^2}{\omega_{ge_u}^2 \omega_{e_ue_g}}, \quad (1.17)$$

where e_g and e_u are the two singlet excited states (the $zzzz$ indices are dropped for clarity). One can then approximate the transition dipole moments, with R_{ab} , the distance between the two centers. Furthermore, $r_K = 2K_{ab}/U$ is defined, where K_{ab} is the exchange integral between the a and b sites and $U = U_{aa} - U_{ab}$ is the difference between on-site and intersite Coulomb integrals, which are both non-diagonal elements of the Hamiltonian. It yields:²⁸⁻³⁰

$$\frac{\gamma}{R_{ab}^4/U^3} = -\underbrace{\frac{8q^4}{(1 + \sqrt{1-q^2})^2 \left(1 - 2r_K + \frac{1}{\sqrt{1-q^2}}\right)^3}}_{\gamma^{(II)}/(R_{ab}^4/U^3)} + \underbrace{\frac{4q^2}{\left(1 - 2r_K + \frac{1}{\sqrt{1-q^2}}\right)^2 \left(\frac{1}{\sqrt{1-q^2}}\right)}}_{\gamma^{(III-2)}/(R_{ab}^4/U^3)}, \quad (1.18)$$

where q is the bond order, defined as $q = 1 - y$, with y , the diradical character. This expression, plotted in Fig. 1.3, shows a maximum for an intermediate diradical character. Thus, by controlling the diradical character, one can tune the second hyperpolarizability.²⁸⁻³⁰ Most of these materials are based on polycyclic aromatic hydrocarbons (PAH), which spontaneously feature some diradical character. Examples include diphenalenyl compounds³² and graphene nanoflakes.^{33,34} The model can also be extended to non-centrosymmetric molecules, as shown in Ref. 35.

Applications

First applications of NLO materials reported in the literature are found in photonic devices.³⁶ The requirements of such are:³⁷ i) large nonlinear optical response, so that the device can be operated with low-power laser source, ii) fast response times, and iii) specific device needs: stability (to optical damages), processability and low optical losses. Hence, developing actual photonic materials requires to overcome different challenges, in order to provide

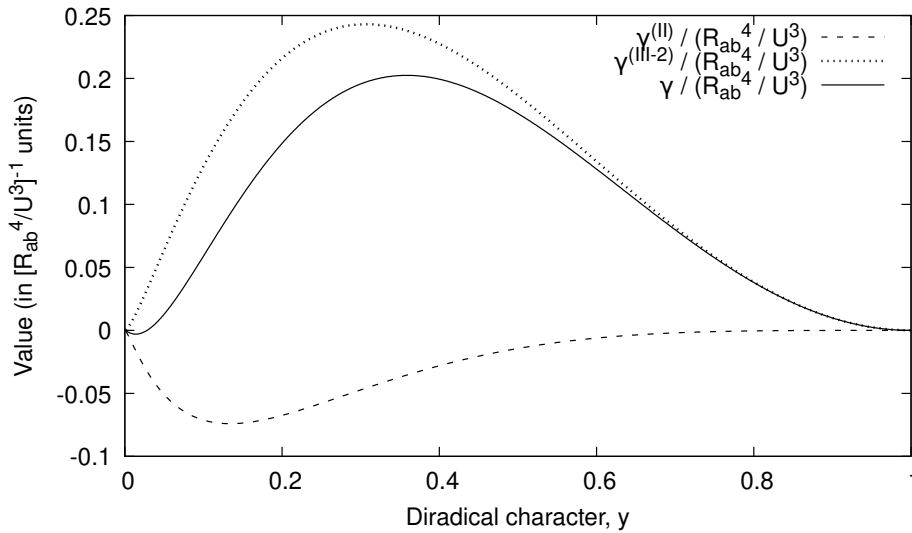


Figure 1.3: Evolution of γ_{zzzz} (the subscripts are omitted for clarity) with the diradical character, γ , as described by Eq. (1.18). Adapted from Ref. 29.

light-driven equivalents to the classical electronic devices (e.g., switches, logical gates, ...).³⁸ It should be already noted that many photonic devices presented in this section rely on the modification of refractive index, so the Pockels, Kerr and DFWM processes (Table 1.1).

One of the successful examples of photonic devices that rely on the first hyperpolarizability (or its macroscopic equivalent, $\chi^{(2)}$) are the poled polymers. They are obtained through the dispersion of NLO chromophores in a polymer matrix or the functionalization of the polymer with NLO-active moieties, followed by electric field poling (alignment of the NLOphores by the application of an external electric field) to avoid global centrosymmetry.³⁹ They can then be used to provide functions such as frequency conversion^{40,41} (e.g., frequency doubling), polarization control⁴² (e.g., Pockels cells and Q-switching) and opto-electronic devices^{43,44} (e.g., modulation or switching of light). An example of the latter is given in Fig. 1.4. Another method to get efficient NLO-powered devices are the Langmuir-Blodgett films which consist of the transfer of a molecular monolayer (giving a preferential orientation of the NLO-active moieties, at least for one mono-layer) from air-water interface onto a surface, with a very controlled thickness.⁴⁵ An advantage of this technique, in the case of frequency doublers, is that it allows a better control on the (quasi) phase matching between SHG beams, which would otherwise destructively interact, lowering the output.

On the other hand, materials with large second hyperpolarizability do not necessarily require preferential orientation (even though poled polymers are also proposed), but the optical losses (generally due to two-photon absorption) should be minimal.^{25,44,46,47} In the photonic area, $\chi^{(3)}$ materials are used to create phase-conjugated mirrors⁴⁸ (i.e., the output of the device is $F(\omega)^*$, with the reverse phase), optical bistability⁴⁹⁻⁵¹ (hysteresis behavior of the output w.r.t. input beam) and more generally, all-optical switches^{44,52-54} (i.e., light controlling light). Still today, they are difficult to achieve with organic-based NLO chromophores.⁴⁴

Out of the photonic topics, a last interesting application is Second-Harmonic Imaging Mi-

croscopy (SHIM). This technique provides high-resolution and structural information in biological imaging.^{55–58} Other advantages include a lower phototoxicity, less out-of-focus photobleaching, and higher penetration in tissues w.r.t. conventional fluorescence.⁵⁹ Finally, it is very complimentary to two-photon-excitation fluorescence (TPEF) microscopy, which gives information about the concentration and localization of chromophores. To achieve good contrasts by this technique one normally relies on intrinsic biological systems (like myosin^{55,58} or collagen triple helix^{60,61}). If not, specific dyes can be used when the signal is not strong enough. Ref. 57 draws the requirements for such biomarkers: i) a strong SHG response at laser frequency (which, usually, has to be enhanced with resonance), ii) high affinity to the (hydrophobic) cell membrane, iii) high density, and iv) overall organization of the chromophores to enhance the signal. Many authors have thus pointed out that fluorescent proteins (FP) are biotags of choice.^{57,62} Indeed, FPs are already in use in biological microscopy, since they are either intrinsically (due to folding) or extrinsically (due to the binding of an external molecule) fluorescent. Let us add that, in the past, quantum chemistry has already helped to understand and rationalize the impact of the FP chromophore on the SHG signal.^{63–67} Based on these clues, a mutant FP (named SHardonnay) was engineered specifically for its improved SHG properties.⁶⁵ Chapter 10 is a step towards improving the strategy to predict the SHG response of such large systems.

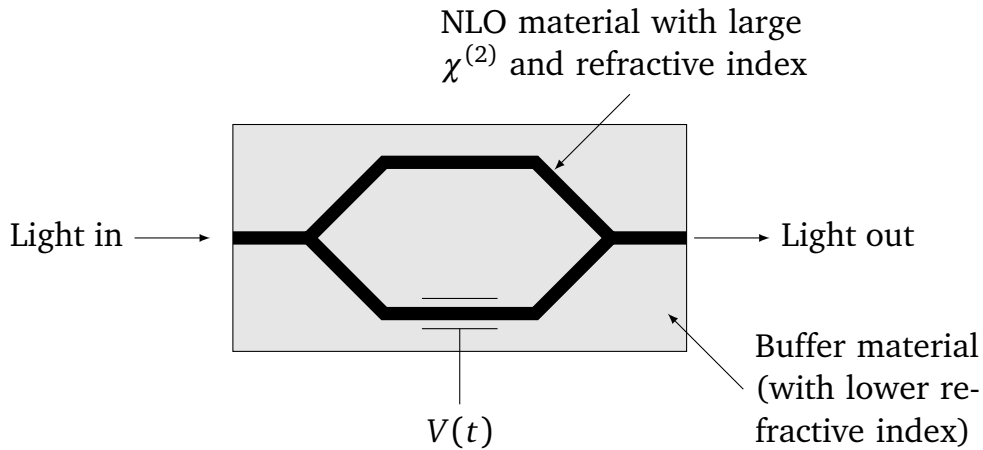


Figure 1.4: Example of photonic device, the Mach-Zehnder interferometer (or modulator): a light beam passes through a waveguide composed by a $\chi^{(2)}$ NLO material. The beam is split in two and recombined at the end. An oscillating electric field can be applied on one of the two arms: the change of refractive index (originating from the dc-Pockels effect) induces a dephasing between the two beams. In the extreme cases, the beams constructively (no phase shift) or destructively (phase shift of $T/2$) interfere, so it becomes a switch. Adapted from Ref. 43.

Section 1.3

NLO molecular switches

Even though there are many examples of biological molecular switches (*e.g.*, the *cis-trans* isomerization of retinal, basis of animal vision), the probably best-known ones (even by the general public) are the pH indicators. This large family also features what is probably the first man-made (synthetic) molecular switch, phenolphthalein, still found today in chemistry laboratories.⁶⁸ Since then, many progresses have been made including up to the 2016 Nobel prize⁶⁹ of Savage, Stoddart, and Feringa “for the design and synthesis of molecular machines”, and the field is still very active.

More generally, a molecular switch is a molecule that adjusts its structural and electronic properties to an external stimulus. The input may be as various as chemical, electrical or optical, and the molecule shifts between (at least) two states. The different states are stable, the transformation is fast and reversible and the system returns to its initial state when the external stimulus is turned off, but those are not absolute requirements. It should be added that, in order to be useful, the different states of a switch should be distinguishable by measurement of a property, and the highest the difference between the forms, the best.^{70–74} Conceptually, the stimulus may be seen as the “writing” operation, while the measurement consists of the “reading” counterpart.

NLO switches based on the first hyperpolarizability

Different methods of classification exist for the (NLO) switches, based on the nature of the stimulus (*e.g.*, light, pH, ...), the one of the molecular switch (*e.g.*, a particular donor or acceptor) or source of the effect (*e.g.*, bond breaking, ...). The latter was explored by Coe in 1999:⁷⁵ starting from the D- π -A architecture, he proposed to categorize the NLO switches depending on the part of the molecule which was modified during commutation, as given in Fig. 1.5. Types I and II compounds generally rely on redox, acido-switching or magnetic⁷⁶ switching, while type III switches encompass a wider range of processes (*e.g.*, thermal⁷⁷).

The advantage of β -NLO switches is the fact that the high sensitivity to geometry and environment of β gives rise to high contrasts. Also, in the specific case of a light-triggered switch, the low-energy light used for the readout operation cannot trigger back the switch. Prototypical examples from the literature^{78–83} are found in Fig. 1.6, and a redox-triggered switch is studied in Chapter 7. Generally, the figure of merit is the contrast between the first hyperpolarizabilities of the different forms. These simple building blocks may eventually be combined with:

1. Polymers, for example through post-functionalization, to form the aforementioned poled polymers.⁸⁴ An important issue is that switching would normally require a reorganiza-

tion of the polymer, which reduces the phenomenon in practice.

2. Surfaces, in the form of self-assembled monolayers⁸⁵ or Langmuir-Blodgett films,⁸⁶ so if the stimulus is applied locally, then the first hyperpolarizability is spatially dependent.
3. Other switching units to form multi-state switches.^{87,88} One of our collaborators, Lionel Sanguinet, is following this path with benzozalooxazolidines (BOXs, Fig. 1.7), see, *e.g.*, Ref. 89 and references therein. Chapters 8 and 9, which study molecules with 2 and 3 BOX units, represents one step towards this goal.

Finally, in their 2013 review, Castet *et al.*⁹⁰ introduced the idea of multi-addressable NLO switches, which react to more than one stimulus. Again, BOXs (Fig. 1.7) are prominent examples, since they can be opened with either light, pH or a difference of potential.⁹¹

NLO switches based on the second hyperpolarizability

The classification proposed in Fig. 1.5 could actually be extended to the second hyperpolarizability switches, since they rely on the same mechanisms (modification of the donor, the acceptor or the π -conjugated path). It is supported by the fact that the authors sometimes check for β and γ at the same time. Note that they generally include the TPA (imaginary part of γ) behavior as well. When γ is the only targeted property, redox switching is generally the main stimulus, especially since it gives a large contrast with organometallic compounds.^{92,93} Ruthenium and iron compounds are, again, generally featured. On the other hand, the derivatives of hydrocarbons have attracted attention in the recent years. Two examples of second hyperpolarizability switches are given in Fig. 1.8.

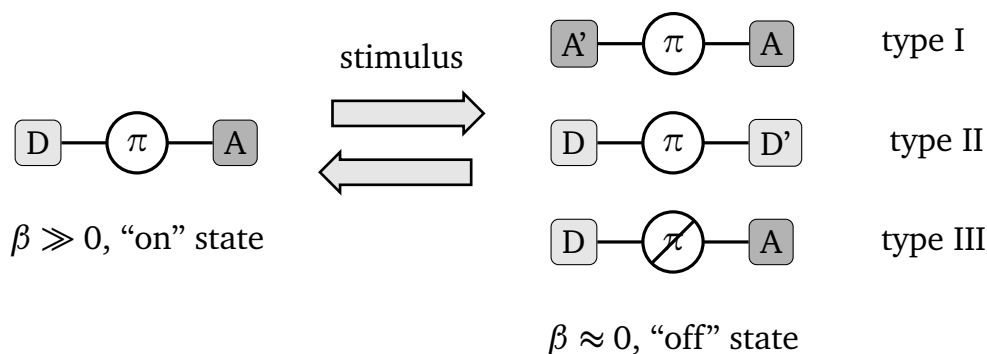


Figure 1.5: Types of strategy for switching the first hyperpolarizability response of dipolar D- π -A molecules, adapted from Ref. 75. The first two types are the modification of the nature of the donor or acceptor moieties, respectively (generally through a redox process), while the last is the alteration of the π -conjugation.

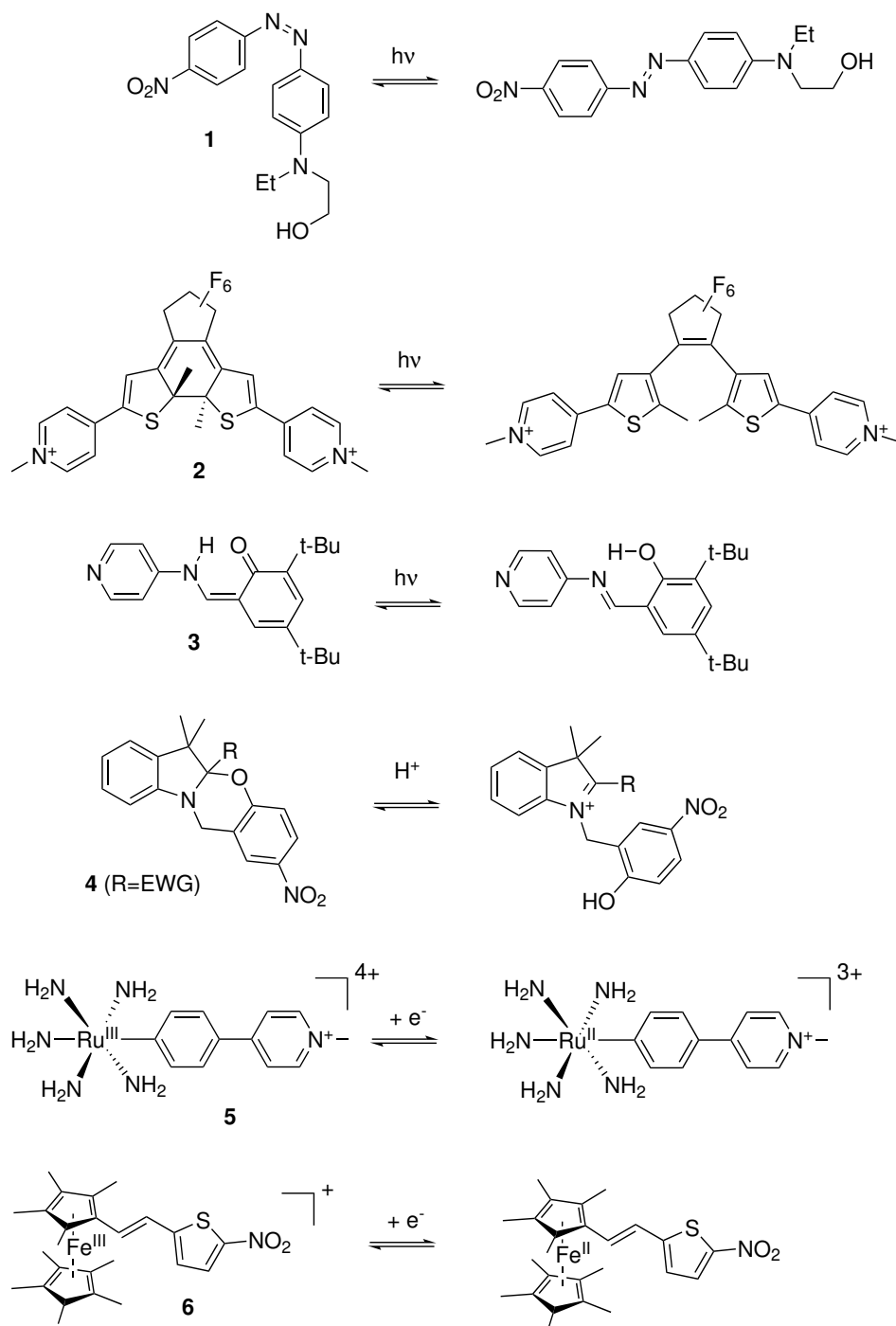


Figure 1.6: Prototypical first hyperpolarizability switches. Types III: disperse red 1 (**1**, cis-trans isomerization of an azobenzene derivative triggered by light, from Ref. 78), diarylethene (**2**, photocyclization triggered by light, from Ref. 79), anil (**3**, phototautomerization, from Ref. 82, also of types I and II), indolinoxazolidine (**4**, acid-assisted ring breaking, from Ref. 83). Types I (triggered by redox): Ruthenium complex (**5**, from Ref. 80) and ferrocene derivative (**6**, from Ref. 81). The forms with the lowest β response are put on the left-hand side.

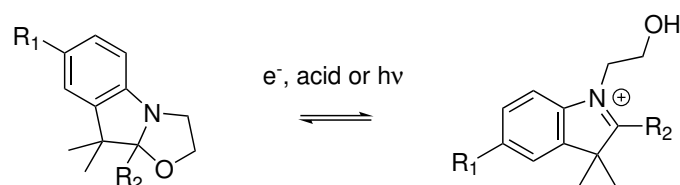


Figure 1.7: The benzozalooxazoline (BOX) multi-addressable NLO switch (see, *e.g.*, Ref. 91). R_1 is generally an acceptor group (or the grafting point in the case of multi-states switches), while R_2 is generally a donor. The form of the left- (right-) hand side is generally referred to as the “closed” (“open”) form, with the lowest (largest) β value.

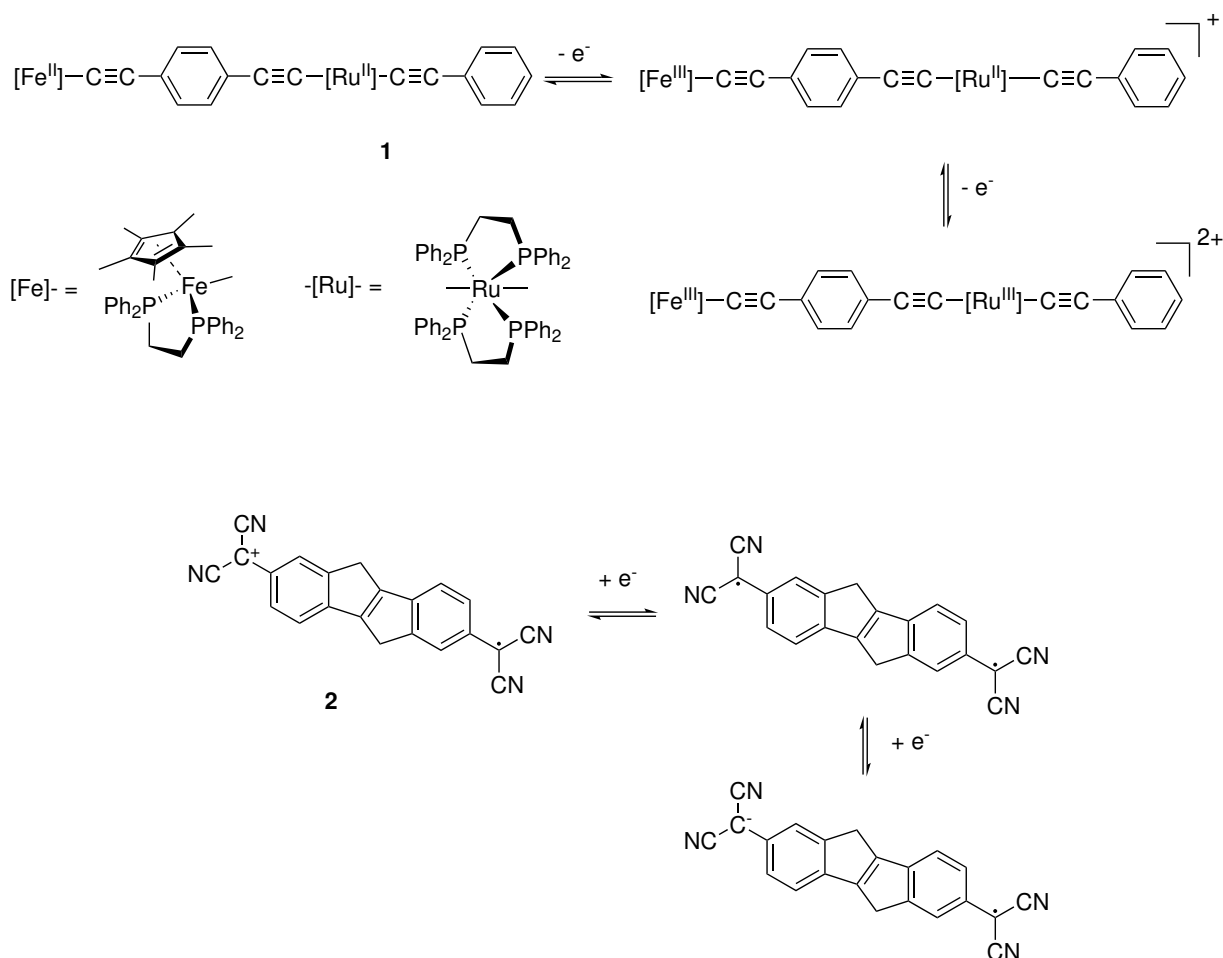


Figure 1.8: Examples of multi-state redox triggered second hyperpolarizability switches: with metallic centers (**1**, “type I”, from Ref. 94) or with a diradical character (**2**, “type II”, from Ref. 95).

Applications

Together with the previously mentioned photonic technologies, three other fields may require (NLO) molecular switches: i) digital processors,⁷⁰ based on molecular gates, which need multi-states switches with orthogonal stimuli, ii) molecular storage or memory, which relies on very stable “on” and “off” states with important contrast, and iii) sensors, which become advantageous if the NLO properties show more contrast than their linear equivalent (see, *e.g.*,

Ref. 96, where a NLO switch is used as a selective cation sensor).

Section 1.4

Objectives

During this first chapter, different kinds of NLO materials have been presented, with multiple applications. They have been made thanks to the interplay between modelisation and experiment. The first has provided design rules and propositions to the second, which in return gives opportunity to improve the theoretical methods to better reproduce the experimental reality. This multidisciplinary approach is the context of our PhD Thesis.

There are two aims in our work. The first is to provide a better description and understanding of the first and second hyperpolarizabilities of reference molecules, which is crucial for the experimental measurement (as explained in Chapter 2). The second is the study of new NLO materials, to understand their properties, provide insights, and help their design. These two goals will highlight the role of quantum chemistry in the present and future of material sciences.

The thesis is therefore divided in four parts. Part I, which includes this chapter, introduces the main concepts. In particular, the next chapter describes the macroscopic quantities associated with the first and second hyperpolarizabilities that are used through the thesis. Then, Chapter 3 reviews the different quantum chemistry methods that are used through the work.

Part II is dedicated to our first goal. The accurate description of the gas phase molecular response of reference molecules is addressed in Chapters 4 and 5 with a hierarchy of Coupled Cluster methods for different NLO processes. In Chapter 4, we concentrate on the agreement with experimental gas phase EFISHG, and Chapter 5 constitutes the first quantum chemical investigation of γ_{THS} (Third Harmonic Scattering) and its decomposition in spherical tensor components (which shows that the response is dominated by its isotropic contribution). Following, in Chapter 6 the impact of the vibrational contributions on both β_{SHS} (Second Harmonic Scattering) and γ_{THS} (again, for the first time), is analyzed with the water molecule as an example. Though small, especially at the usual laser wavelengths, they are nonnegligible.

Part III is devoted to our second goal, the study of complex NLO materials. First of all, in Chapter 7, an octupolar NLO switch with 6 Ruthenium metal centers, triggered by redox, is considered. To better understand its response, it is decomposed and its fragments are also analyzed. Then, Chapters 8 and 9 are dedicated to two multi-state, multi-addressable, NLO switches containing 2 and 3 BOXs, respectively. One of the main conclusions is that these structures can be opened sequentially and are differentiable in term of NLO properties. Additionally, Chapter 10 focuses on the β response of two fluorescent proteins with a simplified approach. In this exploratory work, we focus on two proteins (iLOV and bR), for which it was possible to obtain the first hyperpolarizability with a reasonable amount of computing

ressources (a few days), with a good agreement with experimental values for the bacteriorhodopsin (~ 3850 atoms). Finally, Chapter 11 goes back to the simple few states models, which are generally used as the basis for the design rules, in a systematic study.

Part IV finally reviews and concludes our work and adds some perspectives.

Bibliography

- [1] Franken, P. A.; Hill, A. E.; Peters, C. W.; Weinreich, G. Generation of Optical Harmonics. *Phys. Rev. Lett.* **1961**, 7, 118–119.
- [2] Terhune, R. W.; Maker, P. D.; Savage, C. M. Optical Harmonic Generation in Calcite. *Phys. Rev. Lett.* **1962**, 8, 404–406.
- [3] Reis, H. Problems in the Comparison of Theoretical and Experimental Hyperpolarizabilities Revisited. *J. Chem. Phys.* **2006**, 125, 014506.
- [4] Shelton, D. P.; Rice, J. E. Measurements and Calculations of the Hyperpolarizabilities of Atoms and Small Molecules in the Gas Phase. *Chem. Rev.* **1994**, 94, 3–29.
- [5] Curie, P. Sur la symétrie dans les phénomènes physiques, symétrie d'un champ électrique et d'un champ magnétique. *J. Phys. Théor. Appl.* **1894**, 3, 393–415.
- [6] Brandmüller, J.; Winter, F. X. Influence of Symmetry on the Static and Dynamic Properties of Crystals. *Z. Kristallogr. Cryst. Mater.* **1985**, 172.
- [7] Brandmüller, J. *Symmetry*; Elsevier, 1986; pp 97–100.
- [8] Orr, B.; Ward, J. Perturbation Theory of the Non-Linear Optical Polarization of an Isolated System. *Mol. Phys.* **1971**, 20, 513–526.
- [9] Oudar, J. L.; Chemla, D. S. Hyperpolarizabilities of the Nitroanilines and Their Relations to the Excited State Dipole Moment. *J. Chem. Phys.* **1977**, 66, 2664–2668.
- [10] Lu, D.; Chen, G.; Goddard, W. A. The Valence-bond Charge-transfer-exciton Model for Predicting Nonlinear Optical Properties (Hyperpolarizabilities and Saturation Length) of Polymeric Materials. *J. Chem. Phys.* **1994**, 101, 4920–4930.
- [11] Mulliken, R. S. Molecular Compounds and Their Spectra. II. *J. Am. Chem. Soc.* **1952**, 74, 811–824.
- [12] Lu, D.; Chen, G.; Perry, J. W.; Goddard, W. A. Valence-Bond Charge-Transfer Model for Nonlinear Optical Properties of Charge-Transfer Organic Molecules. *J. Am. Chem. Soc.* **1994**, 116, 10679–10685.
- [13] Meyers, F.; Marder, S. R.; Pierce, B. M.; Brédas, J. L. Electric Field Modulated Nonlinear Optical Properties of Donor-Acceptor Polyenes: Sum-Over-States Investigation of the Relationship between Molecular Polarizabilities (α , β and γ) and Bond Length Alternation. *J. Am. Chem. Soc.* **1994**, 116, 10703–10714.
- [14] Barzoukas, M.; Runser, C.; Fort, A.; Blanchard-Desce, M. A Two-State Description of (Hyper) Polarizabilities of Push-Pull Molecules Based on a Two-Form Model. *Chem. Phys. Lett.* **1996**, 257, 531–537.

- [15] Blanchard-Desce, M.; Barzoukas, M. Two-Form Two-State Analysis of Polarizabilities of Push Pull Molecules. *J. Opt. Soc. Am. B* **1998**, *15*, 302.
- [16] Zyss, J. Molecular Engineering Implications of Rotational Invariance in Quadratic Nonlinear Optics: From Dipolar to Octupolar Molecules and Materials. *J. Chem. Phys.* **1993**, *98*, 6583–6599.
- [17] Zyss, J.; Ledoux, I. Nonlinear Optics in Multipolar Media: Theory and Experiments. *Chem. Rev.* **1994**, *94*, 77–105.
- [18] Coe, B. J. Developing Iron and Ruthenium Complexes for Potential Nonlinear Optical Applications. *Coord. Chem. Rev.* **2013**, *257*, 1438–1458.
- [19] Ashcroft, C. M.; Cole, J. M. In *Handbook of Organic Materials for Electronic and Photonic Devices (Second Edition)*; Ostroverkhova, O., Ed.; Woodhead Publishing Series in Electronic and Optical Materials; Woodhead Publishing, 2019; pp 139–176.
- [20] Costes, J. P.; Lamère, J. F.; Lepetit, C.; Lacroix, P. G.; Dahan, F.; Nakatani, K. Synthesis, Crystal Structures, and Nonlinear Optical (NLO) Properties of New Schiff-Base Nickel(II) Complexes. Toward a New Type of Molecular Switch? *Inorg. Chem.* **2005**, *44*, 1973–1982.
- [21] Lamère, J. F.; Lacroix, P. G.; Farfán, N.; Rivera, J. M.; Santillan, R.; Nakatani, K. Synthesis, Characterization and Nonlinear Optical (NLO) Properties of a Push– Pull Bisboronate Chromophore with a Potential Electric Field Induced NLO Switch. *J. Mater. Chem.* **2006**, *16*, 2913–2920.
- [22] Lacroix, P. G.; Malfant, I.; Lepetit, C. Second-Order Nonlinear Optics in Coordination Chemistry: An Open Door towards Multi-Functional Materials and Molecular Switches. *Coord. Chem. Rev.* **2016**, *308*, 381–394.
- [23] Medishetty, R.; K. Zaręba, J.; Mayer, D.; Samoć, M.; A. Fischer, R. Nonlinear Optical Properties, Upconversion and Lasing in Metal– Organic Frameworks. *Chem. Soc. Rev.* **2017**, *46*, 4976–5004.
- [24] Rustagi, K.; Ducuing, J. Third-Order Optical Polarizability of Conjugated Organic Molecules. *Opt. Commun.* **1974**, *10*, 258–261.
- [25] Brédas, J. L.; Adant, C.; Tackx, P.; Persoons, A.; Pierce, B. M. Third-Order Nonlinear Optical Response in Organic Materials: Theoretical and Experimental Aspects. *Chem. Rev.* **1994**, *94*, 243–278.
- [26] Nakano, M.; Yamaguchi, K. A Proposal of New Organic Third-Order Nonlinear Optical Compounds. Centrosymmetric Systems with Large Negative Third-Order Hyperpolarizabilities. *Chem. Phys. Lett.* **1993**, *206*, 285–292.
- [27] Nakano, M.; Kishi, R.; Nitta, T.; Kubo, T.; Nakasuji, K.; Kamada, K.; Ohta, K.; Champagne, B.; Botek, E.; Yamaguchi, K. Second Hyperpolarizability (γ) of Singlet Diradi-

- cal System: Dependence of γ on the Diradical Character. *J. Phys. Chem. A* **2005**, *109*, 885–891.
- [28] Nakano, M.; Kishi, R.; Ohta, S.; Takebe, A.; Takahashi, H.; Furukawa, S.-i.; Kubo, T.; Morita, Y.; Nakasuji, K.; Yamaguchi, K.; Kamada, K.; Ohta, K.; Champagne, B.; Botek, E. Origin of the Enhancement of the Second Hyperpolarizability of Singlet Diradical Systems with Intermediate Diradical Character. *J. Chem. Phys.* **2006**, *125*, 074113.
- [29] Nakano, M.; Kishi, R.; Ohta, S.; Takahashi, H.; Kubo, T.; Kamada, K.; Ohta, K.; Botek, E.; Champagne, B. Relationship between Third-Order Nonlinear Optical Properties and Magnetic Interactions in Open-Shell Systems: A New Paradigm for Nonlinear Optics. *Phys. Rev. Lett.* **2007**, *99*, 033001.
- [30] Nakano, M. Electronic Structure of Open-Shell Singlet Molecules: Diradical Character Viewpoint. *Top. Curr. Chem.* **2017**, *375*, 47.
- [31] Laporte, O.; Meggers, W. F. Some Rules of Spectral Structure. *J. Opt. Soc. Am.* **1925**, *11*, 459–463.
- [32] Nakano, M.; Minami, T.; Yoneda, K.; Muhammad, S.; Kishi, R.; Shigeta, Y.; Kubo, T.; Rougier, L.; Champagne, B.; Kamada, K.; Ohta, K. Giant Enhancement of the Second Hyperpolarizabilities of Open-Shell Singlet Polyaromatic Diphenalenyl Diradicaloids by an External Electric Field and Donor–Acceptor Substitution. *J. Phys. Chem. Lett.* **2011**, *2*, 1094–1098.
- [33] Nagai, H.; Nakano, M.; Yoneda, K.; Fukui, H.; Minami, T.; Bonness, S.; Kishi, R.; Takahashi, H.; Kubo, T.; Kamada, K.; Ohta, K.; Champagne, B.; Botek, E. Theoretical Study on Third-Order Nonlinear Optical Properties in Hexagonal Graphene Nanoflakes: Edge Shape Effect. *Chem. Phys. Lett.* **2009**, *477*, 355–359.
- [34] Nagai, H.; Nakano, M.; Yoneda, K.; Kishi, R.; Takahashi, H.; Shimizu, A.; Kubo, T.; Kamada, K.; Ohta, K.; Botek, E.; Champagne, B. Signature of Multiradical Character in Second Hyperpolarizabilities of Rectangular Graphene Nanoflakes. *Chem. Phys. Lett.* **2010**, *489*, 212–218.
- [35] Nakano, M.; Champagne, B. Diradical Character Dependences of the First and Second Hyperpolarizabilities of Asymmetric Open-Shell Singlet Systems. *J. Chem. Phys.* **2013**, *138*, 244306.
- [36] Gu, B.; Zhao, C.; Baev, A.; Yong, K.-T.; Wen, S.; Prasad, P. N. Molecular Nonlinear Optics: Recent Advances and Applications. *Adv. Opt. Photonics* **2016**, *8*, 328–369.
- [37] Prasad, P. N.; Orczyk, M. E.; Zieba, J.; Burzynski, R.; Zhang, Y. In *Frontiers of Polymers and Advanced Materials*; Prasad, P. N., Ed.; Springer US: Boston, MA, 1994; pp 75–91.
- [38] Yardley, J. T.; Beeson, K. W.; Ferm, P.; Horn, K.; Knapp, C.; McFarland, M.; Nahata, A.; Shan, J.; Wu, C. In *Frontiers of Polymers and Advanced Materials*; Prasad, P. N., Ed.;

Springer US: Boston, MA, 1994; pp 107–115.

- [39] Singer, K. D.; Andrews, J. H. In *Molecular Nonlinear Optics*; Zyss, J., Ed.; Quantum Electronics–Principles and Applications; Academic Press: San Diego, 1994; pp 245–298.
- [40] Stegeman, G. I. In *Frontiers of Polymer Research*; Prasad, P. N., Nigam, J. K., Eds.; Springer US: Boston, MA, 1991; pp 63–69.
- [41] Ironside, C. N. In *Principles and Applications of Nonlinear Optical Materials*; Munn, R. W., Ironside, C. N., Eds.; Springer Netherlands: Dordrecht, 1993; pp 20–34.
- [42] Yoshimura, T. Design and Evaluation of Organic Nonlinear Optical Materials with a Large Pockels Effect. *Mol. Cryst. Liq. Cryst. Inc. Nonlinear Opt.* **1990**, *182*, 43–50.
- [43] Dubois, J.-C.; Spitz, E. In *Frontiers of Polymers and Advanced Materials*; Prasad, P. N., Ed.; Springer US: Boston, MA, 1994; pp 93–106.
- [44] Wu, J.; Li, Z.; Luo, J.; Jen, A. K.-Y. High-Performance Organic Second- and Third-Order Nonlinear Optical Materials for Ultrafast Information Processing. *J. Mater. Chem. C* **2020**, *8*, 15009–15026.
- [45] Küpfer, M.; Flörsheimer, M.; Bosshard, C.; Looser, H.; Günter, P. In *Frontiers of Polymers and Advanced Materials*; Prasad, P. N., Ed.; Springer US: Boston, MA, 1994; pp 165–173.
- [46] Blau, W. Organic Materials for Nonlinear Optical Devices. *Phys. Technol.* **1987**, *18*, 250–268.
- [47] Kajzar, F.; Charra, F.; Nunzi, J. M.; Raimond, P.; Idiart, E.; Zagorska, M. In *Frontiers of Polymers and Advanced Materials*; Prasad, P. N., Ed.; Springer US: Boston, MA, 1994; pp 141–153.
- [48] Maloney, C.; Byrne, H.; Dennis, W. M.; Blau, W.; Kelly, J. M. Picosecond Optical Phase Conjugation Using Conjugated Organic Molecules. *Chem. Phys.* **1988**, *121*, 21–39.
- [49] Abraham, E.; Smith, S. D. Optical Bistability and Related Devices. *Rep. Prog. Phys.* **1982**, *45*, 815–885.
- [50] Yoon, Y.-K.; Bennink, R. S.; Boyd, R. W.; Sipe, J. Intrinsic Optical Bistability in a Thin Layer of Nonlinear Optical Material by Means of Local Field Effects. *Opt. Commun.* **2000**, *179*, 577–580.
- [51] Gao, T.; Que, W.; Shao, J. Isomerization and Optical Bistability of DR1 Doped Organic–Inorganic Sol–Gel Thin Film. *Opt. Mater.* **2015**, *48*, 198–202.
- [52] Luther-Davies, B.; Samoc, M. Third-Order Nonlinear Optical Organic Materials for Photonic Switching. *Curr. Opin. Solid State Mater. Sci.* **1997**, *2*, 213–219.
- [53] Li, C. In *Nonlinear Optics: Principles and Applications*; Li, C., Ed.; Springer: Singapore, 2017; pp 279–386.
- [54] Cheng, X.; Yao, J.; Zhang, H.; Wang, X.; Bai, J. The Nonlinear Optical Properties of

- Two-Dimensional Metal-Organic Framework. *J. Alloys Compd.* **2021**, 855, 157433.
- [55] Campagnola, P. J.; Wei, M.-d.; Lewis, A.; Loew, L. M. High-Resolution Nonlinear Optical Imaging of Live Cells by Second Harmonic Generation. *Biophys. J.* **1999**, 77, 3341–3349.
- [56] Campagnola, P. J.; Loew, L. M. Second-Harmonic Imaging Microscopy for Visualizing Biomolecular Arrays in Cells, Tissues and Organisms. *Nat. Biotechnol.* **2003**, 21, 1356–1360.
- [57] Reeve, J. E.; Anderson, H. L.; Clays, K. Dyes for Biological Second Harmonic Generation Imaging. *Phys. Chem. Chem. Phys.* **2010**, 12, 13484–13498.
- [58] Campagnola, P. Second Harmonic Generation Imaging Microscopy: Applications to Diseases Diagnostics. *Anal. Chem.* **2011**, 83, 3224–3231.
- [59] Sheppard, C. J. R.; Gu, M. Image Formation in Two-Photon Fluorescence Microscopy. *Optik* **1990**, 86, 104–106.
- [60] Deniset-Besseau, A.; Duboisset, J.; Benichou, E.; Hache, F.; Brevet, P.-F.; Schanne-Klein, M.-C. Measurement of the Second-Order Hyperpolarizability of the Collagen Triple Helix and Determination of Its Physical Origin. *J. Phys. Chem. B* **2009**, 113, 13437–13445.
- [61] de Wergifosse, M.; de Ruyck, J.; Champagne, B. How the Second-Order Nonlinear Optical Response of the Collagen Triple Helix Appears: A Theoretical Investigation. *J. Phys. Chem. C* **2014**, 118, 8595–8602.
- [62] Thorn, K. Genetically Encoded Fluorescent Tags. *Mol. Biol. Cell* **2017**, 28, 848–857.
- [63] De Meulenaere, E.; Asselberghs, I.; de Wergifosse, M.; Botek, E.; Spaepen, S.; Champagne, B.; Vanderleyden, J.; Clays, K. Second-Order Nonlinear Optical Properties of Fluorescent Proteins for Second-Harmonic Imaging. *J. Mater. Chem.* **2009**, 19, 7514.
- [64] De Meulenaere, E.; De Wergifosse, M.; Botek, E.; Spaepen, S.; Champagne, B.; Vanderleyden, J.; Clays, K. Nonlinear Optical Properties of mStrawberry and mCherry for Second Harmonic Imaging. *J. Nonlinear Opt. Phys. Mater.* **2010**, 19, 1–13.
- [65] De Meulenaere, E.; Nguyen Bich, N.; de Wergifosse, M.; Van Hecke, K.; Van Meervelt, L.; Vanderleyden, J.; Champagne, B.; Clays, K. Improving the Second-Order Nonlinear Optical Response of Fluorescent Proteins: The Symmetry Argument. *J. Am. Chem. Soc.* **2013**, 135, 4061–4069.
- [66] De Meulenaere, E.; de Wergifosse, M.; Botek, E.; Vanderleyden, J.; Champagne, B.; Clays, K. Prediction of First Hyperpolarizability of Fluorescent Proteins. Proceedings of The International Conference of Computational Methods in Sciences and Engineering 2010 (ICCMSE-2010). Kos, Greece, 2015; pp 522–525.
- [67] de Wergifosse, M.; Botek, E.; De Meulenaere, E.; Clays, K.; Champagne, B. ONIOM Investigation of the Second-Order Nonlinear Optical Responses of Fluorescent Proteins.

J. Phys. Chem. B **2018**, 122, 4993–5005.

- [68] Szabadvary, F. Indicators: A Historical Perspective. *J. Chem. Educ.* **1964**, 41, 285.
- [69] The Nobel Prize in Chemistry 2016. <https://www.nobelprize.org/prizes/chemistry/2016/summary/>.
- [70] Raymo, F. M. Digital Processing and Communication with Molecular Switches. *Adv. Mater.* **2002**, 14, 401–414.
- [71] Bouas-Laurent, H.; Dürr, H. *Photochromism*; Elsevier, 2003; pp XXVII–LIII.
- [72] Fuentes, N.; Martín-Lasanta, A.; Álvarez de Cienfuegos, L.; Ribagorda, M.; Parra, A.; Cuerva, J. M. Organic-Based Molecular Switches for Molecular Electronics. *Nanoscale* **2011**, 3, 4003.
- [73] Feringa, B. L., Browne, W. R., Eds. *Molecular Switches*, 2nd ed.; Wiley-VCH: Weinheim, Germany, 2011.
- [74] Harris, J. D.; Moran, M. J.; Aprahamian, I. New Molecular Switch Architectures. *Proc. Natl. Acad. Sci.* **2018**, 115, 9414–9422.
- [75] Coe, B. J. Molecular Materials Possessing Switchable Quadratic Nonlinear Optical Properties. *Chem. Eur. J.* **1999**, 5, 2464–2471.
- [76] Lacroix, P. G.; Malfant, I.; Bénard, S.; Yu, P.; Rivière, E.; Nakatani, K. Hybrid Molecular-Based Magnets Containing Organic NLO Chromophores: A Search toward an Interplay between Magnetic and NLO Behavior. *Chem. Mater.* **2001**, 13, 441–449.
- [77] Xing, X.-S.; Sa, R.-J.; Li, P.-X.; Zhang, N.-N.; Zhou, Z.-Y.; Liu, B.-W.; Liu, J.; Wang, M.-S.; Guo, G.-C. Second-Order Nonlinear Optical Switching with a Record-High Contrast for a Photochromic and Thermochromic Bistable Crystal. *Chem. Sci.* **2017**, 8, 7751–7757.
- [78] Loucif-Saïbi, R.; Nakatani, K.; Delaire, J. A.; Dumont, M.; Sekkat, Z. Photoisomerization and Second Harmonic Generation in Disperse Red One-Doped and -Functionalized Poly(Methyl Methacrylate) Films. *Chem. Mater.* **1993**, 5, 229–236.
- [79] Gilat, S. L.; Kawai, S. H.; Lehn, J.-M. Light-Triggered Molecular Devices: Photochemical Switching Of Optical and Electrochemical Properties in Molecular Wire Type Diarylethene Species. *Chem. Eur. J.* **1995**, 1, 275–284.
- [80] Coe, B. J.; Houbrechts, S.; Asselberghs, I.; Persoons, A. Efficient, Reversible Redox-Switching of Molecular First Hyperpolarizabilities in Ruthenium(II) Complexes Possessing Large Quadratic Optical Nonlinearities. *Angew. Chem. Int. Ed.* **1999**, 38, 366–369.
- [81] Asselberghs, I.; Clays, K.; Persoons, A.; McDonagh, A. M.; Ward, M. D.; McCleverty, J. A. In Situ Reversible Electrochemical Switching of the Molecular First Hyperpolarizability. *Chem. Phys. Lett.* **2003**, 368, 408–411.
- [82] Ségerie, A.; Castet, F.; Kanoun, M. B.; Plaquet, A.; Liégeois, V.; Champagne, B. Nonlin-

- ear Optical Switching Behavior in the Solid State: A Theoretical Investigation on Anils. *Chem. Mater.* **2011**, *23*, 3993–4001.
- [83] Beaujean, P.; Bondu, F.; Plaquet, A.; Garcia-Amorós, J.; Cusido, J.; Raymo, F. M.; Castet, F.; Rodriguez, V.; Champagne, B. Oxazines: A New Class of Second-Order Nonlinear Optical Switches. *J. Am. Chem. Soc.* **2016**, *138*, 5052–5062.
- [84] Delaire, J. A.; Nakatani, K. Linear and Nonlinear Optical Properties of Photochromic Molecules and Materials. *Chem. Rev.* **2000**, *100*, 1817–1846.
- [85] Tonnelé, C.; Pielak, K.; Deviers, J.; Muccioli, L.; Champagne, B.; Castet, F. Nonlinear Optical Responses of Self-Assembled Monolayers Functionalized with Indolino–Oxazolidine Photoswitches. *Phys. Chem. Chem. Phys.* **2018**, *20*, 21590–21597.
- [86] Li, J.-X.; Xu, J.-J.; Luo, W.-Q.; Jin, C.-M. Supramolecular Chirality and Photochromism in Langmuir-Blodgett Films of Fabricated Silver-Induced Phenylazoimidazole Derivatives. *Dyes Pigments* **2021**, *187*, 109080.
- [87] Bondu, F.; Quertinmont, J.; Rodriguez, V.; Pozzo, J.-L.; Plaquet, A.; Champagne, B.; Castet, F. Second-Order Nonlinear Optical Properties of a Dithienylethene–Indolinooxazolidine Hybrid: A Joint Experimental and Theoretical Investigation. *Chem. Eur. J.* **2015**, *21*, 18749–18757.
- [88] Quertinmont, J.; Maschio, L.; Datta, A.; Champagne, B. Salicylideneaniline-Based Covalent Organic Frameworks: A New Family of Multistate Second-Order Nonlinear Optical Switches. *J. Phys. Chem. C* **2020**, *124*, 24451–24459.
- [89] Quertinmont, J.; Beaujean, P.; Stiennon, J.; Aidibi, Y.; Leriche, P.; Rodriguez, V.; Sanguinet, L.; Champagne, B. Combining Benzazolo-Oxazolidine Twins toward Multi-State Nonlinear Optical Switches. *J. Phys. Chem. B* **2021**, *125*, 3918–3931.
- [90] Castet, F.; Rodriguez, V.; Pozzo, J.-L.; Ducasse, L.; Plaquet, A.; Champagne, B. Design and Characterization of Molecular Nonlinear Optical Switches. *Acc. Chem. Res.* **2013**, *46*, 2656–2665.
- [91] Bondu, F.; Hadji, R.; Szalóki, G.; Alévêque, O.; Sanguinet, L.; Pozzo, J.-L.; Cavagnat, D.; Buffeteau, T.; Rodriguez, V. Huge Electro-/Photo-/Acidoinduced Second-Order Nonlinear Contrasts From Multiaddressable Indolinooxazolidine. *J. Phys. Chem. B* **2015**, *119*, 6758–6765.
- [92] Humphrey, M. G.; Cifuentes, M. P.; Samoc, M. In *Molecular Organometallic Materials for Optics*; Bozec, H., Guerchais, V., Eds.; Topics in Organometallic Chemistry; Springer: Berlin, Heidelberg, 2010; pp 57–73.
- [93] Green, K. A.; Cifuentes, M. P.; Samoc, M.; Humphrey, M. G. Metal Alkynyl Complexes as Switchable NLO Systems. *Coord. Chem. Rev.* **2011**, *255*, 2530–2541.
- [94] Gauthier, N.; Argouarch, G.; Paul, F.; Toupet, L.; Ladjarafi, A.; Costuas, K.; Halet, J.-F.;

Samoc, M.; Cifuentes, M. P.; Corkery, T. C.; Humphrey, M. G. Electron-Rich Iron/Ruthenium Arylalkynyl Complexes for Third-Order Nonlinear Optics: Redox-Switching between Three States. *Chem. Eur. J.* **2011**, *17*, 5561–5577.

- [95] Qiu, Y.-Q.; Wang, W.-Y.; Ma, N.-N.; Wang, C.-H.; Zhang, M.-Y.; Zou, H.-Y.; Liu, P.-J. Computational Investigation on Redox-Switchable Nonlinear Optical Properties of a Series of Polycyclic p-Quinodimethane Molecules. *J. Mol. Model.* **2013**, *19*, 5479–5487.
- [96] Champagne, B.; Plaquet, A.; Pozzo, J.-L.; Rodriguez, V.; Castet, F. Nonlinear Optical Molecular Switches as Selective Cation Sensors. *J. Am. Chem. Soc.* **2012**, *134*, 8101–8103.

Chapter Two

Second and third harmonic scattering

Abstract

Chapter 2 describes one measurement method, based on second and third harmonic scattering, to get the first and second hyperpolarizability. After a general introduction in the first section, the second is dedicated to the calculation of experimental quantities from the molecular tensors to ease their comparison. Finally, the third section introduces the decomposition of the first and second hyperpolarizability tensors in spherical invariants, with the aim to provide a better understanding of the origin of the response.

Section 2.1

Generation and measurement of harmonics

As shown in the previous Chapter, the interaction between a NLO medium and an oscillating electric field of pulsation ω results in the spontaneous generation of higher order harmonics (multiple of the fundamental frequency) among other phenomenons.

Mechanism

An equivalent description is pictured in Fig. 2.1, where two (three) photons of energy $\hbar\omega$ excite the ground state and are combined to generate a new photon of energy $2\hbar\omega$ ($3\hbar\omega$). More precisely, the first photon interacts with the ground state and excites the molecule to an intermediate, generally virtual (short-lived), state. One (or two) other photon(s) then interact(s) within a close time frame with this excited molecule to bring it to the final virtual state, from which the molecule decays and emits a photon of twice (three times) the energy of the original ones.

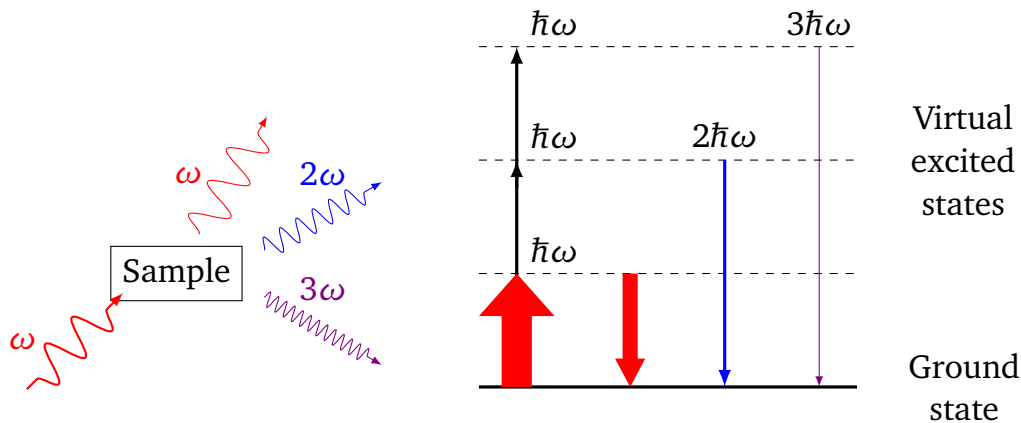


Figure 2.1: Energy-level diagram describing first, second and third harmonic scattering processes, respectively associated with α , β , and γ .

Though the existence of those virtual states is well established, their interpretation differs. For some authors, they are allowed by the time-energy version of the Heisenberg uncertainty principle,¹ given by $\Delta t \Delta E \geq \hbar/2$, so that absorption can occur without breaking the energy conservation principle if the re-emission happens in $\Delta t \leq \hbar/2\Delta E$, hence the *short-lived*. It also explains the low transition probability to such states. For others, the root lies in the interpretation of the time-dependent perturbation theory (see Ref. 2 for a gentle, though provocative, introduction).

Nevertheless, when one of the energies is close to an excited state, the transition probability is enhanced, so that the NLO response becomes large (as predicted by the SOS model, see Eq. (1.12)), which is referred to as *resonance*. Although a desirable experimental feature in

many applications, this may complicate the characterization of the NLO response of a molecule and its prediction (which requires near-resonance theory, *e.g.*, the introduction of damping in response function^{3,4}).

Measurement of harmonic generation from scattering

In this thesis, the measurement of SHG and THG β and γ tensors is assumed to be obtained from the measurement of harmonic scattering (HS). The experimental setup for the measurement of second (SHS) and third (THS) harmonic scattering is pictured in Fig. 2.2. The fundamental light beam (of frequency ω), which is elliptically polarized (Θ and δ describe the state of polarization, and in this case $\delta = \pi/2$), propagates in the Y direction while the Z -linearly polarized component of the scattered beam (of frequency $m\omega$) is recorded in the X direction. One generally distinguishes between two polarization combinations: the VV geometry (vertical-vertical, both incident and scattered lights are vertically polarized, with $\Theta = \pi/2$) and HV [horizontal-vertical, the incident (scattered) light is horizontally- (vertically-) polarized, with $\Theta = 0$]. Note that other combinations of polarization are possible, which probe different components of the hyperpolarizability tensors.⁵⁻⁷

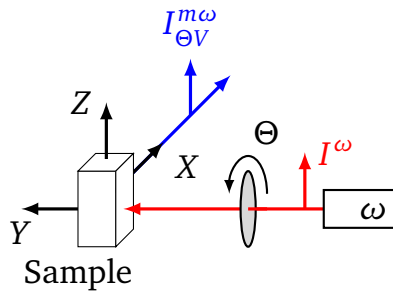


Figure 2.2: Sketch of the experimental SHS ($m\omega = 2\omega$) and THS ($m\omega = 3\omega$) setup.^{5,6,8-11} X , Y and Z stand for the coordinates axes in the laboratory frame. The measurement is done at 90° with respect to the incident beam.

Both gas⁶ and liquid^{10,11} phase measurements are possible, in which it is assumed that only the incoherent scattering contributes to HS, which is a good approximation of the experimental conditions.⁷ The goal is to avoid any intermolecular interaction that would lead to a preferential orientation of the scatterers (which is the case in crystals). What is measured is thus, ideally, the overall response of randomly oriented individual molecules. Therefore, the light intensity $I^{m\omega}$ (for the m^{th} harmonic generation) without any polarization is given by:^{8,11,12}

$$I^{m\omega} = G f_L^2 C \langle \chi^2 \rangle (I^\omega)^m, \quad (2.1)$$

where I^ω is the incident light intensity, G , a constant containing geometrical, optical and electrical factors of the experimental setup, C , the concentration of the chromophore, χ , either β_{HRS} or γ_{THS} (see below), $\langle \chi^2 \rangle$, the rotational averaging of the individual responses (see next

section), and f_L , a local field correction when approximated using the high frequency Lorentz-Lorentz spherical cavity expression, including the refractive reading as:

$$f_L = \left(\frac{n_\omega^2 + 2}{3} \right)^m \left(\frac{n_{m\omega}^2 + 2}{3} \right). \quad (2.2)$$

On the same principle, the I_{VV} intensity is proportional to $\langle \beta_{ZZZ}^2 \rangle$ and $\langle \gamma_{ZZZZ}^2 \rangle$, while I_{HV} is proportional to $\langle \beta_{ZXX}^2 \rangle$ and $\langle \gamma_{ZXXX}^2 \rangle$, respectively. For a non-polarized incident signal, both polarizations have equal probability and the intensity becomes proportional to the sum of the HV and VV observables. This allows defining β_{SHS} and γ_{THS} , the molecular first and second hyperpolarizability determined by HS, as:

$$\beta_{SHS} = \sqrt{\langle \beta_{ZZZ}^2 \rangle + \langle \beta_{ZXX}^2 \rangle}, \quad (2.3)$$

$$\gamma_{THS} = \sqrt{\langle \gamma_{ZZZZ}^2 \rangle + \langle \gamma_{ZXXX}^2 \rangle}. \quad (2.4)$$

Another interesting quantity is the depolarization ratio (DR):

$$DR = \frac{I_{VV}}{I_{HV}} \Leftrightarrow DR_{SHS} = \frac{\langle \beta_{ZZZ}^2 \rangle}{\langle \beta_{ZXX}^2 \rangle}, \text{ and } DR_{THS} = \frac{\langle \gamma_{ZZZZ}^2 \rangle}{\langle \gamma_{ZXXX}^2 \rangle}. \quad (2.5)$$

As shown in the next section, the depolarization ratio takes specific values that depend on the part of the molecule which is responsible for the NLO response, and its symmetry. It should be noted that the SHS experiment is also referred to as the Hyper-Rayleigh scattering (HRS) experiment in the literature,^{13,14} so that β_{SHS} and β_{HRS} are considered to be the same quantity in the present manuscript.

An additional peculiarity of the experimental procedure is that it should be calibrated, either with internal or external references.^{10,15} Generally, He or N₂ (external references) are used for gas phase experiments, while the solvent is used (internal reference) for the liquid phase counterpart. In the end, it relies ultimately on *ab initio* gas phase calculations to calibrate the setup, which is why a part of this thesis (Part II) is dedicated to accurate gas phase calculations.

The advantages of the SHS and THS technique are the following:¹⁶ i) octupolar molecules and charged species can be probed (contrary to the EFISHG technique), ii) the technique is sensitive to the different components, thanks to the possibility to use different combinations of polarizations, and iii) it is relatively simple compared to other techniques. There are also disadvantages, such as i) a strong laser and a very sensitive detection are required (incoherent process), ii) measurements get difficult if close to resonance, and iii) fluorescence at double frequency, if present, should be removed.¹⁷

Section 2.2

From the molecular tensor to the macroscopic quantities

Rotational averaging

When a molecule interacts with the experimental system, the result depends on the molecule orientation and may be described by a function $f(\theta, \phi, \chi)$ of the three Euler angles (Fig. 2.3). The bulk response, $\langle \chi^n \rangle$, is given by:

$$\langle \chi^n \rangle = \frac{1}{8\pi^2} \int_0^\pi d\theta \sin \theta \int_0^{2\pi} d\phi \int_0^{2\pi} d\zeta \chi^n(\theta, \phi, \zeta), \quad (2.6)$$

which perform a per molecule average over all possible orientations of the molecule. Furthermore, the molecular properties are generally expressed in the molecular frame, while the experimental system (e.g., an external electric field) is the same for all molecules in the bulk and defined in the so-called laboratory (of external) frame.¹⁸ Following Andrews and

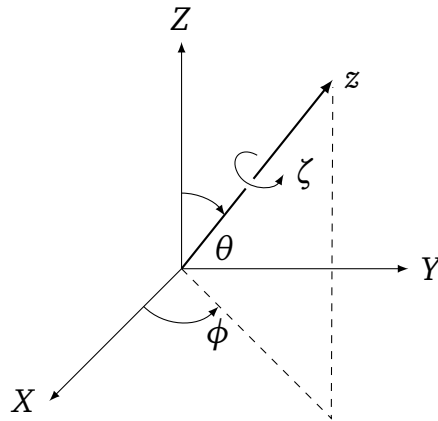


Figure 2.3: Laboratory reference (X , Y , and Z) and molecular reference (x , y , and z) frames. θ , ϕ , and ψ are the Euler angles that relate the coordinate systems. For clarity, only z is shown. Adapted from Ref. 18.

co-workers,^{18–20} the signal, A , associated with a nonlinear interaction is given by:

$$A \propto S_{i_1 \dots i_n} \mathcal{T}_{i_1 \dots i_n}, \quad (2.7)$$

where S is a rank n tensor representing the incident radiation field, $S_{i_1 \dots i_n}$ are the element of these radiation, and \mathcal{T} , a response tensor of the same rank. For incoherent processes involving m photons, the main contribution comes from a term with $n = 2m$, so 6 and 8 for SHS and THS, respectively. S is constructed by the outer product of n vectors describing the polarization of the photons, and their complex conjugates. Here, the $\{i_p\}$ indices indicate that both S and \mathcal{T} are defined in the same coordinate system, which is the one of the incident radiation (so the laboratory frame). A is therefore the signal of a single molecule for which the response

tensor has been expressed in the laboratory frame. Such transformation is performed from the tensor expressed in the molecular frame by the relation:

$$\mathcal{T}_{i_1 \dots i_n} = \sum_{\lambda_1 \dots \lambda_n} L_{i_1 \lambda_1} \cdots L_{i_n \lambda_n} \mathcal{T}_{\lambda_1 \dots \lambda_n} \quad (2.8)$$

where the $L_{i_p \lambda_p}$ are the direction cosines between the \hat{e}_{i_p} and \hat{e}_{λ_p} axes in the molecular frame. The intensity, $I \propto \langle A \rangle$, is obtained by rotational averaging:

$$\langle A \rangle = S_{i_1 \dots i_n} \mathcal{T}_{\lambda_1 \dots \lambda_n} \mathbf{I}_{i_1 \dots i_n \lambda_1 \dots \lambda_n}^{(n)}, \text{ with } \mathbf{I}_{i_1 \dots i_n \lambda_1 \dots \lambda_n}^{(n)} = \langle L_{i_1 \lambda_1} \cdots L_{i_n \lambda_n} \rangle. \quad (2.9)$$

Thus, to get the average signal, the evaluation of the $\mathbf{I}^{(n)}$ is required, which turns out to be 3^{2n} integrals. Although modern computers can evaluate integrals quickly, a simpler way exploits the fact that this matrix is invariant in both the molecular and laboratory frame: it can thus be expressed as a linear combination of isotropic tensors (string of Kronecker delta). Therefore,

$$\mathbf{I}_{i_1 \dots i_n \lambda_1 \dots \lambda_n}^{(n)} = (\mathbf{f}^{(n)})^T \mathbf{M}^{(n)} \mathbf{g}^{(n)}, \quad (2.10)$$

where $\mathbf{f}^{(n)}$ and $\mathbf{g}^{(n)}$ are vectors of laboratory and molecular coordinates, while $\mathbf{M}^{(n)}$ is a coefficient matrix. Their size (and the one of the $\mathbf{M}^{(n)}$ matrix) depends on the rank of the tensor, and amounts to 15 and 91 for the SHS and THS processes, respectively. $\mathbf{M}^{(n)}$ is obtained by a matrix inversion, as explained in Ref. 19. Once $\mathbf{M}^{(n)}$ is found, the average signal rate is given by Eq. (2.9), which is rewritten:

$$\langle A \rangle = \sum_{i, \lambda} [f e^n]_i \mathbf{M}_{i\lambda}^{(n)} [g \mathcal{T}]_\lambda, \quad (2.11)$$

where $[f e^n]_i = S_{i_1 \dots i_n} (\mathbf{f}^{(n)})^T$ and $[g \mathcal{T}]_\lambda = \mathbf{g}^{(n)} \mathcal{T}_{\lambda_1 \dots \lambda_n}$, both rotationally averaged, are referred to as independent observables or rotational invariants.²⁰ In particular, a linear combination of the $[g \mathcal{T}]_\lambda$ can describe $\langle A \rangle$ for any polarization of the photons. Note that from intrinsic permutations (the $n - 1$ incident photons have the same polarization), one can reduce the size of the elements in Eq. (2.11) since some elements are therefore identical. The number of invariants thus drastically reduces if all components are real, to 5 and 7 for SHS and THS, respectively. The strategy to obtain the macroscopic quantities described in Section 2.1 is therefore:

1. Write an expression accounting for the direction and polarization of each photon in the setup to construct the S matrix;
2. Apply intrinsic permutation symmetry^a to get the invariants $[f e^n]_i$ and $[g \mathcal{T}]_\lambda$;
3. Simplify the $\mathbf{M}^{(n)}$ matrix, starting from the ones found in Refs. 19 and 21;
4. Get the expressions of $\langle A \rangle$ (here $\langle \beta^2 \rangle$ and $\langle \gamma^2 \rangle$), using Eq. (2.11).

^aThis part was performed with the help of a Python script, written by myself.

Application to SHS

In the specific case of SHS, one writes:

$$\mathcal{T}_{ABCDEF} = \beta^2 = \beta_{ABC}\beta_{DEF} \quad S_{ABCDEF} = r_A r_B s_C r_D^* r_E^* s_F^* \quad (2.12)$$

where \mathbf{r} describes the polarization of the incidents photons, and \mathbf{s} , the polarization of the scattered photon. For example:

$$\delta_{AB}\delta_{CE}\delta_{DF}\mathcal{T}_{ABCDEF} = \beta_{ij}\beta_{kl} = \delta_{AC}\delta_{BE}\delta_{DF}\mathcal{T}_{ABCDEF} \quad (2.13)$$

$$\delta_{AB}\delta_{CE}\delta_{DF}S_{ABCDEF} = |\mathbf{s} \cdot \mathbf{r}|^2 = \delta_{AC}\delta_{BE}\delta_{DF}S_{ABCDEF}. \quad (2.14)$$

The last equalities are obtained assuming intrinsic permutation symmetry.

With an elliptically polarized incident light propagating along the Y direction and a Z linearly polarized scattered photon, the expressions for \mathbf{r} and \mathbf{s} are:

$$\mathbf{r} = \hat{e}_X \cos(\Theta) - i \hat{e}_Z \cos(\Theta + \delta) \text{ and } \mathbf{s} = \hat{e}_Z, \quad (2.15)$$

where Θ and δ describe the state of polarization, and \hat{e}_Z and \hat{e}_X are unit vectors in the corresponding directions. The phase retardation is $\delta = \pi/2$ (see Fig. 2.2). The matrix $\mathbf{M}^{(6)}$, along with the corresponding rotational invariants are given in Table 2.1, which includes the form of the isotropic tensors and the corresponding polarizations. The application of Eq. (2.11) then gives the following expression for the Θ -dependent intensity:

$$I_{\Theta V}^{2\omega} \propto \langle \beta^2(\Theta) \rangle = \frac{1}{105} \begin{pmatrix} 4 - 26 \cos^2 \Theta + 20 \cos^4 \Theta \\ 4 + 2 \cos^2 \Theta - 8 \cos^4 \Theta \\ 1 - 10 \cos^2 \Theta + 12 \cos^4 \Theta \\ 2 + 8 \cos^2 \Theta - 4 \cos^4 \Theta \\ 4 + 2 \cos^2 \Theta - 8 \cos^4 \Theta \end{pmatrix}^T \begin{pmatrix} [g\beta^2]_A \\ [g\beta^2]_B \\ [g\beta^2]_C \\ [g\beta^2]_D \\ [g\beta^2]_E \end{pmatrix}. \quad (2.16)$$

The VV geometry corresponds to $\Theta = \pi/2$ (all photons have the same polarization), and the HV geometry is when $\Theta = 0$ (the polarization of the incident and scattered photons are perpendicular). In those two cases:

$$\langle \beta_{ZZZ}^2 \rangle = \frac{1}{105} \sum_{ijk}^{xyz} 2\beta_{ijk}^2 + \beta_{ijj}\beta_{ikk} + 4(\beta_{iij}\beta_{jkk} + \beta_{iij}\beta_{kjk} + \beta_{ijk}\beta_{jik}) \quad (2.17)$$

$$\approx \frac{1}{35} \sum_{ijk}^{xyz} 2\beta_{ijk}^2 + 3\beta_{ijj}\beta_{ikk}, \quad (2.18)$$

$$\langle \beta_{ZXX}^2 \rangle = \frac{1}{105} \sum_{ijk}^{xyz} 6\beta_{ijk}^2 + 3\beta_{ijj}\beta_{ikk} - 2(\beta_{iij}\beta_{jkk} + \beta_{iij}\beta_{kjk} + \beta_{ijk}\beta_{jik}) \quad (2.19)$$

$$\approx \frac{1}{105} \sum_{ijk}^{xyz} 4\beta_{ijk}^2 - \beta_{ijj}\beta_{ikk}, \quad (2.20)$$

where Eqs. (2.18) and (2.20) are simplifications of the previous ones if Kleinman's conditions are assumed or satisfied.^{12,22}

$$\mathbf{M}^{(6)} = \frac{1}{210} \begin{bmatrix} 60 & -24 & -20 & 16 & -24 \\ -24 & 32 & 8 & -12 & 4 \\ -20 & 8 & 16 & -10 & 8 \\ 16 & -12 & -10 & 22 & -12 \\ -24 & 4 & 8 & -12 & 32 \end{bmatrix}$$

i or λ	$\mathbf{f}^{(6)}$ or $\mathbf{g}^{(6)}$	$[g\beta^2]_\lambda$	$[fe^6]_i$	$[fe^6]_i$ assuming Eq. (2.15)
A	$\delta_{AB}\delta_{CD}\delta_{EF}$	$\beta_{ijj}\beta_{jkk}$	$\text{Re}[(\mathbf{s} \cdot \mathbf{r})(\mathbf{s}^* \cdot \mathbf{r})(\mathbf{r}^* \cdot \mathbf{r}^*)]$	$2\cos^4\Theta - 3\cos^2\Theta + 1$
B	$\delta_{AB}\delta_{CE}\delta_{DF}$	$\beta_{ijj}\beta_{kjk}$	$ \mathbf{s} \cdot \mathbf{r} ^2$	$1 - \cos^2\Theta$
C	$\delta_{AD}\delta_{BC}\delta_{EF}$	$\beta_{ijj}\beta_{ikk}$	$ \mathbf{r} \cdot \mathbf{r} ^2$	$4\cos^4\Theta - 4\cos^2\Theta + 1$
D	$\delta_{AD}\delta_{BE}\delta_{CF}$	β_{ijk}^2	1	1
E	$\delta_{AE}\delta_{BD}\delta_{CF}$	$\beta_{ijk}\beta_{jik}$	$ \mathbf{s} \cdot \mathbf{r}^* ^2$	$1 - \cos^2\Theta$

Table 2.1: Solution for the SHS case (two identical incident photons of polarization \mathbf{r} and one scattered photon of polarization \mathbf{s}).

Application to THS

In the case of THS:

$$\mathcal{T}_{ABCDEFGH} = \gamma^2 = \gamma_{ABCD}\gamma_{EFGH} \quad S_{ABCDEFGH} = r_A r_B r_C s_D r_E^* r_F^* r_G^* s_H^* \quad (2.21)$$

where \mathbf{r} describes the polarization of the incident photons, and \mathbf{s} , the polarization of the scattered photon. Considering, the same assumption about the polarization of the incident and scattered photons (Eq. 2.15), the matrix $\mathbf{M}^{(8)}$, along with the corresponding rotational invariants, is given in Table 2.2, which includes the form of the isotropic tensors and the corresponding polarizations. It is interesting to note that the polarization parameters are the same as for the SHS case, except for $[fe^8]_A$ and $[fe^8]_F$. The Θ -dependent intensity is thus

given by:²⁰

$$I_{\Theta V}^{3\omega} \propto \langle \gamma^2(\Theta) \rangle = \frac{1}{630} \begin{pmatrix} 6 - 81 \cos^2 \Theta + 198 \cos^4 \Theta - 126 \cos^6 \Theta \\ 24 - 108 \cos^2 \Theta - 72 \cos^4 \Theta + 144 \cos^6 \Theta \\ 12 + 54 \cos^2 \Theta - 90 \cos^4 \Theta + 18 \cos^6 \Theta \\ 6 - 54 \cos^2 \Theta + 36 \cos^4 \Theta + 36 \cos^6 \Theta \\ 4 + 36 \cos^2 \Theta - 12 \cos^4 \Theta - 12 \cos^6 \Theta \\ 6 - 81 \cos^2 \Theta + 198 \cos^4 \Theta - 126 \cos^6 \Theta \\ 12 + 54 \cos^2 \Theta - 90 \cos^4 \Theta + 18 \cos^6 \Theta \end{pmatrix}^T \begin{pmatrix} [g\gamma^2]_A \\ [g\gamma^2]_B \\ [g\gamma^2]_C \\ [g\gamma^2]_D \\ [g\gamma^2]_E \\ [g\gamma^2]_F \\ [g\gamma^2]_G \end{pmatrix}, \quad (2.22)$$

and once again, the two geometries (HV and VV) are distinguished:

$$\langle \gamma_{ZZZZ}^2 \rangle = \frac{1}{315} \sum_{ijkl}^{xyz} \left\{ 2\gamma_{ijkl}^2 + 12\gamma_{iijk}\gamma_{jllk} + 6(\gamma_{iijk}\gamma_{ljlk} + \gamma_{ijkl}\gamma_{jikl}) \right. \\ \left. + 3(\gamma_{ijjk}\gamma_{ikll} + \gamma_{iijj}\gamma_{kllk} + \gamma_{ijjk}\gamma_{kill}) \right\} \quad (2.23)$$

$$\approx \frac{1}{315} \sum_{ijkl}^{xyz} 8\gamma_{ijkl}^2 + 24\gamma_{iijk}\gamma_{jllk} + 3\gamma_{iijj}\gamma_{kllk}, \quad (2.24)$$

$$\langle \gamma_{ZXXX}^2 \rangle = \frac{1}{630} \sum_{ijkl}^{xyz} \left\{ 16\gamma_{ijkl}^2 + 24\gamma_{ijjk}\gamma_{ikll} - 12\gamma_{iijk}\gamma_{jllk} \right. \\ \left. - 6(\gamma_{iijk}\gamma_{ljlk} + \gamma_{ijkl}\gamma_{jikl}) - 3(\gamma_{iijj}\gamma_{kllk} + \gamma_{ijjk}\gamma_{kill}) \right\} \quad (2.25)$$

$$\approx \frac{1}{630} \sum_{ijkl}^{xyz} 10\gamma_{ijkl}^2 + 3\gamma_{iijk}\gamma_{jllk} - 3\gamma_{iijj}\gamma_{kllk}, \quad (2.26)$$

where Eq. (2.24) and (2.26) are a simplification of the previous ones if Kleinman's conditions are assumed.

Section 2.3

Irreducible tensor forms

The concept of irreducible tensors (or spherical tensors) is based on the idea of rotational invariance with respect to the continuous group of rotation-inversion in 3 dimensions [SO(3)]. In other words, in the previous section, the tensors were expressed in Cartesian reference frame, which is affected by a change of the reference system (*i.e.*, the laboratory frame). To circumvent the problem, the solution is to express the tensor in different components on the basis of spherical tensors, thus giving irreducible tensors, or spherical invariants. In the context of SHS and THS, it provides an additional interpretation of the macroscopic quantities, especially the DR.

$$\mathbf{M}^{(8)} = \frac{1}{3780}$$

216	-108	-54	-27	9	-27	27
-108	1512	-540	-432	360	-108	-540
-54	-540	540	189	-225	27	135
-27	-432	189	378	-234	-27	189
9	360	-225	-234	330	9	-225
-27	-108	27	-27	9	216	-54
27	-540	135	189	-225	-54	540

i or λ	$\mathbf{f}^{(8)}$ or $\mathbf{g}^{(8)}$	$[g\gamma^2]_\lambda$	$[fe^8]_i$	$[fe^8]_i$ assuming Eq. (2.15)
A	$\delta_{AB}\delta_{CD}\delta_{EH}\delta_{FG}$	$\gamma_{ijj}\gamma_{klk}$	$\text{Re}[(\mathbf{s}\cdot\mathbf{r})(\mathbf{r}\cdot\mathbf{r})(\mathbf{s}^*\cdot\mathbf{r}^*)(\mathbf{r}^*\cdot\mathbf{r}^*)]$	$-4\cos^6\Theta + 8\cos^4\Theta - 5\cos^2\Theta + 1$
B	$\delta_{AB}\delta_{CE}\delta_{DH}\delta_{FG}$	$\gamma_{ijk}\gamma_{jlk}$	$\text{Re}[(\mathbf{s}\cdot\mathbf{r})(\mathbf{s}^*\cdot\mathbf{r})(\mathbf{r}^*\cdot\mathbf{r}^*)]$	$2\cos^4\Theta - 3\cos^2\Theta + 1$
C	$\delta_{AB}\delta_{CF}\delta_{DH}\delta_{EG}$	$\gamma_{ijk}\gamma_{jlk}$	$ \mathbf{s}\cdot\mathbf{r} ^2$	$1 - \cos^2\Theta$
D	$\delta_{AE}\delta_{BC}\delta_{DF}\delta_{GH}$	$\gamma_{ijk}\gamma_{ikl}$	$ \mathbf{r}\cdot\mathbf{r} ^2$	$4\cos^4\Theta - 4\cos^2\Theta + 1$
E	$\delta_{AE}\delta_{BF}\delta_{CH}\delta_{DG}$	γ_{ijl}^2	1	1
F	$\delta_{AF}\delta_{BC}\delta_{DE}\delta_{GH}$	$\gamma_{ijk}\gamma_{klk}$	$\text{Re}[(\mathbf{s}\cdot\mathbf{r}^*)(\mathbf{r}\cdot\mathbf{r})(\mathbf{s}^*\cdot\mathbf{r})(\mathbf{r}^*\cdot\mathbf{r}^*)]$	$-4\cos^6\Theta + 8\cos^4\Theta - 5\cos^2\Theta + 1$
G	$\delta_{AF}\delta_{BE}\delta_{CG}\delta_{DH}$	$\gamma_{ijkl}\gamma_{jkl}$	$ \mathbf{s}\cdot\mathbf{r}^* ^2$	$1 - \cos^2\Theta$

 Table 2.2: Solution for the THS case (three identical incident photons of polarization \mathbf{r} and one scattered photon of polarization \mathbf{s}).

Procedure

A Cartesian tensor of rank n can be reduced in a sum of irreducible tensors $\mathcal{T}_{J=j}$ of weight J (with $2J + 1$ independent components), with $J \leq n$:^{23–25}

$$\mathcal{T} = \sum_{j=0}^n \mathcal{T}_{J=j}, \text{ with } \mathcal{T}_{J=j} = \sum_{q=1}^{N_j^{(n)}} \mathcal{T}_{(j;q)}, \quad (2.27)$$

where q is the seniority of the irreducible tensor $\mathcal{T}_{(j;q)}$, of weight j and $N_j^{(n)}$, the multiplicity. The goal is to express the average intensity, $I \propto \langle \mathcal{T}^2 \rangle$ (from the previous section), in this new basis:

$$\langle \mathcal{T}^2 \rangle = \sum_{j=0}^n |\mathcal{T}_{J=j}|^2, \text{ with } |\mathcal{T}_{J=j}|^2 = \sum_{pq}^{N_j^{(n)}} \mathcal{T}_{(j;p)} \odot^n \mathcal{T}_{(j;q)}, \quad (2.28)$$

where \odot^n is the (tensor) index product repeated n times. The first equality is coming from the fact that the irreducible tensors are now invariant to rotation and orthogonal to each other, and the last equality assumes that all components are real. The multiplicity is given by:^{25–27}

$$N_j^{(n)} = \sum_{k=0}^{\lfloor (n-j)/3 \rfloor} (-1)^k \binom{n}{k} \binom{2n-3k-j-2}{n-2}. \quad (2.29)$$

The values of the different multiplicities are given in Table 2.3. Note that those multiplicities further decrease if intrinsic or full permutations (Kleinman's conditions) symmetries are taken into account. If the latter is assumed, β is only composed of one dipolar ($J = 1$) and one octupolar ($J = 3$) component, while γ decomposes into an isotropic ($J = 0$), quadrupolar ($J = 2$), and hexadecapolar ($J = 4$) components. Those are the decompositions generally found in literature.

j	$n = 3$			$n = 4$		
	No	Intrinsic	Full	No	Intrinsic	Full
0	1	0	0	3	1	1
1	3	2	1	6	1	0
2	2	1	0	6	2	1
3	1	1	1	3	1	0
4	—	—	—	1	1	1
Total	7	4	2	19	6	3

Table 2.3: Value of the multiplicities $N_j^{(n)}$ for each irreducible tensor of rank n and weight j , as computed by Eq. (2.29), and effects of the intrinsic or full permutation symmetries.^{25–27}

The reduction procedure is based on the formula:²⁵

$$\mathcal{T}_{(j;q)} = \hat{\Pi}_{(j;q)}^{(n|n)} \odot^n \mathcal{T} = \left\{ G_{(0;q)}^{(n|j)} \odot^j \tilde{G}_{(0;q)}^{(j|n)} \right\} \odot^n \mathcal{T}, \quad (2.30)$$

where $\hat{\Pi}$ is the operator that extracts the tensor of weight j and seniority q , which is defined by two other operators: $\tilde{G}_{(0;q)}^{(j|n)}$, which extracts the tensor of rank and weight j , and $G_{(0;q)}^{(n|j)}$, which maps the tensor of rank j to rank n . They are constructed out of isotropic tensors (string of Kronecker deltas), with the resulting operators as found in Refs. 23. Their application extracts the different irreducible tensors, expressed as linear combination of the invariants given in the previous section.^b

Application to SHS

The decomposition of tensors of rank 3, without any assumption on the permutation symmetry, is detailed in Ref. 28. Assuming intrinsic permutation symmetry, four irreducible tensors are obtained (Table 2.3), two of which are of weight $J = 1$, denoted $\beta_{J=1\alpha}$ and $\beta_{J=1\beta}$. From Eq. (2.28) comes 5 different products:

$$|\beta_{J=1\alpha}|^2 = \frac{1}{5} \sum_{ijk}^{xyz} 2 \beta_{ijj} \beta_{ikk}, \quad (2.31)$$

$$|\beta_{J=1\beta}|^2 = \frac{1}{5} \sum_{ijk}^{xyz} 3 \beta_{iij} \beta_{kjk}, \quad (2.32)$$

$$|\beta_{J=1\alpha\beta}|^2 = -\frac{1}{5} \sum_{ijk}^{xyz} \beta_{iij} \beta_{jkk}, \quad (2.33)$$

$$|\beta_{J=2}|^2 = \frac{1}{3} \sum_{ijk}^{xyz} 2\beta_{ijk}^2 - 2\beta_{ijk} \beta_{jik} - \beta_{ijj} \beta_{ikk} - \beta_{iij} \beta_{kjk} + 2\beta_{iij} \beta_{jkk}, \quad (2.34)$$

$$|\beta_{J=3}|^2 = \frac{1}{15} \sum_{ijk}^{xyz} 5\beta_{ijk}^2 + 10\beta_{ijk} \beta_{jik} - \beta_{ijj} \beta_{ikk} - 4\beta_{iij} \beta_{kjk} - 4\beta_{iij} \beta_{jkk}. \quad (2.35)$$

The last equations can also be written in the form of a matrix multiplication:

$$\begin{pmatrix} |\beta_{J=1\alpha}|^2 \\ |\beta_{J=1\beta}|^2 \\ |\beta_{J=1\alpha\beta}|^2 \\ |\beta_{J=2}|^2 \\ |\beta_{J=3}|^2 \end{pmatrix} = \frac{1}{45} \begin{pmatrix} 0 & 0 & 18 & 0 & 0 \\ 0 & 27 & 0 & 0 & 0 \\ -9 & 0 & 0 & 0 & 0 \\ 30 & -15 & -15 & 30 & -30 \\ -12 & -12 & -3 & 15 & 30 \end{pmatrix} \begin{pmatrix} [g\beta^2]_A \\ [g\beta^2]_B \\ [g\beta^2]_C \\ [g\beta^2]_D \\ [g\beta^2]_E \end{pmatrix}, \quad (2.36)$$

so that a matrix inversion in combination with Eq. (2.16) gives:

$$\langle \beta_{ZZZ}^2 \rangle = \frac{1}{30} |\beta_{J=1\alpha}|^2 + \frac{4}{45} |\beta_{J=1\beta}|^2 - \frac{4}{15} |\beta_{J=1\alpha\beta}|^2 + \frac{2}{35} |\beta_{J=3}|^2, \quad (2.37)$$

^bThis part was also performed thanks to symbolic calculus implemented in a home-made Python script.

$$\approx \frac{1}{5} |\beta_{J=1}|^2 + \frac{2}{35} |\beta_{J=3}|^2, \quad (2.38)$$

$$\langle \beta_{ZZX}^2 \rangle = \frac{2}{15} |\beta_{J=1\alpha}|^2 + \frac{1}{45} |\beta_{J=1\beta}|^2 + \frac{4}{15} |\beta_{J=1\alpha\beta}|^2 + \frac{1}{15} |\beta_{J=2}|^2 + \frac{4}{105} |\beta_{J=3}|^2, \quad (2.39)$$

$$\approx \frac{1}{45} |\beta_{J=1}|^2 + \frac{4}{105} |\beta_{J=3}|^2. \quad (2.40)$$

Again, Eqs. (2.38) and (2.40) are the version of the previous ones when the Kleinman's conditions are assumed, with:

$$|\beta_{J=1}|^2 = \frac{3}{5} \sum_{ijk}^{xyz} \beta_{ijj} \beta_{ikk}, \text{ and } |\beta_{J=3}|^2 = \sum_{ijk}^{xyz} \beta_{ijk}^2 - \frac{3}{5} \beta_{ijj} \beta_{ikk}. \quad (2.41)$$

A β -nonlinear anisotropy parameter can be defined to highlight the impact of the dipolar and octupolar contributions to β :^{10,12}

$$\rho_{3/1} = \sqrt{\frac{|\beta_{J=3}|^2}{|\beta_{J=1}|^2}}, \quad (2.42)$$

so that:

$$\text{DR}_{SHS} = \frac{18\rho_{3/1}^2 + 63}{12\rho_{3/1}^2 + 7}. \quad (2.43)$$

Therefore, in the static limit, if the NLOphore is purely dipolar ($\rho_{3/1} \rightarrow 0$), the depolarization ratio is equal to 9, while it amounts to $3/2$ if it is purely octupolar ($\rho_{3/1} \rightarrow \infty$).

Application to THS

The formula for the γ tensor in the specific case of THS can be found in Ref. 20 (based on the work in Ref. 25). This time, it results in six different irreducible tensors, two of which have $J = 2$. One ends up with 7 products:

$$|\gamma_{J=0}|^2 = \frac{1}{5} \sum_{ijkl}^{xyz} \gamma_{iijj} \gamma_{kkll}, \quad (2.44)$$

$$|\gamma_{J=1}|^2 = \frac{1}{10} \sum_{ijkl}^{xyz} 3\gamma_{ijjk} \gamma_{ikll} - 3\gamma_{ijjk} \gamma_{kill}, \quad (2.45)$$

$$|\gamma_{J=2\alpha}|^2 = \frac{1}{42} \sum_{ijkl}^{xyz} 15\gamma_{ijjk} \gamma_{kill} + 15\gamma_{ijjk} \gamma_{ikll} - 10\gamma_{iijj} \gamma_{kllk}, \quad (2.46)$$

$$|\gamma_{J=2\beta}|^2 = \frac{1}{21} \sum_{ijkl}^{xyz} 15\gamma_{iijk} \gamma_{ljlk} - 5\gamma_{iijj} \gamma_{kllk}, \quad (2.47)$$

$$|\gamma_{J=2\alpha\beta}|^2 = \frac{1}{21} \sum_{ijkl}^{xyz} 2\gamma_{iijj}\gamma_{kllk} - 6\gamma_{iijk}\gamma_{jllk}, \quad (2.48)$$

$$|\gamma_{J=3}|^2 = \frac{1}{20} \sum_{ijkl}^{xyz} \left\{ \begin{array}{l} 15\gamma_{ijkl}^2 + 20\gamma_{iijk}\gamma_{jllk} + \gamma_{iijk}\gamma_{kill} \\ -10\gamma_{iijk}\gamma_{ljlk} - 15\gamma_{ijkl}\gamma_{jikl} - 11\gamma_{iijk}\gamma_{ikll} \end{array} \right\}, \quad (2.49)$$

$$|\gamma_{J=4}|^2 = \frac{1}{140} \sum_{ijkl}^{xyz} \left\{ \begin{array}{l} 35\gamma_{ijkl}^2 + 105\gamma_{ijkl}\gamma_{jikl} + 12\gamma_{iijj}\gamma_{kllk} \\ -60\gamma_{iijk}\gamma_{jllk} - 30\gamma_{iijk}\gamma_{ljlk} - 15\gamma_{iijk}\gamma_{ikll} - 15\gamma_{iijk}\gamma_{kill} \end{array} \right\}. \quad (2.50)$$

Or, in a matrix shape:

$$\begin{pmatrix} |\gamma_{J=0}|^2 \\ |\gamma_{J=1}|^2 \\ |\gamma_{J=2\alpha}|^2 \\ |\gamma_{J=2\beta}|^2 \\ |\gamma_{J=2\alpha\beta}|^2 \\ |\gamma_{J=3}|^2 \\ |\gamma_{J=4}|^2 \end{pmatrix} = \frac{1}{420} \begin{pmatrix} 84 & 0 & 0 & 0 & 0 & 0 & 0 \\ 0 & 0 & 0 & 126 & 0 & -126 & 0 \\ -100 & 0 & 0 & 150 & 0 & 150 & 0 \\ -100 & 0 & 300 & 0 & 0 & 0 & 0 \\ 40 & -120 & 0 & 0 & 0 & 0 & 0 \\ 0 & 420 & -210 & -231 & 315 & 21 & -315 \\ 36 & -180 & -90 & -45 & 105 & -45 & 315 \end{pmatrix} \begin{pmatrix} [g\gamma^2]_A \\ [g\gamma^2]_B \\ [g\gamma^2]_C \\ [g\gamma^2]_D \\ [g\gamma^2]_E \\ [g\gamma^2]_F \\ [g\gamma^2]_G \end{pmatrix}. \quad (2.51)$$

The inversion of the coefficient matrix in combination with Eq. (2.22) gives:

$$\langle \gamma_{ZZZZ}^2 \rangle = \frac{1}{5} |\gamma_{J=0}|^2 + \frac{6}{175} |\gamma_{J=2\alpha}|^2 + \frac{6}{175} |\gamma_{J=2\beta}|^2 - \frac{6}{35} |\gamma_{J=2\alpha\beta}|^2 + \frac{8}{315} |\gamma_{J=4}|^2, \quad (2.52)$$

$$\approx \frac{1}{5} |\gamma_{J=0}|^2 + \frac{4}{35} |\gamma_{J=2}|^2 + \frac{8}{315} |\gamma_{J=4}|^2, \quad (2.53)$$

$$\langle \gamma_{ZXXX}^2 \rangle = \frac{1}{10} |\gamma_{J=1}|^2 + \frac{1}{14} |\gamma_{J=2\alpha}|^2 + \frac{2}{175} |\gamma_{J=2\beta}|^2 + \frac{1}{7} |\gamma_{J=2\alpha\beta}|^2 + \frac{1}{35} |\gamma_{J=3}|^2 + \frac{1}{63} |\gamma_{J=4}|^2, \quad (2.54)$$

$$\approx \frac{3}{140} |\gamma_{J=2}|^2 + \frac{1}{63} |\gamma_{J=4}|^2. \quad (2.55)$$

where Eqs. (2.54) and (2.55) are the version of the previous ones when the Kleinman's conditions are assumed, with:

$$|\gamma_{J=2}|^2 = \frac{1}{7} \sum_{ijkl}^{xyz} 6\gamma_{iijk}\gamma_{jklk} - 2\gamma_{iijj}\gamma_{kkll}, \quad (2.56)$$

$$|\gamma_{J=4}|^2 = \frac{1}{35} \sum_{ijkl}^{xyz} 35\gamma_{ijkl}^2 - 30\gamma_{iijk}\gamma_{jklk} + 3\gamma_{iijj}\gamma_{kkll}. \quad (2.57)$$

The γ -nonlinear anisotropy parameters:

$$\rho_{0/2} = \sqrt{\frac{|\gamma_{J=0}|}{|\gamma_{J=2}|}} \text{ and } \rho_{4/2} = \sqrt{\frac{|\gamma_{J=4}|}{|\gamma_{J=2}|}} \quad (2.58)$$

compare the relative contributions of the different components of the second hyperpolarizability tensor with each other. The THS depolarization ratio (Eq. 2.5) is rewritten as:

$$\text{DR}_{THS} = \frac{32\rho_{4/2}^2 + 252\rho_{0/2}^2 + 144}{20\rho_{4/2}^2 + 27}. \quad (2.59)$$

When $\rho_{4/2} \rightarrow \infty$, DR_{THS} converges to the hexadecapolar limit, $8/5$. However, when $\rho_{4/2} \rightarrow 0$, the limit value depends on $\rho_{0/2}$, since:

$$\text{DR}'_{THS} = \lim_{\rho_{4/2} \rightarrow 0} \text{DR}_{THS} = \frac{28}{3}\rho_{0/2}^2 + \frac{16}{3}, \quad (2.60)$$

so that the DR tends to the “pure” quadrupolar limit of $16/3$ when $\rho_{0/2} \rightarrow 0$, and to ∞ when $\rho_{0/2} \rightarrow \infty$, *i.e.*, in the isotropic limit. These relationships, together with Eq. (2.43), are explored in more details in Chapter 5.

Bibliography

- [1] Heisenberg, W. Über den anschaulichen Inhalt der quantentheoretischen Kinematik und Mechanik. *Z. Phys.* **1927**, 43, 172–198.
- [2] Roberts, B. W.; Butterfield, J. Time-Energy Uncertainty Does Not Create Particles. *J. Phys. Conf. Ser.* **2020**, 1638, 012005.
- [3] Norman, P.; Bishop, D. M.; Jensen, H. J. A.; Oddershede, J. Nonlinear Response Theory with Relaxation: The First-Order Hyperpolarizability. *J. Chem. Phys.* **2005**, 123, 194103.
- [4] Norman, P. A Perspective on Nonresonant and Resonant Electronic Response Theory for Time-Dependent Molecular Properties. *Phys. Chem. Chem. Phys.* **2011**, 13, 20519.
- [5] Shelton, D. P.; Rice, J. E. Measurements and Calculations of the Hyperpolarizabilities of Atoms and Small Molecules in the Gas Phase. *Chem. Rev.* **1994**, 94, 3–29.
- [6] Shelton, D. P. Gas Phase Hyper-Rayleigh Scattering Measurements. *J. Chem. Phys.* **2012**, 137, 044312.
- [7] Rodriguez, M. B.; Shelton, D. P. What Is Measured by Hyper-Rayleigh Scattering from a Liquid? *J. Chem. Phys.* **2018**, 148, 134504.
- [8] Andrews, D. L. Harmonic Generation in Free Molecules. *J. Phys. B* **1980**, 13, 4091.
- [9] Heesink, G. J. T.; Ruiter, A. G. T.; van Hulst, N. F.; Bölger, B. Determination of Hyperpolarizability Tensor Components by Depolarized Hyper Rayleigh Scattering. *Phys. Rev. Lett.* **1993**, 71, 999–1002.
- [10] Verbiest, T.; Clays, K.; Rodriguez, V. *Second-Order Nonlinear Optical Characterization Techniques: An Introduction*; Taylor & Francis, 2009.
- [11] Rodriguez, V. Polarization-Resolved Third-Harmonic Scattering in Liquids. *J. Phys. Chem. C* **2017**, 121, 8510–8514.
- [12] Castet, F.; Bogdan, E.; Plaquet, A.; Ducasse, L.; Champagne, B.; Rodriguez, V. Reference Molecules for Nonlinear Optics: A Joint Experimental and Theoretical Investigation. *J. Chem. Phys.* **2012**, 136, 024506.
- [13] Clays, K.; Persoons, A. Hyper-Rayleigh Scattering in Solution. *Phys. Rev. Lett.* **1991**, 66, 2980–2983.
- [14] Hendrickx, E.; Clays, K.; Persoons, A. Hyper-Rayleigh Scattering in Isotropic Solution. *Acc. Chem. Res.* **1998**, 31, 675–683.
- [15] Kaatz, P.; Donley, E. A.; Shelton, D. P. A Comparison of Molecular Hyperpolarizabilities from Gas and Liquid Phase Measurements. *J. Chem. Phys.* **1998**, 108, 849–856.

- [16] Whittall, I. R.; McDonagh, A. M.; Humphrey, M. G.; Samoc, M. In *Advances in Organometallic Chemistry*; Stone, F. G. A., West, R., Eds.; Academic Press, 1998; Vol. 42; pp 291–362.
- [17] De Meulenaere, E.; de Coene, Y.; Russier-Antoine, I.; Vanpraet, L.; Van den Haute, C.; Thevissen, K.; Baekelandt, V.; Bartic, C.; Hofkens, J.; Brevet, P.-F.; Clays, K. Fluorescence-Free First Hyperpolarizability Values of Fluorescent Proteins and Channel Rhodopsins. *J. Photochem. Photobiol. A* **2020**, *400*, 112658.
- [18] Andrews, S. S. Using Rotational Averaging To Calculate the Bulk Response of Isotropic and Anisotropic Samples from Molecular Parameters. *J. Chem. Educ.* **2004**, *81*, 877.
- [19] Andrews, D. L.; Thirunamachandran, T. On Three-dimensional Rotational Averages. *J. Chem. Phys.* **1977**, *67*, 5026–5033.
- [20] Ford, J. S.; Andrews, D. L. Molecular Tensor Analysis of Third-Harmonic Scattering in Liquids. *J. Phys. Chem. A* **2018**, *122*, 563–573.
- [21] Andrews, D. L.; Ghoul, W. A. Eighth Rank Isotropic Tensors and Rotational Averages. *J. Phys. A* **1981**, *14*, 1281.
- [22] Cyvin, S. J.; Rauch, J. E.; Decius, J. C. Theory of Hyper-Raman Effects (Nonlinear Inelastic Light Scattering): Selection Rules and Depolarization Ratios for the Second-Order Polarizability. *J. Chem. Phys.* **1965**, *43*, 4083–4095.
- [23] Coope, J. A. R.; Snider, R. F. Irreducible Cartesian Tensors. II. General Formulation. *J. Math. Phys.* **1970**, *11*, 1003–1017.
- [24] Coope, J. A. R. Irreducible Cartesian Tensors. III. Clebsch-Gordan Reduction. *J. Math. Phys.* **1970**, *11*, 1591–1612.
- [25] Andrews, D. L.; Ghoul, W. A. Irreducible Fourth-Rank Cartesian Tensors. *Phys. Rev. A* **1982**, *25*, 2647–2657.
- [26] Mihailov, V. V. Addition of Arbitrary Number of Identical Angular Momenta. *J. Phys. A* **1977**, *10*, 147.
- [27] Andrews, D. L. Symmetry Characterization in Molecular Multiphoton Spectroscopy. *Spectrochim. Acta A* **1990**, *46*, 871–885.
- [28] Andrews, D. L.; Blake, N. P. Three-Dimensional Rotational Averages in Radiation-Molecule Interactions: An Irreducible Cartesian Tensor Formulation. *J. Phys. A* **1989**, *22*, 49.

Quantum chemistry methods

Abstract

In Chapter 3, one introduces the theoretical concepts and methods. Owing the large number of methods used in our work, this chapter is divided in different sections. The first one is dedicated to the wavefunction approach of quantum mechanics and discusses the Hartree-Fock (HF) method and its extensions. In the second part, the density functional theory (DFT) approach of quantum mechanics is presented. Then, in the third section, one tackles the calculation of molecular properties, either through numerical differentiation or response functions. Finally, the last section introduces methods to include the effects of surroundings.

Note. Atomic units are used in the chapter.

Section 3.1

The wavefunction approaches

In quantum chemistry, the goal is to describe the evolution of a (molecular) system in time and space. One way to achieve such goal is to solve the non-relativistic time-dependent Schrödinger equation:¹

$$\hat{H}\Psi = i\frac{\partial}{\partial t}\Psi, \quad (3.1)$$

where the system is described by a wavefunction, $\Psi(\{\mathbf{r}_p\}, t)$, depending on the positions of the particles, $\{\mathbf{r}_p\}$, and time, t . \hat{H} is the Hamiltonian operator, which basically describes the interactions between the different particles, as well as the impact of a possible environment. Stationary states of the system are thus obtained by solving the time-independent Schrödinger equation:

$$\hat{H}\Psi_i = E_i \Psi_i, \quad (3.2)$$

an eigenvalue problem in which $\{E_i\}$ are the eigenvalues (energies) of the system described by the eigenfunctions $\{\Psi_i\}$, which contain all information on the system at a given time t . The goal of quantum chemistry is therefore to obtain both eigenstates and corresponding eigenfunctions.

The Hamiltonian may be decomposed into:

$$\hat{H} = \hat{T} + \hat{V} + \hat{H}_{ext}, \quad (3.3)$$

where \hat{H}_{ext} describes the influence of the environment, which is assumed to be zero for the moment and addressed in the last section, \hat{T} is the kinetic energy operator, which for a system of N_p particles is written as:

$$\hat{T} = -\frac{1}{2} \sum_p^{N_p} \frac{1}{m_p} \nabla_p^2, \quad (3.4)$$

where m_p is the mass of the particle and ∇_p^2 is the Laplacian. \hat{V} is the potential energy operator, which is due in this case to Coulombic interactions between the N_p particles of charge q_p :

$$\hat{V} = \sum_{P<Q}^N \frac{q_P q_Q}{|\mathbf{r}_P - \mathbf{r}_Q|}, \quad (3.5)$$

For a molecular system, one distinguishes between two types of particles: electrons (e) and nuclei (N), so

$$\hat{T} = \overbrace{-\frac{1}{2} \sum_A^{N_N} \frac{1}{m_A} \nabla_A^2}^{\hat{T}_N} - \overbrace{\frac{1}{2} \sum_i^{N_e} \nabla_i^2}^{\hat{T}_e}, \quad (3.6)$$

$$\hat{V} = \underbrace{\sum_{A < B}^{N_N} \frac{Z_A Z_B}{|\mathbf{r}_A - \mathbf{r}_B|}}_{\hat{V}_{NN}} + \underbrace{\sum_{i < j}^{N_e} \frac{1}{|\mathbf{r}_i - \mathbf{r}_j|}}_{\hat{V}_{ee}} + \underbrace{\sum_i^{N_e} \sum_A^{N_N} \frac{-Z_A}{|\mathbf{r}_i - \mathbf{r}_A|}}_{\hat{V}_{Ne}}, \quad (3.7)$$

where N_N and N_e are the numbers of nuclei and electrons, respectively.

Although exact (in the non-relativistic framework), the Schrödinger equation gets difficult to solve when the number of particles exceeds 2. The goal of the following sections is therefore to explore how to get (reliable) approximate solutions to the problem. Before that, the **Born-Oppenheimer approximation**² proposes to separate the total wavefunction into its nuclear and electronic parts, the latter taking the nuclear coordinates as parameters. This allows one to focus on the electronic Hamiltonian, \hat{H}_e :

$$\hat{H}_e = \hat{T}_e + \hat{V}_{ee} + \hat{V}_{Ne} = -\frac{1}{2} \sum_i^{N_e} \nabla_i^2 + \sum_{i < j}^{N_e} \frac{1}{|\mathbf{r}_i - \mathbf{r}_j|} + \sum_i^{N_e} \sum_A^{N_N} \frac{-Z_A}{|\mathbf{r}_i - \mathbf{r}_A|}. \quad (3.8)$$

For now on, one will focus on the electronic Hamiltonian and its corresponding electronic wavefunction, so the e indices are now dropped for clarity.

Furthermore, since electrons are fermions, the electronic wavefunction should be antisymmetric with respect to the exchange of the coordinates of any pair of electrons (this introduces the so-called Fermi correlation). This property could be fulfilled if one expresses this wavefunction as a **Slater determinant** (or a combination of Slater determinants),³⁻⁵

$$\Psi(\{\mathbf{x}_i\}) = \frac{1}{\sqrt{N!}} \begin{vmatrix} \Theta_1(\mathbf{x}_1) & \Theta_1(\mathbf{x}_2) & \cdots & \Theta_1(\mathbf{x}_N) \\ \Theta_2(\mathbf{x}_1) & \Theta_2(\mathbf{x}_2) & \cdots & \Theta_2(\mathbf{x}_N) \\ \vdots & \vdots & \ddots & \vdots \\ \Theta_N(\mathbf{x}_1) & \Theta_N(\mathbf{x}_2) & \cdots & \Theta_N(\mathbf{x}_N) \end{vmatrix}, \quad (3.9)$$

built out of the occupied spinorbitals, $\Theta_i(\mathbf{x}_1) = \psi_i(\mathbf{r}_1) \sigma_i(\omega_1)$, which are one-electron wavefunctions, \mathbf{r}_1 being the spatial coordinate and ω_1 , the spin coordinate, which may be either up or down (α or β).

The variational principle

Within the framework presented in the previous section, solving the Schrödinger equation would result in finding the combination of spinorbitals so that the corresponding Slater determinant is the best approximation of the ground state wavefunction, Ψ_0 , associated with \hat{H} , if a method to get it was available. The variational principle^{6,7} defines such a road towards Ψ_0 (it is actually more general than this specific case). Indeed, it states that any normalized trial wavefunction, $\tilde{\Psi}$, has a higher energy than the exact ground state energy E_0 :

$$\langle \tilde{\Psi} | \hat{H} | \tilde{\Psi} \rangle \geq E_0 = \langle \Psi_0 | \hat{H} | \Psi_0 \rangle, \quad (3.10)$$

so that the problem actually translates into minimizing the energy of a trial wavefunction.

The Hartree-Fock (HF) method

The HF method proposed by Hartree and Fock⁸⁻¹¹ arises from applying the variational principle to a wavefunction described by one single Slater determinant. For a system with N electrons, the HF method relies on the Fock equation which is, for one spinorbital Θ_i , written as:

$$\hat{f}(\mathbf{r}_1)\Theta_i(\mathbf{x}_1) = \varepsilon_i\Theta_i(\mathbf{x}_1) \quad (3.11)$$

where \hat{f} is the one-electron Fock operator^{12,13} and ε_i , the energy of the spinorbital. \hat{f} can be decomposed in two parts:

$$\hat{f}(\mathbf{r}_1) = \hat{h}(\mathbf{r}_1) + \hat{V}^{HF}(\mathbf{r}_1) \quad (3.12)$$

where:

$$\hat{h}(\mathbf{r}_1) = -\frac{1}{2}\nabla_1^2 - \sum_A^{N_N} \frac{Z_A}{|\mathbf{r}_1 - \mathbf{r}_A|} \quad (3.13)$$

is an operator accounting for the kinetic energy and nuclear attraction of electron 1, while \hat{V}^{HF} is the HF potential, which accounts for the potential experienced by electron 1 arising from the environment constituted by all other electrons, defined as:

$$\hat{V}^{HF}(\mathbf{r}_1) = \sum_j^N \hat{J}_j(\mathbf{r}_1) - \hat{K}_j(\mathbf{r}_1). \quad (3.14)$$

where the sum runs over all other electrons, *i.e.*, over all the occupied spinorbitals. \hat{J}_j is the Coulomb operator, which computes the average Coulomb potential due to the electrons in the spinorbitals Θ_j , defined as:

$$\hat{J}_j(\mathbf{r}_1)\Theta_i(\mathbf{x}_1) = \left[\int d\mathbf{x}_2 \frac{\Theta_j^*(\mathbf{x}_2)\Theta_j(\mathbf{x}_2)}{|\mathbf{r}_1 - \mathbf{r}_2|} \right] \Theta_i(\mathbf{x}_1). \quad (3.15)$$

\hat{K}_j is the exchange operator, defined as

$$\hat{K}_j(\mathbf{r}_1)\Theta_i(\mathbf{x}_1) = \left[\int d\mathbf{x}_2 \frac{\Theta_j^*(\mathbf{x}_2)\Theta_i(\mathbf{x}_2)}{|\mathbf{r}_1 - \mathbf{r}_2|} \right] \Theta_j(\mathbf{x}_1). \quad (3.16)$$

It comes from the antisymmetric nature of the wavefunction, and only appears for spinorbitals with the same spin function.

Therefore,

$$E^{HF} = \langle \Psi | \hat{f} | \Psi \rangle + E_{NN} = \sum_i^N \left\{ h_{ii} + \sum_j^N J_{ij} - K_{ij} \right\} + \sum_{A < B}^{N_N} \frac{Z_A Z_B}{|\mathbf{r}_A - \mathbf{r}_B|}, \quad (3.17)$$

where:

$$h_{ii} = \langle \Theta_i(\mathbf{x}_1) | \hat{h}(\mathbf{r}_1) | \Theta_i(\mathbf{x}_1) \rangle, \quad (3.18)$$

$$J_{ij} = \langle \Theta_i(\mathbf{x}_1) | \hat{J}_j(\mathbf{r}_1) | \Theta_i(\mathbf{x}_1) \rangle = \langle ij | ij \rangle = (ii | jj), \quad (3.19)$$

$$K_{ij} = \langle \Theta_i(\mathbf{x}_1) | \hat{K}_j(\mathbf{r}_1) | \Theta_i(\mathbf{x}_1) \rangle = \langle ij | ji \rangle = (ij | ij), \quad (3.20)$$

obtained through integration over spin and space. $(ii | jj)$ is the Mulliken notation for the corresponding two-electron integrals over spatial orbitals instead of spinorbitals.

With respect to the exact energy, E^{exact} , that would be obtained using the Hamiltonian in Eq. (3.8), the HF method introduces an error called **electron correlation**, $E^{corr} = E^{exact} - E^{HF}$.^{14,15} The sources of error are twofold. First, each eigenstate of the system (including the ground state) is described by a single Slater determinant, where for some systems, more would be needed, which is the so-called “static” electron correlation error. Then, the \hat{J}_j operator only considers the interaction of one electron with the mean field created by the others, it is referred to as the “dynamic” correlation error (also referred to as Coulomb correlation). Both the post-HF methods and density functional theory that are introduced later tackle the electron correlation issue.

The LCAO approximation and Roothaan-Hall formulation of HF

Although it introduces a nice analytic framework, Eq. (3.11) remains difficult to solve for complex systems. It is customary to introduce the Linear Combination of Atomic Orbitals (LCAO) approximation,¹⁶ which states that the molecular orbitals, $\psi_i(\mathbf{r}_1)$, can be advantageously described as linear combinations of atomic orbitals forming a basis set of known (Slater) atomic orbitals $\{\varphi_\mu\}$:

$$\psi_i(\mathbf{r}_1) = \sum_{\mu}^K c_{\mu i} \varphi_{\mu}(\mathbf{r}_1), \quad (3.21)$$

where the $c_{i\mu}$ are the LCAO coefficients and K is the size of the basis set. Introducing this definition into Eq. (3.11) gives:

$$\hat{f}(\mathbf{r}_1) \sum_{\mu} c_{\mu i} \varphi_{\mu}(\mathbf{x}_1) = \varepsilon_i \sum_{\mu} c_{\mu i} \varphi_{\mu}(\mathbf{x}_1), \quad (3.22)$$

which, in matrix notation, transforms into the Roothaan-Hall equation:^{17,18}

$$\mathbf{FC} = \mathbf{SC}\varepsilon, \quad (3.23)$$

where \mathbf{F} is the Fock matrix, \mathbf{C} , the LCAO coefficient matrix, ε , a diagonal matrix containing the MO energies, and \mathbf{S} , the overlap matrix, $S_{\nu\mu} = \langle \varphi_{\mu} | \varphi_{\nu} \rangle$. They are $K \times K$ matrices. Since the Fock matrix depends on the solutions of the problem [the molecular orbitals, see Eq. (3.14)], the problem has to be solved iteratively to get the set of LCAO coefficients (which describe the HF wavefunction) that minimize the energy: the SCF-LCAO-MO cycle.

Using the definition of the density matrix elements,

$$\mathbf{D}_{\mu\nu} = \sum_i^N c_{\mu i} c_{\nu i}, \quad (3.24)$$

Eq. (3.17) becomes

$$E^{HF} = E_{NN} + \sum_{\mu\nu}^K \mathbf{D}_{\mu\nu} (\mathbf{H}_{\nu\mu} + \mathbf{F}_{\nu\mu}), \quad (3.25)$$

where:

$$\mathbf{F}_{\mu\nu} = \sum_{\zeta\eta}^K \mathbf{D}_{\eta\zeta} [2(\mu\nu|\eta\zeta) - (\mu\eta|\nu\zeta)], \text{ and } \mathbf{H}_{\mu\nu} = \langle \varphi_\mu | \hat{h} | \varphi_\nu \rangle, \quad (3.26)$$

Basis sets

When Slater-Type Orbitals ($\text{STO} \propto e^{-r}$) are used, the two-electron integrals of Eq. (3.26) may get difficult to solve. Gaussian Type Orbitals ($\text{GTO} \propto e^{-r^2}$) are usually used instead.¹⁹ To mimic STOs, a contraction of N_{cont} GTOs is used to form a basis function φ_μ . A GTO centered on nucleus A is defined as a so-called primitive function,²⁰

$$G_{nlm,\alpha_{\mu\kappa}}(\mathbf{r} - \mathbf{r}_A) = N_{nlm,\alpha_{\mu\kappa}} (r_x - r_{A,x})^n (r_y - r_{A,y})^l (r_z - r_{A,z})^m e^{-\alpha_{\mu\kappa} |\mathbf{r} - \mathbf{r}_A|^2},$$

$$\text{so that } \varphi_\mu(\mathbf{r}) = \sum_{\kappa}^{N_{cont}} c_{\mu\kappa} G_{lmn,\alpha_{\mu\kappa}}(\mathbf{r} - \mathbf{r}_A) \quad (3.27)$$

where $\alpha_{\mu\kappa}$ is the exponent (which controls the spread of the orbital), $N_{nlm,\alpha_{\mu\kappa}}$, a normalization factor, $c_{\mu\kappa}$, a coefficient depending on the contraction, and $L = n + l + m$ defines the angular momentum (or *shell*) to which the GTO belongs: in analogy to the quantum angular number, $L = 0$ defines *s*-type orbitals, $L = 1$ defines *p*-type orbitals and so on. Constructing a basis set then relies on these three concepts:

1. Minimal basis sets are constructed using one contraction per shell, they are called simple ζ (SZ). If the number of contractions per shell increases, the basis set is labeled *n*-tuple ζ : double ζ (DZ), triple ζ (TZ), ...
2. Then, as from the chemistry point of view valence orbitals are more affected in chemical processes than core orbitals, it is customary to define *split-valence* basis sets, which use a different (usually larger) number of contractions for valence orbitals than for core ones.
3. Finally, basis sets are generally augmented with two special types of GTOs: i) diffuse functions (with a very small exponent α), and ii) polarization functions (with higher values of L than those present in the ground state of the corresponding atom). The first one helps to describe long-distance interactions, while the latter are important for bond description.

In the present work, two main families of basis sets are used:

- The **Pople basis sets**.^{21,22} They are named from the number of contractions and primitives in each of them: the 6-31G basis set (“G” stands for Gaussian) consists in a single contraction (of 6 GTOs) for core orbitals together with 2 contractions (of 3 and 1 GTOs, respectively) for valence orbitals. From the number of contractions for the valence part, it is still referred as double ζ . Triple ζ basis sets also exist, like 6-311G.

Diffuse functions are marked using the “+” sign: the 6-31+G basis set adds diffuse functions to heavy (second row of the periodic table and later) atoms, while 6-31++G contains two sets of diffuse functions on heavy atoms and one on first-row atoms (mainly hydrogens).

Polarization functions are denoted using the shell type of the additional set of functions. For example, 6-31G(d) is a basis set in which d -type ($L = 2$) functions are added to heavy atoms. Extra refinements, like 6-31G(d,p) which add p -type orbitals to first-row atoms, are also possible. Note that an alternative notation for those basis sets is 6-31G* and 6-31G**.

- The **Dunning basis sets**,^{23,24} noted cc-pVXZ, where “cc” stands for *correlation consistent*, “p” for polarization functions (added on all atoms) and “XZ” refers to the number of contractions per shell: DZ, TZ, ... They may be augmented by diffuse functions : the aug-cc-pVXZ and d-aug-cc-pVXZ basis sets used in some part of our works include one and two sets of diffuse functions (on each atom), respectively.

Rayleigh-Schrödinger (RS) perturbation theory

The idea of RS theory^{25,26} is to split the Hamiltonian in two parts, $\hat{H}(\lambda) = \hat{H}_0 + \lambda \hat{V}$ ($\lambda \in [0, 1]$), so that Eq. (3.2) becomes:

$$(\hat{H}_0 + \lambda \hat{V}) \Psi_i = E_i \Psi_i, \quad (3.28)$$

in which \hat{H}_0 is an Hamiltonian for which the solutions, $\{\Psi_i^{(0)}\}$, are known, while \hat{V} is treated as a *perturbation* of such solutions: if $\lambda = 0$, $\Psi = \Psi^{(0)}$. As it is customary in physics and chemistry, if the perturbation is small, a (power) series in λ may be used:

$$\Psi_i = \sum_{k=0}^{\infty} \lambda^k \Psi_i^{(k)} = \Psi_i^{(0)} + \lambda \Psi_i^{(1)} + \dots \quad (3.29)$$

$$E_i = \sum_{k=0}^{\infty} \lambda^k E_i^{(k)} = E_i^{(0)} + \lambda E_i^{(1)} + \dots \quad (3.30)$$

where $\Psi_i^{(k)}$ [and corresponding $E_i^{(k)}$] is the correction at the k^{th} order of the wavefunction (energy) so that:

$$\Psi_i^{(k)} = \frac{1}{k!} \frac{\partial^k \Psi_i}{\partial \lambda^k} \text{ and } E_i^{(k)} = \frac{1}{k!} \frac{\partial^k E_i}{\partial \lambda^k}. \quad (3.31)$$

Note that $\Psi_i^{(k)}$ has to be expressed on the same basis as $\Psi^{(0)}$. Assuming $\langle \Psi_i^{(0)} | \Psi_i^{(k)} \rangle = \delta_{0k}$ (to get $\langle \Psi_i | \Psi_i^{(0)} \rangle = 1$, which is the so-called intermediate normalization condition),

$$\Psi_i^{(k)} = \sum_{\mu} c_{\mu i}^{(k)} \Psi_{\mu}^{(0)} = \sum_{\mu \neq i} \langle \Psi_{\mu}^{(0)} | \Psi_i^{(k)} \rangle \Psi_{\mu}^{(0)}. \quad (3.32)$$

Introducing Eqs. (3.29) and (3.30) into Eq. (3.28) results in:

$$(\hat{H}_0 + \lambda \hat{V}) \left\{ \sum_{k=0}^{\infty} \lambda^k \Psi_i^{(k)} \right\} = \left\{ \sum_{k=0}^{\infty} \lambda^k \Psi_i^{(k)} \right\} \left\{ \sum_{l=0}^{\infty} \lambda^l E_i^{(l)} \right\}, \quad (3.33)$$

which, by grouping terms of same power in λ and setting $\lambda = 1$, results in a set of k equations of the form:

$$\hat{H}_0 \Psi_i^{(k)} + \hat{V} \Psi_i^{(k-1)} - \sum_{l=0}^k E_i^{(l)} \Psi_i^{(k-l)} = 0. \quad (3.34)$$

Multiplying the previous equation to the left by $\Psi_i^{(0)}$ and integrating over space results in:

$$E_i^{(k)} = \begin{cases} \langle \Psi_i^{(0)} | \hat{H}_0 | \Psi_i^{(0)} \rangle & \text{if } k = 0, \\ \langle \Psi_i^{(0)} | \hat{V} | \Psi_i^{(k-1)} \rangle & \text{if } k > 0. \end{cases} \quad (3.35)$$

Therefore, to get the perturbed energy at order k , it is mandatory to know the wavefunction up to order $k-1$. For example, in order to get energy up to order 2, one needs the perturbed contribution to the wavefunction of order 1. The procedure is thus the following: taking Eq. (3.34) for $k = 1$, multiplying the previous to the left by $\Psi_j^{(0)}$ (with $j \neq i$) and integrating over space yields:

$$\langle \Psi_j^{(0)} | \hat{V} | \Psi_i^{(0)} \rangle = (E_i^{(0)} - E_j^{(0)}) \langle \Psi_j^{(0)} | \Psi_i^{(1)} \rangle \Leftrightarrow \langle \Psi_j^{(0)} | \Psi_i^{(1)} \rangle = \frac{\langle \Psi_j^{(0)} | \hat{V} | \Psi_i^{(0)} \rangle}{E_i^{(0)} - E_j^{(0)}}, \quad (3.36)$$

which gives an expression for the overlap to insert into Eq. (3.32),

$$\Psi_i^{(1)} = \sum_{\mu \neq i} \frac{\langle \Psi_{\mu}^{(0)} | \hat{V} | \Psi_i^{(0)} \rangle}{E_i^{(0)} - E_{\mu}^{(0)}} \Psi_{\mu}^{(0)}. \quad (3.37)$$

Finally, with Eq. (3.35),

$$E_i^{(1)} = \langle \Psi_i^{(0)} | \hat{V} | \Psi_i^{(0)} \rangle, \text{ and } E_i^{(2)} = \sum_{\mu \neq i} \frac{|\langle \Psi_{\mu}^{(0)} | \hat{V} | \Psi_i^{(0)} \rangle|^2}{E_i^{(0)} - E_{\mu}^{(0)}}. \quad (3.38)$$

One can carry out this procedure further, up to any order. Note that the first equality is the Hellmann-Feynman theorem.²⁷

Møller-Plesset (MP) perturbation theory

To apply the RS perturbation theory to the electron correlation problem,²⁸ the perturbation is considered to be the difference between the exact Hamiltonian of Eq. (3.8) and the sum of the one-electron Fock operators defined in Eq. (3.12). This turns out to be the difference between the two-electron operators, so that:

$$\hat{H}_0 = \sum_i \hat{f}(\mathbf{r}_i), \text{ and } \hat{V} = \sum_{i<j} \frac{1}{|\mathbf{r}_i - \mathbf{r}_j|} - \hat{V}^{HF}(\mathbf{r}_i). \quad (3.39)$$

From the corrections defined in Eq. (3.38), one recognizes that $E^{HF} = E^{(0)} + E^{(1)}$. The first correction to the HF energy is therefore coming from order 2, where:

$$E_0^{(2)} = \sum_{a<b}^{occ} \sum_{r<s}^{unocc} \frac{|\langle rs||ab \rangle|^2}{\varepsilon_r - \varepsilon_a + \varepsilon_s - \varepsilon_b}, \quad (3.40)$$

in which:

$$\langle rs||ab \rangle = (ab|rs) - (ar|bs) \quad (3.41)$$

is a shorthand notation for two-electron integrals on occupied spinorbitals a and b and unoccupied spinorbitals r and s (of energy ε_r and ε_s). It can thus be interpreted as the contribution of doubly-excited configurations. The MP2 energy of the ground state is given by:

$$E_0^{MP2} = E^{HF} + E_0^{(2)}. \quad (3.42)$$

MP2 is an important step towards including dynamic electron correlation: although more cost-intensive compared to HF (K^5 versus K^3), it may be used on moderate-size systems (nowadays, up to 100 atoms), so it will be used as a reference when Coupled Cluster (see next subsection) is not possible. Moreover, unlike variational methods, the convergence of MPn with respect to the exact energy is not guaranteed, so one will limit ourselves to the second-order correction.

Coupled Cluster (CC) theory

To push further the quest for an accurate description of the exact wavefunction in terms of one electron wavefunction, Čížek²⁹ later proposed to express the wavefunction as the exponential ansatz (educated guess) of a reference wavefunction, here the Hartree-Fock one:

$$\Psi^{CC} = e^{\hat{T}} \Psi^{HF}, \quad (3.43)$$

where \hat{T} is the so-called cluster operator:

$$\hat{T} = \sum_{i=1}^{\infty} \hat{T}_i \quad (3.44)$$

in which \hat{T}_i is the operator of all i -tuple excited configurations. This operator is often truncated: for example, if the excitations are limited to the single and double ones³⁰ (this is referred to as the CCSD level),

$$\hat{T}_1 = \sum_a^{\text{occ}} \sum_r^{\text{unocc}} t_a^r \hat{a}_r^\dagger \hat{a}_a, \text{ and } \hat{T}_2 = \frac{1}{4} \sum_{ab}^{\text{occ}} \sum_{rs}^{\text{unocc}} t_{ab}^{rs} \hat{a}_b^\dagger \hat{a}_r^\dagger \hat{a}_a \hat{a}_b, \quad (3.45)$$

which consists in a sum over occupied (unoccupied) spinorbitals a and b (r and s) where, from second quantization, one recognizes \hat{a}^\dagger and \hat{a} as the creation and annihilation operators (of spinorbitals), respectively. For example,

$$\hat{T}_1 \Psi = \sum_a^{\text{occ}} \sum_r^{\text{unocc}} t_a^r \Psi_a^r, \quad (3.46)$$

where Ψ_a^r is obtained by moving (annihilating) an electron from the occupied spinorbital a to the unoccupied spinorbital r . The t 's are therefore the amplitudes for each corresponding excited configurations or Slater determinants, which are the unknowns of the method. Note that, by virtue of Taylor series, truncating the cluster operators to double excitation does not only include the so-called *connected* single and double excitations (\hat{T}_1 and \hat{T}_2), but also combinations of them: the *disconnected* doubles (\hat{T}_1^2), triples ($\hat{T}_1 \hat{T}_2$), quadruples (\hat{T}_2^2), and so on:

$$e^{\hat{T}_1 + \hat{T}_2} = 1 + (\hat{T}_1 + \hat{T}_2) + \frac{1}{2} (\hat{T}_1^2 + \hat{T}_2^2 + 2\hat{T}_1 \hat{T}_2) + \dots \quad (3.47)$$

The CC energy is given by:

$$E^{CC} = \langle \Psi^{HF} | e^{-\hat{T}} \hat{H} e^{\hat{T}} | \Psi^{HF} \rangle, \quad (3.48)$$

which, using the Baker-Campbell-Hausdorff (BCH) expansion, gives:

$$E^{CC} = E^{HF} + \langle \Psi^{HF} | [\hat{H}, \hat{T}_2] | \Psi^{HF} \rangle + \frac{1}{2} \langle \Psi^{HF} | [[\hat{H}, \hat{T}_1], \hat{T}_1] | \Psi^{HF} \rangle. \quad (3.49)$$

Indeed, cluster operators higher than double do not contribute to energy, because of Brillouin's theorem.³¹ To determine the amplitudes, the variational principle (through Lagrange's multipliers, see below) is used: it results in a set of equations of the form:

$$\forall i > 0 : \langle \mu_i | e^{-\hat{T}} \hat{H} e^{\hat{T}} | \Psi^{HF} \rangle = 0, \quad (3.50)$$

where $\{\mu_i\}$ is the set of all possible i -tuple excited Slater determinants. For example, introducing the \hat{T}_1 transformed Hamiltonian as $\hat{\hat{H}} = e^{-\hat{T}_1} \hat{H} e^{\hat{T}_1}$, the CCSD amplitudes ($i = 1, 2$) are determined by solving

$$\langle \mu_1 | \hat{\hat{H}} + [\hat{\hat{H}}, \hat{T}_2] | \Psi^{HF} \rangle = 0, \quad (3.51)$$

$$\langle \mu_2 | \hat{\hat{H}} + [\hat{\hat{H}}, \hat{T}_2] + \frac{1}{2} [[\hat{\hat{H}}, \hat{T}_2], \hat{T}_2] | \Psi^{HF} \rangle = 0. \quad (3.52)$$

CCSD allows obtaining very accurate energies and properties, but is very cost demanding (K^6 in its iterative version). In order to get an approximation of the impact of double excitations, the second-order approximate coupled cluster single and double model (CC2) may be used instead:³² the idea is the same as in MP theory, which uses the same partition as in Eq. (3.39) (here, the “perturbation” operator \hat{V} is also referred to as the fluctuation operator). Therefore, instead of Eq. (3.52), the following set of equations are solved together with the ones of Eq. (3.51) to give the CC2 amplitudes:

$$\langle \mu_2 | \hat{H} + [\hat{f}, \hat{T}_2] \rangle = 0, \quad (3.53)$$

in which only connected doubles are considered. This gives results of similar quality as MP2 for the energies (both method includes only parts of the double excitations), while it allows using the response function framework, developed later in Section 3.3.

The same idea is found behind CC3,³³ which adds to Eqs. (3.51) and (3.52) terms and equations to account for the impact of (connected) triples to the amplitudes. This results in the hierarchy of CC methods used in this work:

$$\text{CCS} < \text{CC2} < \text{CCSD} < \text{CC3}.$$

Note that if only single excitations are considered, Eq. (3.49) reduces to $E^{\text{CCS}} = E^{\text{HF}}$.

Section 3.2

The density functional theory (DFT) approach

In opposition to the wavefunction approach, the one-electron density $\rho(\mathbf{r}_1)$ is used instead of Ψ . It is obtained from the integration of the square of the norm of the wavefunction over all position and spin coordinates, except one spatial, \mathbf{r}_1 :

$$\rho(\mathbf{r}_1) = N \int \cdots \int d\omega_1 d\mathbf{x}_2 \dots d\mathbf{x}_N |\Psi(\{\mathbf{x}_i\})|^2, \text{ with } N = \int d\mathbf{r} \rho(\mathbf{r}). \quad (3.54)$$

where N is, again, the number of electrons. Even within the Born-Oppenheimer approximation, solving the Schrödinger equation with the electron density requires some guarantees. They are provided, for the ground state, by the two theorems of Hohenberg and Kohn:³⁴

1. *The external potential, V_{ext} , which, in the absence of electromagnetic field, corresponds to nuclei-electron interactions, is uniquely defined (within a trivial additive constant) by the electron density. Thus, the electronic energy is a functional of the density, written $E[\rho]$, and all properties depend on the electron density as well ;*
2. *The energy variational principle is valid for any electron density, so for a trial density ρ ,*

$$E[\rho] \geq E[\rho_0] \quad (3.55)$$

where, similarly to Eq. (3.10), ρ_0 is the exact ground-state density (with ground-state energy $E[\rho_0]$). Again, this principle paves the way towards getting the density and, subsequently, the properties of the system.

Main ideas

The energy is therefore decomposed into different contributions:

$$E[\rho] = E_{NN} + V_{ext}[\rho] + F_{HK}[\rho], \text{ with } F_{HK}[\rho] = T[\rho] + E_{ee}[\rho], \quad (3.56)$$

where E_{NN} is the nuclei-nuclei potential energy, while T is the electron kinetic energy and E_{ee} , the electron-electron potential energy. The last two terms are grouped in the Hohenberg-Kohn functional, F_{HK} . In fact, while E_{NN} is readily available (see above) and $V_{ext}[\rho]$ can be obtained from:

$$V_{ext}[\rho] = \int d\mathbf{r}_1 \hat{V}_{Ne}(\mathbf{r}_1) \rho(\mathbf{r}_1), \quad (3.57)$$

the explicit form of F_{HK} remains unknown. One of the issues is $T[\rho]$, for which there is no exact expression, except if one splits the term into a “non-interacting limit” case (electrons described by a Slater determinant), $T_s[\rho]$, and the remainder. This was the idea of Kohn and Sham,³⁵ which thus reintroduced the concept of spinorbitals into DFT, so that the density of Eq. (3.54) is redefined as:

$$\rho(\mathbf{r}_1) = \sum_i \int d\omega_i |\Theta_i(\mathbf{x}_1)|^2, \quad (3.58)$$

so that:

$$T_s[\rho] = -\frac{1}{2} \sum_i \langle \Theta_i(\mathbf{x}_1) | \nabla^2 | \Theta_i(\mathbf{x}_1) \rangle. \quad (3.59)$$

The, now Kohn-Sham (KS) functional is therefore rewritten:

$$F_{KS}[\rho] = T_s[\rho] + J[\rho] + E_{XC}[\rho], \quad (3.60)$$

where $J[\rho]$ is the Coulomb energy,

$$J[\rho] = \sum_i \langle \Theta_i(\mathbf{x}_1) | \hat{J}(\mathbf{r}_1) | \Theta_i(\mathbf{x}_1) \rangle, \text{ with } \hat{J}(\mathbf{r}_1) = \int d\mathbf{r}_2 \frac{\rho(\mathbf{r}_2)}{|\mathbf{r}_1 - \mathbf{r}_2|}, \quad (3.61)$$

and E_{XC} gathers the unknown parts of the kinetic and potential terms. The set of KS equations to be solved is therefore:

$$\hat{h}_{KS}(\mathbf{r}_1) \Theta_i(\mathbf{x}_1) = \varepsilon_i \Theta_i(\mathbf{x}_1), \quad (3.62)$$

with:

$$\hat{h}_{KS}(\mathbf{r}_1) = -\frac{1}{2} \nabla_1^2 + \underbrace{\hat{V}_{Ne}(\mathbf{r}_1) + \hat{J}(\mathbf{r}_1) + \hat{V}_{XC}(\mathbf{r}_1)}_{\hat{V}_{eff}(\mathbf{r}_1)}, \quad (3.63)$$

where \hat{V}_{eff} is the effective potential and \hat{V}_{XC} is the exchange-correlation (XC) potential, defined as:

$$\hat{V}_{XC}(\mathbf{r}_1) = \frac{\partial E_{XC}[\rho]}{\partial \rho(\mathbf{r}_1)}. \quad (3.64)$$

The expression of E_{XC} is computed from one of the so-called XC-functionals (XCF), which are the cornerstones of DFT. Since this theory can be readily expanded to encompass the LCAO principle, the equations can be expressed in a matrix formalism, similarly to Eq. (3.23), as:

$$\mathbf{F}_{KS} \mathbf{C} = \mathbf{S} \mathbf{C} \epsilon. \quad (3.65)$$

Since it shares similarity with HF, the quantum chemistry codes can be easily extended to include DFT, for a similar cost (computer-wise). Another reason for the popularity of DFT is that it can give better results than HF if the XCF is well chosen, since, contrary to HF, *some* electron correlation is included.

XC functionals

Since the beginning of DFT as a quantum chemistry method, many different XCFs have been developed, based on different underlying principles. In fact, for some functionals, the exchange and correlation functionals may have been developed separately and the XCFs are constructed by mixing the two parts together. For example, the BLYP functional is composed of the Becke³⁶ (B, or more precisely B88) exchange part and the Lee-Yang-Parr³⁷ (LYP) correlation part. All XCFs can be categorized into:³⁸

1. **Local density approximation** (LDA) functionals, that are based on the uniform electron gas as a model, and thus only consider the electron density at a given point to compute the contribution of that density to the XC potential, and energy. An example is the SVWN functional, which combines the Slater³⁴ (S, also referred as “LDA”) exchange functional with the Vosko-Wilk-Nusair³⁹ (VWN) correlation functional;
2. **Generalized Gradient Approximation** (GGA) functionals, which go one step further, by also considering the gradient of the density at point \mathbf{r} to evaluate the potential energy density. Both parts of BLYP are GGA functionals;
3. **Meta-GGA** (m-GGA) functionals, which improve over GGA by including the Laplacian of the density (or kinetic energy density). Among others, M06-L⁴⁰ is a pure m-GGA functional;
4. **Hybrid** functionals, which include a certain amount of (exact) HF exchange to correct the exchange part. The simplest examples are inspired by the adiabatic connection principle,^{41,42} which relates the KS and physical systems by:

$$E_{XC} = E_C + \int_0^1 d\lambda E_X^\lambda \approx E_{XC}^{(m-)\text{GGA}} + \lambda (E_X^{\text{HF}} - E_X^{(m-)\text{GGA}}), \quad (3.66)$$

so that, if E_X is linear in λ , $\lambda = 0$ corresponds to the KS (non-interacting) system, while $\lambda = 1$ corresponds to the fully correlated system (for which the HF exchange is exact). Due to the unknown nature of E_C , the actual value depends on the (m-)GGA that is chosen and thus lies between 0 and 1.

For example, BHandHLYP is based on BLYP with 50 % of HF exchange ($\lambda = 0.5$). Other examples used in our work include some members of the Minnesota family⁴⁰ with M06 (27 % of HF exchange) and M06-2X (twice that amount, so 54 %). Finally, the (in)famous B3LYP functional⁴³ relies on 3 parameters to combine one LDA (S-VWN) and one GGA (BLYP) XCF together with HF exchange:

$$E_{XC}^{B3LYP} = E_{XC}^S + a_1 (E_X^{HF} - E_X^S) + a_2 E_X^{B88} + a_3 (E_C^{LYP} - E_C^{VWN}), \quad (3.67)$$

with, in Gaussian, $a_1 = 0.2$ (20 % of HF exchange), $a_2 = 0.72$, and $a_3 = 0.81$. B3P86 uses the same parametrization with P86⁴⁴ instead of LYP;

5. **Range-corrected hybrid** functionals, which also include HF exchange, but with a varying percentage that depends on the distance $r_{12} = |\mathbf{r}_1 - \mathbf{r}_2|$. In practice, the two-electron operator is splitted into a short- and long-range part, as:⁴⁵

$$\frac{1}{r_{12}} = \underbrace{\frac{1 - [\alpha + \beta \operatorname{erf}(\omega r_{12})]}{r_{12}}}_{\text{short range}} + \underbrace{\frac{\alpha + \beta \operatorname{erf}(\omega r_{12})}{r_{12}}}_{\text{long range}}, \quad (3.68)$$

where ω (written μ in LC-BLYP) is the division parameter. The first part (short range) is associated to the evolution of the DFT exchange, the second part (long range), to the evolution of the HF exchange. Thus α corresponds to the amount of HF exchange at $r_{12} = 0$, while $\alpha + \beta$ to the one at $r_{12} = \infty$. In our work, the CAM-B3LYP⁴⁵ ($\alpha = 19\%$, $\alpha + \beta = 65\%$, $\omega = 0.33 a_0^{-1}$) and LC-BLYP⁴⁶ ($\alpha = 0\%$, $\alpha + \beta = 100\%$, $\omega = 0.47 a_0^{-1}$) functionals were used. The evolution of the DFT exchange with the distance for those two XCFs is compared in Fig. 3.1 to the BHandHLYP case;

6. Finally, **double hybrid** functionals use the KS orbitals to include a MP2 correction to the energy, using Eq. (3.40). B2-PLYP⁴⁷ which is based on B3LYP with 27 % of MP2 correction, is probably the most famous example of this last category.

As an additional refinement which can be applied to any category, the van der Waals (vdW) interactions are not well accounted for in the DFT energy (except with double-hybrids). An empirical correction is possible, like with the DFT-D2, -D3, and -D4 schemes.⁴⁸⁻⁵¹ One example is the ω B97X-D functional,⁵² which is also used in our work. It is a range-corrected hybrid ($\alpha = 16\%$, $\alpha + \beta = 100\%$, $\omega = 0.2 a_0^{-1}$), in which the dispersion is described by the DFT-D2 scheme in Gaussian:⁵³

$$E_{disp} = -s_6 \sum_{A < B}^{N_N} \frac{C_6^{AB}}{|\mathbf{r}_A - \mathbf{r}_B|^6} f_{damp}(|\mathbf{r}_A - \mathbf{r}_B|), \text{ with } f_{damp}(r) = \frac{1}{1 + e^{-d(r/R^{AB}-1)}}, \quad (3.69)$$

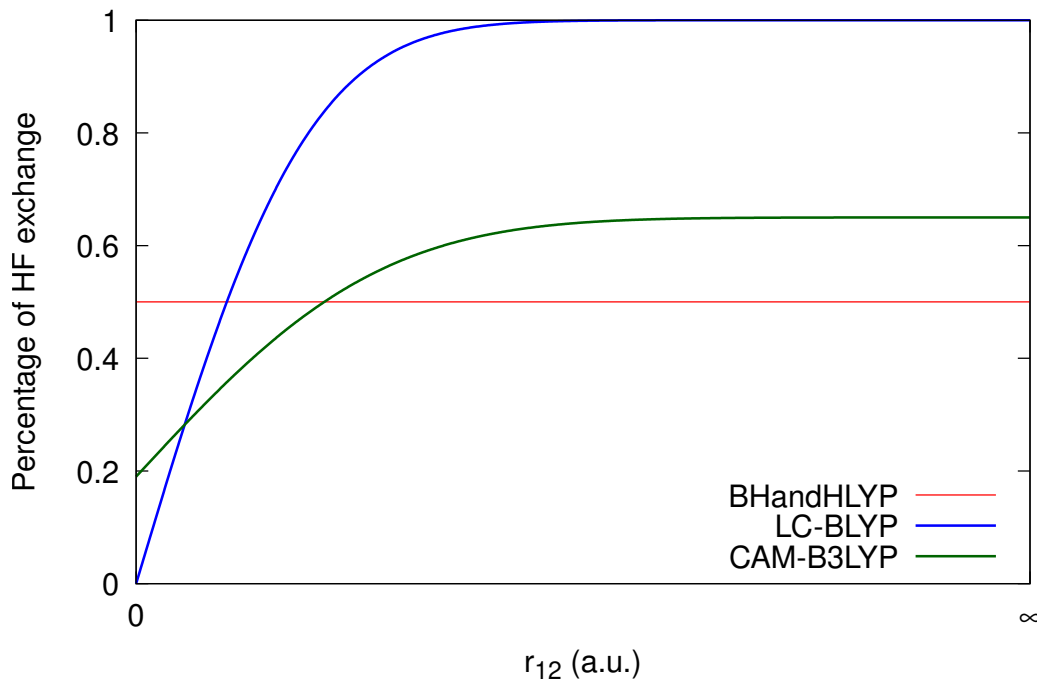


Figure 3.1: Evolution of the percentage of HF exchange with the distance r_{12} for the BHandHLYP, LC-BLYP, and CAM-B3LYP functionals. The percentage tends to $\alpha + \beta$ for $r \rightarrow \infty$. A larger ω parameter makes the function increasing more rapidly.

where s_6 is a global scaling factor, C_6 , a dispersion factor that depends on the AB pair of nuclei, f_{damp} , a damping function, d controls the strength of the dispersion (equal to 6), and R^{AB} is the sum of the vdW radii of atoms A and B .

Tight-binding approximation of DFT (DFTB)

While it is possible to study many small- to medium-size systems (< 500 atoms) with DFT, some interesting problems would require techniques that handle at least one order of magnitude more atoms. In our case, in Chapter 10, our focus turns to be the first hyperpolarizability of fluorescent proteins, which contain (for the smallest system) about 2000 atoms. This is currently out of reach of conventional DFT, even with the constant improvement of modern hardware. Semi-empirical methods are therefore an alternative. In the following, one details the second version (GFN2-xTB⁵⁴) of the tight-binding DFT GFN-xTB methods developed by Grimme's group.⁵⁴⁻⁵⁶

Any tight-binding formulation of DFT is based on a separation of the density $\rho = \rho_0 + \Delta\rho$, where ρ_0 is a reference density and $\Delta\rho$ is a density difference (or fluctuation).⁵⁷ The xTB methods add an additional term, E_{NL} , to the total energy given by Eq. (3.56) to account for non-local correlation. This results in:

$$E_{tot}[\rho] = E_{HT}[\rho_0] + \Delta E_{HT}[\Delta\rho] + E_{XC}[\rho] + E_{NL}[\rho, \rho'], \quad (3.70)$$

where E_{HT} is the (Huckel-Type) energy of the reference density ρ_0 (including the nuclei-nuclei potential E_{NN}) and ΔE_{HT} , the energy difference due to fluctuations. As it is customary in DFTB, the reference density is taken to be the superposition of (neutral and spherical) non-interacting atomic reference densities:

$$\rho_0(\mathbf{r}) = \sum_A^{N_N} \rho_0^A(\mathbf{r}). \quad (3.71)$$

Note that in xTB, as in many other DFTB formulations, only the valence part is taken into account: so, within the LCAO framework, the atomic densities are defined from a minimal set of valence atomic orbitals $\{\psi_\mu\}$. If one Taylor-expands the density around $\delta\rho = 0$, Eq. (3.70) is rewritten as:

$$E[\rho_0 + \Delta\rho] = E^{(0)}[\rho_0] + E^{(1)}[\rho_0, \delta\rho] + E^{(2)}[\rho_0, (\delta\rho)^2] + E^{(3)}[\rho_0, (\delta\rho)^3] + \dots \quad (3.72)$$

where, for example,

$$E^{(2)}[\rho_0, (\delta\rho)^2] = \frac{1}{2} \int d\mathbf{r}_1 \int d\mathbf{r}_2 \left. \frac{\partial^2 E[\rho]}{\partial \rho(\mathbf{r}_1) \partial \rho'(\mathbf{r}_2)} \right|_{\rho, \rho' = \rho_0} \delta\rho(\mathbf{r}_1) \delta\rho'(\mathbf{r}_2). \quad (3.73)$$

The GFN2-xTB method is a so-called DFTB3⁵⁸ formulation, which means that the energy expansion is truncated after the third order term. Thus:

$$E^{(0)}[\rho_0] = E_{HT}[\rho_0] + E_{disp}^{(0)}[\rho_0, \rho'_0], \quad (3.74)$$

$$E^{(1)}[\rho_0, \delta\rho] = \frac{\partial}{\partial \rho} (\Delta E_{HT}[\Delta\rho] + E_{XC}[\rho] + E_{NL}[\rho, \rho']) \delta\rho = E_{disp}^{(1)} + E_{HT}^{(1)}, \quad (3.75)$$

$$E^{(2)}[\rho_0, (\delta\rho)^2] = \frac{\partial^2}{\partial \rho \partial \rho'} (\Delta E_{HT}[\Delta\rho] + E_{XC}[\rho] + E_{NL}[\rho, \rho']) \delta\rho \delta\rho' = E_{disp}^{(2)} + E_{XC}^{(2)} + E_{ES}^{(2)}, \quad (3.76)$$

$$E^{(3)}[\rho_0, (\delta\rho)^3] = \frac{\partial^3 E_{XC}[\rho]}{\partial \rho \partial \rho' \partial \rho''} \delta\rho \delta\rho' \delta\rho'' = E_{XC}^{(3)}. \quad (3.77)$$

Grouping the terms of the same kind together finally gives the following expression for the DFTB3 energy:

$$\begin{aligned} E_{\text{DFTB3}} &= E_{HT}^{(0),(1)} + E_{rep}^{(0)} + E_{disp}^{(0),(1),(2)} + E_{XC}^{(2),(3)} + E_{ES}^{(2)}, \\ &= E_{HT} + E_{rep} + E_{disp} + E_{ES-XC} + E_{\Gamma}, \end{aligned}$$

where E_{XC} comes from the derivatives of the XFC, E_{ES} are the electrostatic (Coulomb) interaction energies, and E_{disp} (specific to GFN2-xTB) arises from derivatives of the non-local interactions. The second-order electrostatic and XC terms are customarily grouped together as $E_{ES-XC} = E_{ES}^{(2)} + E_{XC}^{(2)}$, while the third order XC energy term is generally written $E_{\Gamma} = E_{XC}^{(3)}$.⁵⁸

The GFN2-xTB method

In GFN2-xTB,

- The XCF is a hybrid functional, containing 50 % of HF exchange.
- The (extended) Huckel-Type (HT) energies are given, within the LCAO approximation [Eq. (3.21)], by:

$$E_{HT} = \sum_i^{N_{MO}} \sum_{\mu, \nu}^K n_i C_{i\mu} C_{i\nu} H_{\mu\nu} = \sum_{\mu, \nu}^K D_{\nu\mu} H_{\mu\nu}, \quad (3.78)$$

where $S_{\mu\nu} = S_{\mu\nu}^{(0)} + \delta D_{\mu\nu}$ is a density matrix element [Eq. (3.24)], defined from the fluctuation of the density, while $H_{\mu\nu}$ is a Hamiltonian matrix element, constructed out of shell- and atom-specific parameters. It is the crucial ingredient to describe covalent bonds in all the GFN-XTB methods.

Note that $n_i = n_{i\alpha} + n_{i\beta}$, the occupation of the MO i , is allowed to be fractional to handle open-shell structures and nearly degenerate states. To do so, an additional finite temperature treatment term is added to the energy E_{HT} :

$$G_{Fermi} = k_B T_{el} \sum_i^{N_{MO}} \sum_{\omega}^{\alpha, \beta} n_{i\omega} \ln(n_{i\omega}) + (1 - n_{i\omega}) \ln(1 - n_{i\omega}), \quad (3.79)$$

where k_B is the Boltzmann's constant, T_{el} , the electronic temperature (300 K by default) and $n_{i\omega}$, the fractional occupation of the corresponding spinorbital, computed from:

$$n_{i\omega} = \left\{ \exp \left[\frac{\varepsilon_i - \varepsilon_F^\omega}{k_B T_{el}} \right] - 1 \right\}^{-1}, \quad (3.80)$$

where ε_i , the energy of the spatial orbital i and $\varepsilon_F^\omega = \frac{1}{2}(\varepsilon_{HOMO}^\omega + \varepsilon_{LUMO}^\omega)$, the Fermi level of the $\omega = \alpha$ or β set of spatial orbitals.

- The **repulsion energy** is an atom-pairwise expression:

$$E_{rep}^{(0)} = \sum_{A < B}^{N_N} \frac{Z_{eff}^A Z_{eff}^B}{R_{AB}} e^{-\sqrt{\alpha_A \alpha_B} (R_{AB})^{k_f}}, \quad (3.81)$$

where Z_{eff} (roughly corresponding to effective nuclear charges screened by the reference density) and α are element-specific parameters that define the magnitude of repulsion energy. $k_f = \frac{3}{2}$ is a global parameter, except when A and B are first-row atoms (H or He) for which $k_f = 1$.

- The **dispersion** is treated with a modified DFT-D4 scheme,⁵¹ defined as:

$$E_{disp} = - \sum_n^{6,8} s_n \sum_{A < B}^{N_N} \frac{C_n^{AB}}{R_{AB}^n} f_{damp}^{(n)}(R_{AB})$$

$$-s_9 \sum_{A<B<C}^{N_N} \frac{(3 \cos \theta_{ABC} \cos \theta_{BCA} \cos \theta_{CAB} + 1) C_9^{ABC}}{(R_{AB} R_{AC} R_{BC})^3} f_{damp,0}^{(9)}(R_{AB}, R_{AC}, R_{BC}), \quad (3.82)$$

where R_{AB} is, again, the distance between atoms A and B , θ_{ABC} , the angle between atom A , B , and C (in that order) and, similarly to Eq. (3.69), C_n^{AB} and C_9^{ABC} are dispersion coefficients and f_{damp} is a damping function. It is important to notice that the DFT-D4 scheme, compared to D2 [Eq. (3.69)] or D3, also requires a self-consistent scheme, since the C_n parameters are computed from the atomic (partial) charge and coordination numbers.

- The **second-order energy** is rewritten as a multipole expansion, as:

$$E_{ES-XC} = E_\gamma + E_{AES} + E_{AXC}, \quad (3.83)$$

where E_γ is identified as the isotropic XC-ES potential. Basically, E_γ is a monopole term in the multipole expansion of the second-order energy, while E_{AXC} and E_{AES} are the (anisotropic) higher-order terms up to order 2, that thus involve the atomic dipole and quadrupole moments.

E_γ , common in DFTB2 and 3 other formulations, is here expressed in a shell-specific form:

$$E_\gamma = \sum_{A \leq B}^{N_N} \sum_{\mu \in A} \sum_{\nu \in B} q_\mu q_\nu \gamma_{AB,\mu\nu}, \quad (3.84)$$

where q_μ and q_ν are the (partial) Mulliken shell charges, and the notation $\mu \in A$ ($\nu \in B$) indicates the shells of atom A (atom B). $\gamma_{AB,\mu\nu}$ are short-range damped Coulomb interactions: for large distances, γ_{AB} reduces to $|\mathbf{r}_A - \mathbf{r}_B|^{-1}$, while, at short range, the expression involves the chemical hardness, η , of the two atoms and element-specific scaling factors for the individual shells (k_A^μ). The resulting expression is:

$$\gamma_{AB,\mu\nu} = \frac{1}{\sqrt{|\mathbf{r}_A - \mathbf{r}_B|^2 + \eta_{AB,\mu\nu}^{-2}}}, \text{ with } \eta_{AB,\mu\nu} = \frac{1}{2} [\eta_A (1 + k_A^\mu) + \eta_B (1 + k_B^\nu)]. \quad (3.85)$$

- Finally, the **third-order energy** is also an (isotropic) on-site term, formulated in a shell-specific form:

$$E_\Gamma = \frac{1}{3} \sum_A^{N_N} \sum_{\mu \in A} q_\mu^3 K_\mu^\Gamma \Gamma_A, \quad (3.86)$$

where K_μ^Γ is a global shell-specific parameter, while Γ_A is an element-specific parameter.

More details for the different expressions are found in Refs. 54 and 56. The main specificity of GFN-xTB methods is to avoid as much as possible pair-specific parameters, which would make the parametrization of the method much more complicated. More particularly, GFN2-xTB does not require H- and halogen-bond specific parameters (and thus no atom-pair parameters), due

to the inclusion of E_{AXC} and E_{AES} (it was not the case for GFN-xTB) and features the D4 auto-coherent scheme for the dispersion.

The xtb program (<https://github.com/grimme-lab/xtb>), which implements the SCF-LCAO-KS scheme for the method, also includes a geometry optimizer (based on approximate normal coordinates, ANC⁵⁹). As reported by Schmitz *et al.*,⁶⁰ it very quickly results in accurate optimized geometry for proteins, starting from their crystal structure. It is the basis for the procedure considered in Chapter 10.

Section 3.3

Molecular properties

Even though solving the Schrödinger equation (Sections 3.1 and 3.2) is the first important step in all quantum chemistry calculations, one is generally interested in quantities related to physical phenomena. When they are not directly obtainable from the expectation value of certain operators, molecular properties are defined as the response of the molecular system with respect to an external perturbation (or several). For example,

- A change of molecular geometry ($\Delta \mathbf{x}$) is related to the molecular gradient (first-order term), to the harmonic vibrational frequencies (from the molecular Hessian, second-order), etc:

$$E(\mathbf{x}_0 + \Delta \mathbf{x}) = E_0 + \underbrace{\sum_A^{N_a} \frac{\partial E}{\partial \mathbf{x}_A} \bigg|_0}_{\text{gradient}} \delta \mathbf{x}_A + \frac{1}{2} \underbrace{\sum_{AB}^{N_a} \frac{\partial^2 E}{\partial \mathbf{x}_A \partial \mathbf{x}_B} \bigg|_0}_{\text{Hessian}} \delta \mathbf{x}_A \delta \mathbf{x}_B + \dots \quad (3.87)$$

where \mathbf{x}_A is the change of geometry of nuclei (atom) A .

- From the first chapter, the application of an external electric field (\mathbf{F}) is related to the electric dipole moment (μ), the polarizability (α), etc:

$$E(\Delta \mathbf{F}) = E_0 - \int_0^{\mathbf{F}} d\mathbf{F}' \mu(\mathbf{F}') = E_0 - \underbrace{\sum_i^{xyz} \frac{\partial E}{\partial F_i} \bigg|_0}_{\mu_i} \delta F_i - \frac{1}{2} \underbrace{\sum_{ij}^{xyz} \frac{\partial^2 E}{\partial F_i \partial F_j} \bigg|_0}_{\alpha_{ij}} \delta F_i \delta F_j - \dots \quad (3.88)$$

- The application of an external magnetic field gives rises to the NMR shieldings, etc.

From the computational point of view, two methods are available to compute such derivatives of the energy: **finite field differentiation** or **analytical derivatives**. While the first comes in handy when no implementation of analytical derivatives exists in the target quantum chemistry program (for example for post-HF methods), the latter is useful since it is more precise, generally less computer-intensive, and it can provide time-dependent molecular properties. Let us present these different methods and discuss some of their key aspects.

Finite field (FF) method and the Romberg scheme

The Mac-Laurin series expansion of a function $f(x)$ is given by:

$$f(x) = \sum_{n=0}^{\infty} D^{(n)} \frac{x^n}{n!}, \text{ with } D^{(n)} = \left. \frac{\partial^n f}{\partial x^n} \right|_{x=0}. \quad (3.89)$$

A finite difference approach allows recovering a derivative at order ℓ , $D^{(\ell)}$. It employs a finite change of parameter x , called here h so that $h \in \mathbb{R}_0^+$:

$$D^{(\ell)} \approx D^{(\ell)}(h) = D^{(\ell)} + \sum_{n=1}^{\infty} D^{(\ell+n)} \frac{h^n}{(\ell+n)!} = D^{(\ell)} + \mathcal{O}(h^{\ell+1}), \quad (3.90)$$

where $D^{(\ell)}(h)$ is an approximation to $D^{(\ell)}$. Such finite difference formula is based on the following equality:

$$\frac{h^\ell}{\ell!} D^{(\ell)}(h) = \sum_{i=i_{\min}}^{i_{\max}} C_i f(ih), \quad (3.91)$$

which holds by selecting the correct $\{C_i\}$ coefficients, with $i \in [i_{\min}, i_{\max}]$ ($i_{\min} < i_{\max}$). Note that instead of an arithmetic progression in h , a geometric progression is also possible. To find the coefficients, the procedure is straightforward: given Eq. (3.89), the previous equation is rewritten:

$$\frac{h^\ell}{\ell!} D^{(\ell)}(h) = \sum_{n=0}^N \frac{h^n}{n!} D^{(n)} \sum_{i=i_{\min}}^{i_{\max}} C_i i^n, \quad (3.92)$$

from which it is visible that Eq. (3.91) only holds if:

$$\sum_{i=i_{\min}}^{i_{\max}} C_i i^n = \begin{cases} 1 & \text{if } n = \ell, \\ 0 & \text{otherwise.} \end{cases} \quad (3.93)$$

This defines a set of $N + 1$ equations with $i_{\max} - i_{\min} + 1$ unknowns. The values of i_{\min} and i_{\max} may therefore be arbitrarily chosen to give a solution, and to provide forward-difference ($i_{\min} = 0$), backward-difference ($i_{\max} = 0$) or centered-difference ($i_{\min} = -i_{\max}$) derivatives. It is then possible to know the value of $D^{(\ell)}$ from Eq. (3.91). For example, the polarizability (second-order derivative of the energy) defined in Eq. (3.88) can be computed with a forward-difference derivative formula as:

$$\alpha_{xx} \approx \frac{E(0) - 2E(\mathbf{F}_x) + E(2\mathbf{F}_x)}{\mathbf{F}_x^2} + \mathcal{O}(\mathbf{F}_x^3), \quad (3.94)$$

while the following centered-difference derivative formula may also be used:

$$\alpha_{xx} \approx \frac{E(-\mathbf{F}_x) - 2E(0) + E(\mathbf{F}_x)}{\mathbf{F}_x^2} + \mathcal{O}(\mathbf{F}_x^4) \quad (3.95)$$

where, in this case, \mathbf{F}_x is a x -oriented electric field (in the molecular frame). The latter formula should be preferred, since a centered-difference formula gives a better precision. Note that this procedure is easily adapted for multivariate functions.

The quality of the approximation thus depends on the intensity of h : i) if it is too small, it gives rise to computational (numerical) errors, while ii) if too large, $\mathcal{O}(h^{l+1})$ gets important, which gives rise to precision errors. To circumvent the latter, the Richardson procedure⁶¹ (also called Romberg's scheme) may be employed. Defining a geometric progression with $h = a^k h_0$, where a is the common factor (generally defined as $\sqrt[n]{2}$ with $n \geq 0$) and h_0 is the minimal field and using Eq. (3.90),^{62,63}

$$a^{rm} D^{(l)}(a^k h_0) - D^{(l)}(a^{k+1} h_0) = (a^{rm} - 1) D^{(l)} + \sum_{n=1}^{\infty} D^{(l+n)} \frac{(a^k h_0)^n}{(n+1)!} (a^{rm} - a^n), \quad (3.96)$$

it is possible to remove the n^{th} -term of the contamination by choosing $rm = n$. m is the number of refinement steps or Romberg iterations. Thus, a recurrence relation is defined:

$$D_l(k, m+1) = \frac{a^{rm} D^{(l)}(k, m) - D^{(l)}(k+1, m)}{a^{rm} - 1} + \mathcal{O}(h_0^{rm}), \quad (3.97)$$

starting by $m = 0$. In general, r should be equal to 1 to remove the m_{th} -power contamination, but in the case of centered derivatives, every odd-power term vanishes from the series expansion, so that $r = 2$. The result is a Romberg triangle (Fig. 3.2).

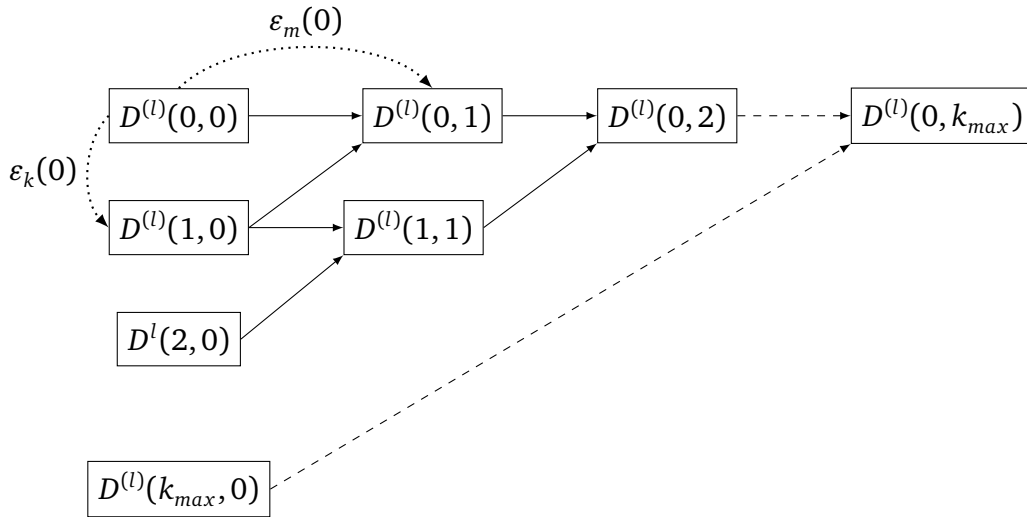


Figure 3.2: Scheme of a Romberg triangle for the Romberg procedure. The ε_k and ε_m are the amplitude and iteration errors, respectively (see text).

If the value of h_0 and k_{max} are chosen well enough, the final value should be the rightmost one [$D^{(l)}(0, k_{\text{max}})$ in Fig. 3.2]. However, without *a priori* knowledge of the ideal window for h , it is necessary to carry out an analysis of the triangle to select the “best” value.⁶³ Two quantities are useful:

$$\varepsilon_k(m) = D^{(l)}(k+1, m) - D^{(l)}(k, m), \quad (3.98)$$

$$\varepsilon_m(k) = D^{(l)}(k, m+1) - D^{(l)}(k, m), \quad (3.99)$$

where ε_k is the amplitude error at iteration m and ε_m , the iteration error for an amplitude k . The best value is chosen according to the flowchart given in Figure 3.3. Such procedure has been implemented in the home-made nachos program to automatically compute the geometrical derivatives of electrical properties up to any order, used in Chapter 6.

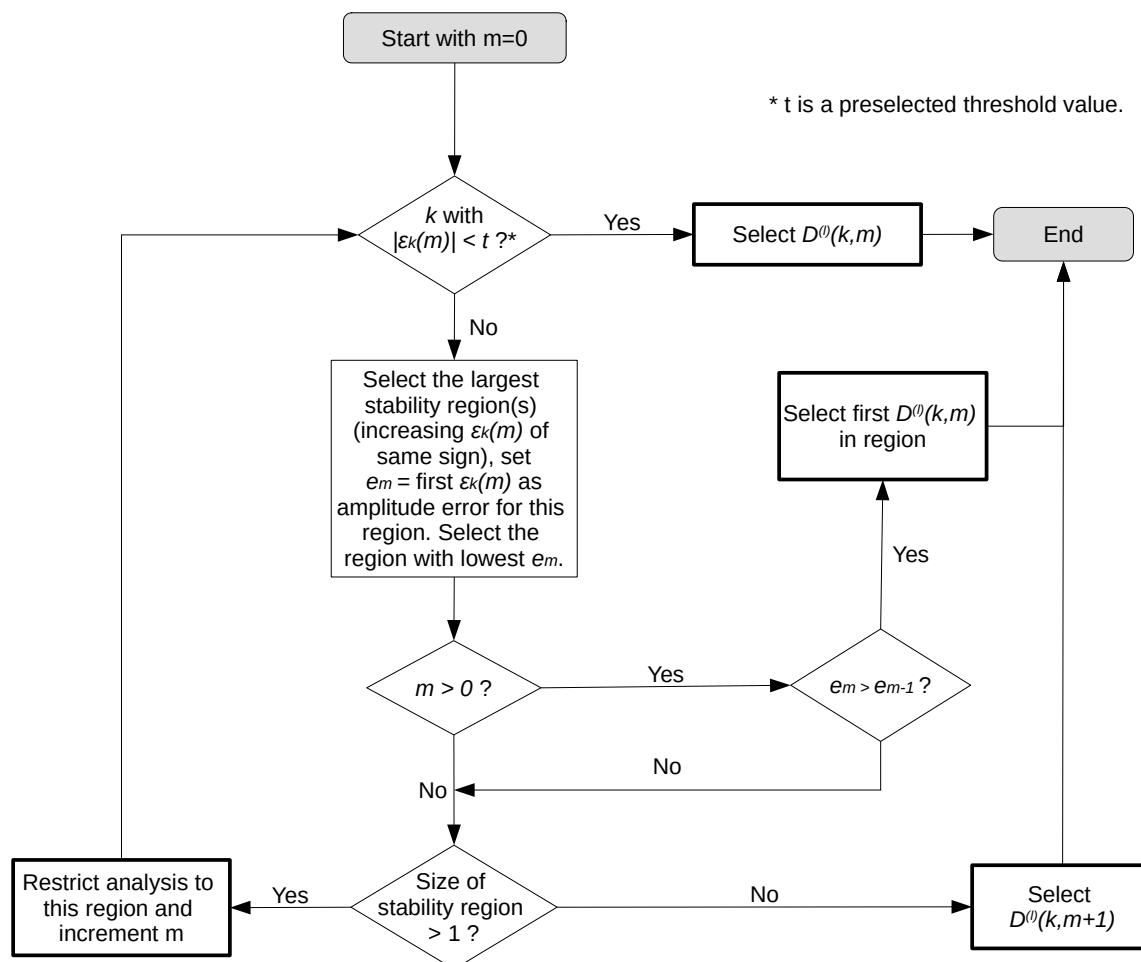


Figure 3.3: Flowchart to select the “best” value in a Romberg triangle in nachos, adapted from the text in Ref. 63.

Static Response Functions (RF)

The analytical expressions for both time-independent and dependent molecular properties rely on the RS perturbation theory, developed above. In the first case, it is a straightforward application, slightly recast to help with the time-dependent theory developed below. A general expression for the electronic energy for a given geometry is:

$$E(\{\kappa_i\}, \lambda) = \langle \Psi(\{\kappa_i\}) | \hat{H}(\lambda) | \Psi(\{\kappa_i\}) \rangle, \quad (3.100)$$

where $\{\kappa_i\}$ is the set of electronic (wavefunction) parameters (e.g., LCAO parameters) and λ , the strength of the perturbation, as in Eq. (3.28): $\hat{H}(\lambda) = \hat{H}_0 + \lambda \hat{V}$. The $\{\kappa_i\}$ thus depends on

the perturbation. Note that if they are determined variationally, then:

$$\forall \kappa_i : \left. \frac{\partial E(\{\kappa_i\}, \lambda)}{\partial \kappa_i} \right|_0 = 0. \quad (3.101)$$

The first-order derivative is therefore given by:

$$\frac{dE}{d\lambda} = \frac{\partial E(\{\kappa_i\}, \lambda)}{\partial \lambda} + \sum_i \underbrace{\frac{\partial E(\{\kappa_i\}, \lambda)}{\partial \kappa_i}}_{=0} \frac{\partial \kappa_i}{\partial \lambda} = \left\langle \Psi(\{\kappa_i\}) \left| \frac{\partial \hat{H}(\lambda)}{\partial \lambda} \right| \Psi(\{\kappa_i\}) \right\rangle \quad (3.102)$$

which is, again, the Hellmann-Feynman theorem.²⁷ The second-order derivative is obtained from differentiating the previous expression, yielding:

$$\frac{d^2 E}{d\lambda^2} = \sum_i \underbrace{\frac{\partial^2 E(\{\kappa_i\}, \lambda)}{\partial \lambda \partial \kappa_i}}_{\text{perturbed electronic gradient}} \frac{\partial \kappa_i}{\partial \lambda}, \quad (3.103)$$

or, in a simplified notation $\langle \langle \hat{V}; \hat{V} \rangle \rangle = (\kappa^\lambda)^T \eta^\lambda$, where $\langle \langle \hat{V}; \hat{V} \rangle \rangle$ is the linear RF, and κ^λ , the first-order response vector to λ , containing all $\partial \kappa_i / \partial \lambda$. It is obtained from the derivatives of the stationary condition Eq. (3.101), which results in a set of equation of the form:

$$\sum_j \underbrace{\frac{\partial^2 E(\{\kappa_i\}, \lambda)}{\partial \kappa_i \partial \kappa_j}}_{\text{electronic Hessian}} \frac{\partial \kappa_j}{\partial \lambda} = - \frac{\partial^2 E(\{\kappa_i\}, \lambda)}{\partial \lambda \partial \kappa_i}, \quad (3.104)$$

or, in a simpler form, $\mathbf{E}^\lambda \kappa^\lambda = -\eta^\lambda$. Therefore, after getting the response vector, one is finally able to compute the static linear response to perturbation with Eq. (3.103).

In the case where the perturbation is a geometrical modification, for example a geometry optimization, the geometric gradient is generally sufficient. The static linear RF gives access to the geometric Hessian, \mathbf{H} [see Eq. 3.87]. The diagonalization of the mass-weighted Hessian \mathbf{H}^m , defined as:

$$\mathbf{H}^m = \mathbf{m}^{1/2} \mathbf{H} \mathbf{m}^{-1/2}, \text{ with } \mathbf{m}_{AB} = m_A \delta_{AB}, \quad (3.105)$$

gives access to the $3N-6$ (or 5 if the molecule is linear) vibrational frequencies of the molecule. The absence of imaginary frequencies is the sign that the geometry sits in a (local) energetic minimum, so a frequency calculation is mandatory after each geometry optimizations. It is also required, together with the electronic energy, to evaluate the thermodynamical properties (e.g., enthalpy, entropy or free Gibbs energy) of a molecule.⁶⁴

RF for non-variational wavefunctions

If the wavefunction depends on non-variational parameters (for example, the CC amplitudes), the Lagrange's method of undetermined multipliers has to be used. In practice, if the

Lagrangian $L(\{c_i\}, \{\bar{c}_i\})$ depends on a set of non-variational parameters $\{c_i\}$, the $\{\bar{c}_i\}$ are the Lagrange's multipliers, used to constraints the Lagrangian:

$$L(\{c_i\}, \{\bar{c}_i\}) = E(\{c_i\}) + \sum_i \bar{c}_i [e(\{c_i\}) - 0], \quad (3.106)$$

where $e(\{c_i\}) = 0$ is a constraint. The set of parameters and multipliers are found by imposing the stationary conditions:

$$\forall c_i : \frac{\partial L(\{c_i\}, \{\bar{c}_i\})}{\partial c_i} = 0 \Leftrightarrow \frac{\partial E(\{c_i\})}{\partial c_i} + \bar{c}_i \frac{\partial e(\{c_i\})}{\partial c_i} = 0, \quad (3.107)$$

$$\forall \bar{c}_i : \frac{\partial L(\{c_i\}, \{\bar{c}_i\})}{\partial \bar{c}_i} = 0. \quad (3.108)$$

The first one allows determining the multipliers, while the second one is used to get the parameters. The Lagrangian, for which the two stationary conditions together are equivalent to Eq. (3.101), can be used instead of the energy in the previous expressions, (3.103) and (3.104), to get the response functions. Such framework is also readily applicable to the dynamic responses (see below).

Dynamic response functions

This time, let the Hamiltonian be time-dependent, such that:

$$\hat{H}(\lambda, t) = H_0 + \hat{V}(\lambda, t), \quad (3.109)$$

where only the perturbation $\hat{V}(\lambda, t)$ is time-dependent (TD). Thus, one can assume that, in the absence of a perturbation, the TD wavefunction reduces to the time-independent wavefunction Ψ_0 . The development of such wavefunction is now governed by the TD Schrödinger equation [Eq. (3.1)]. Different approaches to solve this problem exist. Following the Floquet theory,^{65–68} it is proposed to extract a (position independent) phase factor $F(t)$ from the $\bar{\Psi}(t)$ wavefunction so that:

$$\bar{\Psi}(\{\kappa_i\}, t) = e^{iF(t)} \tilde{\Psi}(\{\kappa_i\}, t), \quad (3.110)$$

where $\tilde{\Psi}$ is the phase isolated wavefunction, which is again assumed to depend on the $\{\kappa_i\}$ parameters. Inserting $\bar{\Psi}$ into Eq. (3.1) results in:

$$\left[\hat{H}(\lambda, t) - i \frac{\partial}{\partial t} \right] \tilde{\Psi}(\{\kappa_i\}, t) = Q(t) \tilde{\Psi}(\{\kappa_i\}, t),$$

$$\text{with } Q(t) = \frac{\partial F(t)}{\partial t} = \left\langle \tilde{\Psi}(\{\kappa_i\}, t) \left| \hat{H}(\lambda, t) - i \frac{\partial}{\partial t} \right| \tilde{\Psi}(\{\kappa_i\}, t) \right\rangle. \quad (3.111)$$

This equation reduces to Eq. (3.2) in the time-independent limit. As a result, $Q(t)$, a real quantity, is called the TD quasienergy since it reduces to the energy E_0 in the time-independent

case. In Floquet theory, the perturbation is assumed to be periodic in time, of period T and frequency ω :

$$\hat{V}(\lambda, t + T) = \hat{V}(\lambda, t), \text{ and } \omega_T = \frac{2\pi}{T}, \quad (3.112)$$

which means that $\hat{V}(\lambda, t)$ oscillates at a multiple of the fundamental frequency ω_T . Note that this implies, since the Hamiltonian becomes periodic, that $\tilde{\Psi}$ oscillates with the same period. Introducing the time average of a given periodic function $g(t)$ as $\{g\}_T$,

$$\{g\}_T = \frac{1}{T} \int_0^T dt g(t), \quad (3.113)$$

the (time-averaged) quasienergy \mathcal{Q} is given by:

$$\mathcal{Q} = \{Q(t)\}_T = \left\{ \left\langle \tilde{\Psi}(\{\kappa_i\}, t) \left| \hat{H}(\lambda, t) - i \frac{\partial}{\partial t} \right| \tilde{\Psi}(\{\kappa_i\}, t) \right\rangle \right\}_T. \quad (3.114)$$

Since

$$\left\{ \frac{dg(t)}{dt} \right\}_T = 0, \quad (3.115)$$

the TD variational principle is:

$$\frac{\partial \mathcal{Q}}{\partial \kappa_i} = 0, \quad (3.116)$$

and the TD version of the Hellmann-Feynman theorem is:

$$\frac{d\mathcal{Q}}{d\lambda} = \left\{ \left\langle \tilde{\Psi}(\{\kappa_i\}, t) \left| \frac{\partial H(\lambda, t)}{\partial \lambda} \right| \tilde{\Psi}(\{\kappa_i\}, t) \right\rangle \right\}_T. \quad (3.117)$$

In a more general case, one uses the Fourier series of the perturbation operator,⁶⁷ given by:

$$\hat{V}(\lambda, t) = \sum_{k=-N}^N \lambda^{\omega_k} \hat{V} e^{-i\omega_k t} \quad (3.118)$$

where ω_k is a multiple of the fundamental frequency ω_T and $\lambda(\omega_k)$ are the perturbation strengths. \hat{V} is a time-independent operator. To ensure that the Hamiltonian remains hermitian: i) $\omega_{-k} = -\omega_k$, ii) \hat{V}^ω is hermitian [$\hat{V} = \hat{V}^\dagger$], and iii) $\lambda^{-\omega} = (\lambda^\omega)^*$. Thus, the ω_k always come in pair, $\pm\omega_k$. Furthermore, differentiating $\hat{V}(t)$ with respect to one strength parameter λ^{ω_k} results in a single periodic perturbation:

$$\frac{\partial \hat{V}(\lambda, t)}{\partial \lambda^{\omega_k}} = \hat{V} e^{-i\omega_k t}. \quad (3.119)$$

Hence, Eq. (3.117) takes the form:

$$\frac{d\mathcal{Q}}{d\lambda^{\omega_0}} = \left\{ \left\langle \tilde{\Psi}(\{\kappa_i\}, t) \left| \hat{V} \right| \tilde{\Psi}(\{\kappa_i\}, t) \right\rangle e^{-i\omega_0 t} \right\}_T. \quad (3.120)$$

Given that if ω_0 is a multiple of the fundamental frequency ω_T , then:

$$\{e^{i\omega_0 t}\}_T = \delta(\omega_0), \quad (3.121)$$

where $\delta(\omega_0)$ is the Dirac delta function (its value is non-zero if the argument, here ω_0 , is zero), Eq. (3.120) is finally rewritten (after expanding the bracket in terms of the perturbation strength) as:^{66–68}

$$\begin{aligned} \frac{d\mathcal{Q}}{d\lambda^{\omega_0}} &= \langle \Psi_0(\{\kappa_i\}) | \hat{V} | \Psi_0(\{\kappa_i\}) \rangle \delta(\omega_0) \\ &+ \sum_{k_1=-N}^N \lambda^{\omega_{k_1}} \langle \langle \hat{V}; \hat{V} \rangle \rangle_{\omega_{k_1}} \delta(\omega_0 + \omega_{k_1}) \\ &+ \frac{1}{2} \sum_{k_1, k_2=-N}^N \lambda^{\omega_{k_1}} \lambda^{\omega_{k_2}} \langle \langle \hat{V}; \hat{V}, \hat{V} \rangle \rangle_{\omega_{k_1}, \omega_{k_2}} \delta(\omega_0 + \omega_{k_1} + \omega_{k_2}) + \dots \end{aligned} \quad (3.122)$$

where Ψ_0 is the time-independent wavefunction. The Dirac functions only allow frequency combinations that sums up to zero : $\omega_0 = -\sum_i \omega_{k_i}$, which ensures energy conservation. Therefore:

$$\langle \langle \hat{A}; \hat{B} \rangle \rangle_{\omega_B} = \left. \frac{d^2 \mathcal{Q}}{d\lambda^{-\omega_B} d\lambda^{\omega_B}} \right|_{\lambda=0} \quad (3.123)$$

is the linear RF at frequency ω_B , and:

$$\langle \langle \hat{A}; \hat{B}, \hat{C} \rangle \rangle_{\omega_B, \omega_C} = \left. \frac{d^3 \mathcal{Q}}{d\lambda^{-\omega_\sigma} d\lambda^{\omega_B} d\lambda^{\omega_C}} \right|_{\lambda=0} \quad (3.124)$$

is the quadratic response, evaluated at frequency $\omega_\sigma = \omega_B + \omega_C$.

The actual analytical expressions are found in a similar manner to the time-independent case.^{66–68} Recognizing that the $\{\kappa_i\}$ are time- (and perturbation-) dependent, they are expanded as:

$$\kappa_i(\lambda, t) = \kappa_i^{(0)} + \kappa_i^{(1)}(\lambda, t) + \dots \quad (3.125)$$

where, for example,

$$\kappa_i^{(1)}(\lambda, t) = \sum_{k_1=-N}^N \kappa_i^{\omega_{k_1}} \lambda^{\omega_{k_1}} e^{-i\omega_{k_1} t},$$

and so on. Again, this implies that $\kappa_i^{-\omega} = (\kappa_i^\omega)^*$. Deriving Eq. (3.120) with respect to another perturbation gives:

$$\frac{\partial^2 \mathcal{Q}}{\partial \lambda^{-\omega} \partial \lambda^\omega} = \sum_i \frac{\partial^2 \mathcal{Q}}{\partial \lambda^{-\omega} \partial \kappa_i^\omega} \frac{\partial \kappa_i^\omega}{\partial \lambda^\omega}, \quad (3.126)$$

or, in a simplified notation, $\langle \langle V; V \rangle \rangle_\omega = (\eta^{-\omega})^\dagger \kappa^\omega$.⁶⁷ On the other hand, the derivation Eq. (3.116), gives a set of equation for the first-order response vectors:

$$\sum_j \frac{\partial^2 \mathcal{Q}}{\partial \kappa_i^{-\omega} \partial \kappa_j^\omega} \frac{\partial \kappa_j^\omega}{\partial \lambda^\omega} = -\frac{\partial^2 \mathcal{Q}}{\partial \kappa_i^{-\omega} \partial \lambda^\omega}, \quad (3.127)$$

or, in a simplified notation, $\mathbf{J}^\omega \kappa^\omega = -\eta^\omega$.⁶⁷ \mathbf{J} is the Jacobian matrix, so that $\mathbf{J}^\omega = \mathbf{E}^\omega - \omega \mathbf{S}$, since:

$$\left\{ \frac{\partial^2 \langle \tilde{\Psi}(\{\kappa_i\}) | \hat{H}_0 | \tilde{\Psi}(\{\kappa_i\}) \rangle}{\partial \kappa_i^{-\omega} \partial \kappa_j^\omega} \right\}_T = \mathbf{E}^\omega, \text{ and } \left\{ \frac{\partial^2 \langle \tilde{\Psi}(\{\kappa_i\}) | -i \frac{\partial}{\partial t} | \tilde{\Psi}(\{\kappa_i\}) \rangle}{\partial \kappa_i^{-\omega} \partial \kappa_j^\omega} \right\}_T = -\omega \mathbf{S}, \quad (3.128)$$

where \mathbf{E}^ω is, again, the electronic Hessian, while \mathbf{S} is an overlap matrix.

Applications to the TDHF, TD-DFT, and nRF-CC level of approximations

On the one hand, the response function framework is readily applicable to the HF level to give the linear (LR), quadratic (QR), etc, response function HF (e.g., LR-TDHF) methods.⁶⁹ For example, given a monochromatic electric field perturbation $\hat{V}(t) = \hat{\mu}(F^\omega e^{-i\omega t} + F^{-\omega} e^{-i\omega t})$, where $\hat{\mu}$ is the dipole moment operator, the dynamic polarizability α is defined as:

$$\alpha_{ij}(-\omega; \omega) = -\langle \langle \mu_i; \mu_j \rangle \rangle_\omega. \quad (3.129)$$

The $\{\kappa_i\}$ parameters of the HF method are the LCAO coefficients, $\{C_{ar}\}$, and \hat{H}_0 is the HF Hamiltonian (the sum of one-electron Fock operators). Given the Hermiticity of \mathbf{E}^ω and η^ω , Eq. (3.127) is written:

$$\left[\begin{pmatrix} \mathbf{A} & \mathbf{B} \\ \mathbf{B}^* & \mathbf{A}^* \end{pmatrix} - \omega \begin{pmatrix} \mathbf{1} & \mathbf{0} \\ \mathbf{0} & -\mathbf{1} \end{pmatrix} \right] \begin{pmatrix} \mathbf{x}_j^\omega \\ \mathbf{y}_j^\omega \end{pmatrix} = \begin{pmatrix} \mu_j \\ \mu_j^* \end{pmatrix}, \quad (3.130)$$

where \mathbf{x}_j^ω and \mathbf{y}_j^ω are the frequency-dependent linear response vectors (to be determined) in the Cartesian direction j , and:

$$\begin{aligned} \mu_{i,ar} &= \frac{\partial \mathcal{Q}_{HF}}{\partial F^{-\omega} \partial C_{ar}^\omega} = -\langle \Psi_a^r | \hat{\mu}_i | \Psi_0 \rangle, \\ \mathbf{A}_{ar,bs} &= \frac{\partial^2 \langle \tilde{\Psi}(t) | \hat{H}_0 - E^{HF} | \tilde{\Psi}(t) \rangle}{\partial C_{ar}^{-\omega} \partial C_{bs}^\omega} = \langle \Psi_a^r | \hat{H}_0 - E_0 | \Psi_b^s \rangle = (\epsilon_r - \epsilon_a) \delta_{ab} \delta_{rs} + \langle rs || ab \rangle, \\ \mathbf{B}_{ar,bs} &= \frac{\partial^2 \langle \tilde{\Psi}(t) | \hat{H}_0 - E^{HF} | \tilde{\Psi}(t) \rangle}{(\partial C_{ar}^{-\omega})^* \partial C_{bs}^\omega} = \langle \Psi_{ab}^{rs} | \hat{H}_0 | \Psi_0 \rangle = \langle rb || as \rangle. \end{aligned} \quad (3.131)$$

where the intermediate integrals for \mathbf{A} and \mathbf{B} are therefore evaluated thanks to the Slater-Condon rules. Then, Eq. (3.129) becomes:

$$\alpha_{ij}(-\omega; \omega) = -\begin{pmatrix} \mu_i \\ \mu_i^* \end{pmatrix}^\dagger \begin{pmatrix} \mathbf{x}_j^\omega \\ \mathbf{y}_j^\omega \end{pmatrix} = -2 \sum_a^{\text{occ}} \sum_r^{\text{unocc.}} \mu_{i,ar} (\mathbf{x}_{j,ai}^\omega + \mathbf{y}_{j,ai}^\omega) \quad (3.132)$$

which is the LR expression of the polarizability. An equivalent expression was obtained by Gerratt and Mills,⁷⁰ based on a pure matrix formalism and starting from the second-order

derivative of Eq. (3.25). This leads to the (standard) TDHF method (implemented in different QM codes^{71,72}). An iterative cycle is used to compute the derivatives of the density matrix, which is equivalent to solving Eq. (3.127).

On the other hand, this should normally not apply to DFT since the Hohenberg-Kohn and Kohn-Sham theorems are only valid for stationary cases (see Section 3.2). Hopefully, Runge and Gross⁷³ extended DFT to the time-dependent realm by showing that the (now TD) density still determines uniquely the TD external potential, and hence the properties, which is the extension of the first HK theorem. Furthermore, van Leeuwen⁷⁴ later proved that KS orbitals satisfy the TD Schrödinger equation. Finally, the adiabatic approximation can be employed, which in this context refers to the use of the (time-independent) XCF, together with the TD density, to approximate the actual time-dependent XCF:

$$\hat{V}_{XC}(\mathbf{r}_1, t) \approx \frac{\partial E_{XC}[\rho]}{\partial \rho(\mathbf{r}_1, t)}. \quad (3.133)$$

Assuming the periodicity of the perturbation, Eq. (3.132) remains valid, though the expression of the **A** and **B** matrices are adapted to include the XC kernel (response of the XCF to the perturbation). In particular, for the hybrid functional:

$$\begin{aligned} \mathbf{A}_{ar,bs} &= (\varepsilon_r - \varepsilon_a) \delta_{ab} \delta_{rs} + 2(ar|bs) - a_x(ab|rs) + (1 - a_x)(ar|f_{XC}|bs), \\ \mathbf{B}_{ar,bs} &= 2(ar|sb) - a_x(as|rb) + (1 - a_x)(ar|f_{XC}|sb), \end{aligned} \quad (3.134)$$

where a_x is the amount of exact HF exchange, and $(ar|f_{XC}|bs)$, the XC kernel contribution. This is the LR-TD-DFT expression of polarizability. Again, a totally equivalent formula is obtained starting from the DFT equivalent of the Roothaan-Hall equation, which leads to the coupled-perturbed KS (CPKS) method.^{75,76}

Finally, the CC response (nRF-CC) uses the time-averaged Lagrangian, $\mathcal{L} = \{L\}_T$, instead of the quasienergy, but the derivation of the linear response is similar. The parameters are the TD cluster amplitudes, $\{t_i^\omega\}$, and the corresponding Lagrange's multipliers are denoted $\{\bar{t}_i^\omega\}$, determined with the TD version of the cluster amplitude equations [e.g., Eqs. (3.51) and (3.52)] as constraints. Defining the perturbed Lagrangian gradients as:

$$\eta_i^\omega = \frac{\partial^2 \mathcal{L}}{\partial t_i^{-\omega} \partial \lambda^\omega} \text{ and } \zeta_i^\omega = \frac{\partial^2 \mathcal{L}}{\partial \bar{t}_i^{-\omega} \partial \lambda^\omega}, \quad (3.135)$$

the set of equations to get the response vectors [equivalent to Eq. (3.127)] is:

$$(\bar{\mathbf{E}}^\omega + \omega \mathbf{1}) \mathbf{t}^\omega = -\boldsymbol{\zeta}^\omega \text{ and } \bar{\mathbf{t}}^\omega (\mathbf{E}^\omega + \omega \mathbf{1}) + \mathbf{R} \mathbf{t}^\omega = -\boldsymbol{\eta}^\omega, \quad (3.136)$$

where the first equation determines \mathbf{t}^ω , the first-order response vector and the second determines $\bar{\mathbf{t}}^\omega$, the first-order multipliers. The \mathbf{E}^ω and $\bar{\mathbf{E}}^\omega$ electronic Hessian matrices are required:

$$\bar{\mathbf{E}}_{ij}^\omega = \frac{\partial^2 \mathcal{L}}{\partial \bar{t}_i^{-\omega} \partial t_j^\omega} \text{ and } \mathbf{E}_{ij}^\omega = \frac{\partial^2 \mathcal{L}}{\partial t_i^{-\omega} \partial t_j^\omega}. \quad (3.137)$$

The polarizability is then:

$$\alpha_{ij}(-\omega; \omega) = -\frac{1}{2} \sum_{\mathcal{P}} [\eta^{-\omega} \mathbf{t}^{\omega} + \bar{\mathbf{t}}^{\omega} \zeta^{-\omega}], \quad (3.138)$$

where the $\sum_{\mathcal{P}}$ is a sum over the 2 permutations of the Cartesian indices (and corresponding frequencies).

The Wigner $2n + 1$ rule^{77,78} states that *for variational wavefunction, the derivatives of the wavefunction to order n determine the derivatives of the energy to order $2n + 1$* . Therefore, the expression of the quadratic response function (QRF) may be expressed only in terms of the linear response vectors κ^{ω} , thus not requiring to solve another set of equations. The expression for the variational QRF is:

$$\langle\langle \hat{A}; \hat{B}, \hat{C} \rangle\rangle_{\omega_1, \omega_2} = \sum_{\mathcal{P}} \left[\frac{1}{2} \mathbf{J}^{-\omega_{\sigma}} + \frac{1}{6} \mathbf{H}^{\omega_1, \omega_2} \kappa^{-\omega_{\sigma}} \right] \kappa^{\omega_1} \kappa^{\omega_2}, \quad (3.139)$$

where $\omega_{\sigma} = \omega_1 + \omega_2$, $\sum_{\mathcal{P}}$ is a sum over the 6 permutations of the Cartesian indices (and corresponding frequencies) and:

$$\mathbf{H}^{\omega_1, \omega_2} = \frac{\partial^3 \mathcal{Q}}{\partial \kappa^{-\omega_{\sigma}} \partial \kappa^{\omega_1} \partial \kappa^{\omega_2}}. \quad (3.140)$$

For TD-DFT, Eq. (3.139) is rewritten as:⁷⁹

$$\beta_{ijk}(-\omega_{\sigma}; \omega_1, \omega_2) = A_{ijk}(-\omega_{\sigma}; \omega_1, \omega_2) - B_{ijk}(-\omega_{\sigma}; \omega_1, \omega_2) + C_{ijk}(-\omega_{\sigma}; \omega_1, \omega_2), \quad (3.141)$$

with:

$$\begin{aligned} A_{ijk}(-\omega_{\sigma}; \omega_1, \omega_2) &= \mathcal{P} \sum_{ab}^{occ} \sum_r^{unocc} \mathbf{x}_{i,ar}^{-\omega_{\sigma}} \left[-\mu_{j,ab} \sum_c^{occ} \sum_s^{unocc} f_{ab,sc} (\mathbf{x}_{j,cs}^{\omega_1} + \mathbf{y}_{j,cs}^{\omega_1}) \right] \mathbf{y}_{k,br}^{\omega_2}, \\ B_{ijk}(-\omega_{\sigma}; \omega_1, \omega_2) &= \mathcal{P} \sum_a^{occ} \sum_{rs}^{unocc} \mathbf{x}_{i,ar}^{-\omega_{\sigma}} \left[-\mu_{j,rs} \sum_b^{occ} \sum_t^{unocc} f_{rs,tb} (\mathbf{x}_{j,bt}^{\omega_1} + \mathbf{y}_{j,bt}^{\omega_1}) \right] \mathbf{y}_{k,as}^{\omega_2}, \\ C_{ijk}(-\omega_{\sigma}; \omega_1, \omega_2) &= \mathcal{P} \sum_{abc}^{occ} \sum_{rst}^{unocc} g_{ra, sb, tc} (\mathbf{x}_{i,ar}^{-\omega_{\sigma}} + \mathbf{y}_{i,ar}^{-\omega_{\sigma}}) (\mathbf{x}_{j,bs}^{\omega_1} + \mathbf{y}_{j,bs}^{\omega_1}) (\mathbf{x}_{k,ct}^{\omega_2} + \mathbf{y}_{k,ct}^{\omega_2}), \end{aligned} \quad (3.142)$$

where $f_{ab,sc}$ is the Hartree XC kernel (related to \mathbf{J}) and $g_{ra, sb, tc}$, the third-order derivative of the XC functional (related to \mathbf{H}).

While the HF, DFT, and CC response functions (up to cubic) are available in the Dalton code,⁸⁰ the TDHF and CPKS approaches are also implemented in Gaussian 16. In particular, the QRF- and CRF-CC approaches to compute precise gas phase hyperpolarizabilities of small molecules are featured in Chapters 4-6.

Simplified TD-DFT (sTD-DFT) for the first hyperpolarizability

In sTD-DFT,^{79,81,82} starting from the $2n + 1$ equations [Eq. (3.142)], simplifications are introduced:

1. The response of the XCF is neglected in the **A** and **B** matrices of Eq. (3.134) and in the *A* and *B* terms of Eq. (3.142). The *C* term of Eq. (3.142) is also dropped. These approximations, though drastic, alleviate the need to evaluate new (XCF dependent!) integrals.^{79,81}
2. The Coulomb and exchange integrals are approximated by short-range damped Coulomb interactions:

$$(pq|rs)' = \sum_{A,B}^{N_A} q_{pq}^A q_{rs}^B \Gamma_{AB}, \quad (3.143)$$

where q_{pq}^A is the transition charge density (determined through a Löwdin population analysis) and Γ_{AB} , the Mataga-Nishimoto-Ohno-Klopman damped Coulomb operator, namely:

$$\begin{aligned} \Gamma_{AB}^J &= \left[\frac{1}{|\mathbf{r}_A - \mathbf{r}_B|^{y_J} + (a_x \eta)^{-y_J}} \right]^{\frac{1}{y_J}}, \\ \Gamma_{AB}^K &= \left[\frac{1}{|\mathbf{r}_A - \mathbf{r}_B|^{y_K} + \eta^{-y_K}} \right]^{\frac{1}{y_K}}, \end{aligned} \quad (3.144)$$

for the Coulomb and exchange integrals, respectively, with η the chemical hardnesses of atom *A* and *B* and a_x the amount of HF exchange. As seen in Chapter 10 y_J and y_K need to be chosen carefully in order to get accurate results.

As a result, instead of Eq. (3.134),

$$\mathbf{A}_{ar,bs} = (\varepsilon_r - \varepsilon_a) \delta_{ab} \delta_{rs} + 2(ar|bs)'_K - (ab|rs)'_J \text{ and } \mathbf{B}_{ar,bs} = 2(ar|sb)'_K - a_x (as|rb)'_K \quad (3.145)$$

are used in Eq. (3.130) to get the first-order response vectors.

3. The 3-centers integrals are not evaluated.
4. A threshold value, $E_{thresh.}$, truncates the configuration space (for both occupied and unoccupied orbitals).

The sTD-DFT was designed to work with any hybrid XCF wavefunctions. Therefore, it may be combined with a modified version (including a more complete basis set) of the xTB scheme to give the sTD-DFT-xTB method, which has provided the first hyperpolarizability of systems up to 3000 atoms.⁸²

The `stda` program (<https://github.com/grimme-lab/stda>) implements the sTD-DFT method for the first hyperpolarizability (as well as UV-VIS spectra,⁸¹ ...). It also features optional simplifications due to the Tamm-Dancoff (TDA) approximation (see below). The `xtb4stda` program (<https://github.com/grimme-lab/xtb4stda>) provides the modified xTB wavefunction for sTD-DFT-xTB calculations (see Ref. 82 for more details).

Excitation energies as the pole of the linear RF

When rewriting Eq. (3.130) into a generalized eigenvalue equation,

$$\begin{pmatrix} \mathbf{A} & \mathbf{B} \\ \mathbf{B}^* & \mathbf{A}^* \end{pmatrix} \begin{pmatrix} \mathbf{X}^{\omega_l} \\ \mathbf{Y}^{\omega_l} \end{pmatrix} = \omega_l \begin{pmatrix} \mathbf{1} & \mathbf{0} \\ \mathbf{0} & -\mathbf{1} \end{pmatrix} \begin{pmatrix} \mathbf{X}^{\omega_l} \\ \mathbf{Y}^{\omega_l} \end{pmatrix}, \quad (3.146)$$

the eigenvalues of this equation, $\{\omega_l\}$, appears as the poles of the linear RF: the vertical excitation energies. This is known as the Casida equation⁸³ in the context of TD-DFT, but it also provides access to the excitation energies for other methods as well, such as HF or CC.

Furthermore, the excitation energies may be approximated by setting $\mathbf{B} = 0$, which corresponds to the TDA approximation,^{84,85} leading to a (true) hermitian eigenvalue equation:

$$\mathbf{A} \mathbf{X}^{\omega'_l} = \omega'_l \mathbf{X}^{\omega'_l}. \quad (3.147)$$

It is comparable to the one giving the Configuration Interaction Singles (CIS) excitation energies. The $\mathbf{X}_{ar}^{\omega'_l}$ are, in this case, the coefficient for the single orbital excitation $a \rightarrow r$, whose square gives the participation of the transition to the excitation. For example, for π -conjugated molecules, the first excitation (with the lowest ω_l) is generally dominated by a HOMO→LUMO transition.

Section 3.4

Effects of the surroundings

Until now, it has been assumed that there is no interaction between the system (described by Ψ) and its surroundings. When compared to experiment, it is useful to include some of these effects, for example when checking against results in solution phase. Although one could fully include the surrounding in Ψ , the computational scaling of the different methods generally prevents such approach. Three levels of embedding are then possible:

1. The **mechanical** embedding: the model system is only influenced by the positions of the atoms in the surrounding, and thus their van der Waals forces.
2. The **electronic** embedding: the charges of the surrounding influence the electronic structure of the model system. It is also referred to as charge embedding, where the (unmodified) charges from a previous calculation are used in further ones.

3. The **polarizable** embedding: the model system also polarizes the charges (and the electronic structure, if treated at a QM level) of the surrounding.

Among the different alternatives, two will be presented: continuum models (GBSA and PCM) and partition methods (ONIOM).

Continuum models

This first approach is dedicated to include the electrostatic effects of the solvent in a “cheap” formulation. The Gibbs free energy of solvation may be decomposed in three terms:

$$\Delta G_{solv} = \underbrace{\Delta G_{cav} + \Delta G_{vdW}}_{\Delta G_{cd}} + \Delta G_{pol}, \quad (3.148)$$

where ΔG_{cav} is the energy to create a solute cavity in the solvent continuum, ΔG_{vdW} accounts for the solute-solvent vdW interactions (dispersion), and ΔG_{pol} is coming from the electrostatic solute-solvent interactions. The first method, the **Generalized Born/Surface Area**^{86–88} (GBSA), proposes to group the first two terms together into a single one, ΔG_{cd} , proportional to the solvent-accessible surface (SAS, Fig. 3.4) area (SASA):

$$\Delta G_{cd} = \sum_A^{N_a} \sigma_A A_A, \quad (3.149)$$

where A_A is the SASA of atom A and σ_A , a parameter for atom A (also referred to as accessible surface tension). On the other hand, the polarization is estimated by a simple function, which interpolates between the short-range Born expression⁸⁹ (solvation of a spherical ion) and the long-range Coulomb behavior (described by the Poisson-Boltzmann equation):

$$\Delta G_{pol} \approx -\frac{1}{2} \left(1 - \frac{1}{\epsilon_s} \right) \sum_{ab}^{N_a} \frac{q_A q_B}{f_{GB}(|\mathbf{r}_A - \mathbf{r}_B|, R_A, R_B)},$$

$$\text{with } f_{GB}(r_{AB}, R_A, R_B) = \left[r_{AB}^2 + R_i R_j \exp \left(-\frac{r_{AB}^2}{4 R_i R_j} \right) \right]^{1/2} \quad (3.150)$$

where ϵ_s is the dielectric constant of the solute, and R_A and R_B are the effective Born radii, which accounts for the burial of the atoms w.r.t. the solute. It has thus to be computed for every atom.⁸⁸

This GBSA model is featured in the `xtb` and `xtb4stda` programs to account for the impact of solvation on the wavefunction. Note that it is not fully accounted in `stda`, so that the computed β values miss the dynamic solvent effects.⁸²

On the other hand, the **Polarizable Continuum Model**^{91,92} (PCM) proposes, again, to approximate the system by a solute placed in a cavity. This time, the procedure is self-consistent: indeed, the charge distribution of the solute polarizes the continuum (represented charges on

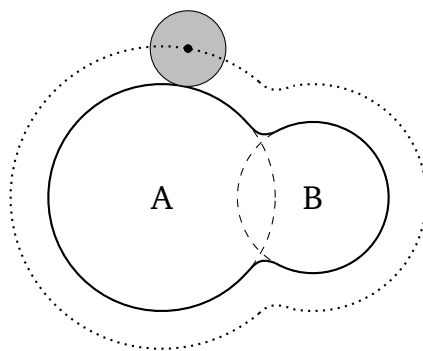


Figure 3.4: Definition of the surfaces for the solvent models in the case of a two-atoms (A and B) molecule: solvent excluded surface (SES, thick lines) and solvent accessible surface (SAS, dotted lines). The latter is traced out the center of a probe representing the solvent (gray circle), using the vdW radii of the atoms. Adapted from Ref. 90.

the surface of the cavity formed by the solvent excluded surface, see Fig. 3.4), which in return polarizes the charge distribution, and so on until convergence. The charge density at the surface, which depends on the potential $V(\mathbf{s})$ at a given point of the surface \mathbf{s} , is given by:⁹⁰

$$\sigma(\mathbf{s}) = -\frac{\epsilon_s - 1}{4\pi\epsilon_s} \frac{\partial V(\mathbf{s})}{\partial \mathbf{n}}, \quad (3.151)$$

where \mathbf{n} is a normal vector to the surface that points towards the solute. $V(\mathbf{r})$ may be partitioned into two contributions, V_ρ which comes from the charge distribution (electrons and nuclei) of the solute and V_σ which comes from the charge at the surface of the cavity. The latter is approximated by discretizing the surface of the cavity into k tesserae of area A_k , so that:

$$V_\sigma(\mathbf{r}) = \int_\sigma d\mathbf{s} \frac{\sigma(\mathbf{s})}{|\mathbf{r} - \mathbf{s}|} \approx \sum_k \frac{\sigma(\mathbf{s}_k) A_k}{|\mathbf{r} - \mathbf{s}_k|}. \quad (3.152)$$

In practice, V_σ is added to the Hamiltonian, and a second iterative cycle (self-consistent reaction field, SCRF) inside each SCF cycle is dedicated to the evaluation of $\sigma(\mathbf{s}_k)$. Approximate formulas are then used to evaluate ΔG_{cd} at the end, which depends on the implementation. An integral equation formalism (IEF) version⁹³ of this procedure is available in Gaussian 16 at the HF or DFT levels (among others). The formalism is also extended to fully account for dynamic solvent effects on the different time-(in)dependent properties.⁹⁴

The ONIOM method

Another approach to reduce the computational cost while accounting for the surroundings is to partition the system into different layers, treated at different levels of theory. It is the basis of the ONIOM (“our Own N-layered integrated molecular Orbital and molecular Mechanics”) approach,⁹⁵ which provides a convenient framework for such calculations in Gaussian 16. In particular, a two-layer approach partition the full (real) system into a region of interest (the model system), which will be treated at a high level of theory and the surroundings, which

will be treated at a lower level of theory. For a property P (such as the energy), the resulting value will be:

$$P^{\text{ONIOM}}(\text{real}) = P^{\text{low}}(\text{real}) - P^{\text{low}}(\text{model}) + P^{\text{high}}(\text{model}), \quad (3.153)$$

which requires three calculations: at the low level on both real and model systems (P^{low}) and at the high level on the model system (P^{high}). These calculations are sometimes referred to as QM:MM or QM:QM, where the left and right side of the colon refers to the treatment of the model and real systems, respectively. Indeed, the real system may be treated at the QM or molecular mechanics (MM) level (Newtonian mechanics).

Since the geometry has a large impact on the first hyperpolarizability, a QM:QM scheme (DFT for the chromophore and its surrounding amino acids within a 4 Å distance, GFN2-xTB for the rest) was used for the geometry optimization of the proteins in Chapter 10. This scheme includes the polarization effects, missing in QM:MM approach.

Bibliography

- [1] Schrödinger, E. An Undulatory Theory of the Mechanics of Atoms and Molecules. *Phys. Rev.* **1926**, 28, 1049–1070.
- [2] Born, M.; Oppenheimer, R. Zur Quantentheorie Der Molekeln. *Ann. Phys.* **1927**, 389, 457–484.
- [3] Dirac, P. A. M.; Fowler, R. H. On the Theory of Quantum Mechanics. *Proc. R. Soc. Lond. A* **1926**, 112, 661–677.
- [4] Heisenberg, W. Mehrkörperproblem und Resonanz in der Quantenmechanik. *Z. Phys.* **1926**, 38, 411–426.
- [5] Slater, J. C. The Theory of Complex Spectra. *Phys. Rev.* **1929**, 34, 1293–1322.
- [6] Ritz, W. Über eine neue Methode zur Lösung gewisser Variationsprobleme der mathematischen Physik. *J. Reine Angew. Math.* **1909**, 1909, 1–61.
- [7] MacDonald, J. K. L. Successive Approximations by the Rayleigh-Ritz Variation Method. *Phys. Rev.* **1933**, 43, 830–833.
- [8] Hartree, D. R. The Wave Mechanics of an Atom with a Non-Coulomb Central Field. Part III. Term Values and Intensities in Series in Optical Spectra. *Math. Proc. Camb. Philos. Soc.* **1928**, 24, 426–437.
- [9] Hartree, D. R. The Wave Mechanics of an Atom with a Non-Coulomb Central Field. Part II. Some Results and Discussion. *Math. Proc. Camb. Philos. Soc.* **1928**, 24, 111–132.
- [10] Hartree, D. R. The Wave Mechanics of an Atom with a Non-Coulomb Central Field. Part I. Theory and Methods. *Math. Proc. Camb. Philos. Soc.* **1928**, 24, 89–110.
- [11] Hartree, D. R.; Hartree, W. Self-Consistent Field, with Exchange, for Beryllium. *Proc. R. Soc. Lond. A* **1935**, 150, 9–33.
- [12] Fock, V. Näherungsmethode zur Lösung des quantenmechanischen Mehrkörperproblems. *Z. Phys.* **1930**, 61, 126–148.
- [13] Fock, V. “Selfconsistent field” mit Austausch für Natrium. *Z. Phys.* **1930**, 62, 795–805.
- [14] Wigner, E. On the Interaction of Electrons in Metals. *Phys. Rev.* **1934**, 46, 1002–1011.
- [15] Löwdin, P.-O. Quantum Theory of Many-Particle Systems. III. Extension of the Hartree-Fock Scheme to Include Degenerate Systems and Correlation Effects. *Phys. Rev.* **1955**, 97, 1509–1520.
- [16] Lennard-Jones, J. E. The Electronic Structure of Some Diatomic Molecules. *Trans. Faraday Soc.* **1929**, 25, 668–686.

- [17] Roothaan, C. C. J. New Developments in Molecular Orbital Theory. *Rev. Mod. Phys.* **1951**, 23, 69–89.
- [18] Hall, G. G.; Lennard-Jones, J. E. The Molecular Orbital Theory of Chemical Valency VIII. A Method of Calculating Ionization Potentials. *Proc. R. Soc. Lond. A* **1951**, 205, 541–552.
- [19] Boys, S. F.; Egerton, A. C. Electronic Wave Functions - I. A General Method of Calculation for the Stationary States of Any Molecular System. *Proc. R. Soc. Lond. A* **1950**, 200, 542–554.
- [20] Jensen, F. Atomic Orbital Basis Sets. *Wiley Interdiscip. Rev. Comput. Mol. Sci.* **2013**, 3, 273–295.
- [21] Ditchfield, R.; Hehre, W. J.; Pople, J. A. Self-Consistent Molecular-Orbital Methods. IX. An Extended Gaussian-Type Basis for Molecular-Orbital Studies of Organic Molecules. *J. Chem. Phys.* **1971**, 54, 724–728.
- [22] Hehre, W. J.; Ditchfield, R.; Pople, J. A. Self-Consistent Molecular Orbital Methods. XII. Further Extensions of Gaussian-Type Basis Sets for Use in Molecular Orbital Studies of Organic Molecules. *J. Chem. Phys.* **1972**, 56, 2257–2261.
- [23] Dunning, T. H. Gaussian Basis Functions for Use in Molecular Calculations. I. Contraction of (9s5p) Atomic Basis Sets for the First-Row Atoms. *J. Chem. Phys.* **1970**, 53, 2823–2833.
- [24] Dunning, T. H. Gaussian Basis Sets for Use in Correlated Molecular Calculations. I. The Atoms Boron through Neon and Hydrogen. *J. Chem. Phys.* **1989**, 90, 1007–1023.
- [25] Rayleigh, J. W. S. B. *The theory of sound*; Macmillan, 1896; Vol. 2.
- [26] Schrödinger, E. Quantisierung Als Eigenwertproblem. *Ann. Phys.* **1926**, 385, 437–490.
- [27] Feynman, R. P. Forces in Molecules. *Phys. Rev.* **1939**, 56, 340–343.
- [28] Møller, C.; Plesset, M. S. Note on an Approximation Treatment for Many-Electron Systems. *Phys. Rev.* **1934**, 46, 618–622.
- [29] Čížek, J. On the Correlation Problem in Atomic and Molecular Systems. Calculation of Wavefunction Components in Ursell-Type Expansion Using Quantum-Field Theoretical Methods. *J. Chem. Phys.* **1966**, 45, 4256–4266.
- [30] Purvis, G. D.; Bartlett, R. J. A Full Coupled-cluster Singles and Doubles Model: The Inclusion of Disconnected Triples. *J. Chem. Phys.* **1982**, 76, 1910–1918.
- [31] Löwdin, P.-O. A Generalization of Brillouin's Theorem and the Stability Conditions in the Quantum-Mechanical Variation Principle in the Case of General Trial Wave Functions. *J. Chem. Sci.* **1986**, 96, 121–126.
- [32] Christiansen, O.; Koch, H.; Jørgensen, P. The Second-Order Approximate Coupled Cluster Singles and Doubles Model CC2. *Chem. Phys. Lett.* **1995**, 243, 409–418.

- [33] Koch, H.; Christiansen, O.; Jørgensen, P.; Sanchez de Merás, A. M.; Helgaker, T. The CC3 Model: An Iterative Coupled Cluster Approach Including Connected Triples. *J. Chem. Phys.* **1997**, *106*, 1808–1818.
- [34] Hohenberg, P.; Kohn, W. Inhomogeneous Electron Gas. *Phys. Rev.* **1964**, *136*, B864–B871.
- [35] Kohn, W.; Sham, L. J. Self-Consistent Equations Including Exchange and Correlation Effects. *Phys. Rev.* **1965**, *140*, A1133–A1138.
- [36] Becke, A. D. Density-Functional Exchange-Energy Approximation with Correct Asymptotic Behavior. *Phys. Rev. A* **1988**, *38*, 3098–3100.
- [37] Lee, n.; Yang, n.; Parr, n. Development of the Colle-Salvetti Correlation-Energy Formula into a Functional of the Electron Density. *Phys. Rev. B* **1988**, *37*, 785–789.
- [38] Tsuneda, T. *Density Functional Theory in Quantum Chemistry*; Springer Japan: Tokyo, 2014.
- [39] Vosko, S. H.; Wilk, L.; Nusair, M. Accurate Spin-Dependent Electron Liquid Correlation Energies for Local Spin Density Calculations: A Critical Analysis. *Can. J. Phys.* **1980**, *58*, 1200–1211.
- [40] Zhao, Y.; Truhlar, D. G. The M06 Suite of Density Functionals for Main Group Thermochemistry, Thermochemical Kinetics, Noncovalent Interactions, Excited States, and Transition Elements: Two New Functionals and Systematic Testing of Four M06-Class Functionals and 12 Other Functionals. *Theor. Chem. Acc.* **2008**, *120*, 215–241.
- [41] Burke, K.; Ernzerhof, M.; Perdew, J. P. The Adiabatic Connection Method: A Non-Empirical Hybrid. *Chem. Phys. Lett.* **1997**, *265*, 115–120.
- [42] Yang, W. Generalized Adiabatic Connection in Density Functional Theory. *J. Chem. Phys.* **1998**, *109*, 10107–10110.
- [43] Becke, A. D. Density-functional Thermochemistry. III. The Role of Exact Exchange. *J. Chem. Phys.* **1993**, *98*, 5648–5652.
- [44] Perdew, J. P. Density-Functional Approximation for the Correlation Energy of the Inhomogeneous Electron Gas. *Phys. Rev. B* **1986**, *33*, 8822–8824.
- [45] Yanai, T.; Tew, D. P.; Handy, N. C. A New Hybrid Exchange–Correlation Functional Using the Coulomb-Attenuating Method (CAM-B3LYP). *Chem. Phys. Lett.* **2004**, *393*, 51–57.
- [46] Iikura, H.; Tsuneda, T.; Yanai, T.; Hirao, K. A Long-Range Correction Scheme for Generalized-Gradient-Approximation Exchange Functionals. *J. Chem. Phys.* **2001**, *115*, 3540–3544.
- [47] Grimme, S. Semiempirical Hybrid Density Functional with Perturbative Second-Order Correlation. *J. Chem. Phys.* **2006**, *124*, 034108.
- [48] Grimme, S. Accurate description of van der Waals complexes by density functional theory

- including empirical corrections. *J. Comput. Chem.* **2004**, *25*, 1463–1473.
- [49] Grimme, S. Semiempirical GGA-type density functional constructed with a long-range dispersion correction. *J. Comput. Chem.* **2006**, *27*, 1787–1799.
- [50] Grimme, S.; Antony, J.; Ehrlich, S.; Krieg, H. A Consistent and Accurate Ab Initio Parametrization of Density Functional Dispersion Correction (DFT-D) for the 94 Elements H-Pu. *J. Chem. Phys.* **2010**, *132*, 154104.
- [51] Caldeweyher, E.; Bannwarth, C.; Grimme, S. Extension of the D3 Dispersion Coefficient Model. *J. Chem. Phys.* **2017**, *147*, 034112.
- [52] Chai, J.-D.; Head-Gordon, M. Long-Range Corrected Hybrid Density Functionals with Damped Atom–Atom Dispersion Corrections. *Phys. Chem. Chem. Phys.* **2008**, *10*, 6615–6620.
- [53] Frisch, M. J. et al. Gaussian 16 Revision A.03. 2016; Gaussian Inc. Wallingford CT.
- [54] Bannwarth, C.; Ehlert, S.; Grimme, S. GFN2-xTB-An Accurate and Broadly Parametrized Self-Consistent Tight-Binding Quantum Chemical Method with Multipole Electrostatics and Density-Dependent Dispersion Contributions. *J. Chem. Theory Comput.* **2019**, *15*, 1652–1671.
- [55] Grimme, S.; Bannwarth, C.; Shushkov, P. A Robust and Accurate Tight-Binding Quantum Chemical Method for Structures, Vibrational Frequencies, and Noncovalent Interactions of Large Molecular Systems Parametrized for All Spd-Block Elements ($Z = 1-86$). *J. Chem. Theory Comput.* **2017**, *13*, 1989–2009.
- [56] Bannwarth, C.; Caldeweyher, E.; Ehlert, S.; Hansen, A.; Pracht, P.; Seibert, J.; Spicher, S.; Grimme, S. Extended Tight-Binding Quantum Chemistry Methods. *Wiley Interdiscip. Rev. Comput. Mol. Sci.* **2021**, *11*, e1493.
- [57] Elstner, M.; Seifert, G. Density Functional Tight Binding. *Philos. Trans. R. Soc. A* **2014**, *372*, 20120483.
- [58] Gaus, M.; Cui, Q.; Elstner, M. DFTB3: Extension of the Self-Consistent-Charge Density-Functional Tight-Binding Method (SCC-DFTB). *J. Chem. Theory Comput.* **2011**, *7*, 931–948.
- [59] Lindh, R.; Bernhardsson, A.; Karlström, G.; Malmqvist, P.-Å. On the Use of a Hessian Model Function in Molecular Geometry Optimizations. *Chem. Phys. Lett.* **1995**, *241*, 423–428.
- [60] Schmitz, S.; Seibert, J.; Ostermeir, K.; Hansen, A.; Göller, A. H.; Grimme, S. Quantum Chemical Calculation of Molecular and Periodic Peptide and Protein Structures. *J. Phys. Chem. B* **2020**, *124*, 3636–3646.
- [61] Richardson, L. F.; Gaunt, J. A. The Deferred Approach to the Limit. Part I. Single Lattice. Part II. Interpenetrating Lattices. *Philos. Trans. R. Soc. Lond. A* **1927**, *226*, 299–361.

- [62] Mohammed, A. A. K.; Limacher, P. A.; Champagne, B. Finding Optimal Finite Field Strengths Allowing for a Maximum of Precision in the Calculation of Polarizabilities and Hyperpolarizabilities. *J. Comput. Chem.* **2013**, *34*, 1497–1507.
- [63] de Wergifosse, M.; Liégeois, V.; Champagne, B. Evaluation of the Molecular Static and Dynamic First Hyperpolarizabilities. *Int. J. Quantum Chem.* **2014**, *114*, 900–910.
- [64] Atkins, P. J. d. *P. Atkins' Physical Chemistry*, ninth edition ed.; Oxford University Press: Oxford, 2010.
- [65] Shirley, J. H. Solution of the Schrödinger Equation with a Hamiltonian Periodic in Time. *Phys. Rev.* **1965**, *138*, B979–B987.
- [66] Olsen, J.; Jørgensen, P. Linear and Nonlinear Response Functions for an Exact State and for an MCSCF State. *J. Chem. Phys.* **1985**, *82*, 3235–3264.
- [67] Christiansen, O.; Jørgensen, P.; Hättig, C. Response Functions from Fourier Component Variational Perturbation Theory Applied to a Time-Averaged Quasienergy. *Int. J. Quantum Chem.* **1998**, *68*, 1–52.
- [68] Pawłowski, F.; Olsen, J.; Jørgensen, P. Molecular Response Properties from a Hermitian Eigenvalue Equation for a Time-Periodic Hamiltonian. *J. Chem. Phys.* **2015**, *142*, 114109.
- [69] Dalgaard, E. Quadratic Response Functions within the Time-Dependent Hartree-Fock Approximation. *Phys. Rev. A* **1982**, *26*, 42–52.
- [70] Gerratt, J.; Mills, I. M. Force Constants and Dipole-Moment Derivatives of Molecules from Perturbed Hartree-Fock Calculations. II. Applications to Limited Basis-Set SCF-MO Wavefunctions. *J. Chem. Phys.* **1968**, *49*, 1730–1739.
- [71] Sekino, H.; Bartlett, R. J. Hyperpolarizabilities of the Hydrogen Fluoride Molecule: A Discrepancy between Theory and Experiment? *J. Chem. Phys.* **1986**, *84*, 2726–2733.
- [72] Karna, S. P.; Dupuis, M. Frequency Dependent Nonlinear Optical Properties of Molecules: Formulation and Implementation in the HONDO Program. *J. Comput. Chem.* **1991**, *12*, 487–504.
- [73] Runge, E.; Gross, E. K. U. Density-Functional Theory for Time-Dependent Systems. *Phys. Rev. Lett.* **1984**, *52*, 997–1000.
- [74] van Leeuwen, R. Causality and Symmetry in Time-Dependent Density-Functional Theory. *Phys. Rev. Lett.* **1998**, *80*, 1280–1283.
- [75] Colwell, S. M.; Murray, C. W.; Handy, N. C.; Amos, R. D. The Determination of Hyperpolarisabilities Using Density Functional Theory. *Chem. Phys. Lett.* **1993**, *210*, 261–268.
- [76] Lee, A. M.; Colwell, S. M. The Determination of Hyperpolarizabilities Using Density Functional Theory with Nonlocal Functionals. *J. Chem. Phys.* **1994**, *101*, 9704–9709.

- [77] von Neumann, J.; Wigner, E. P. Über Das Verhalten von Eigenwerten Bei Adiabatischen Prozessen. *Phys. Z.* **1929**, *30*, 467–470.
- [78] von Neumann, J.; Wigner, E. P. In *The Collected Works of Eugene Paul Wigner: Part A*; Wightman, A. S., Ed.; The Collected Works of Eugene Paul Wigner; Springer: Berlin, Heidelberg, 1993; pp 294–297.
- [79] de Wergifosse, M.; Grimme, S. Nonlinear-Response Properties in a Simplified Time-Dependent Density Functional Theory (sTD-DFT) Framework: Evaluation of the First Hyperpolarizability. *J. Chem. Phys.* **2018**, *149*, 024108.
- [80] Aidas, K. et al. The Dalton Quantum Chemistry Program System. *J. Comp. Chem.* **2014**, *4*, 269–284.
- [81] de Wergifosse, M.; Grimme, S. Nonlinear-Response Properties in a Simplified Time-Dependent Density Functional Theory (sTD-DFT) Framework: Evaluation of Excited-State Absorption Spectra. *J. Chem. Phys.* **2019**, *150*, 094112.
- [82] de Wergifosse, M.; Grimme, S. Perspective on Simplified Quantum Chemistry Methods for Excited States and Response Properties. *J. Phys. Chem. A* **2021**,
- [83] Casida, M. E. *Recent Advances in Density Functional Methods*; Recent Advances in Computational Chemistry; World Scientific, 1995; Vol. Volume 1; pp 155–192.
- [84] Dancoff, S. M. Non-Adiabatic Meson Theory of Nuclear Forces. *Phys. Rev.* **1950**, *78*, 382–385.
- [85] Hirata, S.; Head-Gordon, M. Time-Dependent Density Functional Theory within the Tamm–Dancoff Approximation. *Chem. Phys. Lett.* **1999**, *314*, 291–299.
- [86] Still, W. C.; Tempczyk, A.; Hawley, R. C.; Hendrickson, T. Semianalytical Treatment of Solvation for Molecular Mechanics and Dynamics. *J. Am. Chem. Soc.* **1990**, *112*, 6127–6129.
- [87] Cramer, C. J.; Truhlar, D. G. General Parameterized SCF Model for Free Energies of Solvation in Aqueous Solution. *J. Am. Chem. Soc.* **1991**, *113*, 8305–8311.
- [88] Hawkins, G. D.; Cramer, C. J.; Truhlar, D. G. Pairwise Solute Descreening of Solute Charges from a Dielectric Medium. *Chem. Phys. Lett.* **1995**, *246*, 122–129.
- [89] Onsager, L. Electric Moments of Molecules in Liquids. *J. Am. Chem. Soc.* **1936**, *58*, 1486–1493.
- [90] Tomasi, J.; Mennucci, B.; Cammi, R. Quantum Mechanical Continuum Solvation Models. *Chem. Rev.* **2005**, *105*, 2999–3094.
- [91] Miertuš, S.; Scrocco, E.; Tomasi, J. Electrostatic Interaction of a Solute with a Continuum. A Direct Utilizaion of AB Initio Molecular Potentials for the Prevision of Solvent Effects. *Chem. Phys.* **1981**, *55*, 117–129.

- [92] Miertuš, S.; Tomasi, J. Approximate Evaluations of the Electrostatic Free Energy and Internal Energy Changes in Solution Processes. *Chem. Phys.* **1982**, 65, 239–245.
- [93] Tomasi, J.; Mennucci, B.; Cancès, E. The IEF Version of the PCM Solvation Method: An Overview of a New Method Addressed to Study Molecular Solutes at the QM Ab Initio Level. *Comput. Theor. Chem.* **1999**, 464, 211–226.
- [94] Cammi, R.; Cossi, M.; Mennucci, B.; Tomasi, J. Analytical Hartree–Fock Calculation of the Dynamical Polarizabilities α , β , and γ of Molecules in Solution. *J. Chem. Phys.* **1996**, 105, 10556–10564.
- [95] Dapprich, S.; Komáromi, I.; Byun, K. S.; Morokuma, K.; Frisch, M. J. A New ONIOM Implementation in Gaussian98. Part I. The Calculation of Energies, Gradients, Vibrational Frequencies and Electric Field derivatives. *Comput. Theor. Chem.* **1999**, 461-462, 1–21.

Part II

**Accurate description and understanding of
the first and second hyperpolarizabilities
of reference molecules**

Coupled Cluster evaluation of the frequency dispersion of the first and second hyperpolarizabilities of water, methanol and dimethyl ether

J. Chem. Phys. **2016**, *145*, 044311 (DOI: 10.1063/1.4958736)

Pierre Beaujean and Benoît Champagne

*Laboratory of Theoretical Chemistry, Namur Institute of Structured Matter,
University of Namur, Rue de Bruxelles 61, B-5000 Namur, Belgium*

Abstract

The static and dynamic first ($\beta_{||}$) and the second ($\gamma_{||}$) hyperpolarizabilities of water, methanol, and dimethyl ether have been evaluated within the response function approach using a hierarchy of coupled cluster levels of approximation and doubly-augmented correlation consistent atomic basis sets. For the three compounds, the electronic $\beta_{||}$ and $\gamma_{||}$ values calculated at the CCSD and CC3 levels are in good agreement with gas phase electric field-induced second harmonic generation (EFISHG) measurements. In addition, for dimethyl ether, the frequency dispersion of both properties follows closely recent experimental values [V. W. Couling and D. P. Shelton, *J. Chem. Phys.* **143**, 224307 (2015)] demonstrating the reliability of these methods and levels of approximation. This also suggests that the vibrational contributions to the EFISHG responses of these molecules are small.

► Supporting information are available at <https://doi.org/10.1063/1.4958736>.

Section 4.1

Introduction

The evaluation of the first (β) and second (γ) hyperpolarizability tensors remains a challenge for modern quantum chemistry. Besides the electronic contribution, the vibrational counterpart can be non-negligible and the evaluation of both contributions as well as the description of their frequency dispersion require treatments including electron correlation.^{1–8} During the last 30 years that have witnessed the elaboration of high-level electron-correlation methods, the comparisons between calculation and experiment have turned out to be profitable for increasing the accuracy and precision of both types of methods as well for understanding the origin of the nonlinear optical (NLO) responses.^{1,9–18}

A recent publication due to Couling and Shelton¹⁹ reports measurements of both the first and the second hyperpolarizabilities of dimethyl ether (DME). These measurements have been carried out in gas phase at different frequencies by using the electric field-induced second harmonic generation (ESHG) technique. This new set of data as well as the comparison with water and methanol gives a new opportunity to assess state-of-the-art quantum chemistry methods for predicting the hyperpolarizabilities. Indeed, on the one hand, their small number of atoms allows the use of large basis sets together with high-level post Hartree-Fock methods. On the other hand, these gas phase data prevent from having to account for solvent or surrounding effects, which might be cumbersome.^{20–25}

Following Couling and Shelton, this article is focusing on the two quantities accessible through ESHG experiment, the projection of the vector part of β on the permanent dipole moment ($\vec{\mu}$), $\beta_{||}$, and the isotropic second hyperpolarizability, $\gamma_{||}$, which are defined as:

$$\beta_{||} = \frac{1}{5} \sum_{\zeta}^{x,y,z} \frac{\mu_{\zeta}}{||\vec{\mu}||} \sum_{\eta}^{x,y,z} \beta_{\zeta\eta\eta} + \beta_{\eta\zeta\eta} + \beta_{\eta\eta\zeta} \quad (4.1)$$

$$\gamma_{||} = \frac{1}{15} \sum_{\zeta,\eta}^{x,y,z} \gamma_{\zeta\zeta\eta\eta} + \gamma_{\zeta\eta\eta\zeta} + \gamma_{\zeta\eta\zeta\eta}, \quad (4.2)$$

where ζ, η, \dots are Cartesian coordinates, μ_{ζ} is the ζ component of the permanent dipole moment vector and $||\vec{\mu}||$ its norm. $\beta_{\zeta\eta\eta}$ and $\gamma_{\zeta\eta\eta\zeta}$ are elements of the first and second hyperpolarizability tensors, respectively.

In this contribution, only the electronic hyperpolarizabilities are calculated. They are evaluated by adopting a hierarchy of Coupled Cluster (CC) response function methods, suitable to evaluate the static values as well as their frequency dispersion. The vibrational contributions to β and γ have already been addressed for water^{26–28} and methanol,^{29,30} at different levels of approximation, showing that, at optical frequencies, the vibrational contributions amount to only a few percents of the electronic SHG values.

This paper is organized in three parts: after describing the theoretical frame and the computational details in Section 4.2, the main results for water, methanol and dimethyl ether are presented and discussed in Section 4.3. First, the effects of basis set and electron correlation on the static and dynamic responses are analyzed. This allows selecting “best” values for performing comparisons. Besides comparison with the experimental data of Couling and Shelton,¹⁹ Kaatz et al.,²¹ and Ward and Miller,³¹ comparisons are made with previous theoretical values for water and methanol. To our knowledge, this is the first report on calculated first and second hyperpolarizabilities for DME. The conclusions are drawn in Section 4.4.

Section 4.2

Theoretical methods and computational procedures

The frequency-dependent first and second hyperpolarizabilities are the expansion coefficients of the molecular induced dipole moment as a function of external electric fields, \vec{F} , applied along the η , ξ , ... directions and oscillating at frequencies ω_1 , ω_2 , ...:

$$\begin{aligned} \Delta\mu_\zeta(\vec{F}) &= \sum_{\eta}^{x,y,z} \alpha_{\zeta\eta}(-\omega_\sigma; \omega_1) F_\eta(\omega_1) \\ &+ \frac{1}{2!} \sum_{\eta,\xi}^{x,y,z} \beta_{\zeta\eta\xi}(-\omega_\sigma; \omega_1, \omega_2) F_\eta(\omega_1) F_\xi(\omega_2) + \dots \\ &+ \frac{1}{3!} \sum_{\eta,\xi,\chi}^{x,y,z} \gamma_{\zeta\eta\xi\chi}(-\omega_\sigma; \omega_1, \omega_2, \omega_3) F_\eta(\omega_1) F_\xi(\omega_2) F_\chi(\omega_3) + \dots \end{aligned} \quad (4.3)$$

where $\omega_\sigma = \sum_i \omega_i$ and $\alpha_{\zeta\eta}$ is an element of the polarizability tensors. Depending on the experimental setup and the combination of the static and dynamic electric fields, different NLO processes arise. For the first hyperpolarizability, one distinguishes the linear optoelectronic effect [dc-Pockels, $\beta(-\omega; \omega, 0)$] and the second harmonic generation [SHG, $\beta(-2\omega; \omega; \omega)$]. For the second hyperpolarizability, usual processes encompass the Kerr effect [dc-Kerr, $\gamma(-\omega; \omega, 0, 0)$], the degenerate four wave mixing [DFWM, $\gamma(-\omega; \omega, -\omega, \omega)$], the electric-field induced second harmonic generation [ESHG, $\gamma(-2\omega; \omega, \omega, 0)$], and the third harmonic generation [THG, $\gamma(-3\omega; \omega, \omega, \omega)$].¹

According to Eq. (4.3), the hyperpolarizability tensor elements can be evaluated as the second- and third-order responses of the dipole moment to these fields. Typically, these can be obtained by using response function methods^{32,33} and/or partial finite field numerical derivative techniques.³⁴ Within perturbation theory, β and γ can also be expressed in the form of summations over excited states,^{35,36}

$$P_{\zeta\eta\xi\dots}(-\omega_\sigma; \omega_1, \dots) = \mathcal{P}_{\zeta\eta\dots} \sum_{a_1, a_2, \dots} \frac{\mu_{0a_1}^\zeta \bar{\mu}_{a_1 a_2}^\eta \dots}{(\omega_{a_1} - \omega_\sigma)(\omega_{a_2} - \omega_\sigma + \omega_1) \dots} \quad (4.4)$$

where $P = \alpha, \beta, \gamma$. $\omega_{a_i} = \hbar\omega_{a_i} = E_i - E_0$ is the vertical transition energy between the ground state (0) and the i^{th} excited state, \mathcal{P} is the permutation operator over the pairs of coordinates and frequencies, $(\omega_\sigma, \zeta), (\omega_1, \eta), \dots$. The quantity $\bar{\mu}_{a_i a_j}$ is equal to $\langle i|\hat{\mu}|j\rangle - \delta_{ij} \langle 0|\hat{\mu}|0\rangle$. As a result, the magnitude of the hyperpolarizabilities is inversely proportional to the square (cube) of the excitation energies for β (γ).

Following experimental evidences,³⁷ Bishop^{36,38,39} and, later on, Hättig⁴⁰ demonstrated that the frequency-dependent hyperpolarizabilities [Eq. (4.4)] can be rewritten under the form of a product between the static hyperpolarizabilities, $P(0)$, and a ω_L^2 polynomial:

$$P(-\omega_\sigma; \omega_1, \dots) = P(0)[1 + A\omega_L^2 + B\omega_L^4 + \dots] \quad (4.5)$$

where A, B, \dots are the expansion coefficients, and

$$\omega_L^2 = \sum_i^{\sigma, 1, 2, \dots} \omega_i^2. \quad (4.6)$$

They proved that A is the same for all second-order (third-order) NLO processes but it depends on the molecule. Moreover, B is the same for both ESHG and dc-Kerr processes.^{39,40} Thus, for typical NLO processes with only one optical frequency (ω), ω_L^2 is an integer (k) multiple of ω^2 . For instance, for the SHG and the ESHG processes, k is equal to 6, whereas it amounts to 2 for dc-Pockels and dc-Kerr. This allows defining a frequency dispersion factor, $D(\omega_L^2)$:

$$D(\omega_L^2) = \frac{P(\omega_\sigma; \omega_1, \dots)}{P(0)} - 1 = A\omega_L^2 + B\omega_L^4 + \dots \quad (4.7)$$

These expressions and relationships are valid for average quantities ($\beta_{||}$ and $\gamma_{||}$) as well as for the diagonal tensor elements ($\beta_{\zeta\zeta\zeta}$ and $\gamma_{\zeta\zeta\zeta\zeta}$).

The geometries of the three molecules were optimized at the M06/6-311G(d) level of theory. At first, SHG/ESHG first and second hyperpolarizabilities were evaluated for a range of wavelengths (energies), i.e. ∞ (0), 1064 (9400), 694.3 (14400), 611.3 (16360), 590 (16950), 514.5 (19440) and 488 (20500) nm (cm^{-1}). These hyperpolarizabilities were evaluated at the time-dependent Hartree-Fock (TDHF) level,⁴¹ as well as with a hierarchy of CC models with quadratic and cubic response functions.^{32,33,42,43} Unrelaxed orbitals were assumed. The CC hierarchy, given in increasing order of electron correlation treatment is CCS, CC2, CCSD and CC3.^{32,33,42,43} Those calculations were performed with doubly-augmented correlation consistent polarized valence basis sets, d-aug-cc-pVXZ⁴⁴ ($X=D, T, Q$, and 5 for water, $X=D$ and T for methanol and DME). X determines the splitting level of the valence shell atomic orbitals and also the highest angular momentum quantum number (l_{max}) of the polarization functions. So, for the O atom, if $X = T$ (3), there are three sets of valence s and p functions and $l_{\text{max}} = 3$, corresponding to f polarization functions whereas for $X = Q$ (4), there are 4 valence s and p sets and g polarization functions ($l_{\text{max}} = 4$). This choice of doubly-augmented basis sets is consistent with previous investigations on reference molecules for nonlinear optics.^{16,18}

In a second step, β and γ values for additional NLO processes were calculated. For the latter, the calculations were performed at the [Q,C]RF-CCSD/d-aug-cc-pVDZ level with ω_L^2 values ranging from 0 to $30 \times 10^8 \text{ cm}^{-2}$ by step of $2 \times 10^8 \text{ cm}^{-2}$. All reported β and γ values are given in a.u. [1 a.u. of $\beta = 3.6212 \times 10^{-42} \text{ m}^4 \text{ V}^{-1} = 3.2064 \times 10^{-53} \text{ C}^3 \text{ m}^3 \text{ J}^{-2} = 8.639 \times 10^{-33} \text{ esu}$; 1 a.u. of $\gamma = 7.423 \times 10^{-54} \text{ m}^5 \text{ V}^{-2} = 6.2354 \times 10^{-65} \text{ C}^4 \text{ m}^4 \text{ J}^{-3} = 5.0367 \times 10^{-40} \text{ esu}$] within the T convention.¹ Geometry optimization and TDHF calculations were carried out with the Gaussian 09 D01 package⁴⁵ while response functions at the different coupled-cluster levels were obtained with Dalton 2016.⁴⁶

Section 4.3

Results and discussions

Basis sets and electron correlation effects on β and γ of water

The small water molecule enabled a detailed investigation of electron correlation effects by using basis sets ranging from d-aug-cc-pVDZ to d-aug-cc-pV5Z. The complete data are listed in Tables 4.1, 4.2 for the static and dynamic, quadratic and cubic, responses (their frequency dispersion factors are given in Table S1), respectively. They are summarized in Fig. 4.1. For all properties, static and dynamic β and γ , at any level of approximation, the convergence of the responses with respect to X is fast. Still, it is the fastest at the HF and CCS levels so that differences between the $X = Q$ and $X = 5$ are smaller than or equal to 0.1 (0.3) % for $\beta_{||}$ ($\gamma_{||}$). These differences are larger at the CC2 and CCSD levels but they remain smaller than 1 and 2 %, respectively. Looking at the $X = D, T, Q$ sequence, the differences between $X = Q$ and $X = T$ are smaller than 3 % whereas between $X = T$ and $X = D$ the differences attain 15 % for $\beta_{||}$ but range between 5 and 9 % for $\gamma_{||}$. Similar effects are observed for the frequency dispersion factor, $D(\omega_L^2)$, evaluated at 694.3 nm. Then, for any property and basis set, the magnitude of the responses follows the same ordering:

$$\text{HF} < \text{CCS} < \text{CC3} \approx \text{CCSD} < \text{CC2} \quad (4.8)$$

When considering the quasi-converged d-aug-cc-pVQZ results, the CCSD $\beta_{||}(0)$ value is overestimated by less than 3 % in comparison to the CC3 results, highlighting the small impact of including triples in the CC expansion. On the other hand, the CC2 level overestimates $\beta_{||}(0)$ by about 45 % whereas the HF and CCS methods underestimate the quadratic response by 47 % and 18 %, respectively. In the case of the cubic $\gamma_{||}(0)$ response, the CCSD method overestimates slightly (1 %) the CC3 value and, again, CC2 provides overestimated values (by 38 %) while the HF and CCS methods underestimate it by 41 % and 32 %, respectively. At a wavelength of 1064 nm, the above analysis is confirmed whereas the overestimations and underestimations are typically enhanced by a few percents. Turning to frequency dispersion, the amplitude ordering is $\text{CCS} < \text{HF} < \text{CC3} \approx \text{CCSD} < \text{CC2}$, highlighting an inversion between the HF and CCS methods with respect to the responses ordering as well as between CCSD and CC3, though for the latter the dispersion factors and properties are very similar.

The frequency dispersion factors as well as the amplitudes of the hyperpolarizabilities are determined by the relative values of the lowest excitation energies as well as by the transition dipole moments. Though for molecules like water (and also methanol and DME, *vide infra*) many excited states contribute to Eq. (4.4) and the two-state approximation¹⁰ cannot be invoked, the amplitude ordering of the lowest excitation energies in Table S2 is inverse with respect to the hyperpolarizabilities magnitude:

$$\text{CCS} \approx \text{HF} > \text{CC3} \approx \text{CCSD} > \text{CC2} \quad (4.9)$$

Table S2 also demonstrates the good agreement between the theoretical excitation energy values and those obtained from electron impact data, at both the CCSD and CC3 levels but also using the CC2 method.

Table 4.1: Basis set and electron correlation effects on the static $\beta_{||}$ (a.u.) and $\gamma_{||}$ (a.u.) of water. Relative differences (in %) with respect to d-aug-cc-pV5Z are given in parentheses (except for CC3 for which the comparison is made with d-aug-cc-pVQZ).

	HF	CCS	CC2	CCSD	CC3
$\beta_{ }(0)$					
d-aug-cc-pVDZ	-9.04 (-19.1)	-12.12 (-16.3)	-21.28 (-17.1)	-15.03 (-17.2)	-14.13 (-20.3)
d-aug-cc-pVTZ	-10.85 (-2.8)	-14.16 (-2.2)	-25.46 (-0.8)	-17.90 (-1.4)	-17.22 (-2.9)
d-aug-cc-pVQZ	-11.17 (0.1)	-14.48 (0.03)	-25.81 (0.6)	-18.25 (0.5)	-17.74
d-aug-cc-pV5Z	-11.17	-14.48	-25.66	-18.16	—
$\gamma_{ }(0)$					
d-aug-cc-pVDZ	907 (-9.1)	1063 (-8.7)	2294 (-1.2)	1705 (0.6)	1630 (-4.7)
d-aug-cc-pVTZ	999 (0.2)	1165 (0.1)	2429 (4.6)	1773 (4.6)	1744 (2.0)
d-aug-cc-pVQZ	1001 (0.3)	1167 (0.24)	2366 (1.8)	1722 (1.6)	1710
d-aug-cc-pV5Z	998	1164	2323	1694	—

Table 4.2: Basis set and electron correlation effects on the dynamic (at 1064 nm) $\beta_{||}$ (a.u.) and $\gamma_{||}$ (a.u.) of water. Relative differences (in %) with respect to d-aug-cc-pV5Z are given in parentheses (except for CC3 for which the comparison is made with d-aug-cc-pVQZ for $\beta_{||}$ and d-aug-cc-pVTZ for $\gamma_{||}$).

	HF	CCS	CC2	CCSD	CC3
$\beta_{ }(-2\omega; \omega, \omega)$					
d-aug-cc-pVDZ	-9.67 (-18.7)	-12.83 (-16.1)	-23.61 (-15.8)	-16.50 (-16.1)	-15.54 (-19.9)
d-aug-cc-pVTZ	-11.57 (-2.8)	-14.96 (-2.2)	-27.94 (-0.4)	-19.45 (-1.1)	-18.77 (-2.6)
d-aug-cc-pVQZ	-11.91 (0.1)	-15.30 (0.0)	-28.23 (0.7)	-19.77 (0.6)	-19.28
d-aug-cc-pV5Z	-11.90	-15.30	-28.04	-19.66	—
$\gamma_{ }(-2\omega; \omega, \omega, 0)$					
d-aug-cc-pVDZ	985 (-9.0)	1149 (-8.7)	2607 (-0.2)	1906 (1.5)	1821 (-15.1)
d-aug-cc-pVTZ	1084 (0.1)	1259 (0.1)	2738 (4.9)	1969 (4.9)	2147
d-aug-cc-pVQZ	1086 (0.3)	1261 (0.3)	2662 (1.9)	1909 (1.7)	—
d-aug-cc-pV5Z	1083	1258	2611	1877	—

Basis sets and electron correlation effects on β and γ of methanol and DME

The results on the first and second hyperpolarizabilities of MeOH (Tables 4.3) and DME (Tables 4.4) confirm to a large extent the analysis made on water. In the case of methanol, the differences between $X = T$ and $X = D$ is much smaller than for water, highlighting cooperation effects between basis functions on different atomic centers. Qualitatively, the differences between the various CC levels are consistent with water: the CC3 and CCSD methods provide similar values (the effect of the triples is small), the HF and CCS levels underestimate them while CC2 overestimates them.

Table 4.3: Basis set ($X = D, T$) and electron correlation effects on the static and dynamic (at 1064 nm) $\beta_{||}$ (a.u.) and $\gamma_{||}$ (a.u.) of methanol as well as on their frequency dispersion factor [$D(\omega_L^2)$] at 694.3 nm. Relative errors (in %) with respect to $X = T$ values are given in parentheses.

	X	HF	CCS	CC2	CCSD	CC3
$\beta_{ }(0)$	D	-24.86 (-1.1)	-30.40 (-0.8)	-38.46 (0.5)	-31.11 (-0.1)	-29.93
	T	-25.13	-30.63	-38.26	-31.14	—
$\beta_{ }(-2\omega; \omega, \omega)$	D	-26.59 (-1.0)	-32.29 (-0.7)	-42.01 (1.0)	-33.73 (0.3)	-32.53
	T	-26.86	-32.54	-41.60	-33.64	—
$D(\omega_L^2)$ of $\beta_{ }(-2\omega; \omega, \omega)$	D	0.177 (0.9)	0.159 (0.7)	0.242 (5.9)	0.219 (5.3)	0.226
	T	0.176	0.158	0.228	0.208	—
$\gamma_{ }(0)$	D	2184 (-4)	2592 (-3.5)	4538 (1.8)	3554 (1.8)	3426
	T	2274	2686	4456	3491	—
$\gamma_{ }(-2\omega; \omega, \omega, 0)$	D	2381	2813	5149	3968	—
$D(\omega_L^2)$ of $\gamma_{ }(-2\omega; \omega, \omega, 0)$	D	0.235	0.221	0.374	0.316	—

In the case of DME, differences between $X = T$ and $X = D$ are slightly larger than for methanol but remain smaller than 10 %. The impact of successive improvements of the electron correlation treatment is very similar, qualitatively and quantitatively, to what was observed for water and methanol. Moreover, contrary to water and methanol, enlarging the basis set leads to a decrease of the $\beta_{||}$ and $\gamma_{||}$ amplitudes rather than an increase as in the case of the former.

Comparison with experiment and other theoretical results

Gas phase experimental $\beta_{||}$ and $\gamma_{||}$ values for water and MeOH,^{21,31} as well as for DME,¹⁹ are collected in Table 4.5 together with our best theoretical estimates. These are defined as the values obtained with the highest level of approximation, usually CC3, and then the most extended basis set. Note that previous experimental values have an uncertainty of about 5 % while for the recent values due to Couling and Shelton for DME the uncertainty is improved

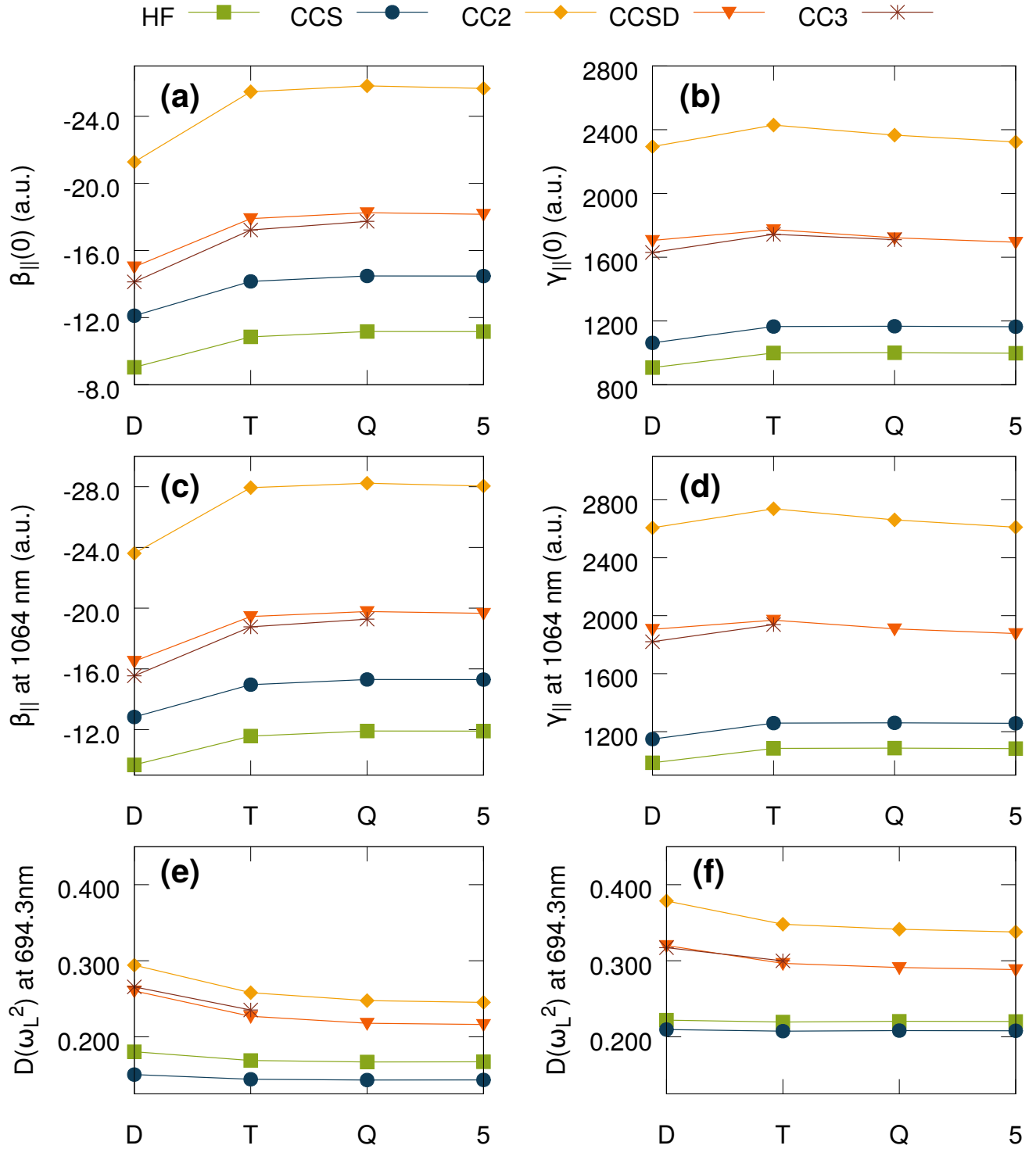


Figure 4.1: Effect of the basis set (d-aug-cc-pVXZ) and of the level of approximation on the first ($\beta_{||}$, a.u., left) and second ($\gamma_{||}$, a.u., right) hyperpolarizabilities of water. Top and middle panels give the static and dynamic (SHG or ESHG at 1064 nm) responses while the bottom panels report the frequency dispersion [$D(\omega_L^2)$] for SHG or ESHG at 694.3 nm.

Table 4.4: Basis set ($X = D, T$) and electron correlation effects on the static and dynamic (at 1064 nm) $\beta_{||}$ (a.u.) and $\gamma_{||}$ (a.u.) of DME as well as on their frequency dispersion factor [$D(\omega_L^2)$] at 694.3 nm. Relative errors (in %) with respect to d-aug-cc-pVTZ values are given in parentheses.

	X	HF	CCS	CC2	CCSD	CC3
$\beta_{ }(0)$	D	-54.20 (1.1)	-66.85 (1.2)	-131.32 (7.8)	-93.65 (7.2)	-90.65
	T	-53.60	-66.08	-121.77	-87.39	—
$\beta_{ }(-2\omega; \omega, \omega)$	D	-58.93 (1.2)	-72.20 (1.2)	-150.67 (8.6)	-105.43 (7.8)	-102.18
	T	-58.26	-71.34	-138.76	-97.83	—
$D(\omega_L^2)$ of $\beta_{ }(-2\omega; \omega, \omega)$	D	0.227 (0.5)	0.207 (0.5)	0.416 (6.9)	0.344 (6.3)	0.348
	T	0.226	0.206	0.389	0.324	—
$\gamma_{ }(0)$	D	4053 (-1.2)	4897 (-0.9)	10147 (7.4)	7313 (6.2)	7033
	T	4101	4941	9450	6886	—
$\gamma_{ }(-2\omega; \omega, \omega, 0)$	D	4480	5386	12025	8417	—
$D(\omega_L^2)$ of $\gamma_{ }(-2\omega; \omega, \omega, 0)$	D	0.279	0.263	0.553	0.429	—

by one order of magnitude. For the three compounds, a very nice agreement is achieved, in particular for water and methanol. For DME, the deviations attain about 8 %, which might be due to the lack of CC3 values with $X = T$ or due to missing vibrational contributions. Then, for DME, the frequency dispersion factors are compared in Fig. 4.2 to those of Ref. 19. For the whole range of wavenumbers, the agreement between the CCSD and CC3 calculations and experiment is very good and even excellent in the case of $\gamma_{||}$. Of course, as already discussed, consistently with the excitation energies, the optical dispersion is overestimated at the CC2 level while underestimated by the HF and CCS methods (Tables S2 and S3).

Now, comparisons with selected previous calculations are made for $\beta_{||}$ and $\gamma_{||}$ of each compound. For $\beta_{||}$ of water (Table 4.6), these highlight i) the consistency between our QRF-CC results and those of Christiansen *et al.*,⁴³ though slightly different geometries are employed, ii) the reliability of the QED-MP2 method, iii) the performance of the modified POL basis set with respect to doubly-augmented correlation consistent basis sets, iv) the underestimation due to using the QRF-CAS approach, and v) overestimations when employing DFT with conventional exchange-correlation functionals.

The analysis of the $\gamma_{||}$ values of water (Table 4.7) shows the good agreement between our results and the CCSD and CCSD(T) static values of Sekino and Bartlett² as well as with the static and dynamic QED-MP2 values of Kobayashi *et al.*⁵³ These comparisons confirm also the underestimations of the HF method with a complete basis set and the overestimations of DFT with a functional missing the long-range behavior.

In the case of methanol, the POL basis set gives RPA³⁰ (*i.e.* HF) and CCSD⁶ $\beta_{||}$ and $\gamma_{||}$ values that are consistent with our TDHF and QRF-CCSD results, respectively. Moreover, all

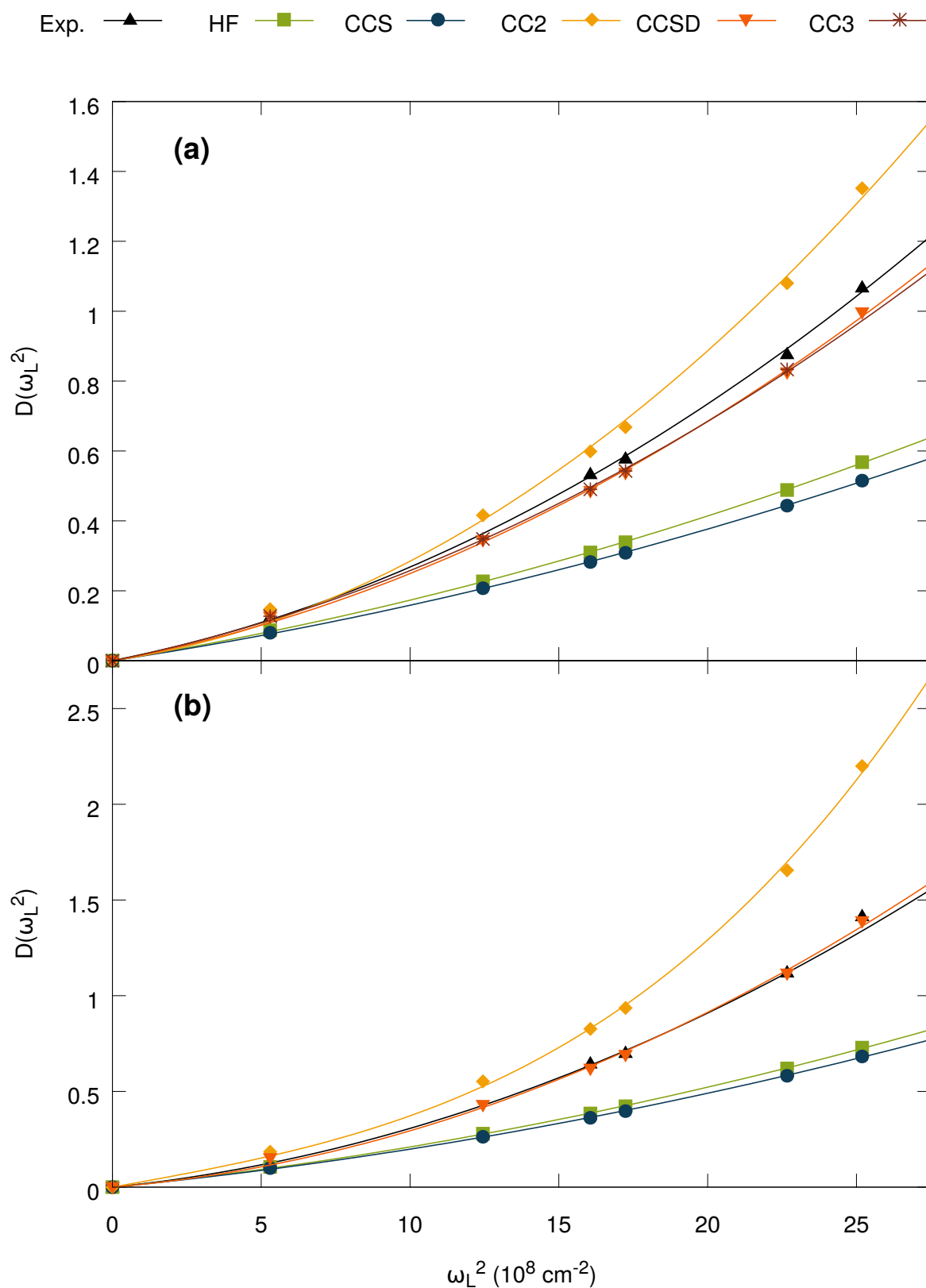


Figure 4.2: Comparison between experimental and calculated frequency dispersions $[D(\omega_L^2)]$ of the (a) first and (b) second hyperpolarizabilities of DME. The calculations were performed at different levels of approximation using the d-aug-cc-pVDZ basis set.

Table 4.5: Experimental $\beta_{||}$ (a.u.) and $\gamma_{||}$ (a.u.) of water, methanol, and DME in comparison with our “best” theoretical values.

λ	Water		Methanol		DME	
	1064 nm ¹	694.3 nm ²	1064 nm ^{1,3}	694.3 nm ²	∞ ^{4,5}	1064 ⁴
Experiment						
$\beta_{ }$	-19.2±0.9	-22.0±0.9	-31.2±1.6	-35.0±2.1	-83.5	-94.0±0.25
$\gamma_{ }$	1800±150	2310±120	3730±190	4590±130	7624	8591±34
Theory						
$\beta_{ }$	-19.28	-21.77	-32.53	-36.69	-90.65	-102.19
$\gamma_{ }$	2147	2266	3968	4677	7033	8417

¹ Ref. 21.

² Ref. 31.

³ Value for CH₃OD instead of CH₃OH.

⁴ Ref. 19, additional frequencies available (see text).

⁵ Static value extrapolated from experimental data using Eq. (4.5).

the CCSD and CC3 results agree with experiment, considering the error bars on the measurements. On the other hand, the dynamic $\gamma_{||}$ evaluated at the Restricted Active Space (RAS) level underestimates experiment by about 30 %.

Comparison of the frequency dispersion for different NLO processes

The frequency dispersion of $\beta_{||}$ and $\gamma_{||}$ was then investigated by considering several second- and third-order NLO processes. This is achieved by plotting the $D(\omega_L^2)$ functions (Eq. (4.7)) as a function of ω_L^2 (Figs. 4.3-4.5). As shown, for the three compounds, the $D(\omega_L^2)$ curves of the different NLO processes (of a given order) are superimposed over a broad range of wavenumbers so that values obtained for a given NLO process can easily be converted into the corresponding values for another NLO process. Though these relationships only apply to the electronic contributions to the first and second hyperpolarizabilities, they open possibilities for comparison with new experimental data. These $D(\omega_L^2)$ dispersion functions were evaluated at the CCSD/d-aug-cc-pVDZ level of approximation. Polynomial fits including terms up to 7th order in ω_L^2 were also performed in order to compare the A coefficients, describing the dispersion at small wavenumbers. Data included in Figs. 4.3-4.5 show that the A coefficients for $\beta_{||}$ behave inversely to the lowest excitation energies (Tables S2 and S3). On the other hand, for $\gamma_{||}$ the A coefficients for water and methanol are similar and smaller than for DME. Note that the A coefficients are systematically larger for $\gamma_{||}$ than for $\beta_{||}$. Finally, the amplitudes of frequency dispersion were compared among the NLO processes of a given order. It is noticed that $D(\omega_L^2)$ of methanol and DME is larger for DFWM $\gamma_{||}$ than for the other processes, for which the dispersion functions are little different over the probed range of wavenumbers. For water,

Table 4.6: Comparison between experimental and calculated static and dynamic (at 694.3 nm) $\beta_{||}$ values (a.u.) of water.

Method	Basis set	Static	Dynamic	
Experiment	—	—	-22.0±0.9	Ref. 31
QRF-CCSD	d-aug-cc-pV5Z	-18.16	-22.08	This work
QRF-CC3	d-aug-cc-pVQZ	-17.74	-21.77	This work
TDHF	modified POL ¹	-10.8	-12.57	Ref. 2
FF ² /HF	HF limit	-11.07	—	Ref. 47
TDDFT/LDA	d-aug-cc-pVTZ	-23.78	-32.12	Ref. 48
TDDFT/BLYP	d-aug-cc-pVTZ	-23.65	-32.76	Ref. 48
TDDFT/B3LYP	d-aug-cc-pVTZ	-18.54	-24.11	Ref. 48
QED-MP2	modified HyPOL ³	-17.67	-21.31	Ref. 49
QRF-CAS	P3 ⁴	-15.68	-19.02	Ref. 27
QRF-CCSD	d-aug-cc-pVTZ	-17.73	-21.72	Ref. 43
QRF-CCSD	d-aug-cc-pVQZ	-18.07	-21.98	Ref. 43
QRF-CC3	d-aug-cc-pVTZ	-17.04	-21.02	Ref. 43
FF ² /CCSD	modified POL ¹	-16.2	—	Ref. 2.
FF ² /CCSD(T)	modified POL ¹	-18.0	—	Ref. 2

¹ Sadlej POL basis set⁵⁰ augmented with a set of *d* functions on H atoms and two sets of *1s1p* functions to describe the lone pairs.

² Finite field numerical derivatives of the energy.

³ Sadlej HyPOL basis set⁵¹ with optimized coefficients.

⁴ [8s5p3d1f/4s2p1d] basis set of Diercksen *et al.*⁵² with a CAS of 8 active orbitals.

there is no such difference and literature shows that the two situations occur. On the one hand for the hydrogen⁵⁵ and helium⁵⁶ atoms as well as for ethylene,⁵⁷ DFWM dispersion is large compared to sum wave mixing processes such as dc-Kerr, ESHG, and THG with only positive frequency arguments. On the other hand, for all-trans hexatriene,⁵⁷ the frequency dispersion is larger for ESHG than DFWM. Finally, for *p*-nitroaniline,⁵⁸ there is hardly any difference.

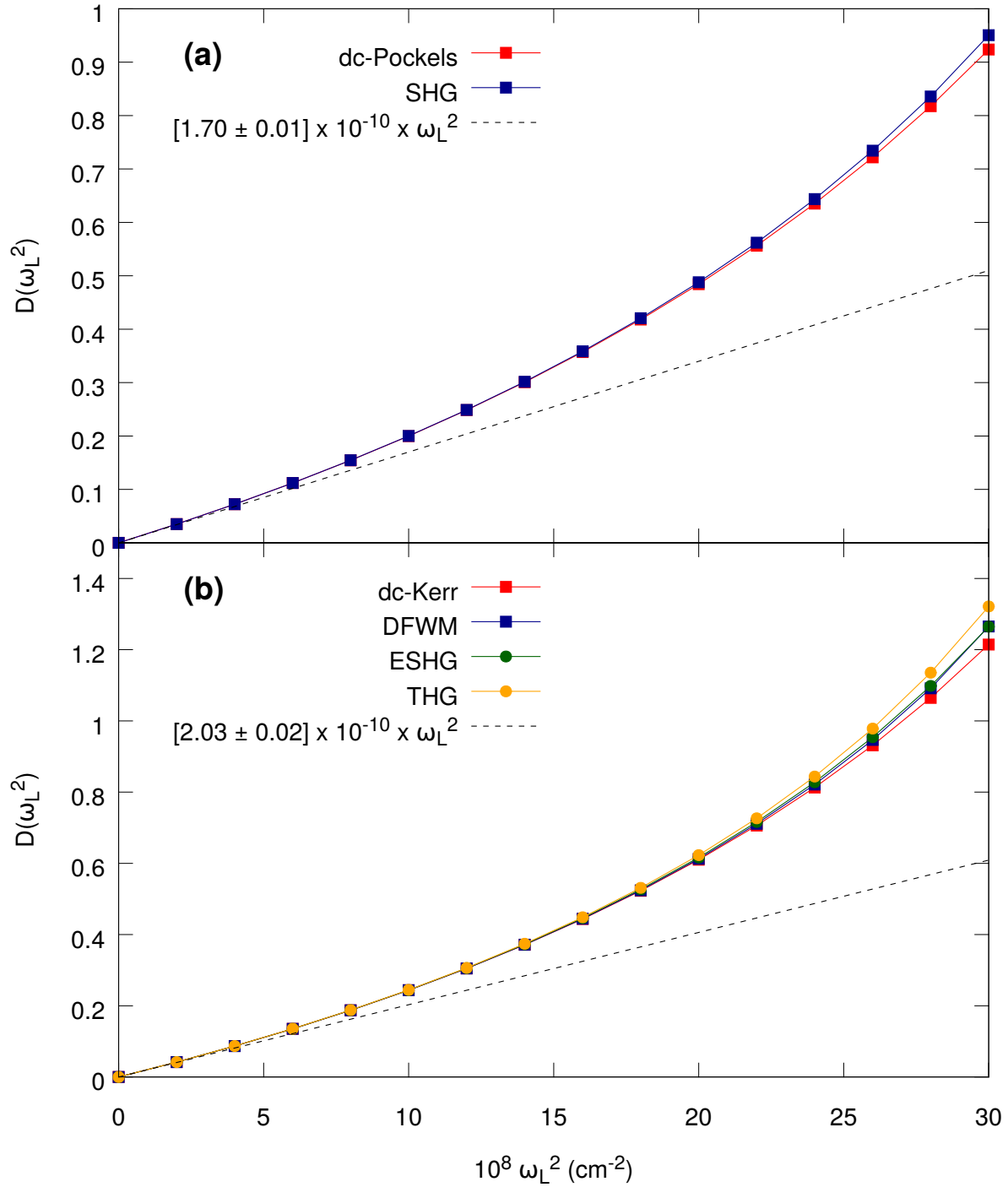


Figure 4.3: CCSD/d-aug-cc-pVDZ frequency dispersion $[D(\omega_L^2)]$ for $\beta_{||}$ (a) and $\gamma_{||}$ (b) of water for different second- and third-order NLO processes. The dashed line corresponds to Eq. (4.7) truncated at the second order.

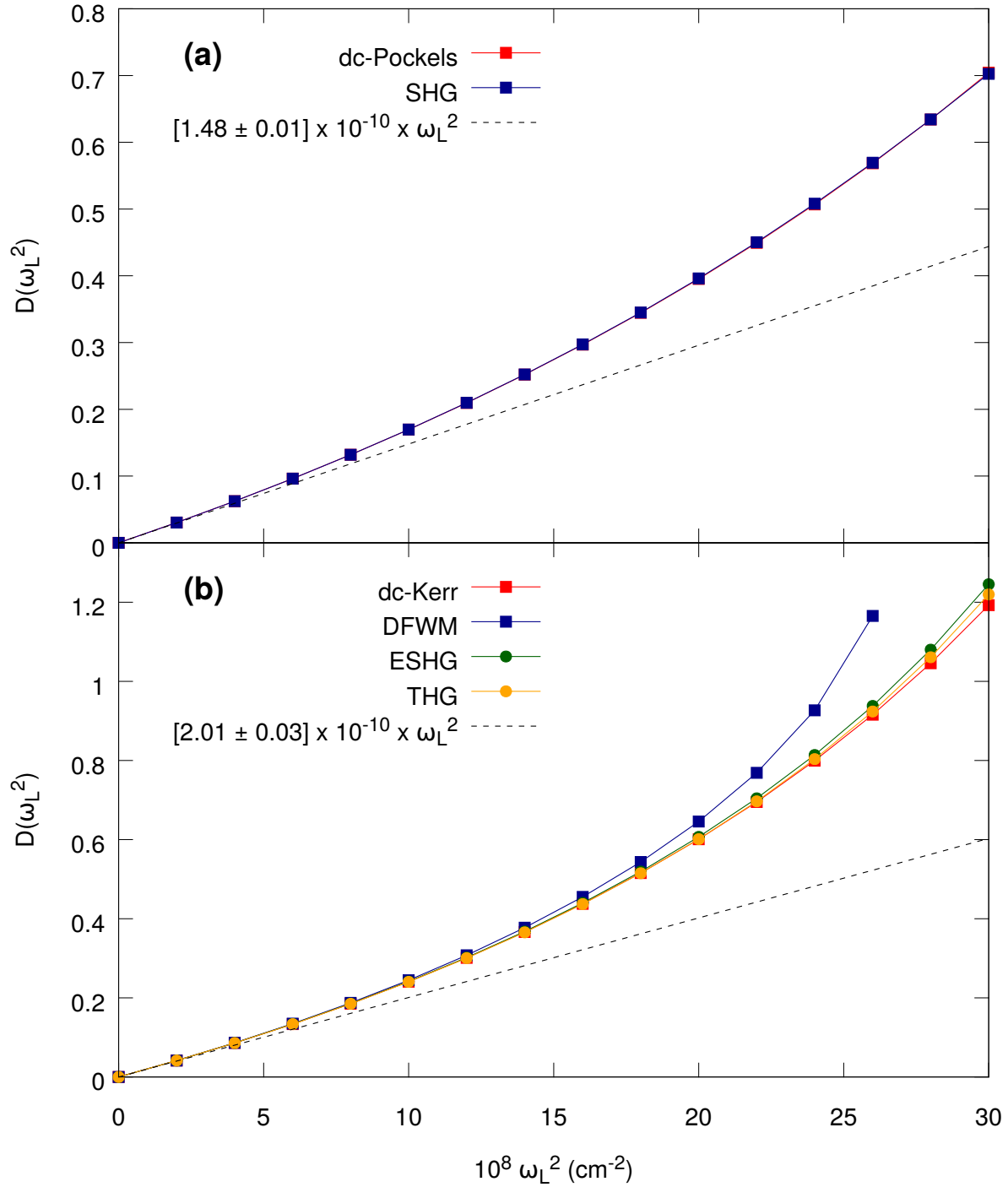


Figure 4.4: CCSD/d-aug-cc-pVDZ frequency dispersion $[D(\omega_L^2)]$ for $\beta_{||}$ (a) and $\gamma_{||}$ (b) of methanol for different second- and third-order NLO processes. The dashed line corresponds to Eq. (4.7) truncated at the second order.

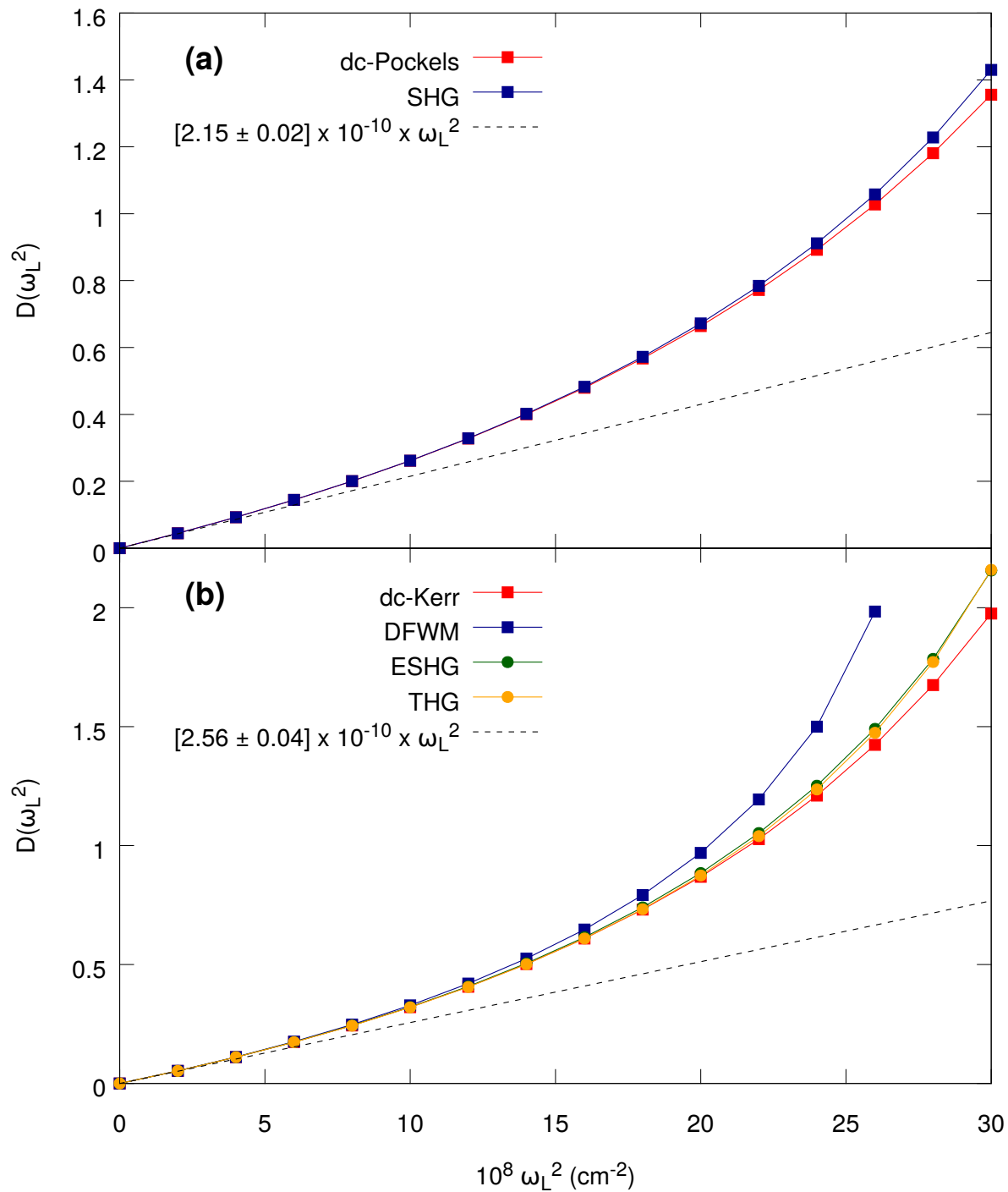


Figure 4.5: CCSD/d-aug-cc-pVDZ frequency dispersion $[D(\omega_L^2)]$ for $\beta_{||}$ (a) and $\gamma_{||}$ (b) of DME for different second- and third-order NLO processes. The dashed line corresponds to Eq. (4.7) truncated at the second order.

Table 4.7: Comparison between experimental and calculated static and dynamic (at 694.3 nm) $\gamma_{||}$ values (a.u.) of water.

Method	Basis set	Static	Dynamic	
Experiment	—	—	2310±120	Ref. 31
CRF-CCSD	d-aug-cc-pVTZ	1773	2299	This work
CRF-CC3	d-aug-cc-pVTZ	1744	2266	This work
TDHF	modified POL	1010	1216	Ref. 2
FF/HF	HF limit	985	—	Ref. 47
TDDFT/BLYP	Extended TZ ¹	3700	4800	Ref. 54
TDDFT/LB94	Extended TZ	1200	1500	Ref. 54
QED-MP2	modified HyPOL	1741.7	2213.8	Ref. 53
FF/CCSD	modified POL	1650.0	—	Ref. 2
FF/CCSD(T)	modified POL	1800.0	—	Ref. 2

¹ Valence triple- ζ basis set with two polarization functions and $2s2p2d2f$ diffuse functions.

Table 4.8: Comparison between experimental and calculated static and dynamic (at 694.3 nm) $\beta_{||}$ (a.u.) and $\gamma_{||}$ (a.u.) values of methanol.

Method	Basis set	Static	Dynamic	
$\beta_{ }(-2\omega; \omega, \omega)$				
Experiment	—	—	-35.0±2.1	Ref. 31
QRF-CCSD	d-aug-cc-pVTZ	-31.14	-37.61	This work
QRF-CC3	d-aug-cc-pVDZ	-29.93	-36.69	This work.
RPA	POL ¹	-24.15	-28.55	Ref. 30
QRF-CCSD	POL	-33.52	-40.61	Ref. 6
$\gamma_{ }(-2\omega; \omega, \omega, 0)$				
Experiment	—	—	4590±130	Ref. 31
CRF-CCSD	d-aug-cc-PVDZ	3554	4677	This work
RPA	POL	2137.3	2619.3	Ref. 30
CRF-CCSD	POL	3502	4550	Ref. 6
CRF-RAS ²	POL	—	3260	Ref. 29

¹ Sadlej's POL basis set.⁵⁰

² The active space is built from 7 occupied and 7 unoccupied orbitals and excitations up to the quadruples are considered.

Section 4.4

Conclusions

The static and dynamic first ($\beta_{||}$) and the second ($\gamma_{||}$) hyperpolarizabilities of water, methanol, and dimethyl ether have been evaluated within the response function approach using a hierarchy of coupled cluster levels of approximation and doubly-augmented correlation consistent atomic basis sets. The first goal was to challenge recent gas phase electric field-induced second harmonic generation (EFISHG) measurements on dimethyl ether and the variations of $\beta_{||}$ and $\gamma_{||}$ among the three compounds. For the three compounds, electronic $\beta_{||}$ and $\gamma_{||}$ values in good agreement with experiment (within the error bars) are obtained at the CCSD and CC3 levels. In addition, for dimethyl ether, the frequency dispersion of both properties follows closely the experimental values, demonstrating the reliability of these methods and levels of approximation. This also suggests that the vibrational contributions to the EFISHG responses of these molecules are small, if not negligible. The variations in dispersion factors among the three compounds have been explained in terms of the smallest excitation energies: the smaller the lowest excitation energies, the larger the frequency dispersion.

Acknowledgments

This work was supported by funds from the Belgian Government (IUAP No P7/5, Functional Supramolecular Systems) and the Francqui Foundation. The calculations were performed on the computers of the Consortium des Équipements de Calcul Intensif, including those of the Technological Platform of High-Performance Computing, for which we gratefully acknowledge the financial support of the FNRS-FRFC (Convention Nos. 2.4.617.07.F and 2.5020.11) and of the University of Namur, as well as on zenobe, the Tier-1 facility of the Walloon Region (Convention 1117545).

Bibliography

- [1] (a) Shelton, D. P.; Rice, J. E. Measurements and Calculations of the Hyperpolarizabilities of Atoms and Small Molecules in the Gas Phase. *Chem. Rev.* **1994**, *94*, 3–29; (b) Brédas, J. L.; Adant, C.; Tackx, P.; Persoons, A.; Pierce, B. M. Third-Order Nonlinear Optical Response in Organic Materials: Theoretical and Experimental Aspects. *Chem. Rev.* **1994**, *94*, 243–278; (c) Kanis, D. R.; Ratner, M. A.; Marks, T. J. Design and Construction of Molecular Assemblies with Large Second-Order Optical Nonlinearities. Quantum Chemical Aspects. *Chem. Rev.* **1994**, *94*, 195–242.
- [2] (a) Sekino, H.; Bartlett, R. J. Hyperpolarizabilities of Molecules with Frequency Dependence and Electron Correlation. *J. Chem. Phys.* **1991**, *94*, 3665–3669; (b) Sekino, H.; Bartlett, R. J. Molecular Hyperpolarizabilities. *J. Chem. Phys.* **1993**, *98*, 3022–3037.
- [3] (a) Maroulis, G. Hyperpolarizability of H₂O. *J. Chem. Phys.* **1991**, *94*, 1182–1190; (b) Sim, F.; Chin, S.; Dupuis, M.; Rice, J. E. Electron Correlation-Effects in Hyperpolarizabilities of P-Nitroaniline. *J. Phys. Chem.* **1993**, *97*, 1158–1163; (c) Maroulis, G. Static Hyperpolarizability of the Water Dimer and the Interaction Hyperpolarizability of Two Water Molecules. *J. Chem. Phys.* **2000**, *113*, 1813–1820.
- [4] (a) Hättig, C.; Christiansen, O.; Koch, H.; Jørgensen, P. Frequency-Dependent First Hyperpolarizabilities Using Coupled Cluster Quadratic Response Theory. *Chem. Phys. Lett.* **1997**, *269*, 428–434; (b) Hammond, J. R.; Kowalski, K. Parallel Computation of Coupled-Cluster Hyperpolarizabilities. *J. Chem. Phys.* **2009**, *130*, 194108; (c) Hammond, J. R.; Kowalski, K. Parallel Computation of Coupled-Cluster Hyperpolarizabilities. *J. Chem. Phys.* **2009**, *130*, 194108; (d) Robinson, J. B.; Knowles, P. J. Application of the Quasi-Variational Coupled Cluster Method to the Nonlinear Optical Properties of Model Hydrogen Systems. *J. Chem. Phys.* **2012**, *137*, 054301; (e) Coe, J. P.; Paterson, M. J. Approaching Exact Hyperpolarizabilities via Sum-over-States Monte Carlo Configuration Interaction. *J. Chem. Phys.* **2014**, *141*, 124118.
- [5] (a) Bishop, D. M.; Norman, P. Effects of Vibration on the Polarizability and the First and Second Hyperpolarizabilities of HF, HCl, and HBr. *J. Chem. Phys.* **1999**, *111*, 3042–3050; (b) Gao, B.; Ringholm, M.; Bast, R.; Ruud, K.; Thorvaldsen, A. J.; Jaszuński, M. Analytic Density Functional Theory Calculations of Pure Vibrational Hyperpolarizabilities: The First Dipole Hyperpolarizability of Retinal and Related Molecules. *J. Phys. Chem. A* **2014**, *118*, 748–756.
- [6] Dutra, A. S.; Castro, M. A.; Fonseca, T. L.; Fileti, E. E.; Canuto, S. Hyperpolarizabilities of the Methanol Molecule: A CCSD Calculation Including Vibrational Corrections. *J. Chem. Phys.* **2010**, *132*, 034307.

- [7] (a) Jacquemin, D.; Champagne, B.; Hättig, C. Correlated Frequency-Dependent Electronic First Hyperpolarizability of Small Push–Pull Conjugated Chains. *Chem. Phys. Lett.* **2000**, *319*, 327–334; (b) Norman, P. A Perspective on Nonresonant and Resonant Electronic Response Theory for Time-Dependent Molecular Properties. *Phys. Chem. Chem. Phys.* **2011**, *13*, 20519; (c) Campo, J.; Wenseleers, W.; Hales, J. M.; Makarov, N. S.; Perry, J. W. Practical Model for First Hyperpolarizability Dispersion Accounting for Both Homogeneous and Inhomogeneous Broadening Effects. *J. Phys. Chem. Lett.* **2012**, *3*, 2248–2252.
- [8] de Wergifosse, M.; Champagne, B.; Ito, S.; Fukuda, K.; Nakano, M. Challenging Compounds for Calculating Molecular Second Hyperpolarizabilities: The Triplet State of the Trimethylenemethane Diradical and Two Derivatives. *Phys. Chem. Chem. Phys.* **2016**, *18*, 6420–6429.
- [9] Verbiest, T.; Clays, K.; Rodriguez, V. *Second-Order Nonlinear Optical Characterization Techniques: An Introduction*; Taylor & Francis, 2009.
- [10] Oudar, J. L.; Chemla, D. S. Hyperpolarizabilities of the Nitroanilines and Their Relations to the Excited State Dipole Moment. *J. Chem. Phys.* **1977**, *66*, 2664–2668.
- [11] (a) Gorman, C. B.; Marder, S. R. An Investigation of the Interrelationships between Linear and Nonlinear Polarizabilities and Bond-Length Alternation in Conjugated Organic Molecules. *Proc. Natl. Acad. Sci. U.S.A.* **1993**, *90*, 11297–11301; (b) Murugan, N. A.; Kongsted, J.; Rinkevicius, Z.; Ågren, H. Breakdown of the First Hyperpolarizability/Bond-Length Alternation Parameter Relationship. *Proc. Natl. Acad. Sci. U.S.A.* **2010**, *107*, 16453–16458; (c) Hu, X.; Xiao, D.; Keinan, S.; Asselberghs, I.; Therien, M. J.; Clays, K.; Yang, W.; Beratan, D. N. Predicting the Frequency Dispersion of Electronic Hyperpolarizabilities on the Basis of Absorption Data and Thomas-Kuhn Sum Rules. *J. Phys. Chem. C* **2010**, *114*, 2349–2359; (d) Coe, B. J.; Pilkington, R. A. Theoretical Studies on Two-Dimensional Nonlinear Optical Chromophores with Pyrazinyl Cores and Organic or Ruthenium(II) Ammine Electron Donors. *J. Phys. Chem. A* **2014**, *118*, 2253–2268.
- [12] Kirtman, B.; Toto, J. L.; Breneman, C.; de Melo, C. P.; Bishop, D. M. Comment on “The Hyperpolarizability of *Trans*-Butadiene: A Critical Test Case for Quantum Chemical Models” [*J. Chem. Phys.* **106**, 1827 (1997)]. *J. Chem. Phys.* **1998**, *108*, 4355–4357.
- [13] (a) Suponitsky, K. Y.; Liao, Y.; Masunov, A. E. Electronic Hyperpolarizabilities for Donor-Acceptor Molecules with Long Conjugated Bridges: Calculations versus Experiment. *J. Phys. Chem. A* **2009**, *113*, 10994–11001; (b) Johnson, L. E.; Dalton, L. R.; Robinson, B. H. Optimizing Calculations of Electronic Excitations and Relative Hyperpolarizabilities of Electrooptic Chromophores. *Acc. Chem. Res.* **2014**, *47*, 3258–3265.
- [14] (a) Mançois, F.; Pozzo, J.-L.; Pan, J.; Adamietz, F.; Rodriguez, V.; Ducasse, L.; Castet, F.; Plaquet, A.; Champagne, B. Two-Way Molecular Switches with Large Nonlinear Optical

- Contrast. *Chem. Eur. J.* **2009**, *15*, 2560–2571; (b) Boixel, J.; Guerchais, V.; Le Bozec, H.; Jacquemin, D.; Amar, A.; Boucekkine, A.; Colombo, A.; Dragonetti, C.; Marinotto, D.; Roberto, D.; Righetto, S.; De Angelis, R. Second-Order NLO Switches from Molecules to Polymer Films Based on Photochromic Cyclometalated Platinum(II) Complexes. *J. Am. Chem. Soc.* **2014**, *136*, 5367–5375; (c) Cariati, E.; Dragonetti, C.; Lucenti, E.; Nisic, F.; Righetto, S.; Roberto, D.; Tordin, E. An Acido-Triggered Reversible Luminescent and Nonlinear Optical Switch Based on a Substituted Styrylpyridine: EFISH Measurements as an Unusual Method to Reveal a Protonation– Deprotonation NLO Contrast. *Chem. Commun.* **2014**, *50*, 1608.
- [15] (a) Hohm, U. Experimental Static Dipole– Dipole Polarizabilities of Molecules. *J. Mol. Struct.* **2013**, *1054-1055*, 282–292; (b) Thakkar, A. J.; Wu, T. How Well Do Static Electronic Dipole Polarizabilities from Gas-Phase Experiments Compare with Density Functional and MP2 Computations? *J. Chem. Phys.* **2015**, *143*, 144302.
- [16] de Wergifosse, M.; Castet, F.; Champagne, B. Frequency Dispersion of the First Hyperpolarizabilities of Reference Molecules for Nonlinear Optics. *J. Chem. Phys.* **2015**, *142*, 194102.
- [17] Beaujean, P.; Bondu, F.; Plaquet, A.; Garcia-Amorós, J.; Cusido, J.; Raymo, F. M.; Castet, F.; Rodriguez, V.; Champagne, B. Oxazines: A New Class of Second-Order Nonlinear Optical Switches. *J. Am. Chem. Soc.* **2016**, *138*, 5052–5062.
- [18] Castet, F.; Bogdan, E.; Plaquet, A.; Ducasse, L.; Champagne, B.; Rodriguez, V. Reference Molecules for Nonlinear Optics: A Joint Experimental and Theoretical Investigation. *J. Chem. Phys.* **2012**, *136*, 024506.
- [19] Couling, V. W.; Shelton, D. P. Hyperpolarizability Dispersion Measured for (CH₃)₂O. *J. Chem. Phys.* **2015**, *143*, 224307.
- [20] Mikkelsen, K. V.; Luo, Y.; Ågren, H.; Jørgensen, P. Sign Change of Hyperpolarizabilities of Solvated Water. *J. Chem. Phys.* **1995**, *102*, 9362–9367.
- [21] Kaatz, P.; Donley, E. A.; Shelton, D. P. A Comparison of Molecular Hyperpolarizabilities from Gas and Liquid Phase Measurements. *J. Chem. Phys.* **1998**, *108*, 849–856.
- [22] Ferrighi, L.; Frediani, L.; Ruud, K. Degenerate Four-Wave Mixing in Solution by Cubic Response Theory and the Polarizable Continuum Model. *J. Phys. Chem. B* **2007**, *111*, 8965–8973.
- [23] Takimoto, Y.; Isborn, C. M.; Eichinger, B. E.; Rehr, J. J.; Robinson, B. H. Frequency and Solvent Dependence of Nonlinear Optical Properties of Molecules. *J. Phys. Chem. C* **2008**, *112*, 8016–8021.
- [24] Lu, S.-I.; Chiu, C.-C.; Wang, Y.-F. Density Functional Theory Calculations of Dynamic First Hyperpolarizabilities for Organic Molecules in Organic Solvent: Comparison to

- Experiment. *J. Chem. Phys.* **2011**, *135*, 134104.
- [25] Quertinmont, J.; Champagne, B.; Castet, F.; Hidalgo Cardenuto, M. Explicit versus Implicit Solvation Effects on the First Hyperpolarizability of an Organic Biphotochrome. *J. Phys. Chem. A* **2015**, *119*, 5496–5503.
- [26] Bishop, D. M.; Kirtman, B.; Kurtz, H. A.; Rice, J. E. Calculation of Vibrational Dynamic Hyperpolarizabilities for H₂O, CO₂, and NH₃. *J. Chem. Phys.* **1993**, *98*, 8024–8030.
- [27] Luo, Y.; Ågren, H.; Vahtras, O.; Jørgensen, P.; Spirko, V.; Hettema, H. Frequency-dependent Polarizabilities and First Hyperpolarizabilities of Water. *J. Chem. Phys.* **1993**, *98*, 7159–7164.
- [28] Quinet, O.; Kirtman, B.; Champagne, B. Analytical Time-Dependent Hartree-Fock Evaluation of the Dynamic Zero-Point Vibrationally Averaged (ZPVA) First Hyperpolarizability. *J. Chem. Phys.* **2003**, *118*, 505–513.
- [29] Norman, P.; Luo, Y.; Ågren, H. Vibrational Corrections to Static and Dynamic Hyperpolarizabilities of Pure Liquids: Calculations on Methanol. *J. Chem. Phys.* **1998**, *109*, 3580–3588.
- [30] Wang, Y.-H.; Wang, C.-K.; Luo, Y. Vibrational Contributions to Nonlinear Optical Properties of Methanol, Ethanol and Propanol. *Comput. Theor. Chem.* **2005**, *717*, 223–230.
- [31] Ward, J. F.; Miller, C. K. Measurements of Nonlinear Optical Polarizabilities for Twelve Small Molecules. *Phys. Rev. A* **1979**, *19*, 826–833.
- [32] Hättig, C.; Jørgensen, P. Dispersion coefficients for second hyperpolarizabilities using coupled cluster cubic response theory. *Adv. Quantum Chem.* **1999**, *35*, 111–148.
- [33] Helgaker, T.; Coriani, S.; Jørgensen, P.; Kristensen, K.; Olsen, J.; Ruud, K. *Chem. Rev.* **2012**, *112*, 543.
- [34] de Wergifosse, M.; Liégeois, V.; Champagne, B. Evaluation of the Molecular Static and Dynamic First Hyperpolarizabilities. *Int. J. Quantum Chem.* **2014**, *114*, 900–910.
- [35] Orr, B.; Ward, J. Perturbation Theory of the Non-Linear Optical Polarization of an Isolated System. *Mol. Phys.* **1971**, *20*, 513–526.
- [36] Bishop, D. M. General Dispersion Formulas for Molecular Third-order Nonlinear Optical Properties. *J. Chem. Phys.* **1989**, *90*, 3192–3195.
- [37] Mizrahi, V.; Shelton, D. P. Deviations from Kleinman Symmetry Measured for Several Simple Atoms and Molecules. *Phys. Rev. A* **1985**, *31*, 3145–3154.
- [38] Bishop, D. M. Dispersion Formulas for Certain Nonlinear Optical Processes. *Phys. Rev. Lett.* **1988**, *61*, 322–324.
- [39] Bishop, D. M.; De Kee, D. W. The Frequency Dependence of Nonlinear Optical Processes. *J. Chem. Phys.* **1996**, *104*, 9876–9887.

- [40] Hattig, C. Dispersion Formulas for Hyperpolarizability Averages. *Mol. Phys.* **1998**, *94*, 455–460.
- [41] Karna, S. P.; Dupuis, M. Frequency Dependent Nonlinear Optical Properties of Molecules: Formulation and Implementation in the HONDO Program. *J. Comput. Chem.* **1991**, *12*, 487–504.
- [42] Hättig, C. Dispersion formulas for the second hyperpolarizability components $\gamma_{||}$, γ and γ_K . *Chem. Phys. Lett.* **1998**, *296*, 245–252.
- [43] Christiansen, O.; Gauss, J.; Stanton, J. F. Frequency-Dependent Polarizabilities and First Hyperpolarizabilities of CO and H₂O from Coupled Cluster Calculations. *Chem. Phys. Lett.* **1999**, *305*, 147–155.
- [44] Dunning, T. H. Gaussian Basis Sets for Use in Correlated Molecular Calculations. I. The Atoms Boron through Neon and Hydrogen. *J. Chem. Phys.* **1989**, *90*, 1007–1023.
- [45] Frisch, M. J. et al. Gaussian 09 Revision D.01. 2013; Gaussian Inc. Wallingford CT 2009.
- [46] Aidas, K. et al. The Dalton quantum chemistry program system. *Wiley Interdiscip. Rev. Comput. Mol. Sci.* **2014**, *4*, 269–284.
- [47] Maroulis, G. Hyperpolarizability of H₂O Revisited: Accurate Estimate of the Basis Set Limit and the Size of Electron Correlation Effects. *Chem. Phys. Lett.* **1998**, *289*, 403–411.
- [48] Sałek, P.; Helgaker, T.; Vahtras, O.; Ågren, H.; Jonsson, D.; Gauss, J. A Comparison of Density-Functional-Theory and Coupled-Cluster Frequency-Dependent Polarizabilities and Hyperpolarizabilities. *Mol. Phys.* **2005**, *103*, 439–450.
- [49] Kobayashi, T.; Sasagane, K.; Aiga, F.; Yamaguchi, K. Calculation of Frequency-Dependent First Hyperpolarizabilities Using the Second-Order Møller–Plesset Perturbation Theory. *J. Chem. Phys.* **1999**, *110*, 11720–11733.
- [50] Sadlej, A. J. Medium-Size Polarized Basis Sets for High-Level Correlated Calculations of Molecular Electric Properties. *Collect. Czechoslov. Chem. Commun.* **1988**, *53*, 1995–2016.
- [51] Pluta, T.; Sadlej, A. J. HyPol Basis Sets for High-Level-Correlated Calculations of Electric Dipole Hyperpolarizabilities. *Chem. Phys. Lett.* **1998**, *297*, 391–401.
- [52] Diercksen, G. H. F.; Kellö, V.; Sadlej, A. J. Perturbation Theory of the Electron Correlation Effects for Atomic and Molecular Properties. VII. Complete Fourth-order MBPT Study of the Dipole Moment and Dipole Polarizability of H₂O. *J. Chem. Phys.* **1983**, *79*, 2918–2923.
- [53] Kobayashi, T.; Sasagane, K.; Aiga, F.; Yamaguchi, K. Calculation of Frequency-Dependent Second Hyperpolarizabilities for Electric Field Induced Second Harmonic Generation in the Second-Order Møller–Plesset Perturbation Theory. *J. Chem. Phys.* **1999**, *111*, 842–848.

- [54] van Gisbergen, S. J. A.; Snijders, J. G.; Baerends, E. J. Accurate Density Functional Calculations on Frequency-Dependent Hyperpolarizabilities of Small Molecules. *J. Chem. Phys.* **1998**, *109*, 10657–10668.
- [55] Shelton, D. P. Hyperpolarizability of the Hydrogen Atom. *Phys. Rev. A* **1987**, *36*, 3032–3041.
- [56] Bishop, D. M.; Lam, B. Ab Initio Study of Third-Order Nonlinear Optical Properties of Helium. *Phys. Rev. A* **1988**, *37*, 464–469.
- [57] Karna, S. P.; Talapatra, G. B.; Wijekoon, W. M. K. P.; Prasad, P. N. Frequency Dependence of Linear and Nonlinear Optical Properties of Conjugated Polyenes: An Ab Initio Time-Dependent Coupled Hartree-Fock Study. *Phys. Rev. A* **1992**, *45*, 2763–2770.
- [58] Karna, S. P.; Prasad, P. N.; Dupuis, M. Nonlinear Optical Properties of *p*-nitroaniline: An Ab Initio Time-dependent Coupled Perturbed Hartree-Fock Study. *J. Chem. Phys.* **1991**, *94*, 1171–1181.

Coupled cluster evaluation of the second and third harmonic scattering responses of small molecules

Theo. Chem. Acc. **2018**, 137, 50 (DOI: 10.1007/s00214-018-2219-y)

Pierre Beaujean and Benoît Champagne

*Laboratory of Theoretical Chemistry, Namur Institute of Structured Matter,
University of Namur, Rue de Bruxelles 61, B-5000 Namur, Belgium*

Abstract

The static and dynamic second harmonic (β_{SHS}) and third harmonic (γ_{THS}) scattering hyperpolarizabilities and depolarization ratios of water, carbon tetrachloride, chloroform, dichloromethane, chloromethane, and acetonitrile have been evaluated at the coupled cluster response theory level of approximation. Following two recent publications on their measurements, this is the first quantum chemical investigation on γ_{THS} and on its decomposition into its spherical tensor components. Substantial electron correlation and basis set effects are evidenced for β_{SHS} and γ_{THS} and for their depolarization ratios and they depend on the nature of the molecule. Then, using the selected CCSD/d-aug-cc-pVDZ level, the chlorinated methane derivatives have been studied, showing that i) the γ_{THS} response is dominated by its isotropic contribution whereas ii) for β_{SHS} the dipolar contribution increases from carbon tetrachloride to dichloromethane, chloroform, chloromethane, and acetonitrile. Comparisons with the experimental data obtained from measurements in liquid phase i) show that the increase of γ_{THS} with the number for chlorine atoms is well reproduced by the calculations and ii) suggest that the solvation effects are smaller for γ_{THS} than for β_{SHS} .

► Supporting information are available at <https://doi.org/10.1007/s00214-018-2219-y>.

Section 5.1

Introduction

Since the first observation of the Second Harmonic Generation (SHG) phenomenon by Franken *et al.*¹ in 1961 and of the Third Harmonic Generation (THG) phenomenon, one year later by Terhune and co-workers,² these phenomena have been exploited to understand the properties of molecules and their interactions with electro-magnetic fields.³ In parallel, the development of accurate theoretical methods has provided complementary tools for the evaluation of the corresponding molecular properties, the first (β) and the second (γ) hyperpolarizabilities.^{4–10} This has led to the deduction of the necessary structure-NLO (nonlinear optical) property relationships to design molecules with large β and γ responses as well as interpretation tools when these properties are used to probe the structures, properties, and dynamics of molecules and matter.

Recently, Van Steerteghem and co-workers¹¹ and Rodriguez¹² have shown that γ can also be determined from Third Harmonic Scattering (THS) measurements, opening a new direction for investigating structure- γ relationships as well as to assess the potential of THS γ as a probe of molecular structures and properties. THS technique is the next-order analog of Second Harmonic Scattering (SHS), usually called Hyper Rayleigh Scattering (HRS), which has already permitted β measurements for a broad range of molecules and ions,^{13–17} including organic and organometallic compounds as well as, more recently, molecular switches.^{3,18–25}

In most cases, both SHS and THS experimental determinations of β and γ rely on relative rather than on absolute measurements, which requires a precise knowledge of the responses of these reference compounds, typically small molecules.^{3,10,26} As shown over the last decades, the definition of reference values results often from joint experimental and theoretical/quantum chemical investigations. On the one hand, the small size of these reference compounds allows using high-level methods (extended basis sets, high-order electron correlation treatment, vibrational contributions, effects of the surrounding).^{27–38} On the other hand, they allow assessing the reliability of more approximate methods. For instance, Castet *et al.*^{39,40} have reported experimental SHS results (on β and its depolarization ratio) of five small molecules in solution and have discussed the performance of various *ab initio* methods to reproduce qualitatively and quantitatively the experimental data.

In this paper, a hierarchy of Coupled Cluster (CC) methods is employed to perform the first quantum chemistry investigation of the THS responses of reference molecules. The present study follows two recent contributions of our group^{41,42} on other NLO responses. Six molecules have been selected: water (H_2O), chloromethane (CH_3Cl), dichloromethane (CH_2Cl_2), chloroform (CHCl_3), carbon tetrachloride (CCl_4), and acetonitrile (CH_3CN). H_2O has been chosen because its small size enables a detailed investigation of basis set and electron correlation effects, as we demonstrated in a recent paper.⁴² The other molecules enable

to unravel the effect of molecular symmetry on the THS response: CCl_4 belongs to the T_d point group, CH_3Cl , CHCl_3 , and CH_3CN belong to C_{3v} , while CH_2Cl_2 (and H_2O) to C_{2v} . Note also that the later four compounds have already been studied experimentally by THS in Refs.^{11,12} and by SHS in Ref.⁴⁰ Besides γ_{THS} , for the sake of completeness, the present study also reports the β_{SHS} results. Then, only the electronic contribution to the first and second hyperpolarizabilities is computed. In the case of second-harmonic generation β and third-harmonic generation γ the pure vibrational contributions are indeed expected to be small at optical frequencies^{43,44} whereas considering the zero-point vibrational average is beyond the scope of this investigation.

This paper is divided in four Section: i) Section 5.2 gives a short description of SHS and THS methods and their target quantities; ii) the computational details are presented in Section 5.3; iii) the main results are presented and analyzed in Section 5.4: first, the electron correlation and basis set effects are investigated on the static first and second hyperpolarizabilities of the water molecule and then on the frequency dispersion of the second- and third-order scattering responses of acetonitrile. Then, a selected method is employed to study the static and dynamic SHS and THS hyperpolarizabilities of the four other molecules; iv) the conclusions are drawn in Section 5.5.

Section 5.2

The SHS and THS spectroscopies

At the molecular scale, the frequency-dependent first and second hyperpolarizabilities are the expansion coefficients of the molecular induced dipole moment as a function of external electric fields, \vec{F} , applied along the i, j, \dots directions (note that lower-case letters stand for coordinates in the molecular frame) and oscillating at frequencies $\omega_1, \omega_2, \dots$:

$$\begin{aligned} \Delta\mu_i(\vec{F}) = & \sum_j^{x,y,z} \alpha_{ij}(-\omega_\sigma; \omega_1) F_j(\omega_1) \\ & + \frac{1}{2!} \sum_{jk}^{x,y,z} \beta_{ijk}(-\omega_\sigma; \omega_1, \omega_2) F_j(\omega_1) F_k(\omega_2) \\ & + \frac{1}{3!} \sum_{jkl}^{x,y,z} \gamma_{ijkl}(-\omega_\sigma; \omega_1, \omega_2, \omega_3) F_j(\omega_1) F_k(\omega_2) F_l(\omega_3) + \dots \end{aligned} \quad (5.1)$$

where $\omega_\sigma = \sum_i \omega_i$, α_{ij} is an element of the polarizability tensor, while β_{ijk} and γ_{ijkl} are elements of the first and second hyperpolarizability tensors, respectively. Depending on the combination of static and dynamic electric fields, different NLO processes arise. The second and third harmonic generation responses are noted $\beta(-2\omega; \omega, \omega)$ and $\gamma(-3\omega; \omega, \omega, \omega)$, respectively.

For an isotropic medium composed of identical molecules or scatterers, the intensity of incoherent contribution to the harmonic scattered light $I^{m\omega}$ reads :

$$I^{m\omega} = G f_L^2 C \langle \chi^2 \rangle (I^\omega)^m, \quad (5.2)$$

where $I^{m\omega}$ is the light intensity at the second ($m=2$) or third ($m=3$) harmonic, I^ω is the incident intensity, G is a constant containing geometrical, optical, and electrical factors of the experimental setup, C is the scatterers concentration, χ is either β or γ , and f_L is a local field correction depending on the refractive indices of the medium at frequencies ω and $m\omega$. The brackets refer to an isotropic (or rotational) averaging of the tensor over all possible molecular orientations.^{3,12,40,45}

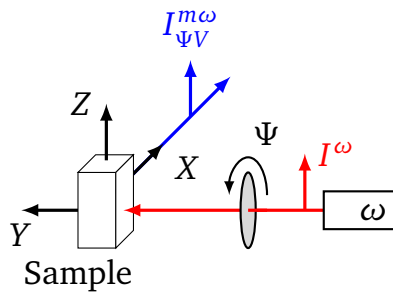


Figure 5.1: Sketch of the experimental SHS ($m\omega = 2\omega$) and THS ($m\omega = 3\omega$) setup.^{3,12,16,45} X, Y and Z stand for the coordinates axes in the laboratory frame.

In the conventional experimental setup (Fig. 5.1), the scattered light is analyzed at a 90° angle with respect to the direction of propagation. So, the fundamental light beam (of frequency ω), which is elliptically polarized (Ψ and δ describe the state of polarization, and in this case $\delta = \pi/2$), propagates in the Y direction while the Z-linearly polarized component of the scattered beam (of frequency $m\omega$) is recorded in the X direction. One generally distinguishes between two polarization combinations: the VV geometry (vertical-vertical, both incident and scattered lights are vertically-polarized, with $\Psi = \pi/2$) and HV [horizontal-vertical, the incident (scattered) light is horizontally(verticaly)-polarized, with $\Psi = 0$]. For SHS and THS, the I_{VV} intensity is proportional to $\langle \beta_{ZZZ}^2 \rangle$ and $\langle \gamma_{ZZZZ}^2 \rangle$, while I_{HV} is proportional to $\langle \beta_{ZXX}^2 \rangle$ and $\langle \gamma_{ZXXX}^2 \rangle$, respectively. The expressions for those averages can be derived following the technique described by Andrew and Thirunamachandran.⁴⁶ For SHS,^{47–49} the resulting expressions are:

$$\langle \beta_{ZZZ}^2 \rangle = \frac{1}{105} \sum_{ijk}^{x,y,z} 2\beta_{ijk}^2 + \beta_{ijj}\beta_{ikk} + 4\beta_{iij}\beta_{jkk} + 4\beta_{iij}\beta_{kkj} + 4\beta_{ijk}\beta_{jik}, \quad (5.3)$$

$$\langle \beta_{ZXX}^2 \rangle = \frac{1}{105} \sum_{ijk}^{x,y,z} 6\beta_{ijk}^2 + 3\beta_{ijj}\beta_{ikk} - 2\beta_{iij}\beta_{jkk} - 2\beta_{iij}\beta_{kkj} - 2\beta_{ijk}\beta_{jik}, \quad (5.4)$$

while for THS they read:

$$\langle \gamma_{ZZZZ}^2 \rangle = \frac{1}{315} \sum_{ijkl}^{x,y,z} \left\{ \begin{aligned} &2\gamma_{ijkl}^2 + 12\gamma_{iijk}\gamma_{jllk} + 6\gamma_{iijk}\gamma_{ljlk} + 6\gamma_{ijkl}\gamma_{jikl} \\ &+ 3\gamma_{ijjk}\gamma_{ikll} + 3\gamma_{iijj}\gamma_{kllk} + 3\gamma_{ijjk}\gamma_{kill} \end{aligned} \right\}, \quad (5.5)$$

$$\langle \gamma_{ZXXX}^2 \rangle = \frac{1}{630} \sum_{ijkl}^{x,y,z} \left\{ \begin{aligned} &16\gamma_{ijkl}^2 + 24\gamma_{ijjk}\gamma_{ikll} - 12\gamma_{iijk}\gamma_{jllk} - 6\gamma_{iijk}\gamma_{ljlk} \\ &- 6\gamma_{ijkl}\gamma_{jikl} - 3\gamma_{iijj}\gamma_{kllk} - 3\gamma_{ijjk}\gamma_{kill} \end{aligned} \right\}. \quad (5.6)$$

Note that these expressions undergo simplifications if Kleinman's conditions (full permutation of the tensors components) are assumed (see below). For a non-polarized incident signal, both polarizations have equal probability and the intensity becomes proportional to the sum of the HV and VV observables. This allows defining β_{SHS} and γ_{THS} :

$$\beta_{SHS} = \sqrt{\langle \beta_{ZZZ}^2 \rangle + \langle \beta_{ZXX}^2 \rangle}, \quad (5.7)$$

$$\gamma_{THS} = \sqrt{\langle \gamma_{ZZZZ}^2 \rangle + \langle \gamma_{ZXXX}^2 \rangle}, \quad (5.8)$$

and their associated depolarization ratios (DR):

$$DR = \frac{I_{VV}}{I_{HV}} \Rightarrow DR_{SHS} = \frac{\langle \beta_{ZZZ}^2 \rangle}{\langle \beta_{ZXX}^2 \rangle}, \quad (5.9)$$

$$\Rightarrow DR_{THS} = \frac{\langle \gamma_{ZZZZ}^2 \rangle}{\langle \gamma_{ZXXX}^2 \rangle}. \quad (5.10)$$

To further analyze the β and γ tensors, they are decomposed into their irreducible spherical components.⁵⁰ These analyses have been pioneered by Kielich and co-workers^{51,52} and later on used by Brasselet and Zyss⁵³ for SHS. When assuming the Kleinman's conditions, β contains a dipolar ($J = 1$) and an octupolar ($J = 3$) component,⁵³ expressed as:

$$|\beta_{J=1}|^2 = \frac{3}{5} \sum_{ijk}^{x,y,z} \beta_{ijj} \beta_{ikk}, \quad (5.11)$$

$$|\beta_{J=3}|^2 = \sum_{ijk}^{x,y,z} \beta_{ijk}^2 - \frac{3}{5} \beta_{ijj} \beta_{ikk}. \quad (5.12)$$

Consequently, in the static limit, the averaged β quantities [Eqs. (5.3) and (5.4)] can be rewritten under the following form:

$$\langle \beta_{ZZZ}^2 \rangle = \frac{9}{45} |\beta_{J=1}|^2 + \frac{6}{105} |\beta_{J=3}|^2, \quad (5.13)$$

$$\langle \beta_{ZXX}^2 \rangle = \frac{1}{45} |\beta_{J=1}|^2 + \frac{4}{105} |\beta_{J=3}|^2. \quad (5.14)$$

A β -nonlinear anisotropy parameter, $\rho_{3/1} = |\beta_{J=3}|/|\beta_{J=1}|$, can also be defined to highlight whether the first hyperpolarizability is dominated by dipolar or octupolar contributions. The depolarization ratio is then rewritten as a function of $\rho_{3/1}$:

$$\text{DR}_{SHS} = \frac{18\rho_{3/1}^2 + 63}{12\rho_{3/1}^2 + 7}, \quad (5.15)$$

so that, if the NLOphore is purely dipolar ($\rho_{3/1} \rightarrow 0$), the depolarization ratio is equal to 9, while it amounts to $3/2$ if it is purely octupolar ($\rho_{3/1} \rightarrow \infty$).

On the other hand, the static γ tensor is composed of an isotropic ($J = 0$), a quadrupolar ($J = 2$), and a hexadecapolar ($J = 4$) spherical tensor component,⁵² with:

$$|\gamma_{J=0}|^2 = \frac{1}{5} \sum_{ijkl}^{x,y,z} \gamma_{iijj} \gamma_{kkll}, \quad (5.16)$$

$$|\gamma_{J=2}|^2 = \frac{1}{7} \sum_{ijkl}^{x,y,z} 6\gamma_{iijk} \gamma_{jjkl} - 2\gamma_{iijj} \gamma_{kkll}, \quad (5.17)$$

$$|\gamma_{J=4}|^2 = \frac{1}{35} \sum_{ijkl}^{x,y,z} 35\gamma_{ijkl}^2 - 30\gamma_{iijk} \gamma_{jjkl} + 3\gamma_{iijj} \gamma_{kkll}. \quad (5.18)$$

This allows rewriting the expressions for the average γ quantities [Eqs. (5.5) and (5.6)]:⁵²

$$\langle \gamma_{ZZZZ}^2 \rangle = \frac{1}{5} |\gamma_{J=0}|^2 + \frac{4}{35} |\gamma_{J=2}|^2 + \frac{8}{315} |\gamma_{J=4}|^2, \quad (5.19)$$

$$\langle \gamma_{ZXXX}^2 \rangle = \frac{3}{140} |\gamma_{J=2}|^2 + \frac{1}{63} |\gamma_{J=4}|^2, \quad (5.20)$$

showing there is no isotropic contribution to $\langle \gamma_{ZXXX}^2 \rangle$. The γ -nonlinear anisotropy parameters, $\rho_{0/2} = |\gamma_{J=0}|/|\gamma_{J=2}|$ and $\rho_{4/2} = |\gamma_{J=4}|/|\gamma_{J=2}|$, compare the relative contributions of the different components of the second hyperpolarizability tensor with each other. Note that these definitions differ from those of Rodriguez¹² (which, using the same notations, would be written $\rho_{2/0}$ and $\rho_{4/0}$). Our choice was motivated by the fact that the isotropic contribution is generally larger than the two other ones, resulting in nonlinear anisotropy parameters $\ll 1$ (*vide infra*). In this new framework, the THS depolarization ratio [Eq. (5.10)] is rewritten as:

$$\text{DR}_{THS} = \frac{32\rho_{4/2}^2 + 252\rho_{0/2}^2 + 144}{20\rho_{4/2}^2 + 27}. \quad (5.21)$$

The evolution of DR_{THS} as a function of $\rho_{4/2}$ for different values of $\rho_{0/2}$ is plotted in Fig. 5.2. When $\rho_{4/2} \rightarrow \infty$, DR_{THS} converges to the hexadecapolar limit, $8/5$. However, when $\rho_{4/2} \rightarrow 0$ (left part of Fig. 5.2), the limit value depends on $\rho_{0/2}$, since

$$\text{DR}'_{THS} = \lim_{\rho_{4/2} \rightarrow 0} \text{DR}_{THS} = \frac{28}{3} \rho_{0/2}^2 + \frac{16}{3}, \quad (5.22)$$

so that the depolarization ratio tends to the “pure” quadrupolar limit of $16/3$ when $\rho_{0/2} \rightarrow 0$, and to ∞ when $\rho_{0/2} \rightarrow \infty$, *i.e.* in the isotropic limit.

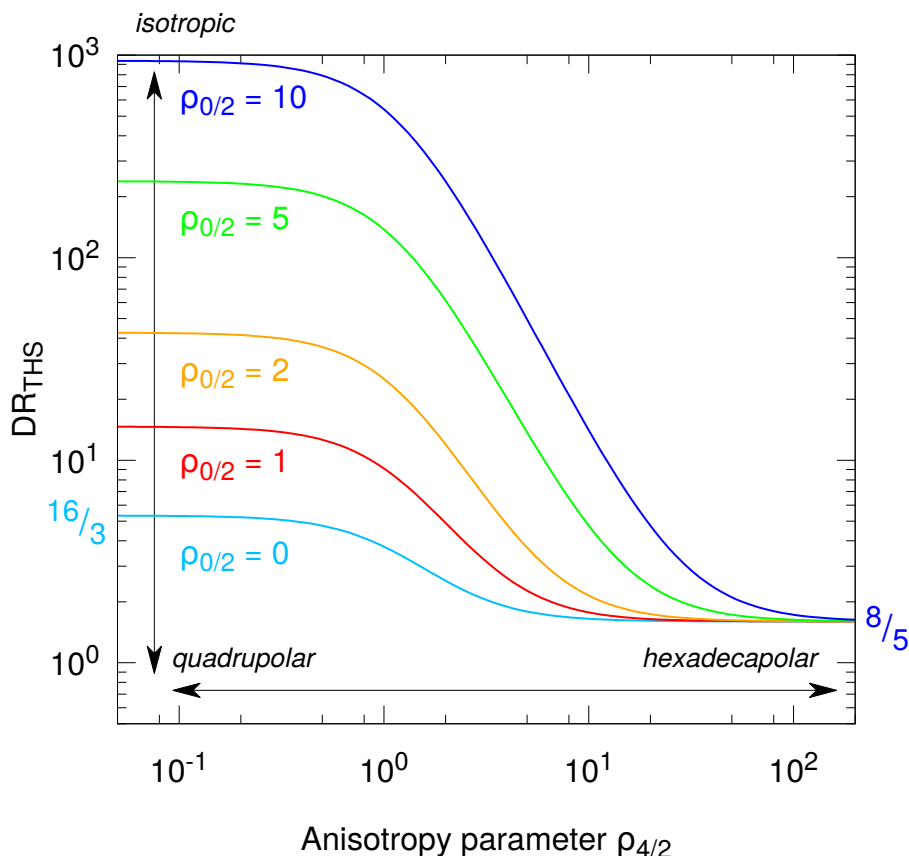


Figure 5.2: Evolution of the THS depolarization ratio as a function of $\rho_{4/2}$ for different values of $\rho_{0/2}$. A logarithmic scale is used. When $\rho_{4/2}$ increases, the curves tend to the hexadecapolar limit ($8/5$), while the quadrupolar limit ($16/3$) is visible at the beginning of the curve for $\rho_{0/2} = 0$ (see text for more details).

Section 5.3

Computational methodology

For the water molecule, the geometry from Ref. 42 was used to facilitate the comparison with previous results on electric field-induced second harmonic generation (EFISHG) quantities. The geometry of the five other molecules was optimized at the MP2/cc-pVTZ level of approximation. Static first and second hyperpolarizabilities were computed with the Dalton 2016 program⁵⁴ with a hierarchy of coupled clusters (CC) methods in combination with the quadratic/cubic response function approaches.^{55–58} Unrelaxed orbitals were assumed. The employed CC hierarchy, given in increasing order of electron correlation content, is HF, CCS, CC2, and CCSD.^{55–58} Following the results of a previous investigation on related properties showing that CCSD and CC3 results are very close,⁴² no attempt was made to go beyond CCSD. The correlation consistent polarized valence basis sets of Dunning,⁵⁹ singly- or doubly-augmented with diffuse functions, (d-)aug-cc-pVXZ, were employed, in a consistent way with

respect to previous investigations on small reference molecules for nonlinear optics.^{40–42} Both static and dynamic quantities were calculated. Wavelengths of 1500, 1300 (typical for γ_{THS}), and 1064 nm (typical for β_{SHS}) were selected to analyze the frequency dispersion of β and γ using the following frequency dispersion factor:

$$D(\omega_L^2) = \frac{\chi(\omega_\sigma; \omega_1, \dots)}{\chi(0)} - 1, \text{ with } \omega_L^2 = \sum_i^{\sigma, 1, \dots} \omega_i^2 \quad (5.23)$$

where χ is either β or γ and $\chi(0)$ is the corresponding static value. All reported β and γ values are given in a.u. [1 a.u. of $\beta = 3.6212 \times 10^{-42} \text{ m}^4 \text{ V}^{-1} = 3.2064 \times 10^{-53} \text{ C}^3 \text{ m}^3 \text{ J}^{-2} = 8.639 \times 10^{-33} \text{ esu}$; 1 a.u. of $\gamma = 7.423 \times 10^{-54} \text{ m}^5 \text{ V}^{-2} = 6.2354 \times 10^{-65} \text{ C}^4 \text{ m}^4 \text{ J}^{-3} = 5.0367 \times 10^{-40} \text{ esu}$] and within the T convention.

Section 5.4

Results and discussions

Basis sets and electron correlation effects

The SHS and THS responses of water and acetonitrile molecules were calculated first in order to investigate the basis sets and electron correlation effects. For water, the results are reported in Table 5.1 for the static first and second hyperpolarizabilities, and they are summarized in Fig. 5.3. The convergence with the size of the basis set is fast for β_{SHS} . At the four levels of approximation considered, the differences with respect to d-aug-cc-pV5Z are already below 10 % when using the smallest basis set (aug-cc-pVDZ). Moreover, although the singly- and doubly-augmented cc-pVDZ basis sets present similar efficiency, d-aug-cc-pVTZ is clearly superior to aug-cc-pVTZ. DR_{SHS} is systematically underestimated no matter which basis set is used, which corresponds to an overestimation of the octupolar contribution (which was previously reported⁴⁰). Its convergence with basis set size is consistent with that of β_{SHS} .

On the other hand, the basis set convergence of γ_{THS} is much slower than for β_{SHS} . A clear difference between the singly- and doubly-augmented basis sets appears for the triple- ζ basis sets: γ_{THS} is underestimated by up to 25-30 % with aug-cc-pVTZ whereas the error is reduced to less than 5 % with d-aug-cc-pVTZ. A similar behavior with respect to adding diffuse functions has already been reported for the two-photon absorption cross section of water and has been explained by the contribution of very diffuse Rydberg excited states.⁶⁰ Moreover, differences with respect to d-aug-cc-pV5Z are still of the order of 10 % when using aug-cc-pV5Z. A satisfactory (less than 5 % of difference) agreement requires d-aug-cc-pVTZ. When using singly-augmented basis sets, DR_{THS} is systematically overestimated (with relative errors of about 20 % for the aug-cc-pV5Z basis set) whereas the opposite behavior is observed for the doubly-augmented ones but the amplitude of the underestimations is smaller. These basis set

Table 5.1: Basis set and electron correlation effects on the static β_{SHS} (a.u.) and γ_{THS} (a.u.) of water (geometry from Ref. 42) and on their depolarization ratios (DR). Relative differences (in %) with respect to d-aug-cc-pV5Z are given in parentheses.

	HF	CCS	CC2	CCSD
$\beta_{SHS}(0)$				
aug-cc-pVDZ	8.24 (7.6)	9.91 (4.5)	14.36 (-9.1)	11.37 (0.4)
aug-cc-pVTZ	8.29 (8.2)	10.07 (6.2)	15.83 (0.2)	11.85 (4.7)
aug-cc-pVQZ	7.85 (2.5)	9.63 (1.5)	15.66 (-0.9)	11.42 (0.9)
aug-cc-pV5Z	7.83 (2.3)	9.63 (1.6)	15.85 (0.3)	11.46 (1.3)
d-aug-cc-pVDZ	6.89 (-10.1)	8.49 (-10.5)	13.57 (-14.1)	9.87 (-12.7)
d-aug-cc-pVTZ	7.52 (-1.9)	9.32 (-1.7)	15.71 (-0.6)	11.19 (-1.1)
d-aug-cc-pVQZ	7.66 (0.0)	9.48 (0.0)	15.89 (0.6)	11.37 (0.5)
d-aug-cc-pV5Z	7.66	9.48	15.80	11.32
DR_{SHS}				
aug-cc-pVDZ	3.41 (-33.0)	4.14 (-32.1)	5.27 (-36.9)	4.77 (-38.7)
aug-cc-pVTZ	4.56 (-10.5)	5.45 (-10.6)	7.15 (-14.3)	6.58 (-15.4)
aug-cc-pVQZ	4.77 (-6.3)	5.74 (-5.9)	7.75 (-7.2)	7.16 (-7.9)
aug-cc-pV5Z	4.98 (-2.3)	5.95 (-2.4)	8.06 (-3.4)	7.48 (-3.7)
d-aug-cc-pVDZ	3.79 (-25.7)	4.76 (-21.9)	6.90 (-17.4)	6.01 (-22.6)
d-aug-cc-pVTZ	4.94 (-3.1)	5.96 (-2.2)	8.27 (-1.0)	7.65 (-1.6)
d-aug-cc-pVQZ	5.10 (0.2)	6.10 (0.1)	8.35 (0.1)	7.79 (0.2)
d-aug-cc-pV5Z	5.09	6.10	8.35	7.77
$\gamma_{THS}(0)$				
aug-cc-pVDZ	610 (-40.5)	719 (-39.6)	1363 (-43.9)	1066 (-39.5)
aug-cc-pVTZ	751 (-26.7)	890 (-25.3)	1686 (-30.6)	1278 (-27.4)
aug-cc-pVQZ	854 (-16.7)	1008 (-15.4)	1924 (-20.7)	1439 (-18.3)
aug-cc-pV5Z	924 (-9.9)	1084 (-9.0)	2097 (-13.6)	1554 (-11.8)
d-aug-cc-pVDZ	940 (-8.3)	1095 (-8.1)	2436 (0.4)	1801 (2.2)
d-aug-cc-pVTZ	1028 (0.3)	1193 (0.2)	2546 (4.9)	1849 (4.9)
d-aug-cc-pVQZ	1028 (0.3)	1194 (0.3)	2475 (1.9)	1792 (1.7)
d-aug-cc-pV5Z	1025	1191	2428	1762
DR_{THS}				
aug-cc-pVDZ	236 (98.0)	301 (116.2)	102 (38.9)	117 (40.9)
aug-cc-pVTZ	212 (77.9)	257 (84.6)	103 (39.7)	118 (42.1)
aug-cc-pVQZ	165 (38.5)	196 (40.4)	92 (25.4)	104 (25.7)
aug-cc-pV5Z	145 (21.8)	170 (22.3)	85 (16.1)	97 (16.2)
d-aug-cc-pVDZ	90 (-24.8)	106 (-24.0)	54 (-26.3)	60 (-28.4)
d-aug-cc-pVTZ	115 (-3.3)	135 (-3.1)	69 (-5.7)	78 (-6.5)
d-aug-cc-pVQZ	118 (-1.2)	138 (-1.2)	72 (-2.3)	81 (-2.3)
d-aug-cc-pV5Z	119	139	74	83

Note: For aug-cc-pVXZ, the number of contracted GTO's (Gaussian Type Orbitals) is 41 (X=D), 92 (X=T), 172 (X=Q), and 287 (X=5); for d-aug-cc-pVXZ, it is 58 (X=D), 126 (X=T), 229 (X=Q), and 564 (X=5).

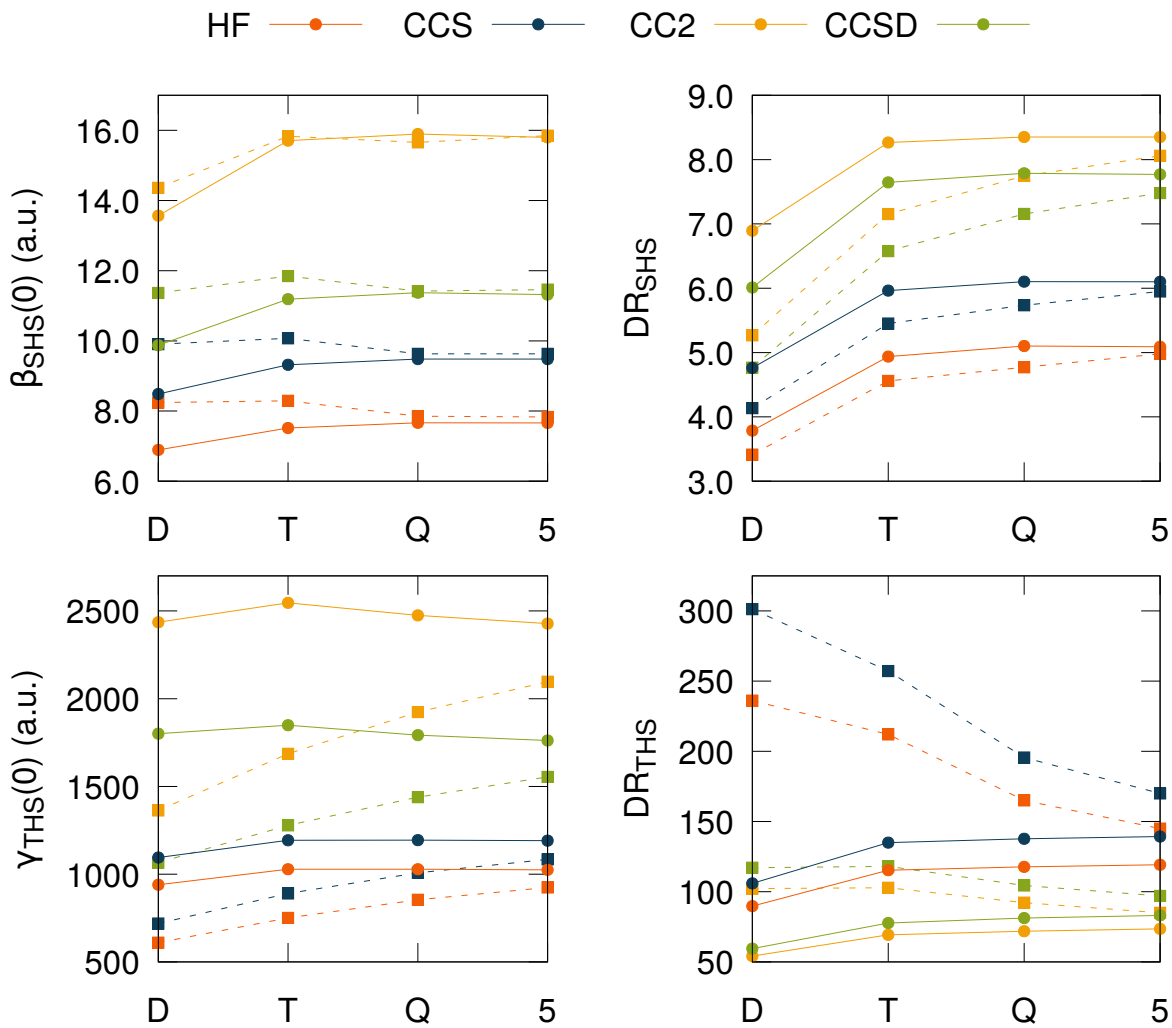


Figure 5.3: Effect of the basis set (aug-cc-pVXZ, dashed lines and d-aug-cc-pVXZ, plain lines) and of the level of approximation on the first (above) and second (below) hyperpolarizabilities of water. Left panels report averaged quantities (β_{SHS} , γ_{THS} , a.u.) while right panels report the depolarization ratios.

effects on both β_{SHS} and γ_{THS} are supported by an analysis of the different tensor components (Figs. S1 and S2), for which the convergence with respect to the basis set follows the same trend as for the average quantities.

The magnitude of both β_{SHS} and γ_{THS} responses as a function of electron correlation content follows a systematic trend: HF < CCS < CCSD < CC2. Employing the results obtained with the largest basis set, the HF and CCS levels underestimate the reference CCSD β_{SHS} (γ_{THS}) values by 32 and 16 % (42 and 32 %), respectively. On the other hand, CC2 overestimate both quantities, by 40 % (38 %) for the first (second) hyperpolarizability. These results are comparable to those reported for $\beta_{||}$ (although the error with respect to the largest basis set are larger for this EFISHG quantity) and $\gamma_{||}$.⁴² The dipolar contribution to DR_{SHS} increases from HF and CCS (34 and 16 % of underestimation with respect to CCSD, for the largest basis set) to CC2 (7% of overestimation). The DR_{SHS} values satisfy the following ordering: HF < CCS < CCSD < CC2. The almost opposite order is observed for DR_{THS} : CCS > HF > CCSD

> CC2. Still, the differences with respect to CCSD are larger than in the case of DR_{SHS} : 68 and 48 % of overestimation for CCS and HF, 11 % of underestimation for CC2. Clearly, HF and CCS do not appear as reliable methods to predict DR_{THS} values.

The first and second hyperpolarizabilities of acetonitrile were computed at the HF, CCS, CC2, and CCSD levels with both the aug-cc-pVTZ and d-aug-cc-pVTZ basis sets (Tables 5.2 and S1 and Fig. 5.4). For β_{SHS} , the differences between these two basis sets is similar to those observed for the water case discussed above. For γ_{SHS} , the basis set effects are smaller (smaller than 4 %), underlying the cooperation effects between basis functions on different atomic centers. The effects of adding a second set of diffuse functions on the depolarization ratio are larger for the second than for the first hyperpolarizability responses. With respect to the reference CCSD/d-aug-cc-pVTZ values, frequency dispersion effects on β_{SHS} are generally slightly overestimated when using the aug-cc-pVTZ basis set as well as when adopting the CCS and CC2 levels of approximation. These effects get smaller when going from SHS to THS quantities. Electron correlation effects are substantial on β_{SHS} of acetonitrile, with an increase by a factor of 3 between CCS (and HF) and CCSD (and CC2) (together with an increase of the depolarization ratio from octupolar at the HF and CCS level to dipolar at the CC2 and CCSD level). On the other hand, the differences between the CC2 and CCSD β_{SHS} and γ_{SHS} values are much smaller than for water. Moreover, the CCS method strongly underestimates (overestimates) the CCSD DR_{SHS} (DR_{THS}) values.

SHS and THS of 6 reference molecules

Based on the results of the previous Section, the CCSD/d-aug-cc-pVDZ level of approximation has been used to calculate the static and dynamic first and second hyperpolarizabilities of the whole set of 6 reference molecules (Tables 5.3 and 5.4). As previously reported,⁴⁰ this set of molecules spreads over a broad range of dipolar/octupolar character, as evidenced by DR_{SHS} values ranging from 1.5 (octupolar CCl_4 molecule) to *circa* six (dipolar, H_2O and CH_3CN molecules). The octupolar contribution dominates the β_{SHS} value of chlorinated methanes (since $\rho_{3/1} > 1$), especially in the case of chloroform and dichloromethane. In the CH_xCl_y series, $CHCl_3$ presents the largest β_{SHS} value, followed by CCl_4 , which has no dipolar contribution, and then the CH_2Cl_2 and CH_3Cl molecules. The acetonitrile displays a large β response, due its dipolar contribution (originating from the cyano group).

The γ responses vary over a broader range of amplitudes, with γ_{THS} of CCl_4 150 % larger than in CH_3Cl . With its four polarizable chlorine atoms, CCl_4 possesses the largest γ_{THS} response and each time a chlorine atom is replaced by an hydrogen atom, γ_{THS} decreases by about 20 %. The smaller γ_{THS} values of acetonitrile and water are explained by their correspondingly lower $J = 0$ contribution. For all compounds, the isotropic component is in fact dominant, followed by the quadrupolar contribution (except for CCl_4 , where it is zero by symmetry). Therefore, γ_{THS} is governed by the $\langle \gamma_{ZZZZ}^2 \rangle$ term [Eq. (5.19)], all $\rho_{0/2}$ values

Table 5.2: Basis set and electron correlation effects on the static and dynamic (1500, 1300 and 1064 nm) β_{SHS} (a.u.) and γ_{THS} (a.u.) of acetonitrile, with their corresponding depolarization ratios (DR). Relative errors with respect to d-aug-cc-pVTZ (right) are given in parentheses for the d-aug-cc-pVDZ (left) values.

	d-aug-cc-pVDZ ^a				d-aug-cc-pVTZ			
	HF	CCS	CC2	CCSD	HF	CCS	CC2	CCSD
$\beta_{SHS}(-2\omega; \omega, \omega)$								
static	6.42 (-2.7)	4.42 (-9.3)	17.26 (2.4)	16.74 (6.8)	6.59	4.83	16.84	15.61
1500 nm	6.65 (-2.4)	4.52 (-8.8)	17.91 (2.6)	17.41 (6.9)	6.81	4.92	17.45	16.21
1300 nm	6.73 (-2.3)	4.56 (-8.7)	18.14 (2.6)	17.64 (6.9)	6.88	4.96	17.66	16.42
1064 nm	6.89 (-2.1)	4.64 (-8.3)	18.59 (2.7)	18.11 (7.0)	7.03	5.02	18.09	16.84
DR_{SHS}								
static	2.53 (10.1)	1.52 (1.4)	5.96 (9.8)	5.87 (11.7)	2.27	1.50	5.38	5.18
1500 nm	2.58 (10.3)	1.54 (2.2)	5.92 (9.7)	5.84 (11.6)	2.31	1.50	5.35	5.16
1300 nm	2.60 (10.4)	1.54 (2.5)	5.90 (9.6)	5.82 (11.5)	2.33	1.50	5.33	5.15
1064 nm	2.64 (10.5)	1.55 (3.1)	5.87 (9.5)	5.80 (11.4)	2.36	1.51	5.31	5.14
$\gamma_{THS}(-3\omega; \omega, \omega, \omega)$								
static	2986 (-2.6)	3559 (-3.0)	4577 (3.1)	4037 (3.2)	3064	3664	4435	3907
1500 nm	3256 (-2.5)	3862 (-2.9)	5030 (3.4)	4420 (3.5)	3339	3973	4860	4263
1300 nm	3355 (-2.5)	3972 (-2.8)	5196 (3.5)	4558 (3.6)	3439	4084	5014	4392
1064 nm	3562 (-2.5)	4203 (-2.8)	5548 (3.7)	4853 (3.9)	3650	4319	5342	4666
DR_{THS}								
static	156 (-42.9)	175 (-45.1)	56 (-15.9)	70 (-22.1)	223	253	65	85
1500 nm	153 (-40.1)	170 (-42.4)	54 (-14.8)	67 (-20.7)	214	243	62	81
1300 nm	152 (-39.2)	169 (-41.6)	53 (-14.4)	66 (-20.3)	211	239	61	80
1064 nm	149 (-37.4)	167 (-39.9)	51 (-13.8)	64 (-19.4)	205	233	58	77

^a For d-aug-cc-pVXZ: 135 (X=D) and 282 (X=T) contracted GTO's are used.

Table 5.3: CCSD/d-aug-cc-pVDZ static SHS and THS responses for the six reference molecules: β_{SHS} (a.u.) and γ_{THS} (a.u.), their depolarization ratios (DR), their spherical tensor decompositions, and the corresponding nonlinear anisotropy parameters.

	CCl_4	CH_2Cl_2	CHCl_3	CH_3Cl	CH_3CN	H_2O
β_{SHS}	15.63	13.41	16.32	12.32	16.74	9.87
DR_{SHS}	1.50	1.53	1.57	2.94	5.87	6.01
$ \beta_{J=1} $	~ 0	3.67	6.59	18.22	32.71	19.40
$ \beta_{J=3} $	50.65	43.09	51.91	28.61	21.14	12.06
$\rho_{3/1}$	$\sim \infty$	11.75	7.88	1.57	0.65	0.62
γ_{THS}	12719	8474	10993	5065	4037	1801
DR_{THS}	5744	90	169	414	70	60
DR'_{THS}	$\sim \infty$	94	176	440	72	61
$ \gamma_{J=0} $	28434	18296	24130	11241	8623	3813
$ \gamma_{J=2} $	~ 0	5923	5638	1647	3221	1565
$ \gamma_{J=4} $	1332	1522	1412	475	680	263
$\rho_{0/2}$	$\sim \infty$	3.089	4.280	6.823	2.677	2.437
$\rho_{4/2}$	$\sim \infty$	0.257	0.250	0.288	0.211	0.168

Table 5.4: Static and dynamic (1500, 1300 and 1064 nm) β_{SHS} (a.u.) and γ_{THS} (a.u.) of the six reference compounds, together with their depolarization ratios (DR) in parentheses, as obtained at the CCSD/d-aug-cc-pVDZ level.

	CCl_4	CH_2Cl_2	CHCl_3	CH_3Cl	CH_3CN	H_2O
$\beta_{SHS}(-2\omega; \omega, \omega)$ (DR_{SHS})						
static	15.63 (1.50)	13.41 (1.53)	16.32 (1.57)	12.32 (2.94)	16.74 (5.87)	9.87 (6.01)
1500 nm	16.28 (1.50)	14.22 (1.54)	17.12 (1.57)	13.25 (2.96)	17.41 (5.84)	10.29 (6.22)
1300 nm	16.50 (1.50)	14.51 (1.54)	17.40 (1.57)	13.59 (2.97)	17.64 (5.82)	10.43 (6.30)
1064 nm	16.97 (1.50)	15.11 (1.54)	17.99 (1.57)	14.27 (2.98)	18.11 (5.80)	10.73 (6.46)
$\gamma_{THS}(-3\omega; \omega, \omega, \omega)$ (DR_{THS})						
static	12719 (5744)	8474 (90)	10993 (169)	5065 (414)	4037 (70)	1801 (60)
1500 nm	14279 (5451)	9575 (85)	12389 (161)	5672 (454)	4420 (67)	2027 (48)
1300 nm	14859 (5358)	9989 (84)	12910 (158)	5899 (471)	4558 (66)	2113 (44)
1064 nm	16118 (5182)	10892 (80)	14044 (152)	6394 (512)	4853 (64)	2304 (38)

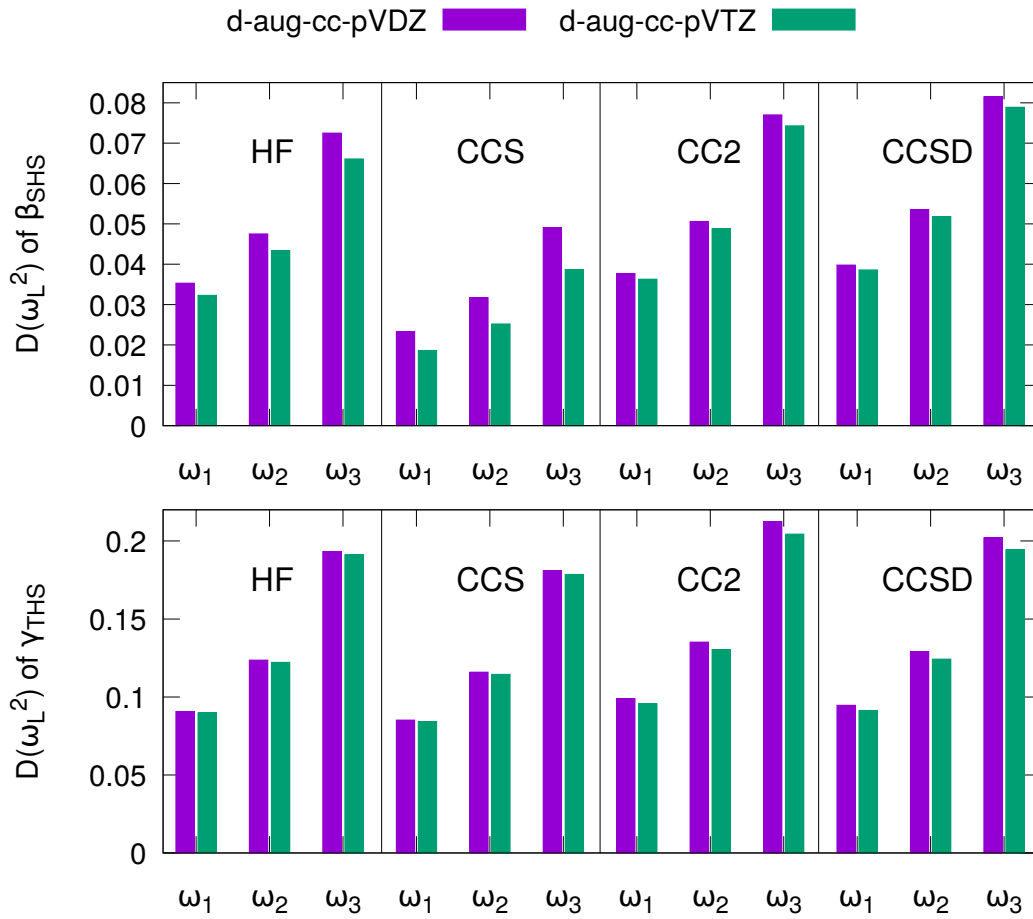


Figure 5.4: Effect of the electron correlation and basis set on the frequency dispersion [$D(\omega_L^2)$] of the first (β_{SHS}) and second (γ_{THS}) hyperpolarizabilities of acetonitrile ($\omega_1=1500$ nm, $\omega_2=1300$ nm, and $\omega_3=1064$ nm).

are larger than 1, and all $\rho_{4/2}$ values are smaller than 1 (the $\rho_{4/2}$ values are far from the hexadecapolar limit).

These analyses are confirmed for the dynamic quantities (Table 5.4) because the photon energies of the second and third harmonics are still far from the electronic resonances of the molecules. Indeed, for a wavelength of 1064 nm, the third harmonics photons have an energy close to 3.5 eV, while the first excitation energy is, at least, twice larger (for example, it amounts to 7.4 eV in the case of water⁶¹).

For the three wavelengths considered, frequency dispersion (Table S2) remains i) between 8 and 16 % for β_{SHS} (at 1064 nm the ordering of the $D(\omega_L^2)$ values satisfies $\text{CH}_3\text{CN} \approx \text{CCl}_4 \approx \text{H}_2\text{O} < \text{CHCl}_3 < \text{CH}_2\text{Cl}_2 < \text{CH}_3\text{Cl}$) and ii) between 20 and 30 % for γ_{THS} ($\text{CH}_3\text{CN} < \text{CCl}_4 \approx \text{CH}_3\text{Cl} < \text{CHCl}_3 \approx \text{H}_2\text{O} < \text{CH}_2\text{Cl}_2$). The frequency dispersion has a negligible effect on DR_{SHS} , with the exception of water where the increase attains 7 % for 1064 nm. The variations are larger for DR_{THS} , of about 10 % at 1064 nm, except for chloromethane and water (24 and 36 %, respectively). These DR_{THS} variations are associated with an increase of the quadrupolar (hexacapolar) contribution for water (chloromethane).

Though experiments have been carried out in solutions, it is interesting to see how good is

the agreement with the CCSD γ_{THS} values obtained for the isolated molecule. This comparison is achieved for a wavelength of 1300 nm, employed in Ref. 11. Note that in the latter reference, the B-convention was adopted so that their γ_{THS} values have been multiplied by a factor of 6 to match with the T-convention. For acetonitrile, the experimental value (68×10^2 a.u.) is about 30 % larger than our CCSD prediction (46×10^2 a.u., Table 5.4). The agreement is however much better for dichloromethane (exp. value of 111×10^2 a.u. versus 100×10^2 a.u. at the CCSD level), chloroform (126×10^2 a.u. versus 129×10^2 a.u. at the CCSD level), and carbon tetrachloride (152×10^2 a.u. versus 149×10^2 a.u. at the CCSD level), with differences with respect to the CCSD values of 10 % or less. These good agreements suggest that the Liq/Gas ratios are close to one, at least for the chlorinated species. This contrasts with what has been observed for the β_{SHS} response.⁴⁰

Section 5.5

Conclusions

The static and dynamic second harmonic (β_{SHS}) and third harmonic (γ_{THS}) scattering hyperpolarizabilities of water, carbon tetrachloride, chloroform, dichloromethane, chloromethane, and acetonitrile have been evaluated by using a hierarchy of coupled cluster response methods in combination with atomic basis sets of increasing size. The focus of this paper goes beyond the prediction of benchmark β_{SHS} and γ_{THS} quantities and deals with the depolarization ratios as well as with the decomposition of the rank-3 and rank-4 tensors into their spherical invariants (dipolar and octupolar for β_{SHS} , isotropic, quadrupolar, and hexadecapolar for γ_{THS}). To our knowledge, this is the first quantum chemical investigation of γ_{THS} , following two recent papers on their measurements.^{11,12} Substantial electron correlation and basis set effects are evidenced and depend on the nature of the molecule. On the basis of a detailed investigation of the second- and third-order responses of water and acetonitrile, the CCSD/d-aug-cc-pVDZ level has been selected to study the chlorinated methane derivatives. CCSD results demonstrate that γ_{THS} of these compounds is dominated by its isotropic component while the second largest contribution is the quadrupolar one (with the exception of carbon tetrachloride, where it is zero). In the case of β_{SHS} , its dipolar character increases from carbon tetrachloride to chloromethane. Comparisons with experimental data obtained from measurements in liquid phase show that the increase of γ_{THS} with the number for chlorine atoms is well reproduced by the calculations. These comparisons also suggest that the solvation effects are smaller for γ_{THS} than for β_{SHS} .

Acknowledgments

At the occasion of his 60th birthday, it is a pleasure to dedicate this paper to Prof. Antonio RIZZO, who is pioneering since several decades the evaluation of high-order optical effects and their confrontation with experiment, leading to an improved understanding of the interactions between light and matter. This work was supported by funds from the Francqui Foundation. The calculations were performed on the computers of the Consortium des Équipements de Calcul Intensif, including those of the Technological Platform of High-Performance Computing, for which we gratefully acknowledge the financial support of the FNRS-FRFC (Convention Nos. 2.4.617.07.F and 2.5020.11) and of the University of Namur.

Bibliography

- [1] Franken, P. A.; Hill, A. E.; Peters, C. W.; Weinreich, G. Generation of Optical Harmonics. *Phys. Rev. Lett.* **1961**, 7, 118–119.
- [2] Terhune, R. W.; Maker, P. D.; Savage, C. M. Optical Harmonic Generation in Calcite. *Phys. Rev. Lett.* **1962**, 8, 404–406.
- [3] Verbiest, T.; Clays, K.; Rodriguez, V. *Second-Order Nonlinear Optical Characterization Techniques: An Introduction*; Taylor & Francis, 2009.
- [4] Kanis, D. R.; Ratner, M. A.; Marks, T. J. Design and Construction of Molecular Assemblies with Large Second-Order Optical Nonlinearities. Quantum Chemical Aspects. *Chem. Rev.* **1994**, 94, 195–242.
- [5] Brédas, J. L.; Adant, C.; Tackx, P.; Persoons, A.; Pierce, B. M. Third-Order Nonlinear Optical Response in Organic Materials: Theoretical and Experimental Aspects. *Chem. Rev.* **1994**, 94, 243–278.
- [6] Bishop, D. M.; Norman, P. In *Handbook of advanced electronic and photonic materials and devices*; Nalwa, H. S., Ed.; Acad. Press: San Diego, Calif., 2001; pp 1– 62.
- [7] Champagne, B.; Kirtman, P. In *Handbook of advanced electronic and photonic materials and devices*; Nalwa, H. S., Ed.; Acad. Press: San Diego, Calif., 2001; pp 63–127.
- [8] Papadopoulos, M. G.; Sadlej, A. J.; Leszczynski, J. In *Challenges and advances in computational chemistry and physics*; Papadopoulos, M. G., Sadlej, A. J., Leszczynski, J., Eds.; Challenges and Advances in Computational Chemistry and Physics 1; Springer: Dordrecht, 2006; OCLC: 72145327.
- [9] Castet, F.; Rodriguez, V.; Pozzo, J.-L.; Ducasse, L.; Plaquet, A.; Champagne, B. Design and Characterization of Molecular Nonlinear Optical Switches. *Acc. Chem. Res.* **2013**, 46, 2656–2665.
- [10] (a) Shelton, D. P.; Rice, J. E. Measurements and Calculations of the Hyperpolarizabilities of Atoms and Small Molecules in the Gas Phase. *Chem. Rev.* **1994**, 94, 3–29.
- [11] Van Steerteghem, N.; Clays, K.; Verbiest, T.; Van Cleuvenbergen, S. Third-Harmonic Scattering for Fast and Sensitive Screening of the Second Hyperpolarizability in Solution. *Anal. Chem.* **2017**, 89, 2964–2971.
- [12] Rodriguez, V. Polarization-Resolved Third-Harmonic Scattering in Liquids. *J. Phys. Chem. C* **2017**, 121, 8510–8514.
- [13] Terhune, R. W.; Maker, P. D.; Savage, C. M. Measurements of Nonlinear Light Scattering. *Phys. Rev. Lett.* **1965**, 14, 681–684.

- [14] Clays, K.; Persoons, A. Hyper-Rayleigh Scattering in Solution. *Phys. Rev. Lett.* **1991**, *66*, 2980–2983.
- [15] Hendrickx, E.; Clays, K.; Persoons, A. Hyper-Rayleigh Scattering in Isotropic Solution. *Acc. Chem. Res.* **1998**, *31*, 675–683.
- [16] Heesink, G. J. T.; Ruiter, A. G. T.; van Hulst, N. F.; Bölger, B. Determination of Hyperpolarizability Tensor Components by Depolarized Hyper Rayleigh Scattering. *Phys. Rev. Lett.* **1993**, *71*, 999–1002.
- [17] Shelton, D. P. Gas Phase Hyper-Rayleigh Scattering Measurements. *J. Chem. Phys.* **2012**, *137*, 044312.
- [18] Ostroverkhov, V.; Petschek, R. G.; Singer, K. D.; Sukhomlinova, L.; Twieg, R. J.; Wang, S.-X.; Chien, L. C. Measurements of the Hyperpolarizability Tensor by Means of Hyper-Rayleigh Scattering. *J. Opt. Soc. Am. B* **2000**, *17*, 1531–1542.
- [19] Mançois, F.; Sanguinet, L.; Pozzo, J.-L.; Guillaume, M.; Champagne, B.; Rodriguez, V.; Adamietz, F.; Ducasse, L.; Castet, F. Acido-Triggered Nonlinear Optical Switches: Benzazolo-Oxazolidines. *J. Phys. Chem. B* **2007**, *111*, 9795–9802.
- [20] Duncan, T.; Song, K.; Hung, S.-T.; Miloradovic, I.; Nayak, A.; Persoons, A.; Verbiest, T.; Therien, M.; Clays, K. Molecular Symmetry and Solution-Phase Structure Interrogated by Hyper-Rayleigh Depolarization Measurements: Elaborating Highly Hyperpolarizable D₂-Symmetric Chromophores. *Angew. Chem. Int. Ed.* **2008**, *120*, 3020–3023.
- [21] Asselberghs, I.; Flors, C.; Ferrighi, L.; Botek, E.; Champagne, B.; Mizuno, H.; Ando, R.; Miyawaki, A.; Hofkens, J.; der Auweraer, M. V.; Clays, K. Second-Harmonic Generation in GFP-like Proteins. *J. Am. Chem. Soc.* **2008**, *130*, 15713–15719.
- [22] Garrett, K.; Sosa Vazquez, X.; Egri, S. B.; Wilmer, J.; Johnson, L. E.; Robinson, B. H.; Isborn, C. M. Optimum Exchange for Calculation of Excitation Energies and Hyperpolarizabilities of Organic Electro-Optic Chromophores. *J. Chem. Theory Comput.* **2014**, *10*, 3821–3831.
- [23] Quertinmont, J.; Champagne, B.; Castet, F.; Hidalgo Cardenuto, M. Explicit versus Implicit Solvation Effects on the First Hyperpolarizability of an Organic Biphotochrome. *J. Phys. Chem. A* **2015**, *119*, 5496–5503.
- [24] Beaujean, P.; Bondu, F.; Plaquet, A.; Garcia-Amorós, J.; Cusido, J.; Raymo, F. M.; Castet, F.; Rodriguez, V.; Champagne, B. Oxazines: A New Class of Second-Order Nonlinear Optical Switches. *J. Am. Chem. Soc.* **2016**, *138*, 5052–5062.
- [25] Coe, B. J.; Foxon, S. P.; Pilkington, R. A.; Sánchez, S.; Whittaker, D.; Clays, K.; Van Steerteghem, N.; Brunschwig, B. S. Rhenium(I) Tricarbonyl Complexes with Peripheral N-Coordination Sites: A Foundation for Heterotrimetallic Nonlinear Optical Chromophores. *Organometallics* **2016**, *35*, 3014–3024.

- [26] Bishop, D. M. In *Advances in Quantum Chemistry*; Sabin, J. R., Zerner, M. C., Eds.; Academic Press, 1994; Vol. 25; pp 1–45, DOI: 10.1016/S0065-3276(08)60017-9.
- [27] Maroulis, G. Hyperpolarizability of H₂O. *J. Chem. Phys.* **1991**, *94*, 1182–1190.
- [28] Sekino, H.; Bartlett, R. J. Molecular Hyperpolarizabilities. *J. Chem. Phys.* **1993**, *98*, 3022–3037.
- [29] Bishop, D. M.; Norman, P. Effects of Vibration on the Polarizability and the First and Second Hyperpolarizabilities of HF, HCl, and HBr. *J. Chem. Phys.* **1999**, *111*, 3042–3050.
- [30] Christiansen, O.; Gauss, J.; Stanton, J. F. Frequency-Dependent Polarizabilities and First Hyperpolarizabilities of CO and H₂O from Coupled Cluster Calculations. *Chem. Phys. Lett.* **1999**, *305*, 147–155.
- [31] Rizzo, A.; Coriani, S.; Fernández, B.; Christiansen, O. A Coupled Cluster Response Study of the Electric Dipole Polarizability, First and Second Hyperpolarizabilities of HCl. *Phys. Chem. Chem. Phys.* **2002**, *4*, 2884–2890.
- [32] Luis, J. M.; Reis, H.; Papadopoulos, M.; Kirtman, B. Treatment of Nonlinear Optical Properties Due to Large Amplitude Anharmonic Vibrational Motions: Umbrella Motion in NH₃. *J. Chem. Phys.* **2009**, *131*, 034116.
- [33] Maroulis, G.; Menadakis, M. Polarizability and Hyperpolarizability of COS and NNO. *Chem. Phys. Lett.* **2010**, *494*, 144–149.
- [34] Dutra, A. S.; Castro, M. A.; Fonseca, T. L.; Fileti, E. E.; Canuto, S. Hyperpolarizabilities of the Methanol Molecule: A CCSD Calculation Including Vibrational Corrections. *J. Chem. Phys.* **2010**, *132*, 034307.
- [35] Bast, R.; Ekström, U.; Gao, B.; Helgaker, T.; Ruud, K.; Thorvaldsen, A. J. The Ab Initio Calculation of Molecular Electric, Magnetic and Geometric Properties. *Phys. Chem. Chem. Phys.* **2011**, *13*, 2627–2651.
- [36] Bulik, I. W.; Zaleśny, R.; Bartkowiak, W.; Luis, J. M.; Kirtman, B.; Scuseria, G. E.; Avramopoulos, A.; Reis, H.; Papadopoulos, M. G. Performance of Density Functional Theory in Computing Nonresonant Vibrational (Hyper)Polarizabilities. *J. Comput. Chem.* **2013**, *34*, 1775–1784.
- [37] Coe, J. P.; Paterson, M. J. Approaching Exact Hyperpolarizabilities via Sum-over-States Monte Carlo Configuration Interaction. *J. Chem. Phys.* **2014**, *141*, 124118.
- [38] Zaleśny, R.; Baranowska-Łączkowska, A.; Medved', M.; Luis, J. M. Comparison of Property-Oriented Basis Sets for the Computation of Electronic and Nuclear Relaxation Hyperpolarizabilities. *J. Chem. Theory Comput.* **2015**, *11*, 4119–4128.
- [39] Castet, F.; Champagne, B. Assessment of DFT Exchange–Correlation Functionals for Evaluating the Multipolar Contributions to the Quadratic Nonlinear Optical Responses of Small Reference Molecules. *J. Chem. Theory Comput.* **2012**, *8*, 2044–2052.

- [40] Castet, F.; Bogdan, E.; Plaquet, A.; Ducasse, L.; Champagne, B.; Rodriguez, V. Reference Molecules for Nonlinear Optics: A Joint Experimental and Theoretical Investigation. *J. Chem. Phys.* **2012**, *136*, 024506.
- [41] de Wergifosse, M.; Castet, F.; Champagne, B. Frequency Dispersion of the First Hyperpolarizabilities of Reference Molecules for Nonlinear Optics. *J. Chem. Phys.* **2015**, *142*, 194102.
- [42] Beaujean, P.; Champagne, B. Coupled Cluster Evaluation of the Frequency Dispersion of the First and Second Hyperpolarizabilities of Water, Methanol, and Dimethyl Ether. *J. Chem. Phys.* **2016**, *145*, 044311.
- [43] Bishop, D. M.; Kirtman, B.; Kurtz, H. A.; Rice, J. E. Calculation of Vibrational Dynamic Hyperpolarizabilities for H₂O, CO₂, and NH₃. *J. Chem. Phys.* **1993**, *98*, 8024–8030.
- [44] Bishop, D. M.; Gu, F. L.; Cybulski, S. M. Static and Dynamic Polarizabilities and First Hyperpolarizabilities for CH₄, CF₄, and CCl₄. *J. Chem. Phys.* **1998**, *109*, 8407–8415.
- [45] Andrews, D. L. Harmonic Generation in Free Molecules. *J. Phys. B* **1980**, *13*, 4091.
- [46] Andrews, D. L.; Thirunamachandran, T. On Three-dimensional Rotational Averages. *J. Chem. Phys.* **1977**, *67*, 5026–5033.
- [47] Terhune, R. W.; Maker, P. D.; Savage, C. M. Measurements of Nonlinear Light Scattering. *Phys. Rev. Lett.* **1965**, *14*, 681–684.
- [48] Cyvin, S. J.; Rauch, J. E.; Decius, J. C. Theory of Hyper-Raman Effects (Nonlinear Inelastic Light Scattering): Selection Rules and Depolarization Ratios for the Second-Order Polarizability. *J. Chem. Phys.* **1965**, *43*, 4083–4095.
- [49] Bersohn, R.; Pao, Y.-H.; Frisch, H. L. Double-Quantum Light Scattering by Molecules. *J. Chem. Phys.* **1966**, *45*, 3184–3198.
- [50] Jerphagnon, J.; Chemla, D.; Bonneville, R. The Description of the Physical Properties of Condensed Matter Using Irreducible Tensors. *Adv. Phys.* **1978**, *27*, 609–650.
- [51] Alexiewicz, W.; Ozgo, Z.; Kielich, S. Spectra Theory of Third-Harmonic Light Scattering by Molecular Liquids. *Acta Phys. Pol. A* **1975**, *48*, 243.
- [52] Tadeusz, B.; Zdzislaw, O. Irreducible Spherical Representation of Some Fourth-Rank Tensors. *J. Comput. Methods Sci. Eng.* **2010**, 129–138.
- [53] Brasselet, S.; Zyss, J. Multipolar Molecules and Multipolar Fields: Probing and Controlling the Tensorial Nature of Nonlinear Molecular Media. *J. Opt. Soc. Am. B* **1998**, *15*, 257.
- [54] Aidas, K. et al. The Dalton quantum chemistry program system. *Wiley Interdiscip. Rev. Comput. Mol. Sci.* **2014**, *4*, 269–284.
- [55] Helgaker, T.; Coriani, S.; Jørgensen, P.; Kristensen, K.; Olsen, J.; Ruud, K. *Chem. Rev.*

2012, 112, 543.

- [56] Hättig, C. Dispersion formulas for the second hyperpolarizability components $\gamma_{||}$, γ and γ_K . *Chem. Phys. Lett.* **1998**, 296, 245–252.
- [57] Hättig, C.; Jørgensen, P. Dispersion coefficients for second hyperpolarizabilities using coupled cluster cubic response theory. *Adv. Quantum Chem.* **1999**, 35, 111–148.
- [58] Christiansen, O.; Gauss, J.; Stanton, J. F. Frequency-Dependent Polarizabilities and First Hyperpolarizabilities of CO and H₂O from Coupled Cluster Calculations. *Chem. Phys. Lett.* **1999**, 305, 147–155.
- [59] Dunning, T. H. Gaussian Basis Sets for Use in Correlated Molecular Calculations. I. The Atoms Boron through Neon and Hydrogen. *J. Chem. Phys.* **1989**, 90, 1007–1023.
- [60] Paterson, M. J.; Christiansen, O.; Pawłowski, F.; Jørgensen, P.; Hättig, C.; Helgaker, T.; Sałek, P. Benchmarking Two-Photon Absorption with CC3 Quadratic Response Theory, and Comparison with Density-Functional Response Theory. *J. Chem. Phys.* **2006**, 124, 054322.
- [61] Chutjian, A.; Hall, R. I.; Trajmar, S. Electron-impact Excitation of H₂O and D₂O at Various Scattering Angles and Impact Energies in the Energy-loss Range 4.2–12 eV. *J. Chem. Phys.* **1975**, 63, 892–898.

Coupled Cluster investigation of the vibrational and electronic second and third harmonic scattering hyperpolarizabilities of the water molecule

J. Chem. Phys. **2019**, *151*, 064303 (DOI: 10.1063/1.5110375)

Pierre Beaujean and Benoît Champagne

*Laboratory of Theoretical Chemistry, Namur Institute of Structured Matter,
University of Namur, Rue de Bruxelles 61, B-5000 Namur, Belgium*

Abstract

The vibrational contributions to the average polarizability ($\bar{\alpha}$), to the second harmonic scattering (SHS) first hyperpolarizability (β_{SHS}) and depolarization ratio (DR_{SHS}), as well as to the third harmonic scattering (THS) second hyperpolarizability (γ_{THS}) and depolarization ratio (DR_{THS}) have been evaluated for the water molecule using the Bishop and Kirtman perturbative theory approach, in combination with finite differentiation techniques to evaluate the higher-order derivatives. From a hierarchy of Coupled Clusters techniques and extended atomic basis sets, the CCSD/d-aug-cc-pVTZ level has been selected to assess the importance of the ZPVA contributions and of the pure vibrational contributions with respect to their electronic counterparts. This is the first investigation demonstrating electronic and vibrational SHS and THS responses can be computed for small molecules, with the perspective of performing comparisons with recent experimental data [Anal. Chem. **89**, 2964 (2017) and J. Phys. Chem. C **121**, 8510 (2017)]. Numerical results on the water molecule highlight that i) the vibrational contributions to the dynamic

$\tilde{\alpha}$, β_{SHS} , and γ_{THS} are small but non negligible, ii) they amount to respectively 3, 10, and 4 % at the typical 1064 nm wavelength, iii) the mechanical anharmonicity term dominates the zero-point vibrational average contribution, iv) the double harmonic terms dominate the pure vibrational contributions, v) the stretching vibrations provide the largest contributions to the dynamic (hyper)polarizabilities, and vi) these conclusions are strongly impacted in the static limit where the vibrational contributions are much larger, in particular the double harmonic pure vibrational terms, and even more in the case of the first hyperpolarizability.

► Supporting information are available at <https://doi.org/10.1063/1.5110375>.

Section 6.1

Introduction

The interactions between light and matter constitute a bottomless topic, with scientific, technological, philosophical, and medical aspects. Among these, nonlinear effects present their own interest and characteristics. Since their first observations, usually attributed to the discovery of lasers, many nonlinear optical (NLO) effects have been revealed and their study has led to the development of analytical or spectroscopic tools for characterizing molecular structures and for imaging as well as to the elaboration of optics-based devices.^{1–4} the present work focuses on the Second Harmonic Scattering^{4,5} (SHS, also called hyper-Rayleigh Scattering, HRS) and Third Harmonic Scattering (THS)^{6,7} phenomena. At the molecular scale, the NLO effects, including SHS and THS, are described by the first (β) and second (γ) hyperpolarizabilities and numerous studies have dwelled on their relationships with the molecular structure.^{8–13} In parallel to instrumental developments as well as to synthesis and characterization of highly active compounds, the hyperpolarizabilities have been a topic of intense theoretical and computational activities to derive structure-property relationships in order to design compounds with high efficiency but also because the hyperpolarizabilities are challenging quantities to calculate and to interpret.^{13,14} In particular, numerous works have highlighted the large electron correlation effects,^{15–19} the impact of the surrounding (solvent, self-assembled monolayer, solid),^{20–25} the specific frequency dispersion,^{26,27} and the importance of the vibrational contributions. This last topic has been the subject of extended studies, to select reliable computational levels of approximation^{28–34} as well as to unravel the structure-property relationships for molecules,^{35–38} clusters,^{39,40} solids,⁴¹ or new materials.^{42–44} Owing its small size and omnipresence, the determination of the water electrical properties has always been the subject of numerous investigations and it was often considered when testing new methods, for instance in the case of the polarizability,⁴⁵ the first and second hyperpolarizabilities,⁴⁶ and their related multipolar properties.^{47,48}

When electron correlation is included at an appropriate level and with a well-chosen basis set, usually an extended basis set with diffuse functions, accurate electronic (hyper)polarizability values are obtained.^{49–54} Nevertheless, within the Born-Oppenheimer approximation, along with this electronic contribution, they are additional contributions, called vibrational contributions. They originate from the electric field-induced nuclear reorganizations as well as from the electric field dependence of the potential energy surface.⁵⁵ Within the perturbation theory approach, these vibrational responses are divided into pure vibrational and zero-point vibrational average (ZPVA) contributions. Their expressions have been derived by Bishop, Luis, and Kirtman^{56–58} by expanding in Taylor series the potential energy surface and the electrical properties around the equilibrium geometry, leading to contributions of higher and higher orders in mechanical and electrical anharmonicities.

Previous studies^{59–68} have shown that, in the static limit as well as for specific NLO processes involving one or more static field, the correction that originates from the pure vibrational contributions can be of similar magnitude to the electronic contribution and cannot be neglected. On the other hand, in the case of “fully” optical phenomena, like SHS and THS, those contributions are usually neglected. Indeed, the pure vibrational part is expected to be much smaller at optical frequencies because it is damped by the $(\omega_a/\omega)^{2n}$ ($n \geq 1$) multiplicative factor, where ω_a is a vibrational mode (angular) frequency and ω is the frequency of the incident light. In addition, the ZPVA represents usually only a few percents of the electronic response and it is, therefore, often neglected. Moreover, there are fewer results on the ZPVA contributions since it is anharmonic in nature and it requires computationally expensive calculations of, at least, the cubic force constants as well as of second-order derivatives of the electrical properties with respect to the normal mode coordinates. In this paper, we address this simplification by tackling the water molecule with a hierarchy of Coupled Cluster (CC) methods combined with extended basis sets. The importance of the different vibrational contributions is then assessed as a function of ω , while the validity of Kleinmann’s symmetry conditions is checked. Emphasis is also put on the contributions of the different vibrational normal modes, in relation to their symmetry representation.

This paper is divided in five sections. After a description, in Section 6.2, of the vibrational contributions to α , β and γ , and the target quantities, Section 6.3 presents the computational details. Then, in Section 6.4, the main results are presented and analyzed. First the effects of the level of approximation and of the atomic basis set are assessed. Then, using a selected method, the relative amplitudes of the vibrational contributions are discussed at the light of their electronic counterpart and they are traced back to the contributions of the vibrational normal modes. Moreover, comparisons are made with previous calculations of both the electronic and vibrational (hyper)polarizabilities of water. Finally conclusions are drawn in Section 6.5.

Section 6.2

Theoretical aspects

Electronic and vibrational hyperpolarizabilities

At the molecular scale, the frequency-dependent polarizability, first and second hyperpolarizabilities are the Taylor series expansion coefficients of the molecular induced dipole moment as a function of external electric fields, \vec{F} , applied along the i, j, \dots directions (note that lower-case letters stand for coordinates in the molecular frame) and oscillating at frequencies

$\omega_1, \omega_2, \dots$:

$$\begin{aligned} \Delta\mu_i(\vec{F}) = & \sum_j^{x,y,z} \alpha_{ij}(-\omega_\sigma; \omega_1) F_j(\omega_1) + \frac{1}{2!} \sum_{jk}^{x,y,z} \beta_{ijk}(-\omega_\sigma; \omega_1, \omega_2) F_j(\omega_1) F_k(\omega_2) \\ & + \frac{1}{3!} \sum_{jkl}^{x,y,z} \gamma_{ijkl}(-\omega_\sigma; \omega_1, \omega_2, \omega_3) F_j(\omega_1) F_k(\omega_2) F_l(\omega_3) + \dots \end{aligned} \quad (6.1)$$

with $\omega_\sigma = \sum_i \omega_i$. α_{ij} is an element of the polarizability tensor, β_{ijk} and γ_{ijkl} are elements of the first and second hyperpolarizability tensors, respectively. Depending on the combination of static and dynamic electric fields, different NLO processes arise. The SHS and THS responses are noted $\beta(-2\omega; \omega, \omega)$ and $\gamma(-3\omega; \omega, \omega, \omega)$, respectively.

When electric fields interact with a molecule, different phenomena occur. Within the clamped-nucleus approximation,⁵⁵ the effects on the electronic and nuclear motions are considered sequentially, rather than simultaneously. First, the electronic distribution changes, giving rise to the electronic responses, P^e , with $P = \alpha, \beta$, or γ . This induces a modification of the ground state potential energy surface, therefore of the equilibrium geometry and of the vibrational zero-point energy, leading to the so-called nuclear relaxation and curvature contributions to the (hyper)polarizabilities, or, globally, the vibrational responses, P^v . Note that, under the application of external electric fields, the molecule can also rotate to align its (induced) dipole moment on the external field but this contribution is neglected for optical electric fields because the molecular response time is too slow with respect to the incident light frequency.

The total electrical property, P^{tot} , reads therefore $P^{tot} = P^e + P^v$. To provide tractable equations, Bishop and Kirtman⁵⁶ started from the sum-over-states (SOS) perturbation theory expressions of the (hyper)polarizabilities in the adiabatic approximation,⁶⁹ and decomposed these into two terms, the electronic [$P^e(\text{SOS})$] and the pure vibrational [$P^{pv}(\text{SOS})$] contributions. These expressions were then further simplified by invoking the clamped nucleus approximation, leading to SOS expressions where the electronic states are employed instead of vibronic states. As a result, the corresponding electronic contribution [$P^e(\text{CN})$] involves a zero-point vibrational averaging over the vibrational ground state wavefunction of the electronic ground state so that it can be written as the sum of the electronic contribution at the equilibrium ground state geometry (P^e) and a ZPVA correction (ΔP^{ZPVA}). These ZPVA contributions present therefore the same type of frequency dispersion as their electronic counterparts. For $P^{pv}(\text{CN})$, Bishop and Kirtman⁵⁶ assumed that, in non-resonant regimes, optical frequencies can be neglected in comparison to electronic transition frequencies. Note that this approximation holds in the static and infinite frequency limit, but some corrections would be needed for optical fields, as discussed by Kirtman and Luis.⁷⁰ Finally, the treatment of Ref.⁵⁶ leads to the decomposition of the pure vibrational contributions P^{pv} into square bracket quan-

tities, involving lower-order electrical properties:

$$\alpha^{pv} = [\mu^2], \quad (6.2)$$

$$\beta^{pv} = [\mu\alpha] + [\mu^3], \quad (6.3)$$

$$\gamma^{pv} = [\alpha^2] + [\mu\beta] + [\mu^2\alpha] + [\mu^4]. \quad (6.4)$$

Then, for both P^{pv} and ΔP^{ZPVA} quantities, it is assumed that the power series expansions of the electrical properties around the equilibrium geometry and of the potential energy are convergent. This allows treating electrical (when second- and higher-order derivatives of the electrical properties are considered) and mechanical (when third- and higher-order derivatives of the potential energy are considered) anharmonicities by ordinary double perturbation theory and writing the different quantities as sums of harmonic and anharmonic terms. In the present investigation, the following terms are included:

$$\Delta P^{ZPVA} = [P]^I, \quad (6.5)$$

$$\alpha^{pv} = [\mu^2]^0 + [\mu^2]^II, \quad (6.6)$$

$$\beta^{pv} = [\mu\alpha]^0 + [\mu^3]^I + [\mu\alpha]^II, \quad (6.7)$$

$$\gamma^{pv} = [\alpha^2]^0 + [\mu\beta]^0 + [\mu^2\alpha]^I + [\alpha^2]^II + [\mu\beta]^II + [\mu^4]^II, \quad (6.8)$$

where $[X]^0 = [X]^{0,0}$, $[X]^I = [X]^{1,0} + [X]^{0,1}$, and $[X]^II = [X]^{1,1} + [X]^{2,0} + [X]^{0,2}$. The $[X]^{m,n}$ notation associates m with the order of electrical anharmonicity and n with the order of mechanical anharmonicity. Still, the expressions for $[X]^{2,0}$ and $[X]^{0,2}$ were truncated so that they do not contain third-order derivatives of electrical properties nor quartic force constants, respectively. The detailed expressions for those contributions were derived by Bishop, Luis, and Kirtman^{56–58} and are used in the present work.

Hyperpolarizability tensor components and target quantities

All components of the electronic and vibrational (hyper)polarizability tensors were calculated in order to evaluate quantities that can be extracted from experiment. For the polarizability, these quantities are its isotropic average ($\bar{\alpha}$) and its anisotropy ($\Delta\alpha$), defined as

$$\bar{\alpha} = \frac{1}{3} \sum_i^{x,y,z} \alpha_{ii}, \quad (6.9)$$

$$\Delta\alpha = \left[\frac{1}{2} \sum_{i,j}^{x,y,z} 3\alpha_{ij}^2 - \alpha_{ii}\alpha_{jj} \right]^{1/2}. \quad (6.10)$$

The higher-order target quantities are the second harmonic scattering first hyperpolarizability (β_{SHS}) and the third harmonic scattering second hyperpolarizability (γ_{THS}) as well as their depolarization ratios (DR_{SHS} and DR_{THS}):

$$\beta_{SHS} = \sqrt{\langle \beta_{ZZZ}^2 \rangle + \langle \beta_{ZXX}^2 \rangle}, \quad (6.11)$$

$$DR_{SHS} = \frac{\langle \beta_{ZZZ}^2 \rangle}{\langle \beta_{ZXX}^2 \rangle}, \quad (6.12)$$

$$\gamma_{THS} = \sqrt{\langle \gamma_{ZZZZ}^2 \rangle + \langle \gamma_{ZXXX}^2 \rangle}, \quad (6.13)$$

$$DR_{THS} = \frac{\langle \gamma_{ZZZZ}^2 \rangle}{\langle \gamma_{ZXXX}^2 \rangle}. \quad (6.14)$$

β_{SHS} and γ_{THS} characterize the scattering intensities for non-polarized incident light and observation of plane-polarized scattered light made perpendicularly to the propagation plane. $\langle \beta_{ZZZ}^2 \rangle$ ($\langle \gamma_{ZZZZ}^2 \rangle$) and $\langle \beta_{ZXX}^2 \rangle$ ($\langle \gamma_{ZXXX}^2 \rangle$) are orientational averages of the β (γ) tensor components describing the SHS (THS) intensities when the incident light is vertically- or horizontally-polarized, respectively. Their detailed expressions can be found in Refs. 71–74. Still, owing to its symmetry (water belongs to the C_{2v} point group) and specific NLO processes, out of the 27 (β) or 81 (γ) tensor components, only a reduced number of components have to be calculated. So, the number of non-zero independent tensor components amounts to 3 (xx, yy and zz) for the polarizability, to 5 [x(xz), y(yz), zxx, zyy, and zzz, parentheses indicate permutations that leave invariant the tensor component] for the first hyperpolarizability, and 9 [xxxx, x(xyy), x(xzz), y(xxy), yyyy, y(yzz), z(xxz), z(yyz), and zzzz] for the second hyperpolarizability.⁷² In the static limit, Kleinman's conditions are fulfilled and any permutation of the tensor indices leave invariant the tensor components so that the number of non-zero independent tensor components is further reduced to 3 and 6 for the first and second hyperpolarizabilities, respectively.

Symmetry has also an impact on the number of derivatives to calculate, *i.e.* the derivatives of the molecular electrical properties with respect to the vibrational normal coordinates (see Appendix). Indeed, the water molecule possesses three vibrational normal modes: a bending (associated with Q_1 , of A_1 irreducible representation), a symmetric (Q_2 , A_1) and an anti-symmetric (Q_3 , B_2) stretching.

To assess the importance of the electronic and vibrational contributions on the total value of a given (hyper)polarizability, a missing-contribution analysis was used, with \mathcal{C}_A a measure, in percents, of the A contribution:

$$\mathcal{C}_A = 100 \times \left\{ 1 - \frac{P^{(-A)}}{P_{tot}} \right\}, \quad (6.15)$$

where $P^{(-A)}$ is the property for which the A contribution is missing. For any tensor component, the curly bracket is equivalent to $\frac{P^A}{P_{tot}}$. The impact of a vibrational mode on a given vibrational

contribution to P^v was assessed in the same way, using the missing mode analysis:

$$\mathcal{C}_a = 100 \times \left\{ 1 - \frac{P^{v(-a)}}{P^v} \right\}, \quad (6.16)$$

where $P^{v(-a)}$ is the vibrational property computed by using all the normal modes but mode a . All α , β , and γ quantities are given within the T convention (Eq. 1) in a.u.:

- 1 a.u. of $\alpha = 1.648 \times 10^{-41} \text{ C}^2 \text{ m}^2 \text{ J}^{-1} = 0.14818 \text{ \AA}^3$;
- 1 a.u. of $\beta = 3.6212 \times 10^{-42} \text{ m}^4 \text{ V}^{-1} = 3.2064 \times 10^{-53} \text{ C}^3 \text{ m}^3 \text{ J}^{-2} = 8.639 \times 10^{-33} \text{ esu}$;
- 1 a.u. of $\gamma = 7.423 \times 10^{-54} \text{ m}^5 \text{ V}^{-2} = 6.2354 \times 10^{-65} \text{ C}^4 \text{ m}^4 \text{ J}^{-3} = 5.0367 \times 10^{-40} \text{ esu}$.

Section 6.3

Computational aspects

The water molecule lies in the YZ plane with its C_2 axis coinciding with the Cartesian Z axis (the oxygen atom points in the direction of negative Z). Its geometry was optimized in gas phase at different levels of approximation (HF, CCS, ⁷⁵ CC2, ⁷⁵ CCSD⁷⁶) and with different basis sets ([d-]aug-cc-pVXZ, ⁷⁷ with X=D, T). The static and dynamic (at 1500, 1300, 1064 and 694.3 nm wavelengths) electronic properties (polarizability, SHS first hyperpolarizability, and THS second hyperpolarizability) were computed at the same levels of approximation for both equilibrium and distorted geometries, using the linear, ⁷⁸ quadratic (QRF), ^{79,80} and cubic (CRF) ^{81,82} response function methods.

In order to calculate the geometrical derivatives of the electrical properties with respect to the atomic Cartesian coordinates, the central finite difference method was employed and combined with the Romberg (or Richardson) quadrature ($k_{\max}=4$, distortion amplitude = $0.01 a_0$, common ratio = 2) to remove higher-order contaminations. ^{83–86} These derivatives were finally projected over the normal coordinates in order to obtain the derivatives with respect to the vibrational normal mode coordinates. At the Hartree-Fock level, the Hessian required to compute the vibrational normal modes and frequencies was calculated analytically, using the coupled-perturbed Hartree-Fock scheme, but the cubic force constants numerically, as the first-order derivatives of the Hessian using the same method as described above for the geometrical derivatives of the electrical properties. At the CC levels, both quadratic and cubic force constants were calculated from the analytical gradients, as their first- and second-order derivatives, respectively. The masses used for the hydrogen and oxygen atoms in the computation of the mass-weighted Hessian are $m_H=1.00794 \text{ a.m.u.}$ and $m_O=15.9994 \text{ a.m.u.}$ ⁸⁷

The geometry optimizations and electrical property calculations were performed using Dalton 2016⁸⁸ while a homemade program was employed to calculate the numerical deriva-

tives and the subsequent vibrational (hyper)polarizabilities. The SCF convergence was set to 10^{-11} a.u. and CPHF (or its CC counterparts) QRF and CRF convergences to 10^{-10} a.u.

Section 6.4

Results and discussions

Geometries and vibrational frequencies

Table S1 describes the impact of the level of approximation and basis set on the equilibrium geometrical parameters of the water molecule, which are also plotted in Fig. 6.1. Changes from double- to triple- ζ basis sets or from CCS to CCSD leads to concerted variations in the bond length and valence angle: when R increases, δ decreases. Going from double- to triple- ζ basis sets increases the valence angle by 0.3 - 0.4° while a decrease of the bond length by 0.007 - 0.008\AA is observed when going from the CCS to CCSD level. On the other hand, the addition of a second set of diffuse functions has a much smaller effect. Then, electron correlation leads to a lengthening of the O-H bond by about 0.02\AA and to a smaller valence angle by about 2° . The differences between CC2 and CCSD are smaller.

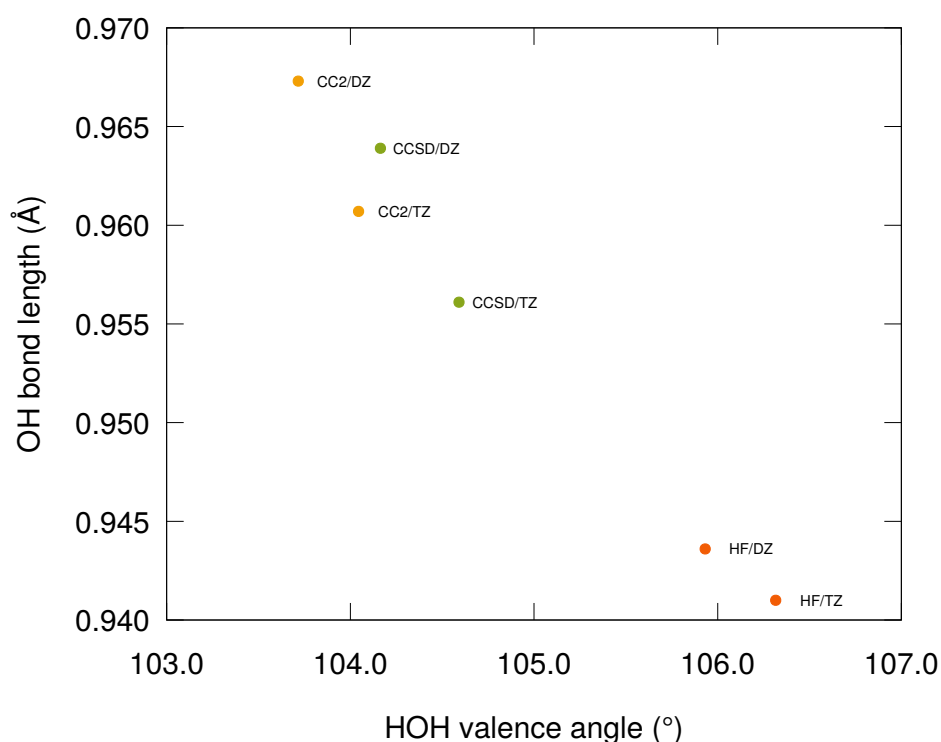


Figure 6.1: Impact of the level of approximation and basis set (XZ=aug-cc-pVXZ) on the equilibrium geometrical parameters of water.

The impact of the method of calculation on the vibrational frequencies is presented in Table 6.1. The effect of the basis set depends on the method and impacts mostly the stretching modes. While the HF frequencies vary by 5 to 15 cm^{-1} , there is a larger impact at the

CC2 and CCSD levels (up to 50 cm^{-1} for the stretchings). On the other hand, the additional set of diffuse functions impacts the frequencies by less than 6 cm^{-1} , the B_2 stretching being mostly affected. Taking CCSD/d-aug-cc-pVTZ as reference, the HF frequencies evaluated with the same basis set are overestimated by 5 % for the bending and by as much as 8 % for the stretchings, while the CC2 frequencies are underestimated by less than 2 %.

Table 6.1: Basis set and electron correlation effects on the harmonic vibrational frequencies of water (ω_1 , A_1 bending; ω_2 , A_1 symmetric stretching; ω_3 , B_2 anti-symmetric stretching, in cm^{-1}).

	D			T		
	ω_1	ω_2	ω_3	ω_1	ω_2	ω_3
aug-cc-pVXZ						
HF = CCS	1744.2	4130.0	4237.4	1745.0	4120.29	4222.6
CC2	1617.3	3770.6	3907.5	1619.0	3812.5	3935.0
CCSD	1649.8	3823.9	3939.4	1654.7	3880.8	3982.0
d-aug-cc-pVXZ						
HF = CCS	1749.8	4130.1	4238.8	1745.8	4121.3	4222.5
CC2	1623.7	3768.6	3907.0	1620.9	3806.1	3929.0
CCSD	1656.3	3822.0	3938.9	1656.5	3874.3	3975.8

Polarizabilities and hyperpolarizabilities

The total (electronic + ZPVA + pv) static and dynamic (1064 nm) (hyper)polarizabilities calculated at the different levels of approximation are given in Tables 6.2-6.4. On the basis of our recent investigations on the first and second electronic hyperpolarizabilities of water, methanol, and dimethylether,^{52,74} the CCSD/d-aug-cc-pVTZ results are considered as reference values. This allows assessing, on the one hand, the contribution of electron correlation to the (hyper)polarizabilities, i.e., the differences between the HF and CCSD results, as well as to check how close or different are the more approximate CC2 values. On the other hand, these reference values are employed to estimate the importance of including a second set of diffuse functions and of using triple- ζ instead of double- ζ basis sets.

With respect to CCSD, the HF and CCS response property values are underestimated ($\Delta\alpha$ and DR_{THS} are overestimated), while CC2 overestimates the different quantities ($\Delta\alpha$ and DR_{THS} are underestimated). These results, on both the static and dynamic linear and nonlinear responses, are consistent with the results on the electronic responses only.^{52,74} Within the four basis sets employed in this work, basis set effects on the isotropic polarizability are of the order of 2%. They increase to about 10% for β_{SHS} . For γ_{THS} these can attain 50%. Still, like in Ref. 74, the basis set effects on the depolarization ratios are much larger. These are also stronger on the polarizability anisotropy than on the average polarizability.

The vibrational contribution to the average polarizability range between 5 and 7 % in the static limit and decreases to about 3 % at 1064 nm. Changing the basis set has a negligible influence on these percentages whereas changing the method leads to variations of the order of 1 % with respect to the Hartree-Fock case. The impact of including the vibrational contributions to the polarizability anisotropy is much stronger, with contributions between 25 and 60 %, as a function of the method and basis set. Using CCSD/d-aug-cc-pVTZ, the static vibrational counterpart amounts to 50 % of the total anisotropy value whereas, at 1064 nm, it still represents one third of the total response.

For static quantities, the vibrational contribution is detrimental to the β_{SHS} amplitude. At the reference level, it amounts to -16% of the total value but it reaches as much as 50 % at the HF and CCS levels. The impact of including vibrational contributions to the static DR_{SHS} depends strongly on the method and is rather negligible at the reference level. The situation is opposite for the dynamic β_{SHS} (at 1064 nm) since the vibrational contribution increases the response by about 10 %. Again the relative vibrational counterpart gets larger at the HF and CCS levels. The contribution of the vibrations is modest on the dynamic DR_{SHS} , being of the order of -5% . Like for its static analog, changing the method leads to substantial variations of the vibrational contribution but, percentagewise, it remains small.

Finally, for γ_{THS} , at the reference level, the vibrational contribution amounts to 13 % in the static limit and to 4 % at 1064 nm. These are a rather small contributions, smaller than for the first hyperpolarizability. The vibrational contributions have a much larger effect on the static DR_{THS} and they lead to an increase by about 50 %. The latter presents also a substantial dependence on the method and basis set. Note that owing to its large DR_{THS} values, γ_{THS} of the water molecule is typically dominated by its isotropic rather than by its quadrupolar and hexadecapolar components. At 1064 nm, the vibrational contribution to DR_{THS} is small, of the same order of magnitude as the contribution to γ_{THS} .

These results have evidenced that the vibrational contributions to the dynamic α , β , and γ are small but not negligible, and non-systematic. Then, owing to the large effects of the method and basis set, it turns out that the CCSD/d-aug-cc-pVTZ level is mandatory for investigating the impact of vibrational contributions on the (hyper)polarizabilities of water.

Owing the larger computational cost of the vibrational contributions, a hybrid approach has been tested, where the electronic contribution is evaluated at the CCSD level, while the vibrational ones are calculated at the HF or CC2 levels of approximation (Table S9). If reliable, this hybrid method would be an efficient alternative to grasp most of the vibrational contributions. For instance, the resulting hybrid $\bar{\alpha}$ are in close agreement with the reference full CCSD value for the dynamic responses, and especially for the pure vibrational contributions, which are negligible. However, the differences amount to about 10 % for the static $\Delta\alpha$. The agreement for the dynamic β is less good because of the differences between the ZPVA contributions, which can be larger than 50 %. For instance, the vibrational contribution to the $\beta_{||}(-2\omega; \omega, \omega)$ response is overestimated by 50 % at the CC2 level, raising question about

the reliability of this hybrid scheme. On the other hand, the pure vibrational contribution are small for the dynamic responses. In the static limit, both the ZPVA and the pure vibrational contributions to the first hyperpolarizabilities varies substantially from one method to another. Finally, in the case the dynamic second hyperpolarizability, neither the HF, nor the CC2 method represent a good alternative to evaluate the vibrational contributions because the former underestimates these by about a factor of 3, while the latter underestimates it by more than a factor of 2. Again, the pure vibrational contributions are negligible.

Frequency dispersion and decomposition into the different vibrational contributions

Now, we focus on the impact of each vibrational contribution to the total value and we describe their frequency dispersions. The results are listed in Tables 6.5-6.7. Additional details are provided in Tables S2-S4 where the independent non-zero tensor components are listed.

Table 6.2: Basis set and electron correlation effects on the total ($\alpha^e + \Delta\alpha^{ZPVA} + \alpha^{pv}$) static (top) and dynamic (bottom, 1064 nm) isotropic polarizability of water and its anisotropy. The amplitude of the vibrational counterpart (\mathcal{C}_v , %) is given in parentheses.

	HF	CCS	CC2	CCSD
$\bar{\alpha}(0)$				
aug-cc-pVDZ	8.54 (6.7)	8.98 (6.5)	10.49 (5.6)	9.85 (5.5)
aug-cc-pVTZ	8.81 (6.6)	9.26 (6.4)	10.73 (5.6)	10.01 (5.5)
d-aug-cc-pVDZ	8.94 (6.6)	9.39 (6.4)	11.20 (5.5)	10.43 (5.4)
d-aug-cc-pVTZ	8.93 (6.6)	9.38 (6.4)	10.99 (5.6)	10.20 (5.5)
$\Delta\alpha(0)$				
aug-cc-pVDZ	1.84 (26.9)	2.02 (25.0)	1.44 (27.2)	1.52 (26.2)
aug-cc-pVTZ	1.62 (34.2)	1.78 (31.5)	1.16 (42.8)	1.26 (39.1)
d-aug-cc-pVDZ	1.45 (39.5)	1.60 (35.9)	0.85 (58.0)	1.01 (49.5)
d-aug-cc-pVTZ	1.50 (39.0)	1.66 (35.5)	0.93 (61.4)	1.09 (50.6)
$\bar{\alpha}(1064\text{nm})$				
aug-cc-pVDZ	8.23 (2.7)	8.67 (2.7)	10.30 (3.1)	9.64 (2.9)
aug-cc-pVTZ	8.49 (2.6)	8.93 (2.6)	10.52 (3.0)	9.78 (2.7)
d-aug-cc-pVDZ	8.62 (2.6)	9.07 (2.7)	11.01 (3.1)	10.23 (2.8)
d-aug-cc-pVTZ	8.61 (2.6)	9.06 (2.6)	10.78 (3.0)	9.97 (2.7)
$\Delta\alpha(1064\text{nm})$				
aug-cc-pVDZ	1.59 (15.7)	1.78 (15.1)	1.27 (20.2)	1.35 (19.2)
aug-cc-pVTZ	1.30 (18.6)	1.47 (17.6)	0.87 (27.7)	0.99 (24.7)
d-aug-cc-pVDZ	1.11 (22.4)	1.28 (20.9)	0.56 (42.9)	0.74 (35.1)
d-aug-cc-pVTZ	1.15 (20.9)	1.32 (19.6)	0.55 (42.1)	0.75 (32.2)

Like its electronic counterpart, the ZPVA contribution to the isotropic polarizability increases slightly with the optical frequency. From 694 nm to the static limit, it amounts to roughly 3 %. The mechanical anharmonicity contributes the most to the (first order) ZPVA correction, in a 2:1 ratio with respect to the electrical anharmonicity term. The pure vibrational term has, in the static limit, a similar amplitude to the ZPVA correction but it drops strongly in the dynamic regime. Note that the harmonic term is the main pure vibrational contribution, much larger than the second-order anharmonicity term. For the polarizability anisotropy, in the static limit the ZPVA correction and pure vibrational term are again of the same order of magnitude but in the dynamic regime the ZPVA term dominates again the whole vibrational response. Moreover, the mechanical anharmonicity term is also the largest and about twice bigger than the electrical anharmonicity one. The frequency dispersion of the harmonic term is characterized by a decrease of its amplitude with the frequency (like for the isotropic average) whereas the second-order anharmonic term presents a non-monotonic frequency dispersion, due a resonance in those terms, between the optical frequency and the

Table 6.3: Basis set and electron correlation effect on the total ($\beta^e + \Delta\beta^{ZPVA} + \beta^{pv}$) static (top) and dynamic (bottom, 1064 nm) SHS hyperpolarizability of water and of its depolarization ratio (DR). The amplitude of the vibrational counterpart (\mathcal{C}_v , %) is given in parentheses.

	HF	CCS	CC2	CCSD
$\beta_{SHS}(0)$				
aug-cc-pVDZ	5.28 (-42.7)	6.31 (-44.6)	12.42 (-20.0)	9.52 (-21.9)
aug-cc-pVTZ	4.96 (-51.0)	6.26 (-46.9)	13.75 (-16.0)	9.66 (-21.2)
d-aug-cc-pVDZ	4.11 (-51.8)	5.30 (-46.3)	12.64 (-10.1)	8.66 (-15.4)
d-aug-cc-pVTZ	4.47 (-51.3)	5.85 (-44.9)	14.32 (-10.1)	9.49 (-16.3)
$DR_{SHS}(0)$				
aug-cc-pVDZ	1.93 (-77.2)	2.38 (-76.3)	3.90 (-38.7)	3.24 (-50.6)
aug-cc-pVTZ	3.46 (-35.4)	4.32 (-30.2)	6.55 (-10.6)	5.76 (-16.1)
d-aug-cc-pVDZ	3.08 (-24.7)	4.00 (-21.9)	6.67 (-3.5)	5.52 (-15.4)
d-aug-cc-pVTZ	4.64 (-10.9)	5.64 (-10.0)	8.20 (-1.1)	7.55 (-2.4)
$\beta_{SHS}(1064\text{ nm})$				
aug-cc-pVDZ	9.64 (18.4)	11.31 (16.1)	17.91 (10.7)	13.84 (10.6)
aug-cc-pVTZ	9.59 (17.9)	11.45 (16.0)	18.97 (9.4)	13.89 (9.9)
d-aug-cc-pVDZ	8.27 (20.4)	10.09 (19.2)	17.02 (10.1)	12.14 (10.9)
d-aug-cc-pVTZ	8.81 (18.8)	10.69 (16.6)	18.90 (8.9)	13.19 (9.5)
$DR_{SHS}(1064\text{ nm})$				
aug-cc-pVDZ	3.71 (3.0)	3.96 (-11.5)	5.98 (-4.4)	5.30 (-5.6)
aug-cc-pVTZ	4.77 (-3.2)	5.62 (-5.3)	7.69 (-4.9)	6.96 (-5.9)
d-aug-cc-pVDZ	4.03 (0.7)	4.95 (-2.4)	7.07 (-4.7)	6.15 (-3.9)
d-aug-cc-pVTZ	5.09 (-5.3)	6.05 (-6.9)	8.43 (-3.5)	7.76 (-5.8)

sum of the two stretching vibrational frequencies close to 1300 nm. Analyzing the tensor components (Table S2), the largest static and dynamic ZPVA component is α_{yy} and, in the static limit, α^{pv} is determined by the α_{zz} component. Note that there is no pure vibrational contribution to α_{xx} since, $\forall a, \left(\frac{\partial \mu_x}{\partial Q_a}\right)_0 = 0$.

The frequency dispersion of the first hyperpolarizability presents similarities to that of the polarizability, though it is naturally exalted owing to its SHG character. The ZPVA correction evolves smoothly with the frequency, as does the electronic contribution. Again, the mechanical anharmonicity term is the largest, with a 3:1 ratio with respect to the electrical anharmonicity. In the pure vibrational contribution, the $[\mu\alpha]^0$ harmonic term is the largest, followed by $[\mu\alpha]^{\text{II}}$, and they both fade out when the optical frequency increases. On the other hand, the static β^{pv} is much larger than the dynamic one. It is of the opposite sign to the electronic counterpart and it dominates the vibrational response. The inclusion of vibrational contributions modifies DR_{SHS} by at most 10 % with a non-monotonic frequency dispersion that originates from the pure vibrational (harmonic) contribution. The amplitudes of the three

Table 6.4: Basis set and electron correlation effect on the total ($\gamma^e + \Delta\gamma^{\text{ZPVA}} + \gamma^{pv}$) static (top) and dynamic (bottom, 1064 nm) THS hyperpolarizability of water and of its depolarization ratio (DR). The amplitude of the vibrational counterpart (\mathcal{C}_v , %) is given in parentheses.

	HF	CCS	CC2	CCSD
$\gamma_{\text{THS}}(0)$				
aug-cc-pVDZ	759 (22.2)	885 (21.4)	1690 (18.8)	1303 (18.2)
aug-cc-pVTZ	910 (20.2)	1064 (19.2)	2012 (16.8)	1506 (16.3)
d-aug-cc-pVDZ	1103 (17.2)	1274 (16.5)	2871 (14.5)	2084 (13.6)
d-aug-cc-pVTZ	1190 (16.3)	1371 (15.7)	2938 (14.0)	2101 (13.3)
$\text{DR}_{\text{THS}}(0)$				
aug-cc-pVDZ	660 (70.0)	699 (64.3)	309 (66.9)	416 (71.8)
aug-cc-pVTZ	1465 (88.0)	1820 (88.4)	290 (65.5)	417 (72.7)
d-aug-cc-pVDZ	312 (74.0)	380 (74.9)	100 (46.9)	126 (53.5)
d-aug-cc-pVTZ	411 (74.9)	504 (76.2)	127 (46.8)	166 (54.3)
$\gamma_{\text{THS}}(1064 \text{ nm})$				
aug-cc-pVDZ	728 (4.2)	792 (-2.9)	1904 (5.3)	1406 (3.9)
aug-cc-pVTZ	891 (3.9)	976 (-2.9)	2276 (5.3)	1635 (3.9)
d-aug-cc-pVDZ	1127 (3.5)	1301 (3.5)	3486 (6.1)	2402 (4.1)
d-aug-cc-pVTZ	1226 (3.6)	1410 (3.6)	3497 (6.0)	2387 (4.2)
$\text{DR}_{\text{THS}}(1064 \text{ nm})$				
aug-cc-pVDZ	132 (22.4)	68 (-81.6)	38 (0.9)	50 (5.6)
aug-cc-pVTZ	128 (20.6)	178 (32.3)	46 (1.3)	60 (5.7)
d-aug-cc-pVDZ	69 (14.5)	80 (14.9)	32 (0.6)	39 (3.7)
d-aug-cc-pVTZ	86 (13.9)	99 (14.3)	42 (0.7)	51 (3.8)

non-zero independent $\beta^e(0; 0, 0)$ tensor components (Table S3) satisfy the $\beta_{xxz} < \beta_{yyz} < \beta_{zzz}$ ordering. The pure vibrational contribution is also dominated by β_{zzz} , followed by β_{zyy} , which are much larger than β_{zxx} . For these dominant tensor components, contrary to the electronic and ZPVA contributions, the harmonic contribution to β^{pv} is positive but it is partly canceled by the $[\mu^3]^I$ first-order anharmonic term. On the other hand, for the ZPVA correction, the largest component is β_{yyz} , followed by β_{zzz} , and both are also much larger than β_{xxz} . The small $\beta_{(xxz)}$ contributions are again explained by the zero $\left(\frac{\partial \mu_x}{\partial Q_a}\right)_0$ quantities. For both β^e and $\Delta\beta^{ZPVA}$, these relative amplitudes remain when considering the dynamic responses, with small differences between the Kleinman-related tensor components [e.g. $\beta_{x(xz)}$ and β_{zxx}]. Finally, it is interesting to note that, at 1064 nm, deviations with respect to Kleinman's conditions are much larger for the pure vibrational contribution than for the ZPVA correction. Indeed, if one compares e.g. the β_{zyy} and β_{yyz} components, the difference attains 22 % at 1064 nm for $[\mu\alpha]^0$, while 0.6 % for $\Delta\beta^{ZPVA}$.

The ZPVA correction to γ_{THS} increases with the frequency, from 4 % in the static limit to 6 % at 694.3 nm (Table 6.7). Again, it is dominated by the mechanical anharmonicity term, though the electrical anharmonicity term increases faster with the frequency. The pure vibrational contributions to γ_{THS} are small, even in the static limit where it attains only 10 %. At optical frequency, the whole γ^{pv} as well as any of its components contribute to less than 1 % and can therefore be considered negligible. Note that the largest contribution to γ^{pv} comes from the $[\alpha^2]^0$ Raman term. Vibrational contributions are larger on DR_{THS} , in particular for the static value, which is strongly enhanced by the harmonic $[\alpha^2]^0$ and $[\mu\beta]^0$ terms. At optical frequencies, the pure vibrational contribution to DR_{THS} is small whereas its ZPVA correction

Table 6.5: Electronic and vibrational contributions to the average polarizability and polarizability anisotropy as computed at the CCSD/d-aug-cc-pVTZ level at different wavelengths.

	Total	Electronic	ZPVA			Pure vibrational			\mathcal{C}_v
			$\mathcal{C}_{[\alpha]^1,0}$	$\mathcal{C}_{[\alpha]^0,1}$	\mathcal{C}_{ZPVA}	$\mathcal{C}_{[\mu^2]^0}$	$\mathcal{C}_{[\mu^2]^II}$	\mathcal{C}_{pv}	
$\bar{\alpha}$									
∞	10.20	9.64	0.9	1.9	2.8	2.8	-0.1	2.7	5.5
1500 nm	9.92	9.67	0.9	2.0	2.9	-0.4	0.0	-0.3	2.6
1300 nm	9.96	9.68	0.9	2.0	2.9	-0.3	0.2	-0.1	2.8
1064 nm	9.97	9.70	0.9	2.0	2.9	-0.2	0.0	-0.2	2.7
694.3 nm	10.08	9.79	0.9	2.0	2.9	-0.1	0.0	-0.1	2.9
$\Delta\alpha$									
∞	1.09	0.54	7.9	12.1	19.6	25.6	-1.1	26.7	50.6
1500 nm	0.74	0.52	12.9	22.0	34.8	-6.4	1.1	-5.3	29.7
1300 nm	0.78	0.52	12.3	20.9	33.1	-4.0	4.7	0.7	34.0
1064 nm	0.75	0.51	13.0	21.9	34.8	-2.5	-0.3	-2.7	32.2
694.3 nm	0.72	0.47	13.7	22.8	36.3	-0.9	0.0	-1.0	35.4

is slightly larger. At 694.3 nm, both vibrational contributions are strongly reduced. Contrary to the lower-order properties, the largest electronic component (in amplitude) is γ_{xxxx} , then γ_{zzzz} and γ_{yyyy} (Table S4). In the static limit, the dominant tensor components to γ^{pv} satisfy the following ordering: $\gamma_{yyyy} > \gamma_{zzzz} > \gamma_{yyzz}$ whereas for the ZPVA correction it is $\gamma_{xxxx} > \gamma_{yyyy} > \gamma_{zzzz}$. Owing to their negligible values, the $\gamma^{pv}(-3\omega; \omega, \omega, \omega)$ tensor components are not discussed. For $\Delta\gamma^{ZPVA}(-3\omega; \omega, \omega, \omega)$ γ_{xxxx} is still the largest component whereas the amplitudes of the two other diagonal components are in reverse order. For those components that satisfy Kleinman's conditions in the static limit, the differences amount to about 10 % for the electronic and pure vibrational contributions while it can be twice larger for the ZPVA correction.

Contributions of the vibrational normal modes

An analysis of the vibrational normal mode contributions is provided in Fig. 6.2 as well as in Table S5. At 1064 nm, the symmetric stretching vibration contributes most to the linear and nonlinear optical responses, followed by the antisymmetric stretching and finally the bending mode. In the static limit, the percentage contributions of modes 2 and 3 change but mode 2 still provides larger contributions than mode 3. On the other hand, for $\bar{\alpha}$ and β_{SHS} , the bending mode contributes substantially with contributions of the same ($\bar{\alpha}$) or opposite (β_{SHS}) signs. In details, on the one hand, the large cubic force constant of the A_1 stretching explains the large $[\]^{0,1}$ contributions in both the static and dynamic cases. On the other hand, a large $\left(\frac{\partial \mu_z}{\partial Q_1}\right)_0$ is at the origin of the large P^{pv} contributions of the A_1 bending mode, in the static case.

Table 6.6: Electronic and vibrational contributions to the SHS first hyperpolarizability and DR as computed at the CCSD/d-aug-cc-pVTZ level at different wavelengths.

	Total	Electronic	ZPVA			Pure vibrational				\mathcal{C}_v
			$\mathcal{C}_{[\beta]^{\text{I},0}}$	$\mathcal{C}_{[\beta]^{\text{0},1}}$	\mathcal{C}_{ZPVA}	$\mathcal{C}_{[\mu\alpha]^0}$	$\mathcal{C}_{[\mu\alpha]^{\text{II}}}$	$\mathcal{C}_{[\mu^3]^{\text{I}}}$	\mathcal{C}_{pv}	
β_{SHS}										
∞	9.49	11.04	1.9	5.8	7.6	-36.1	-5.2	15.5	-24.2	-16.3
1500 nm	13.22	11.47	1.6	4.5	6.1	8.3	-1.2	0.1	7.2	13.2
1300 nm	12.91	11.62	1.7	4.7	6.3	5.7	-2.0	0.0	3.7	10.0
1064 nm	13.19	11.93	1.7	4.7	6.4	3.4	-0.2	0.0	3.2	9.5
694.3 nm	14.51	13.37	2.0	4.8	6.8	1.2	-0.1	0.0	1.1	7.9
DR_{SHS}										
∞	7.55	7.73	-0.9	-1.5	-2.3	-7.6	1.0	17.7	0.7	-2.4
1500 nm	7.26	7.96	-1.0	-1.8	-2.8	-6.6	0.2	0.1	-6.2	-9.6
1300 nm	7.30	8.04	-1.0	-1.8	-2.8	-4.3	-2.2	0.0	-6.6	-10.0
1064 nm	7.76	8.21	-1.1	-1.9	-3.0	-2.6	0.1	0.0	-2.6	-5.8
694.3 nm	8.72	9.06	-1.0	-1.9	-2.8	-1.0	0.0	0.0	-1.0	-3.9

Table 6.7: Electronic and vibrational contributions to the THS second hyperpolarizability and DR as computed at the CCSD/d-aug-cc-pVTZ level at different wavelengths.

		ZPVA			Pure vibrational									
		$\mathcal{C}_{[\gamma]^{1,0}}$	$\mathcal{C}_{[\gamma]^{0,1}}$	\mathcal{C}_{ZPVA}	$\mathcal{C}_{[\alpha^2]^0}$	$\mathcal{C}_{[\alpha^2]^{\text{III}}}$	$\mathcal{C}_{[\mu\beta]^0}$	$\mathcal{C}_{[\mu\beta]^{\text{III}}}$	$\mathcal{C}_{[\mu^2\alpha]^{\text{I}}}$	$\mathcal{C}_{[\mu^4]^{\text{III}}}$	\mathcal{C}_{pv}	\mathcal{C}_v		
													γ_{THS}	
∞	2101	1821	1.1	2.5	3.5	7.3	1.7	-0.5	0.0	0.9	0.5	9.8	13.3	
1500 nm	2108	2033	1.3	2.8	4.1	-0.6	0.0	0.1	0.0	0.0	0.0	-0.5	3.6	
1300 nm	2195	2113	1.3	2.9	4.2	-0.4	0.0	0.1	0.0	0.0	0.0	-0.4	3.8	
1064 nm	2387	2288	1.4	3.0	4.4	-0.3	0.0	0.0	0.0	0.0	0.0	-0.2	4.2	
694.3 nm	3622	3401	2.4	3.8	6.2	-0.1	0.0	0.0	0.0	0.0	0.0	-0.1	6.1	
													DR_{THS}	
∞	166	76	4.7	1.6	6.3	42.3	13.3	-5.1	-0.9	5.9	3.0	50.7	54.3	
1500 nm	64	61	3.9	2.3	6.2	-3.9	-0.2	1.7	-0.1	0.0	0.0	-2.3	4.0	
1300 nm	60	57	3.7	2.0	5.8	-2.7	-0.2	1.1	-0.1	0.0	0.0	-1.8	4.1	
1064 nm	51	49	3.3	1.5	4.8	-1.5	-0.1	0.6	0.0	0.0	0.0	-1.1	3.8	
694.3 nm	23	24	-0.4	-1.3	-1.8	-0.3	0.0	0.1	0.0	0.0	0.0	-0.2	-2.1	

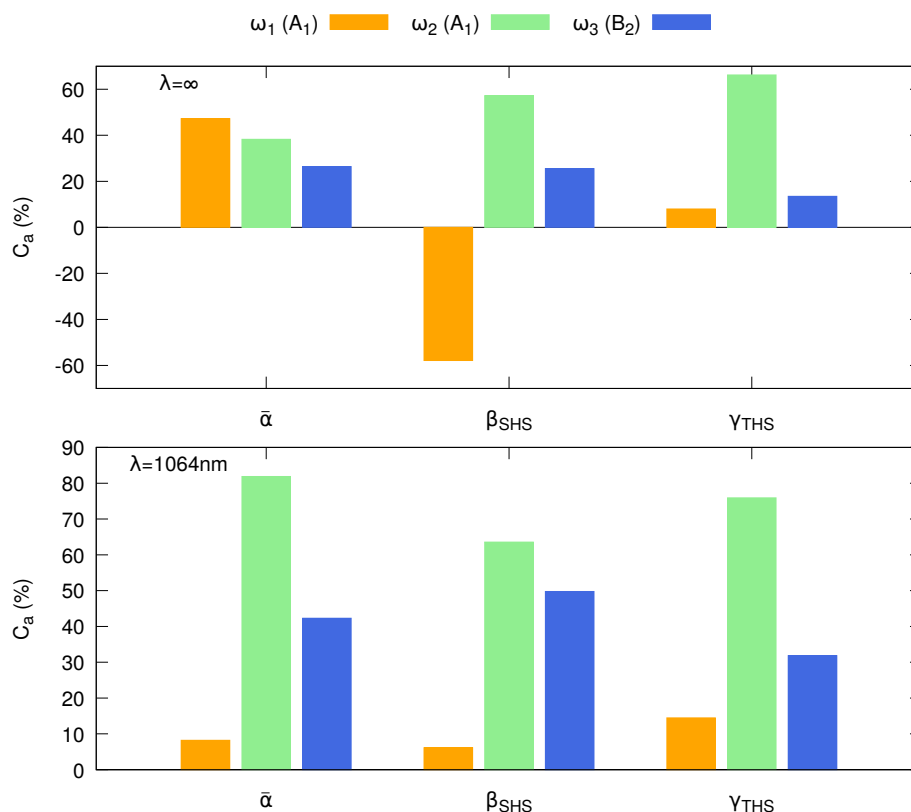


Figure 6.2: Missing mode analysis [\mathcal{C}_a , %] (ω_1 , A_1 bending; ω_2 , A_1 symmetric stretching; ω_3 , B_2 antisymmetric stretching) to the static (top) and dynamic ($\lambda = 1064 \text{ nm}$, bottom) total vibrational contributions to $\bar{\alpha}$, β_{SHS} , and γ_{THS}), as computed at the CCSD/d-aug-cc-pVTZ level.

Comparison with other theoretical investigations

Comparisons with previous works focusing on the whole responses and their contributions are given in Tables 6.8 (polarizability) and 6.9 (first and second hyperpolarizabilities). A selection of additional data are listed in Tables S6-S8 for the electronic counterpart. In the case of the vibrational responses, in order to provide a more detailed comparison between levels of approximation, in Table 6.9, the more common (static and dynamic) $\beta_{||}(-2\omega; \omega, \omega)$ quantity is considered instead of β_{SHS} while γ_{THS} is replaced by the static $\gamma_{||}$ since no dynamic third harmonic γ values were available. Note that in several cases, the listed quantities were calculated from the different tensor components reported in the corresponding original investigations.

The analysis of the electronic contributions (Tables S6-S8) reminds several known or less known effects, including (i) basis set effects are stronger for computing the hyperpolarizabilities than the polarizability, (ii) the impact of the triple excitations is rather small, as estimated by comparison with the CCSD(T) results of Maroulis⁸⁹ and the CC3 ones due to Christiansen,⁸⁰ (iii) electron correlation effects are large and increase with the order of the response, (iv) the MP2 approach provides a good agreement with higher-level calculations (though this agreement worsens at the MP3 and MP4 levels) and the QED-MP2 method of Kobayashi *et al.*^{90,91} quantitatively reproduces the frequency dispersion of the first hyperpolarizability, (v) the MR-

CI approach of Spelsberg *et al.*⁹² slightly overestimates the first hyperpolarizabilities, (vi) most reported DFT results overestimate the molecular responses and their frequency dispersion, though the use of hybrid exchange-correlation functionals (like mPW91PW91) improves the agreement and the exact exchange functional formalism of Bokhan and Bartlett⁹³ gives results close to the Hartree-Fock ones, (vii) these limitations of DFT with conventional exchange-correlation functionals are exalted in the case of the higher-order response properties,

The first reports on the ZPVA contributions to the polarizability of the water molecule⁹⁴⁻⁹⁷ have employed the HF level and the POL basis set.⁹⁸ They predict that, in the static limit, $\Delta\alpha^{ZPVA}$ amounts to a few percents of the electronic polarizability (3 %) and that it increases by less than one percent at 694.3 nm, which whom values are in good agreement with more recent correlated results, thought slightly smaller (15 %). In the case of the polarizability anisotropy, the HF values are typically 25 % larger than at the CCSD level. Moreover, the ZPVA contributions to the polarizability as estimated at the MP2 level by Cohen *et al.*⁹⁹ after including higher-order derivatives are similar to those obtained using the sum of the two first contributions, $[\alpha]^{1,0} + [\alpha]^{0,1}$. In the case of the first hyperpolarizability, the HF ZPVA values are larger than those obtained at correlated (MP2 and CCSD) levels so that their relative contribution to the total first hyperpolarizability increases by about a factor of two since, at the same time, the electronic contributions are underestimated. We note also that there is a nice consistency between the MP2 and CCSD $\Delta\alpha^{ZPVA}$ and $\Delta\beta^{ZPVA}$ values while the MP2/POL $\Delta\gamma^{ZPVA}$ values are smaller than the CCSD/d-aug-cc-pVTZ results, by about 30 %. The agreement between the vibrational CI results of Christiansen and co-workers¹⁰⁰⁻¹⁰³ and ours, for the polarizability, first and second hyperpolarizabilities, employing the same electronic structure method, is excellent.

Considering now the pure vibrational counterpart, Bishop *et al.*¹⁰⁴ already reported in 1993 its contributions to the first and second hyperpolarizabilities of the water molecule (without the $[\mu\alpha]^{0,2}$ and $[\mu^4]^{0,2}$ terms). In the static limit, they found that the HF \mathcal{C}_{pv} values attain as much as 47 % (17 %) for the first (second) hyperpolarizabilities, and that these percentages decrease to 11 % (16 %) at the MP2 level. Later,¹⁰⁵ they detailed the different contributions to the second hyperpolarizability tensor at the HF level, and pinpointed the importance of the $[\alpha^2]$ term over the other ones. Moreover, Cohen *et al.*⁹⁹ investigated the impact of the third-order derivatives of μ to the pv contributions and found it to be small. Also, the nuclear relaxation approach due to Luis *et al.*⁹⁵ predicted very similar results to those obtained with perturbation theory. Static MP2 results have later been calculated by Reis *et al.*,¹⁰⁶ showing that the pure vibrational contribution amounts to 3 % of the polarizability, 27 % of the first hyperpolarizability (note that the difference with respect to Ref. 104 can be explained by the inclusion of the $[\mu\alpha]^{0,2}$ term) and 13 % of the second hyperpolarizability (in close agreement with our results). More recently, Thorvaldsen *et al.*¹⁰⁷ studied the impact of the basis set on the HF vibrational contributions (only including the so-called double harmonic, $m=n=0$ terms) and advocated the use of d-aug-cc-pVTZ or POL. Finally, the VCI approach of Christiansen and

co-workers¹⁰² provides similar results to those of the present study in the static limit as well as for the SHS first hyperpolarizability at 694.3 nm.

Table 6.8: α^e , $\Delta\alpha^{ZPVA}$, and α^{pv} contributions to the static and dynamic (at 694.3 nm) isotropic polarizability ($\bar{\alpha}$, a.u.) and polarizability anisotropy ($\Delta\alpha$, a.u.) of the water molecule, as calculated at different levels of approximation.

Method	Basis set	Frequency	Contributions			Reference
			P^e	ΔP^{ZPVA}	P^{pv}	
$\bar{\alpha}(-\omega; \omega)$						
HF	POL	static	—	0.247	—	94
HF	POL	static	—	0.247	0.333	95
HF	POL	static	8.362	0.247	—	96
HF	POL	694.3 nm	8.461 ¹	0.266 ¹	—	96
HF	d-aug-cc-pVTZ	static	8.602	—	0.378	107
MP2	POL	static	—	0.292	—	94
MP2	POL	static	9.944	0.292	0.286	106
CCSD + VCI	d-aug-cc-pVTZ	static	9.638	0.285	0.295	100 and 101
CCSD	d-aug-cc-pVTZ	static	9.638	0.286	0.276	This work
CCSD + VCI	d-aug-cc-pVTZ	694.3 nm	9.788	0.296	-0.006	100 and 101
CCSD	d-aug-cc-pVTZ	694.3 nm	9.788	0.296	-0.006	This work
$\Delta\alpha(-\omega; \omega)$						
HF	POL	static	—	0.268	—	94
HF	POL	static	—	0.268	0.348	95
MP2	POL	static	—	0.242	—	94
MP2 ^c	POL	static	0.527	0.242	0.722	106
CCSD + VCI	d-aug-cc-pVTZ	static	0.537	0.265	0.743	100 and 101
CCSD	d-aug-cc-pVTZ	static	0.536	0.262	0.664	This work
CCSD + VCI	d-aug-cc-pVTZ	694.3 nm	0.467	0.270	0.009	100 and 101
CCSD	d-aug-cc-pVTZ	694.3 nm	0.466	0.264	0.009	This work

¹ Interpolated using the frequency dispersion.

Table 6.9: Static (and dynamic, at 694.3 nm) electronic, ZPVA, and pure vibrational contributions to $\beta_{||}(-2\omega; \omega, \omega)$ and $\gamma_{||}$ (in a.u.) of the water molecule, as calculated at different levels of approximation.

Method	Basis set	Frequency	Contributions			Reference
			P^e	ΔP^{ZPVA}	P^{pv}	
$\beta_{ }(-2\omega; \omega, \omega)$						
HF	POL	static	—	—	3.983	104
HF	POL	static	—	-1.397	4.141	95
HF	POL	static	-7.53	-1.397	—	97
HF	POL	694.3 nm	-8.97 ¹	-1.687 ¹	—	97
HF	d-aug-cc-pVTZ	static	-11.01	—	9.351	107
MP2	POL	static	—	—	1.472	104
MP2	POL	static	-13.59	-0.95	3.73	106
CCSD + VCI	d-aug-cc-pVTZ	static	-17.70	-1.039	2.645	102
CCSD	d-aug-cc-pVTZ	static	-17.70	-1.101	3.647	This work
CCSD + VCI	d-aug-cc-pVTZ	694.3 nm	-21.68	-1.438	-0.243	102
CCSD	d-aug-cc-pVTZ	694.3 nm	-21.68	-1.488	-0.237	This work
$\gamma_{ }$						
HF	POL	static	—	—	150.1	104 and 105
HF	POL	static	—	—	148.9	95
HF	d-aug-cc-pVTZ	static	999	—	144.6	107
MP2	POL	static	1400	—	235.2	53 and 104
MP2	POL	static	1447	51	187	106
CCSD + VCI	d-aug-cc-pVTZ	static	1736	75.8	171.6	103
CCSD	d-aug-cc-pVTZ	static	1745	75.6	240.4	This work

¹ Interpolated using the frequency dispersion expressions.

Section 6.5

Conclusions

Second harmonic scattering (SHS) first hyperpolarizability (β_{SHS}) and third harmonic scattering (THS) second hyperpolarizability (γ_{THS}) are all-optical nonlinear optical processes. For such processes, theoretical models predict that the pure vibrational contributions are small while the zero-point vibrational averages (ZPVA) are modest, which explains why they are neglected in most quantum chemical investigations. In addition, THS has mostly been ignored until the last three years and the publication of two experimental papers.^{6,7} This gives the incentive for investigating, by employing quantum chemistry methods, the vibrational contributions to SHS and THS of the water molecule and for comparing these to their electronic counterparts. Thus, this paper has reported on the vibrational contributions to the average polarizability ($\bar{\alpha}$), to β_{SHS} and its depolarization ratio (DR_{SHS}), as well as to γ_{THS} and its depolarization ratio (DR_{THS}) by using the Bishop and Kirtman perturbative theory approach in combination with finite differentiation techniques to evaluate the higher-order derivatives. This has been performed by employing a hierarchy of Coupled Clusters techniques and extended atomic basis sets, from which the CCSD/d-aug-cc-pVTZ level has been selected to assess the importance of the ZPVA contributions and of the pure vibrational contributions with respect to their electronic counterparts. Numerical results on the water molecules highlight that i) the vibrational contributions to the dynamic $\bar{\alpha}$, β_{SHS} , and γ_{THS} are small but still not negligible, ii) they amount to respectively 3, 10, and 4 % at the typical wavelength of 1064 nm, iii) the mechanical anharmonicity term dominates the zero-point vibrational average (ZPVA) contribution, iv) the double harmonic terms dominate the pure vibrational contributions, v) the stretching vibrations provide the largest contributions to the dynamic (hyper)polarizabilities, and vi) these conclusions are strongly impacted in the static limit where the vibrational contributions are much larger, in particular the double harmonic pure vibrational terms, and even more in the case of β_{SHS} . It was further interesting to observe that the relative vibrational contributions to the optical responses do not increase with the order of the response. Still, confirmations about their absolute and relative amplitudes deserve investigating other compounds, from small reference systems like those studied in Ref. 74 to NLO active molecules like (push-pull) π -conjugated molecules.

Acknowledgments

The calculations were performed on the computers of the Consortium des Équipements de Calcul Intensif, including those of the Technological Platform of High-Performance Comput-

ing, for which we gratefully acknowledge the financial support of the FNRS-FRFC, of the Walloon Region, and of the University of Namur (Conventions No. 2.5020.11, GEQ U.G006.15, 1610468, and RW/GEQ2016).

Bibliography

- [1] Wagnière, G. H. *Linear and Nonlinear Optical Properties of Molecules*; Verl. Helvetica Chimica Acta: Basel, 1993; OCLC: 246731393.
- [2] Bosshard, C. *Organic Nonlinear Optical Materials*; Gordon and Breach: Basel, Switzerland, 1995; OCLC: 33261662.
- [3] Papadopoulos, M. G.; Sadlej, A. J.; Leszczynski, J. In *Non-Linear Optical Properties of Matter: From Molecules to Condensed Phases*; Papadopoulos, M. G., Sadlej, A. J., Leszczynski, J., Eds.; Challenges and Advances in Computational Chemistry and Physics 1; Springer: Dordrecht, 2006; OCLC: 762167749.
- [4] Verbiest, T.; Clays, K.; Rodriguez, V. *Second-Order Nonlinear Optical Characterization Techniques: An Introduction*; Taylor & Francis, 2009.
- [5] Clays, K.; Persoons, A. Hyper-Rayleigh Scattering in Solution. *Phys. Rev. Lett.* **1991**, 66, 2980–2983.
- [6] Van Steerteghem, N.; Clays, K.; Verbiest, T.; Van Cleuvenbergen, S. Third-Harmonic Scattering for Fast and Sensitive Screening of the Second Hyperpolarizability in Solution. *Anal. Chem.* **2017**, 89, 2964–2971.
- [7] Rodriguez, V. Polarization-Resolved Third-Harmonic Scattering in Liquids. *J. Phys. Chem. C* **2017**, 121, 8510–8514.
- [8] Marder, S. R.; Cheng, L.-T.; Tiemann, B. G.; Friedli, A. C.; Blanchard-Desce, M.; Perry, J. W.; Skindhøj, J. Large First Hyperpolarizabilities in Push-Pull Polyenes by Tuning of the Bond Length Alternation and Aromaticity. *Science* **1994**, 263, 511–514.
- [9] Zyss, J.; Ledoux, I. Nonlinear Optics in Multipolar Media: Theory and Experiments. *Chem. Rev.* **1994**, 94, 77–105.
- [10] Kanis, D. R.; Ratner, M. A.; Marks, T. J. Design and Construction of Molecular Assemblies with Large Second-Order Optical Nonlinearities. Quantum Chemical Aspects. *Chem. Rev.* **1994**, 94, 195–242.
- [11] Hu, X.; Xiao, D.; Keinan, S.; Asselberghs, I.; Therien, M. J.; Clays, K.; Yang, W.; Beratan, D. N. Predicting the Frequency Dispersion of Electronic Hyperpolarizabilities on the Basis of Absorption Data and Thomas-Kuhn Sum Rules. *J. Phys. Chem. C* **2010**, 114, 2349–2359.
- [12] List, N. H.; Zaleśny, R.; Murugan, N. A.; Kongsted, J.; Bartkowiak, W.; Ågren, H. Relation between Nonlinear Optical Properties of Push–Pull Molecules and Metric of Charge Transfer Excitations. *J. Chem. Theory Comput.* **2015**, 11, 4182–4188.

- [13] Brédas, J. L.; Adant, C.; Tackx, P.; Persoons, A.; Pierce, B. M. Third-Order Nonlinear Optical Response in Organic Materials: Theoretical and Experimental Aspects. *Chem. Rev.* **1994**, *94*, 243–278.
- [14] Shelton, D. P.; Rice, J. E. Measurements and Calculations of the Hyperpolarizabilities of Atoms and Small Molecules in the Gas Phase. *Chem. Rev.* **1994**, *94*, 3–29.
- [15] Kobayashi, T.; Sasagane, K.; Aiga, F.; Yamaguchi, K. Calculation of Frequency-Dependent First Hyperpolarizabilities Using the Second-Order Møller–Plesset Perturbation Theory. *J. Chem. Phys.* **1999**, *110*, 11720–11733.
- [16] Maroulis, G. On the Bond-Length Dependence of the Static Electric Polarizability and Hyperpolarizability of F₂. *Chem. Phys. Lett.* **2007**, *442*, 265–269.
- [17] Wheatley, R. J. Time-Dependent Coupled-Cluster Calculations of Polarizabilities and Dispersion Energy Coefficients. *J. Comput. Chem.* **2008**, *29*, 445–450.
- [18] Norman, P. A Perspective on Nonresonant and Resonant Electronic Response Theory for Time-Dependent Molecular Properties. *Phys. Chem. Chem. Phys.* **2011**, *13*, 20519.
- [19] Coe, J. P.; Paterson, M. J. Approaching Exact Hyperpolarizabilities via Sum-over-States Monte Carlo Configuration Interaction. *J. Chem. Phys.* **2014**, *141*, 124118.
- [20] Bishop, D. M. Effect of the Surroundings on Atomic and Molecular Properties. *Int. Rev. Phys. Chem.* **1994**, *13*, 21–39.
- [21] Champagne, B.; Bishop, D. M. *Advances in Chemical Physics*; John Wiley & Sons, Ltd, 2003; pp 41–92.
- [22] Kongsted, J.; Osted, A.; Mikkelsen, K. V.; Christiansen, O. Second Harmonic Generation Second Hyperpolarizability of Water Calculated Using the Combined Coupled Cluster Dielectric Continuum or Different Molecular Mechanics Methods. *J. Chem. Phys.* **2004**, *120*, 3787–3798.
- [23] Seidler, T.; Stadnicka, K.; Champagne, B. Investigation of the Linear and Second-Order Nonlinear Optical Properties of Molecular Crystals within the Local Field Theory. *J. Chem. Phys.* **2013**, *139*, 114105.
- [24] Mishina, E.; Miyakita, Y.; Yu, Q.-K.; Nakabayashi, S.; Sakaguchi, H. Nonlinear Optical Properties of Oligothiophene Self-Assembled Monolayers on Gold Substrate. *J. Chem. Phys.* **2002**, *117*, 4016–4021.
- [25] Tonnelé, C.; Pielak, K.; Deviers, J.; Muccioli, L.; Champagne, B.; Castet, F. Nonlinear Optical Responses of Self-Assembled Monolayers Functionalized with Indolino–Oxazolidine Photoswitches. *Phys. Chem. Chem. Phys.* **2018**, *20*, 21590–21597.
- [26] Dalskov, E. K.; Jensen, H. J. A. A.; Oddershede, J. Does Scaling or Addition Provide the Correct Frequency Dependence of $\beta_{||}(-\omega_{\sigma}; \omega_1, \omega_2)$ at the Correlated Level? an Investigation for Six Molecules. *Mol. Phys.* **1997**, *90*, 3–14.

- [27] de Wergifosse, M.; Castet, F.; Champagne, B. Frequency Dispersion of the First Hyperpolarizabilities of Reference Molecules for Nonlinear Optics. *J. Chem. Phys.* **2015**, *142*, 194102.
- [28] Zaleśny, R.; Bulik, I. W.; Bartkowiak, W.; Luis, J. M.; Avramopoulos, A.; Papadopoulos, M. G.; Krawczyk, P. Electronic and Vibrational Contributions to First Hyperpolarizability of Donor–Acceptor-Substituted Azobenzene. *J. Chem. Phys.* **2010**, *133*, 244308.
- [29] Dutra, A. S.; Castro, M. A.; Fonseca, T. L.; Fileti, E. E.; Canuto, S. Hyperpolarizabilities of the Methanol Molecule: A CCSD Calculation Including Vibrational Corrections. *J. Chem. Phys.* **2010**, *132*, 034307.
- [30] Lacivita, V.; Rérat, M.; Kirtman, B.; Orlando, R.; Ferrabone, M.; Dovesi, R. Static and Dynamic Coupled Perturbed Hartree-Fock Vibrational (Hyper)Polarizabilities of Polyacetylene Calculated by the Finite Field Nuclear Relaxation Method. *J. Chem. Phys.* **2012**, *137*, 014103.
- [31] Bulik, I. W.; Zaleśny, R.; Bartkowiak, W.; Luis, J. M.; Kirtman, B.; Scuseria, G. E.; Avramopoulos, A.; Reis, H.; Papadopoulos, M. G. Performance of Density Functional Theory in Computing Nonresonant Vibrational (Hyper)Polarizabilities. *J. Comput. Chem.* **2013**, *34*, 1775–1784.
- [32] Gao, B.; Ringholm, M.; Bast, R.; Ruud, K.; Thorvaldsen, A. J.; Jaszuński, M. Analytic Density Functional Theory Calculations of Pure Vibrational Hyperpolarizabilities: The First Dipole Hyperpolarizability of Retinal and Related Molecules. *J. Phys. Chem. A* **2014**, *118*, 748–756.
- [33] Naves, E. S.; Castro, M. A.; Fonseca, T. L. Vibrational Corrections to Hyperpolarizabilities of the O₃, SO₂, N₂O and CO₂ Molecules: A Comparison between Variational and Perturbation Methods. *Chem. Phys. Lett.* **2014**, *608*, 130–135.
- [34] Zaleśny, R.; Baranowska-Łączkowska, A.; Medved', M.; Luis, J. M. Comparison of Property-Oriented Basis Sets for the Computation of Electronic and Nuclear Relaxation Hyperpolarizabilities. *J. Chem. Theory Comput.* **2015**, *11*, 4119–4128.
- [35] Naves, E. S.; Castro, M. A.; Fonseca, T. L. Dynamic (Hyper)Polarizabilities of the Ozone Molecule: Coupled Cluster Calculations Including Vibrational Corrections. *J. Chem. Phys.* **2011**, *134*, 054315.
- [36] Naves, E. S.; Castro, M. A.; Fonseca, T. L. Dynamic (Hyper)Polarizabilities of the Sulphur Dioxide Molecule: Coupled Cluster Calculations Including Vibrational Corrections. *J. Chem. Phys.* **2012**, *136*, 014303.
- [37] Zaleśny, R.; Garcia-Borràs, M.; Góra, R. W.; Medved', M.; Luis, J. M. On the Physical Origins of Interaction-Induced Vibrational (Hyper)Polarizabilities. *Phys. Chem. Chem. Phys.* **2016**, *18*, 22467–22477.

- [38] Marques, S.; Castro, M. A.; Leão, S. A.; Fonseca, T. L. Electronic and Vibrational Hyperpolarizabilities of Lithium Substituted (Aza)Benzenes and (Aza)Naphthalenes. *J. Phys. Chem. A* **2018**, *122*, 7402–7412.
- [39] Garcia-Borràs, M.; Solà, M.; Luis, J. M.; Kirtman, B. Electronic and Vibrational Nonlinear Optical Properties of Five Representative Electrides. *J. Chem. Theory Comput.* **2012**, *8*, 2688–2697.
- [40] Feitoza, L.; Castro, M. A.; Leão, S. A.; Fonseca, T. L. Electronic and Vibrational Second Hyperpolarizabilities of (MgO)_n Clusters. *J. Chem. Phys.* **2017**, *146*, 144309.
- [41] Casassa, S.; Baima, J.; Mahmoud, A.; Kirtman, B. Ab Initio Investigation of Electronic and Vibrational Contributions to Linear and Nonlinear Dielectric Properties of Ice. *J. Chem. Phys.* **2014**, *140*, 224702.
- [42] Kang, L. Z.; Inerbaev, T.; Kirtman, B.; Gu, F. L. Alkali Metal Doping Effect on Static First Hyperpolarizabilities of PMI Chains. *Theor. Chem. Acc.* **2011**, *130*, 727–737.
- [43] Avramopoulos, A.; Reis, H.; Otero, N.; Karamanis, P.; Pouchan, C.; Papadopoulos, M. G. A Series of Novel Derivatives with Giant Second Hyperpolarizabilities, Based on Radiaannulenes, Tetrathiafulvalene, Nickel Dithiolene, and Their Lithiated Analogues. *J. Phys. Chem. C* **2016**, *120*, 9419–9435.
- [44] Torrent-Sucarrat, M.; Navarro, S.; Marcos, E.; Anglada, J. M.; Luis, J. M. Design of Hückel–Möbius Topological Switches with High Nonlinear Optical Properties. *J. Phys. Chem. C* **2017**, *121*, 19348–19357.
- [45] Avila, G. Ab Initio Dipole Polarizability Surfaces of Water Molecule: Static and Dynamic at 514.5nm. *J. Chem. Phys.* **2005**, *122*, 144310.
- [46] Purvis, G. D.; Bartlett, R. J. Molecular Hyperpolarizabilities. II. A Correlated Study of H₂O. *Phys. Rev. A* **1981**, *23*, 1594–1599.
- [47] Bishop, D. M.; Pipin, J. Field and Field-Gradient Polarizabilities of H₂O. *Theor. Chim. Acta* **1987**, *71*, 247–253.
- [48] Gubskaya, A. V.; Kusalik, P. G. The Multipole Polarizabilities and Hyperpolarizabilities of the Water Molecule in Liquid State: An Ab Initio Study. *Mol. Phys.* **2001**, *99*, 1107–1120.
- [49] Bishop, D. M.; Lam, B. Ab Initio Study of Third-Order Nonlinear Optical Properties of Helium. *Phys. Rev. A* **1988**, *37*, 464–469.
- [50] Stähelin, M.; Moylan, C. R.; Burland, D. M.; Willetts, A.; Rice, J. E.; Shelton, D. P.; Donley, E. A. A Comparison of Calculated and Experimental Hyperpolarizabilities for Acetonitrile in Gas and Liquid Phases. *J. Chem. Phys.* **1993**, *98*, 5595–5603.
- [51] Pecul, M.; Pawłowski, F.; Jørgensen, P.; Köhn, A.; Hättig, C. High-Order Correlation Effects on Dynamic Hyperpolarizabilities and Their Geometric Derivatives: A Comparison with Density Functional Results. *J. Chem. Phys.* **2006**, *124*, 114101.

- [52] Beaujean, P.; Champagne, B. Coupled Cluster Evaluation of the Frequency Dispersion of the First and Second Hyperpolarizabilities of Water, Methanol, and Dimethyl Ether. *J. Chem. Phys.* **2016**, *145*, 044311.
- [53] Sekino, H.; Bartlett, R. J. Molecular Hyperpolarizabilities. *J. Chem. Phys.* **1993**, *98*, 3022–3037.
- [54] Rizzo, A.; Coriani, S.; Fernández, B.; Christiansen, O. A Coupled Cluster Response Study of the Electric Dipole Polarizability, First and Second Hyperpolarizabilities of HCl. *Phys. Chem. Chem. Phys.* **2002**, *4*, 2884–2890.
- [55] Bishop, D. M. Molecular Vibrational and Rotational Motion in Static and Dynamic Electric Fields. *Rev. Mod. Phys.* **1990**, *62*, 343–374.
- [56] Bishop, D. M.; Kirtman, B. A Perturbation Method for Calculating Vibrational Dynamic Dipole Polarizabilities and Hyperpolarizabilities. *J. Chem. Phys.* **1991**, *95*, 2646–2658.
- [57] Bishop, D. M.; Kirtman, B. Compact Formulas for Vibrational Dynamic Dipole Polarizabilities and Hyperpolarizabilities. *J. Chem. Phys.* **1992**, *97*, 5255–5256.
- [58] Bishop, D. M.; Luis, J. M.; Kirtman, B. Additional Compact Formulas for Vibrational Dynamic Dipole Polarizabilities and Hyperpolarizabilities. *J. Chem. Phys.* **1998**, *108*, 10013–10017.
- [59] Norman, P.; Luo, Y.; Ågren, H. Vibrational Corrections to Static and Dynamic Hyperpolarizabilities of Pure Liquids: Calculations on Methanol. *J. Chem. Phys.* **1998**, *109*, 3580–3588.
- [60] Quinet, O.; Champagne, B. Vibrational Second Hyperpolarizability of CH₄-nFn Molecules with N=0–4. *J. Chem. Phys.* **1998**, *109*, 10594–10602.
- [61] Quinet, Q.; Champagne, B. *New Trends in Quantum Systems in Chemistry and Physics*; Kluwer Academic Publishers: Dordrecht, 2002; Vol. 6; pp 375–392.
- [62] Torrent-Sucarrat, M.; Luis, J. M.; Duran, M.; Solà, M. The Hardness Profile as a Tool to Detect Spurious Stationary Points in the Potential Energy Surface. *J. Chem. Phys.* **2004**, *120*, 10914–10924.
- [63] Torrent-Sucarrat, M.; Luis, J. M.; Kirtman, B. Variational Calculation of Vibrational Linear and Nonlinear Optical Properties. *J. Chem. Phys.* **2005**, *122*, 204108.
- [64] Loboda, O.; Zaleśny, R.; Avramopoulos, A.; Luis, J.-M.; Kirtman, B.; Tagmatarchis, N.; Reis, H.; Papadopoulos, M. G. Linear and Nonlinear Optical Properties of [60]Fullerene Derivatives. *J. Phys. Chem. A* **2009**, *113*, 1159–1170.
- [65] Skwara, B.; Góra, R. W.; Zaleśny, R.; Lipkowski, P.; Bartkowiak, W.; Reis, H.; Papadopoulos, M. G.; Luis, J. M.; Kirtman, B. Electronic Structure, Bonding, Spectra, and Linear and Nonlinear Electric Properties of Ti@C₂₈. *J. Phys. Chem. A* **2011**, *115*, 10370–10381.

- [66] Avramopoulos, A.; Reis, H.; Luis, J. M.; Papadopoulos, M. G. On the Vibrational Linear and Nonlinear Optical Properties of Compounds Involving Noble Gas Atoms: HXeOXeH, HXeOXeF, and FXeOXeF. *J. Comput. Chem.* **2013**, *34*, 1446–1455.
- [67] Bishop, D. M.; Gu, F. L.; Cybulski, S. M. Static and Dynamic Polarizabilities and First Hyperpolarizabilities for CH₄, CF₄, and CCl₄. *J. Chem. Phys.* **1998**, *109*, 8407–8415.
- [68] Luis, J. M.; Reis, H.; Papadopoulos, M.; Kirtman, B. Treatment of Nonlinear Optical Properties Due to Large Amplitude Anharmonic Vibrational Motions: Umbrella Motion in NH₃. *J. Chem. Phys.* **2009**, *131*, 034116.
- [69] Orr, B.; Ward, J. Perturbation Theory of the Non-Linear Optical Polarization of an Isolated System. *Mol. Phys.* **1971**, *20*, 513–526.
- [70] Kirtman, B.; Luis, J. M. On the contribution of mixed terms in response function treatment of vibrational nonlinear optical properties. *Int. J. Quantum Chem.* **2011**, *111*, 839–847.
- [71] Bersohn, R.; Pao, Y.-H.; Frisch, H. L. Double-Quantum Light Scattering by Molecules. *J. Chem. Phys.* **1966**, *45*, 3184–3198.
- [72] Andrews, D. L.; Allcock, P. *Optical Harmonics in Molecular Systems*; Wiley-VCH: Weinheim, 2002; OCLC: ocm48468465.
- [73] Ford, J. S.; Andrews, D. L. Molecular Tensor Analysis of Third-Harmonic Scattering in Liquids. *J. Phys. Chem. A* **2018**, *122*, 563–573.
- [74] Beaujean, P.; Champagne, B. Coupled Cluster Evaluation of the Second and Third Harmonic Scattering Responses of Small Molecules. *Theor. Chem. Acc.* **2018**, *137*, 50.
- [75] Christiansen, O.; Koch, H.; Jørgensen, P. The Second-Order Approximate Coupled Cluster Singles and Doubles Model CC2. *Chem. Phys. Lett.* **1995**, *243*, 409–418.
- [76] Purvis, G. D.; Bartlett, R. J. A Full Coupled-cluster Singles and Doubles Model: The Inclusion of Disconnected Triples. *J. Chem. Phys.* **1982**, *76*, 1910–1918.
- [77] Dunning, T. H. Gaussian Basis Sets for Use in Correlated Molecular Calculations. I. The Atoms Boron through Neon and Hydrogen. *J. Chem. Phys.* **1989**, *90*, 1007–1023.
- [78] Hald, K.; Halkier, A.; Jørgensen, P.; Coriani, S. Orbital Nonrelaxed Coupled Cluster Singles and Doubles with Perturbative Triples Corrections Calculations of First-Order One-Electron Properties. *J. Chem. Phys.* **2002**, *117*, 9983–9990.
- [79] Hättig, C.; Christiansen, O.; Koch, H.; Jørgensen, P. Frequency-Dependent First Hyperpolarizabilities Using Coupled Cluster Quadratic Response Theory. *Chem. Phys. Lett.* **1997**, *269*, 428–434.
- [80] Christiansen, O.; Gauss, J.; Stanton, J. F. Frequency-Dependent Polarizabilities and First Hyperpolarizabilities of CO and H₂O from Coupled Cluster Calculations. *Chem. Phys.*

Lett. **1999**, 305, 147–155.

- [81] Hättig, C. Dispersion formulas for the second hyperpolarizability components $\gamma_{||}$, γ and γ_K . *Chem. Phys. Lett.* **1998**, 296, 245–252.
- [82] Hättig, C.; Jørgensen, P. Dispersion coefficients for second hyperpolarizabilities using coupled cluster cubic response theory. *Adv. Quantum Chem.* **1999**, 35, 111–148.
- [83] Richardson, L. F.; Gaunt, J. A. The Deferred Approach to the Limit. Part I. Single Lattice. Part II. Interpenetrating Lattices. *Philos. Trans. R. Soc. Lond. A* **1927**, 226, 299–361.
- [84] Bloor, J. E. Finite Field Ab Initio Calculations of the Dipole Polarizabilities and First and Second Hyperpolarizabilities Using Multiple Sets of Polarization Funct. *Comput. Theor. Chem.* **1991**, 234, 173–183.
- [85] Mohammed, A. A. K.; Limacher, P. A.; Champagne, B. Finding Optimal Finite Field Strengths Allowing for a Maximum of Precision in the Calculation of Polarizabilities and Hyperpolarizabilities. *J. Comput. Chem.* **2013**, 34, 1497–1507.
- [86] de Wergifosse, M.; Liégeois, V.; Champagne, B. Evaluation of the Molecular Static and Dynamic First Hyperpolarizabilities. *Int. J. Quantum Chem.* **2014**, 114, 900–910.
- [87] Wieser, M. E. Atomic Weights of the Elements 2005 (IUPAC Technical Report). *Pure Appl. Chem.* **2006**, 78, 2051–2066.
- [88] Aidas, K. et al. The Dalton quantum chemistry program system. *Wiley Interdiscip. Rev. Comput. Mol. Sci.* **2014**, 4, 269–284.
- [89] Maroulis, G. Hyperpolarizability of H₂O Revisited: Accurate Estimate of the Basis Set Limit and the Size of Electron Correlation Effects. *Chem. Phys. Lett.* **1998**, 289, 403–411.
- [90] Kobayashi, T.; Sasagane, K.; Aiga, F.; Yamaguchi, K. Calculation of Frequency-Dependent First Hyperpolarizabilities Using the Second-Order Møller–Plesset Perturbation Theory. *J. Chem. Phys.* **1999**, 110, 11720–11733.
- [91] Kobayashi, T.; Sasagane, K.; Aiga, F.; Yamaguchi, K. Calculation of Frequency-Dependent Second Hyperpolarizabilities for Electric Field Induced Second Harmonic Generation in the Second-Order Møller–Plesset Perturbation Theory. *J. Chem. Phys.* **1999**, 111, 842–848.
- [92] Spelsberg, D.; Meyer, W. Ab Initio Dynamic Multipole Polarizabilities and Hyperpolarizabilities of H₂O and the Long-Range Interaction Coefficients for Its Dimer. *J. Chem. Phys.* **1998**, 108, 1532–1543.
- [93] Bokhan, D.; Bartlett, R. J. Exact-Exchange Density Functional Theory for Hyperpolarizabilities. *J. Chem. Phys.* **2007**, 127, 174102.
- [94] Russell, A. J.; Spackman, M. A. Vibrational Averaging of Electrical Properties. *Mol. Phys.* **1995**, 84, 1239–1255.

- [95] Luis, J. M.; Duran, M.; Andrés, J. L.; Champagne, B.; Kirtman, B. Finite Field Treatment of Vibrational Polarizabilities and Hyperpolarizabilities: On the Role of the Eckart Conditions, Their Implementation, and Their Use in Characterizing Key Vibrations. *J. Chem. Phys.* **1999**, *111*, 875–884.
- [96] Quinet, O.; Champagne, B.; Kirtman, B. Analytical TDHF Second Derivatives of Dynamic Electronic Polarizability with Respect to Nuclear Coordinates. Application to the Dynamic ZPVA Correction. *J. Comput. Chem.* **2001**, *22*, 1920–1932.
- [97] Quinet, O.; Kirtman, B.; Champagne, B. Analytical Time-Dependent Hartree-Fock Evaluation of the Dynamic Zero-Point Vibrationally Averaged (ZPVA) First Hyperpolarizability. *J. Chem. Phys.* **2003**, *118*, 505–513.
- [98] Sadlej, A. J. Medium-Size Polarized Basis Sets for High-Level Correlated Calculations of Molecular Electric Properties. *Collect. Czechoslov. Chem. Commun.* **1988**, *53*, 1995–2016.
- [99] Cohen, M. J.; Willetts, A.; Amos, R. D.; Handy, N. C. Vibrational Contributions to Static Polarizabilities and Hyperpolarizabilities. *J. Chem. Phys.* **1994**, *100*, 4467–4476.
- [100] Kongsted, J.; Christiansen, O. Automatic Generation of Force Fields and Property Surfaces for Use in Variational Vibrational Calculations of Anharmonic Vibrational Energies and Zero-Point Vibrational Averaged Properties. *J. Chem. Phys.* **2006**, *125*, 124108.
- [101] Christiansen, O.; Kongsted, J.; Paterson, M. J.; Luis, J. M. Linear Response Functions for a Vibrational Configuration Interaction State. *J. Chem. Phys.* **2006**, *125*, 214309.
- [102] Hansen, M. B.; Christiansen, O.; Hättig, C. Automated Calculation of Anharmonic Vibrational Contributions to First Hyperpolarizabilities: Quadratic Response Functions from Vibrational Configuration Interaction Wave Functions. *J. Chem. Phys.* **2009**, *131*, 154101.
- [103] Hansen, M. B.; Christiansen, O. Vibrational Contributions to Cubic Response Functions from Vibrational Configuration Interaction Response Theory. *J. Chem. Phys.* **2011**, *135*, 154107.
- [104] Bishop, D. M.; Kirtman, B.; Kurtz, H. A.; Rice, J. E. Calculation of Vibrational Dynamic Hyperpolarizabilities for H₂O, CO₂, and NH₃. *J. Chem. Phys.* **1993**, *98*, 8024–8030.
- [105] Bishop, D. M.; Dalskov, E. K. Analysis of the Vibrational, Static and Dynamic, Second Hyperpolarizability of Five Small Molecules. *J. Chem. Phys.* **1996**, *104*, 1004–1011.
- [106] Reis, H.; Raptis, S.; Papadopoulos, M. Electrostatic Calculation of Linear and Non-Linear Optical Properties of Ice Ih, II, IX and VIII. *Chem. Phys.* **2001**, *263*, 301–316.
- [107] Thorvaldsen, A. J.; Ruud, K.; Jaszuński, M. Analytic Calculations of Vibrational Hyperpolarizabilities in the Atomic Orbital Basis. *J. Phys. Chem. A* **2008**, *112*, 11942–11950.

Part III

Study of complex NLO molecules

Unraveling the Symmetry Effects on the Second-Order Nonlinear Optical Responses of Molecular Switches: the Case of Ruthenium Complexes

Abstract

Owing to their odd order, second-order nonlinear optical (NLO) responses are very sensitive to the symmetry. So, within hyper-Rayleigh scattering (HRS) technique, the symmetry modifies the amplitude of the molecular responses, the HRS first hyperpolarizability (β_{HRS}), but also the value of the depolarization ratio (DR). Starting from a challenging octupolar structure bearing 6 ruthenium(II) ammine centers π -conjugated via quaterpyridyl moieties to a tris-chelated zinc(II) core, together with its Λ -shape and one-dimensional analogs built by replacing one or two Ru-quaterpyridyl by bipyridine moieties, (time-dependent) density functional theory calculations have been enacted to unravel the symmetry-NLO response relationships as well as their Ru^{II/III} redox-triggered switching effects. The one-dimensional and Λ -shape NLOphores present β_{HRS} values about three times larger than the octupolar system, for both Ru oxidation states. However, using the few-state valence bond-charge transfer models demonstrates that the β_{HRS} response of the octupolar compound can become larger than those of its analogs provided stronger donor-acceptor groups are employed. In parallel, the DRs decrease from a strong dipolar character (DR \approx 6) for the one-dimensional chromophore to a weaker dipolar character (DR \approx 5) for the Λ -shape one, and to a clear octupolar character (DR \approx 1.7) for the last one. In all cases, the β responses originate mostly from the metal-to-ligand charge transfer excited states, as revealed using a new scheme for describing the variations of electron density upon excitation. The Ru^{II/III} oxidations lead to a strong decrease of the β_{HRS} responses, which is attributed to the loss of the donor character of the Ru centers and therefore to the reduction of the push-pull π -conjugation. These results demonstrate that the NLO contrast and the NLO switching behavior of these Ru compounds are maintained for the

different molecular symmetries. Finally, the character of the β responses of the oxidized species, as revealed by the DR values, further evidences a clear evolution from dipolar to octupolar NLOphores.

► Supporting information are available in Appendix A, page 319.

Section 7.1

Introduction

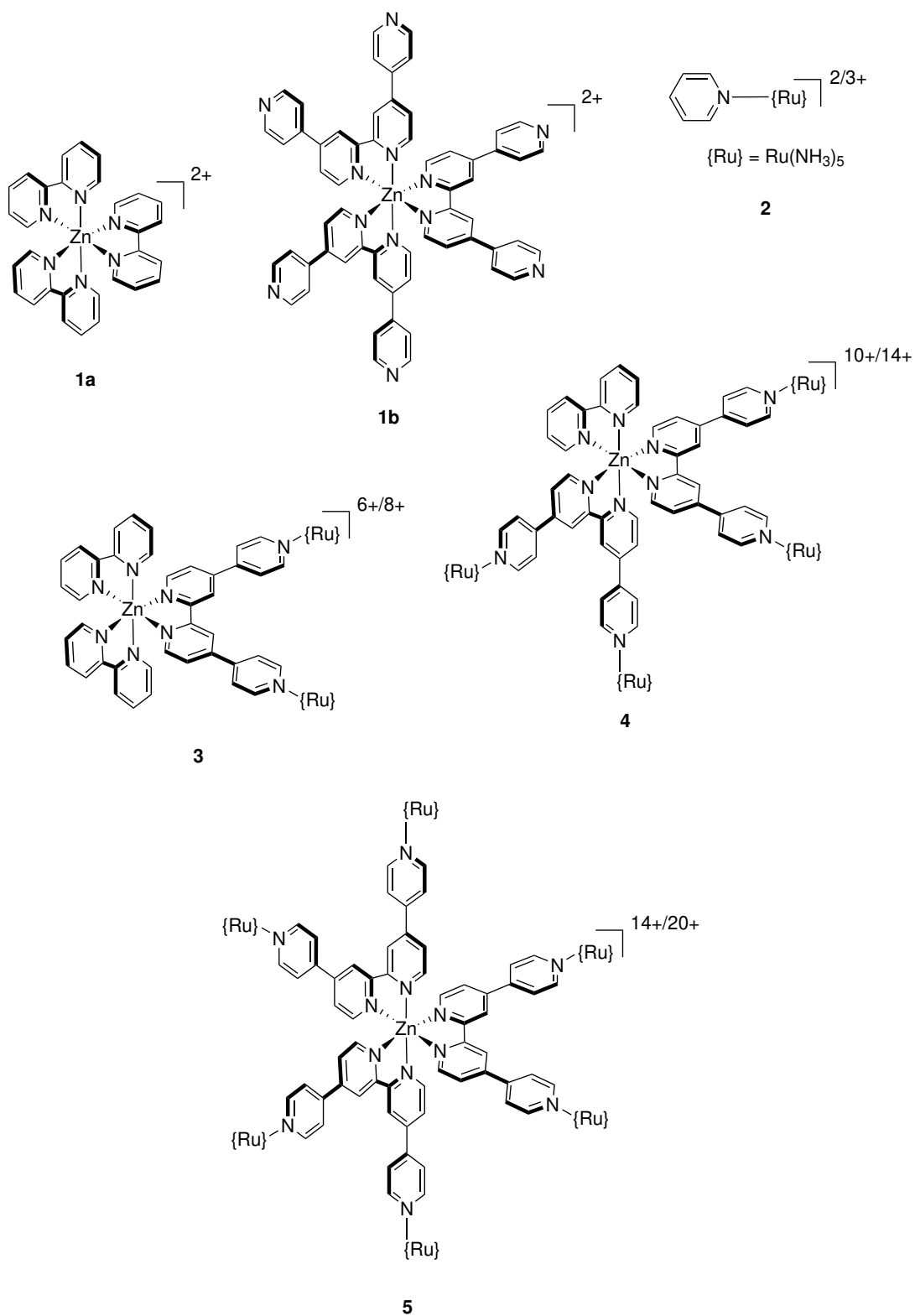
For many years, the field of nonlinear optical (NLO) switches has drawn attention for their applications in optoelectronics and photonics.^{1–5} The trigger can actually take different forms: light irradiation, pH or redox potential modifications, recognition of specific analytes, etc. At the molecular level, the central property of these switches is generally the first hyperpolarizability, β . The β characteristics can be probed experimentally by using phenomena and techniques such as hyper-Rayleigh Scattering^{6–8} (HRS), Stark spectroscopy,⁹ and electric-field induced second harmonic generation (EFISHG).^{10,11} In parallel, theoretical tools have been developed to rationalize the results as well as to design new, improved, structures.^{11–14}

In the past, many one-dimensional dipolar NLO switches have been studied. To a good approximation, their β response is dictated by one low-excitation energy charge transfer (CT) excited state.^{15–20} Among them, Ruthenium complexes, which constitute the broadest family of organometallic NLO compounds, were extensively scrutinized by Coe and co-workers,²¹ first from experimental^{22–31} point of view, owing to the large first hyperpolarizabilities of the Ru^{II} species. These studies have also fostered quantum chemistry investigations^{32–39} targeting the interpretation of the NLO response of these Ru-containing compounds, contributing therefore to their design, or aiming at the assessment of their performance (*e.g.*, choice of atomic basis sets, role of electron correlation, description of frequency dispersion). These large β values have been ascribed to a strong metal-to-ligand charge transfer (MLCT) excited state, which can be altered reversibly through a Ru^{II/III} redox switching. Besides one-dimensional dipolar structures, already 30 years ago, Zyss has drawn attention on alternative architectures,⁴⁰ such as the octupolar compounds, which can also exhibit large β values, similar to those of their dipolar counterparts. These results were rationalized using theoretical means, *e.g.*, a simple 4-state model.⁴¹ Here, challenged by Benjamin Coe^a, we study a rather complex example of such octupolar transition metal NLO switches: compound **5** (Scheme 7.1), which contains 6 switchable Ruthenium centers arranged in a D₃ fashion. The primary goal is to study, by using well-selected quantum chemistry methods, its first hyperpolarizability, at the light of its geometrical and electronic structures as well as of its UV/VIS absorption properties. In order to get such an insight on the structure-property relationships, different substructures of **5** (compounds **1–4**) are also characterized and, when available, the quantum chemistry results are compared to experimental data. Note that, we restrict ourselves to the fully reduced (all Ru atoms are in the oxidation state II, noted \mathbf{x}^{II}) or fully oxidized (\mathbf{x}^{III}) cases. A secondary goal is to unravel the relationships between the first hyperpolarizability and the molecular symmetry since, starting from compound **5**, the removal of the Ru units on one arm leads to the Λ -shape compound **4**, while the removal of a pair of such units restores a

^aCoe, B. Private communication.

one-dimensional structure (compound **3**). From these analyses, design strategies to enhance the β contrast are then suggested.

This paper is divided in four parts: after describing the methodological and computational issues in Section 7.2, the results (geometrical structures, then first hyperpolarizabilities, and their analysis *via* the few-state approximations) are presented and discussed in Section 7.3. Finally, Section 7.4 summarizes the key results and draws conclusions.



Scheme 7.1: Compound 5 and its substructures (1-4). For the structures with Ru atoms, the first (second) charge corresponds to the fully reduced (oxidized) form.

Section 7.2

Methodological and Computational Elements

HRS responses

The focus of this paper is the first hyperpolarizabilities as it can be measured using the HRS technique.^{6–8} The following setup is considered: within the laboratory frame, the incident light propagates along the Y axis, and the Z -polarized scattered light is collected in the X direction. According to the parallel (Z -polarized) or perpendicular (X -polarized) polarization of the incident light, the intensity is proportional to the orientational averages $\langle\beta_{ZZZ}^2\rangle$ and $\langle\beta_{ZXX}^2\rangle$, respectively. Also, for a non-polarized incident light, the square of the molecular β_{HRS} is defined to be the sum of those two quantities:

$$\beta_{HRS} = \sqrt{\langle\beta_{ZZZ}^2\rangle + \langle\beta_{ZXX}^2\rangle}, \quad (7.1)$$

while the depolarization ratio,

$$DR = \frac{\langle\beta_{ZZZ}^2\rangle}{\langle\beta_{ZXX}^2\rangle}, \quad (7.2)$$

is indicative of the geometry and the symmetry of the NLOphore: in the static limit, $DR = 1.5$ for perfect octupolar compounds while $DR=9$ for purely dipolar geometries.^{42–44} All reported β values are given in a.u. [1 a.u. of $\beta = 3.6212 \times 10^{-42} \text{ m}^4 \text{ V}^{-1} = 3.2064 \times 10^{-53} \text{ C}^3 \text{ m}^3 \text{ J}^{-2} = 8.639 \times 10^{-33} \text{ esu}$] within the T convention.¹¹

DFT Molecular geometries

Full geometry optimizations were performed for each compound using the Gaussian 16 A03 package.⁴⁵ In order to select a reliable level of approximation for the geometry optimization, different combinations of DFT exchange-correlation functionals (XCFs) and basis sets were employed and the results compared to available XRD structures for compound **2** in its reduced and oxidized forms. These structures are referenced in the Cambridge Structural Database⁴⁶ as NEFXUR for **2**^{II} (reduced form, singlet) and NEFYAY **2**^{III} (oxidized form, doublet).⁴⁷ Emphasis was put on the reproduction of the modification of bond lengths (mostly those involving the Ru atom) induced by the redox switching. Tables A.1-A.2 demonstrate that a triple- ζ basis set is mandatory for the first and second-row atoms as well as for Ru. This led to selecting the B3P86⁴⁸/6-311G(d)/LANL2TZ^{49,50} [and 6-31G(d) for Zn] and to use it to optimize the structure of **1** as well as of both the fully reduced and oxidized forms of **3-5**. Vibrational frequency calculations were also carried out on the optimized structures at the same level of approximation to check for the absence of imaginary frequencies and confirm that structures are minima on the potential energy surface.

TDDFT first hyperpolarizabilities

The level of approximation was also selected for calculating the NLO properties of those compounds. These calculations were enacted using the coupled-perturbed Kohn-Sham (CPKS) scheme^{51,52} for the static values and the time-dependent DFT scheme⁵³ for the dynamic ones. The XCF/basis set combination was selected such as to approach, at the CPKS level, reference values obtained at the MP2/cc-pVTZ/LANL2TZ(f)⁵⁴ level for both oxidation states of **2**. Note that the MP2 values are evaluated using the finite-field method, corresponding to a numerical differentiation^{55–58} of the field-dependent energy whereas the CPKS and TDDFT values were obtained using a self-consistent analytical derivative scheme. As shown in Table A.3, all tested XCFs overestimate the β_{HRS} of the oxidized form. The LC-BLYP⁵⁹/6-311G(d)/LANL2TZ [with 6-31G(d) for Zn] level was chosen because it provides a correct description of the β value of **2^{II}**, though it underestimates the **2^{II}** / **2^{III}** ratio. All CPKS/TDDFT calculations were performed in the static limit as well as at typical wavelengths (1907 and 1064 nm). They were performed using Gaussian 16. The molecules are modeled in acetonitrile solution ($\epsilon_0 = 35.688$, $\epsilon_\infty = 1.806874$), and these surroundings effects are simulated within the IEF-PCM implicit solvent formalism.^{60–62}

TDDFT excitation energies and electron density reorganization

To rationalize the first hyperpolarizabilities, the first 100 excited states were computed using Gaussian 16 at the same level of approximation as the first hyperpolarizabilities. Note that the LC-BLYP is known to overestimate the transition energies of Ru derivatives with respect to experiment,^{36,37} but the trends are correct while this choice allows a consistent treatment of both linear and nonlinear optical responses. Note that those compounds present inherent difficulties for quantum chemistry treatments: first of all, the presence of Ru atoms can imply low-energy state partially described by doubly-excited configuration state functions, which would require a multireference treatment, while the large size of **5** currently prevents this kind of approach. Nevertheless, on this topic, Escudero et al.³⁹ compared standard TDDFT to DFT/MRCI and ADC(2) and concluded that DFT was suitable to recover correct trends. For the dominant (large oscillator strength) excited states, the electron densities evaluated ensuring a non-equilibrium solvation model were used to determine the difference between the ground (GS) and excited state (ES) densities:

$$\delta\rho(\mathbf{r}) = \rho^{ES}(\mathbf{r}) - \rho^{GS}(\mathbf{r}) = \rho^+(\mathbf{r}) - \rho^-(\mathbf{r}) \quad (7.3)$$

where, following Jacquemin et al.,⁶³ one has partitioned the excitation-induced electron density difference into its positive

$$\rho^+(\mathbf{r}) = \begin{cases} \delta\rho(\mathbf{r}) & \text{if } \delta\rho(\mathbf{r}) > 0 \\ 0 & \text{otherwise,} \end{cases} \quad (7.4)$$

and negative [$\rho^-(\mathbf{r}) = \delta\rho(\mathbf{r})$ if $\delta\rho(\mathbf{r}) < 0$] parts, so that the amount of charge transfer is estimated as

$$q_{CT} = \int d\mathbf{r} \rho^+(\mathbf{r}) = - \int d\mathbf{r} \rho^-(\mathbf{r}), \quad (7.5)$$

while the charge transfer distance is given by

$$d_{CT} = |\langle \mathbf{r} \rangle^- - \langle \mathbf{r} \rangle^+|, \text{ with } \langle \mathbf{r} \rangle^\pm = \pm \frac{1}{q_{CT}} \int d\mathbf{r} \mathbf{r} \rho^\pm(\mathbf{r}). \quad (7.6)$$

Owing to the shape of the compounds, it was advantageous to use an alternative approach and to represent the radial distribution of this excitation-induced electron difference around a given center (generally the origin of the axes if properly defined according to group theory). The corresponding positive/negative radial electron distributions $\rho_r^\pm(r)$ are then defined, within spherical coordinates, as

$$\rho_r^\pm(r) = \frac{d\rho^\pm(\mathbf{r})}{dr} = \int_0^{2\pi} d\phi \int_0^\pi d\theta \rho^\pm(r, \theta, \phi) r^2 \sin \theta. \quad (7.7)$$

Similarly to q_{CT} , the amount of radial charge transfer reads

$$q_{r,CT} = \pm \int dr \rho_r^\pm(r), \quad (7.8)$$

while, in parallel to d_{CT} , a charge transfer radius, r_{CT} , reads:

$$r_{CT} = \langle r \rangle^+ - \langle r \rangle^-, \text{ with } \langle r \rangle^\pm = \pm \frac{1}{q_{r,CT}} \int dr r \rho_r^\pm(r), \quad (7.9)$$

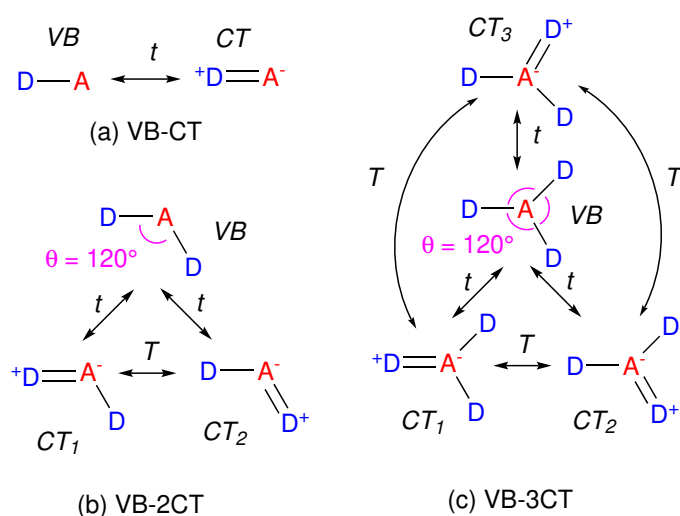
which represents the radial charge transfer distance. Analysis of the $\rho_r^\pm(r)$ graphs also helps to determine how each (group of) atom contributes to the change of electron density: $\rho_r(r) = \rho_r^+(r) - \rho_r^-(r)$ is therefore representative of the electronic reorganization along the transition. Note that the sign of r_{CT} now indicates, upon excitation, whether the electron density moves from the center to the periphery of the structure ($r_{CT} > 0$), or the opposite.

The cubegen utility (with the default options) of Gaussian 16 was used to extract the densities. To gather the charge transfer properties, the numerical integration of Eqs. (7.7)-(7.9) were performed with a homemade code, by linear interpolation of the density with $\Delta r = 0.05 \text{ \AA}$, $\Delta\theta = \Delta\phi = \frac{\pi}{20}$.

Valence Bond-Charge Transfer Models

Owing to the shape diversity when going from compound **5** to its fragments, successive valence-bond n charge transfer (VB- n CT) states models were applied. They are adequate to provide qualitative insights when discussing structures with multiple donor moieties, like compounds **3-5**. Those molecules are described by one covalent (VB) and n charge-transfer

states: $n=1$ for compound **3**, 2 for compound **4**, and 3 for compound **5** (Scheme 7.2).^{41,64} These models employ effective Hamiltonians to predict the eigenstates (ground and excited states) and their eigenvalues, and therefore the excitation energies, transition dipoles and state dipoles so that the first hyperpolarizability can be modeled as a function of the 3 + 1 parameters: the transfer integrals (t for VB-CT, T for CT-CT), and the mixing coefficient (m_{CT}) between the VB and CT states, which is clamped between -1 and 1 and describes the amount of CT character of each (ground or excited) state, as introduced by Barzoukas, Blanchard-Desce, and co-workers.^{16,20,65} For the ground state, a m_{CT} value close to -1 (to 1) means that it is dominated by the VB (CT) state. $m_{CT} = 0$ is the case of an equal mixing of the CT and VB states, the so-called cyanine limit.



Scheme 7.2: Representation of the successive VB- n CT models (adapted from Cho et al.,⁶⁶ with the charge transfer integrals t and T).

Those VB- n CT models were combined with the sum-over-states expression of Orr and Ward,⁶⁷ to determine the different components of the β tensor as a function of the shape of the compound. To do so, a last parameter is required: the charge-transfer dipole moment, μ_{CT} , which by definition is proportional to the product between the charge of the donor and acceptor (q_{CT}) and the distance (d_{CT}).

Spin multiplicity issues

The oxidized forms are spin multiplets so that the exact $\langle S^2 \rangle$ expectation values should be equal to 0.75 (**2**^{III}, doublet), 2 (**3**^{III}, triplet), 6 (**4**^{III}, quintuplet) and 12 (**5**^{III}, sextuplet). TDDFT excited states are known to exhibit spin contamination when starting from open-shell ground state.⁶⁸ For these multiplets, following Casida and co-workers,^{68,69} the $\Delta \langle \hat{S}^2 \rangle = \langle \hat{S}^2 \rangle_e - \langle \hat{S}^2 \rangle_g$ value was also reported for each relevant excited state e , to estimate the spin contamination of the corresponding excited state. Moreover, spin contaminations were monitored for both the ground and excited states. Note that the spin densities reveal that the excess of electrons are located only on the Ru atoms.

Section 7.3

Results and discussions

Geometrical parameters

To begin, the impact of oxidation on the geometrical parameters are discussed in two steps: first, the impact on the “core” part of the molecules (around the central Zn atom, Figure 7.1a) then on the “Ruthenium” part (Figure 7.1b). The different quantities are reported in Table 7.1, in which they are averaged over the different moieties (e.g., the 6 Ru centers). A standard deviation is also reported.

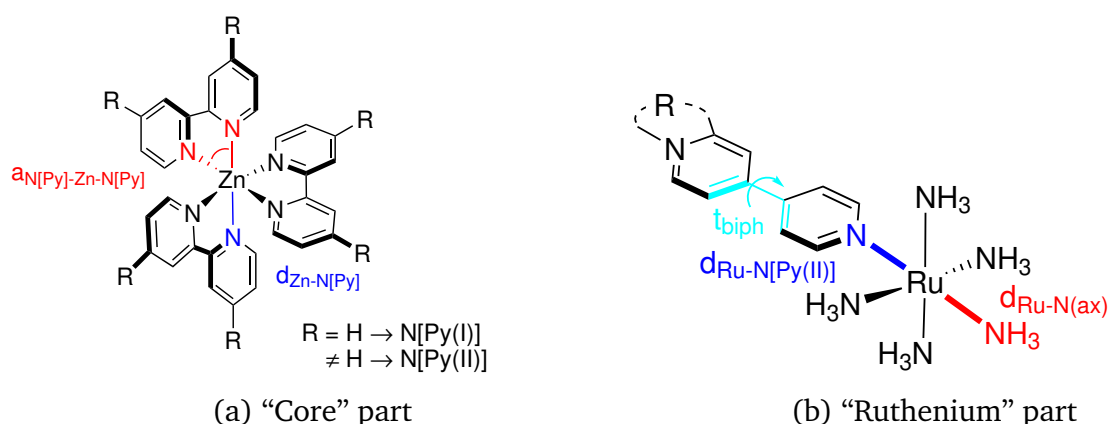


Figure 7.1: Definition of the geometrical parameters. A distinction is made between the bipyridine bearing Ru-donating moieties [Py(II)] and the ones without [Py(I)]. “biph” stands for *biphenyl*.

On the one hand, for the “core” part, the presence of Ru-donating moieties (**1a**→**3**, **4**, **5**) and of oxidation ($x^{II} \rightarrow x^{III}$) both lead to slight decrease of the N[Py(II)]-Zn-N[Py(II)] angles and an increase of the Zn-N[Py(II)] bond lengths. Overall, this part of the molecules remains mostly unaffected because the oxidation effects are localized on the Ru moiety. On the other hand, for the “Ruthenium” moieties, the modifications are one order of magnitude larger. Again, both the presence of the Ru-containing ligands and the oxidation impact the geometry in the same way, though the later is more important: the Ru-N[Py(II)] bond (dark-blue in Figure 7.1b) lengths increase, while the Ru-N(ax) bond (red in Figure 7.1b) lengths decrease. Both effects are consistent with the weakening, upon oxidation, of the *back bonding* between the Ru atoms and the pyridyl ligands. An additional clue comes from the modification of the torsion angle between the pyridine rings, which increases upon oxidation. These oxidation-induced modifications are in agreement with the observation of Zhang et al.,³⁶ although more important due to the multiple Ru centers. In conclusion, the effect of oxidation is the reduction of the π -conjugation between the Ru and Zn moieties.

	1a	1b	2	3	4	5
	\mathbf{x}^{II}					
$a_{\text{N}}[\text{Py}(\text{II})]-\text{Zn}-\text{N}[\text{Py}(\text{II})]$	—	—	—	75.7	75.9 ± 0.0	75.8 ± 0.0
$a_{\text{N}}[\text{Py}(\text{I})]-\text{Zn}-\text{N}[\text{Py}(\text{I})]$	76.4 ± 0.0	76.2 ± 0.0	—	76.6 ± 0.0	76.5	—
$d_{\text{Zn}-\text{N}}[\text{Py}(\text{II})]$	—	—	—	2.160 ± 0.002	2.157 ± 0.005	2.159 ± 0.004
$d_{\text{Zn}-\text{N}}[\text{Py}(\text{I})]$	2.155 ± 0.000	2.154 ± 0.002	—	2.151 ± 0.002	2.153 ± 0.005	—
$d_{\text{Ru}-\text{N}}[\text{Py}(\text{II})]$	—	—	2.083	2.071 ± 0.001	2.070 ± 0.001	2.070 ± 0.001
$d_{\text{Ru}-\text{N}}(\text{ax})$	—	—	2.165	2.164 ± 0.000	2.163 ± 0.001	2.163 ± 0.001
t_{biph}	—	37.1 ± 0.5	—	34.7 ± 0.5	32.1 ± 3.1	32.9 ± 2.7
	\mathbf{x}^{III}					
$a_{\text{N}}[\text{Py}(\text{II})]-\text{Zn}-\text{N}[\text{Py}(\text{II})]$	—	—	—	75.1	75.6 ± 0.0	75.7 ± 0.0
$a_{\text{N}}[\text{Py}(\text{I})]-\text{Zn}-\text{N}[\text{Py}(\text{I})]$	—	—	—	76.8 ± 0.0	76.9	—
$d_{\text{Zn}-\text{N}}[\text{Py}(\text{II})]$	—	—	—	2.177 ± 0.001	2.166 ± 0.007	2.166 ± 0.004
$d_{\text{Zn}-\text{N}}(\text{I})$	—	—	—	2.144 ± 0.002	2.145 ± 0.003	—
$d_{\text{Ru}-\text{N}}[\text{Py}(\text{II})]$	—	—	2.100	2.107 ± 0.001	2.110 ± 0.002	2.116 ± 0.002
$d_{\text{Ru}-\text{N}}(\text{ax})$	—	—	2.142	2.138 ± 0.001	2.134 ± 0.001	2.136 ± 0.002
t_{biph}	—	—	—	38.2 ± 1.6	38.0 ± 0.5	41.5 ± 3.1
	$\Delta(\mathbf{x}^{\text{III}}-\mathbf{x}^{\text{II}})$					
$a_{\text{N}}[\text{Py}(\text{II})]-\text{Zn}-\text{N}[\text{Py}(\text{II})]$	—	—	—	-0.7	-0.4	-0.1
$a_{\text{N}}[\text{Py}(\text{I})]-\text{Zn}-\text{N}[\text{Py}(\text{I})]$	—	—	—	0.3	0.4	—
$d_{\text{Zn}-\text{N}}[\text{Py}(\text{II})]$	—	—	—	0.017	0.009	0.007
$d_{\text{Zn}-\text{N}}[\text{Py}(\text{I})]$	—	—	—	-0.006	-0.009	0.000
$d_{\text{Ru}-\text{N}}[\text{Py}(\text{II})]$	—	—	0.017	0.036	0.040	0.046
$d_{\text{Ru}-\text{N}}(\text{ax})$	—	—	-0.023	-0.026	-0.029	-0.027
t_{biph}	—	—	—	3.4	5.9	8.6

Table 7.1: Impact of oxidation on the average geometrical parameters defined in Figure 7.1a (bond lengths d , in Å, angles a , in °, and their standard deviations) obtained by the geometry optimization of **1** and **3-5** at the IEF-PCM(acetonitrile)/B3P86/6-311G(d)/LANL2TZ level. A distinction is made between the bipyridine bearing Ru-bearing moieties [Py(II)] and the ones without [Py(I)].

First hyperpolarizabilities

The static and dynamic (1907 and 1064 nm) first hyperpolarizabilities of all compounds are reported in Table 7.2. The ordering of the β_{HRS} amplitudes of the reduced forms follows:

$$1b < 1a \ll 2^{II} < 5^{II} \ll 3^{II} \approx 4^{II},$$

at the three considered wavelengths. Going from compound **1a** to **3** i.e. by adding a pair of Ru-based donor moieties results in a huge enhancement of the first hyperpolarizability. Then, adding a second pair increases only slightly β_{HRS} while it decreases upon the inclusion of a third pair so that the β value becomes comparable to that of compound **2**. The depolarization ratios are close to 5-6 for compounds **2-4**, while close to 1.7 for compounds **1** and **5**, evidencing the octupolar character of β associated with the D_3 -like symmetry. The DR of compound **3** is actually the largest, corresponding to the most pronounced dipolar character. Moreover, the dynamic β_{HRS} responses of compounds **1** and **2** are smaller than the static ones, which originates from a dynamic permittivity of acetonitrile that is smaller than its static counterpart.

After oxidation, β_{HRS} decreases but the trend among the different Ru-containing compounds remains:

$$2^{III} < 5^{III} < 4^{III} \approx 3^{III},$$

except in the static limit, where $3^{III} < 5^{III}$. This inversion is related to frequency dispersion. Therefore in the dynamic regime, the contrast between the two oxidation states are slightly larger than 3 and follows the ordering

$$2 \approx 5 < 3 < 4.$$

Those ratios are comparable to the one reported by Zhang et al.³⁶ for a one-dimensional-like derivatives of compound **2**. They also reported that LC-BLYP tends to underestimate the ratios with respect to the experimental values.

	Reduced (\mathbf{x}^{II})			Oxidized (\mathbf{x}^{III})			$\mathbf{x}^{\text{II}} / \mathbf{x}^{\text{III}}$		
	static	1907 nm	1064 nm	static	1907 nm	1064 nm	static	1907 nm	1064 nm
1a	83 (1.50)	42 (1.50)	49 (1.50)	—	—	—	—	—	—
1b	57 (1.50)	7 (1.65)	14 (1.46)	—	—	—	—	—	—
2	652 (4.65)	475 (4.67)	612 (4.74)	128 (3.04)	159 (4.02)	192 (4.21)	5.08	2.99	3.19
3	3070 (6.08)	2875 (5.93)	4194 (5.98)	251 (4.49)	837 (6.01)	1055 (6.34)	12.25	3.44	3.98
4	3164 (5.10)	3035 (4.67)	4359 (4.81)	210 (3.03)	682 (3.81)	917 (3.90)	15.13	4.45	4.76
5	986 (1.72)	934 (1.72)	1478 (1.79)	354 (2.92)	343 (1.54)	436 (1.54)	2.79	2.73	3.39

Table 7.2: Static and dynamic (1907 and 1064 nm) first hyperpolarizability (β_{HRS} , a.u.) of \mathbf{x} ($\mathbf{x}=\mathbf{1-5}$) together with their ratio between the two oxidation states ($\mathbf{x}^{\text{II}} / \mathbf{x}^{\text{III}}$), as computed at the LC-BLYP/6-311G(d)/LANL2TZ level in acetonitrile (IEF-PCM). The depolarization ratio (DR) is given in parentheses.

Insights from the VB- n CT models

The first hyperpolarizability of the reduced forms, which are large and dominated by CT transitions, can be analyzed using simple VB- n CT models. The evolution of the static β_{HRS} with the CT character (m_{CT}) given in Figure 7.2, shows variations as a function of the shape: i) in the simple D/A case, β_{HRS} presents two maxima at $m_{CT} = \pm\sqrt{5}/5 \approx \pm 0.45$,^{16,20} ii) in the VB-2CT model, with $\theta = 120^\circ$ (which corresponds to the angle between the CT dipoles of compound 4), it exhibits only one maximum located in the $m_{CT} \approx 0.3$ area,⁶⁴ while iii) for the VB-3CT model with a D_3 -like structure, β_{HRS} increases monotonically with m_{CT} .^{40,41} So, i) D/A pairs of moderate strength favor large β_{HRS} response with one bidentate ligand (featuring 2 Ru-containing linkers), then ii) stronger D/A pairs lead to large responses for structures with two or three bidentate ligands, and, finally, iii) the octupolar species has the largest response in the limit of very large m_{CT} . Assuming that the VB- n CT parameters can be considered similar between the compounds, these models help to rationalize the differences of β_{HRS} between **3**^{II}-**5**^{II}, which are governed by the symmetry and from comparing the relative β_{HRS} amplitudes of **3**-**5**, it is deduced that $m_{CT} \sim -0.1$, which is not far from the cyanine limit.

Two design strategies to enhance β are suggested by this analysis. The simplest consists

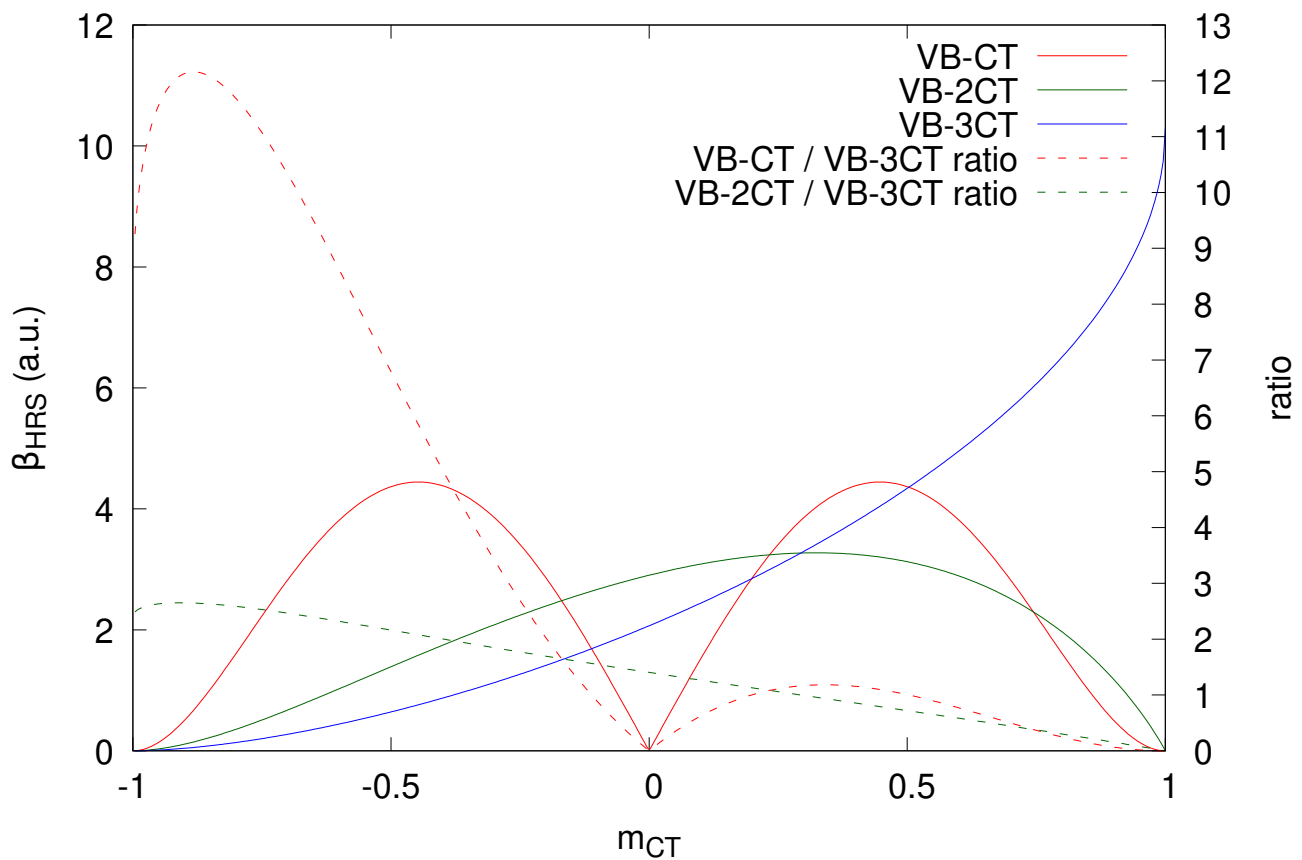


Figure 7.2: Evolution of β_{HRS} (a.u.) as a function of the CT mixing parameter (m_{CT}) for the 3 models (thick lines, obtained with $t = T = 0.1 E_h$ and $\mu_{CT} = 1 e a_0$) as well as their ratios (dashed lines).

in increasing m_{CT} (by modification of the donor/acceptor pair), which will increase β of the octupolar architecture with respect to those of the others. Another, indirect, issue consists in lengthening the π -conjugation path. While this leads to a decrease of m_{CT} ,⁶⁵ it comes together with an increase of the CT dipole moment, which globally leads to an enhancement of β_{HRS} , even though an appropriate balance between the two effects needs to be found. In such case, the one-dimensional and Λ -shape structures would present larger responses than their octupolar analogues. This strategy was explored by Zhang and Champagne in Ref. 37 for the reduced forms, resulting in a fourfold increase of β_{HRS} for derivatives of compound **2**, when increasing the length of the polyenic segment between the pyridine and pyridinium rings.

Excited States

Figure 7.3 displays the simulated absorption spectra of compounds **1a** and **1b**. In order to confirm the predictions of the VB- n CT models, the important excited states are analyzed and their characteristics are detailed in Table 7.3. The spectrum presents a first absorption band around 260 nm. Going from **1a** to **1b** slightly increases both the wavelength and the oscillator strength of this band, which is associated with the lengthening of the π -conjugated path. A second, more intense, band around 220 nm shows up for compound **1b**. Both are ILCT, $\pi \rightarrow \pi^*$, transitions which do not involve the Zn atom. This first absorption band is

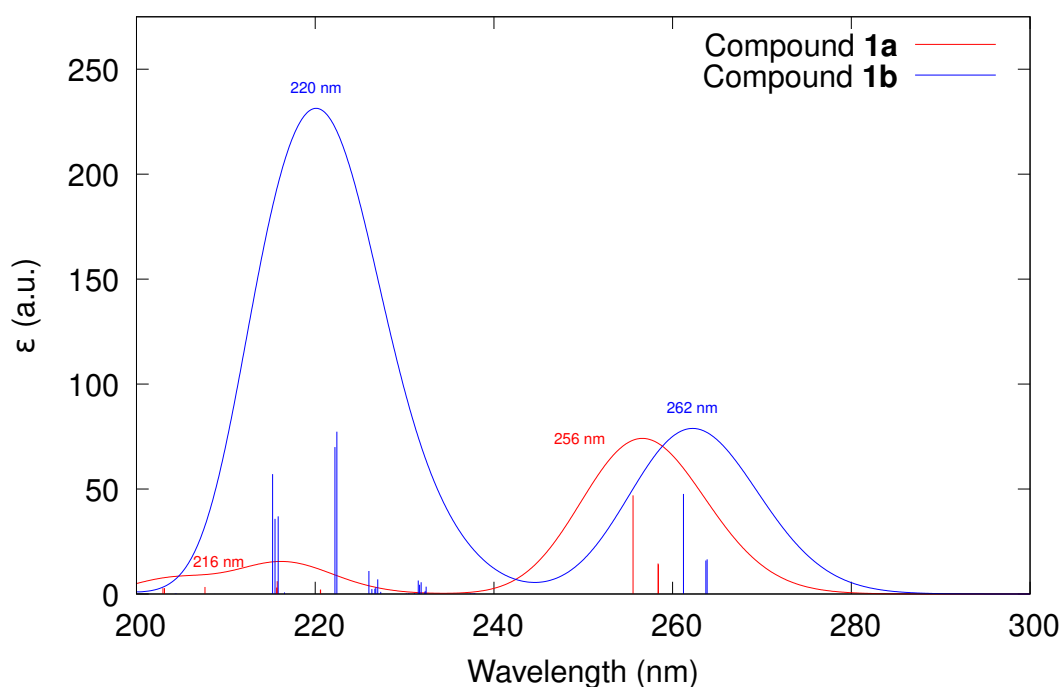


Figure 7.3: Simulated UV/VIS absorption spectra of compounds **1a** and **1b**, as computed at the LC-BLYP/6-311G(d)/LANL2TZ level in acetonitrile (IEF-PCM). Each transition is represented by a Gaussian function (FWHM=0.3 eV), together with its impulse, which is proportional to the oscillator strength. The different maxima of the curves are also reported.

composed of 2 (#1 and #2, located on two ligands) + 1 (#3, located on the three ligands and having the largest intensity) electronic transitions. As expected for ILCT transition, the charge transfer distances (d_{CT}) are quite small for all three, with a moderate ($0.4e$) charge transfer.

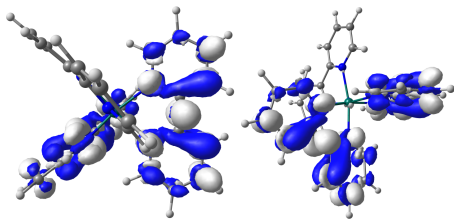
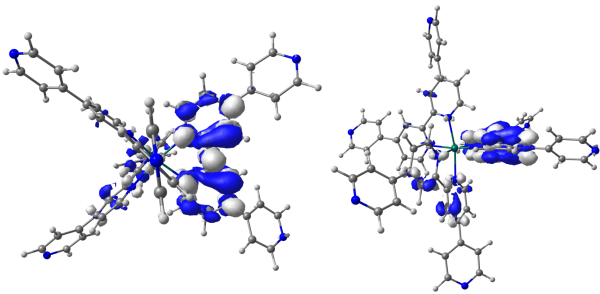
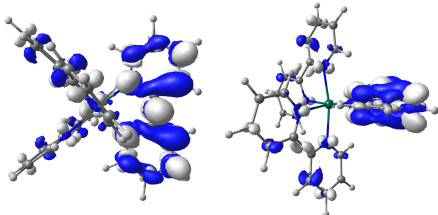
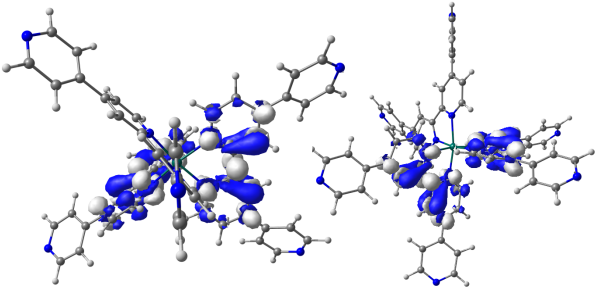
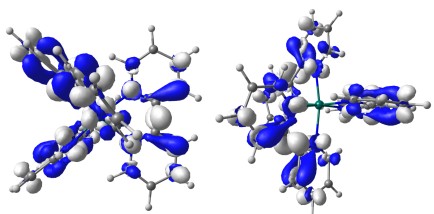
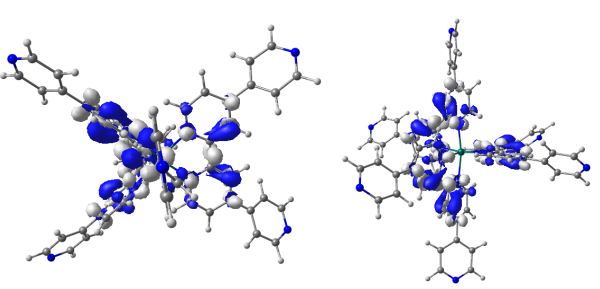
1a	1b
ES #1, 258 nm (0.234)	ES #1, 264 nm (0.274)
	
$q_{CT} = 0.43e$, $d_{CT} = 0.17\text{ \AA}$ $r_{CT} = -0.09\text{ \AA}$	$q_{CT} = 0.45e$, $d_{CT} = 0.02\text{ \AA}$ $r_{CT} = 0.38\text{ \AA}$
ES #2, 258 nm (0.241)	ES #2, 264 nm (0.264)
	
$q_{CT} = 0.42e$, $d_{CT} = 0.18\text{ \AA}$ $r_{CT} = -0.13\text{ \AA}$	$q_{CT} = 0.46e$, $d_{CT} = 0.01\text{ \AA}$ $r_{CT} = 0.30\text{ \AA}$
ES #3, 255 nm (0.779)	ES #3, 261 nm (0.790)
	
$q_{CT} = 0.40e$, $d_{CT} = 0.01\text{ \AA}$ $r_{CT} = -0.09\text{ \AA}$	$q_{CT} = 0.49e$, $d_{CT} = 0.01\text{ \AA}$ $r_{CT} = 0.34\text{ \AA}$

Table 7.3: Nature of the main electron transitions (vertical excitation energy and oscillator strength in parentheses) and electron density difference (negative in blue, isovalue of 0.001 a.u., two orientations) together with the related quantities (charge transfer amplitude, q_{CT} , distance, d_{CT} , and radius, r_{CT}) of **1a** and **1b** as computed at the LC-BLYP/6-311G(d)/LANL2TZ level in acetonitrile (IEF-PCM). Two molecular orientation are proposed for each transition state.

The radial charge densities are similar for all first 3 excited states of **1a** and **1b** (Figure A.1). A representative example (ES #3) is given in Figure 7.4. For the zone below $r = 6 \text{ \AA}$, the shapes for **1a** and **1b** are similar: the electron density moves mostly from C_3 and C_5 to N_1 and C_4 . The peak around 3 \AA in ρ_r^+ is due to an increase of the density in the π orbital between C_6 and C_6' . When $r > 6 \text{ \AA}$, while $\rho_r^\pm(r)$ tend towards 0 for **1a**, the second ring also slightly contributes for **1b**. This results in i) larger r_{CT} values for **1b** than for **1a** (around -0.1 \AA for **1a** and 0.3 \AA for **1b**), and ii) a change of sign, *i.e.*, of direction.

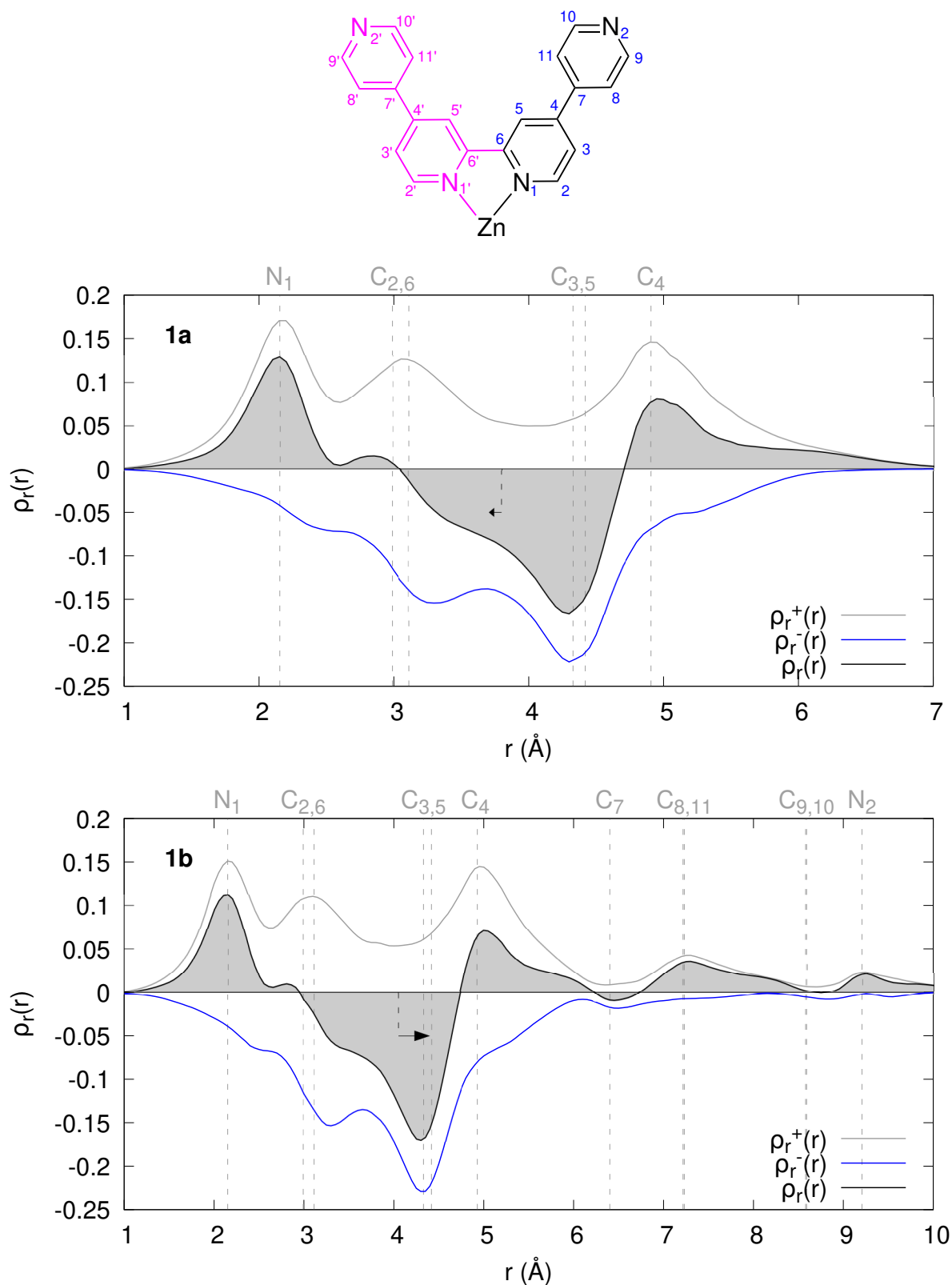


Figure 7.4: Radial distribution of the electron density difference (centered on the Zn atom) of ES #3 of **1a** (middle, numbering of the atoms on top, the atoms in purple are equivalent by symmetry) and **1b** (bottom) as computed at the LC-BLYP/6-311G(d)/LANL2TZ level in acetonitrile (IEF-PCM). The (small) black arrow represents $r_{CT} = \langle r \rangle^+ - \langle r \rangle^-$.

Figure 7.5 displays the simulated absorption spectrum of both forms of **2**, while Table 7.4 details the main transitions. The singlet reduced form (**2^{II}**) displays two important band, located around 250 and 200 nm, with large q_{CT} , d_{CT} and $|r_{CT}|$. Upon oxidation (**2^{III}**, doublet), the first excitation band disappears, while two ES appear around 230 nm. The topology of the electron density differences changes, and is accompanied by a decrease of the oscillator strength (together with a decrease of q_{CT} and d_{CT}). Note that the spin contamination remains moderate ($0.15 < \Delta \langle S^2 \rangle < 0.4$).

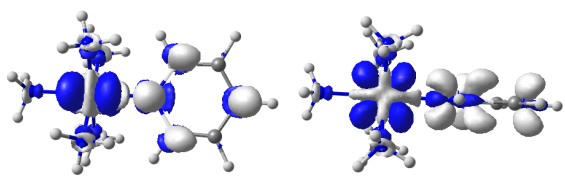
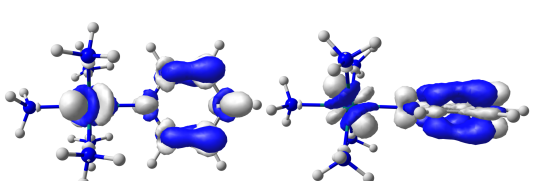
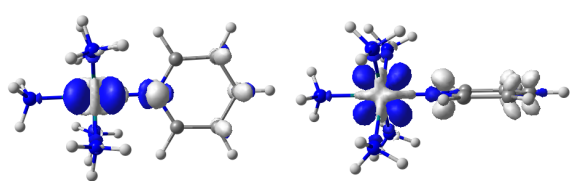
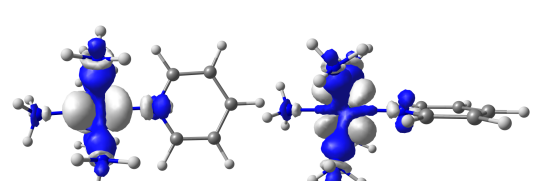
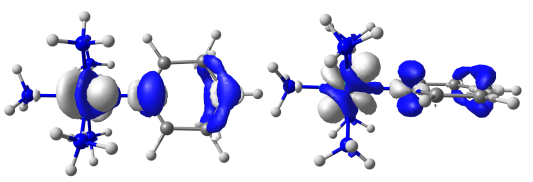
2^{II}		2^{III}	
ES #1, 251 nm (0.237)		ES #1, 239 nm (0.048), $\Delta \langle S^2 \rangle = 0.35$	
			
$q_{CT} = 1.00 e$, $d_{CT} = 2.16 \text{ \AA}$ $r_{CT} = -1.71 \text{ \AA}$		$q_{CT} = 0.71 e$, $d_{CT} = 1.05 \text{ \AA}$ $r_{CT} = 1.10 \text{ \AA}$	
ES #2, 201 nm (0.155)		ES #2, 228 nm (0.051), $\Delta \langle S^2 \rangle = 0.20$	
			
$q_{CT} = 0.65 e$, $d_{CT} = 2.26 \text{ \AA}$ $r_{CT} = -1.72 \text{ \AA}$		$q_{CT} = 0.74 e$, $d_{CT} = 0.28 \text{ \AA}$ $r_{CT} = 0.13 \text{ \AA}$	
		ES #3, 206 nm (0.097), $\Delta \langle S^2 \rangle = 0.16$	
			
		$q_{CT} = 0.75 e$, $d_{CT} = 1.81 \text{ \AA}$ $r_{CT} = 1.37 \text{ \AA}$	

Table 7.4: Nature of the main electron transitions (vertical excitation energy and oscillator strength in parentheses) and electron density difference (negative in blue, isovalue of 0.001 a.u., two orientations) together with the related quantities (charge transfer amplitude, q_{CT} , distance, d_{CT} , and radius, r_{CT}) of both oxidation states of compound **2** as computed at the LC-BLYP/6-311G(d)/LANL2TZ level in acetonitrile (IEF-PCM). Two molecular orientation are proposed for each transition state.

The radial distributions of the electron density difference are plotted in Figure 7.6 for these excited states. The two transitions in **2^{II}** have a similar shape, describing mostly a displacement of the electron density from the Ru atom to the pyridine ring [positive $\rho_r(r)$

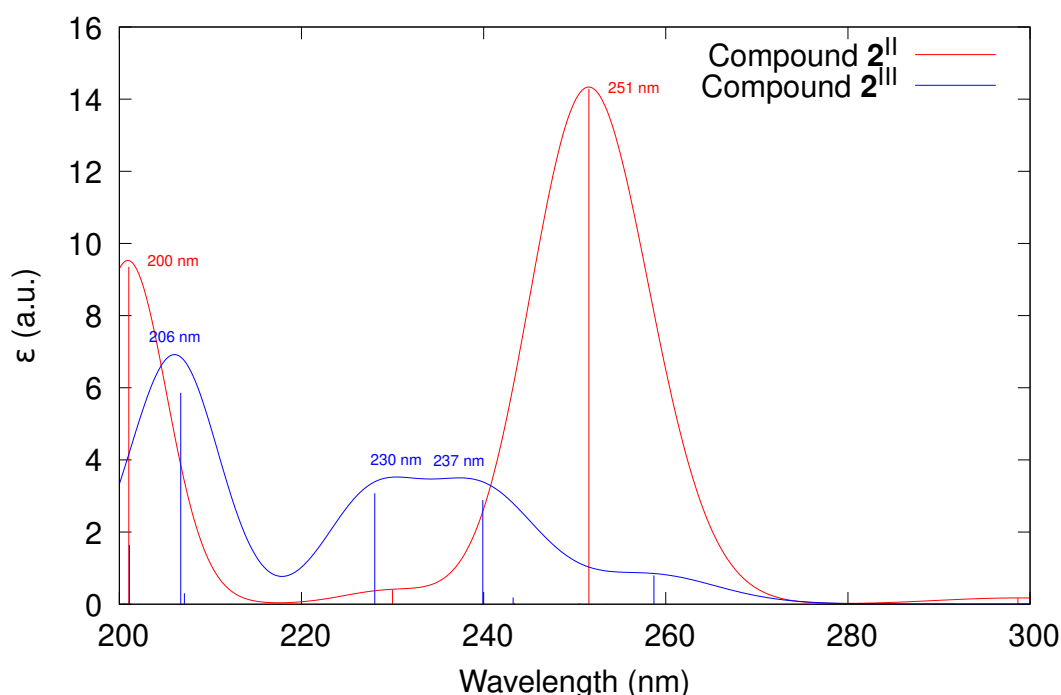


Figure 7.5: Simulated UV/VIS absorption spectra of compounds **2^{II}**, as computed at the LC-BLYP/6-311G(d)/LANL2TZ level in acetonitrile (IEF-PCM). Each transition is represented by a Gaussian function (FWHM=0.3 eV), together with its impulse. The different maxima of the curves are also reported.

when $r < 4\text{\AA}$, especially around N_1]. This corresponds to a MLCT transition. On the other hand, $\rho_r(r)$ shows the opposite trend for ES #1 and #3 of **2^{III}**. ES #2 of **2^{III}** is mostly located on the Ru center which corresponds to intra-metal charge transfer (IMCT). It is also noticeable that r_{CT} is positive for **2^{III}**, which indicates a change of the direction of the electron density displacement upon excitation with respect to the reduced form.

In overall, the important excited states of **1a** and **1b** are ILCT within the pyridine rings. In **2^{II}**, the first two bands show a clear MLCT character, which disappears upon oxidation, leading to LMCT and IMCT transitions. This observation is consistent with the drastic decrease of β_{HRS} from **2^{II}** to **2^{III}** as calculated at the TDDFT level, as well as with the analysis from the VB-CT model (due to the reduction of q_{CT} and d_{CT}). Now, it is interesting to analyze the corresponding behavior in **3-5**, which combine the **1** and **2** moieties.

Compounds 3-5

The simulated absorption spectra of both oxidation states of compounds **3-5** are reported in Figure 7.7. For the reduced forms, the spectra displays three maxima: around 285, 260, and 210 nm. While their positions remain mostly unaffected (the corresponding ES are slightly redshifted) by addition of Ru-bearing moieties (**3^{II}→5^{II}**), the intensity of the first and the last ones grows, mostly due to the addition of extra ES (the oscillator strengths of the corresponding transitions remain similar). The analysis of the difference of density of the important ES

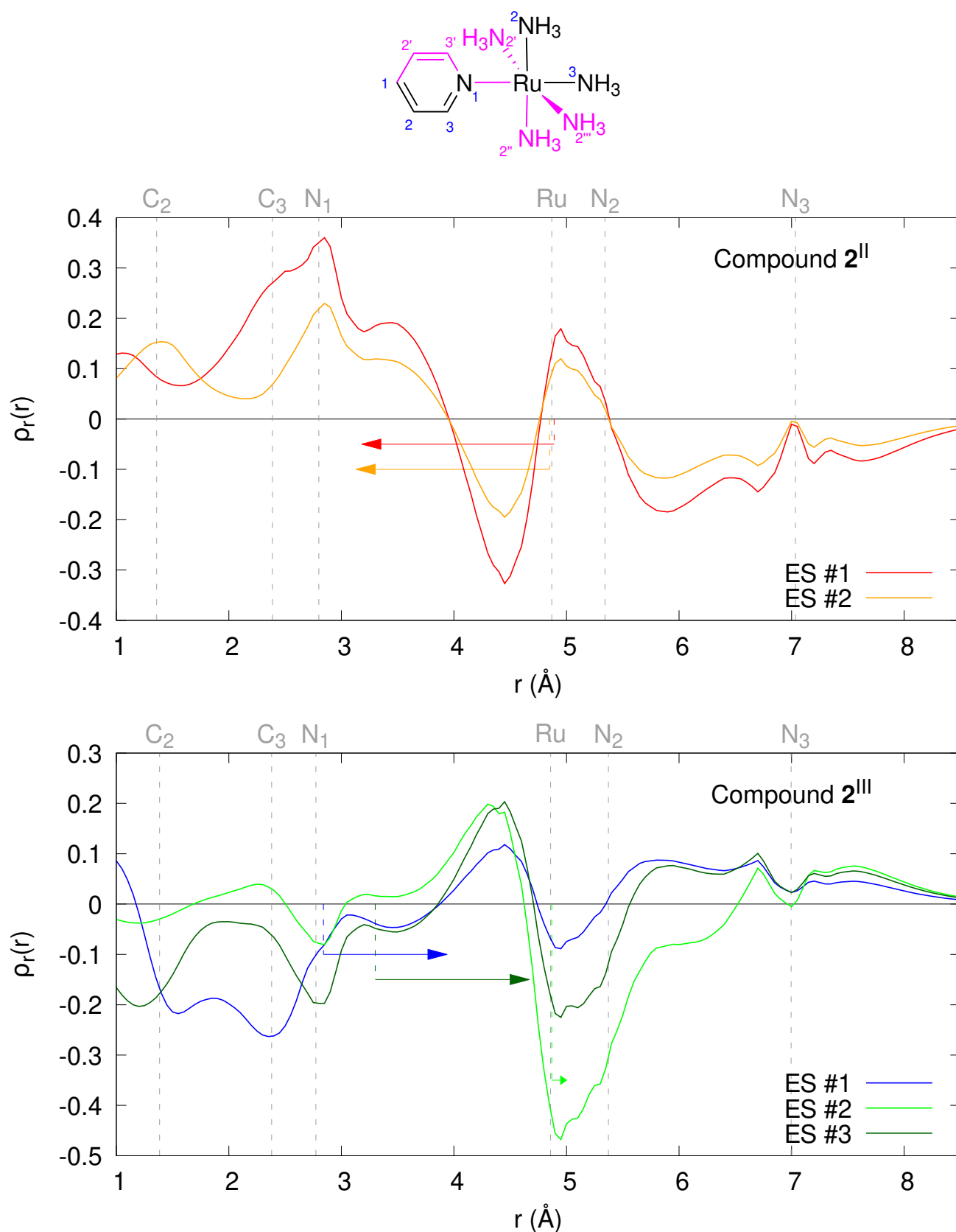


Figure 7.6: Radial distribution of the electron density difference (centered on the C_1 atom) of the first important excited states of **2^{II}** (middle, numbering of the atoms on top, the atoms in purple are equivalent by symmetry) and **2^{III}** (bottom) as computed at the LC-BLYP/6-311G(d)/LANL2TZ level in acetonitrile (IEF-PCM). Arrows indicate $r_{CT} = \langle r \rangle^+ - \langle r \rangle^-$.

(Tables A.5-A.7, Figures 7.8-7.10) show that the first peak is constituted of MLCT transitions as expected (like ES #1 of **2^{II}**, but redshifted since the π -conjugated path is more important), while the two others have an ILCT character close to the ones of **1b**. Concerning the oxidized forms, the change are comparable to the oxidation of **2**: the MLCT character is lost in favor of ILCT, together with an inversion of the displacement of the electron density upon excitation (Tables A.8-A.10, Figures 7.8-7.10). Note that there are many transitions with weak oscillator strengths, so that only the first peak of **5^{III}** (peaking at 268 nm) is obtained when including the first 100 excited states.

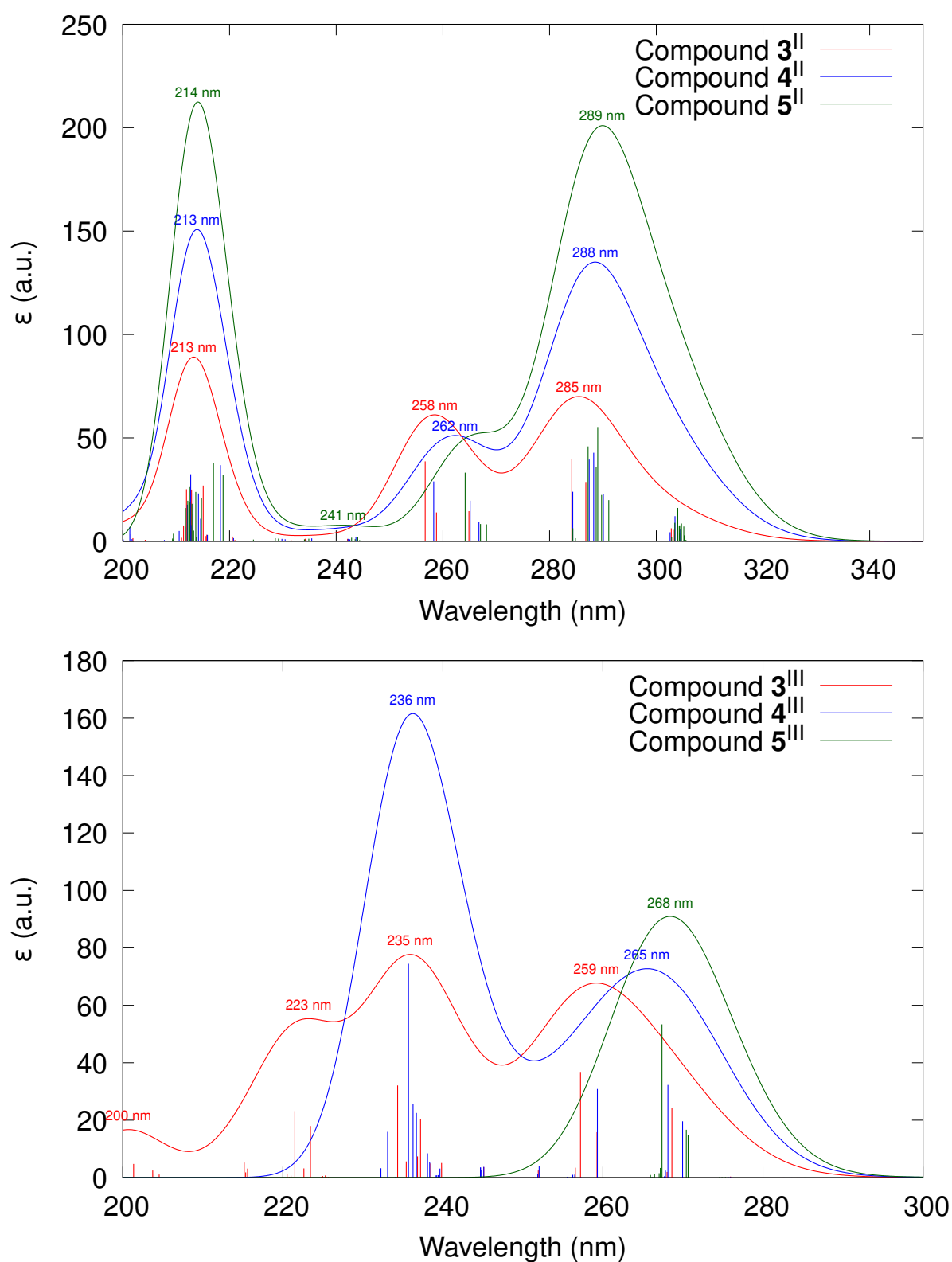


Figure 7.7: Simulated UV/VIS absorption spectra of compounds **3^{II}-5^{II}** (top) and **3^{III}-5^{III}**, as computed at the LC-BLYP/6-311G(d)/LANL2TZ level in acetonitrile (IEF-PCM). Each transition is represented by a Gaussian function (FWHM=0.3 eV), together with its impulse. The different maxima of the curves are also reported.

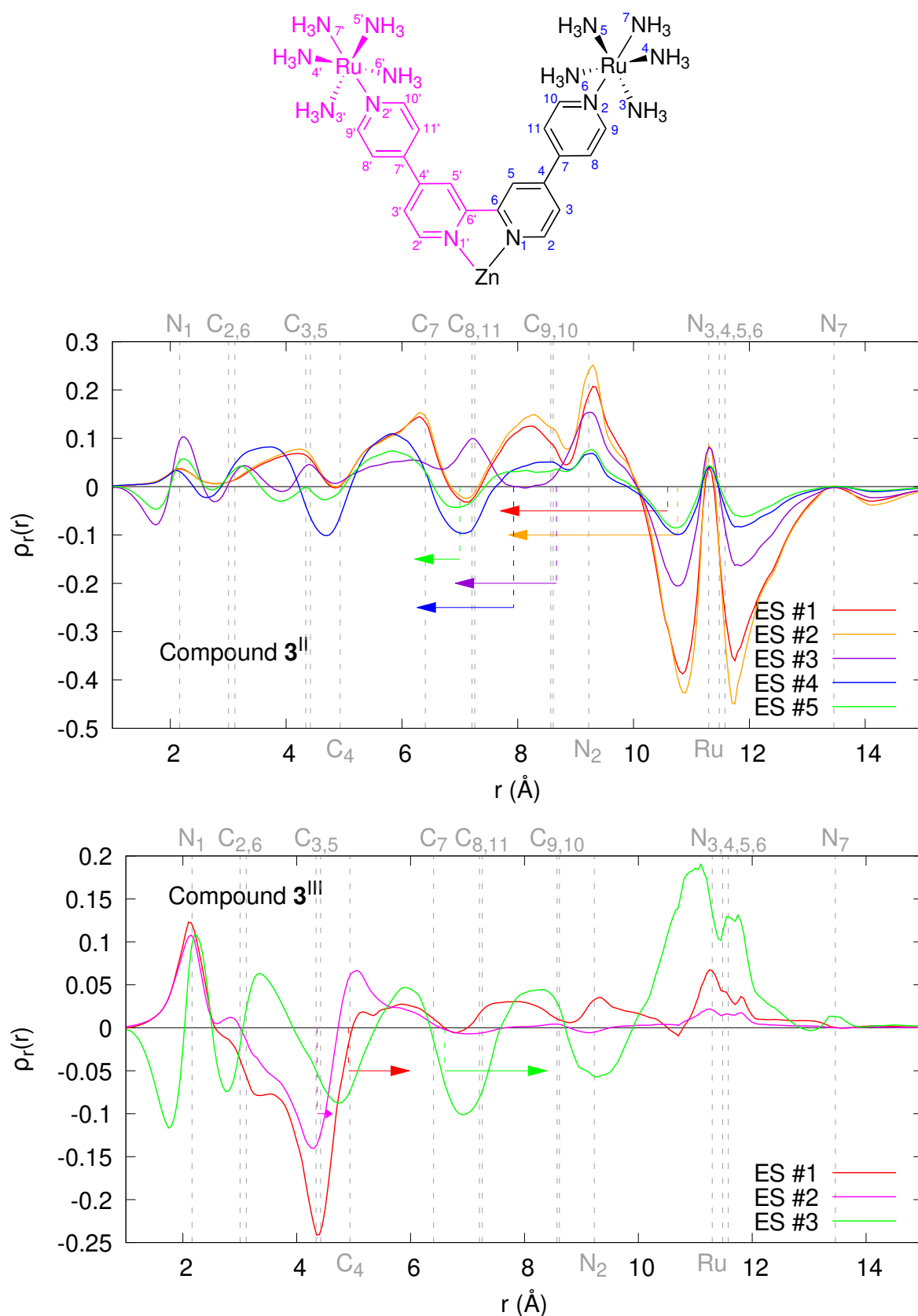


Figure 7.8: Radial distribution of the electron density difference (centered in Zn) of the first important excited states of **3^{II}** (middle, numbering of the atoms on top, the atoms in purple are equivalent by symmetry) and **3^{III}** (bottom) as computed at the LC-BLYP/6-311G(d)/LANL2TZ level in acetonitrile (IEF-PCM). Arrows indicate r_{CT} .

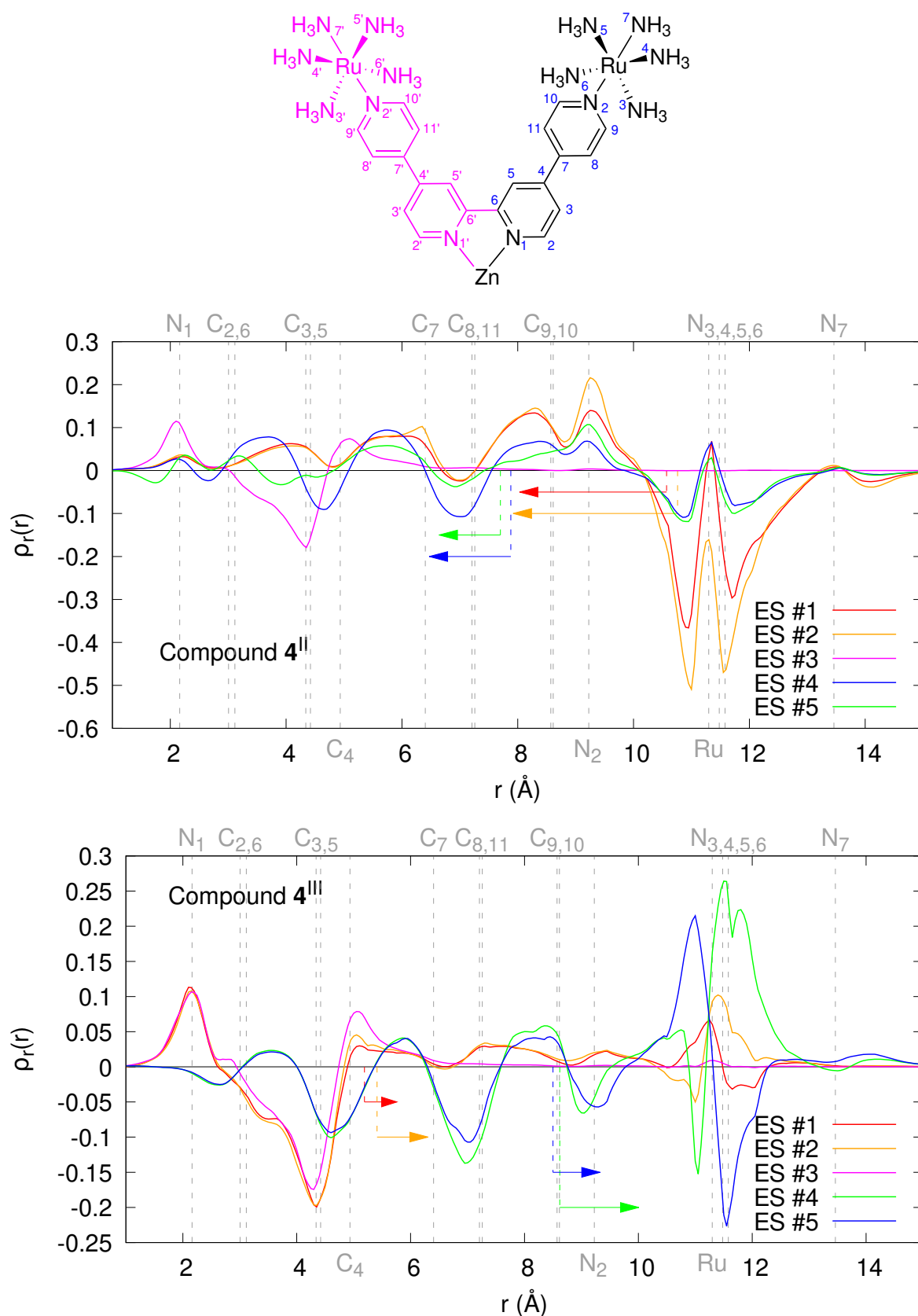


Figure 7.9: Radial distribution of the electron density difference (centered on the Zn atom) of the first important excited states of **4^{II}** (middle, numbering of the atoms on top, the atoms in purple are equivalent by symmetry) and **4^{III}** (bottom) as computed at the LC-BLYP/6-311G(d)/LANL2TZ level in acetonitrile (IEF-PCM). Arrows indicate r_{CT} .

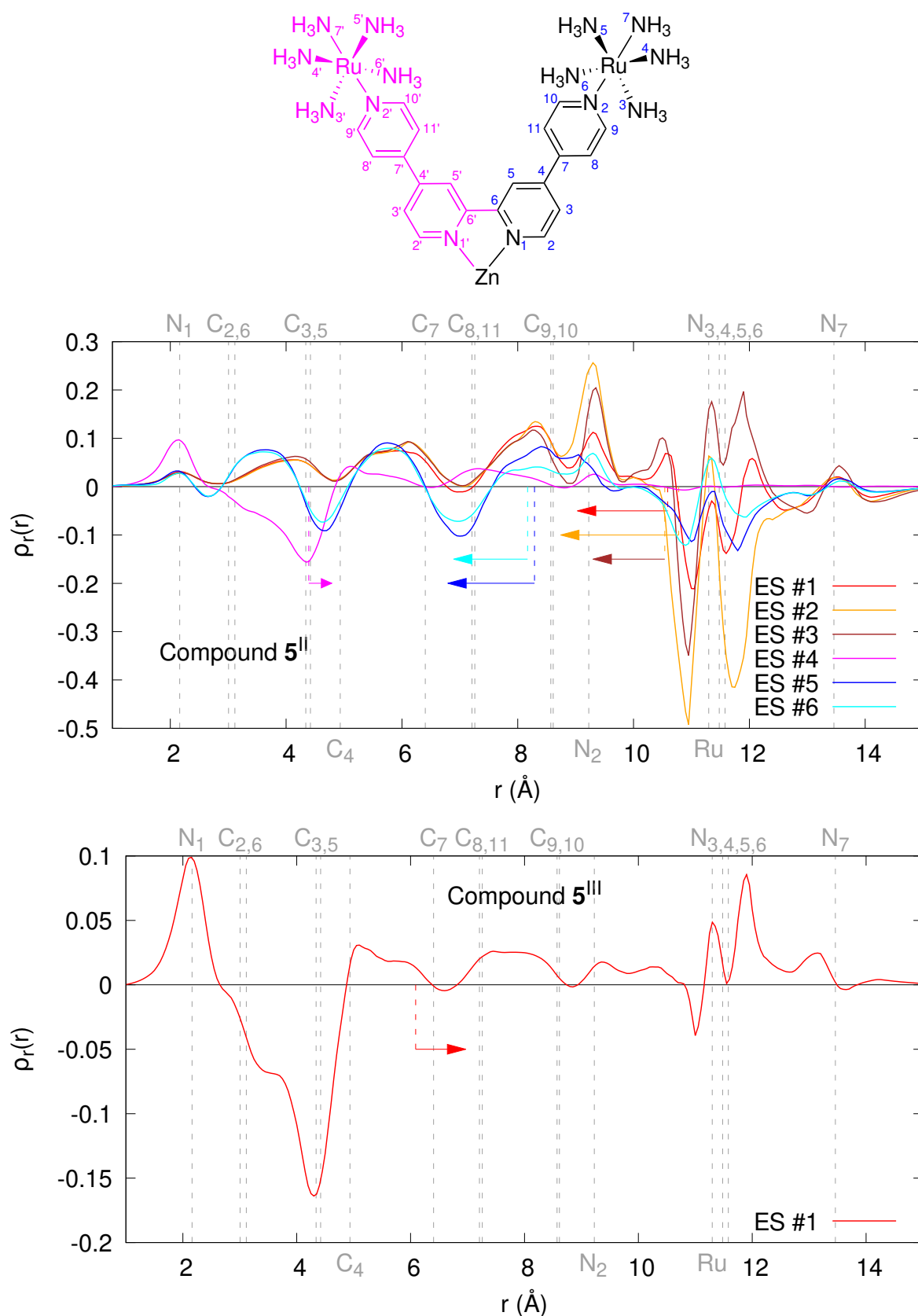


Figure 7.10: Radial distribution of the electron density difference (centered on the Zn atom) of the first important excited states of **5^{II}** (middle, numbering of the atoms on top, the atoms in purple are equivalent by symmetry) and **5^{III}** (bottom) as computed at the LC-BLYP/6-311G(d)/LANL2TZ level in acetonitrile (IEF-PCM). Arrows indicate r_{CT} .

Section 7.4

Conclusions and outlook

In this paper, (time-dependent) density functional theory calculations are enacted to study an octupolar molecular switch bearing six Ru centers, associated with 3 bidentate ligands complexing the central Zn atom. This switch can be triggered by redox, corresponding to the Ru(II)-to-Ru(III) transformations, and *vice versa*. The linear and second-order nonlinear optical properties of this challenging compound have been studied in its fully-reduced and fully-oxidized forms. The first hyperpolarizability of the reduced form is 3 to 4 times larger than the one of the oxidized form, as a result of substantial contributions from low-energy metal(Ru) to ligand charge transfer excited states. On the other hand, upon oxidation, there is a reversal of the direction of charge transfer and a reduction of its amplitude, which explains its smaller first hyperpolarizability. These modifications of the electronic and optical properties upon oxidation have been shown to be associated with a reduction of π -conjugation via a weakening of back bonding between the Ru atoms and the pyridyl ligands, which is evidenced by comparing the ground state geometries.

The first hyperpolarizability of both oxidation states of this octupolar molecular switch has been further analyzed by studying its fragments, in particular those structures obtained by removing one or two bidentate ligands. By removing one ligand, the switch contains 4 Ru centers and corresponds to a Λ -shape NLOphore while after removal of two of such ligands, the structure resembles a one-dimensional push-pull NLOphore. For these Λ -shape and one-dimensional systems, the calculations predict, for the reduced form, an enhancement of the first hyperpolarizability by about a factor of 3. These results have been rationalized by adopting the VB-*n*CT models. Subsequently, this model is used to propose design rules to enhance the first hyperpolarizability of such compounds with multiple Ru centers. In particular, in the case of the octupolar structures, it appears important to achieve larger charge transfer character in the ground state.

Besides unraveling structure/symmetry-property relationships, this paper has discussed the choice of an appropriate density functional theory level of calculations, by probing the effects of the exchange-correlation functional and of the atomic basis set on the structural and nonlinear optical properties. Finally, the few-state model analysis has been facilitated by adapting to octupolar systems the method for analyzing the ground-to-excited state electron density differences.

Acknowledgments

The calculations were performed on the computers of the Consortium des Équipements de Calcul Intensif, including those of the Technological Platform of High-Performance Computing, for which we gratefully acknowledge the financial support of the FNRS-FRFC, of the Walloon Region, and of the University of Namur (Conventions No. 2.5020.11, GEQ U.G006.15, 1610468, and RW/GEQ2016).

Bibliography

- [1] Nalwa, H. S., Ed. *Handbook of Advanced Electronic and Photonic Materials and Devices*; Acad. Press: San Diego, Calif., 2001.
- [2] Coe, B. J. Molecular Materials Possessing Switchable Quadratic Nonlinear Optical Properties. *Chem. Eur. J.* **1999**, *5*, 2464–2471.
- [3] Delaire, J. A.; Nakatani, K. Linear and Nonlinear Optical Properties of Photochromic Molecules and Materials. *Chem. Rev.* **2000**, *100*, 1817–1846.
- [4] Bouas-Laurent, H.; Dürr, H. *Photochromism*; Elsevier, 2003; pp XXVII–LIII.
- [5] Castet, F.; Rodriguez, V.; Pozzo, J.-L.; Ducasse, L.; Plaquet, A.; Champagne, B. Design and Characterization of Molecular Nonlinear Optical Switches. *Acc. Chem. Res.* **2013**, *46*, 2656–2665.
- [6] Verbiest, T.; Clays, K.; Rodriguez, V. *Second-Order Nonlinear Optical Characterization Techniques: An Introduction*; Taylor & Francis, 2009.
- [7] Clays, K.; Persoons, A. Hyper-Rayleigh Scattering in Solution. *Phys. Rev. Lett.* **1991**, *66*, 2980–2983.
- [8] Hendrickx, E.; Clays, K.; Persoons, A. Hyper-Rayleigh Scattering in Isotropic Solution. *Acc. Chem. Res.* **1998**, *31*, 675–683.
- [9] Bublitz, G. U.; Boxer, S. G. Stark Spectroscopy: Applications in Chemistry, Biology, and Materials Science. *Annu. Rev. Phys. Chem.* **1997**, *48*, 213–242.
- [10] Finn, R. S.; Ward, J. F. Dc-Induced Optical Second-Harmonic Generation in the Inert Gases. *Phys. Rev. Lett.* **1971**, *26*, 285–289.
- [11] Shelton, D. P.; Rice, J. E. Measurements and Calculations of the Hyperpolarizabilities of Atoms and Small Molecules in the Gas Phase. *Chem. Rev.* **1994**, *94*, 3–29.
- [12] Kanis, D. R.; Ratner, M. A.; Marks, T. J. Design and Construction of Molecular Assemblies with Large Second-Order Optical Nonlinearities. Quantum Chemical Aspects. *Chem. Rev.* **1994**, *94*, 195–242.
- [13] Papadopoulos, M. G.; Sadlej, A. J.; Leszczynski, J. In *Non-Linear Optical Properties of Matter: From Molecules to Condensed Phases*; Papadopoulos, M. G., Sadlej, A. J., Leszczynski, J., Eds.; Challenges and Advances in Computational Chemistry and Physics 1; Springer: Dordrecht, 2006.
- [14] Champagne, B.; Beaujean, P.; de Wergifosse, M.; Cardenuto, M. H.; Liégeois, V.; Castet, F. In *Frontiers of Quantum Chemistry*; Wójcik, M. J., Nakatsuji, H., Kirtman, B., Ozaki, Y., Eds.; Springer Singapore: Singapore, 2018; pp 117–138.

- [15] Bourhill, G.; Brédas, J.-L.; Cheng, L.-T.; Marder, S. R.; Meyers, F.; Perry, J. W.; Tie-
mann, B. G. Experimental Demonstration of the Dependence of the First Hyperpolar-
izability of Donor-Acceptor-Substituted Polyenes on the Ground-State Polarization and
Bond Length Alternation. *J. Am. Chem. Soc.* **1994**, *116*, 2619–2620.
- [16] Barzoukas, M.; Fort, A.; Blanchard-Desce, M. A Two-Form Description of Push-Pull
Molecules: Correlations between Structure, Intramolecular Charge Transfer and (Hy-
per) Polarizabilities. *J. Nonlinear Opt. Phys. Mater.* **1996**, *05*, 757–765.
- [17] Kirtman, B.; Champagne, B.; Bishop, D. M. Electric Field Simulation of Substituents in
Donor-Acceptor Polyenes: A Comparison with Ab Initio Predictions for Dipole Moments,
Polarizabilities, and Hyperpolarizabilities. *J. Am. Chem. Soc.* **2000**, *122*, 8007–8012.
- [18] Lu, D.; Chen, G.; Goddard, W. A. The Valence-bond Charge-transfer-exciton Model for
Predicting Nonlinear Optical Properties (Hyperpolarizabilities and Saturation Length)
of Polymeric Materials. *J. Chem. Phys.* **1994**, *101*, 4920–4930.
- [19] Lu, D.; Chen, G.; Perry, J. W.; Goddard, W. A. Valence-Bond Charge-Transfer Model for
Nonlinear Optical Properties of Charge-Transfer Organic Molecules. *J. Am. Chem. Soc.*
1994, *116*, 10679–10685.
- [20] Barzoukas, M.; Runser, C.; Fort, A.; Blanchard-Desce, M. A Two-State Description of
(Hyper) Polarizabilities of Push-Pull Molecules Based on a Two-Form Model. *Chem. Phys.*
Lett. **1996**, *257*, 531–537.
- [21] Coe, B. J. Developing Iron and Ruthenium Complexes for Potential Nonlinear Optical
Applications. *Coord. Chem. Rev.* **2013**, *257*, 1438–1458.
- [22] Coe, B. J.; Essex-Lopresti, J. P.; Harris, J. A.; Houbrechts, S.; Persoons, A. Ruthenium(II)
Ammine Centres as Efficient Electron Donor Groups Forquadratic Non-Linear Optics.
Chem. Commun. **1997**, 1645–1646.
- [23] Coe, B. J.; Chamberlain, M. C.; Essex-Lopresti, J. P.; Gaines, S.; Jeffery, J. C.;
Houbrechts, S.; Persoons, A. Large Molecular Quadratic Hyperpolarizabilities in
Donor/Acceptor-Substituted Trans-Tetraammineruthenium(II) Complexes. *Inorg. Chem.*
1997, *36*, 3284–3292.
- [24] Coe, B. J.; Harris, J. A.; Harrington, L. J.; Jeffery, J. C.; Rees, L. H.; Houbrechts, S.; Per-
soons, A. Enhancement of Molecular Quadratic Hyperpolarizabilities in Ruthenium(II)
4,4'-Bipyridinium Complexes by N-Phenylation. *Inorg. Chem.* **1998**, *37*, 3391–3399.
- [25] Coe, B. J.; Harris, J. A.; Brunschwig, B. S.; Garín, J.; Orduna, J.; Coles, S. J.; Hurst-
house, M. B. Contrasting Linear and Quadratic Nonlinear Optical Behavior of Dipolar
Pyridinium Chromophores with 4-(Dimethylamino)Phenyl or Ruthenium(II) Ammine
Electron Donor Groups. *J. Am. Chem. Soc.* **2004**, *126*, 10418–10427.
- [26] Coe, B. J. In *Non-Linear Optical Properties of Matter: From Molecules to Condensed Phases*;

- Papadopoulos, M. G., Sadlej, A. J., Leszczynski, J., Eds.; Challenges and Advances in Computational Chemistry and Physics; Springer Netherlands: Dordrecht, 2006; pp 571–608.
- [27] Coe, B. J.; Fielden, J.; Foxon, S. P.; Asselberghs, I.; Clays, K.; Brunschwig, B. S. Two-Dimensional, Pyrazine-Based Nonlinear Optical Chromophores with Ruthenium(II) Ammine Electron Donors. *Inorg. Chem.* **2010**, *49*, 10718–10726.
- [28] Coe, B. J.; Pilkington, R. A. Theoretical Studies on Two-Dimensional Nonlinear Optical Chromophores with Pyrazinyl Cores and Organic or Ruthenium(II) Ammine Electron Donors. *J. Phys. Chem. A* **2014**, *118*, 2253–2268.
- [29] Coe, B. J.; Peers, M. K.; Scrutton, N. S. Syntheses and Electronic and Optical Properties of Complexes of the Bis(2,2'-Bipyrazyl)Ruthenium Unit. *Polyhedron* **2015**, *96*, 57–65.
- [30] Coe, B. J.; Sánchez, S. Synthesis and Properties of New Mononuclear Ru(II)-Based Photocatalysts Containing 4,4'-Diphenyl-2,2'-Bipyridyl Ligands. *Dalton Trans.* **2016**, *45*, 5210–5222.
- [31] Coe, B. J.; Houbrechts, S.; Asselberghs, I.; Persoons, A. Efficient, Reversible Redox-Switching of Molecular First Hyperpolarizabilities in Ruthenium(II) Complexes Possessing Large Quadratic Optical Nonlinearities. *Angew. Chem. Int. Ed.* **1999**, *38*, 366–369.
- [32] Zhang, L.-T.; Ondrechen, M. J. The Electronic Structure of Pentaammine (Pyrazine) Ruthenium (II) and (III): The Metal-Ligand π Conjugation and Its Implications in Electron Delocalization. *Inorg. Chim. Acta* **1994**, *226*, 43–51.
- [33] Coe, B. J.; Beljonne, D.; Vogel, H.; Garín, J.; Orduna, J. Theoretical Analyses of the Effects on the Linear and Quadratic Nonlinear Optical Properties of N-Arylation of Pyridinium Groups in Stilbazolium Dyes. *J. Phys. Chem. A* **2005**, *109*, 10052–10057.
- [34] Escudero, D.; González, L. RASPT2/RASSCF vs Range-Separated/Hybrid DFT Methods: Assessing the Excited States of a Ru(II)Bipyridyl Complex. *J. Chem. Theor. Comput.* **2012**, *8*, 203–213.
- [35] Coe, B. J.; Avramopoulos, A.; Papadopoulos, M. G.; Pierloot, K.; Vancoillie, S.; Reis, H. Theoretical Modelling of Photoswitching of Hyperpolarisabilities in Ruthenium Complexes. *Chem. Eur. J.* **2013**, *19*, 15955–15963.
- [36] Zhang, Y.; Castet, F.; Champagne, B. Theoretical Investigation of the First Hyperpolarizability Redox-Switching in a Ruthenium Complex. *Chem. Phys. Lett.* **2013**, *574*, 42–46.
- [37] Zhang, Y.; Champagne, B. Understanding the Second-Order Nonlinear Optical Properties of One-Dimensional Ruthenium(II) Ammine Complexes. *J. Phys. Chem. C* **2013**, *117*, 1833–1848.
- [38] Escudero, D.; Thiel, W. Assessing the Density Functional Theory-Based Multireference Configuration Interaction (DFT/MRCI) Method for Transition Metal Complexes. *J. Chem.*

Phys. **2014**, *140*, 194105.

- [39] Escudero, D.; Thiel, W.; Champagne, B. Spectroscopic and Second-Order Nonlinear Optical Properties of Ruthenium(II) Complexes: A DFT/MRCI and ADC(2) Study. *Phys. Chem. Chem. Phys.* **2015**, *17*, 18908–18912.
- [40] Zyss, J. Molecular Engineering Implications of Rotational Invariance in Quadratic Nonlinear Optics: From Dipolar to Octupolar Molecules and Materials. *J. Chem. Phys.* **1993**, *98*, 6583–6599.
- [41] Cho, M.; Kim, H.-S.; Jeon, S.-J. An Elementary Description of Nonlinear Optical Properties of Octupolar Molecules: Four-State Model for Guanidinium-Type Molecules. *J. Chem. Phys.* **1998**, *108*, 7114–7120.
- [42] Bersohn, R.; Pao, Y.-H.; Frisch, H. L. Double-Quantum Light Scattering by Molecules. *J. Chem. Phys.* **1966**, *45*, 3184–3198.
- [43] Andrews, D. L.; Allcock, P. *Optical Harmonics in Molecular Systems*; Wiley-VCH: Weinheim, 2002; OCLC: ocm48468465.
- [44] Beaujean, P.; Champagne, B. Coupled Cluster Evaluation of the Second and Third Harmonic Scattering Responses of Small Molecules. *Theor. Chem. Acc.* **2018**, *137*, 50.
- [45] Frisch, M. J. et al. Gaussian 16 Revision A.03. 2016; Gaussian Inc. Wallingford CT.
- [46] Groom, C. R.; Bruno, I. J.; Lightfoot, M. P.; Ward, S. C. The Cambridge Structural Database. *Acta Crystallogr. B* **2016**, *72*, 171–179.
- [47] Shin, Y.-g. K.; Szalda, D. J.; Brunschwig, B. S.; Creutz, C.; Sutin, N. Electronic and Molecular Structures of Pentaammineruthenium Pyridine and Benzonitrile Complexes as a Function of Oxidation State. *Inorg. Chem.* **1997**, *36*, 3190–3197.
- [48] Perdew, J. P.; Wang, Y. Accurate and Simple Analytic Representation of the Electron-Gas Correlation Energy. *Phys. Rev. B* **1992**, *45*, 13244–13249.
- [49] Hay, P. J.; Wadt, W. R. Ab Initio Effective Core Potentials for Molecular Calculations. Potentials for K to Au Including the Outermost Core Orbitals. *J. Chem. Phys.* **1985**, *82*, 299–310.
- [50] Roy, L. E.; Hay, P. J.; Martin, R. L. Revised Basis Sets for the LANL Effective Core Potentials. *J. Chem. Theory Comput.* **2008**, *4*, 1029–1031.
- [51] Colwell, S. M.; Murray, C. W.; Handy, N. C.; Amos, R. D. The Determination of Hyperpolarisabilities Using Density Functional Theory. *Chem. Phys. Lett.* **1993**, *210*, 261–268.
- [52] Lee, A. M.; Colwell, S. M. The Determination of Hyperpolarizabilities Using Density Functional Theory with Nonlocal Functionals. *J. Chem. Phys.* **1994**, *101*, 9704–9709.
- [53] van Gisbergen, S. J. A.; Snijders, J. G.; Baerends, E. J. Accurate Density Functional Calculations on Frequency-Dependent Hyperpolarizabilities of Small Molecules. *J. Chem.*

Phys. **1998**, *109*, 10657–10668.

- [54] Ehlers, A. W.; Böhme, M.; Dapprich, S.; Gobbi, A.; Höllwarth, A.; Jonas, V.; Köhler, K. F.; Stegmann, R.; Veldkamp, A.; Frenking, G. A Set of F-Polarization Functions for Pseudo-Potential Basis Sets of the Transition Metals ScCu, YAg and LaAu. *Chem. Phys. Lett.* **1993**, *208*, 111–114.
- [55] Richardson, L. F.; Gaunt, J. A. The Deferred Approach to the Limit. Part I. Single Lattice. Part II. Interpenetrating Lattices. *Philos. Trans. R. Soc. Lond. A* **1927**, *226*, 299–361.
- [56] Bloor, J. E. Finite Field Ab Initio Calculations of the Dipole Polarizabilities and First and Second Hyperpolarizabilities Using Multiple Sets of Polarization Funct. *Comput. Theor. Chem.* **1991**, *234*, 173–183.
- [57] Mohammed, A. A. K.; Limacher, P. A.; Champagne, B. Finding Optimal Finite Field Strengths Allowing for a Maximum of Precision in the Calculation of Polarizabilities and Hyperpolarizabilities. *J. Comput. Chem.* **2013**, *34*, 1497–1507.
- [58] de Wergifosse, M.; Liégeois, V.; Champagne, B. Evaluation of the Molecular Static and Dynamic First Hyperpolarizabilities. *Int. J. Quantum Chem.* **2014**, *114*, 900–910.
- [59] Iikura, H.; Tsuneda, T.; Yanai, T.; Hirao, K. A Long-Range Correction Scheme for Generalized-Gradient-Approximation Exchange Functionals. *J. Chem. Phys.* **2001**, *115*, 3540–3544.
- [60] Corozzi, A.; Mennucci, B.; Cammi, R.; Tomasi, J. Structure versus Solvent Effects on Nonlinear Optical Properties of Push-Pull Systems: A Quantum-Mechanical Study Based on a Polarizable Continuum Model. *J. Phys. Chem. A* **2009**, *113*, 14774–14784.
- [61] Cammi, R.; Cossi, M.; Mennucci, B.; Tomasi, J. Analytical Hartree–Fock Calculation of the Dynamical Polarizabilities α , β , and γ of Molecules in Solution. *J. Chem. Phys.* **1996**, *105*, 10556–10564.
- [62] Tomasi, J.; Mennucci, B.; Cancès, E. The IEF Version of the PCM Solvation Method: An Overview of a New Method Addressed to Study Molecular Solutes at the QM Ab Initio Level. *Comput. Theor. Chem.* **1999**, *464*, 211–226.
- [63] Jacquemin, D.; Bahers, T. L.; Adamo, C.; Ciofini, I. What Is the “Best” Atomic Charge Model to Describe through-Space Charge-Transfer Excitations? *Phys. Chem. Chem. Phys.* **2012**, *14*, 5383.
- [64] Yang, M.; Champagne, B. Large Off-Diagonal Contribution to the Second-Order Optical Nonlinearities of Λ -Shaped Molecules. *J. Phys. Chem. A* **2003**, *107*, 3942–3951.
- [65] Blanchard-Desce, M.; Barzoukas, M. Two-Form Two-State Analysis of Polarizabilities of Push Pull Molecules. *J. Opt. Soc. Am. B* **1998**, *15*, 302.
- [66] Cho, M.; An, S.-Y.; Lee, H.; Ledoux, I.; Zyss, J. Nonlinear Optical Properties of Tetrahedral Donor– Acceptor Octupolar Molecules: Effective Five-State Model Approach. *J. Chem.*

Phys. **2002**, *116*, 9165–9173.

- [67] Orr, B.; Ward, J. Perturbation Theory of the Non-Linear Optical Polarization of an Isolated System. *Mol. Phys.* **1971**, *20*, 513–526.
- [68] Ipatov, A.; Cordova, F.; Doriol, L. J.; Casida, M. E. Excited-State Spin-Contamination in Time-Dependent Density-Functional Theory for Molecules with Open-Shell Ground States. *Comput. Theor. Chem.* **2009**, *914*, 60–73.
- [69] Myneni, H.; Casida, M. E. On the Calculation of $\Delta\langle S^2 \rangle$ for Electronic Excitations in Time-Dependent Density-Functional Theory. *Comput. Phys. Commun.* **2017**, *213*, 72–91.

Multi-state nonlinear optical switches: a quantum chemical investigation of compounds bearing two identical multi-addressable benzazolo-oxazolidine units

J. Phys. Chem. B **2021**, 125, 3918 (DOI: 10.1021/acs.jpcc.1c01962)

Jean Quertinmont[†], Pierre Beaujean[†], Julien Stiennon[†], Youssef Aidibi[‡], Philippe Leriche[‡],
Vincent Rodriguez[§], Lionel Sanguinet[‡], and Benoît Champagne[†]

[†]*Laboratory of Theoretical Chemistry, Namur Institute of Structured Matter,
University of Namur, Rue de Bruxelles 61, B-5000 Namur, Belgium*

[‡]*MOLTECH-Anjou (CNRS-UMR 6200),
Université d'Angers, F-49045 Angers, France*

[§]*Institut des Sciences Moléculaires (ISM, UMR CNRS 5255),
Université de Bordeaux, 351 cours de la Libération, F-33405 Talence, France*

Abstract

Molecular switches are chemical compounds exhibiting the possibility of reversible transformations between their different forms accompanied by a modification in their properties. Among these, switching of multi-addressable Benzazolo-OXazolidines (BOXs) from a closed form to an open form results in drastic modifications in their linear and non-linear optical properties. Here, we target molecules containing two identical BOX units

(diBOX) connected by different π -conjugated linkers, and we combine synthesis, UV/visible absorption, and hyper-Rayleigh scattering (HRS) measurements, together with density functional theory (DFT) calculations. Three derivatives have been considered, which differ by the linker: i) a bithiophene moiety (Bt), ii) two 3,4-ethylenedioxythiophene (EDOT) units, and iii) a triad composed of an EDOT-thiophene-EDOT sequence (TtO). As a matter of fact, these systems can adopt three states (**CF-CF**, **POF-POF**, and **CF-POF**) depending on the closed form (CF) or the protonated open form (POF) of each BOX unit. Despite chemical equivalence, stepwise switching of such systems under the addition of a chemical acid or an oxidant has been experimentally evidenced for two of them (**diBOX-Bt** and **diBOX-TtO**). Then, DFT calculations show that the first BOX opening leads to the formation of a push-pull π -conjugated segment, exhibiting a huge increase in the first hyperpolarizability (β) and a bathochromic shift with respect to the fully closed form. On the contrary, the second BOX opening induces not only a slight bathochromic shift but also a reduction in their β values conferring the great and uncommon abilities to modulate their linear and nonlinear properties over three discrete levels. Among these results, those on **diBOX-Bt** agree with the experimental data obtained by HRS measurements and further shed light on their structure-property relationship.

► Supporting information are available at <https://doi.org/10.1021/acs.jpcb.1c01962>.

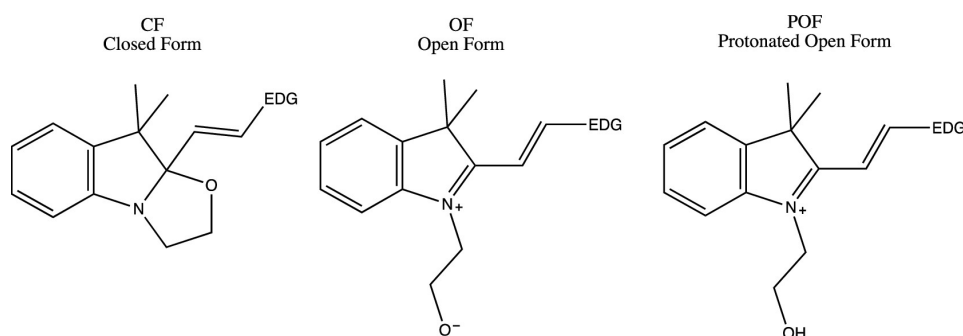
Section 8.1

Introduction

Molecular switches constitute a class of compounds that can undergo, under an external stimulation, reversible transformations between at least two metastable states.^{1–4} Due to a change of structure, this switching results in a variation of the molecular properties where the modification of the absorption spectrum, and therefore the color, is certainly one of the most noticeable phenomenon. These color changing systems are generally classified as a function of the nature of the stimulation. Halochromism (also referenced as acidochromism)⁵ defining a color change with the pH is certainly the most widespread with applications such as pH indicators. Nevertheless, many other chromisms phenomena have been reported so far: thermochromism (temperature), photochromism (light irradiation), electrochromism (electrical potential), solvatochromism (solute-solvent interactions), and piezochromism (pressure) to name a few.⁶

These molecular property changes go beyond the absorption spectrum. They can also encompass motion,⁷ change of emission (fluorescence, phosphorescence)⁸ like in fluorescent proteins, variation of the nonlinear optical responses,^{9–11} and modifications of the reactivity.

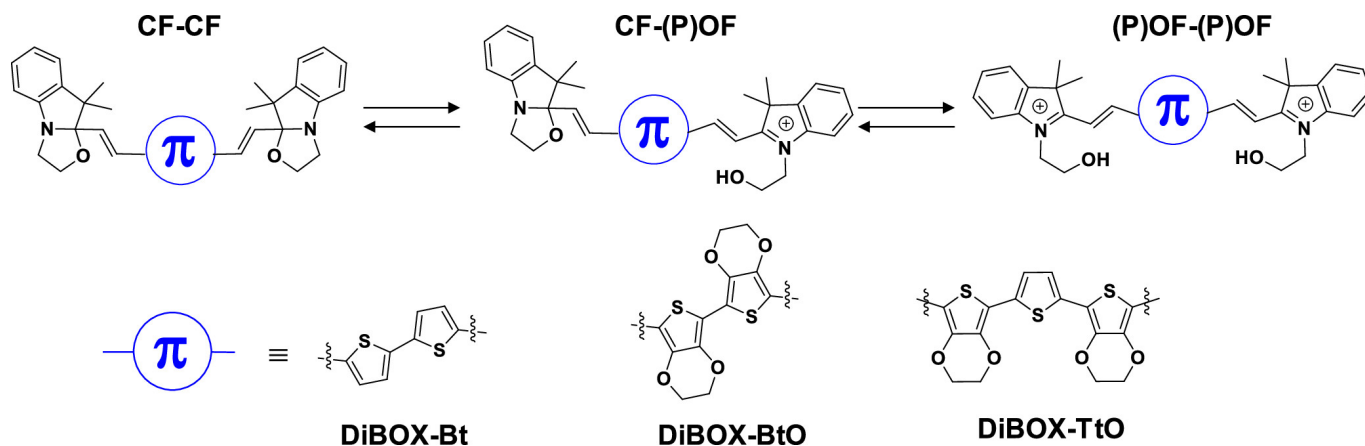
Since the last decades, we and others are interested in the modulation of the quadratic hyperpolarizabilities where molecular systems based on Benzazolo-OXazolidines switchable unit (abbreviated BOX's) have demonstrated remarkable abilities.^{12,13} Under stimulation, the oxazolidine ring opening leads to the formation of an indoleninium unit, which acts as strong electron withdrawing group (EWG). Combined with an electron-donating group (EDG) through a π -conjugated bridge, the open form of BOX's behaves as a push-pull system providing a drastic enhancement of the first hyperpolarizability (β) and leading to observed high β contrasts between the closed and open forms (Scheme 8.1). Systems incorporating a BOX unit can switch between two discrete levels, generally referenced as ON and OFF states. Their efficiency (the β contrast) can be maximized by appropriately selecting the EDG and the substituents on the EWG.¹⁴



Scheme 8.1: BOX in its three different forms: CF, OF, and POF. EDG stands for an aromatic fragment with electron donating character, which could bear different types of substituents.

Interestingly, the opening of the oxazolidine ring can be induced by using different kinds of stimulation conferring to BOX's some photo-, electro-, and acido-chromic properties.¹⁵ If the protonation leads directly to the formation of the positively-charged Protonated Open Form (POF), UV light irradiation leads to the formation of the meta-stable zwitterionic Open Form (OF) through cleavage of the C-O bond. In protic media, this later is able to capture a proton and readily converted in POF form. Noticeably, for a given BOX, both open forms (OF and POF) do not display any difference in their UV/Vis absorption spectra, leading to the conclusion that the state of protonation on the O atom negligibly affects the electronic properties of the molecule. From another point of view, the first excitation energy is not affected by the protonation of the open BOX.^{16,17} As consequence, regeneration of the Closed Form (CF) is generally obtained by treatment with a base or, more rarely, by irradiation with visible light. Aside from photochromism and acidochromism, the BOX's electrochemical properties were investigated more lately.¹⁸ Additionally to direct oxidation, the oxazolidine ring opening under an electrochemical potential can be obtained by an electromediated process when the BOX unit is associated to a bithiophene moiety as EDG. The latter is known to form stable radical cation and enhances the electrochemical properties of the BOX.^{14,19} In that case, the assumed mechanism for the opening by oxidation is the following: i) the oxidation occurs on the bithiophene, leading to the formation of a radical-cation species, ii) the radical is delocalized to the BOX, before iii) the homolytic cleavage of the C-O bond occurs, and then, iv) the POF is formed.¹⁵

To modulate a molecular property over more than two discrete levels, one strategy consists of building units that can switch between more than two states, like dinitrobenzylpyridine²⁰ and oxazines.²¹ In another approach leading to the formation of multi-state molecular switches several switching units are combined. So, a system combining n different two-state molecular switches displays 2^n different forms, each one possessing its own properties. An illustration is given by the system built from the following three different units: a BOX, a diarylethene, and an alkene linker (which can display two conformations: *cis* and *trans*), leading to an octa-state molecular switch.²²⁻²⁵ However, in that case, the different reactions of switching can be in competition and may lead to difficulties in controlling one or more forms of the molecular switch, especially if the reactions of photoisomerization are achieved in similar conditions. This is particularly true when the different molecular switches are chemically close to each other. Nevertheless, we have recently demonstrated that a stepwise opening selectivity between two identical BOX units is reachable when they are grafted on a same π -conjugated core.^{26,27} If such systems did not obey to the classical " 2^n states" rule, they are able to commute between three different states (**CF-CF**, **CF-POF**, and **POF-POF**) (Scheme 8.2). As we assessed in this work, from one state to the others, the successive openings of the oxazolidine rings must induce drastic changes in the molecular electronic structures, leading to the first compounds possessing two identical BOX units able to modulate their NLO properties over three discrete levels.



Scheme 8.2: Different Levels of Opening of Molecular Switches Combining Two BOX Units, Linked Together by a π -Conjugated Bridge (Top) and the Nature of These Linkers in **diBOX-Bt**, **diBOX-BtO**, and **diBOX-TtO** Compounds (Bottom)

Within this context, molecular switches containing two identical BOX units (referenced as diBOX's) rise several questions: i) since the different BOX's are chemically equivalent, is it possible to control the level of opening of these molecules?, ii) does the chemical nature of the linker affect the selectivity of the successive openings?, and iii) how does the level of opening of the switch modulate the linear and nonlinear optical properties of these systems? These questions are addressed here by considering three diBOX's, which differ by the linker connecting the BOX units. The linker of the first compound is composed of a Bithiophene (Bt), the second one contains two 3,4-EthyleneDiOxyThiophene (EDOT) units (BtO), and the last one is composed of an EDOT-thiophene-EDOT sequence (called TtO) (Scheme 8.2). In this way, comparison between **diBOX-Bt** and **diBOX-BtO** enables to study the impact of a stronger donating π -linker (BtO) while the comparisons between these and TtO tackles the effects of the linker length and π -electron delocalization. These questions are addressed by adopting a multidisciplinary approach that combines synthesis, experimental characterizations, and quantum chemical calculations. The synthesis of **diBOX-Bt** has already been reported together with the control of its successive openings and their impact on the linear optical properties.²⁶ Depicting the limitation of diBOX system synthesis, we present here the synthesis of **diBOX-TtO** in our effort to extend the series to more donating π cores. Then, in addition to the characterization of the linear and nonlinear optical properties of both compounds under their different opening states, we present a detailed quantum chemical investigation of their structural, electronic, and optical properties. The latter are performed at the density functional theory (DFT) and time-dependent DFT (TDDFT) levels of approximation.

Section 8.2

Methods

UV/vis Absorption and hyper-Rayleigh Scattering Measurements

UV/visible absorption spectra were acquired with a Varian Cary 50 single beam spectrometer with a 0.1 s integration time every 1 nm. Solvent used is commercially available spectroscopic grade acetonitrile without further purification. Quartz cuvettes were used with a 1 cm optical path.

The first hyperpolarizabilities were determined by using a homemade set up. An OPG picosecond laser source (signal: 720-1000 nm, idler: 1150-2200 nm) is used as probing source to adjust the incident energy (ω) to tune the SHS (2ω). A block power, constituted of a half-wave plate and a polarizer, is placed after the source in order to control the incident intensity and deliver linear vertical polarization. This fundamental relative intensity is precisely determined via the measurement of the scattered light intensity by the half-wave plate routed through an optical fiber to a photodiode connected at an oscilloscope. More important, the polarization of the incident beam can be continuously controlled (P, S, left/right circular polarization and all intermediate elliptic polarizations) thanks to the juxtaposition of a half-wave plate and a rotatable quarter-wave plate. This tunability of the incident beam polarization allows to probe different beta tensor components. The scattered light is collected at 90° and analyzed by a spectrograph using CCD detector. The β_{HRS} of each form of **diBOX-Bt** was investigated in acetonitrile solution (varying between 0.25 and 1.0×10^{-4} M) by using the solvent as internal reference.²⁸ An incident excitation wavelength of 1300 nm has been chosen as a good compromise to avoid both absorption of the fundamental beam from acetonitrile in the near-IR range (ω) and absorption of the scattered harmonic beam (2ω) from the diBOX samples. The **CF-POF** and **POF-POF** species were obtained from stimulating the **CF-CF** species by adding 1 and 2 equiv of the chemical oxidant, respectively. Figure S6 gathers all the results and shows the variations of the incoherent scattered light at optical frequency 2ω as a function of the concentration of the chromophore and also of the incident power. Then, Figure S7 shows the extracted polarization curves from the different forms. In the case of **diBOX-TtO**, the β_{HRS} measurements could not be conducted due to too strong two-photon-induced fluorescence that almost fully hampered the HRS response.

Theoretical and Computational Aspects

The geometries of all compounds were fully optimized at the DFT level with the M06 XC functional,²⁹ the 6-311G(d) basis set, and by accounting for solvent effects using the integral equation formalism of the polarizable continuum model (IEF-PCM) (the solvent is acetonitrile).³⁰ Real vibrational frequencies demonstrate the optimized geometries are minima on the

potential energy hyper-surface. Since the diBOX compounds are mostly composed of cyclic units and conjugated segments, the numbers of stable conformers in solution are rather small and the search of those conformers possessing a non-negligible weight within the Maxwell-Boltzmann (MB) statistics can be carried out in a systematic manner. This was done i) by defining the key torsion angles to distinguish the main conformations (Scheme S1), ii) by performing rigid scans to locate the extrema of the potential energy hyper-surface, iii) by combining the minima of the rigid scans to preselect conformations, and iv) then by performing full geometry optimizations. Finally, only those conformers within an energy window of 12.5 kJ mol^{-1} were kept to calculate the MB populations, on the basis of the Gibbs free energies, ΔG^0 at 298.15 K. These results are presented in SI. This approach is efficient to locate the key conformations because the torsion angles are far enough from each other and, in first approximation, their impact on the total energy is considered as independent from each other, leading to a quasi-additive behavior. Note that, contrary to Ref.,²³ the *cis-trans* isomerizations are not considered here. Indeed, as observed in calculations not detailed here, the fraction of the *cis* form is negligible, so that only the *trans* alkene forms are taken into account.

The vertical excitation energies (ΔE_{ge}) and the transition dipole moments (μ_{ge}) were calculated for at least the 10 lowest-energy excited states at the TDDFT level using the M06-2X XC functional,²⁹ and accounting for solvent effects using the IEF-PCM scheme. The μ_{ge} quantities were used to calculate the oscillator strengths ($f_{ge} = 2/3 \Delta E_{ge} \mu_{ge}^2$) and then employed to plot the UV/vis absorption spectra (each transition was associated with a Gaussian function, centered on ΔE_{ge} , of intensity proportional to f_{ge} , and of full width at half maximum of 0.3 eV). The differences of dipole moment between the ground and key excited states, $\Delta\mu_{ge} = \mu_e - \mu_g$, were then evaluated. The calculations of all these excited state-related properties, including μ_e , employ the nonequilibrium solvation approach since electronic excitation processes are very fast with respect to the solvent reorganization.³¹ Nonequilibrium solvation TDDFT calculations were performed to evaluate the difference of electronic density between the ground and excited states, $\Delta\rho(\vec{r}) = \rho_e(\vec{r}) - \rho_g(\vec{r})$. Following the procedure described by Le Bahers et al.,³² the barycenters of the positive [$\Delta\rho^+(\vec{r})$] and negative [$\Delta\rho^-(\vec{r})$] electronic density variations were evaluated. The distance between these barycenters defines the charge-transfer distance (d_{CT}) while their integration over the whole space gives the amount of charge transferred (q_{CT}). The product of these two quantities gives $\Delta\mu_{ge} = q_{CT} \times d_{CT}$.

The β tensor components were calculated using the TDDFT method^{33,34} with the M06-2X XC functional, the 6-311+G(d) basis set, and the IEFPCM scheme to account for solvent effects. Both static and dynamic (for incident wavelengths of 1907, 1300, and 1064 nm) responses were evaluated. In this work, in parallel to the experimental data, we concentrated on the second harmonic generation (SHG) phenomenon, $\beta(-2\omega; \omega, \omega)$, and more precisely on the hyper-Rayleigh scattering (HRS) first hyperpolarizabilities, $\beta_{\text{HRS}}(-2\omega; \omega, \omega)$, and their decompositions.³⁵ For an experimental set-up where the incident light is non-polarized and the vertically polarized (along the Z axis of the laboratory frame) signal scattered at 90° with

respect to the propagation direction (Y axis) is detected, the HRS intensity is proportional to the square of $\beta_{\text{HRS}}(-2\omega; \omega, \omega)$, which depends on two ensemble averages ($\langle \beta_{\text{ZZZ}}^2 \rangle$ and $\langle \beta_{\text{ZXX}}^2 \rangle$) over the molecular orientations:

$$\beta_{\text{HRS}}(-2\omega; \omega, \omega) = \sqrt{\langle \beta_{\text{ZZZ}}^2 \rangle + \langle \beta_{\text{ZXX}}^2 \rangle} = \sqrt{\langle \beta_{\text{ZZZ}}^2 \rangle \left(1 + \frac{1}{\text{DR}}\right)} \quad (8.1)$$

The depolarization ratio DR, which reflects the chromophore shape, is the ratio between the scattered intensities obtained when the incident light is vertically ($\langle \beta_{\text{ZZZ}}^2 \rangle$) and horizontally ($\langle \beta_{\text{ZXX}}^2 \rangle$) polarized, respectively. The relationships between these averages (in the laboratory frame) and the molecular tensor components (in the molecular frame) are available from previous papers.^{28,36}[41,49] In the case of a push-pull π -conjugated system, the β tensor is often dominated by a single diagonal tensor component (namely β_{zzz} so that $\text{DR} = 5$ and $\beta_{\text{HRS}} = \sqrt{6/35}\beta_{\text{zzz}}$). The static β_{HRS} responses were also analyzed in terms of the β irreducible spherical representations,^{37,38} namely $|\beta_{J=1}|$, the dipolar contribution, and $|\beta_{J=3}|$, the octupolar one:

$$\beta_{\text{HRS}}(-2\omega; \omega, \omega) = \sqrt{\frac{10}{45} |\beta_{J=1}|^2 + \frac{10}{105} |\beta_{J=3}|^2} = |\beta_{J=1}| \sqrt{\frac{2}{3} \left(\frac{1}{3} + \frac{1}{7}\rho^2\right)} \quad (8.2)$$

where $\rho = |\beta_{J=3}| / |\beta_{J=1}|$ is the nonlinear anisotropy factor, describing the relative importance of the octupolar contribution with respect to the dipolar one. Note that ρ and DR are related:

$$\text{DR} = 9 \left(\frac{1 + \frac{2}{7}\rho^2}{1 + \frac{12}{7}\rho^2} \right) \quad (8.3)$$

For purely dipolar responses, $\text{DR} = 9$ and $\rho = 0$ whereas for octupolar ones, $\text{DR} = 1.5$ and $\rho = \infty$. For one-dimensional (1D) NLO-phore with a unique dominant diagonal β tensor component, $\text{DR} = 5$ and $\rho = 0.82$.

To visualize the β tensor, the unit sphere representation (USR), initially proposed for the first hyperpolarizability tensor,³⁹ was adopted. It consists i) in computing an effective induced dipole moment (either static or dynamic like the current SHG responses):

$$\vec{\mu}_{\text{ind}} = \overleftrightarrow{\beta} : \vec{E}^2(\theta, \phi) \quad (8.4)$$

where the tensor nature of β has been evidenced and $\vec{E}^2(\theta, \phi)$ is a unit vector of electric field, of which the polarization direction is defined in spherical coordinates by the θ and ϕ angles, and ii) by representing all the induced dipole moment vectors on a sphere centered on the center of mass of the compound. This enables highlighting the directions where the second-order polarization is the strongest (it corresponds to the largest induced dipoles), its orientation (the acceptor-donor direction), and subsequently showing how much the β response is dipolar/octupolar. These USR were plotted using the Drawmol package.⁴⁰ All reported β

values are given in a.u. [1 a.u. of $\beta = 3.6212 \times 10^{-42} \text{ m}^4 \text{ V}^{-1} = 3.2064 \times 10^{-53} \text{ C}^3 \text{ m}^3 \text{ J}^{-2} = 8.639 \times 10^{-33} \text{ esu}$] within the T convention.⁴¹

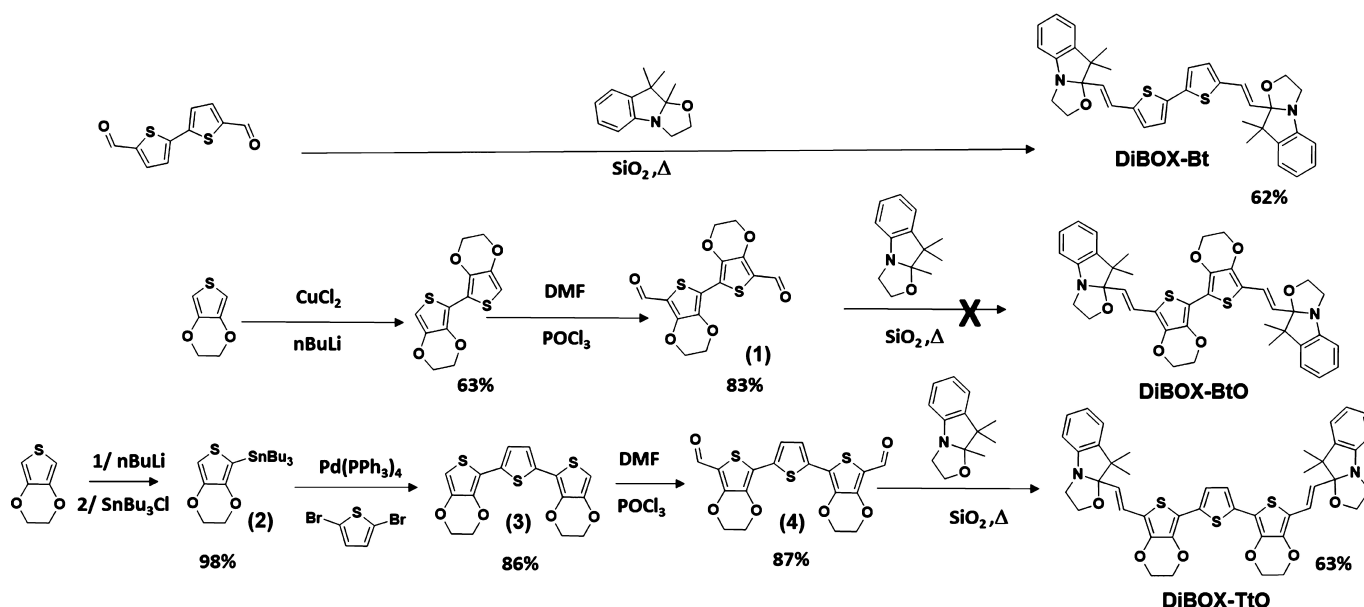
As noted, a different XC functional was used for calculating the linear and nonlinear optical properties (M06-2X, 54 % HF exchange) than the structural and thermodynamic data (M06, 27 % HF exchange). This is consistent with previous studies on related compounds,¹⁴ which show that a larger amount of exact Hartree-Fock (HF) exchange is needed to calculate the optical properties.^{42–46} All (TD)DFT calculations were carried out using the Gaussian16 package.⁴⁷

Section 8.3

Results and Discussion

Synthesis

The preparation of diBOX compounds has already been reported in the literature. The corner stone of most of them is the condensation of an aromatic core bearing two carbonyl functions with trimethylindolino-oxazolidine derivatives. If many experimental conditions have been described to perform such condensation (protic/aprotic solvent, with and without acid/base catalysis, ...) recent solvent-free methodology using silica powder⁴⁸ have demonstrated high efficiency and allowing the preparation of **diBOX-Bt** in good yield.²⁶ In order to



Scheme 8.3: Preparation of three diBOX derivatives by solvent-free silica mediated condensation between trimethyl indolino[2,1-b]oxazolidine and three bis-aldehyde aromatics prepared by Vilsmeier-Haack reaction according to reported procedures.

prepare **diBOX-BtO** we have synthesized 5,5'-dicarbaldehyde-2,2'-bis-EDOT (**1**) according to already-reported procedures,⁴⁹ but the replacement of thiophene by EDOT moieties comes

with a drop of the solubility of the corresponding bis-aldehyde. Due to this lack of stability, it was impossible to carry out its condensation with 2,3,3-trimethylindolino[2,1,b]oxazolidine in classical conditions. Unfortunately, all our attempts to circumvent this problem by changing either the experimental condition or our synthetic strategy to prepare **diBOX-BtO** have been up to now unsuccessful. Starting from this, a thiophene was introduced between both EDOT units in order to improve the solubility. A Stille coupling performed on 2,5-dibromothiophene⁵⁰ followed by a classical Vilsmeier-Haack reaction allowed to prepare 2,5-di(5'-carbaldehyde-EDOT)thiophene (**4**). Exhibiting a better solubility than **2**, its condensation with 2,3,3-trimethylindolino[2,1,b]oxazolidine leading to **diBOX-TtO** did not raise any particular problem. Noticeably, it should be mentioned that the higher donor ability of this π -conjugated core, compared to bithiophene, impacts the reaction efficiency as the time of the reaction has to be increased of up to 7 hours in order to reach similar yield. All syntheses are resumed below in Scheme 8.3. More details are provided in the Supporting Information.

Geometrical Structures

The linear and nonlinear optical properties of chromophores can often be analyzed in light of their π -electron conjugation, characterized by simple geometrical quantities, the bond length alternation (BLA), and the torsion or dihedral angles of the π -conjugated segment. Therefore, the geometries of all compounds were fully optimized at the IEF-PCM (acetonitrile)/M06/6-311G(d) level of approximation. For each diBOX and each of their three states, Supporting Information provide a summary of the key geometrical parameters (torsion angles and bond length alternations (BLA's)) of the most stable conformers, their relative Gibbs free enthalpies (ΔG^0) and their populations with Maxwell-Boltzmann (MB) approach, and a brief analysis of the optimal torsion angles between the aromatic moieties (Scheme S1, Tables S1-S9). To better describe the π -conjugated segments, instead of one, two types of BLA's were considered: a "global" BLA, taken from one BOX to the other one (noted *BLA*) and "local" BLA's, measured individually on each vinylene bridge (Scheme S1) and denoted *BLA'* and *BLA''*. For **CF-POF**, the two local BLA's are noted *BLA'* when associated with the vinylene on the CF while *BLA''* with the POF side. The global BLA values decrease upon the successive openings (Table 8.1):

$$BLA[\text{POF-POF}] < BLA[\text{CF-POF}] < BLA[\text{CF-CF}]$$

while for the local *BLA'* and *BLA''* the following trend is observed:

$$BLA''[\text{CF-POF}] < BLA''[\text{POF-POF}] \ll BLA'[\text{CF-CF}] < BLA''[\text{CF-POF}]$$

Two trends are evidenced. First, the presence of indoleninium moieties, which corresponds to the transformation of a sp^3 C atom into a sp^2 one, increases the general π -electron delocalization (expressed by a smaller BLA's). Therefore, a decrease of the excitation energies

is expected to come alongside the successive openings. In parallel, opening a BOX strongly reduces the local BLA values ($BLA'' \ll BLA'$) due to the better π -electron delocalization. Noticeably, this transformation of only one BOX unit has an impact on the electron delocalization of both vinylene bridges, as evidenced by a slight increase of the BLA' between **CF-CF** and **CF-POF** forms. Surprisingly, the second BOX opening has antagonistic effects because smaller global BLA values are associated with larger BLA'' for state **POF-POF** than **CF-POF**. These results seem to indicate that the indoleninium-linker delocalization is the strongest when only one BOX is open.

As observed with the status of the BOX unit, BLA' values are less affected by the nature of the linker, since all BLA' range between 0.132 Å to 0.139 Å. On the other hand, the BLA'' values depend on the nature of the linker: the BLA'' becomes smaller when the thiophenes are substituted by EDOT. This is due to the ether functions of the EDOT, which enhance the delocalization between the linker and the indoleninium(s) by strengthening the donor character of the linker.^{51,52} For the diBOX's in **POF-POF**, the length of the linker has an additional effect on the BLA'' , it is smaller for **diBOX-TtO** than **diBOX-BtO** (0.026 Å vs 0.035 Å). This BLA analysis — as well as the differences between the global and local BLA's — find its roots in the way the successive CF openings impact the C–C bond lengths from one BOX to the other (Figure S1). The presence of indoleninium moieties in the π -conjugated system results in a better delocalization, leading to a decrease of BLA . When induced by a single BOX in POF, this delocalization attenuates after one aromatic ring. This delocalization is the strongest for the diBOX's in **CF-POF**, with a stronger weight of the quinoïdal form. This effect is then further enhanced by the substitution of a thiophene by an EDOT, as illustrated by the variation of

Table 8.1: BLA's values (in Å) for the diBOX's in their different forms as evaluated from geometry optimizations at the M06/6-311G(d)/IEF-PCM (acetonitrile) level of approximation. These values are averaged over the MB distributions, using the data from Tables S1-S9.

		diBOX-Bt	diBOX-BtO	diBOX-TtO
CF-CF	BLA^a	0.081	0.079	0.072
	BLA'	0.136	0.133	0.133
CF-POF	BLA	0.048	0.041	0.042
	BLA'	0.139	0.136	0.135
	BLA''	0.032	0.013	0.015
POF-POF	BLA	0.032	0.026	0.024
	BLA''	0.049	0.035	0.026

^a all BLA values being negative, their absolute values are reported.

BLA'' .

UV/Visible Absorption Spectra and Related Properties

Recording the experimental UV/vis absorption spectra upon stimulation represents certainly the easiest way to monitor the switching abilities of **diBOX-Bt** and **diBOX-TtO**. As a multi-modal switch, acid or chemical oxidant (generally NOSbF_6) aliquots can be generally used in such purpose. However, stimulation by acid is known to be less selective for switching the diBOX system, leading to the coexistence of its three different states. As already performed for **diBOX-Bt**,^{18,19,24} the electrochromic behavior of **diBOX-TtO** was checked by spectroelectrochemistry experiments (Figure S3), confirming the reversible opening/closing of BOX units under application of an electrochemical potential (at 0.35 and -0.95 V vs Fc/Fc^+ , respectively). More conveniently, the titration of **diBOX-Bt** and **diBOX-TtO** with NOSbF_6 was monitored by UV/vis spectroscopy (see Methods section for more details). Figures 8.1 and 8.2 (with more details in Figures S4 and S5) show that the switching abilities of the diBOX are not affected by the nature of the π -conjugated linker. As already reported for **diBOX-Bt**, a stepwise transformation of **diBOX-TtO** is observed under electrochemical stimulation leading successively to the **CF-POF**, then **POF-POF** form from the **CF-CF** form. In both cases, the first BOX opening induces a huge bathochromic shift of the absorption maxima wavelength (151 and 218 nm (corresponding to 0.94 and 0.98 eV) for **diBOX-Bt** and **diBOX-TtO**, respectively, Table 8.2). On the contrary, the second BOX opening induces only a moderate variation of the absorption maxima wavelength (17 and 20 nm (0.07 and 0.06 eV) for **diBOX-Bt** and **diBOX-TtO**, respectively). This stepwise switching under external stimulation is translated by an irregular evolution of the UV/vis spectra along the titration with acid or oxidant aliquots. Such as presented for electrochemical stimulation (Figures 8.1 and 8.2), below one equivalent two isosbestic points are noticed in each case (321/427 and 368/476 nm for **diBOX-Bt** and **diBOX-TtO**, respectively). When the stimulation is pushed further, an enhancement of the coloration is observed and, more important, this increment did not allow maintaining the observation of the previous isosbestic points which are replaced by new ones (326 and 358/464 nm for **diBOX-Bt** and **diBOX-TtO**, respectively).

Turning now to the QC calculations, using the populations given in Supporting Information, the weighted averages of the excitation energies were evaluated at the M06-2X/6-311+G(d)/IEF-PCM (acetonitrile) level of approximation. The oscillator strengths were calculated with the objective of simulating the UV/Vis absorption spectra (Table 8.2). The charge-transfer character of the first dominant excitation are also listed. These quantities are indeed often useful to interpret the dominant diagonal (in the following expression, along the z axis) first hyperpolarizability tensor components within the two-state approximation (TSA)⁵³

$$\beta_{zzz} = 9 \frac{f_{ge} \Delta\mu_{ge}}{\Delta E_{ge}^3} \quad (8.5)$$

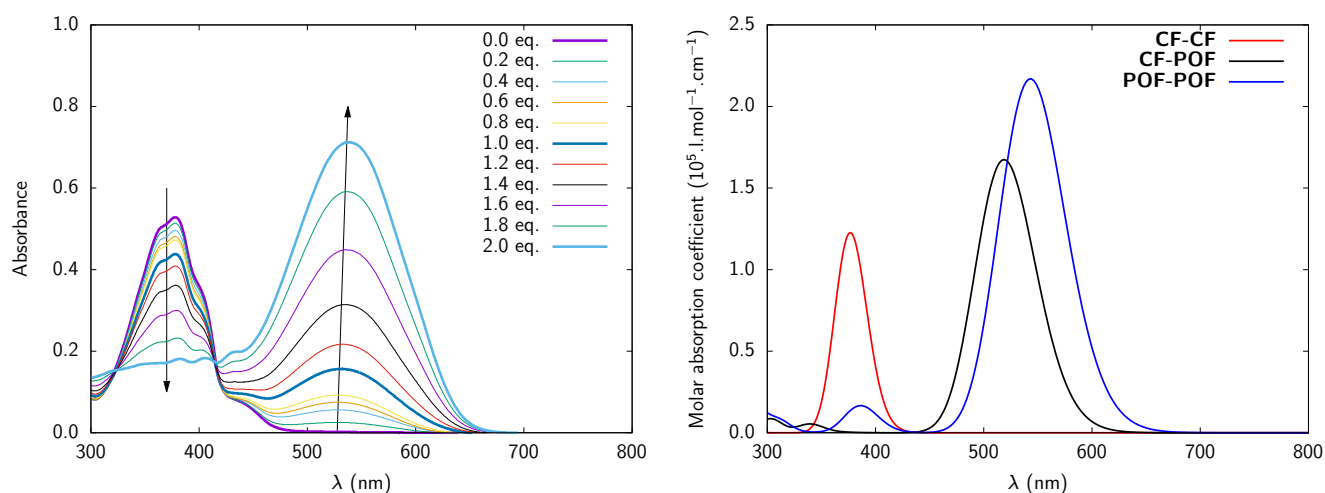


Figure 8.1: Experimental (left) and simulated (right) UV/vis absorption spectra of **diBOX-Bt**. The experimental ones are obtained in acetonitrile (0.086 M) along a titration with NOSbF_6 as chemical oxidant. The simulated spectra are given for three different forms (red: **CF-CF**, black: **CF-POF** and blue: **POF-POF**) using the weighted average results as calculated at the M06-2X/6-311+G(d)/IEF-PCM (acetonitrile) level of theory.

As a matter of fact, large β responses can be achieved by 1) a low ΔE_{ge} , 2) a strong absorbance (large oscillator strength, f_{ge}), and, 3) a large variation of the dipole moment ($\Delta\mu_{ge}$) between the ground and that excited state.

The low-excitation energy peak in the UV/Vis spectrum is attributed to a $S_0 \rightarrow S_1$ excitation since the contributions of the other excitation bands are negligible. We can notice a good agreement between the experimental maximum wavelengths of absorption and the calculated vertical excitation wavelengths of this first transition (Table 8.2, Figures 8.1 and 8.2). This substantiates the selection of the M06-2X XC functional for the investigation of the linear optical properties of these systems as a function of the nature of the π -conjugated linker. Numerical simulations confirm that the global evolution of the linear optical properties as a function of the level of opening are not affected by the nature of the linker. In each case, a bathochromic shift accompanies the successive openings (Figures 8.1 and 8.2). This shift is more important for the first opening (0.74-0.90 eV) than for the second (0.11-0.23 eV). Still, the value of ΔE_{ge} is strongly influenced by the nature of the linker. By increasing the electron donor character of the π -conjugated linker (*vide supra*), it seems possible to reduce ΔE_{ge} and, as consequence, generates higher dominant diagonal first hyperpolarizability tensor components. As consequence, the substitution of thiophene(s) by EDOT(s) moieties and the enhancement of the linker length results in the smallest ΔE_{ge} values for **diBOX-TtO** regardless of the considered form, while **diBOX-BtO** presents values in-between the two other compounds.

For the second key parameter in order to reach larger β responses, the evolution of the oscillator strength of the **diBOX**'s is mainly affected by the successive **BOX** openings but also by the nature of the π -conjugated linker. Indeed, f_{ge} increases by about the same amount

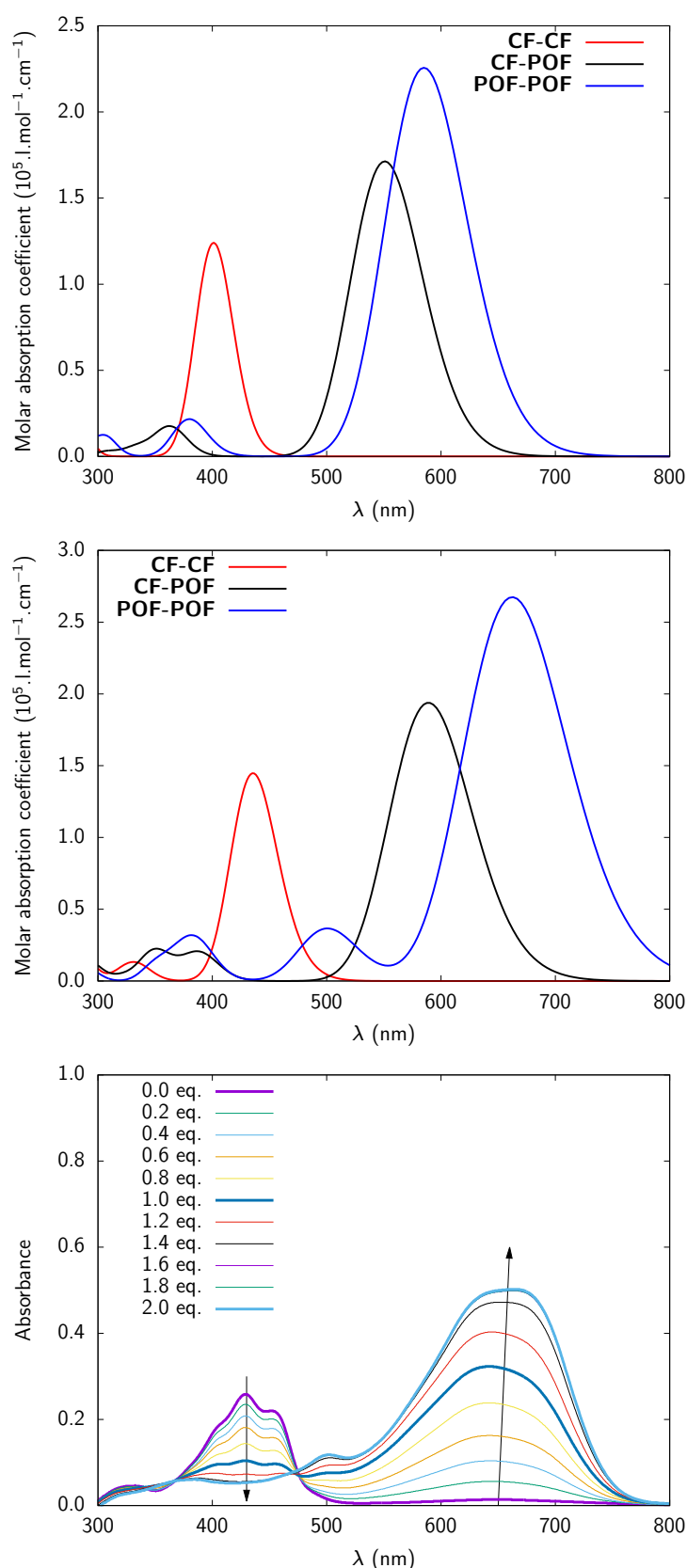


Figure 8.2: Simulated (top) UV/vis absorption spectra of **diBOX-BtO** and comparison between the simulated (middle) and experimental (bottom) UV/vis absorption spectra of **diBOX-TtO**. The simulated spectra are given for three different forms (red: **CF-CF**, black: **CF-POF** and blue: **POF-POF**) using the weighted average results as calculated at the M06-2X/6-311+G(d)/IEF-PCM (acetonitrile) level of theory. The experimental ones are obtained in acetonitrile (0.06 M) along a titration with NOSbF_6 as chemical oxidant.

(~ 0.40 - 0.60) after each oxazolidine ring opening. For a given form, the absorbance does not vary much between **diBOX-Bt** and **diBOX-BtO**. On the contrary, the length of the linker affects the oscillator strength: **diBOX-TtO** possesses the largest f_{ge} values (~ 0.30 higher than **diBOX-Bt** and **diBOX-BtO**).

Then, achieving large β responses requires a large variation of the dipole moment ($\Delta\mu_{ge}$) between the ground and excited states. This third parameter can be expressed as the product of the charge-transfer associated with the (first) excitation, q_{CT} , by its distance d_{CT} . Concerning q_{CT} the following trend is observed for the three molecules:

$$q_{CT}[\text{CF-CF}] < q_{CT}[\text{POF-POF}] < q_{CT}[\text{CF-POF}]$$

$q_{CT}[\text{CF-CF}]$ and $q_{CT}[\text{CF-POF}]$ do not vary much between the different compounds, between $0.38 e$ and $0.41 e$, and between $0.49 e$ and $0.56 e$, respectively. Obviously, the $q_{CT}[\text{CF-POF}]$ values depend on the nature of the linker and follows the evolution of electron donor ability of the π -conjugated linker (**diBOX-BtO**: 0.49 , **diBOX-Bt**: $0.55 e$, and **diBOX-TtO**: $0.60 e$). Concerning the distance of charge transfer, its evolution is specific to the degree of opening and it depends on the nature of the linker. For **diBOX-Bt**, one observes:

$$d_{CT}[\text{CF-CF}] < d_{CT}[\text{POF-POF}] \ll d_{CT}[\text{CF-POF}]$$

Table 8.2: Experimental (maximum absorption) wavelengths (λ_{exp} , nm), computed (vertical) excitation wavelengths (λ_{ge} , nm), excitation energies (ΔE_{ge} , eV), oscillator strengths (f_{ge}), amounts of charge transfer (q_{CT} , e), distances of charge transfer (d_{CT} , Å), and variations of dipole moment ($\Delta\mu_{ge}$, D) associated with the $S_0 \rightarrow S_1$ excitation of the three diBOX's in their different forms, as evaluated at the M06-2X/6-311+G(d)/IEF-PCM (acetonitrile) level of approximation. The averages are weighted using the populations of conformers at 298.15 K.

		λ_{exp}	λ_{ge}	ΔE_{ge}	f_{ge}	q_{CT}	d_{CT}	$\Delta\mu_{ge}$
diBOX-Bt	CF-CF	375 ^a	377	3.29	1.39	0.395	0.090	0.176
	CF-POF	530 ^a	519	2.39	1.87	0.550	3.287	8.697
	POF-POF	545 ^a	543	2.28	2.43	0.494	0.182	0.433
diBOX-BtO	CF-CF		401	3.09	1.38	0.384	0.022	0.040
	CF-POF		551	2.25	1.91	0.498	2.546	6.098
	POF-POF		585	2.12	2.55	0.490	0.020	0.046
diBOX-TtO	CF-CF	428	437	2.84	1.70	0.410	0.425	0.840
	CF-POF	646	589	2.10	2.16	0.601	4.137	11.945
	POF-POF	666	662	1.87	2.98	0.563	0.222	0.600

^a From Ref. 26.

while for **diBOX-BtO**:

$$d_{CT}[\text{POF-POF}] \sim d_{CT}[\text{CF-CF}] \ll d_{CT}[\text{CF-POF}]$$

and **diBOX-TtO**:

$$d_{CT}[\text{POF-POF}] < d_{CT}[\text{CF-CF}] \ll d_{CT}[\text{CF-POF}].$$

For the three compounds, the **CF-POF** form displays a large d_{CT} , owing to its push-pull π -conjugated character and the CT character of the lowest-energy excitation. Since $\Delta\mu_{ge}$ is the product of q_{CT} by d_{CT} , and since d_{CT} is more affected by the level of opening than q_{CT} , the variations of $\Delta\mu_{ge}$ follow those of d_{CT} . The variations of the amplitude of charge transfer between the different diBOX and the different forms can be rationalized in terms of the topology of the molecular orbitals implied in the first excitation (Figure 8.3). For all structures, the first excitation corresponds mostly to a HOMO to LUMO electronic transition. Both frontier orbitals are quite delocalized over the π -conjugated system. For the **CF-CF** form, these orbitals are distributed symmetrically on the linker. For the other symmetric form (**POF-POF**), their distributions extend towards the indoleninium groups, in particular for the HOMO. Finally, for the **CF-POF** form, the distributions are a mixed of those of the symmetric forms. Subsequently, the variations of electron density also spread over the molecule (Figure 8.4), with alternant positive and negative regions but globally, the electronic charge goes from the linker to the oxazolidine, especially when it is open.

Note that for diBOX's in **CF-CF** and **POF-POF**, d_{CT} depends on the conformation of the linker. Indeed, the conformation affects the symmetry of the molecule and modulates the amplitude of d_{CT} . This is particularly true for **diBOX-Bt**, where the bithiophene linker can adopt both *syn* and *anti* conformations. The *anti* conformation corresponds to a centrosymmetric structure, resulting in a $\Delta\mu_{ge}$ close to zero. On the other hand, the *syn* conformation leads to a structure displaying a C_{2v} -like symmetry. As a result, switching from the *anti* to the *syn* conformation of the bithiophene (θ_3 : $180^\circ \rightarrow 0^\circ$) results in an increase of the amplitude of $\Delta\mu_{ge}$ (Tables S10 and S12). This effect is further enhanced by the $0^\circ \rightarrow 180^\circ$ switching of the θ_2 - θ_4 torsion angles. It corresponds to a $\Delta\mu_{ge}$ increase from 0.056 D to 0.451 D for **CF-CF** and from 0.002 D to 1.379 D for **POF-POF**. Furthermore, the change of conformation of **diBOX-Bt** from *anti* to *syn* in **CF-CF** and **POF-POF** is associated with a reduction of the intensity of the $S_0 \rightarrow S_1$ absorption. For **CF-CF**, the f_{ge} value associated with the $S_0 \rightarrow S_1$ excitation decreases from ~ 1.35 - 1.45 to ~ 1.15 - 1.20 , while f_{ge} of $S_0 \rightarrow S_2$ is ~ 0.30 - 0.40 when the bithiophene adopts a *syn* conformation. For **POF-POF**, the θ_2 - θ_4 torsion angles impact also f_{ge} of the two first excitations. For the second excitation, conformer 6 (θ_2 and θ_4 : *s-cis*) has $f_{ge} = 0.12$, conformer 4 (θ_2 : *s-trans* and θ_2 : *s-cis*) has $f_{ge} = 0.39$ and conformer 2 (θ_2 and θ_4 : *s-trans*) has $f_{ge} = 0.77$. For the form with the largest oscillator strength associated with the second excitation (**POF-POF-2**), this excitation was further analyzed. ΔE_{ge} is larger than the first excitation (3.22 eV vs 2.28 eV), the oscillator strength is relatively weak (0.77 vs 2.42), still its $\Delta\mu_{ge}$ is relatively high for this considered conformer (0.62 D), but its contribution to the

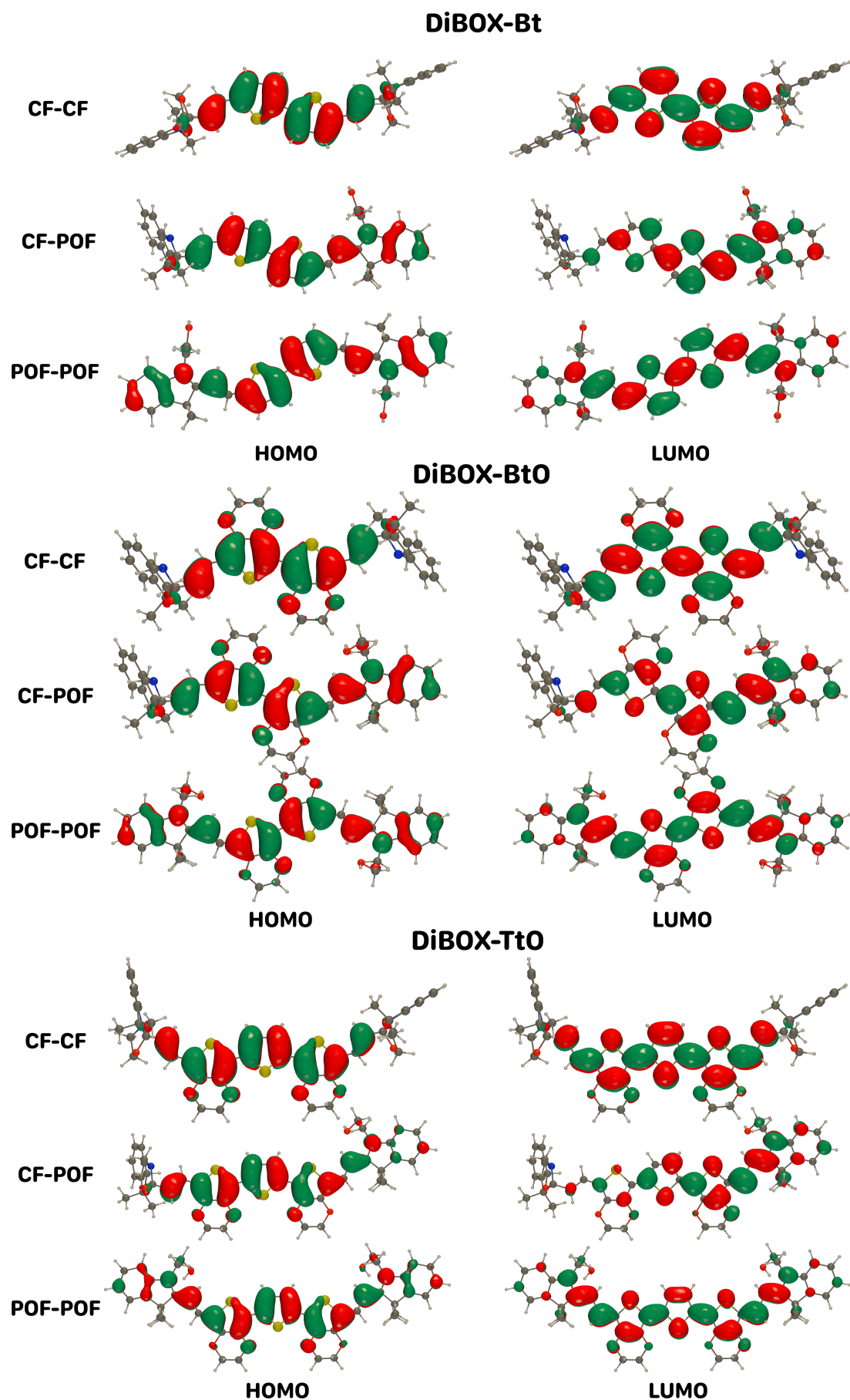


Figure 8.3: HOMO and LUMO of diBOX's (in their most stable conformations), which mostly determine the first excitation of these compounds as evaluated at the M06-2X/6-311+G(d)/IEF-PCM (acetonitrile) level of theory. Green = negative, Red = positive, isovalue = 0.02 a.u..

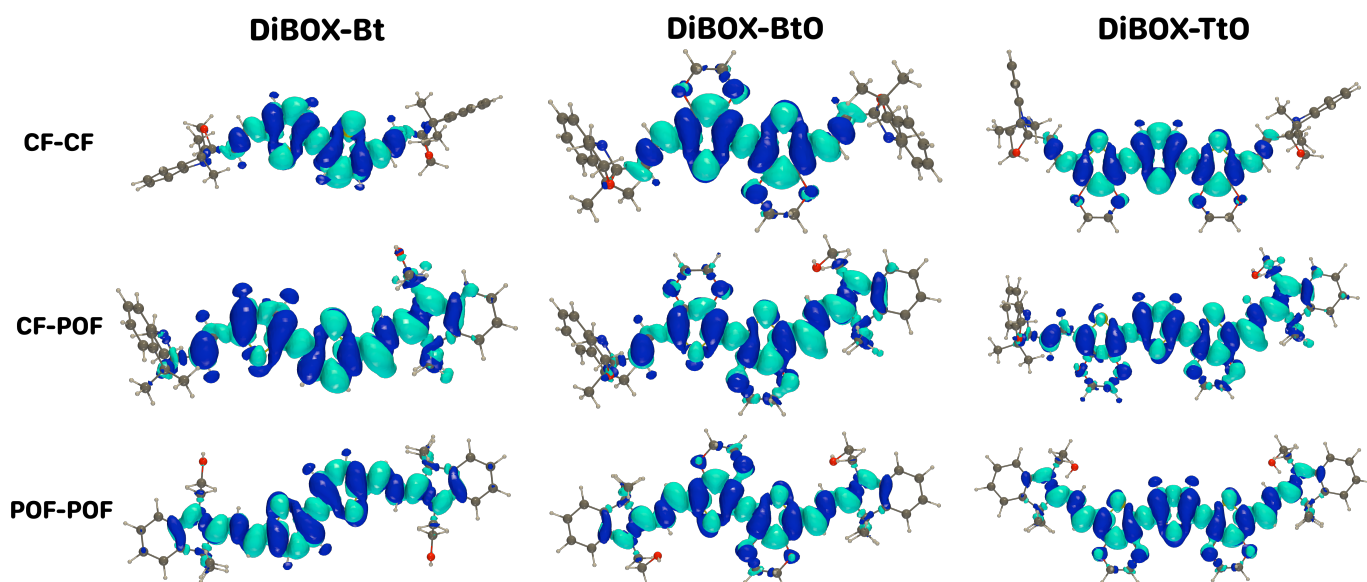


Figure 8.4: Variation of electron density associated with the first excitation for the three diBOX's (in their most stable conformations) as evaluated at the M06-2X/6-311+G(d)/IEF-PCM (acetonitrile) level of approximation. Cyan: positive, Blue: negative, isovalue: 0.0004 a.u..

SOS expression of β is expected to be small since this conformer only represents 18.5 % of the total population at 298.15 K (*vide infra*).

For **diBOX-BtO**, the two EDOT units adopt an *anti* conformation due to the repulsion between these units, resulting in a small $\Delta\mu_{ge}$, especially for **CF-CF** (between 0.04 and 0.05 D) and **POF-POF** (between 0.03 and 0.12 D) (Tables S13 and S14). Since the linker of **diBOX-TtO** possesses three thiophene-based units, it cannot display a centrosymmetric structure. The **CF-CF** and **POF-POF** forms correspond to V-shaped NLO-phores, with C_2 symmetry. The displacement of the electron cloud occurring along the first excitation is a displacement from the center of the linker to the BOX moieties. The amplitude of d_{CT} (and $\Delta\mu_{ge}$) can be enhanced by constraining the linker, *e.g.* switching from *anti* to *syn* conformation between the thiophene-based units ($\theta_3\text{-}\theta_4$: $180^\circ \rightarrow 0^\circ$). Indeed, for **CF-CF** and **POF-POF** $\Delta\mu_{ge}$ varies between 0.37 D and 1.58 D, and between 0.54 D and 1.47 D, as a function of the conformation of the linker (Tables S16 and S18). In the next paragraph, we present the first hyperpolarizability values for the different compounds in each of their three states and we see that these can be rationalized, to a given extent, by using the linear optical responses.

Nonlinear Optical Properties

The key second-order NLO properties of the diBOX compounds, evaluated at TDDFT/M06-2X/6-311+G(d)/IEF-PCM (acetonitrile) level of approximation, are listed in Table 8.3. For all three diBOX derivatives, to act as efficient NLO switches, the three different states should present very distinct β_{HRS} . For a large range of wavelengths, calculations reveal that the smallest β_{HRS} values are achieved with the fully closed forms where the EWG potential of the BOX is not expressed. The first BOX opening, leading to **CF-POF** from **CF-CF** induces a

substantial increase of β_{HRS} , at least by a factor of 30 but often by two orders of magnitude. In this form exhibiting the largest $\Delta\mu_{ge}$, the second smallest ΔE (yet close to the smallest one), and the smallest local BLA's, all systems present logically the largest β_{HRS} value. In this state, the systems present a dipolar character whatever the nature of the π -conjugated linker and a depolarization ratio (DR) close to 5 [DR = 4.79 (**diBOX-Bt**), 4.67 (**diBOX-BtO**), and 4.84 (**diBOX-TtO**)].

Table 8.3: β_{HRS} (10^3 a.u., static, $\lambda = \infty$ nm and dynamic fields at $\lambda = 1907$ nm, 1300 nm, and 1064 nm) as well as static β_{ZZZ} , β_{ZXX} , $|\beta_{J=1}|$, $|\beta_{J=3}|$ 10^3 a.u., DR, and ρ for the diBOX's in their different forms as evaluated at the TDDFT/M06-2X/6-311+G(d)/IEF-PCM (acetonitrile) level of theory. These are averaged values calculated using the Boltzmann's populations at 298.15 K. The last column reports experimental data at 1300 nm with their DR in parentheses.

		β_{HRS}				Exp. 1300
		∞	1907	1300	1064	
diBOX-Bt	CF-CF	0.4	0.3	0.4	0.5	4.1 ± 0.2 (2.49)
	CF-POF	36.2	33.7	77.9	739.0	88.3 ± 4.5 (4.01)
	POF-POF	9.5	6.6	11.0	41.5	47.3 ± 2.4 (2.74)
diBOX-BtO	CF-CF	1.3	1.2	1.7	2.6	
	CF-POF	37.4	33.4	95.9	466.0	
	POF-POF	0.4	0.3	1.3	1.6	
diBOX-TtO	CF-CF	2.1	1.8	2.7	5.1	
	CF-POF	80.6	87.6	392.0	416.0	
	POF-POF	9.0	8.9	48.4	40.5	

		β_{ZZZ}	β_{ZXX}	DR	$ \beta_{J=1} $	$ \beta_{J=3} $	ρ
diBOX-Bt	CF-CF	0.4	0.2	3.74	0.7	0.8	1.19
	CF-POF	32.9	15.0	4.79	66.5	57.4	0.86
	POF-POF	8.4	4.3	3.76	15.7	18.3	1.16
diBOX-BtO	CF-CF	1.2	0.5	4.98	2.5	2.0	0.82
	CF-POF	34.0	15.7	4.67	68.5	61.2	0.89
	POF-POF	0.3	0.2	2.26	0.4	1.0	2.28
diBOX-TtO	CF-CF	1.9	0.9	4.51	3.8	3.5	0.93
	CF-POF	73.4	33.4	4.84	150.0	127.0	0.85
	POF-POF	7.6	4.7	2.58	12.2	22.3	1.82

The second BOX opening leading to **POF-POF** from **CF-POF** generates a β_{HRS} decreases. As explained above, due to the (partial) centro-symmetry, the EWG characters of the indoleninium groups cancel each other, which prevent the systems to exhibit large β_{HRS} re-

sponses. This is especially the case of **diBOX-BtO** where the *syn* form of the bis-EDOT linker has a vanishingly small MB weight (*vide infra*), resulting in a contrast ratio around 0.01 for the **CF-POF** to **POF-POF** transition (at $\lambda = 1300$ nm). On the other hand, in **diBOX-Bt** V-shape structures are more stable (steric interactions between the thiophene groups are smaller than between the EDOT's) and in **diBOX-TtO** V-shape structures are naturally present owing to the EDOT-Th-EDOT structure of linker, conducting to observe smaller contrast ratios, 0.14 and 0.12, respectively (again at $\lambda = 1300$ nm). The comparison of the β_{HRS} contrasts of the three diBOX's is summarized in Figure 8.5.

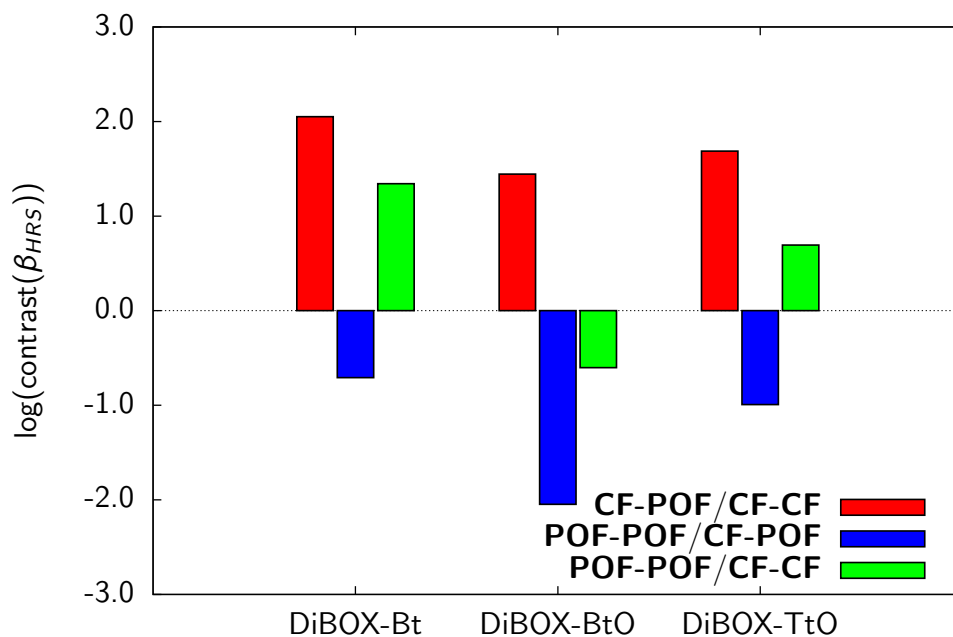


Figure 8.5: Effect of the linker on the β_{HRS} contrasts for an incident wavelength of 1907 nm, as calculated at the TDDFT/M06-2X/6-311+G(d)/IEF-PCM (acetonitrile) level of approximation.

While the **CF-POF** species present a strong dipolar character ($|\beta_{J=1}|$ larger than $|\beta_{J=3}|$ and $\rho < 1$) in all cases, the dipolar/octupolar character of the other forms (**CF-CF** and **POF-POF**) depends on the nature of the linker. For **diBOX-Bt**, for which the linker can be centrosymmetric or not (in the latter case, when the bithiophene adopts a *syn* conformation, the molecule can adopt a C_{2v} -like symmetry), the DR amounts to 3.54 and 3.74 for **CF-CF** and **POF-POF**, respectively. These values correspond to a slight predominance of the octupolar character ($\rho \sim 1.2$). In both cases, this is due to the fact that some of the contributing conformers have a V-shape structure (DR around 3) while others have a 1-D NLOphore character (DR close to 5). As it was discussed before, the change of conformation of the bithiophene from *anti* to *syn* results in an increase of $\Delta\mu_{ge}$. Since within the two-state approximation, β is directly proportional to $\Delta\mu_{ge}$, the β response of **diBOX-Bt** increases upon the *anti* to *syn* switching, as illustrated in Figure 8.6 for the **POF-POF** using the unit sphere representation.³⁹

When the bithiophene is replaced by a bis-EDOT moiety as π -conjugated linker, the *syn* conformation is impeded due to steric hindrance between the two EDOT units. As conse-

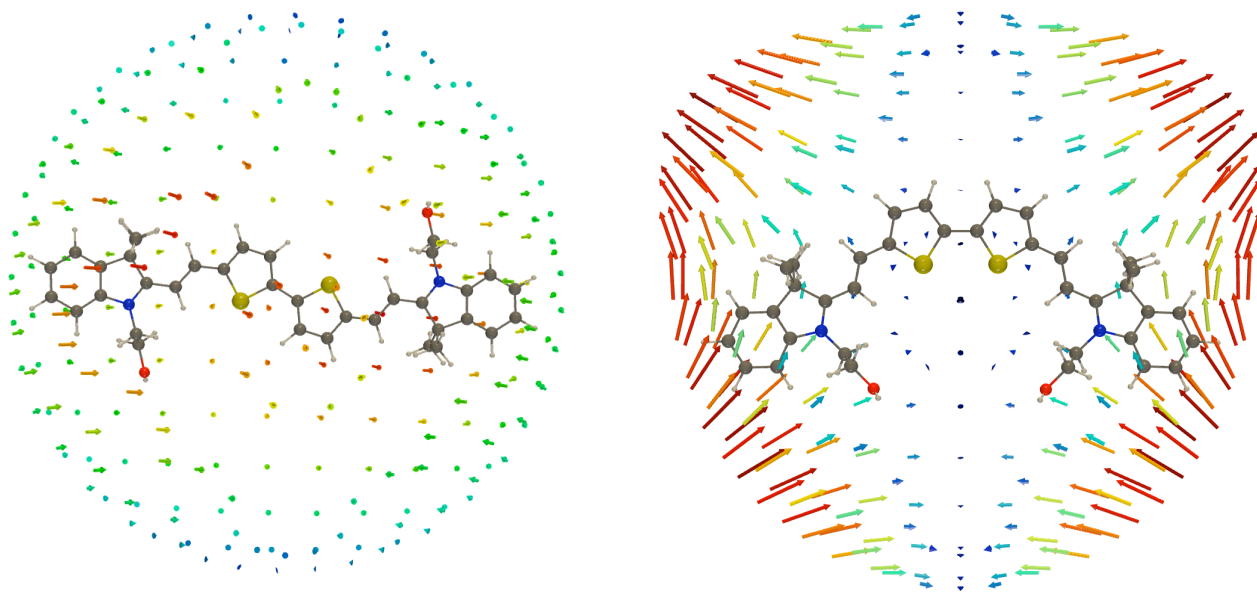


Figure 8.6: Progressive increase of the static β response of **diBOX-Bt** in **POF-POF** upon the C_i -like $\rightarrow C_{2v}$ -like change of symmetry. Left, conformer 1 ($\beta_{HRS} < 0.1 \times 10^3$ a.u.) and right: conformer 2 ($\beta_{HRS} < 13 \times 10^3$ a.u., DR = 2.31). A USR factor of 1×10^{-4} (5 \AA a.u.^{-1}) was used for conformers 2 (1).

quence, **POF-POF** of **diBOX-BtO** exhibits a very small β response but we can also notice a significantly smaller DR than in **diBOX-Bt** (2.26 versus 3.76), "translating" an enhancement of the octupolar character of the system. An antagonist effect is observed on **CF-CF** state, though the β responses are small. Under this state, bis-EDOT exhibits a more pronounced dipolar character translated by a DR closer to 5 than **diBOX-Bt** (3.74). This is explained by the existence for **CF-CF** state of non-centrosymmetric conformers with non-negligible MB weights.

Last, the **CF-CF** and **POF-POF** states of **diBOX-TtO** have ρ values equal to 0.92 and 1.83, respectively. These values are similar than their analogs of **diBOX-BtO** (0.82 and 2.20), but not necessarily for the same reasons. Indeed, many conformers contribute to the MB population of the **CF-CF** state and larger β_{HRS} responses are associated with DR values close to 5, *i.e.* typical of 1-D NLOphores (Conformers 5, 6, 12, 14, and 15, Table S25). Then, for the fully open species, the octupolar character is always dominant ($1.8 < \rho < 2.1$) no matter whether both θ_3 and θ_4 correspond to a anti conformation ($\sim 180^\circ$) or only one. Therefore, for **diBOX-Bt** with the bithiophene in syn conformation and **diBOX-TtO** with trans conformations of the thiophene-EDOT units, the **POF-POF** state corresponds to V-shaped (or Λ -shaped) A-D-A (attractor-donor-attractor) NLO-phores, with larger β responses than in **diBOX-BtO**. In order to enhance the β responses of the **POF-POF** form, several strategies can be foreseen to constrain the conformation of the linker so that the EWG's draw a V-shape form. This can be achieved by using rigid linkers or, like in the present study, by combining an odd number of aromatic units adopting an *anti* conformation (**diBOX-TtO**) or an even number of aromatic

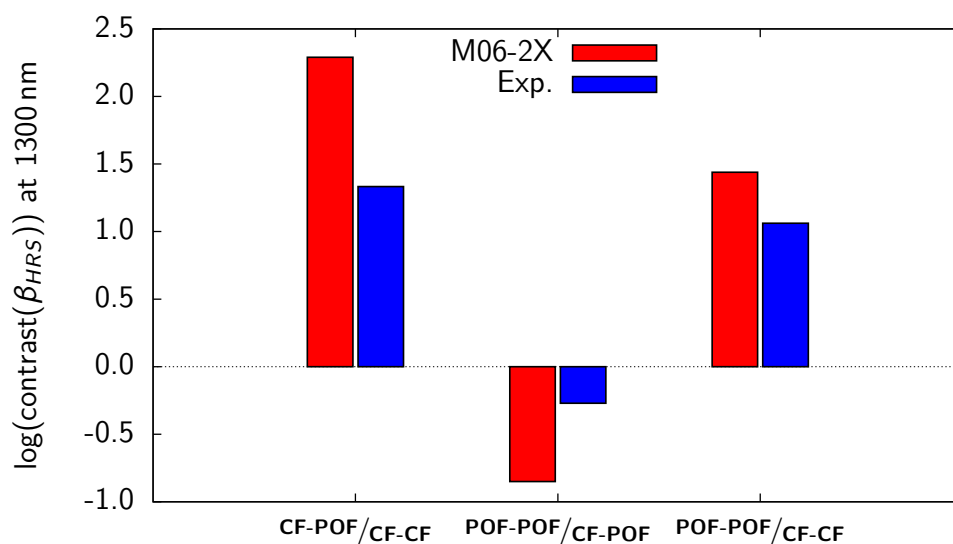


Figure 8.7: Contrasts of the β_{HRS} responses for the individual opening reactions of **diBOX-Bt** as well as for the whole switching from the fully closed to the fully open forms, as represented by their $\log(\text{contrast}(\beta_{HRS}))$ at 1300 nm. The experimental results are compared to the calculations enacted at the TDDFT/M06-2X/6-311+G(d)/IEF-PCM (acetonitrile) level of theory.

units allowing *syn* conformation (**diBOX-Bt**).

The diBOX-BT results were confronted to experimental data at 1300 nm (Table 8.3). For **CF-POF** the computational and the experimental procedures give responses of the same order of magnitude (78×10^3 a.u. *versus* 88×10^3 a.u., respectively). On the other hand, the computations underestimate strongly the responses of the **CF-CF** and **POF-POF**. This leads to a general overestimation of the β_{HRS} contrasts. Nevertheless, as illustrated in Figure 8.7, the experimental trends are reproduced. Yet, as discussed in the Methods Section, measurements were only made for **diBOX-Bt** because we did not succeed in synthesizing **diBOX-BtO** while HRS measurements on **diBOX-TtO** were hampered by huge two-photon fluorescence.

Section 8.4

Further Discussions, Conclusions, and Outlook

By adopting a multidisciplinary approach that combines synthesis, UV/vis absorption and hyper-Rayleigh scattering measurements, together with quantum chemical calculations performed at the DFT level it has been shown that diBOX derivatives possessing two identical BOX units are efficient NLO switches. Since each BOX can be either closed or open, these systems can adopt three different states (**CF-CF**, **CF-POF**, and **POF-POF**). In these compounds, the acceptor character of the BOX units is unleashed when it opens to form an indoleninium unit, so that low excitation energies are obtained for the **CF-POF** and **POF-POF** states. Then, since non-centrosymmetry is required to achieve non-zero first hyperpolarizability, only the

non-symmetric **CF-POF** state is expected to exhibit a substantial β response. Indeed, calculations show that the $\beta(\text{CF-POF})/\beta(\text{CF-CF})$ contrast is larger than 10, corresponding to the opening of the first BOX, while $\beta(\text{POF-POF})/\beta(\text{CF-POF})$ is smaller than 1/3 for the opening of the second. Still, these contrasts depend on the nature of the linker, which controls the extent of the π -electron delocalization but also the symmetry of the system. In particular, better contrasts are achieved when centro-symmetry can be enforced for the fully open and fully closed states; in other words when these two states have zero or negligible first hyperpolarizabilities. From the DFT analysis, it is shown that such centro-symmetry can be enforced when the linker between the BOX's contains two EDOT units (in the case of the **diBOX-BtO** compound) because they can adopt a *anti* centro-symmetric conformation while the *syn* conformation is prevented due to steric hindrance. On the other hand, when the central part of the linker is replaced by a bithiophene (**diBOX-Bt** compound), there is a non-zero population of the *syn* conformation. Similarly, when the linker is an EDOT-thiophene-EDOT sequence, a V-shape conformation is the most stable, leading to β responses that are not negligible — though still smaller — with respect to those of the corresponding **CF-POF** state. Beyond this static or stationary picture of the compounds, there are vibrational motions that can lift these pseudo-symmetries and lead to additional contributions to the β_{HRS} responses, like the so-called zero-point vibrational average responses.

Calculations have further evidenced that the largest β_{HRS} responses (in the **CF-POF** state) are achieved with the largest linker, EDOT-thiophene-EDOT, owing to better push-pull π -delocalization effects, as shown by the largest $\Delta\mu_{ge}$ among the three diBOX's (Table 8.2). Taking advantage of the two-state approximation (TSA)⁵³ where $\beta \propto f_{ge}\Delta\mu_{ge}/\Delta E_{ge}^3$ and assuming a dominant 1D characteristic for the static first hyperpolarizability, the following relationship holds

$$\beta_{HRS} = \sqrt{\frac{6}{35}}\beta_{zzz} = 3.73 \frac{f_{ge}\Delta\mu_{ge}}{\Delta E_{ge}^3} \quad (8.6)$$

Then, using the MB averages of Table 8.2, the corresponding TSA β_{HRS} values of the **CF-POF** state of **diBOX-Bt**, **diBOX-BtO**, and **diBOX-TtO** amount to 35×10^3 , 30×10^3 , and to 82×10^3 a.u., respectively. These values match nicely the full values given in Table 8.3.

To complement the experimental investigations of the successive switching steps, that can operate by the addition of acid or of oxidant, and therefore to analyze the control of the level of opening of these molecules, the Gibbs free energies were calculated for the following reactions (298.15 K in acetonitrile; the most stable conformer of each state was considered)



where HA is an acid and A^- its conjugate base. Besides the irreversibility of the reactions [$\Delta G^0(1)$ and/or $(2) < 0$], in particular we concentrated on their difference, [$\Delta\Delta G^0 = \Delta G^0(2) - \Delta G^0(1)$], because a negative value would mean that the second opening is easier than the first

one and therefore that the level of opening cannot be controlled, which would be in contradiction with experiment. For **diBOX-Bt**, using the M06 XC functional, the 6-311G(d) basis set and IEFPCM, positive $\Delta G^0(1)$ values of 61 and 31 kJ mol⁻¹ were calculated when HA is acetic acid and formic acid, demonstrating these are poor acids to trigger the transformation, respectively. On the other hand, with HClO₄ $\Delta G^0(1)$ amounts to -81 kJ mol⁻¹ and to -15 kJ mol⁻¹ for trifluoroacetic acid (TFA), the acid that is often employed experimentally. We then considered only TFA as acid and found that the opening reaction is facilitated in the case of **diBOX-BtO** [$\Delta G^0(1) = -59$ kJ mol⁻¹] and **diBOX-TtO** [$\Delta G^0(1) = -50$ kJ mol⁻¹]. Finally, calculations were performed, for **diBOX-Bt**, at the ω B97X-D/6-311+G(d)/IEFPCM level and it was found that the second opening is less favorable [$\Delta G^0(2) = -10$ kJ mol⁻¹] than the first [$\Delta G^0(1) = -24$ kJ mol⁻¹] so that $\Delta\Delta G^0(1) = 14$ kJ mol⁻¹.

The opening by oxidation was then investigated (also by considering the most stable conformers). It consists of four steps (Scheme S2): i) the oxidation of the CF to form a radical cation, ii) the C–O bond breaking (homolytic cleavage), iii) the reduction of the product, and iv) its protonation to obtain the POF. The rate determining step is the first one (Table S28) so that the potential of oxidation versus the Fc/Fc⁺ electrode (ferrocene/ferrocenium system) was evaluated. In the case of **diBOX-Bt**, M06/6-311G(d)/IEFPCM calculations predict that the oxidation potential amounts to 0.34 V for the **CF-CF** state while for **CF-POF** it amounts to 0.71 V. This larger value is attributed to the fact that it is more difficult to extract an electron from **CF-POF**, which bears a positive charge. In the case of **diBOX-BtO**, the successive redox potentials versus the Fc/Fc⁺ electrode amount to -0.12 V and 0.39 V, evidencing the role of the better electron donating bis-EDOT with respect to bithiophene. These redox potentials further decrease in the case of the EDOT-thiophene-EDOT linker with values of -0.18 eV and 0.18 eV, highlighting now the role of a larger π -conjugated linker. Therefore, owing to the fact that the redox potentials are larger for the second opening and that they are sufficiently different (differences of 0.51 V for **diBOX-BtO**, 0.37 V for **diBOX-Bt**, and 0.36 V for **diBOX-TtO**), the calculations also demonstrate that the level of opening can also be controlled by redox reactions. These results also evidence that this computational protocol can be employed to other, not yet synthesized, compounds in the process of designing new multi-state switches with a control of its successive transformations. The analysis of the spin density distribution of the oxidized species (Figure S2) and the related atomic spin densities (Table S29) demonstrates it is delocalized over the π -linker with large values on the vinyl C atom adjacent to the BOX (named C_{BOX}, Scheme S3). This atom is directly involved in the cleavage step and its larger atomic spin density in [**CF-POF**]^{•+} than [**CF-CF**]^{•+} accounts for the fact that the cleavage is less endergonic for the second opening than the first (Table S28). Calculations further show that these C_{BOX} spin densities are similar for **diBOX-BtO** but smaller for **diBOX-TtO**, where the spin density is delocalized over three rings rather than two.

The general good agreement between the calculations on **diBOX-Bt** and experiment demonstrates that the same approach can be used to study other multi-state multi-addressable BOX

derivatives and therefore to help selecting the best ones for the synthesis. Current directions of investigation encompass the study of i) diBOX with asymmetric linkers and ii) TriBOX and TetraBOX derivatives with symmetric or asymmetric linkers in order to improve the control of the switching process as well as to maximize the linear and nonlinear optical property contrasts. Different functionalization patterns can also be investigated.⁵⁴ Among these, the use of linkers able to chelate transition metals would open the field considerably.^{55–57} Though it does not affect the design strategy, from the methodological and computational viewpoint, it is important to explain why the predicted β_{HRS} values of the **CF-CF** and **POF-POF** states of **diBOX-Bt** are underestimated with respect to experiment. This could require using sequential Molecular Dynamics then Quantum Chemistry approaches like done recently for ion pairs and chromophores embedded in lipid bilayers.^{58,59}

Acknowledgments

J.Q. thanks the “Actions de Recherche Concertées” (ARC) de la Direction générale de l’Enseignement non obligatoire et de la Recherche scientifique-Direction de la Recherche scientifique-Communauté française de Belgique under convention no. 15/20-068 for his PhD grant. This work, carried out within the MORIARTY project, has benefited from the financial support from Wallonie-Bruxelles International (WBI), from the Fund for Scientific Research (F.R.S.-FNRS), from the French Ministry of Foreign and European Affairs, and from the Ministry of Higher Education and Research in the frame of the Hubert Curien partnerships. V.R. is grateful to F. Adamietz for experimental support and technical developments and also thanks the Région Nouvelle Aquitaine for financial support (CRA: 2015-1R10205-00004858). This work has been partly done in the frame of the Investments for the future Programme IdEx Bordeaux-LAPHIA (ANR-10-IDEX-03-02). The calculations were performed on the computers of the Consortium des Équipements de Calcul Intensif (CÉCI, <http://www.cec-i-hpc.be>) and particularly those of the Technological Platform of High-Performance Computing, for which the authors gratefully acknowledge the financial support of the FNRS-FRFC, of the Walloon Region, and of the University of Namur (convention nos. 2.5020.11, GEQ U.G006.15, 1610468, and RW/GEQ2016), as well as on zenobe, the Tier-1 facility of the Walloon Region (convention 1117545).

Bibliography

- [1] Bissell, R. A.; Córdova, E.; Kaifer, A. E.; Stoddart, J. F. A chemically and electrochemically switchable molecular shuttle. *Nature* **1994**, *369*, 133–137.
- [2] de Silva, A. P.; Vance, T. P.; West, M. E. S.; Wright, G. D. Bright Molecules with Sense, Logic, Numeracy and Utility. *Org. Biomol. Chem.* **2008**, *6*, 2468.
- [3] Feringa, B. L., Browne, W. R., Eds. *Molecular Switches*, 2nd ed.; Wiley-VCH: Weinheim, Germany, 2011.
- [4] Andréasson, J.; Pischel, U. Molecules with a Sense of Logic: A Progress Report. *Chem. Soc. Rev.* **2015**, *44*, 1053–1069.
- [5] Muller, P. Glossary of terms used in physical organic chemistry (IUPAC Recommendations 1994). *Pure Appl. Chem.* **1994**, *66*, 1077–1184.
- [6] Bamfield, P. *Chromic Phenom.*; Royal Society of Chemistry: Cambridge, 2010; Chapter 1, pp 9–140.
- [7] Kassem, S.; van Leeuwen, T.; Lubbe, A. S.; Wilson, M. R.; Feringa, B. L.; Leigh, D. A. Artificial molecular motors. *Chem. Soc. Rev.* **2017**, *46*, 2592–2621.
- [8] McConnell, A. J.; Wood, C. S.; Neelakandan, P. P.; Nitschke, J. R. Stimuli-Responsive MetalLigand Assemblies. *Chem. Rev.* **2015**, *115*, 7729–7793.
- [9] Coe, B. J.; Houbrechts, S.; Asselberghs, I.; Persoons, A. Efficient, Reversible Redox-Switching of Molecular First Hyperpolarizabilities in Ruthenium(II) Complexes Possessing Large Quadratic Optical Nonlinearities. *Angew. Chem. Int. Ed.* **1999**, *38*, 366–369.
- [10] Delaire, J. A.; Nakatani, K. Linear and Nonlinear Optical Properties of Photochromic Molecules and Materials. *Chem. Rev.* **2000**, *100*, 1817–1846.
- [11] Castet, F.; Rodriguez, V.; Pozzo, J.-L.; Ducasse, L.; Plaquet, A.; Champagne, B. Design and Characterization of Molecular Nonlinear Optical Switches. *Acc. Chem. Res.* **2013**, *46*, 2656–2665.
- [12] Mançois, F.; Sanguinet, L.; Pozzo, J.-L.; Guillaume, M.; Champagne, B.; Rodriguez, V.; Adamietz, F.; Ducasse, L.; Castet, F. Acido-Triggered Nonlinear Optical Switches: Benzazolo-Oxazolidines. *J. Phys. Chem. B* **2007**, *111*, 9795–9802.
- [13] (a) Mançois, F.; Pozzo, J.-L.; Pan, J.; Adamietz, F.; Rodriguez, V.; Ducasse, L.; Castet, F.; Plaquet, A.; Champagne, B. Two-Way Molecular Switches with Large Nonlinear Optical Contrast. *Chem. Eur. J.* **2009**, *15*, 2560–2571.
- [14] Pielak, K.; Bondu, F.; Sanguinet, L.; Rodriguez, V.; Champagne, B.; Castet, F. Second-Order Nonlinear Optical Properties of Multiaddressable Indolinoxazolidine Derivatives:

- Joint Computational and Hyper-Rayleigh Scattering Investigations. *J. Phys. Chem. C* **2017**, *121*, 1851–1860.
- [15] Szalóki, G.; Sanguinet, L. In *Photon-Working Switches*; Yokoyama, Y., Nakatani, K., Eds.; Springer Japan: Tokyo, 2017; pp 69–91.
- [16] Sanguinet, L.; Pozzo, J.-L.; Rodriguez, V.; Adamietz, F.; Castet, F.; Ducasse, L.; Champagne, B. Acido- and Phototriggered NLO Properties Enhancement. *J. Phys. Chem. B* **2005**, *109*, 11139–11150.
- [17] Bondu, F.; Hadji, R.; Szalóki, G.; Alévêque, O.; Sanguinet, L.; Pozzo, J.-L.; Cavagnat, D.; Buffeteau, T.; Rodriguez, V. Huge Electro-/Photo-/Acidoinduced Second-Order Nonlinear Contrasts From Multiaddressable Indolinoxazolodine. *J. Phys. Chem. B* **2015**, *119*, 6758–6765.
- [18] Hadji, R.; Szalóki, G.; Alévêque, O.; Levillain, E.; Sanguinet, L. The Stepwise Oxidation of Indolino[2,1-b]Oxazolidine Derivatives. *J. Electroanal. Chem.* **2015**, *749*, 1–9.
- [19] Szalóki, G.; Alévêque, O.; Pozzo, J.-L.; Hadji, R.; Levillain, E.; Sanguinet, L. Indolinoxazolodine: A Versatile Switchable Unit. *J. Phys. Chem. B* **2015**, *119*, 307–315.
- [20] Houbrechts, S.; Clays, K.; Persoons, A.; Pikramenou, Z.; Lehn, J.-M. Hyper-Rayleigh scattering investigation of nitrobenzyl pyridine model compounds for optical modulation of the hyperpolarisability. *Chem. Phys. Lett.* **1996**, *258*, 485–489.
- [21] Beaujean, P.; Bondu, F.; Plaquet, A.; Garcia-Amorós, J.; Cusido, J.; Raymo, F. M.; Castet, F.; Rodriguez, V.; Champagne, B. Oxazines: A New Class of Second-Order Nonlinear Optical Switches. *J. Am. Chem. Soc.* **2016**, *138*, 5052–5062.
- [22] Sevez, G.; Gan, J.; Delbaere, S.; Vermeersch, G.; Sanguinet, L.; Levillain, E.; Pozzo, J.-L. Photochromic Performance of a Dithienylethene–Indolinoxazolodine Hybrid. *Photochem. Photobiol. Sci.* **2010**, *9*, 131–135.
- [23] Szalóki, G.; Sevez, G.; Berthet, J.; Pozzo, J.-L.; Delbaere, S. A Simple Molecule-Based Octastate Switch. *J. Am. Chem. Soc.* **2014**, *136*, 13510–13513.
- [24] Bondu, F.; Quertinmont, J.; Rodriguez, V.; Pozzo, J.-L.; Plaquet, A.; Champagne, B.; Castet, F. Second-Order Nonlinear Optical Properties of a Dithienylethene–Indolinoxazolodine Hybrid: A Joint Experimental and Theoretical Investigation. *Chem. Eur. J.* **2015**, *21*, 18749–18757.
- [25] Sanguinet, L.; Berthet, J.; Szalóki, G.; Alévêque, O.; Pozzo, J.-L.; Delbaere, S. 13 Metastable States Arising from a Simple Multifunctional Unimolecular System. *Dyes Pigments* **2017**, *137*, 490–498.
- [26] Aidibi, Y.; Guerrin, C.; Alévêque, O.; Leriche, P.; Delbaere, S.; Sanguinet, L. BT-2-BOX: An Assembly toward Multimodal and Multilevel Molecular System Simple as a Breeze. *J. Phys. Chem. C* **2019**, *123*, 11823–11832.

- [27] Guerrin, C.; Aidibi, Y.; Sanguinet, L.; Leriche, P.; Aloise, S.; Orio, M.; Delbaere, S. When Light and Acid Play Tic-Tac-Toe with a Nine-State Molecular Switch. *J. Am. Chem. Soc.* **2019**, *141*, 19151–19160.
- [28] Castet, F.; Bogdan, E.; Plaquet, A.; Ducasse, L.; Champagne, B.; Rodriguez, V. Reference Molecules for Nonlinear Optics: A Joint Experimental and Theoretical Investigation. *J. Chem. Phys.* **2012**, *136*, 024506.
- [29] Zhao, Y.; Truhlar, D. G. The M06 Suite of Density Functionals for Main Group Thermochemistry, Thermochemical Kinetics, Noncovalent Interactions, Excited States, and Transition Elements: Two New Functionals and Systematic Testing of Four M06-Class Functionals and 12 Other Functionals. *Theor. Chem. Acc.* **2008**, *120*, 215–241.
- [30] Tomasi, J.; Mennucci, B.; Cammi, R. Quantum Mechanical Continuum Solvation Models. *Chem. Rev.* **2005**, *105*, 2999–3094.
- [31] Scalmani, G.; Frisch, M. J.; Mennucci, B.; Tomasi, J.; Cammi, R.; Barone, V. Geometries and Properties of Excited States in the Gas Phase and in Solution: Theory and Application of a Time-Dependent Density Functional Theory Polarizable Continuum Model. *J. Chem. Phys.* **2006**, *124*, 094107.
- [32] Le Bahers, T.; Adamo, C.; Ciofini, I. A Qualitative Index of Spatial Extent in Charge-Transfer Excitations. *J. Chem. Theory Comput.* **2011**, *7*, 2498–2506.
- [33] van Gisbergen, S. J. A.; Snijders, J. G.; Baerends, E. J. Accurate Density Functional Calculations on Frequency-Dependent Hyperpolarizabilities of Small Molecules. *J. Chem. Phys.* **1998**, *109*, 10657–10668.
- [34] Helgaker, T.; Coriani, S.; Jørgensen, P.; Kristensen, K.; Olsen, J.; Ruud, K. Recent Advances in Wave Function-Based Methods of Molecular-Property Calculations. *Chem. Rev.* **2012**, *112*, 543–631.
- [35] Verbiest, T.; Clays, K.; Rodriguez, V. *Second-Order Nonlinear Optical Characterization Techniques: An Introduction*; Taylor & Francis: New York, 2009.
- [36] Bersohn, R.; Pao, Y.-H.; Frisch, H. L. Double-Quantum Light Scattering by Molecules. *J. Chem. Phys.* **1966**, *45*, 3184–3198.
- [37] Rodriguez, V.; Grondin, J.; Adamietz, F.; Danten, Y. Local Structure in Ionic Liquids Investigated by Hyper-Rayleigh Scattering. *J. Phys. Chem. B* **2010**, *114*, 15057–15065.
- [38] Brasselet, S.; Zyss, J. Multipolar Molecules and Multipolar Fields: Probing and Controlling the Tensorial Nature of Nonlinear Molecular Media. *J. Opt. Soc. Am. B* **1998**, *15*, 257.
- [39] Tuer, A.; Krouglov, S.; Cisek, R.; Tokarz, D.; Barzda, V. Three-Dimensional Visualization of the First Hyperpolarizability Tensor. *J. Comput. Chem.* **2011**, *32*, 1128.
- [40] Liégeois, V. DrawMol. UNamur, <https://www.unamur.be/drawmol>.

- [41] Shelton, D. P.; Rice, J. E. Measurements and Calculations of the Hyperpolarizabilities of Atoms and Small Molecules in the Gas Phase. *Chem. Rev.* **1994**, *94*, 3–29.
- [42] de Wergifosse, M.; Champagne, B. Electron Correlation Effects on the First Hyperpolarizability of Push–Pull π -Conjugated Systems. *J. Chem. Phys.* **2011**, *134*, 074113.
- [43] Johnson, L. E.; Dalton, L. R.; Robinson, B. H. Optimizing Calculations of Electronic Excitations and Relative Hyperpolarizabilities of Electrooptic Chromophores. *Acc. Chem. Res.* **2014**, *47*, 3258–3265.
- [44] Garrett, K.; Sosa Vazquez, X.; Egri, S. B.; Wilmer, J.; Johnson, L. E.; Robinson, B. H.; Isborn, C. M. Optimum Exchange for Calculation of Excitation Energies and Hyperpolarizabilities of Organic Electro-Optic Chromophores. *J. Chem. Theory Comput.* **2014**, *10*, 3821–3831.
- [45] Champagne, B.; Beaujean, P.; de Wergifosse, M.; Cardenuto, M. H.; Liégeois, V.; Castet, F. In *Frontiers of Quantum Chemistry*; Wójcik, M. J., Nakatsuji, H., Kirtman, B., Ozaki, Y., Eds.; Springer Singapore: Singapore, 2018; pp 117–138.
- [46] Lescos, L.; Sitkiewicz, S. P.; Beaujean, P.; Blanchard-Desce, M.; Champagne, B.; Matito, E.; Castet, F. Performance of DFT Functionals for Calculating the Second-Order Nonlinear Optical Properties of Dipolar Merocyanines. *Phys. Chem. Chem. Phys.* **2020**, *22*, 16579–16594.
- [47] Frisch, M. J. et al. Gaussian 16 Revision A.03. 2016; Gaussian Inc. Wallingford CT.
- [48] Szalóki, G.; Sanguinet, L. Silica-Mediated Synthesis of Indolinoxazolidine-Based Molecular Switches. *J. Org. Chem.* **2015**, *80*, 3949–3956.
- [49] Leriche, P.; Turbiez, M.; Monroche, V.; Frère, P.; Blanchard, P.; Skabara, P. J.; Roncali, J. Strong π -electron donors based on a self-rigidified 2,2'-bi(3,4-ethylenedioxy)thiophenetetrathiafulvalene hybrid π -conjugated system. *Tetrahedron Lett.* **2003**, *44*, 649–652.
- [50] Imae, I.; Sagawa, H.; Mashima, T.; Komaguchi, K.; Ooyama, Y.; Harima, Y. Synthesis of Soluble Polythiophene Partially Containing 3,4-Ethylenedioxythiophene and 3-Hexylthiophene by Polycondensation. *Open J. Polym. Chem.* **2014**, *04*, 83–93.
- [51] Blanchard, P.; Cravino, A.; Levillain, E. In *Handb. Thiophene-Based Mater.*; Perepichka, I. F., Perepichka, D. F., Eds.; John Wiley & Sons, Ltd: Chichester, UK, 2009; Chapter 9, pp 419–453.
- [52] Chevallier, F.; Charlot, M.; Mongin, F.; Champagne, B.; Franz, E.; Clays, K.; Blanchard-Desce, M. Synthetic, Optical and Theoretical Study of Alternating Ethylenedioxythiophene-Pyridine Oligomers: Evolution from Planar Conjugated to Helicoidal Structure towards a Chiral Configuration. *ChemPhysChem* **2016**, *17*, 4090–4101.
- [53] Oudar, J. L.; Chemla, D. S. Hyperpolarizabilities of the Nitroanilines and Their Relations

- to the Excited State Dipole Moment. *J. Chem. Phys.* **1977**, *66*, 2664–2668.
- [54] Bureš, F. Fundamental Aspects of Property Tuning in Push– Pull Molecules. *RSC Adv.* **2014**, *4*, 58826–58851.
- [55] Yam, V. W.-W.; Ko, C.-C.; Zhu, N. Photochromic and Luminescence Switching Properties of a Versatile Diarylethene-Containing 1,10-Phenanthroline Ligand and Its Rhenium(I) Complex. *J. Am. Chem. Soc.* **2004**, *126*, 12734–12735.
- [56] Guerchais, V.; Ordronneau, L.; Le Bozec, H. Recent Developments in the Field of Metal Complexes Containing Photochromic Ligands: Modulation of Linear and Nonlinear Optical Properties. *Coord. Chem. Rev.* **2010**, *254*, 2533–2545.
- [57] Pielak, K.; Bondu, F.; Sanguinet, L.; Rodriguez, V.; Castet, F.; Champagne, B. Acido-Triggered Switching of the Second-Order Nonlinear Optical Properties of a Ferrocenyl-Containing Indolino-Oxazolidine Derivative. *Dye. Pigment.* **2019**, *160*, 641–646.
- [58] Pielak, K.; Tonnelé, C.; Sanguinet, L.; Cariati, E.; Righetto, S.; Muccioli, L.; Castet, F.; Champagne, B. Dynamical Behavior and Second Harmonic Generation Responses in Acido-Triggered Molecular Switches. *J. Phys. Chem. C* **2018**, *122*, 26160–26168.
- [59] Bouquiaux, C.; Tonnelé, C.; Castet, F.; Champagne, B. Second-Order Nonlinear Optical Properties of an Amphiphilic Dye Embedded in a Lipid Bilayer. A Combined Molecular Dynamics–Quantum Chemistry Study. *J. Phys. Chem. B* **2020**, *124*, 2101–2109.

When the π -conjugation of a connector cheats the statistical transformation of an octastate multimodal molecular switch: a theoretical characterization

Abstract

Benzazolooxazolidines (BOXs) have already demonstrated their benefits for the elaboration of multichromophoric systems. However, so far, this has been limited to symmetrical compounds containing two BOX units, which reduces the number of possible states. In this contribution, quantum chemistry calculations have been enacted to study molecular switches containing three BOX units. Then, besides the first compound where the three linkers are equivalent, this investigation has been extended to unsymmetrical triBOX, leading to 8 distinct states whereas the symmetrical compound only contains four. The main results are the following: i) the first opening leads to synergic changes in the (non)linear optical properties, ii) the following openings are accompanied by modest variations of these properties, though the variation of the depolarization ratio could help distinguishing between the different states, iii) the protonation as well as the oxidation are predicted to be sequential, and iv) for the unsymmetrical compound, the sequence is the same for both stimuli.

Note. This chapter corresponds to a manuscript in an early redaction stage. It gathers the contributions from J. Stiennon, M. Hodée, J. Quertinmont, P. Beaujean, B. Champagne, Y. Aidibi, and L. Sanguinet.

Section 9.1

Introduction

Due to their numerous application fields, the elaboration of molecular switches continues to raise a great attention. They are defined as molecular systems which are able to undergo a reversible conversion between, at least, 2 (meta)stable states under the application of an external stimulation.¹ Exhibiting different physicochemical properties from each other, this switching between the different forms conducts to the possibility to elaborate materials where a desired property can be modulated on demand. In this context, numberless molecular systems were reported in the literature to modulate the color, the luminescence, the electrochemical potential, the conductivity or the supramolecular assembly of the systems.² To classify them, the nature of the trigger is generally used conducting to define several families such as halochromic (pH changes), photochromic (light irradiation), electrochromic (change of electrochemical potential), thermochromic (temperature) and piezochromic (pressure) compounds to name a few.³

The search of more performant systems allowing a modulation of a molecular property over several discrete levels has driven the research to the elaboration of multichromophoric systems. To prepare them, the general strategy consists in combining several switchable units, issued from one or several families, by covalent linkage^{4,5} or via a supramolecular assembly process.⁶ Indeed, a multichromophoric system gathering n two-state switches can theoretically exhibit up to 2^n distinct states. Such systems represent then a promising approach to the design of molecular-scale high-density optical memory or multinary logic devices.⁷⁻⁹

In this context, the elaboration of photo- and redox-active materials is particularly appealing due to their potential applications in data storage or molecular logic gates.¹⁰⁻¹² Despite the synthetic efforts to overcome in order to prepare such multi-chromophoric systems, the selective addressability of the different constitutive switching units is still challenging. As highlighted by numerous studies on systems combining several diarylethene (DAE) units, one of the most studied photoswitch family,¹³⁻¹⁹ their selective addressability is not efficient when a metal complex center is used to combine them. At the opposite, the photocyclization of one DAE unit impedes the photoreactivity of the remaining ones when they are connected through a π -conjugated linker. As a consequence, the fully closed form of these kinds of multichromophoric systems can hardly be obtained.²⁰ In a similar manner, azobenzene based multichromophoric systems have also been thoroughly studied.²¹⁻²⁴ As in DAE-based multichromophoric systems, the photoswitching capacity of the different azobenzene units is detrimentally affected by the electronic delocalization. Using a π -conjugated core to connect several azobenzene leads generally to a reduction of the photoswitching capacity. At the opposite, a saturated spacer ensures a complete electronic decoupling of the different photochromic units but it conducts also to an independent behavior of these photochromic unit

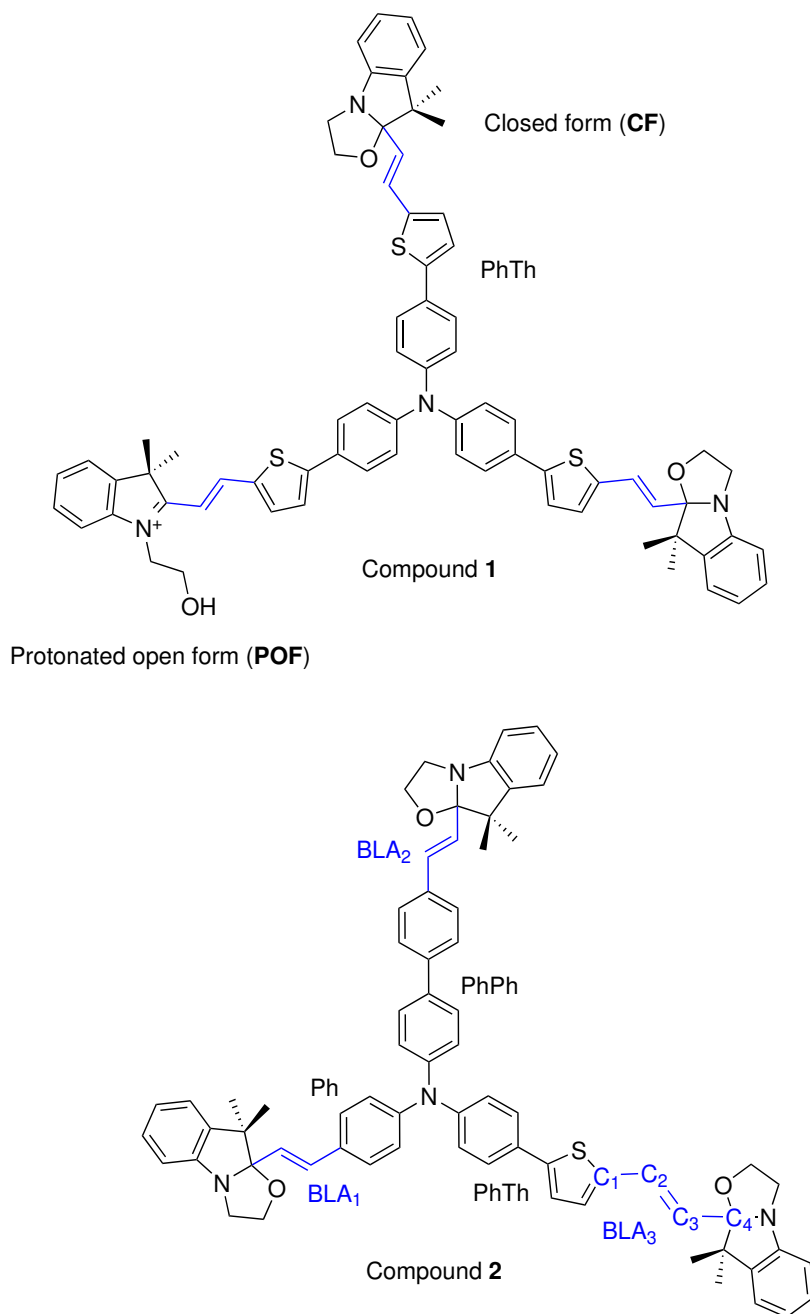
and to the formation of complex mixtures of the different isomers under light irradiation. As a consequence, the implementation of multiple switches in a unique molecular system is not a trivial task and actually many efforts are devoted to optimize the substitution pattern in order to combine photoactivity, selective addressability and molecular properties modulation.^{25,26}

To overcome this situation, we and others are involved in the elaboration and in the study of multistimuli-responsiveness molecular systems.²⁷ Including multiple active parts that can be addressed by using orthogonal stimuli, such systems appear as promising solutions to reach some molecular machines or data storage materials exhibiting a higher degree of complexity and functionality. In this framework, indolino[2,1-b]oxazolidine derivatives (later referenced as BOX) have particularly caught our attention. Firstly, reported at the end of the last century,²⁸ these systems were known to present acido- and photochromic properties.^{29,30} Resulting from the opening of the oxazolidine ring by adding some acid or UV light irradiation, the possibility to address them was recently extended to electrochemical stimulation. The electro-induced opening of the oxazolidine results either from the direct oxidation of the BOX³¹ or from an indirect electromediated process when a redox active system is present on position 2.³² In both cases, the oxidation of the colorless form conducts to the formation of the corresponding radical cation, which is forthwith converted to the colored protonated open form, after abstraction of a hydrogen atom from the surrounding media.^{32–34} Restoration of the initial closed state from the open form can then be obtained indifferently by using either a base treatment or an electrochemical reduction and, in more rare cases, by visible light irradiation.

As importantly, BOX units have already demonstrated their benefits for the elaboration of performant multichromophoric systems. Their combination with some other photochromic units such as a DAE has led to molecular systems exhibiting an impressive number of metastable states.^{35,36} Unfortunately, the generation of each of them results from a clever and successive use of different types of stimulation (UV/visible light; acid/base; oxidation/reduction) which can be detrimental for some applications. Linking two identical BOX units in direct electronic conjugation also conducts to promising molecular systems.^{37–40} With an easy and straightforward synthesis, these systems have revealed interesting and complex switching behavior. If a stepwise opening of both oxazolidine rings is globally observed whatever the nature of the stimulation (proton, electron, photon), electrochemical stimulation allows a perfect selective addressability of each BOX. Unfortunately, multi-BOX systems are, to the best of our knowledge, restricted to symmetric compounds, which limits drastically the number of reachable states.³⁹ The elaboration of unsymmetrical structures involving several BOX units is then appealing to overcome this limitation and to prepare more performant systems.

In such purpose, and following the methodology used for diBOX,⁴⁰ we present here the theoretical characterization of a system based on symmetrical (1) and unsymmetrical (2) tri-arylamine bearing three BOX units (Scheme 9.1). Focusing on the forms obtained through protonation and dropping the cis-trans isomerization, up to 2^3 states are thus possible. The presentation of this work is organized in three parts: after a review of the computational

details in Section 9.2, the main results for the two triBOX are presented in Section 9.3. First, the structural properties are analyzed, following by the study of the reactivity upon addition of different equivalents of acid. Then, the linear and nonlinear properties of the different forms are reviewed. Finally, Section 9.4 draws the main conclusions.



Scheme 9.1: Structure of the triBOX **1** (top) and **2** (bottom), with the nomenclature of the two forms of the BOX (closed and protonated open), of the different π -conjugated linkers (phenyl [Ph], biphenyl [PhPh], and phenylthiophene [PhTh]), and definition of the different segments where the BLA are calculated (in blue).

Section 9.2

Theoretical and computational aspects

The geometries of all compounds and of the different forms obtained by opening 1, 2, or the 3 BOXs were fully optimized at the DFT level with the ω B97X-D XC functional,^{41,42} the 6-311G(d) basis set, and by accounting for solvent effects using the integral equation formalism of the polarizable continuum model (IEF-PCM) (the solvent is acetonitrile).⁴³ Real vibrational frequencies demonstrate that the optimized geometries are minima on the potential energy hyper-surface. Since the triBOX compounds are mostly composed of cyclic units and conjugated segments, the numbers of stable conformers in solution are rather small and the search of those conformers possessing a non-negligible weight within the Maxwell-Boltzmann (MB) statistics can be carried out in a systematic manner. This was done i) by defining the key torsion angles to distinguish the main conformations, ii) then by performing rigid scans to locate the extrema of the potential energy hyper-surface, iii) by combining the minima of the rigid scans to preselect conformations, and then iv) by performing full geometry optimizations on the latter. Finally, only those conformers within an energy window of 12.5 kJ mol^{-1} higher than the most stable conformer were kept to calculate the MB populations, on the basis of the Gibbs free energies, ΔG^0 , at 298.15 K. Such approach is efficient to locate the key conformers because the torsion angles are far enough from each other and, in first approximation, their impact on the total energy is considered as independent from each other, leading to a quasi-additive behavior. In the following, averaged results following the MB populations of conformers are reported. Note that, in this contribution, it is assumed that there is no equilibrium between forms with different levels of opening when computing the MB populations.

To assess the impact of the state of opening on the structure and on the π -conjugation of the molecules, the bond length alternation (BLA) of the vinylidene segment between the linker and the BOX units were analyzed. Given the π -conjugated segment $C_1-C_2=C_3-C_4$ (Scheme 9.1), the BLA is computed as

$$\text{BLA} = \frac{1}{2} (l_{12} + l_{34} - 2l_{23}), \quad (9.1)$$

where l_{ij} is the distance between carbon i and j .

For each form, the vertical excitation energies (ΔE_{ge}) and the transition dipole moments (μ_{ge}) were calculated for, at least, the 10 lowest-energy excited states at the TDDFT level using the M06-2X XC functional,⁴⁴ the 6-311+G(d) basis set, and accounting for solvent effects using the IEF-PCM scheme. The quantities were used to calculate the oscillator strengths ($f_{ge} = \frac{2}{3} \Delta E_{ge} \mu_{ge}^2$) and then employed to plot the UV/vis absorption spectra (each transition was associated with a Gaussian function, centered on ΔE_{ge} , of intensity proportional to f_{ge} , and of full width at half maximum of 0.3 eV). Further TDDFT calculations were also performed to evaluate the difference of electronic density between the ground and excited

states, $\Delta\rho(\mathbf{r}) = \rho_e(\mathbf{r}) - \rho_g(\mathbf{r})$. Following the procedure described by Le Bahers et al.,⁴⁵ the barycenters of the positive $[\Delta\rho^+(\mathbf{r})]$ and negative $[\Delta\rho^-(\mathbf{r})]$ electronic density variations were evaluated. The distance between these barycenters defines the charge-transfer distance (d_{CT}) while their integration over the whole space gives the amount of charge transferred (q_{CT}). The product of these two quantities gives the difference between the ground and key excited state, $\Delta\mu_{ge} = \mu_e - \mu_g$. The calculations of all these excited state-related properties, including the electronic densities, employed the nonequilibrium solvation approach since electronic excitation processes are very fast with respect to the solvent reorganization.⁴⁶

Finally, the NLO properties were computed for each form at the same level of approximation [M06-2X/6-311+G(d) in acetonitrile (IEF-PCM)]. Here, we focus on the evaluation of the quantities obtained in the Hyper-Rayleigh scattering (HRS) experiment: β_{HRS} and its depolarization ratio (DR) as defined by the sum and ratio of the β -tensor orientational averages,⁴⁷ respectively, according to:

$$\beta_{HRS} = \sqrt{\langle\beta_{ZZZ}^2\rangle + \langle\beta_{ZXX}^2\rangle} \text{ and } DR = \frac{\langle\beta_{ZZZ}^2\rangle}{\langle\beta_{ZXX}^2\rangle}. \quad (9.2)$$

as depicted in Chapter 2. From the two-state approximation of β ⁴⁸, One can also derive an effective β^{2ST} based on the quantities extracted from UV/visible spectra, as:

$$\beta^{2ST} = \sqrt{\frac{6}{35}} |\beta_{zzz}| = 6 \sqrt{\frac{6}{35}} \frac{(\mu_{ge})^2 |\Delta\mu_{ge}|}{\Delta E_{ge}^2} = 9 \sqrt{\frac{6}{35}} \frac{f_{ge} |\Delta\mu_{ge}|}{\Delta E_{ge}^3}. \quad (9.3)$$

The two-state approximation is generally useful for understanding and designing NLO compounds (further developments are presented in Chapter 11).

As noted, a different XC functional was used for calculating the linear and nonlinear optical properties (M06-2X, 54 % HF exchange) and the structural and thermodynamic data (ω B97X-D, 16 % and 100 % of HF exchange at short- and long-range, respectively, with a range-separating parameter $\omega = 0.2 a_0^{-1}$). This is consistent with previous studies on related compounds,⁴⁹ which show that range-separated hybrids generally overestimate the excitation energies while hybrids with about 50 % of HF exchange provide closer agreement.^{50–53} All (TD)DFT calculations were carried out using the Gaussian 16 package.⁵⁴

Section 9.3

Results and discussion

Structural properties

The BLA values, found in Table 9.1, are all positive. They demonstrate the impact of openings: the BLA of the vinylidene path decreases substantially as the corresponding BOX opens.

This is interpreted as an increase of the π -conjugation. Moreover, the influence of the linker (compound **2**) is also visible, since the BLA of the Ph and PhPh linkers are slightly larger than the one of the PhTh linker (0.157 versus 0.147 Å) for the CCC form. Upon opening, the trend becomes PhTh < Ph < PhPh, which indicates that the delocalization is the strongest for the phenylthiophene linker and the weakest for the biphenyl, as expected from the non-negligible torsion angle between the phenyl rings that results in steric hindrance. Concerning the PhTh linker, note that its BLA values are similar in compounds **1** and **2**. A more subtle effect is evidenced by the sequential openings in compound **1** (but also found in compound **2**), in which the BLA, and so the π -conjugation, slightly increases, revealing that the BOX units are competing.

	BLA ₁	BLA ₂	BLA ₃
Compound 1			
CCC	0.147	0.147	0.147
OCC	0.059	0.147	0.147
OOC	0.061	0.061	0.147
OOO	0.062	0.062	0.062
Compound 2			
Ph(C)-PhPh(C)-PhTh(C)	0.156	0.157	0.147
Ph(C)-PhPh(C)-PhTh(O)	0.157	0.157	0.056
Ph(C)-PhPh(O)-PhTh(C)	0.156	0.085	0.147
Ph(O)-PhPh(C)-PhTh(C)	0.064	0.157	0.147
Ph(C)-PhPh(O)-PhTh(O)	0.157	0.086	0.058
Ph(O)-PhPh(C)-PhTh(O)	0.069	0.157	0.061
Ph(O)-PhPh(O)-PhTh(C)	0.067	0.087	0.147
Ph(O)-PhPh(O)-PhTh(O)	0.070	0.087	0.062

Table 9.1: BLA values (Å) of the different forms of the two triBOX compounds, as evaluated at the ω B97X-D/6-311-G(d)/IEF-PCM (acetonitrile) level of theory. These are averaged values using the MB population at 298.15 K as calculated at the ω B97X-D/6-311-G(d)/IEF-PCM (acetonitrile) level of theory.

Acidochromic and electrochromic properties

Using the whole set of conformers, Figure 9.1a shows that the opening of the BOX by protonation can be sequential since the successive openings are less and less exergonic. It is also predicted to be spontaneous with trifluoroacetic acid (TFA). The differences of ΔG^0 values along these successive openings are larger in the case of compound **2** than **1**, which is attributed to the presence of different π -conjugated linkers. For compound **2**, following

the most spontaneous sequence of opening, **Ph(O)-PhPh(C)-PhTh(C)** (61 % of **OCC**) and **Ph(O)-PhPh(C)-PhTh(O)** (87 % of **OOC**) are the most prevalent. This prediction indicates that adressability is thus possible, though not perfect (especially for **OCC**).

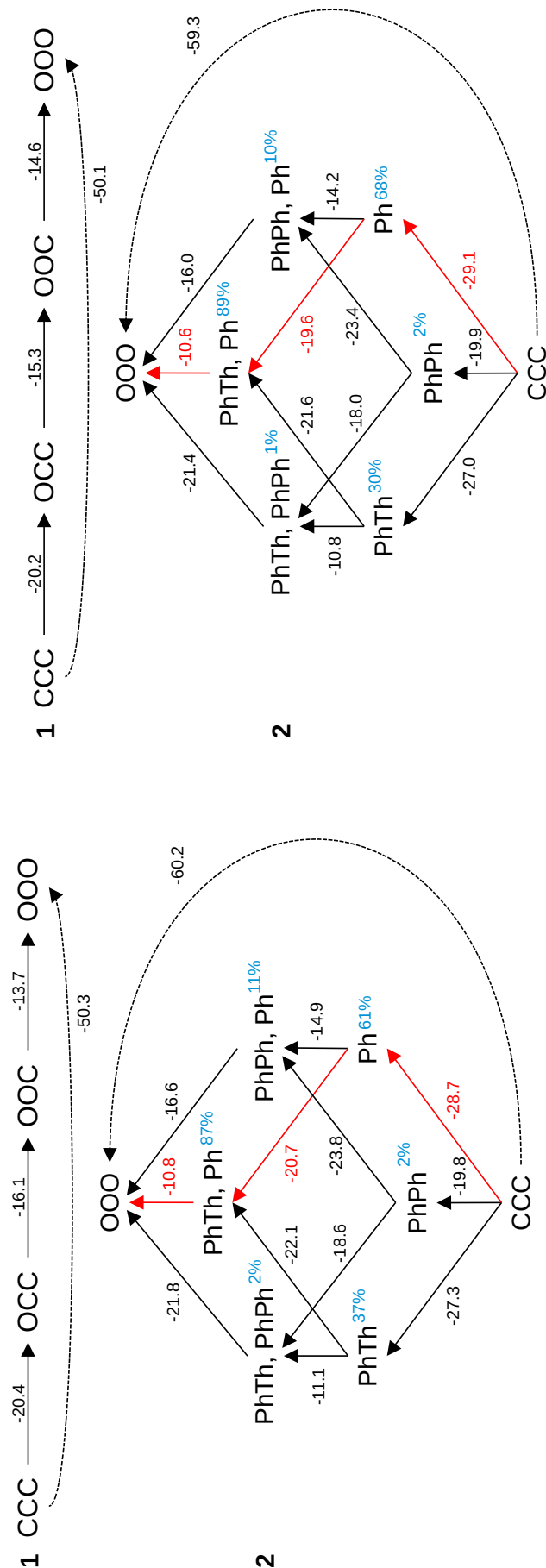
If only the most stable conformers of each form are considered (Figure 9.1b), the predicted ΔG^0 are affected by 1 kJ mol^{-1} or less, which leads to the same conclusion concerning the sequence of opening. It shows that accurate results can also be obtained, in first approximation, by only considering the most stable conformer.

To confirm that the electrochromic behavior was similar, Figure 9.2 presents analogous results, beside the fact that only the most stable conformer of each form of compound **2** was considered. If the whole set of conformers was considered, we expect the change to be similar to the one of Figure 9.1. The underlying electrochemical mechanism is considered to be a three-step process: i) an oxidation (removing of an electron) occurs, leaving a radical species $[\text{triBOX}-\text{CF}]^{\bullet+}$ (first arrow in Figure 9.2), ii) a homolytic cleavage of the C–O bond in a BOX unit occurs, giving $[\text{triBOX}-\text{OF}]^{\bullet+}$ (second arrow in Figure 9.2), and iii) a hydrogen abstraction (generally from the solvent) occurs, resulting in $[\text{triBOX}-\text{POF}]^+$. The potential of oxidation (step 1) tends to increase with the number of already opened BOX units, while, at a given level of opening, the linkers modulate this behavior: oxidizing the compound with an open BOX on the Ph arm requires the largest potential of oxidation, while it is the lowest with the PhPh linker. Furthermore, for the first opening, the C–O cleavage in the BOX (step 2) which is beared by the Ph linker is least exergonic, followed by the one of the PhPh arm for the second opening. Thus, the preferential sequence of opening is equivalent to the one observed with protonation.

Nonlinear optical properties

Table 9.2 reports the static and dynamic NLO properties (β_{HRS} and DR) of compounds **1** and **2**. The β_{HRS} values are similar, though slightly smaller for compound **2**. The **CCC** form possesses the weakest NLO response, while the β_{HRS} responses of the others are similar, and in the order **OOO** < **OOC** < **OCC** at all frequencies for compound **2** (the last two are reversed for **1**, except at 1064 nm). Moreover, there is a large enhancement at 1064 nm for the open forms, which indicates a (near) resonance. Table 9.3 details the impact of the different linkers for compound **2**: for **OCC**, the β_{HRS} values follow the PhPh < Ph < PhTh ordering, where the designated linker is attached to the open BOX. For **OOC**, the largest value is achieved when the open BOXs are linked to the Ph and PhTh units. Those two observations are consistent with the BLA values. Indeed the smaller the BLA, the larger the β value. Figure 9.3 reports the different contrasts of β_{HRS} at 1907 nm: the largest contrasts are the ones involving **CCC** (especially in compound **1**), the others being of lesser amplitude (close to unity).

To continue in the analysis of the HRS responses, the evolution of the DR is prototypical: at the first opening, the triBOX compounds go from octupolar ($\text{DR} \sim 1.7$, due to their C_3 -like topology) to linear ($\text{DR} \sim 5$), since the response of the latter is dominated by the open



(a) Computed using the weighted average results as calculated at the ω B97X-D/6-311-G(d)/IEF-PCM (acetonitrile) level of theory.

Figure 9.1: Gibbs free energy (ΔG^0 , kJ mol^{-1}) at 298.15 K of the successive protonation reactions of triBOs 1 and 2 with trifluoroacetic acid (TFA) as a function of the level of opening, with (left) or without (right) the weighted average. The calculation used the ω B97X-D/6-311-G(d)/IEF-PCM (acetonitrile) level of theory for the triBOX, and the ω B97X-D/6-311-G(d)/IEF-PCM (acetonitrile) level of theory for the TFA. The dashed arrows indicate the total change of ΔG^0 of the 3 successive protonations, while, for 2, the red arrows indicate the most spontaneous sequence of openings ($\text{Ph} \rightarrow \text{PhTh} \rightarrow \text{PhPh}$) and the population (in percent) is given in blue for the intermediate (1 and 2 equivalent of acid) forms.

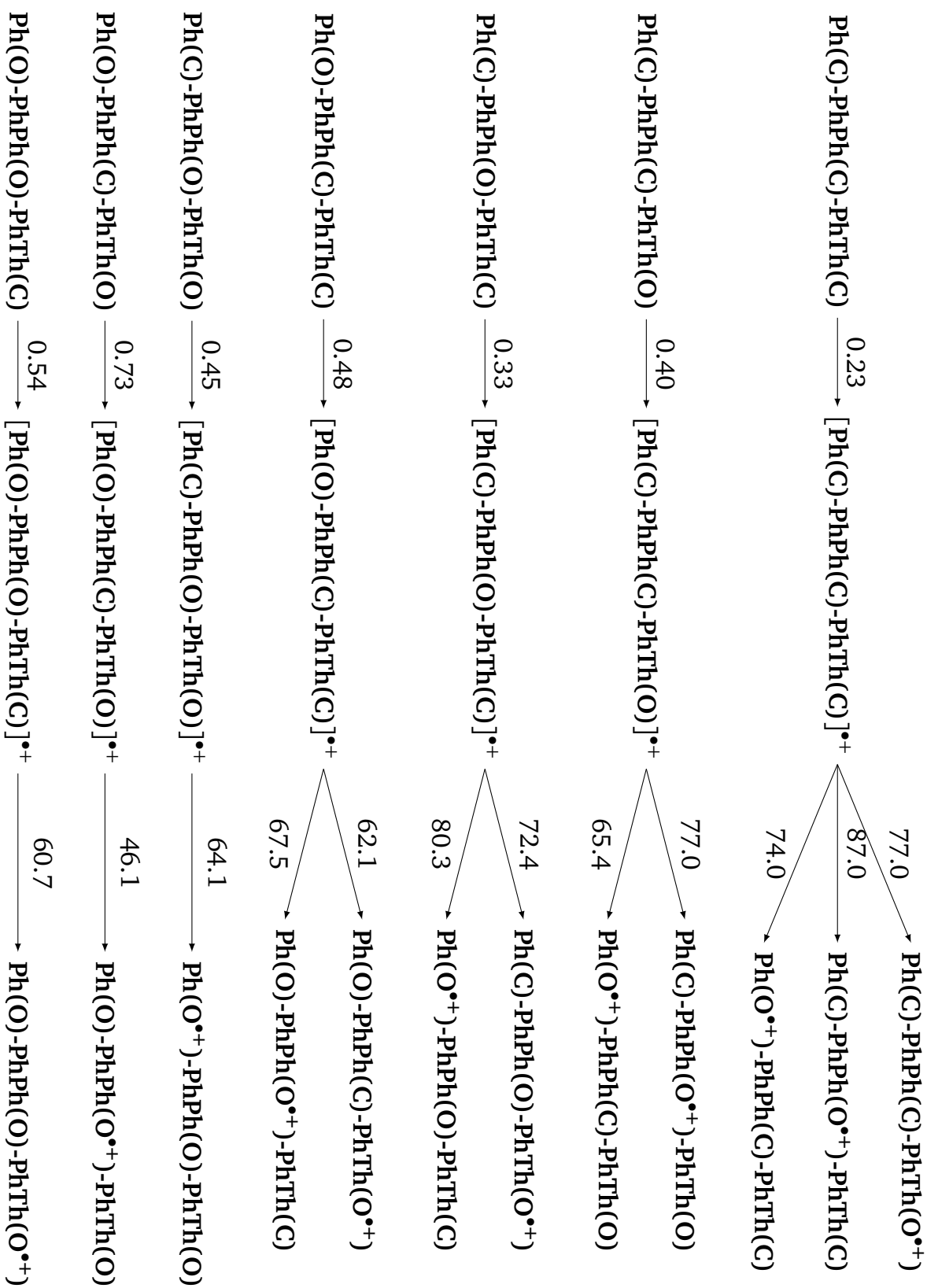


Figure 9.2: Oxidation potential (ΔG^0 , kJ mol⁻¹, first arrow) and Gibbs free energy (ΔG^0 , kJ mol⁻¹, second arrow) of the following C–O bond cleavage of triBOX **2** as a function of the level of opening calculated at the ω B97X-D/6-311-G(d)/IEF-PCM (acetonitrile) level of theory on the most stable conformers at 298.15 K.

		Static	1907 nm	1300 nm	1064 nm
Compound 1	CCC	4.2 (1.72)	4.4 (1.64)	6.0 (1.61)	6.6 (1.59)
	OCC	43.1 (4.47)	52.5 (4.54)	114.9 (4.74)	528.1 (4.96)
	OOC	45.4 (2.92)	55.2 (2.91)	116.2 (3.07)	514.4 (2.94)
	OOO	39.8 (1.52)	50.3 (1.47)	105.7 (1.46)	410.4 (1.46)
Compound 2	CCC	3.6 (1.64)	3.6 (1.63)	5.0 (1.65)	7.0 (1.68)
	OCC	35.6 (4.65)	37.3 (4.70)	76.7 (4.82)	281.9 (4.93)
	OOC	34.9 (3.19)	36.2 (3.12)	68.2 (3.24)	202.0 (3.16)
	OOO	30.7 (3.24)	32.8 (3.16)	62.4 (3.37)	179.2 (3.84)

Table 9.2: Computed static and dynamic first hyperpolarizabilities (β_{HRS} in 10^3 a.u., DR in parentheses) of triBOX **1** and **2** in their different forms, as evaluated at the TDDFT/M06-2X/6-311+G(d)/IEF-PCM (acetonitrile) level of approximation. These are averaged values using the MB population at 298.15 K as calculated at the ω B97X-D/6-311-G(d)/IEF-PCM (acetonitrile) level of theory.

		Static	1907 nm	1300 nm	1064 nm
	Ph(C)-PhPh(C)-PhTh(O)	42.2 (4.66)	48.3 (4.69)	108.8 (4.83)	502.4 (4.92)
OCC	Ph(C)-PhPh(O)-PhTh(C)	27.5 (4.13)	33.5 (4.31)	62.5 (4.52)	148.9 (4.75)
	Ph(O)-PhPh(C)-PhTh(C)	32.0 (4.67)	30.8 (4.71)	58.0 (4.82)	154.6 (4.93)
	Ph(C)-PhPh(O)-PhTh(O)	33.8 (2.93)	39.3 (2.92)	83.6 (3.28)	347.8 (3.68)
OOC	Ph(O)-PhPh(C)-PhTh(O)	35.8 (3.23)	36.9 (3.16)	69.8 (3.27)	206.6 (3.11)
	Ph(O)-PhPh(O)-PhTh(C)	31.4 (3.19)	32.7 (3.12)	58.2 (3.24)	151.3 (3.16)

Table 9.3: Details of the computed static and dynamic first hyperpolarizabilities (β_{HRS} in 10^3 a.u., DR in parentheses) of triBOX **2** in their different forms after one or two protonations (and BOX openings), as evaluated at the TDDFT/M06-2X/6-311+G(d)/IEF-PCM (acetonitrile) level of approximation. These are averaged values using the MB population at 298.15 K as calculated at the ω B97X-D/6-311-G(d)/IEF-PCM (acetonitrile) level of theory.

BOX unit, creating one preferential charge-transfer direction. Then, the octupolar character increases with the second opening, as expected for V-shaped compounds.⁵⁵ Table 9.3 confirms that this trend and the previous are similar for all 3 linkers. Finally, when forming the totally opened form, **OOO**, the octupolar character is restored for compound **1**, while it is less marked for compound **2**, owing the influence of the less conjugated PhPh linker. Nevertheless, the DR provides a (additional) way to differentiate between the different forms.

UV/visible absorption spectra and related properties

Figure 9.4 and the data of Table 9.4 demonstrate that for compound **1**, i) the first opening is associated with a substantial bathochromic shift (140 nm or 1.0 eV), ii) the second and third

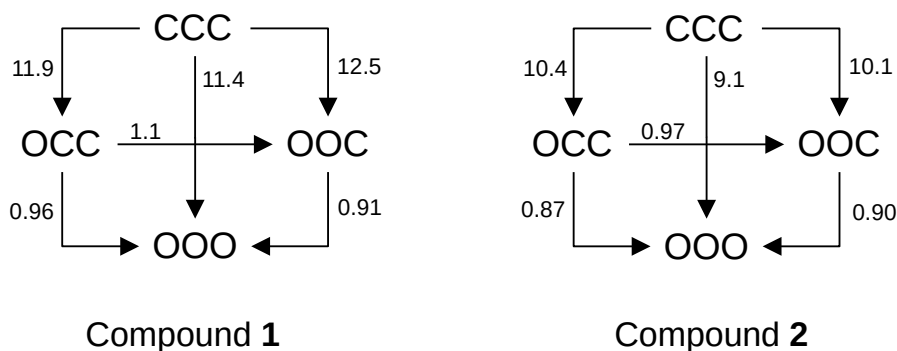


Figure 9.3: Contrasts of dynamic (at 1907 nm) first hyperpolarizability [given by $\beta(\text{end}) / \beta(\text{start})$ on the arrows] of triBOXs **1** and **2** in their different forms, as evaluated at the TDDFT/M06-2X/6-311+G(d)/IEF-PCM (acetonitrile) level of approximation. These are averaged values using the MB population at 298.15 K as calculated at the ω B97X-D/6-311-G(d)/IEF-PCM (acetonitrile) level of theory.

openings are only associated with negligible shifts, but iii) these second and third openings lead to a substantial increase of the intensity of the low-energy absorption band. Moreover, the charge transfer character of that low-energy transition, as estimated from $\Delta\mu_{ge}$, increases by a factor of 3 from the **CCC** to the **OCC** form. The second opening leads to a $\Delta\mu_{ge}$ value that is only 40 % of the one of **OCC** while the fully open structure presents a $\Delta\mu_{ge}$ value, which is 50 % of that of the **OCC** form.

		λ_{ge}	ΔE_{ge}	f_{ge}	q_{CT}	d_{CT}	$\Delta\mu_{ge}$	β^{2ST}
Compound 1	CCC*	359	3.45	1.55	0.57	2.21	6.10	6.7 (4.2)
	OCC	500	2.48	1.79	0.64	5.79	23.22	80.3 (43.1)
	OOC	505	2.45	2.41	0.79	2.95	11.13	53.7 (45.4)
	OOO*	493	2.51	2.43	0.74	3.20	11.35	51.3 (39.8)
Compound 2	CCC	353	3.51	1.44	0.57	2.79	7.64	7.5 (3.6)
	OCC	483	2.57	1.76	0.75	4.49	16.41	49.4 (35.6)
	OOC	488	2.54	2.29	0.70	2.63	8.90	36.8 (34.9)
	OOO	486	2.55	1.93	0.70	2.37	7.91	27.1 (30.7)

Table 9.4: Vertical excitation wavelengths (λ_{ge} , nm), excitation energies (ΔE_{ge} , eV), oscillator strengths (f_{ge}), amounts of charge transfer (q_{CT} , e), distances of charge transfer (d_{CT} , Å), variations of dipole moment ($\Delta\mu_{ge}$, D), and effective β (β^{2ST} , in 10^3 a.u., corresponding static β_{HRS} in parentheses) associated with the $S_0 \rightarrow S_1$ excitation of triBOX **1** (doubly-degenerated transitions are marked with a star) and **2** in their different forms, as evaluated at the M06-2X/6-311+G(d)/IEF-PCM (acetonitrile) level of approximation. These are averaged values using the MB population at 298.15 K as calculated at the ω B97X-D/6-311-G(d)/IEF-PCM (acetonitrile) level of theory.

In the case of compound **2**, the global behavior along the successive openings is similar, with a major bathochromic shift of 130 nm or 0.9 eV occurring at the first opening. Again, the openings are associated with an increase of the absorption intensity but also with a broadening of the absorption band because of the presence of different π -conjugated linkers between the open BOX(s) and the central electron-donating triarylamine unit, having their own optical characteristics. This is illustrated in Figure 9.5, where, for the **OCC** form, opening the BOX on the PhPh, Ph, and PhTh arms results in bathochromic shifts of 101, 120, and 148 nm, respectively (which is, again, consistent with the trends in BLA). Similarly, for the **OOC** form, the λ_{ge} values differ by 20 nm depending on which BOX is open or closed. In addition, like

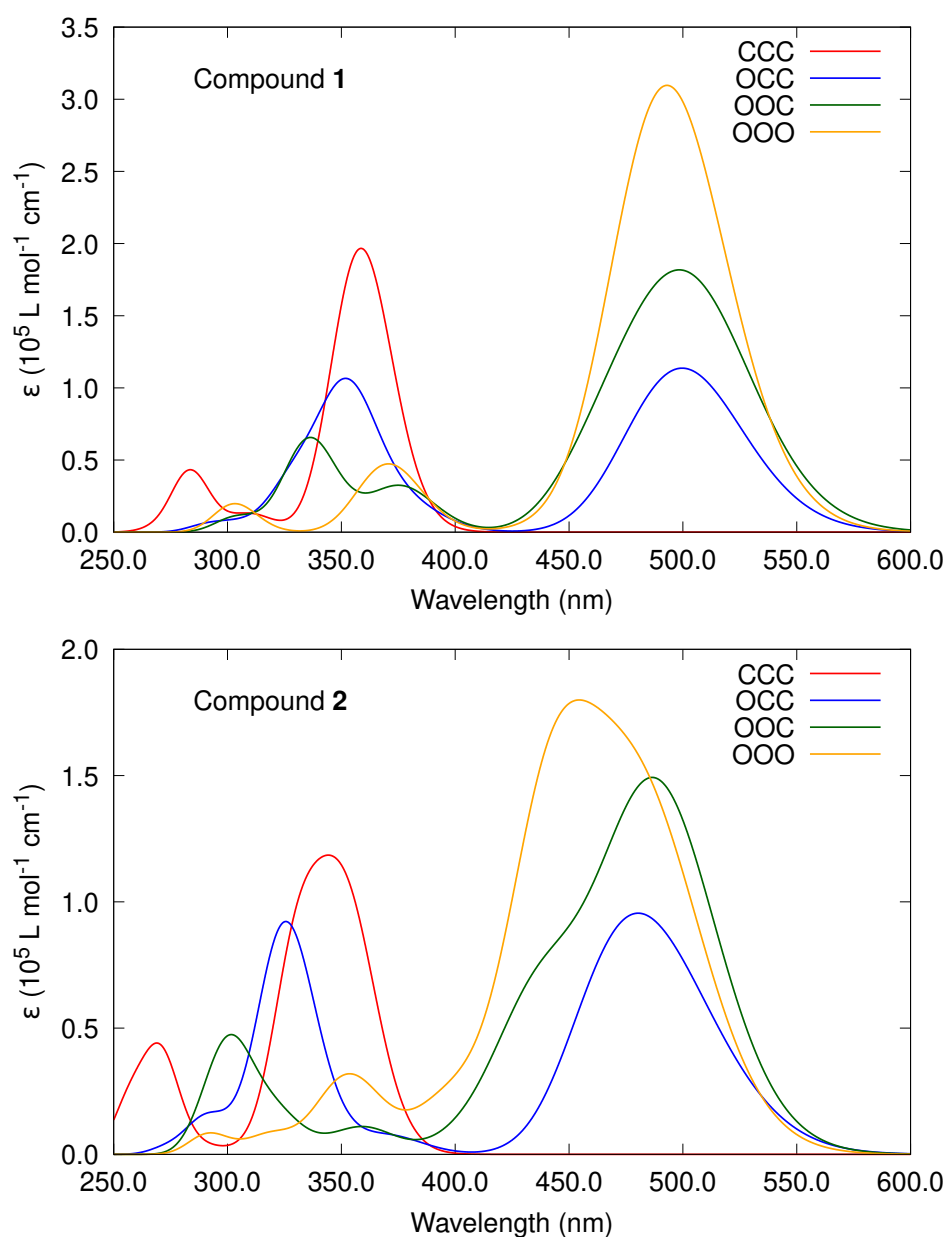


Figure 9.4: TDDFT/M06-2X/6-311+G(d)/IEF-PCM (acetonitrile) simulated UV/vis absorption spectra of triBOX **1** (top) and **2** (bottom) after successively adding, 0, 1, 2, and 3 equivalents of TFA using the weighted average results as calculated at the ω B97X-D/6-311-G(d)/IEF-PCM (acetonitrile) level of theory.

	λ_{ge}	ΔE_{ge}	f_{ge}	q_{CT}	d_{CT}	$\Delta\mu_{ge}$	β^{2ST}
Ph(C)-PhPh(C)-PhTh(O)	501	2.47	1.66	0.83	5.30	21.01	68.2 (42.2)
OCC Ph(C)-PhPh(O)-PhTh(C)	454	2.73	1.45	1.04	6.73	33.64	70.5 (27.5)
Ph(O)-PhPh(C)-PhTh(C)	473	2.62	1.83	0.69	3.94	13.10	39.2 (32.0)
Ph(C)-PhPh(O)-PhTh(O)	495	2.50	2.06	0.80	4.75	18.26	71.2 (33.8)
OOC Ph(O)-PhPh(C)-PhTh(O)	490	2.53	2.34	0.70	2.47	8.31	35.5 (35.8)
Ph(O)-PhPh(O)-PhTh(C)	475	2.61	1.95	0.70	3.55	12.00	39.0 (31.4)

Table 9.5: Detail of the vertical excitation wavelengths (λ_{ge} , nm), excitation energies (ΔE_{ge} , eV), oscillator strengths (f_{ge}), amounts of charge transfer (q_{CT} , e), distances of charge transfer (d_{CT} , Å), variations of dipole moment ($\Delta\mu_{ge}$, D), and effective β (β^{2ST} , in 10^3 a.u., corresponding static β_{HRS} in parentheses) associated with the $S_0 \rightarrow S_1$ excitation of triBOX **2** in their different forms, as evaluated at the M06-2X/6-311+G(d)/IEF-PCM (acetonitrile) level of approximation. These are averaged values using the MB population at 298.15 K as calculated at the ω B97X-D/6-311-G(d)/IEF-PCM (acetonitrile) level of theory.

for **1**, the largest charge transfer ($\Delta\mu_{ge}$) is observed for the **OCC** form whereas they differ by little for the other forms. From Table 9.5, it is found that the opening of the BOX on the PhPh π -conjugated linker leads to the largest $\Delta\mu_{ge}$ value. The excitation energy values also enable to confirm that the large β values at 1064 nm originates from the (near) resonant effect.

The different optical properties have then been employed to estimate the static β_{HRS} values within the two-state approximation (Eq. 9.3). Though the model can be extended by including additional excited states,^{55,56} there is an overall good qualitative agreement between the two sets of data, with a general tendency of the two-state approximation to overestimate the β_{HRS} values. In particular, for the **OCC**, **OOC**, and **OOO** forms, this model reproduces the reduction of β_{HRS} values when going from compound **1** to compound **2**, further substantiating the dominant role of the lowest-excitation energy state in the second-order NLO response.

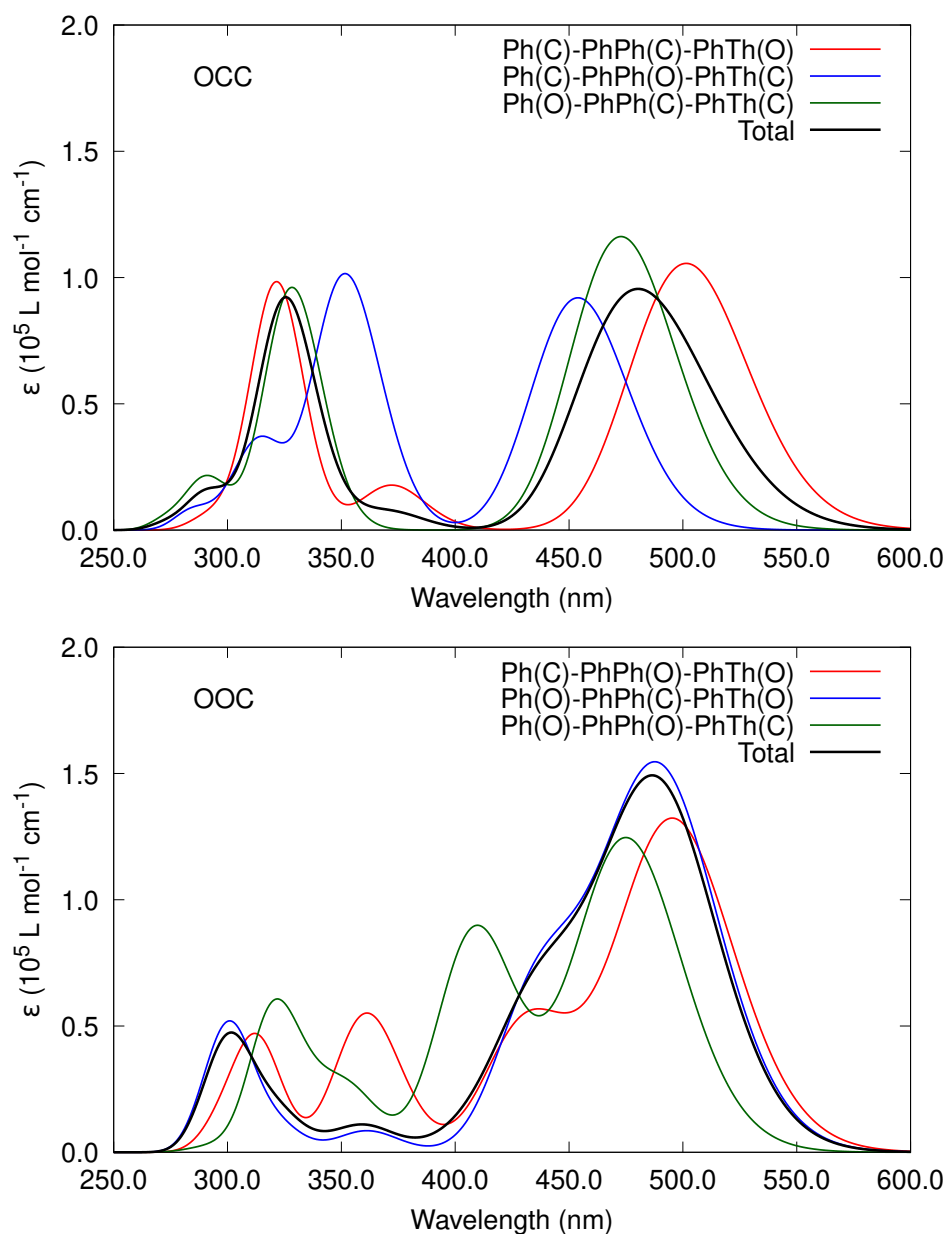


Figure 9.5: Detail of the TDDFT/M06-2X/6-311+G(d)/IEF-PCM (acetonitrile) simulated UV/vis absorption spectra of **2** after one or two protonation (and BOX openings) using the weighted average results as calculated at the ω B97X-D/6-311-G(d)/IEF-PCM (acetonitrile) level of theory.

Section 9.4

Conclusions

In this study, molecular switches containing three BOX units have been studied by using quantum chemistry calculations at the DFT and TDDFT levels. Two molecular switches have been considered. The first one (**1**) is built from a central triarylamine unit substituted by identical arms containing a thienyl group, an ethylenic linker, and a BOX. It is a symmetrical triBOX that can adopt four different states as a function of the number of open/closed BOX(s).

Indeed, the BOXs are the switchable units that can be close or open and when the BOX is open, it creates a push-pull π -conjugated charge-transfer moiety with the triarylamine one. The second triBOX (**2**) is unsymmetrical, owing to the different arms between the central nitrogen atom and the BOX (Ph, PhPh, and PhTh). As a function of the level of opening and which arm(s) bear(s) the open BOX(s), triBOX **2** can adopt 8 different states. Calculations have shown that i) the first opening leads to a large change in linear (bathochromic shift) and nonlinear optical properties (tenfold increase of β_{HRS}), ii) the following openings see modest variations of the first excitation energy and β , even though the corresponding absorption band intensity increases, iii) nevertheless, the second and third openings are also accompanied by a change of depolarization ratio, which may help to further differentiate the different forms, iv) the opening mechanism upon protonation is sequential, with partial addressability in the case of **2** (Ph \rightarrow PhTh \rightarrow PhPh), which has been rationalized, and v) this trend is similar upon oxidation.

Bibliography

- [1] Feringa, B. L., Browne, W. R., Eds. *Molecular Switches*, 2nd ed.; Wiley-VCH: Weinheim, Germany, 2011.
- [2] Goulet-Hanssens, A.; Eisenreich, F.; Hecht, S. Enlightening Materials with Photo-switches. *Adv. Mater.* **2020**, *32*, 1905966.
- [3] Bouas-Laurent, H.; Dürr, H. *Photochromism*; Elsevier, 2003; pp XXVII–LIII.
- [4] Andréasson, J.; Pischel, U. Smart Molecules at Work- Mimicking Advanced Logic Operations. *Chem. Soc. Rev.* **2009**, *39*, 174–188.
- [5] Gust, D.; Andréasson, J.; Pischel, U.; Moore, T. A.; Moore, A. L. Data and Signal Processing Using Photochromic Molecules. *Chem. Commun.* **2012**, *48*, 1947–1957.
- [6] Sun, Z.; Huang, Q.; He, T.; Li, Z.; Zhang, Y.; Yi, L. Multistimuli-Responsive Supramolecular Gels: Design Rationale, Recent Advances, and Perspectives. *ChemPhysChem* **2014**, *15*, 2421–2430.
- [7] Andréasson, J.; Pischel, U. Smart Molecules at Work- Mimicking Advanced Logic Operations. *Chem. Soc. Rev.* **2009**, *39*, 174–188.
- [8] Andréasson, J.; Pischel, U. Storage and Processing of Information Using Molecules: The All-Photonic Approach with Simple and Multi-Photochromic Switches. *Isr. J. Chem.* **2013**, *53*, 236–246.
- [9] Andréasson, J.; Pischel, U. Molecules with a Sense of Logic: A Progress Report. *Chem. Soc. Rev.* **2015**, *44*, 1053–1069.
- [10] Browne, W. R.; Pollard, M. M.; de Lange, B.; Meetsma, A.; Feringa, B. L. Reversible Three-State Switching of Luminescence: A New Twist to Electro- and Photochromic Behavior. *J. Am. Chem. Soc.* **2006**, *128*, 12412–12413.
- [11] Ivashenko, O.; Logtenberg, H.; Areephong, J.; Coleman, A. C.; Wesenhagen, P. V.; Geertsema, E. M.; Heureux, N.; Feringa, B. L.; Rudolf, P.; Browne, W. R. Remarkable Stability of High Energy Conformers in Self-Assembled Monolayers of a Bistable Electro- and Photoswitchable Overcrowded Alkene. *J. Phys. Chem. C* **2011**, *115*, 22965–22975.
- [12] Oms, O.; Hakouk, K.; Dessapt, R.; Deniard, P.; Jobic, S.; Dolbecq, A.; Palacin, T.; Nadjo, L.; Keita, B.; Marrot, J.; Mialane, P. Photo- and Electrochromic Properties of Covalently Connected Symmetrical and Unsymmetrical Spiropyran– Polyoxometalate Dyads. *Chem. Commun.* **2012**, *48*, 12103–12105.
- [13] Matsuda, K.; Irie, M. Diarylethene as a Photoswitching Unit. *J. Photochem. Photobiol. C* **2004**, *5*, 169–182.

- [14] Irie, M. Photochromism of Diarylethene Single Molecules and Single Crystals. *Photochem. Photobiol. Sci.* **2010**, *9*, 1535–1542.
- [15] Fukaminato, T. Single-Molecule Fluorescence Photoswitching: Design and Synthesis of Photoswitchable Fluorescent Molecules. *J. Photochem. Photobiol. C* **2011**, *12*, 177–208.
- [16] Bertarelli, C.; Bianco, A.; Castagna, R.; Pariani, G. Photochromism into Optics: Opportunities to Develop Light-Triggered Optical Elements. *J. Photochem. Photobiol. C* **2011**, *12*, 106–125.
- [17] Szalóki, G.; Pozzo, J.-L. Synthesis of Symmetrical and Nonsymmetrical Bisthiénylcyclopentenes. *Chem. Eur. J.* **2013**, *19*, 11124–11132.
- [18] Irie, M.; Fukaminato, T.; Matsuda, K.; Kobatake, S. Photochromism of Diarylethene Molecules and Crystals: Memories, Switches, and Actuators. *Chem. Rev.* **2014**, *114*, 12174–12277.
- [19] Harvey, E. C.; Feringa, B. L.; Vos, J. G.; Browne, W. R.; Pryce, M. T. Transition Metal Functionalized Photo- and Redox-Switchable Diarylethene Based Molecular Switches. *Coord. Chem. Rev.* **2015**, *282-283*, 77–86.
- [20] Jacquemin, D.; Perpète, E. A.; Maurel, F.; Perrier, A. TD-DFT Simulations of the Electronic Properties of Star-Shaped Photochromes. *Phys. Chem. Chem. Phys.* **2010**, *12*, 7994–8000.
- [21] Cisnetti, F.; Ballardini, R.; Credi, A.; Gandolfi, M. T.; Masiero, S.; Negri, F.; Pieraccini, S.; Spada, G. P. Photochemical and Electronic Properties of Conjugated Bis(Azo) Compounds: An Experimental and Computational Study. *Chem. Eur. J.* **2004**, *10*, 2011–2021.
- [22] Bléger, D.; Dokić, J.; Peters, M. V.; Grubert, L.; Saalfrank, P.; Hecht, S. Electronic Decoupling Approach to Quantitative Photoswitching in Linear Multiazobenzene Architectures. *J. Phys. Chem. B* **2011**, *115*, 9930–9940.
- [23] Bahrenburg, J.; Sievers, C. M.; Schönborn, J. B.; Hartke, B.; Renth, F.; Temps, F.; Näther, C.; Sönnichsen, F. D. Photochemical Properties of Multi-Azobenzene Compounds. *Photochem. Photobiol. Sci.* **2013**, *12*, 511–518.
- [24] Kind, J.; Kaltschnee, L.; Leyendecker, M.; Thiele, C. M. Distinction of Trans– Cis Photoisomers with Comparable Optical Properties in Multiple-State Photochromic Systems – Examining a Molecule with Three Azobenzenes via in Situ Irradiation NMR Spectroscopy. *Chem. Commun.* **2016**, *52*, 12506–12509.
- [25] Zhao, F.; Grubert, L.; Hecht, S.; Bléger, D. Orthogonal Switching in Four-State Azobenzene Mixed-Dimers. *Chem. Commun.* **2017**, *53*, 3323–3326.
- [26] Galanti, A.; Santoro, J.; Mannancherry, R.; Duez, Q.; Diez-Cabanes, V.; Valášek, M.; De Winter, J.; Cornil, J.; Gerbaux, P.; Mayor, M.; Samorì, P. A New Class of Rigid Multi(Azobenzene) Switches Featuring Electronic Decoupling: Unravelling the Isomerization in Individual Photochromes. *J. Am. Chem. Soc.* **2019**, *141*, 9273–9283.

- [27] Jeong, M.; Park, J.; Kwon, S. Molecular Switches and Motors Powered by Orthogonal Stimuli. *Eur. J. Org. Chem.* **2020**, 2020, 7254–7283.
- [28] Zaitseva, E. L.; Prokhoda, A. L.; Kurkovskaya, L. N.; Shifrina, R. R.; Kardash, N. S.; Drapkina, D. A.; Krongauz, V. A. Photochromy of organic substances VI. Preparation of N-methacryloylhydroxyethyl derivatives of indoline spiropyrans. *Khim. Geterotsikl. Soedin.* **1973**, 1362, 1362–1369.
- [29] Sertova, N.; Nunzi, J. M.; Petkov, I.; Deligeorgiev, T. Photochromism of Styryl Cyanine Dyes in Solution. *J. Photochem. Photobiol. A* **1998**, 112, 187–190.
- [30] Petkov, I.; Charra, F.; Nunzi, J. M.; Deligeorgiev, T. Photochemistry of 2-[(1,3,3-Trimethylindoline-2(1H)-Ylidene)Propen-1-Yl]-3,3-Dimethylindolino[1,2-b]-Oxazolidine in Solution. *J. Photochem. Photobiol. A* **1999**, 128, 93–96.
- [31] Hadji, R.; Szalóki, G.; Alévêque, O.; Levillain, E.; Sanguinet, L. The Stepwise Oxidation of Indolino[2,1-b]Oxazolidine Derivatives. *J. Electroanal. Chem.* **2015**, 749, 1–9.
- [32] Szalóki, G.; Alévêque, O.; Pozzo, J.-L.; Hadji, R.; Levillain, E.; Sanguinet, L. Indolinoxazolidine: A Versatile Switchable Unit. *J. Phys. Chem. B* **2015**, 119, 307–315.
- [33] Szalóki, G.; Sanguinet, L. In *Photon-Working Switches*; Yokoyama, Y., Nakatani, K., Eds.; Springer Japan: Tokyo, 2017; pp 69–91.
- [34] Sanguinet, L.; Berthet, J.; Szalóki, G.; Alévêque, O.; Pozzo, J.-L.; Delbaere, S. 13 Metastable States Arising from a Simple Multifunctional Unimolecular System. *Dyes Pigments* **2017**, 137, 490–498.
- [35] Szalóki, G.; Sevez, G.; Berthet, J.; Pozzo, J.-L.; Delbaere, S. A Simple Molecule-Based Octastate Switch. *J. Am. Chem. Soc.* **2014**, 136, 13510–13513.
- [36] Bondu, F.; Quertinmont, J.; Rodriguez, V.; Pozzo, J.-L.; Plaquet, A.; Champagne, B.; Castet, F. Second-Order Nonlinear Optical Properties of a Dithienylethene–Indolinoxazolidine Hybrid: A Joint Experimental and Theoretical Investigation. *Chem. Eur. J.* **2015**, 21, 18749–18757.
- [37] Szalóki, G.; Sanguinet, L. Silica-Mediated Synthesis of Indolinoxazolidine-Based Molecular Switches. *J. Org. Chem.* **2015**, 80, 3949–3956.
- [38] Aidibi, Y.; Guerrin, C.; Alévêque, O.; Leriche, P.; Delbaere, S.; Sanguinet, L. BT-2-BOX: An Assembly toward Multimodal and Multilevel Molecular System Simple as a Breeze. *J. Phys. Chem. C* **2019**, 123, 11823–11832.
- [39] Guerrin, C.; Aidibi, Y.; Sanguinet, L.; Leriche, P.; Aloise, S.; Orio, M.; Delbaere, S. When Light and Acid Play Tic-Tac-Toe with a Nine-State Molecular Switch. *J. Am. Chem. Soc.* **2019**, 141, 19151–19160.
- [40] Quertinmont, J.; Beaujean, P.; Stiennon, J.; Aidibi, Y.; Leriche, P.; Rodriguez, V.; Sanguinet, L.; Champagne, B. Combining Benzazolo-Oxazolidine Twins toward Multi-State

- Nonlinear Optical Switches. *J. Phys. Chem. B* **2021**, 125, 3918–3931.
- [41] Chai, J.-D.; Head-Gordon, M. Systematic Optimization of Long-Range Corrected Hybrid Density Functionals. *J. Chem. Phys.* **2008**, 128, 084106.
- [42] Chai, J.-D.; Head-Gordon, M. Long-Range Corrected Hybrid Density Functionals with Damped Atom–Atom Dispersion Corrections. *Phys. Chem. Chem. Phys.* **2008**, 10, 6615–6620.
- [43] Tomasi, J.; Mennucci, B.; Cancès, E. The IEF Version of the PCM Solvation Method: An Overview of a New Method Addressed to Study Molecular Solutes at the QM Ab Initio Level. *Comput. Theor. Chem.* **1999**, 464, 211–226.
- [44] Zhao, Y.; Truhlar, D. G. The M06 Suite of Density Functionals for Main Group Thermochemistry, Thermochemical Kinetics, Noncovalent Interactions, Excited States, and Transition Elements: Two New Functionals and Systematic Testing of Four M06-Class Functionals and 12 Other Functionals. *Theor. Chem. Acc.* **2008**, 120, 215–241.
- [45] Le Bahers, T.; Adamo, C.; Ciofini, I. A Qualitative Index of Spatial Extent in Charge-Transfer Excitations. *J. Chem. Theory Comput.* **2011**, 7, 2498–2506.
- [46] Scalmani, G.; Frisch, M. J.; Mennucci, B.; Tomasi, J.; Cammi, R.; Barone, V. Geometries and Properties of Excited States in the Gas Phase and in Solution: Theory and Application of a Time-Dependent Density Functional Theory Polarizable Continuum Model. *J. Chem. Phys.* **2006**, 124, 094107.
- [47] Verbiest, T.; Clays, K.; Rodriguez, V. *Second-Order Nonlinear Optical Characterization Techniques: An Introduction*; Taylor & Francis, 2009.
- [48] Oudar, J. L.; Chemla, D. S. Hyperpolarizabilities of the Nitroanilines and Their Relations to the Excited State Dipole Moment. *J. Chem. Phys.* **1977**, 66, 2664–2668.
- [49] Tonnelé, C.; Pielak, K.; Deviers, J.; Muccioli, L.; Champagne, B.; Castet, F. Nonlinear Optical Responses of Self-Assembled Monolayers Functionalized with Indolino–Oxazolidine Photoswitches. *Phys. Chem. Chem. Phys.* **2018**, 20, 21590–21597.
- [50] Johnson, L. E.; Dalton, L. R.; Robinson, B. H. Optimizing Calculations of Electronic Excitations and Relative Hyperpolarizabilities of Electrooptic Chromophores. *Acc. Chem. Res.* **2014**, 47, 3258–3265.
- [51] Garrett, K.; Sosa Vazquez, X.; Egri, S. B.; Wilmer, J.; Johnson, L. E.; Robinson, B. H.; Isborn, C. M. Optimum Exchange for Calculation of Excitation Energies and Hyperpolarizabilities of Organic Electro-Optic Chromophores. *J. Chem. Theory Comput.* **2014**, 10, 3821–3831.
- [52] Lescos, L.; Sitkiewicz, S. P.; Beaujean, P.; Blanchard-Desce, M.; Champagne, B.; Matito, E.; Castet, F. Performance of DFT Functionals for Calculating the Second-Order Nonlinear Optical Properties of Dipolar Merocyanines. *Phys. Chem. Chem. Phys.* **2020**,

22, 16579–16594.

- [53] Champagne, B.; Beaujean, P.; de Wergifosse, M.; Cardenuto, M. H.; Liégeois, V.; Castet, F. In *Frontiers of Quantum Chemistry*; Wójcik, M. J., Nakatsuji, H., Kirtman, B., Ozaki, Y., Eds.; Springer Singapore: Singapore, 2018; pp 117–138.
- [54] Frisch, M. J. et al. Gaussian 16 Revision A.03. 2016; Gaussian Inc. Wallingford CT.
- [55] Yang, M.; Champagne, B. Large Off-Diagonal Contribution to the Second-Order Optical Nonlinearities of Λ -Shaped Molecules. *J. Phys. Chem. A* **2003**, *107*, 3942–3951.
- [56] Cho, M.; Kim, H.-S.; Jeon, S.-J. An Elementary Description of Nonlinear Optical Properties of Octupolar Molecules: Four-State Model for Guanidinium-Type Molecules. *J. Chem. Phys.* **1998**, *108*, 7114–7120.

All-atom quantum mechanical calculation of the second-harmonic generation of fluorescent proteins

Submitted.

Pierre Beaujean[†], Benoît Champagne[†], Stefan Grimme[‡] and Marc de Wergifosse[‡]

*[†]Laboratory of Theoretical Chemistry, Namur Institute of Structured Matter,
University of Namur, Rue de Bruxelles 61, B-5000 Namur, Belgium*

*[‡]Mulliken Center for Theoretical Chemistry,
Institut für Physikalische und Theoretische Chemie der Universität Bonn,
Berings. 4, D-53115 Bonn, Germany*

Abstract

Fluorescent proteins (FPs) are biotags of choice for second-harmonic imaging microscopy (SHIM). Because of their large size, computing their second-harmonic generation (SHG) response represents a great challenge for quantum chemistry. In this contribution, we propose a new all-atom quantum mechanics methodology to compute SHG of large systems. This is now possible because of two recent implementations: the tight-binding GFN2-xTB method to optimize geometries and a related version of the simplified time-dependent density functional theory (sTD-DFT-xTB) to evaluate quadratic response functions. In addition, a new dual-threshold configuration selection scheme is introduced to reduce the computational costs while retaining overall similar accuracy. This methodology was tested to evaluate the SHG of the proteins iLOV and bacteriorhodopsin (bR). In

the case of bR, quantitative agreement with respect to experiment was reached for the out-of-resonance low-energy part of the β_{HRS} frequency dispersion. This work paves the way towards an accurate prediction of the SHG of large structures, a requirement for the design of new and improved SHIM biotags.

► Supporting information are available in Appendix B, page 337.

Fluorescent proteins (FPs)^{1–4} are used as genetically engineered biotags for the second-harmonic imaging microscopy (SHIM).^{5–7} SHIM is a high-resolution bioimaging technique that provides contrast for non-centrosymmetric molecular arrangements. The phenomenon is the second-harmonic generation (SHG)^{8,9} for which the response is governed by the first hyperpolarizability (β). While β is very sensitive to the local non-centrosymmetry and the polarization,^{8,9} SHIM presents a low phototoxicity, less out-of-focus photobleaching, and higher penetration in biological tissues with respect to traditional fluorescence.^{10–12} Reeve et al.⁵ described requirements for good SHIM biotags, in particular a strong SHG response at the laser frequency (usually in the cell transparent region) and a high affinity for the hydrophobic cell membrane. The green fluorescent protein (GFP)-like family perfectly fits these requirements.^{1–4}

Reports^{13,14} showed that GFP was already employed as biotag for SHIM a couple of decades ago. Quantitative β values from hyper-Rayleigh scattering (HRS) experiments were obtained for a full rainbow of FPs.^{1–4} These experimental findings were supported by quantum mechanics (QM) calculations. SHardonnay³ was specifically engineered to remove eYFP local centrosymmetry and to enhance its SHG signal. HRS measurements were also reported for the bacteriorhodopsin¹⁵ as well as other GFP-like proteins and several channel rhodopsins.¹⁶

All-atom QM calculations on such large biological systems are challenging. Most of the theoretical studies on photoreceptor proteins applies multi-scale modeling in which only a small fraction of the protein is treated at the QM level.^{17–21} Specific difficulties on this subject were recently reviewed by Mrogiński et al.²¹ To evaluate β for FPs or other complex systems, previous attempts pinpointed the importance of considering the environment:³ either implicitly (polarizable continuum^{22,23} or charge embedding²⁴) or explicitly (ONIOM schemes^{3,4} or fragmentation methods²⁵). The partitioning between different parts of the structure and their levels of approximation is also important choices to make.²¹

In this communication, we propose a new all-atom QM methodology to generally compute β for FPs. This is now possible because of two recent developments and implementations: the GFN2-xTB method²⁶ to optimize geometries with the xtb program²⁷ and the evaluation of quadratic response functions²⁸ with the simplified time-dependent density functional theory (sTD-DFT)^{28–30} and in particular its tight-binding version (sTD-DFT-xTB)³¹ available in the freely available stda program.³² The geometry of large proteins can now be optimized fully quantum mechanically³³ before computing their β values^{28,34} with modest CPU requirements. This QM protocol retains most of the quality expected from higher levels of theory as it was demonstrated for the dynamical structural effects on β of tryptophan-rich amino peptides.³⁴ The reader interested in simplified quantum chemistry methods for evaluating response properties and excited states can consult our recent perspective articles^{35,36} on the subject. Shortly, three approximations are introduced in the simplified scheme: a) two-electron integrals are approximated by damped short-range Coulomb interactions with two globally fitted y_J and y_K parameters, b) the configuration state function (CSF) space is truncated to cover a spectral

Single threshold method

◆ Truncation of the MO space

$$\epsilon > \epsilon_{HOMO} - 2(1 + 0.8a_x)E_{thr.}$$

$$\epsilon < \epsilon_{LUMO} + 2(1 + 0.8a_x)E_{thr.}$$

◆ Selection of P-CSFs $i \rightarrow a$

$$A_{ia,ia} \leq E_{thr.}$$

◆ Selection of S-CSFs $j \rightarrow b$ for $A_{jb,jb} > E_{thr.}$

$$E_{jb}^{(2)} = \sum_{ia}^{P-CSFs} \frac{|A_{ia,jb}|^2}{A_{ia,ia} - A_{jb,jb}} > 10^{-4}E_h$$

$$\#CSFs = \#P-CSFs + \#S-CSFs$$

Dual threshold method

◆ Truncation of the MO space

$$\epsilon > \epsilon_{HOMO} - 2(1 + 0.8a_x)E_{high}$$

$$\epsilon < \epsilon_{LUMO} + 2(1 + 0.8a_x)E_{high}$$

◆ Select occ. MOs for both threshold

$$\zeta_i = \sum_{\alpha \in \text{high layer}} C_{ai}^2$$

$$\zeta_i > 0.1 \rightarrow E_{high}$$

$$\zeta_i \leq 0.1 \rightarrow E_{low}$$

1. For the high layer:

◆ Selection of P-CSFs-H $i \rightarrow a$

$$A_{ia,ia} \leq E_{high}$$

◆ Range of S-CSFs-H $j \rightarrow b$ for $A_{jb,jb} > E_{high}$

2. For the low layer:

◆ Selection of P-CSFs-low $i \rightarrow a$

$$A_{ia,ia} \leq E_{low}$$

◆ Range of S-CSFs-H $j \rightarrow b$ for $E_{low} < A_{jb,jb} < 2(1 + 0.8a_x)E_{low}$

3. For both layers:

◆ Selection of S-CSFs

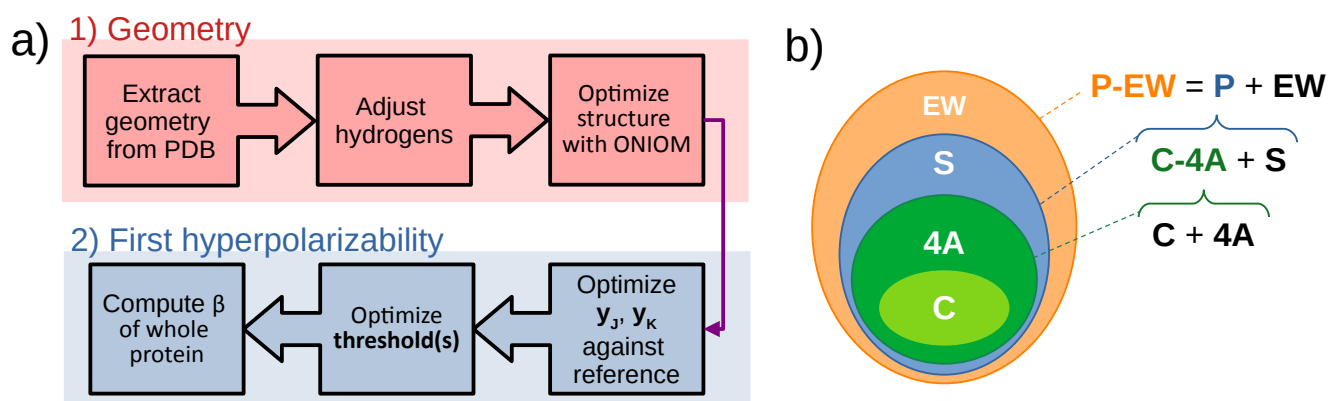
$$E_{jb}^{(2)} = \sum_{ia}^{P-CSFs} \frac{|A_{ia,jb}|^2}{A_{ia,ia} - A_{jb,jb}} > 10^{-4}E_h$$

$$\#CSFs = \#P-CSFs-H + \#P-CSFs-L + \#S-CSFs$$

Scheme 10.1: Details of the sTD-DFT single and dual-threshold response methods. a_x is the Hartree-Fock exchange percentage, i and j refer to occupied molecular orbitals (MOs) while a and b to unoccupied ones, C_{ai} is the LCAO coefficient considering atomic orbital (AO) α and MO i , $A_{ia,jb}$ is an element of the linear response matrix A . P- and S-CSFs stand for primary and secondary configuration state functions, respectively.³⁵

range up to $E_{thresh.}$, and c) the response of the exchange-correlation potential is neglected. The game-changer strategy^{28,34} is to fine-tune the y_J and y_K parameters to reproduce affordable high-level calculations for the chromophore only. This gives to the simplified calculations on FPs a similar accuracy at many orders of magnitude lower computational cost. $E_{thresh.}$ is adjusted to provide a sufficient but still tractable expansion space consisting of typically thousands of CSF.

Considering systems such as FPs, for which only few protein parts contribute significantly to the β response (mostly the chromophore), on top of the previous developments, we propose here a new dual-threshold method. Its motivation is to drastically reduce the configuration space and thereof the memory. In the dual-threshold method, the occupied (occ.) molecular orbitals (MOs) of the protein are partitioned into two layers. The high layer includes occ. MOs that are mostly located on the chromophore and selected important residues (with an electron density $\zeta_i > 0.1$). The remaining occ. MOs constitute the low layer. To determine the truncated space of CSFs, a tighter energy threshold E_{high} is employed for the high layer than for the low layer: $E_{low} < E_{high}$. Thus, with respect to a usual sTD-DFT calculation at a given $E_{thresh.}$, considering that $E_{low} = E_{thresh.}$, the dual-threshold method is increasing the active space but only for parts included in the high layer while the low layer stays unchanged. This allows to keep computational costs reasonable with respect to simply increasing $E_{thresh.}$. The molecular response property is then computed considering this extended set of CSFs. Scheme



Scheme 10.2: Left: the all-atom QM methodology to compute the first hyperpolarizability of a fluorescent protein. Right: different parts of the protein and their acronyms: chromophore (C), 4-Å amino acids surrounding the chromophore (4A), rest of the surrounding amino acids and internal water molecules (S) and external water molecules (EW). Acronyms are also provided for combinations of parts.

10.1 summarizes details of the whole implementation.

Scheme 10.2a presents the all-atom QM methodology used to compute β of FPs. This procedure is divided in two parts: the protein geometry optimization and the evaluation of β . Starting geometries are usually obtained from the protein data bank (PDB).³⁷ Hydrogen atoms are added to the PDB geometry with the PlayMolecule web interface³⁸ at the experimental pH and manually for the chromophore to comply with its pK_a . The global charge of the system (Table S1) is determined according to the amino acid protonation states and inherent charges from other parts (chromophore, ions,...). Because β is highly sensitive to structural details, we used an ONIOM³⁹ QM/QM scheme to optimize the protein geometry. This approach is similar to a QM/MM mechanical embedding but the use of the GFN2-xTB method for the low layer improves the treatment with respect to a MM method as it was demonstrated by Schmitz et al.³³ The chromophore (C, Scheme 10.2b) and the surrounding amino acids in a 4 Å radius (4A) are treated within the high layer at the ω B97X-D/6-31G* level (in gas phase). This was chosen to correctly account for the non-covalent interaction with the chromophore, while keeping a reasonable number of atoms within the high layer. We expect that this protocol should be applicable to other fluorescent proteins where one chromophore dominates the response but also more generally to large systems with a central NLOphore. The rest of the structure, including a few external water molecules, is optimized with the GFN2-xTB method²⁶ (in water, treated with the GBSA model⁴⁰). These calculations were done with the Gaussian 16 A03 package⁴¹ and the xtb 6.2.2 program.^{27,42}

The second part concerns the evaluation of the β_{HRS} and the depolarization ratio (DR) for the FP as defined by the mean and ratio of the β -tensor orientations,⁹ respectively, according

to:

$$\beta_{HRS} = \sqrt{\langle \beta_{ZZZ}^2 \rangle + \langle \beta_{XXX}^2 \rangle} \quad DR = \frac{\langle \beta_{ZZZ}^2 \rangle}{\langle \beta_{XXX}^2 \rangle}, \quad (10.1)$$

where in a HRS experiment, both incident and scattered photons are polarized, either parallel to the X (= horizontal) or to the Z (= vertical) axes for the incident photons and parallel to Z for the scattered photons. The y_J and y_K parameters in the sTD-DFT method are fine-tuned with respect to MP2/6-31+G* results to provide sTD-DFT-xTB values for the chromophore with a similar accuracy. The frequency dispersion is obtained by a multiplicative scheme⁴³ with either ω B97X-D or M06-2X exchange-correlation functionals using TD-DFT for the frequency dependence. Convergence of the β_{HRS} for the chromophore as a function of $E_{thresh.}$ is then assessed to select a sufficiently large number of CSFs. With these y_J , y_K and $E_{thresh.}$ parameters, β_{HRS} values are then computed for the optimized FP structure at the sTD-DFT-xTB level. Note that solvation effects are accounted for by the implicit GBSA solvation model⁴⁰ but only for the generation of MOs. The reference values are obtained with the Gaussian 16 A03, while a development version of the `stda` program³² is used for the sTD-DFT-xTB calculations.

To illustrate this new methodology, we selected two example FPs of increasing size: iLOV (~ 2000 atoms) and the bacteriorhodopsin (bR, ~ 3850 atoms). Figure 10.1 displays their chromophore structures. iLOV is an engineered extrinsically fluorescent protein that binds the flavine mononucleotide (FMN).^{44,45} bR is a light-driven transmembrane protein pump. Its retinal chromophore is covalently linked via a Schiff base to the protein backbone.⁴⁶ From the PDB, we used as input geometries 4EES for iLOV⁴⁷ and 6G7H for bR.⁴⁶ Both structures were protonated considering an experimental pH of 5. A full discussion about their optimizations is provided in the SI. Shortly, structural deviations (Figures S2-S3) for the optimized geometries with respect to X-ray data (0.52 and 0.32 Å for iLOV and bR, respectively) are within the experimental uncertainty of 0.5 Å. For iLOV, the FMN undergoes a displacement of its ribityl tail but without much modification of its π -conjugated pathway. The π -conjugation is also well preserved for the retinal schiff-base of bR (Figure S4).

At these geometries, we obtained sTD-DFT-xTB optimized parameters of $y_J = 2.0$ and $y_K = 0.15$ for both systems (Figure S5). Concerning the truncation of the CSF space (Figure S6), the β_{HRS} value of bR rapidly converges so that a $E_{thresh.}$ of 9 eV was selected. For iLOV, a larger value is required. To balance computational cost and accuracy, we selected $E_{thresh.} = 10$ eV. Note that for bR with $E_{thresh.} = 9$ eV, 35 701 CSFs are included in the computation which took less than 74 hours on a AMD Epyc CPU with 64 cores (2.0 GHz). Moving now towards the dual-threshold scheme, the high layer contains only the chromophore. We use the following notation to refer to those calculation: E_{High} - E_{Low} . For example, the “9-7” calculation on bR used 3399 CSFs when $E_{High} = 9$ eV and $E_{Low} = 7$ eV. This calculation run only 5 hours (instead of 74).

Figure 10.2 presents the impact of the two thresholds on the static β_{HRS} value for both proteins as well as the number of included CSFs. For iLOV, the β_{HRS} value is gradually im-

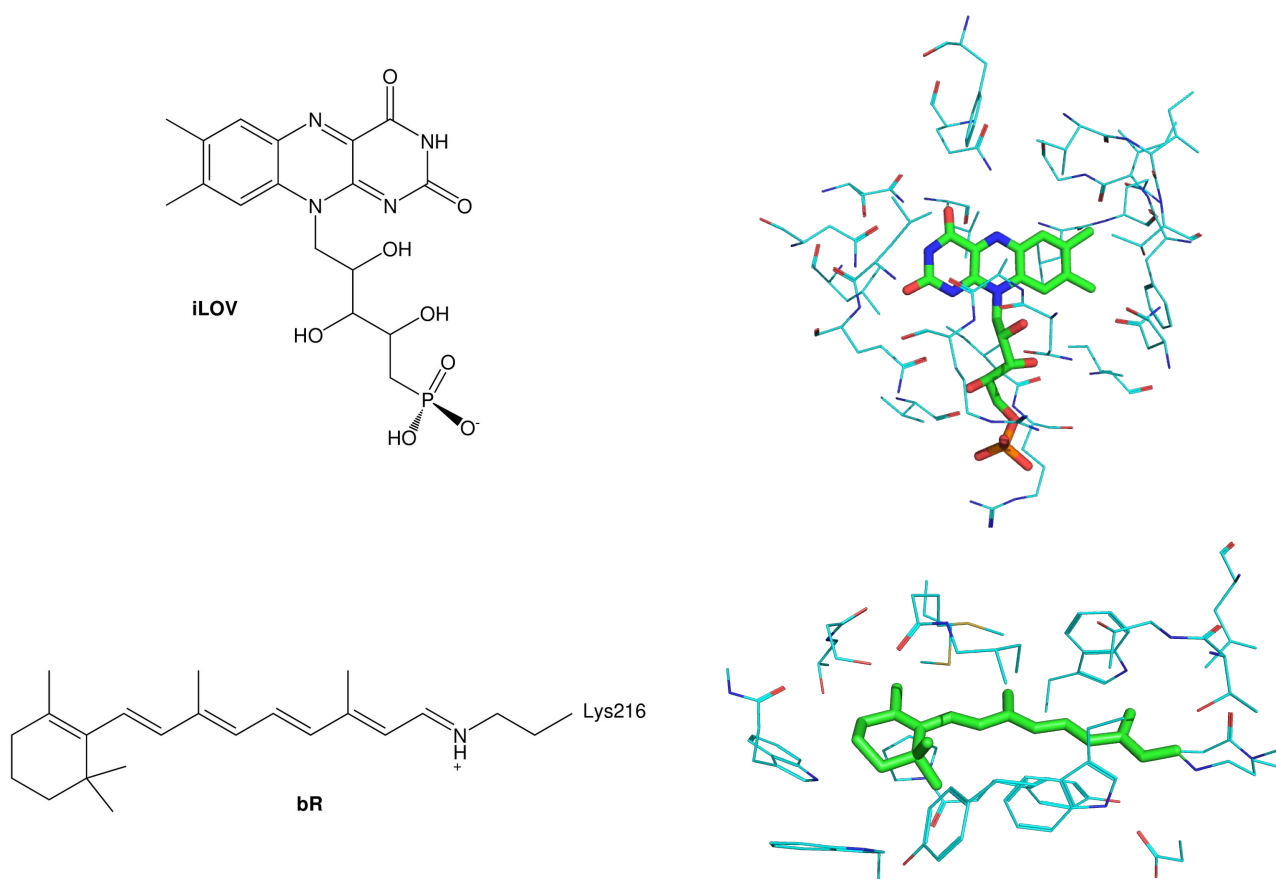


Figure 10.1: NLO-active chromophores (C) of the different proteins, in their experimental protonation state (left) and with their first shell of surrounding amino acids (right, chromophore in green, hydrogens hidden for clarity): iLOV (top, flavine mononucleotide) and bR (bottom, retinal schiff-base, in its native all-trans state conformation).

proved with the number of CSFs in comparison to the value obtained at $E_{thresh.} = 10$ eV (62 882 CSFs). The β_{HRS} value with $E_{thresh.} = 9$ eV is already converged within 10 % for a smaller configuration space (14 978 CSFs). With the dual-threshold method, including important CSFs for the chromophore with $E_{High} = 10$ eV but smaller E_{Low} drastically improves the efficiency of the treatment while maintaining its accuracy. For example, the β_{HRS} value at 10-7 is only 5 % lower than the value with a unique threshold of 10 eV while only accounting for 17 203 CSFs. Going from 10-8 to 10-9, a small increase of β_{HRS} is observed similar to the one from $E_{thresh.} = 8$ to 9 eV. The convergence with E_{Low} could even be smoother by including all tyrosine and tryptophan amino acids into the high layer (Figure S7), though at a slightly higher computational cost. For bR, the calculation with a threshold of 7 eV (1522 CSFs) already retains most of the physics with only 3 % difference with respect to the β_{HRS} value at a threshold of 9 eV (35 701 CSFs). Using the dual-threshold method, the convergence is even smoother.

To assess the impact of the chromophore surroundings on the response, Table 10.1 presents the β_{HRS} and DR for different parts of both structures. For iLOV, the β_{HRS} for the FMN in water

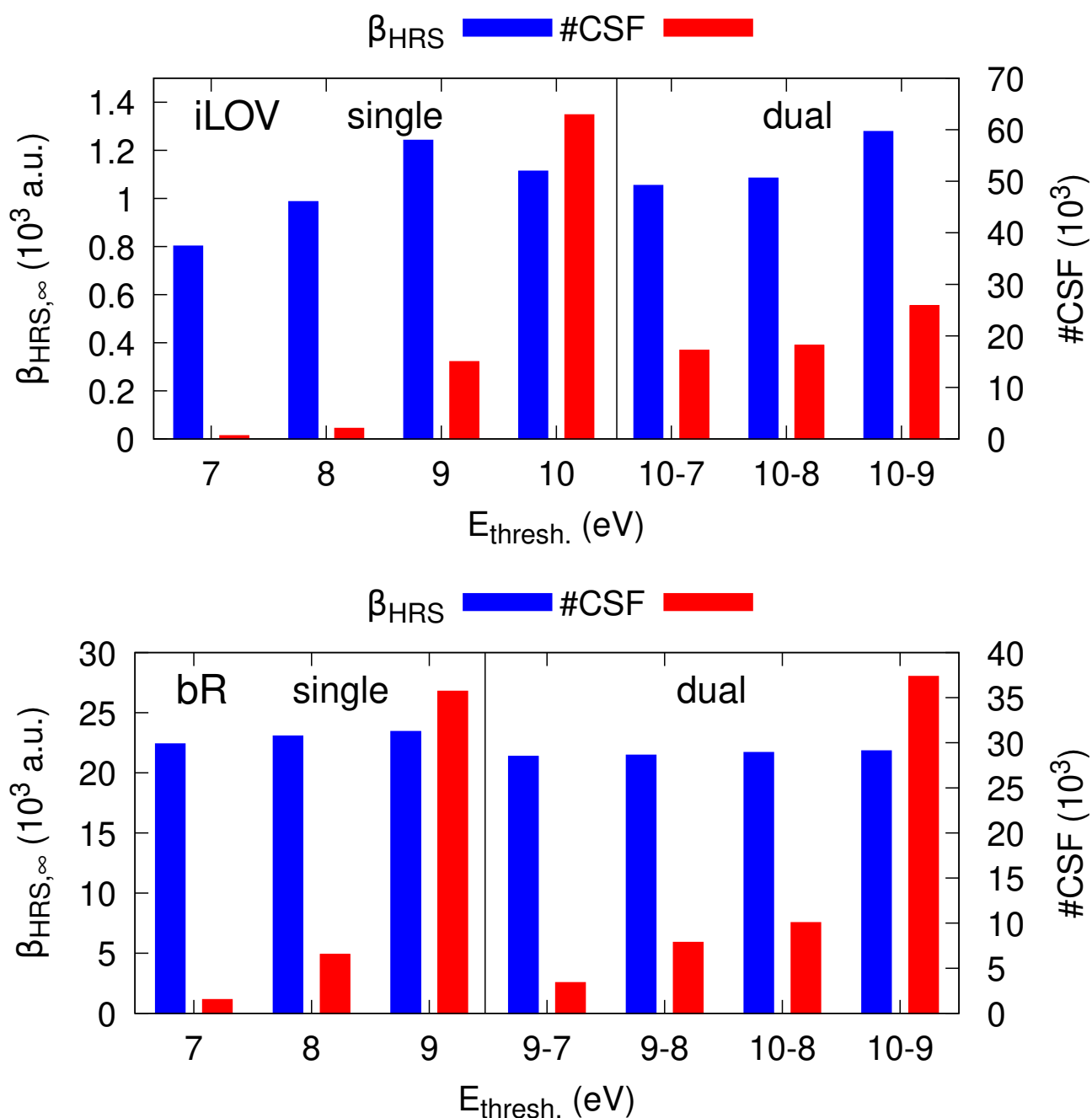


Figure 10.2: Influence of $E_{\text{thresh.}}$ on the static β_{HRS} of iLOV (top) and bR (bottom), as computed at the sTD-DFT-xTB level of theory (with $y_J = 2.0$ and $y_K = 0.15$) in water (GBSA), and corresponding numbers of CSFs. For the dual-threshold scheme, the first number indicates E_{High} and the second E_{Low} .

	sTD-DFT-xTB				MP2:sTD-DFT-xTB	
	C	4A	C-4A	P-EW	C-4A	P-EW
iLOV	1.09 (4.8)	0.16 (2.3)	1.37 (6.2)	1.11 (3.6)	1.57 (5.7)	1.26 (3.6)
bR	17.32 (4.7)	0.66 (5.9)	21.08 (4.9)	23.43 (5.0)	22.04 (5.0)	24.40 (5.2)

Table 10.1: Static β_{HRS} (in 10^3 a.u., DR in parentheses) of the chromophore (C), of its surroundings (4A, with extra hydrogens to saturate bonds) the C-4A region (ONIOM high layer, with extra hydrogens to saturate bonds), and of the whole protein (P-EW), as computed at the sTD-DFT-xTB level of theory (with $y_J = 2.0$, $y_K = 0.15$) in water (GBSA) with a threshold value of 10 eV for iLOV and 9 eV for bR. ONIOM MP2:sTD-DFT-xTB results are also provided.

is close to the one for the whole protein but the DR goes from 4.8 to a more octupolar value of 3.6 for the full protein. For bR, the β_{HRS} increases monotonically with the increasing size of the surroundings but its DR is almost unchanged. The sTD-DFT-xTB calculations are compared to ONIOM MP2:sTD-DFT-xTB results to assess their accuracy and demonstrate an excellent agreement (Table 10.1) for both structures. This confirms the suitability of the empirically fine-tuned y_J and y_K parameters to emulate higher-level QM methods.

Fig. 10.3 (Table S2) presents the β_{HRS} frequency dispersions for both FPs, which are mostly impacted by the first two-photon resonance. The β_{HRS} spectrum for bR was recorded by Clays and coworkers.¹⁵ Usually, β_{HRS} is extrapolated to the static limit by different levels of refinement based on the two-state approximation.^{48,49} We used a simple vibronic model (SVM), of which the key parameters were determined such that the experimental UV-visible spectrum is reproduced. Details about the SVM are given in the SI (Figure S8). Figure 10.4 compares the computed β_{HRS} spectrum to the experimental one as well as to SVM results. The sTD-DFT-xTB β_{HRS} frequency dispersion reproduces quantitatively the first three low-energy experimental points (those below the two-photon resonance) and follows well the extrapolation to the static limit by the SVM. Because of the divergent nature of our response theory in the resonance regime, it was expected that this frequency region could not be reproduced. Nevertheless, for low energy values, quantitative agreement with experiment is striking showing the suitability of this methodology. We obtained a static β_{HRS} value of 23.4×10^3 a.u. close to the extrapolated experimental value of 29.5×10^3 a.u..

In conclusion, the proposed methodology enables computing the SHG of proteins (here with about 4000 atoms) fully quantum mechanically in a reasonable amount of computation time. The key concept is to refit only two empirical parameters in the sTD-DFT-xTB method to reproduce higher level β results for parts of the system (mostly the chromophore), providing a similar accuracy. In addition, a dual-threshold method is introduced to truncate specifically the single-excitation space for two different layers of the system, reducing the computational costs. We tested this approach for iLOV and the bacteriorhodopsin. For bR where experimental data are available, the agreement between sTD-DFT-xTB and experimental low-energy β_{HRS} frequency dispersion is excellent. This kind of comparison could not be achieved by only

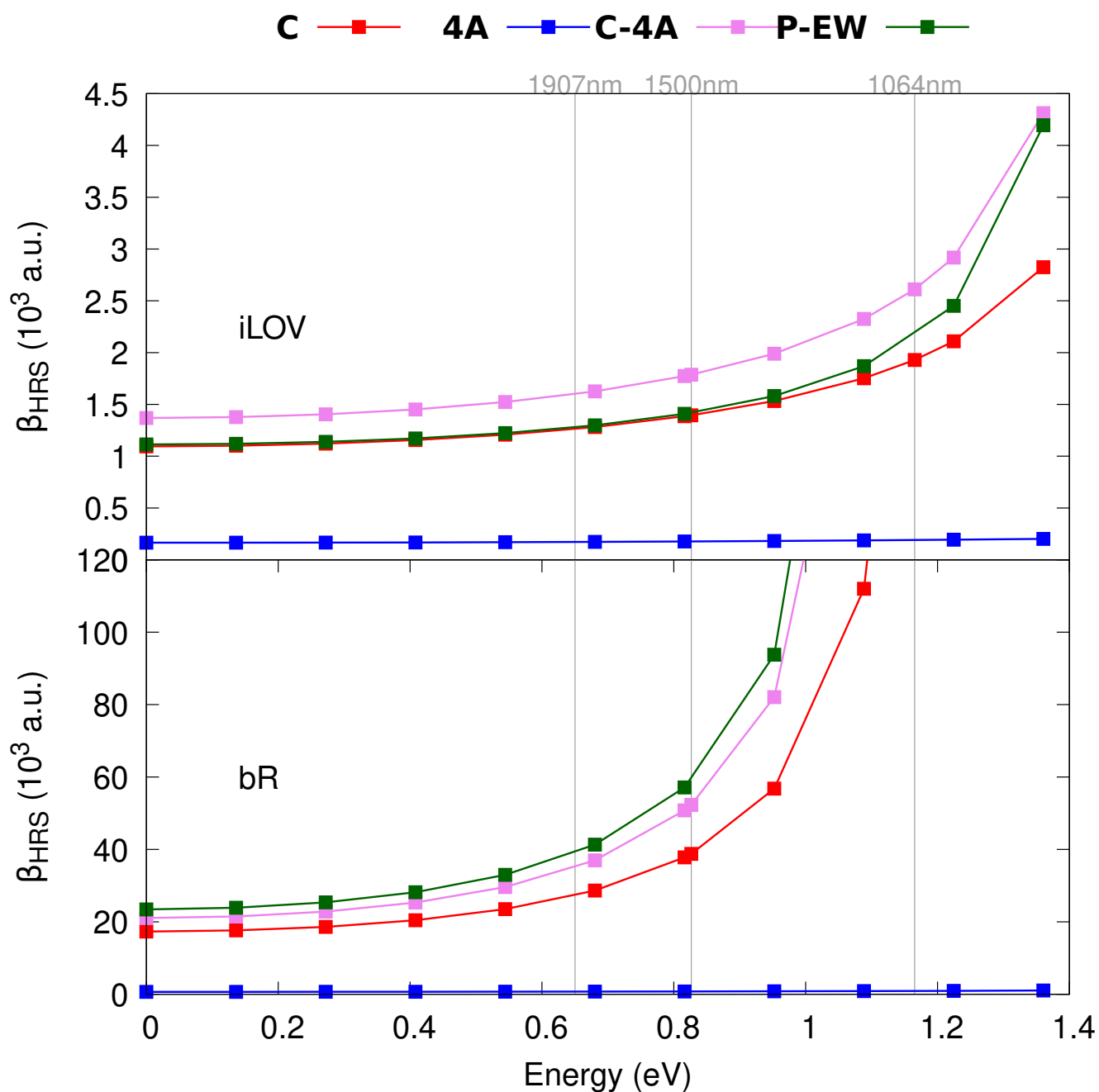


Figure 10.3: Comparison between the β_{HRS} of the chromophore (C), of its surrounding amino acids (4A), of the ONIOM “high” layer (C-4A), and of the total protein (P-EW), as computed at the sTD-DFT-xTB level (with $y_J = 2.0$, $y_K = 0.15$) in water (GBSA) with a threshold value of 10 eV for iLOV (top) and 9 eV for bR (bottom).

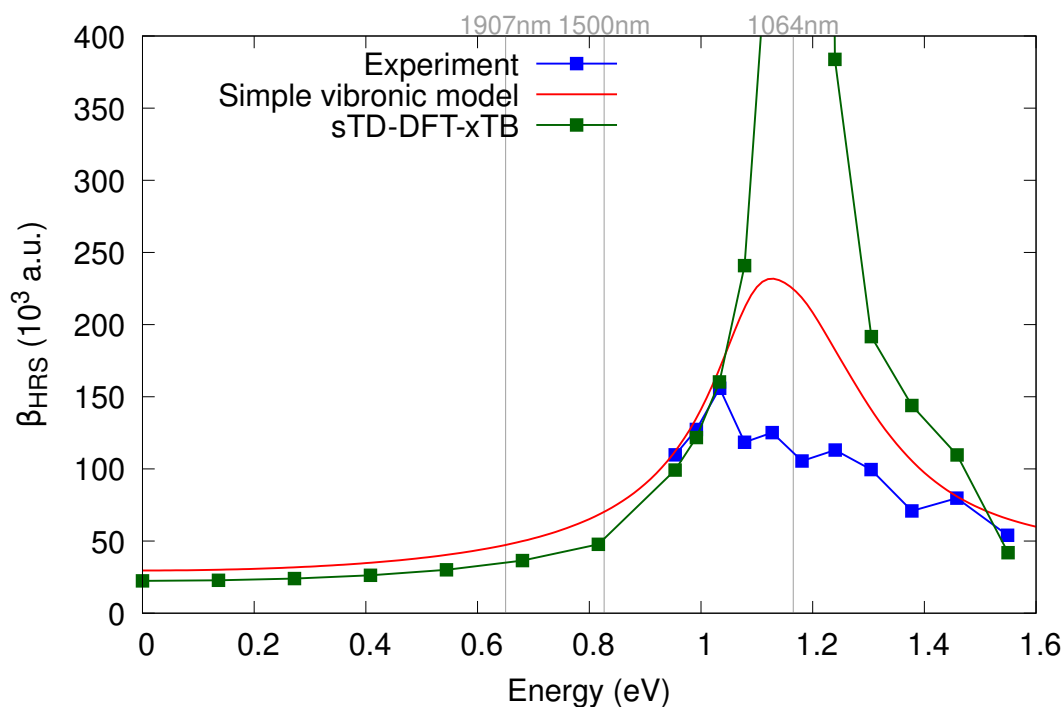


Figure 10.4: Experimental versus calculated β_{HRS} frequency dispersion of bR. The experimental one¹⁵ has been extrapolated (red curve) to the static limit by using a vibronic model. The calculations were carried out at the sTD-DFT-xTB level ($y_J = 2.0$, $y_K = 0.15$, and $E_{thresh.} = 9$ eV) in water (GBSA).

considering parts of the protein. This substantiates the importance to account for the whole protein (or at least large parts of it) into the calculation and the suitability of this workflow. In a near future, we should extend this methodology to the characterization of dynamical structural effects, e.g protein conformations as well as the impact of the truncation of the explicit solvation shell around the system.

Acknowledgments

The authors thank Prof. K. Clays for fruitful discussions. This work was supported by the DFG in the framework of the project "Theoretical studies of nonlinear optical properties of fluorescent proteins by novel low-cost quantum chemistry methods" (Nr. 450959503). The calculations were performed on the computers of the Consortium des Équipements de Calcul Intensif, including those of the Technological Platform of High-Performance Computing, for which we gratefully acknowledge the financial support of the FNRS-FRFC, of the Walloon Region, and of the University of Namur (Conventions No. 2.5020.11, GEQ U.G006.15, 1610468, and RW/GEQ2016).

Bibliography

- [1] Asselberghs, I.; Flors, C.; Ferrighi, L.; Botek, E.; Champagne, B.; Mizuno, H.; Ando, R.; Miyawaki, A.; Hofkens, J.; der Auweraer, M. V.; Clays, K. Second-Harmonic Generation in GFP-like Proteins. *J. Am. Chem. Soc.* **2008**, *130*, 15713–15719.
- [2] De Meulenaere, E.; Asselberghs, I.; de Wergifosse, M.; Botek, E.; Spaepen, S.; Champagne, B.; Vanderleyden, J.; Clays, K. Second-Order Nonlinear Optical Properties of Fluorescent Proteins for Second-Harmonic Imaging. *J. Mater. Chem.* **2009**, *19*, 7514.
- [3] De Meulenaere, E.; Nguyen Bich, N.; de Wergifosse, M.; Van Hecke, K.; Van Meervelt, L.; Vanderleyden, J.; Champagne, B.; Clays, K. Improving the Second-Order Nonlinear Optical Response of Fluorescent Proteins: The Symmetry Argument. *J. Am. Chem. Soc.* **2013**, *135*, 4061–4069.
- [4] de Wergifosse, M.; Botek, E.; De Meulenaere, E.; Clays, K.; Champagne, B. ONIOM Investigation of the Second-Order Nonlinear Optical Responses of Fluorescent Proteins. *J. Phys. Chem. B* **2018**, *122*, 4993–5005.
- [5] Reeve, J. E.; Anderson, H. L.; Clays, K. Dyes for Biological Second Harmonic Generation Imaging. *Phys. Chem. Chem. Phys.* **2010**, *12*, 13484–13498.
- [6] Campagnola, P. J.; Loew, L. M. Second-Harmonic Imaging Microscopy for Visualizing Biomolecular Arrays in Cells, Tissues and Organisms. *Nat. Biotechnol.* **2003**, *21*, 1356–1360.
- [7] Campagnola, P. Second Harmonic Generation Imaging Microscopy: Applications to Diseases Diagnostics. *Anal. Chem.* **2011**, *83*, 3224–3231.
- [8] Franken, P. A.; Hill, A. E.; Peters, C. W.; Weinreich, G. Generation of Optical Harmonics. *Phys. Rev. Lett.* **1961**, *7*, 118–119.
- [9] Verbiest, T.; Clays, K.; Rodriguez, V. *Second-Order Nonlinear Optical Characterization Techniques: An Introduction*; Taylor & Francis, 2009.
- [10] Denk, W.; Strickler, J. H.; Webb, W. W. Two-Photon Laser Scanning Fluorescence Microscopy. *Science* **1990**, *248*, 73–76.
- [11] So, P. T. C.; Dong, C. Y.; Masters, B. R.; Berland, K. M. Two-Photon Excitation Fluorescence Microscopy. *Annu. Rev. Biomed. Eng.* **2000**, *2*, 399–429.
- [12] Sheppard, C. J. R.; Gu, M. Image Formation in Two-Photon Fluorescence Microscopy. *Optik* **1990**, *86*, 104–106.
- [13] Lewis, A.; Khatchatourians, A.; Treinin, M.; Chen, Z.; Peleg, G.; Friedman, N.; Bouevitch, O.; Rothman, Z.; Loew, L.; Sheres, M. Second-Harmonic Generation of Biological

- Interfaces: Probing the Membrane Protein Bacteriorhodopsin and Imaging Membrane Potential around GFP Molecules at Specific Sites in Neuronal Cells of *C. Elegans*. *Chem. Phys.* **1999**, *245*, 133–144.
- [14] Khatchatouriants, A.; Lewis, A.; Rothman, Z.; Loew, L.; Treinin, M. GFP Is a Selective Non-Linear Optical Sensor of Electrophysiological Processes in *Caenorhabditis Elegans*. *Biophys. J.* **2000**, *79*, 2345–2352.
- [15] de Coene, Y.; Van Cleuvenbergen, S.; Van Steerteghem, N.; Baekelandt, V.; Verbiest, T.; Bartic, C.; Clays, K. Fluorescence-Free Spectral Dispersion of the Molecular First Hyperpolarizability of Bacteriorhodopsin. *J. Phys. Chem. C* **2017**, *121*, 6909–6915.
- [16] De Meulenaere, E.; de Coene, Y.; Russier-Antoine, I.; Vanpraet, L.; Van den Haute, C.; Thevissen, K.; Baekelandt, V.; Bartic, C.; Hofkens, J.; Brevet, P-F.; Clays, K. Fluorescence-Free First Hyperpolarizability Values of Fluorescent Proteins and Channel Rhodopsins. *J. Photochem. Photobiol. A* **2020**, *400*, 112658.
- [17] List, N. H.; Olsen, J. M. H.; Jensen, H. J. A.; Steindal, A. H.; Kongsted, J. Molecular-Level Insight into the Spectral Tuning Mechanism of the DsRed Chromophore. *J. Phys. Chem. Lett.* **2012**, *3*, 3513–3521.
- [18] Steindal, A. H.; Olsen, J. M. H.; Ruud, K.; Frediani, L.; Kongsted, J. A Combined Quantum Mechanics/Molecular Mechanics Study of the One- and Two-Photon Absorption in the Green Fluorescent Protein. *Phys. Chem. Chem. Phys.* **2012**, *14*, 5440–5451.
- [19] Ding, L.; Chung, L. W.; Morokuma, K. Reaction Mechanism of Photoinduced Decarboxylation of the Photoactivatable Green Fluorescent Protein: An ONIOM(QM:MM) Study. *J. Phys. Chem. B* **2013**, *117*, 1075–1084.
- [20] Nemukhin, A. V.; Grigorenko, B. L.; Khrenova, M. G.; Krylov, A. I. Computational Challenges in Modeling of Representative Bioimaging Proteins: GFP-Like Proteins, Flavoproteins, and Phytochromes. *J. Phys. Chem. B* **2019**, *123*, 6133–6149.
- [21] Mroginiski, M.-A. et al. Frontiers in Multiscale Modeling of Photoreceptor Proteins. *Photochem. Photobiol.* **2021**, *97*, 243–269.
- [22] Ferrighi, L.; Frediani, L.; Cappelli, C.; Sałek, P.; Ågren, H.; Helgaker, T.; Ruud, K. Density-Functional-Theory Study of the Electric-Field-Induced Second Harmonic Generation (EFISHG) of Push–Pull Phenylpolyenes in Solution. *Chem. Phys. Lett.* **2006**, *425*, 267–272.
- [23] Marrazzini, G.; Giovannini, T.; Egidi, F.; Cappelli, C. Calculation of Linear and Non-Linear Electric Response Properties of Systems in Aqueous Solution: A Polarizable Quantum/Classical Approach with Quantum Repulsion Effects. *J. Chem. Theory Comput.* **2020**, *16*, 6993–7004.
- [24] Bouquiaux, C.; Tonnelé, C.; Castet, F.; Champagne, B. Second-Order Nonlinear Optical

- Properties of an Amphiphilic Dye Embedded in a Lipid Bilayer. A Combined Molecular Dynamics–Quantum Chemistry Study. *J. Phys. Chem. B* **2020**, *124*, 2101–2109.
- [25] Zahariev, F.; Gordon, M. S. Nonlinear Response Time-Dependent Density Functional Theory Combined with the Effective Fragment Potential Method. *J. Chem. Phys.* **2014**, *140*, 18A523.
- [26] Bannwarth, C.; Ehlert, S.; Grimme, S. GFN2-xTB—An Accurate and Broadly Parametrized Self-Consistent Tight-Binding Quantum Chemical Method with Multipole Electrostatics and Density-Dependent Dispersion Contributions. *J. Chem. Theory Comput.* **2019**, *15*, 1652–1671.
- [27] Bannwarth, C.; Caldeweyher, E.; Ehlert, S.; Hansen, A.; Pracht, P.; Seibert, J.; Spicher, S.; Grimme, S. Extended tightbinding quantum chemistry methods. *Wiley Interdiscip. Rev. Comput. Mol. Sci.* **2020**, *11*, e01493.
- [28] de Wergifosse, M.; Grimme, S. Nonlinear-Response Properties in a Simplified Time-Dependent Density Functional Theory (sTD-DFT) Framework: Evaluation of the First Hyperpolarizability. *J. Chem. Phys.* **2018**, *149*, 024108.
- [29] de Wergifosse, M.; Grimme, S. A Unified Strategy for the Chemically Intuitive Interpretation of Molecular Optical Response Properties. *J. Chem. Theory Comput.* **2020**, *16*, 7709–7720.
- [30] de Wergifosse, M.; Grimme, S. Nonlinear-Response Properties in a Simplified Time-Dependent Density Functional Theory (sTD-DFT) Framework: Evaluation of Excited-State Absorption Spectra. *J. Chem. Phys.* **2019**, *150*, 094112.
- [31] Grimme, S.; Bannwarth, C. Ultra-Fast Computation of Electronic Spectra for Large Systems by Tight-Binding Based Simplified Tamm-Dancoff Approximation (sTDA-xTB). *J. Chem. Phys.* **2016**, *145*, 054103.
- [32] de Wergifosse, M.; Bannwarth, C.; Shushkov, P.; Grimme, S. stda program for computing excited states and response properties via the simplified TD-DFT methods, version 1.6.2. Code available at <https://github.com/grimme-lab/stda>.
- [33] Schmitz, S.; Seibert, J.; Ostermeir, K.; Hansen, A.; Göller, A. H.; Grimme, S. Quantum Chemical Calculation of Molecular and Periodic Peptide and Protein Structures. *J. Phys. Chem. B* **2020**, *124*, 3636–3646.
- [34] Seibert, J.; Champagne, B.; Grimme, S.; de Wergifosse, M. Dynamic Structural Effects on the Second-Harmonic Generation of Tryptophane-Rich Peptides and Gramicidin A. *J. Phys. Chem. B* **2020**, *124*, 2568–2578.
- [35] de Wergifosse, M.; Grimme, S. Perspective on Simplified Quantum Chemistry Methods for Excited States and Response Properties. *J. Phys. Chem. A* **2021**, *125*, 3841–3851.
- [36] Grimme, S.; Bohle, F.; Hansen, A.; Pracht, P.; Spicher, S.; Stahn, M. Efficient Quantum

- Chemical Calculation of Structure Ensembles and Free Energies for Nonrigid Molecules. *J. Phys. Chem. A* **2021**, *125*, 4039–4054.
- [37] Berman, H. M.; Westbrook, J.; Feng, Z.; Gilliland, G.; Bhat, T. N.; Weissig, H.; Shindyalov, I. N.; Bourne, P. E. The Protein Data Bank. *Nucleic Acids Res.* **2000**, *28*, 235–242.
- [38] Martínez-Rosell, G.; Giorgino, T.; De Fabritiis, G. PlayMolecule ProteinPrepare: A Web Application for Protein Preparation for Molecular Dynamics Simulations. *J. Chem. Inf. Model.* **2017**, *57*, 1511–1516.
- [39] Dapprich, S.; Komáromi, I.; Byun, K. S.; Morokuma, K.; Frisch, M. J. A New ONIOM Implementation in Gaussian98. Part I. The Calculation of Energies, Gradients, Vibrational Frequencies and Electric Field derivatives. *Comp. Theor. Chem.* **1999**, *461-462*, 1–21.
- [40] Still, W. C.; Tempczyk, A.; Hawley, R. C.; Hendrickson, T. Semianalytical Treatment of Solvation for Molecular Mechanics and Dynamics. *J. Am. Chem. Soc.* **1990**, *112*, 6127–6129.
- [41] Frisch, M. J. et al. Gaussian 16 Revision A.03. 2016; Gaussian Inc. Wallingford CT.
- [42] Ehlert, S.; Bannwarth, C.; Grimme, S. Semiempirical Extended Tight-Binding Program Package xtb, version 6.2.2. <https://github.com/grimme-lab/xtb/>, Accessed: 2019-12-19. See also xTB documentation at <https://xtb-docs.readthedocs.io/en/latest/>.
- [43] Sekino, H.; Bartlett, R. J. Molecular Hyperpolarizabilities. *J. Chem. Phys.* **1993**, *98*, 3022–3037.
- [44] Christie, J. M.; Hitomi, K.; Arvai, A. S.; Hartfield, K. A.; Mettlen, M.; Pratt, A. J.; Tainer, J. A.; Getzoff, E. D. Structural Tuning of the Fluorescent Protein iLOV for Improved Photostability. *J. Biol. Chem.* **2012**, *287*, 22295–22304.
- [45] Cardoso Ramos, F.; Cupellini, L.; Mennucci, B. Computational Investigation of Structural and Spectroscopic Properties of LOV-Based Proteins with Improved Fluorescence. *J. Phys. Chem. B* **2021**, *125*, 1768–1777.
- [46] Nogly, P. et al. Retinal Isomerization in Bacteriorhodopsin Captured by a Femtosecond X-Ray Laser. *Science* **2018**, *361*, eaat0094.
- [47] Christie, J. M.; Hitomi, K.; Arvai, A. S.; Hartfield, K. A.; Mettlen, M.; Pratt, A. J.; Tainer, J. A.; Getzoff, E. D. Structural Tuning of the Fluorescent Protein iLOV for Improved Photostability. *J. Biol. Chem.* **2012**, *287*, 22295–22304.
- [48] Campo, J.; Wenseleers, W.; Goovaerts, E.; Szablewski, M.; Cross, G. H. Accurate Determination and Modeling of the Dispersion of the First Hyperpolarizability of an Efficient Zwitterionic Nonlinear Optical Chromophore by Tunable Wavelength Hyper-Rayleigh Scattering. *J. Phys. Chem. C* **2008**, *112*, 287–296.

- [49] Oudar, J. L.; Chemla, D. S. Hyperpolarizabilities of the Nitroanilines and Their Relations to the Excited State Dipole Moment. *J. Chem. Phys.* **1977**, 66, 2664–2668.

Few-state description of the first hyperpolarizability

Abstract

This paper aims at providing a comparative study of VB- n CT ($n \in [1, 4]$) models found in the literature to rationalize the second-order nonlinear optical (NLO) responses of molecules. It focuses particularly on the quantities obtained from the hyper-Rayleigh scattering (HRS) measurements, the first hyperpolarizability (β_{HRS}) and its depolarization ratio. The expression of the different components have been derived using a set of (up to) 5 parameters, which allows to tackle a wide diversity of architectures, from C_{2v} to $C_{\infty v}$, including D_{3h} and T_d . The analysis shows that i) to be competitive against the one-dimensional dipolar NLO compounds, a large CT character is required for the other architectures, ii) if this character is very large, the D_{3h} architecture is the most interesting of all, and iii) for intermediate CT characters, the C_{2v} and C_{3v} architectures should be considered.

Note. The chapter corresponds to a manuscript in a early redaction stage. It gathers the contributions from P. Beaujean and B. Champagne.

► Supporting information are available in Appendix C, page 351.

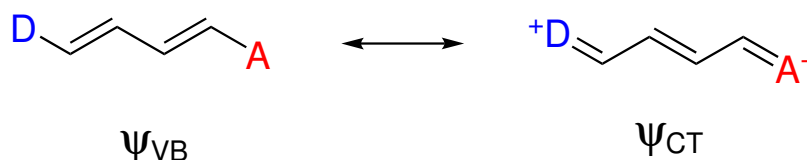
Section 11.1

Introduction

The discovery of Second Harmonic Generation (SHG) by Franken et al.¹ has fostered a large amount of research activities, aiming at applications in materials and life sciences. Among these, the search for materials with large second harmonic generation (SHG) responses for applications in frequency doublers² and the design of SHG sensors.^{3–5} The latter are typically exogenous dyes employed to monitor the structure and dynamics of living matter.⁶ At the molecular level, the SHG intensity is governed by the first hyperpolarizability, β .^{7,8} β can also add a dimension to the molecular switches, leading to multi-addressable, multi-function, and multi-state switches.^{9–12}

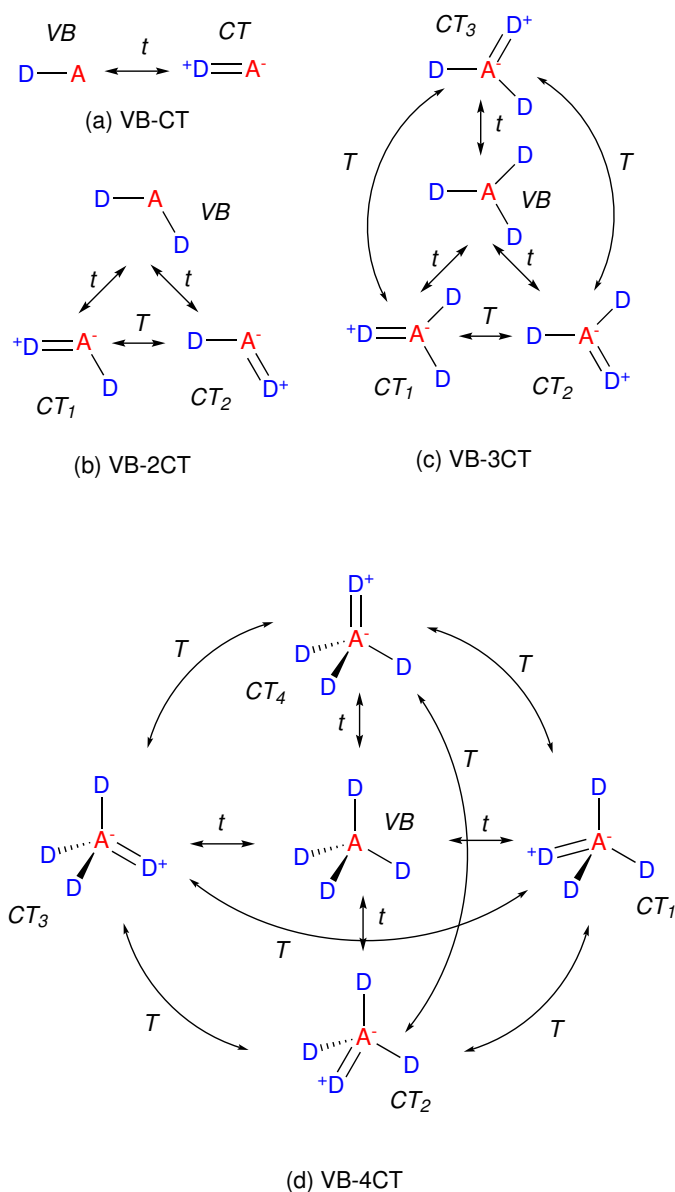
Promising architectures for such molecules belong to the push-pull family, *i.e.*, groups connected by a π -conjugated segment, which allows the “communication” between the two moieties. To maximize β , two (non-orthogonal) strategies have been broadly employed: i) choosing an appropriate pair of donor and acceptor, and ii) controlling the length and nature of the π -conjugated path. To explain this matter of fact, simple models have been developed since they allow, with a handful of parameters, to get insight into complex phenomena.

Pioneered by Mulliken,¹³ the VB-CT (valence-bond charge transfer) model was successfully applied to the first hyperpolarizabilities (in addition to UV/VIS absorption characteristics and other physico-chemical properties¹⁴) of push-pull polyenes and related structures^{15–19} in order to unravel simple structure-activity relationships. It assumes that the electronic state of a system can be described as a combination of two limiting states, a ψ_{VB} state and a ψ_{CT} state (Scheme 11.1), related by the displacement of an electron from the donor to the acceptor. So, using simple quantities associated with the ionization energy of the donor, the electron affinity of the acceptor, and the coupling between the two limiting states, linear and nonlinear properties have been scrutinized. Although quite simple, this model is versatile enough to be extended to encompass the presence of multiple donor/acceptor groups, leading to 3-,^{20–22} 4-²³ and 5-²⁴ state models, as shown in Scheme 11.2. They allowed to get a better understanding on the impact of the molecular geometry and symmetry on β .



Scheme 11.1: Limiting forms of the VB-CT model.

This paper aims at providing a comparative analysis of the VB- n CT models with $n=1-4$, in the context of the hyper-Rayleigh scattering (HRS) technique, broadly employed to measure the first hyperpolarizability of molecules in solution^{25–27} as well as in gas phase.²⁸ It is orga-



Scheme 11.2: Simplified representation of the successive VB- n CT models ($n \in [1, 4]$, adapted from Cho et al.,²⁴ with the charge transfer integrals t and T). Donor (D, in blue) and acceptor (A, in red) can be swapped without loss of generality.

nized as follows: after a brief reminder about the different formulations of the VB- n CT model and of the HRS technique in Section 11.2, Section 11.3 derives the main results for the 4 types of systems and compares them. Finally, Section 11.4 draws conclusions and perspectives.

Section 11.2

Theory

The VB- n CT model

Given that the nature of all the CT states are the same, the Hamiltonian, which is represented by a $(n+1) \times (n+1)$ matrix, is assumed to have the following form:

$$H_{ij} = \begin{cases} E_{VB} & \text{if } i = j = 1, \\ E_{CT} & \text{if } i = j \neq 1, \\ -t & \text{if } i \neq j \wedge (i = 1 \vee j = 1), \\ -T & \text{otherwise,} \end{cases} \quad (11.1)$$

where E_{VB} is the VB state energy, E_{CT} is the CT state energy, $t = -\langle \psi_{VB} | \hat{H} | \psi_{CT,i} \rangle$ is the transfer integral between the VB and any CT state, and $T = -\langle \psi_{CT,i} | \hat{H} | \psi_{CT,j} \rangle$ is the transfer integral between two (different) CT states. The dipole moment integrals are usually approximated as follow:¹⁵

$$\begin{aligned} \langle \psi_{VB} | \hat{\mu} | \psi_{VB} \rangle &= 0, \\ \langle \psi_{VB} | \hat{\mu} | \psi_{CT,i} \rangle &= 0, \\ \langle \psi_{CT,i} | \hat{\mu} | \psi_{CT,i} \rangle &= \mu_{CT}, \text{ and} \\ \langle \psi_{CT,i} | \hat{\mu} | \psi_{CT,j} \rangle &= 0 \text{ if } i \neq j. \end{aligned} \quad (11.2)$$

The eigenvalues, in a general form, were given by Cho *et al.* in 2002.²⁴ They are:

$$\begin{aligned} E_g &= \frac{1}{2} \left\{ E_{VB} + E_{CT} - (n-1)T - \left[(V - (n-1)T)^2 + 4nt^2 \right]^{1/2} \right\}, \\ E_{e_i} &= E_{CT} + T, \\ E_f &= \frac{1}{2} \left\{ E_{VB} + E_{CT} - (n-1)T + \left[(V - (n-1)T)^2 + 4nt^2 \right]^{1/2} \right\}, \end{aligned} \quad (11.3)$$

where $V = E_{CT} - E_{VB}$, g is the ground state, $\{e_i\}$ are the $(n-1)$ -fold degenerate excited states, and f is a single non-degenerate excited state. The corresponding eigenfunctions of (11.1) are

$$|\Psi_g\rangle = \cos \delta |\psi_{VB}\rangle + \frac{\sin \delta}{\sqrt{n}} \sum_j^n |\psi_{CT,j}\rangle, \quad (11.4)$$

$$|\Psi_{e_i}\rangle = \frac{1}{\sqrt{i(i+1)}} \left\{ i |\Psi_{CT,i+1}\rangle - \sum_j^i |\psi_{CT,j}\rangle \right\}, \quad (11.5)$$

$$|\Psi_f\rangle = \sin \delta |\psi_{VB}\rangle - \frac{\cos \delta}{\sqrt{n}} \sum_j^n |\psi_{CT,j}\rangle. \quad (11.6)$$

where the δ parameterization has been introduced, with $\delta \in [0, \pi/2]$. Therefore, when $0 \leq \delta < \pi/4$, the ground state is dominated by the VB state, while it is the opposite when $\pi/4 < \delta \leq \pi/2$, so that $\delta = \pi/4$ is the so-called *cyanine limit*. Minimizing the ground state energy, E_g , with respect to δ results in the following relationship between the parameters:

$$\frac{\partial E_g(\delta)}{\partial \delta} = 0 \Leftrightarrow V - (n-1)T = 2t \sqrt{n} \cot(2\delta), \quad (11.7)$$

Then, setting the energy origin to be

$$E_{VB} + E_{CT} - (n-1)T = 0, \quad (11.8)$$

this allows to express the eigenvalues in a simpler form:

$$\begin{aligned} E_g &= -\frac{1}{2} \left\{ (2t \sqrt{n} \cot(2\delta))^2 + 4nt^2 \right\}^{1/2} = -\sqrt{n} \frac{t}{\sin(2\delta)}, \\ E_{e_i} &= nT + t \sqrt{n} \cot(2\delta), \\ E_f &= \sqrt{n} \frac{t}{\sin(2\delta)}, \end{aligned} \quad (11.9)$$

In the following analysis, differences between the state energies are employed:

$$\begin{aligned} E_{ge} &= E_{e_i} - E_g = nT + t \sqrt{n} \cot(2\delta) + \sqrt{n} \frac{t}{\sin(2\delta)} = t \sqrt{n} \cot(\delta) + nT, \\ E_{gf} &= E_f - E_g = \frac{2t \sqrt{n}}{\sin(2\delta)}. \end{aligned} \quad (11.10)$$

In this frame, the molecular properties are monitored as a function of the δ parameter, which describes the amount of VB and CT forms in the ground (excited) state. This is performed as a function of t as well of the t/T ratio.

Alternative parameterization: the CT character

To monitor the variation of the molecular properties, one can introduce the CT character (of the ground state),²²⁻²⁴ as

$$\ell_{CT} = \frac{1}{n} \sin^2 \delta. \quad (11.11)$$

Note that while $\delta \in [0, \pi/2]$, $\ell_{CT} \in [0, 1/n]$. $\ell_{CT} = 0$ means that the ground state is fully described by the VB form whereas a $\ell_{CT} = 1/n$ corresponds to the opposite situation. The eigenvalues become:

$$E_g = -\frac{t}{2 \sqrt{\ell_{CT} (1 - n\ell_{CT})}},$$

$$\begin{aligned}
E_{e_i} &= nT + \frac{t(1 - 2n\ell_{CT})}{2\sqrt{\ell_{CT}(1 - n\ell_{CT})}}, \\
E_f &= \frac{t}{2\sqrt{\ell_{CT}(1 - n\ell_{CT})}},
\end{aligned} \tag{11.12}$$

and $|\Psi_g\rangle$ and $|\Psi_f\rangle$ may be also defined as ($|\Psi_{e_i}\rangle$ remains the same):

$$\begin{aligned}
|\Psi_g\rangle &= \sqrt{1 - n\ell_{CT}} |\psi_{VB}\rangle + \sqrt{\ell_{CT}} \sum_j^n |\psi_{CT,j}\rangle, \\
|\Psi_f\rangle &= \sqrt{n\ell_{CT}} |\psi_{VB}\rangle - \sqrt{\frac{1}{n} - \ell_{CT}} \sum_j^n |\psi_{CT,j}\rangle,
\end{aligned} \tag{11.13}$$

while the excitation energies become:

$$E_{ge} = nT + t \sqrt{\frac{1}{\ell_{CT}} - n}, \tag{11.14}$$

$$E_{gf} = \frac{t}{\sqrt{\ell_{CT}(1 - n\ell_{CT})}}. \tag{11.15}$$

Alternative parameterization: the mixing character

Another interesting parameter, introduced by Barzoukas and co-workers,¹⁷⁻¹⁹ describes the mixing between the VB and CT states and it is defined as:

$$m_{CT} = -\cos(2\delta) = 2n\ell_{CT} - 1. \tag{11.16}$$

Thus m_{CT} ranges between -1 (dominated by VB) and 1 (dominated by CT). In that framework, the eigenvalues become:

$$\begin{aligned}
E_g &= -t \sqrt{\frac{n}{1 - m_{CT}^2}}, \\
E_{e_i} &= nT - t \sqrt{n} \frac{m_{CT}}{\sqrt{1 - m_{CT}^2}}, \\
E_f &= t \sqrt{\frac{n}{1 - m_{CT}^2}},
\end{aligned} \tag{11.17}$$

and the excitation energies read:

$$\begin{aligned}
E_{ge} &= nT + t \sqrt{n \frac{1 - m_{CT}}{1 + m_{CT}}}, \\
E_{gf} &= 2t \sqrt{\frac{n}{1 - m_{CT}^2}}.
\end{aligned} \tag{11.18}$$

Again, $|\Psi_g\rangle$ and $|\Psi_f\rangle$ may be redefined as:

$$\begin{aligned} |\Psi_g\rangle &= \sqrt{\frac{1-m_{CT}}{2}} |\psi_{VB}\rangle + \sqrt{\frac{1+m_{CT}}{2n}} \sum_j^n |\psi_{CT,j}\rangle, \\ |\Psi_f\rangle &= \sqrt{\frac{1+m_{CT}}{2}} |\psi_{VB}\rangle - \sqrt{\frac{1-m_{CT}}{2n}} \sum_j^n |\psi_{CT,j}\rangle. \end{aligned} \quad (11.19)$$

First hyperpolarizability and HRS spectroscopy

The elements of the first hyperpolarizability are defined using the sum-over-states (SOS) expression of Orr-Ward-Bishop.^{15,29} In the static limit, it reads as:

$$\beta_{ijk} = \sum_{\mathcal{P}}^{i,j,k} \sum_{a_1,a_2}^N \frac{\mu_{0a_1}^i \bar{\mu}_{a_1a_2}^j \mu_{a_20}^k}{\omega_{a_1} \omega_{a_2}}, \quad (11.20)$$

where i, j, k are the Cartesian coordinates x, y, z (in the molecular frame), \sum_{a_1,a_2} is a sum over the N excited states, $\bar{\mu}_{a_1a_2}^j = \mu_{a_1a_2}^j - \delta_{a_1a_2} \mu_0^j$ and $\sum_{\mathcal{P}}$ is the sum of the different permutations over the i, j, k components. Eq. (11.20) can be decomposed in the so-called *dipolar* or diagonal terms, β^D (where $a_i = a_j$) and *two-photon*, octupolar, or off-diagonal terms, β^{TP} (where $a_i \neq a_j$):

$$\beta_{ijk} = \beta_{ijk}^D + \beta_{ijk}^{TP} = \sum_{\mathcal{P}}^{i,j,k} \sum_{a_1}^N \frac{\mu_{0a_1}^i (\mu_{a_1}^j - \mu_0^j) \mu_{a_10}^k}{\omega_{a_1}^2} + 2 \sum_{\mathcal{P}}^{i,j,k} \sum_{a_1 < a_2}^N \frac{\mu_{0a_1}^i \mu_{a_1a_2}^j \mu_{a_20}^k}{\omega_{a_1} \omega_{a_2}}. \quad (11.21)$$

For an isotropic medium composed of identical molecules or scatterers, the intensity, I , of the incoherent contribution to the second harmonic scattered light is proportional to an isotropic (or rotational) averaging of the tensor elements over all possible molecular orientations.^{30–33} In the conventional experimental setup for the hyper-Rayleigh scattering (HRS) technique,²⁷ the scattered light is analyzed at a 90° angle with respect to the direction of propagation (Y), the fundamental light beam (of frequency ω) is Z - or X -polarized (in the laboratory frame), while the Z -linearly polarized component of the scattered beam (of frequency 2ω) is recorded in the X direction. One can thus distinguish between two polarization combinations: the VV geometry (vertical-vertical, both incident and scattered lights are Z -polarized) and HV [horizontal-vertical, the incident (scattered) light is X (Z)-polarized]. The I_{VV} intensity is proportional to $\langle \beta_{ZZZ}^2 \rangle$, while I_{HV} is proportional to $\langle \beta_{ZXX}^2 \rangle$. The resulting expressions are:^{30,33}

$$\langle \beta_{ZZZ}^2 \rangle = \frac{1}{105} \sum_{ijk}^{x,y,z} 2 \beta_{ijk}^2 + \beta_{ijj} \beta_{ikk} + 4 \beta_{iij} \beta_{jkk} + 4 \beta_{ijj} \beta_{kkj} + 4 \beta_{ijk} \beta_{jik}, \quad (11.22)$$

$$\langle \beta_{ZXX}^2 \rangle = \frac{1}{105} \sum_{ijk}^{x,y,z} 6 \beta_{ijk}^2 + 3 \beta_{ijj} \beta_{ikk} - 2 \beta_{iij} \beta_{jkk} - 2 \beta_{iij} \beta_{kkj} - 2 \beta_{ijk} \beta_{jik}. \quad (11.23)$$

For a non-polarized incident signal, both polarizations have equal probability and the intensity becomes proportional to the sum of the HV and VV observables. This allows defining β_{HRS} and its associated depolarization ratio (DR):

$$\beta_{HRS} = \sqrt{\langle \beta_{ZZZ}^2 \rangle + \langle \beta_{ZXX}^2 \rangle}, \text{ and DR} = \frac{\langle \beta_{ZZZ}^2 \rangle}{\langle \beta_{ZXX}^2 \rangle}. \quad (11.24)$$

Section 11.3

Results and discussion

The successive VB- n CT schemes (with $n \in [1, 4]$) are now derived. They are then further analyzed at the end of this section.

2-state $C_{\infty v}$ systems

These molecules are built from a D/A pair, usually at the extremities of a π -conjugated linker, and, for our convenience, they extent here in the z -direction. In the static limit, there is only one nonzero component, β_{zzz} . Given the parameterization,

$$\mu_g = \langle \Psi_g | \hat{\mu} | \Psi_g \rangle = \mu_{CT} \sin^2 \delta = \ell_{CT} \mu_{CT} = \frac{1 + m_{CT}}{2} \mu_{CT}, \quad (11.25)$$

$$\mu_f = \langle \Psi_f | \hat{\mu} | \Psi_f \rangle = \mu_{CT} \cos^2 \delta = (1 - \ell_{CT}) \mu_{CT} = \frac{1 - m_{CT}}{2} \mu_{CT}, \quad (11.26)$$

$$\mu_{gf} = \langle \Psi_g | \hat{\mu} | \Psi_f \rangle = -\frac{1}{2} \mu_{CT} \sin(2\delta) = -\mu_{CT} \sqrt{\ell_{CT}(1 - \ell_{CT})} = -\frac{\mu_{CT}}{2} \sqrt{1 - m_{CT}^2}, \quad (11.27)$$

$$\Delta\mu_{gf} = \mu_f - \mu_g = \mu_{CT} \cos(2\delta) = (1 - 2\ell_{CT}) \mu_{CT} = -m_{CT} \mu_{CT}. \quad (11.28)$$

From relation (11.20) and assuming that μ_{CT} is only in the z direction, this gives¹⁷⁻¹⁹

$$\begin{aligned} \beta_{zzz} &= \beta_{zzz}^D = 6 \frac{(\mu_{gf}^z)^2 (\mu_f^z - \mu_g^z)}{E_{gf}^2} \\ &= \frac{3}{8} \sin^4(2\delta) \cos(2\delta) \frac{\mu_{CT}^3}{t^2} \\ &= 6\ell_{CT}^2 (1 - \ell_{CT})^2 (1 - 2\ell_{CT}) \frac{\mu_{CT}^3}{t^2} \\ &= -\frac{3}{8} m_{CT} (1 - m_{CT}^2)^2 \frac{\mu_{CT}^3}{t^2}. \end{aligned} \quad (11.29)$$

Thus, there is a minimum when $m_{CT} \in \{-1, 0, 1\}$, while β_{zzz} is maximal at $m_{CT} = \pm \frac{\sqrt{5}}{5}$. This is actually the classical trend for a 2-state system.¹⁸ The evolution with m_{CT} of the different quantities are pictured in Figs. C.1 and C.2.

3-state C_{2v} system

Let's assume that the two CT axes form an angle $\theta \in [0, \pi/2]$ from the z axis,²² as represented in Scheme 11.3. In the static limit, at most two independent components are now nonzero: $\beta_{(zxx)}$ and β_{zzz} (which is the only one that remains if $\Theta = \pi/2$). Indeed,

$$\vec{\mu}_{CT,1} = \mu_{CT} (\sin \theta, 0, \cos \theta) \text{ and } \vec{\mu}_{CT,2} = \mu_{CT} (-\sin \theta, 0, \cos \theta). \quad (11.30)$$

Given the parameterization,

$$\begin{aligned} \vec{\mu}_g &= \langle \Psi_g | \hat{\mu} | \Psi_g \rangle \\ &= \mu_{CT} \sin^2 \delta (0, 0, \cos \theta) = 2 \ell_{CT} \mu_{CT} (0, 0, \cos \theta) = \frac{1 + m_{CT}}{2} (0, 0, \cos \theta), \end{aligned} \quad (11.31)$$

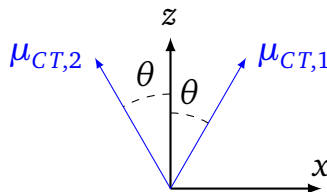
$$\vec{\mu}_e = \langle \Psi_e | \hat{\mu} | \Psi_e \rangle = \mu_{CT} (0, 0, \cos \theta), \quad (11.32)$$

$$\begin{aligned} \vec{\mu}_f &= \langle \Psi_f | \hat{\mu} | \Psi_f \rangle \\ &= \mu_{CT} \cos^2 \delta (0, 0, \cos \theta) = (1 - 2 \ell_{CT}) \mu_{CT} (0, 0, \cos \theta) = \frac{1 - m_{CT}}{2} (0, 0, \cos \theta), \end{aligned} \quad (11.33)$$

$$\begin{aligned} \vec{\mu}_{ge} &= \langle \Psi_g | \hat{\mu} | \Psi_e \rangle \\ &= \mu_{CT} \sin \delta (-\sin \theta, 0, 0) = \sqrt{2 \ell_{CT}} \mu_{CT} (-\sin \theta, 0, 0) \\ &= \sqrt{\frac{1 + m_{CT}}{2}} \mu_{CT} (-\sin \theta, 0, 0), \end{aligned} \quad (11.34)$$

$$\begin{aligned} \vec{\mu}_{gf} &= \langle \Psi_g | \hat{\mu} | \Psi_f \rangle \\ &= \frac{\mu_{CT}}{2} \sin(2\delta) (0, 0, -\cos \theta) = \sqrt{2 \ell_{CT} (1 - 2 \ell_{CT})} \mu_{CT} (0, 0, -\cos \theta) \\ &= \frac{\mu_{CT}}{2} \sqrt{1 - m_{CT}^2} (0, 0, -\cos \theta), \end{aligned} \quad (11.35)$$

$$\begin{aligned} \vec{\mu}_{ef} &= \langle \Psi_e | \hat{\mu} | \Psi_f \rangle \\ &= \mu_{CT} \cos \delta (\sin \theta, 0, 0) = \sqrt{1 - 2 \ell_{CT}} \mu_{CT} (\sin \theta, 0, 0) \\ &= \mu_{CT} \sqrt{\frac{1 - m_{CT}}{2}} (\sin \theta, 0, 0). \end{aligned} \quad (11.36)$$



Scheme 11.3: Representation of the charge-transfer dipoles (μ_{CT}) in the 3-state model.

and,

$$\begin{aligned}\Delta\vec{\mu}_{ge} &= \vec{\mu}_e - \vec{\mu}_g = \mu_{CT} \cos^2 \delta (0, 0, \cos \theta) = (1 - 2\ell_{CT}) \mu_{CT} (0, 0, \cos \theta) \\ &= \frac{1 - m_{CT}}{2} (0, 0, \cos \theta),\end{aligned}\quad (11.37)$$

$$\begin{aligned}\Delta\vec{\mu}_{gf} &= \vec{\mu}_f - \vec{\mu}_g = \mu_{CT} \cos(2\delta) (0, 0, \cos \theta) = (1 - 4\ell_{CT}) \mu_{CT} (0, 0, \cos \theta) \\ &= -m_{CT} \mu_{CT} (0, 0, \cos \theta).\end{aligned}\quad (11.38)$$

For β_{zzz} , relation (11.20) reduces to the dipolar term and the second excited state,

$$\begin{aligned}\beta_{zzz} &= \beta_{zzz}^D = 6 \frac{(\mu_{gf}^z)^2 (\mu_f^z - \mu_g^z)}{E_{gf}^2} \\ &= \frac{3}{16} \sin^4(2\delta) \cos(2\delta) \frac{\mu_{CT}^3}{t^2} \cos^3 \theta \\ &= 12\ell_{CT}^2 (1 - 2\ell_{CT})^2 (1 - 4\ell_{CT}) \frac{\mu_{CT}^3}{t^2} \cos^3 \theta \\ &= -\frac{3}{16} m_{CT} (1 - m_{CT}^2)^2 \frac{\mu_{CT}^3}{t^2} \cos^3 \theta.\end{aligned}\quad (11.39)$$

This expression is identical to the 2-state case, although modulated by the $\cos^3 \theta$ factor. On the other hand, for $\beta_{(zxx)}$ (the parentheses indicate the permutation of the indices):

$$\beta_{(zxx)} = \beta_{(zxx)}^D + \beta_{(zxx)}^{TP}, \quad (11.40)$$

with:

$$\begin{aligned}\beta_{(zxx)}^D &= 2 \frac{(\mu_{ge}^x)^2 (\mu_e^z - \mu_g^z)}{E_{ge}^2} \\ &= \frac{\sin^2(2\delta)}{2} \frac{\mu_{CT}^3}{(2T + t\sqrt{2} \cot \delta)^2} \sin^2 \theta \cos \theta \\ &= 4\ell_{CT} (1 - 2\ell_{CT}) \frac{\mu_{CT}^3}{\left(2T + t\sqrt{\frac{1}{\ell_{CT}} - 2}\right)^2} \sin^2 \theta \cos \theta \\ &= \frac{1 - m_{CT}^2}{2} \frac{\mu_{CT}^3}{\left(2T + t\left[2\frac{1 - m_{CT}}{1 + m_{CT}}\right]^{1/2}\right)^2} \sin^2 \theta \cos \theta,\end{aligned}\quad (11.41)$$

and:

$$\beta_{(zxx)}^{TP} = 4 \frac{\mu_{ge}^x \mu_{ef}^x \mu_{fg}^z}{E_{ge} E_{gf}}$$

$$\begin{aligned}
&= \sin^3(2\delta) \frac{\mu_{CT}^3}{(2T + t\sqrt{2}\cot\delta)(2t\sqrt{2})} \sin^2\theta \cos\theta \\
&= 8\ell_{CT}(1-2\ell_{CT}) \frac{\mu_{CT}^3}{\left(2T + t\sqrt{\frac{1}{\ell_{CT}}-2}\right)\left(\frac{t}{\sqrt{\ell_{CT}(1-2\ell_{CT})}}\right)} \sin^2\theta \cos\theta \\
&= (1-m_{CT}^2) \frac{\mu_{CT}^3}{2t\left[\frac{2}{1-m_{CT}^2}\right]^{1/2}\left(2T + t\left[2\frac{1-m_{CT}}{1+m_{CT}}\right]^{1/2}\right)} \sin^2\theta \cos\theta, \tag{11.42}
\end{aligned}$$

so that:

$$\begin{aligned}
\beta_{(xxx)} &= \frac{1-m_{CT}^2}{2} \mu_{CT}^3 \sin^2\theta \cos\theta \\
&\times \left\{ \frac{1}{\left(2T + t\left[2\frac{1-m_{CT}}{1+m_{CT}}\right]^{1/2}\right)^2} + \frac{2}{2t\left[\frac{2}{1-m_{CT}^2}\right]^{1/2}\left(2T + t\left[2\frac{1-m_{CT}}{1+m_{CT}}\right]^{1/2}\right)} \right\}. \tag{11.43}
\end{aligned}$$

This analysis is in agreement with Ref. 22. Note that when $\theta = 90^\circ$, both β_{zzz} and $\beta_{(xxx)}$ goes to zero, since it corresponds to a situation with a center of inversion ($D_{\infty h}$). The evolution with T/t (in the case where $\theta = 60^\circ$) of the different quantities are pictured in Figs. C.3-C.5.

4-state C_{3v} system

Let us, now, assume that the projection of the three dipole moments xy plane are at 120° from each other in the xy plane (and the first one points to the y direction), but that there is a $\theta \in [0, \pi/2]$ angle between the dipoles and the z axis, as in Scheme 11.4. There are, in this configuration, at most 3 independent β components that are non zero: $\beta_{(zyy)}$, β_{zzz} (which is the only one that remains if $\Theta = \pi/2$), and β_{yyy} (which is the only one that remains if $\Theta = 0$). Thus,

$$\vec{\mu}_{CT,1} = \mu_{CT}(0, \sin\theta, \cos\theta), \vec{\mu}_{CT,2,3} = \frac{\mu_{CT}}{2}(\pm\sqrt{3}\sin\theta, -\sin\theta, 2\cos\theta) \tag{11.44}$$

Given the parameterization, one gets:

$$\begin{aligned}
\vec{\mu}_g &= \langle \Psi_g | \hat{\mu} | \Psi_g \rangle \\
&= \mu_{CT} \sin^2\delta(0, 0, \cos\theta) = 3\ell_{CT}\mu_{CT}(0, 0, \cos\theta) = \frac{1+m_{CT}}{2}(0, 0, \cos\theta), \tag{11.45}
\end{aligned}$$

$$\vec{\mu}_{e_1} = \langle \Psi_{e_1} | \hat{\mu} | \Psi_{e_1} \rangle = \frac{\mu_{CT}}{4}(-\sqrt{3}\sin\theta, \sin\theta, 4\cos\theta), \tag{11.46}$$

$$\vec{\mu}_{e_2} = \langle \Psi_{e_2} | \hat{\mu} | \Psi_{e_2} \rangle = \frac{\mu_{CT}}{4}(\sqrt{3}\sin\theta, -\sin\theta, 4\cos\theta), \tag{11.47}$$

$$\begin{aligned}\vec{\mu}_f &= \langle \Psi_f | \hat{\mu} | \Psi_f \rangle \\ &= \mu_{CT} \cos^2 \delta (0, 0, \cos \theta) = (1 - 3\ell_{CT}) \mu_{CT} (0, 0, \cos \theta) = \frac{1 - m_{CT}}{2} (0, 0, \cos \theta), \quad (11.48)\end{aligned}$$

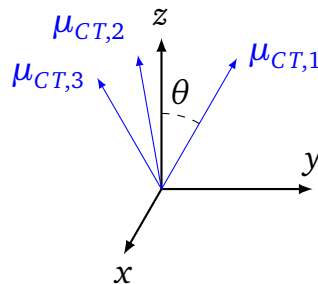
$$\begin{aligned}\vec{\mu}_{ge_1} &= \langle \Psi_g | \hat{\mu} | \Psi_{e_1} \rangle \\ &= \frac{1}{4} \mu_{CT} \sin \delta (\sqrt{3} \sin \theta, -\sqrt{6} \sin \theta, 0) = \frac{1}{4} \sqrt{3\ell_{CT}} \mu_{CT} (\sqrt{3} \sin \theta, -\sqrt{6} \sin \theta, 0) \\ &= \frac{1}{4} \sqrt{\frac{1 + m_{CT}}{2}} \mu_{CT} (\sqrt{3} \sin \theta, -\sqrt{6} \sin \theta, 0), \quad (11.49)\end{aligned}$$

$$\begin{aligned}\vec{\mu}_{ge_2} &= \langle \Psi_g | \hat{\mu} | \Psi_{e_2} \rangle \\ &= \frac{\sqrt{2}}{4} \mu_{CT} \sin \delta (-\sqrt{3} \sin \theta, -\sin \theta, 0) = \frac{\sqrt{2}}{4} \sqrt{3\ell_{CT}} \mu_{CT} (-\sqrt{3} \sin \theta, -\sin \theta, 0) \\ &= \frac{\sqrt{2}}{4} \sqrt{\frac{1 + m_{CT}}{2}} \mu_{CT} (-\sqrt{3} \sin \theta, -\sin \theta, 0), \quad (11.50)\end{aligned}$$

$$\begin{aligned}\vec{\mu}_{gf} &= \langle \Psi_g | \hat{\mu} | \Psi_f \rangle \\ &= \frac{\mu_{CT}}{2} \sin(2\delta) (0, 0, -\cos \theta) = \sqrt{3\ell_{CT}(1 - 3\ell_{CT})} \mu_{CT} (0, 0, -\cos \theta) \\ &= \frac{\mu_{CT}}{2} \sqrt{1 - m_{CT}^2} (0, 0, -\cos \theta), \quad (11.51)\end{aligned}$$

$$\vec{\mu}_{e_1 e_2} = \langle \Psi_{e_1} | \hat{\mu} | \Psi_{e_2} \rangle = \frac{1}{4} \mu_{CT} (-\sin \theta, \sqrt{3} \sin \theta, 0), \quad (11.52)$$

$$\begin{aligned}\vec{\mu}_{e_1 f} &= \langle \Psi_{e_1} | \hat{\mu} | \Psi_f \rangle \\ &= \frac{\sqrt{2}}{4} \mu_{CT} \cos \delta (-\sin \theta, \sqrt{3} \sin \theta, 0) = \frac{\sqrt{2}}{4} \sqrt{1 - 3\ell_{CT}} \mu_{CT} (-\sin \theta, \sqrt{3} \sin \theta, 0) \\ &= \frac{\sqrt{2}}{4} \sqrt{\frac{1 - m_{CT}}{2}} \mu_{CT} (-\sin \theta, \sqrt{3} \sin \theta, 0), \quad (11.53)\end{aligned}$$



Scheme 11.4: Representation of the charge-transfer dipoles (μ_{CT}) in the 3-state model.

$$\begin{aligned}
\vec{\mu}_{e_2f} &= \langle \Psi_{e_2} | \hat{\mu} | \Psi_f \rangle \\
&= \frac{\sqrt{2}}{4} \mu_{CT} \cos \delta (\sqrt{3} \sin \theta, \sin \theta, 0) = \frac{\sqrt{2}}{4} \sqrt{1 - 3\ell_{CT}} \mu_{CT} (\sqrt{3} \sin \theta, \sin \theta, 0) \\
&= \frac{\sqrt{2}}{4} \sqrt{\frac{1 - m_{CT}}{2}} \mu_{CT} (\sqrt{3} \sin \theta, \sin \theta, 0).
\end{aligned} \tag{11.54}$$

and,

$$\begin{aligned}
\Delta \vec{\mu}_{ge_1} &= \vec{\mu}_{e_1} - \vec{\mu}_g = \mu_{CT} \left(\frac{\sqrt{3}}{4} \sin \theta, \frac{1}{4} \sin \theta, \cos^2 \delta \cos \theta \right) \\
&= \mu_{CT} \left(\frac{\sqrt{3}}{4} \sin \theta, \frac{1}{4} \sin \theta, (1 - 2\ell_{CT}) \cos \theta \right) \\
&= \mu_{CT} \left(\frac{\sqrt{3}}{4} \sin \theta, \frac{1}{4} \sin \theta, \frac{1 - m_{CT}}{2} \cos \theta \right),
\end{aligned} \tag{11.55}$$

$$\begin{aligned}
\Delta \vec{\mu}_{ge_2} &= \vec{\mu}_{e_2} - \vec{\mu}_g = \mu_{CT} \left(-\frac{\sqrt{3}}{4} \sin \theta, -\frac{1}{4} \sin \theta, \cos^2 \delta \cos \theta \right) \\
&= \mu_{CT} \left(-\frac{\sqrt{3}}{4} \sin \theta, -\frac{1}{4} \sin \theta, (1 - 2\ell_{CT}) \cos \theta \right) \\
&= \mu_{CT} \left(-\frac{\sqrt{3}}{4} \sin \theta, -\frac{1}{4} \sin \theta, \frac{1 - m_{CT}}{2} \cos \theta \right),
\end{aligned} \tag{11.56}$$

$$\begin{aligned}
\Delta \vec{\mu}_{gf} &= \vec{\mu}_f - \vec{\mu}_g = \mu_{CT} \cos(2\delta) (0, 0, \cos \theta) = (1 - 6\ell_{CT}) \mu_{CT} (0, 0, \cos \theta) \\
&= -m_{CT} \mu_{CT} (0, 0, \cos \theta).
\end{aligned} \tag{11.57}$$

For β_{zzz} , only one dipolar channel (through $\vec{\mu}_{gf}$, since it is the only one with a non-null z component) is possible:

$$\begin{aligned}
\beta_{zzz} &= \beta_{zzz}^D = 6 \frac{(\mu_{gf}^z)^2 (\mu_f^z - \mu_g^z)}{E_{gf}^2} \\
&= \frac{1}{8} \sin^4(2\delta) \cos(2\delta) \frac{\mu_{CT}^3}{t^2} \cos^3 \theta \\
&= 18\ell_{CT}^2 (1 - 3\ell_{CT})^2 (1 - 6\ell_{CT}) \frac{\mu_{CT}^3}{t^2} \cos^3 \theta \\
&= -\frac{1}{8} m_{CT} (1 - m_{CT}^2)^2 \frac{\mu_{CT}^3}{t^2} \cos^3 \theta.
\end{aligned} \tag{11.58}$$

The form is, again, very similar to the one of the 2-state system, as expected. Concerning $\beta_{(zyy)}$ component, two excitation channels are possible:

$$\beta_{(zyy)} = \beta_{(zyy)}^D + \beta_{(zyy)}^{TP}, \tag{11.59}$$

with:

$$\begin{aligned}
 \beta_{(zyy)}^D &= 2 \frac{(\mu_{ge_1}^y)^2 (\mu_{e_1}^z - \mu_g^z)}{E_{ge}^2} + 2 \frac{(\mu_{ge_2}^y)^2 (\mu_{e_2}^z - \mu_g^z)}{E_{ge}^2} \\
 &= \frac{\sin^2(2\delta)}{4} \frac{\mu_{CT}^3}{(3T + t\sqrt{3} \cot \delta)^2} \sin^2 \theta \cos \theta \\
 &= 3\ell_{CT} (1 - 3\ell_{CT}) \frac{\mu_{CT}^3}{\left(3T + t\sqrt{\frac{1}{\ell} - 3}\right)^2} \sin^2 \theta \cos \theta \\
 &= \frac{1}{4} (1 - m_{CT}^2) \frac{\mu_{CT}^3}{\left(3T + t \left[3 \frac{1-m_{CT}}{1+m_{CT}}\right]^{1/2}\right)^2} \sin^2 \theta \cos \theta, \tag{11.60}
 \end{aligned}$$

and:

$$\begin{aligned}
 \beta_{(zyy)}^{TP} &= 4 \frac{\mu_{ge_1}^y \mu_{e_1f}^y \mu_{fg}^z}{E_{ge} E_{gf}} + 4 \frac{\mu_{ge_2}^y \mu_{e_2f}^y \mu_{fg}^z}{E_{ge} E_{gf}} \\
 &= \frac{1}{2} \sin^3(2\delta) \frac{\mu_{CT}^3}{(3T + t\sqrt{3} \cot \delta)(2t\sqrt{3})} \sin^2 \theta \cos \theta \\
 &= 6\ell_{CT} (1 - 3\ell_{CT}) \frac{\mu_{CT}^3}{\left(2T + t\sqrt{\frac{1}{\ell_{CT}} - 2}\right) \left(\frac{t}{\sqrt{\ell_{CT}(1-2\ell_{CT})}}\right)} \sin^2 \theta \cos \theta \\
 &= \frac{1}{2} (1 - m_{CT}^2) \frac{\mu_{CT}^3}{2t \left[\frac{3}{1-m_{CT}^2}\right]^{1/2} \left(3T + t \left[3 \frac{1-m_{CT}}{1+m_{CT}}\right]^{1/2}\right)} \sin^2 \theta \cos \theta, \tag{11.61}
 \end{aligned}$$

so that:

$$\begin{aligned}
 \beta_{(zyy)} &= \frac{1 - m_{CT}^2}{4} \mu_{CT}^3 \sin^2 \theta \cos \theta \\
 &\quad \times \left\{ \frac{1}{\left(3T + t \left[3 \frac{1-m_{CT}}{1+m_{CT}}\right]^{1/2}\right)^2} + \frac{2}{2t \left[\frac{3}{1-m_{CT}^2}\right]^{1/2} \left(3T + t \left[3 \frac{1-m_{CT}}{1+m_{CT}}\right]^{1/2}\right)} \right\}, \tag{11.62}
 \end{aligned}$$

which is reminiscent of $\beta_{(zxx)}$ in the 3-state system. Note that $\beta_{(zxx)} = \beta_{(zyy)}$, as expected from the C_{3v} symmetry. Finally, concerning β_{yyy} , excitation channels cannot go through $\vec{\mu}_{gf}$, and so, there are two D terms, and one TP term:

$$\beta_{yyy}^D = 6 \frac{(\mu_{ge}^y)^2 (\mu_{e_1}^y - \mu_g^y)}{E_{ge}^2} + 6 \frac{(\mu_{ge_2}^y)^2 (\mu_{e_2}^y - \mu_g^y)}{E_{ge}^2}$$

$$\begin{aligned}
&= \frac{3}{8} \sin^2 \delta \frac{\mu_{CT}^3}{(3T + t\sqrt{3} \cot \delta)^2} \sin^3 \theta \\
&= \frac{9\ell_{CT}}{8} \frac{\mu_{CT}^3}{\left(3T + t\sqrt{\frac{1}{\ell_{CT}} - 3}\right)^2} \sin^3 \theta \\
&= \frac{3}{16} (1 + m_{CT}) \frac{\mu_{CT}^3}{\left(3T + t\left[3\frac{1-m_{CT}}{1+m_{CT}}\right]^{1/2}\right)^2} \sin^3 \theta, \tag{11.63}
\end{aligned}$$

$$\begin{aligned}
\beta_{yyy}^{TP} &= 12 \frac{\mu_{ge_1}^y \mu_{e_1e_2}^y \mu_{e_2g}^y}{E_{ge}^2} \\
&= \frac{9}{8} \sin^2 \delta \frac{\mu_{CT}^3}{(3T + t\sqrt{3} \cot \delta)^2} \sin^3 \theta \\
&= \frac{27\ell_{CT}}{8} \frac{\mu_{CT}^3}{\left(3T + t\sqrt{\frac{1}{\ell_{CT}} - 3}\right)^2} \sin^3 \theta \\
&= \frac{9}{16} (1 + m_{CT}) \frac{\mu_{CT}^3}{\left(3T + t\left[3\frac{1-m_{CT}}{1+m_{CT}}\right]^{1/2}\right)^2} \sin^3 \theta. \tag{11.64}
\end{aligned}$$

So that:

$$\beta_{yyy} = \frac{3}{4} (1 + m_{CT}) \frac{\mu_{CT}^3}{\left(3T + t\left[3\frac{1-m_{CT}}{1+m_{CT}}\right]^{1/2}\right)^2} \sin^3 \theta. \tag{11.65}$$

The relationship $\beta_{yyy} = -\beta_{(yxx)}$ holds in this model,^a as expected from C_{3v} symmetry. Furthermore, all other components are zero by symmetry. Note that when $\theta = 90^\circ$, the system corresponds to a D_{3h} symmetry, with $\beta_{zzz} = \beta_{(zyy)} = \beta_{(zxx)} = 0$. The evolution with T/t (in the case where $\theta = 90^\circ$) of the different quantities are pictured in Figs. C.6-C.8.

5-states T_d system

The T_d geometry was first reviewed by Cho *et al.*²⁴ The only independent non-zero component is, in this case, $\beta_{(xyz)}$. The dipole moments are given by:

$$\begin{aligned}
\vec{\mu}_{CT,1} &= \mu_{CT} \frac{\sqrt{3}}{3} (1, 1, 1), \vec{\mu}_{CT,2} = \mu_{CT} \frac{\sqrt{3}}{3} (1, -1, -1), \\
\vec{\mu}_{CT,3} &= \mu_{CT} \frac{\sqrt{3}}{3} (-1, -1, 1), \text{ and } \vec{\mu}_{CT,4} = \mu_{CT} \frac{\sqrt{3}}{3} (-1, 1, -1). \tag{11.66}
\end{aligned}$$

^aSymmetry tables generally reports $\beta_{yyy} = -\beta_{(yyx)}$, but it is just a matter of defining the σ_v . Also, this definition is consistent with D_{3h} .

Given the parameterization, one gets:

$$\vec{\mu}_g = \langle \Psi_g | \hat{\mu} | \Psi_g \rangle = \vec{0}, \quad (11.67)$$

$$\vec{\mu}_{e_1} = \langle \Psi_{e_1} | \hat{\mu} | \Psi_{e_1} \rangle = \mu_{CT} \frac{\sqrt{3}}{3} (1, 0, 0), \quad (11.68)$$

$$\vec{\mu}_{e_2} = \langle \Psi_{e_2} | \hat{\mu} | \Psi_{e_2} \rangle = \mu_{CT} \frac{\sqrt{3}}{9} (-1, -2, 2), \quad (11.69)$$

$$\vec{\mu}_{e_3} = \langle \Psi_{e_3} | \hat{\mu} | \Psi_{e_3} \rangle = \mu_{CT} \frac{2\sqrt{3}}{9} (-1, 1, -1), \quad (11.70)$$

$$\vec{\mu}_f = \langle \Psi_f | \hat{\mu} | \Psi_f \rangle = \vec{0}. \quad (11.71)$$

Due to the fact that $\vec{\mu}_{gf} = \vec{0}$ in this case, the excitation path for β cannot go through Ψ_f . Therefore, the only transition dipoles needed are:

$$\begin{aligned} \vec{\mu}_{ge_1} &= \langle \Psi_g | \hat{\mu} | \Psi_{e_1} \rangle \\ &= \frac{\sqrt{6}}{6} \mu_{CT} \sin \delta (0, -1, -1) = \frac{\sqrt{6}}{6} \sqrt{4\ell_{CT}} \mu_{CT} (0, -1, -1) \\ &= \frac{\sqrt{6}}{6} \sqrt{\frac{1+m_{CT}}{2}} \mu_{CT} (0, -1, -1), \end{aligned} \quad (11.72)$$

$$\begin{aligned} \vec{\mu}_{ge_2} &= \langle \Psi_g | \hat{\mu} | \Psi_{e_2} \rangle \\ &= \frac{3\sqrt{2}}{18} \mu_{CT} \sin \delta (-2, -1, 1) = \frac{3\sqrt{2}}{18} \sqrt{4\ell_{CT}} \mu_{CT} (-2, -1, 1) \\ &= \frac{3\sqrt{2}}{18} \sqrt{\frac{1+m_{CT}}{2}} \mu_{CT} (-2, -1, 1), \end{aligned} \quad (11.73)$$

$$\begin{aligned} \vec{\mu}_{ge_3} &= \langle \Psi_g | \hat{\mu} | \Psi_{e_3} \rangle \\ &= \frac{1}{3} \mu_{CT} \sin \delta (-1, 1, -1) = \frac{1}{3} \sqrt{4\ell_{CT}} \mu_{CT} (-1, 1, -1) \\ &= \frac{1}{3} \sqrt{\frac{1+m_{CT}}{2}} \mu_{CT} (-1, 1, -1), \end{aligned} \quad (11.74)$$

$$\vec{\mu}_{e_1e_2} = \langle \Psi_{e_1} | \hat{\mu} | \Psi_{e_2} \rangle = \frac{1}{3} \mu_{CT} (0, 1, 1), \quad (11.75)$$

$$\vec{\mu}_{e_1e_3} = \langle \Psi_{e_1} | \hat{\mu} | \Psi_{e_3} \rangle = \frac{\sqrt{2}}{6} \mu_{CT} (0, 1, 1), \quad (11.76)$$

$$\vec{\mu}_{e_2e_3} = \langle \Psi_{e_2} | \hat{\mu} | \Psi_{e_3} \rangle = \frac{\sqrt{6}}{18} \mu_{CT} (2, 1, -1). \quad (11.77)$$

Both D and TP channels are possible. In fact,

$$\begin{aligned}
 \beta_{(xyz)}^{TP} &= \frac{1}{E_{ge}^2} \sum_{\mathcal{P}}^{xyz} [\mu_{ge_1}^x (\mu_{e_1}^y - \mu_g^y) \mu_{ge_1}^z + \mu_{ge_2}^x (\mu_{e_1}^y - \mu_g^y) \mu_{ge_2}^z + \mu_{ge_3}^x (\mu_{e_3}^y - \mu_g^y) \mu_{ge_3}^z] \\
 &= \frac{10\sqrt{3}}{27} \sin^2 \delta \frac{\mu_{CT}^3}{(4T + 2t \cot \delta)^2} \\
 &= \frac{40\sqrt{3} \ell_{CT}}{27} \frac{\mu_{CT}^3}{\left(4T + t \sqrt{\frac{1}{\ell_{CT}} - 4}\right)^2} \\
 &= (1 + m_{CT}) \frac{5\sqrt{3}}{27} \frac{\mu_{CT}^3}{\left(4T + 2t \sqrt{\frac{1-m_{CT}}{1+m_{CT}}}\right)^2}, \tag{11.78}
 \end{aligned}$$

and:

$$\begin{aligned}
 \beta_{(xyz)}^D &= \frac{2}{E_{ge}^2} \sum_{\mathcal{P}}^{xyz} [\mu_{ge_1}^x \mu_{e_1e_2}^y \mu_{ge_2}^z + \mu_{ge_1}^x \mu_{e_1e_3}^y \mu_{ge_3}^z + \mu_{ge_2}^x \mu_{e_2e_3}^y \mu_{ge_3}^z] \\
 &= \frac{8\sqrt{3}}{27} \sin^2 \delta \frac{\mu_{CT}^3}{(4T + 2t \cot \delta)^2} \\
 &= \frac{32\sqrt{3} \ell_{CT}}{27} \frac{\mu_{CT}^3}{\left(4T + t \sqrt{\frac{1}{\ell_{CT}} - 4}\right)^2} \\
 &= (1 + m_{CT}) \frac{4\sqrt{3}}{27} \frac{\mu_{CT}^3}{\left(4T + 2t \sqrt{\frac{1-m_{CT}}{1+m_{CT}}}\right)^2}, \tag{11.79}
 \end{aligned}$$

thus:

$$\beta_{(xyz)} = (1 + m_{CT}) \frac{\sqrt{3}}{3} \frac{\mu_{CT}^3}{\left(4T + 2t \left[\frac{1-m_{CT}}{1+m_{CT}}\right]^{1/2}\right)^2}, \tag{11.80}$$

which is in agreement with Cho *et al.*²⁴ This is reminiscent of $\beta_{(yyy)}$ in the 4-state model, which evolves like E_{ge}^{-2} (favored by large m_{CT} and small T). The evolution with T/t of the different quantities are pictured in Fig. C.9: the situation is similar to the one of Fig. C.6. Note that the transition dipole moments are not represented since there are too many of them, but the trends are similar to the ones presented in Fig. C.7.

Analysis of the components expressions

If the goal is to maximize the β_{HRS} , one should first understand the evolution of the different tensor components. In the following, it is described as the product of 4 terms:

$$\beta \propto \mu_{CT}^3 \times M(m_{CT}) \times E(m_{CT}, t, T) \times \Theta(\theta). \tag{11.81}$$

Following this decomposition, the components are summarized in Table 11.1, together with the main conclusion of the following discussion.

In more details, the key terms of this decomposition are the different $E(m_{CT}, t, T)$. They are plotted in Figure 11.1. E_{ge}^{-2} and E_{gf}^{-2} goes to zero when $m_{CT} \rightarrow -1$ and the second one does the same when $m_{CT} \rightarrow 1$. E_{ge}^{-2} presents a maximum at $m_{CT} = 1$, which amounts $E_{ge}^{-2} = (nT)^{-2}$, and E_{gf}^{-2} is maximal at $m_{CT} = 0$ for which $E_{gf}^{-2} = (4n)^{-1}t^{-2}$. The maximum of $E_{ge}^{-2} + 2E_{ge}^{-1}E_{gf}^{-1}$ is a little bit difficult to grasp, since the analytical position of it and its value is quite a complicated expression. To get some insight, we will first describe the evolution of $E_{ge}E_{gf}$,

$$E_{ge}E_{gf} = 2nt \left[T\sqrt{n}M_1(m_{CT}) + tM_2(m_{CT}) \right],$$

$$\text{with } M_1(m_{CT}) = \sqrt{\frac{1}{1-m_{CT}^2}} \text{ and } M_2(m_{CT}) = \sqrt{\frac{1}{(1+m_{CT})^2}}. \quad (11.82)$$

Given the form of M_1 , its minimum is located at $m_{CT} = 0$, while the one of M_2 is located at $m_{CT} = 1$, thus the minimum of the sum should be located between 0 and 1. A crude approximation is to expand the function as a Taylor series,

$$E_{ge}E_{gf} \approx 2nt \left[A - t m_{CT} + \frac{A+t}{2} m_{CT}^2 \right] + \mathcal{O}(m_{CT}^3), \text{ with } A = T\sqrt{n} + t, \quad (11.83)$$

so that the minimum is located at:

$$\arg \min_{m_{CT}} \{E_{ge}E_{gf}\} = \frac{t}{A+t} = \frac{t}{T\sqrt{n} + 2t},$$

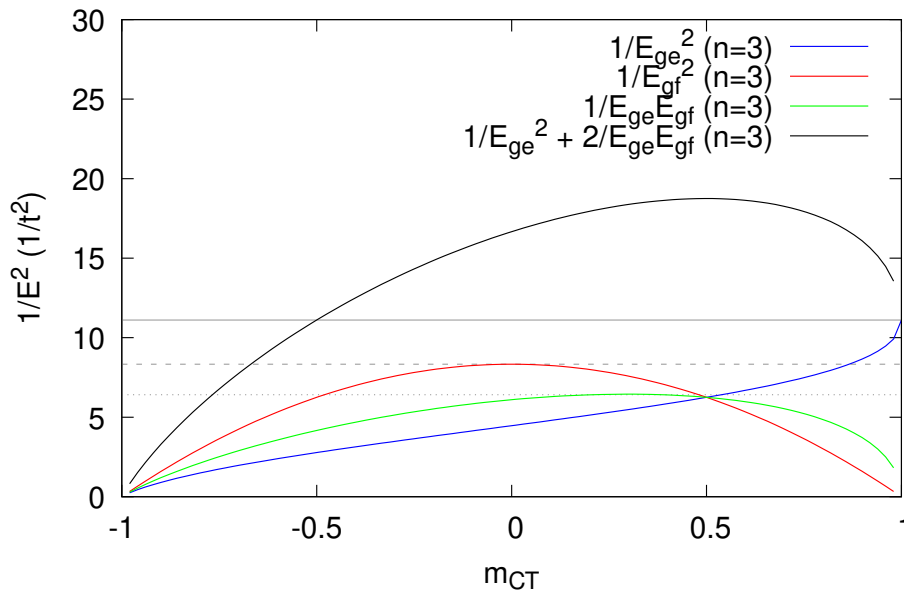


Figure 11.1: Evolution of the square of the inverse of the different excitation energies as a function of m_{CT} (with $n = 3$ and $t = T$). The plain gray line is $1/E^2 = (nT)^{-2}$, the dashed gray line is $1/E^2 = (4n)^{-1}t^{-2}$ and the dotted line is the approximated maximum of $E_{ge}^{-1}E_{gf}^{-1}$ given by Eq. (11.84).

$M(m_{CT})$	$E(m_{CT}, t, T)$	$\Theta(\theta)$	Extrema	Zeros
<hr/>				
2-state $C_{\infty v}$				
β_{zzz}^{2ST}	$-m_{CT}(1-m_{CT}^2) \frac{1}{E_{gf}^2}$	1	$m_{CT} \in [-\sqrt{5}/5, 0[\cup]0, \sqrt{5}/5]$, small t	$m_{CT} \in \{\pm 0, 1\}$, large t
<hr/>				
3-state $C_{2v} (\Theta \neq 90^\circ) \rightarrow D_{\infty h} (\Theta = 90^\circ)$				
β_{zzz}^{3ST}	$-m_{CT}(1-m_{CT}^2) \frac{1}{E_{gf}^2}$	$\cos^3 \theta$	$\theta = 0^\circ \wedge m_{CT} \in [-\sqrt{5}/5, 0[\cup]0, \sqrt{5}/5]$, small t	$\theta = 90^\circ \vee m_{CT} \in \{\pm 0, 1\}$, large t
$\beta_{(zxx)}^{3ST}$	$(1-m_{CT}^2) \frac{1}{E_{ge}^2} + \frac{2}{E_{ge}E_{gf}}$	$\sin^2 \theta \cos \theta$	$\theta \sim 60^\circ \wedge m_{CT} \in [0, 1[$, small t and $T < t$	$\theta = 0^\circ \vee m_{CT} = \pm 1$, large t or $T > t$
<hr/>				
4-state $C_{3v} (\Theta \neq 90^\circ) \rightarrow D_{3h} (\Theta = 90^\circ)$				
β_{zzz}^{4ST}	$-m_{CT}(1-m_{CT}^2) \frac{1}{E_{gf}^2}$	$\cos^3 \theta$	$\theta = 0^\circ \wedge m_{CT} \in [-\sqrt{5}/5, 0[\cup]0, \sqrt{5}/5]$, small t	$\theta = 90^\circ \vee m_{CT} \in \{\pm 0, 1\}$, large t
$\beta_{(zyy)}^{3ST}$	$(1-m_{CT}^2) \frac{1}{E_{ge}^2} + \frac{2}{E_{ge}E_{gf}}$	$\sin^2 \theta \cos \theta$	$\theta \sim 60^\circ \wedge m_{CT} > 0$, small t and $T < t$	$\theta = 0^\circ \vee m_{CT} = \pm 1$, large t or $T > t$
β_{yyy}^{4ST}	$(1+m_{CT}) \frac{1}{E_{ge}^2}$	$\sin^3 \theta$	$\theta = 90^\circ \wedge m_{CT} = 1$, small t and $T < t$	$\theta = 0^\circ \vee m_{CT} = -1$, large t or $T > t$
<hr/>				
5-states T_d				
β_{xyz}^{5ST}	$(1+m_{CT}) \frac{1}{E_{ge}^2}$	1	$m_{CT} = 1$, small t and $T < t$	$m_{CT} = -1$, large t or $T > t$

Table 11.1.1: Decomposition of the components of a C_{2v} , C_{3v} and T_d system, and approximate location of the remarkable points.

$$\text{and } \min\{E_{ge}E_{gf}\} \approx 2nt \left[A - \frac{t^2}{2A + 2t} \right] = 2nt \left[T\sqrt{n} + t - \frac{t^2}{2T\sqrt{n} + 4t} \right]. \quad (11.84)$$

Note that this maximum is, due to the positive value of t and T , always in $m_{CT} \in [0; 1]$. Furthermore, given $T = \zeta t$,

$$\arg \min_{m_{CT}} \{E_{ge}E_{gf}\} = \frac{1}{\zeta \sqrt{n} + 2}, \quad (11.85)$$

it seems that the (approximate) minimum is actually located in $m_{CT} \in [0; 1/2]$. This approximate minimum is the (approximate) position of the maximum of $E_{ge}^{-1}E_{gf}^{-1}$.

The evolution of the more complex $E_{ge}^{-2} + 2E_{ge}^{-1}E_{gf}^{-1}$ (black curve in Figure 11.2) follows the one of $E_{ge}^{-1}E_{gf}^{-1}$, but its maximum is shifted toward more positive m_{CT} due to the E_{ge}^{-2} contribution. To further comment on the evolution of $E(m_{CT}, t, T)$ with t and T , they are plotted in Figure 11.2. E_{gf}^{-2} is not plotted, since it does not depend on T . This is in agreement with the previous analysis: both E_{ge}^{-2} and $E_{ge}^{-2} + 2E_{ge}^{-1}E_{gf}^{-1}$ are large when $T < t$, and the latter is comparable to the graph of $E_{ge}^{-1}E_{gf}^{-1}$. The last graph in Figure 11.2 therefore shows that the maximum of $E_{ge}^{-1}E_{gf}^{-1}$ moves toward smaller m_{CT} when T increases, which indicates how the one $E_{ge}^{-2} + 2E_{ge}^{-1}E_{gf}^{-1}$ evolves. The synopsis of this previous discussion is given in Table 11.2, in the form of the different remarkable points. The $M(m_{CT})$ part (plotted in Figure C.10) is also detailed in the same table, since its evolution with m_{CT} is straightforward due to the simplicity of the expressions and thus requires no special comment.

An additional difficulty for the 3- and 4-state systems is the $\Theta(\theta)$ part (plotted in Figure C.11). The most complex function, $\sin^2 \theta \cos \theta$, found in the $\beta_{(zxx)}$ of 3-state and in $\beta_{(zyy)}$ of 4-state, presents a maximum for an angle of $\theta = \tan^{-1}(\sqrt{2}) = 54.72^\circ \sim 60^\circ$, while minimal at $\theta \in \{0, 90\}^\circ$.

To conclude this discussion, the approximate location for the extrema of the different components are reported in Table 11.1. It leads to favor positive m_{CT} , with small t and smaller T .

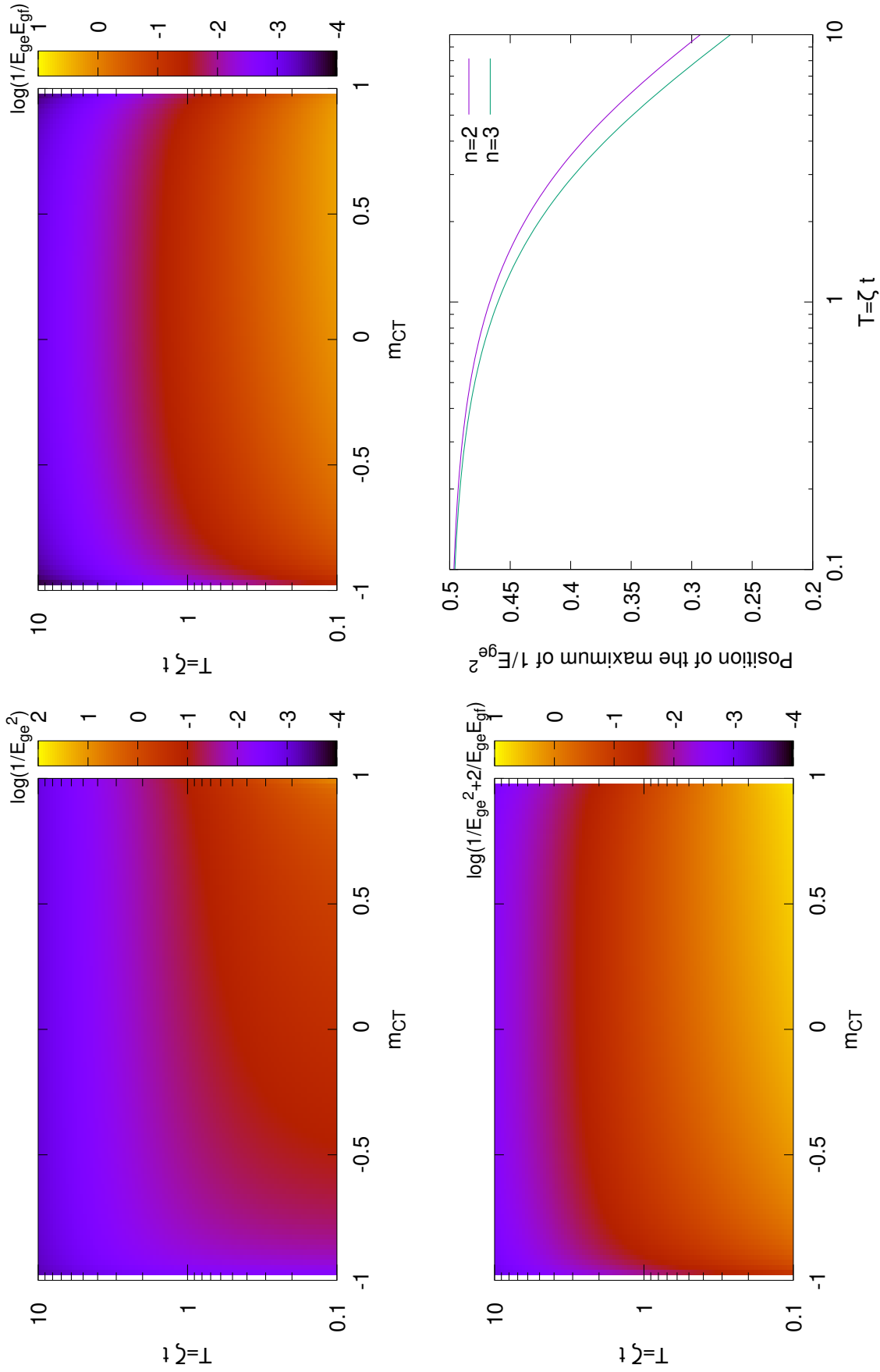


Figure 11.2: Evolution of $\log(E_{ge}^{-2})$ (top left), $\log(E_{ge}^{-1}E_{gf}^{-1})$ (top right) and $\log(E_{ge}^{-2} + 2E_{ge}^{-1}E_{gf}^{-1})$ (bottom left) as a function of m_{CT} and T (defined as a multiple of t , $T = \zeta t$, and with $n = 3$), and evolution of the position of the maximum of $E_{ge}^{-1}E_{gf}^{-1}$ with $T = \zeta t$ (bottom right), as given by Eq. (11.85).

Function	Found in	Extrema	Zeros
$M(m_{CT}) = -m_{CT}(1 - m_{CT}^2)$	$\beta_{2ST}, \beta_{3ST}, \beta_{4ST}$ $\beta_{zzz}, \beta_{zzz}, \beta_{zzz}$	$m_{CT} = \pm \frac{\sqrt{5}}{5}$	$m_{CT} \in \{\pm 1, 0\}$
$M(m_{CT}) = 1 - m_{CT}^2$	β_{3ST}, β_{4ST} $\beta_{(zzx)}, \beta_{(zyy)}$	$m_{CT} = 0$	$m_{CT} = \pm 1$
$M(m_{CT}) = 1 + m_{CT}$	β_{4ST}, β_{5ST} β_{yyz}, β_{xyz}	$m_{CT} = 1$	$m_{CT} = -1$
$E(m_{CT}, t, T) = E_{ge}^{-2}$	$\beta_{3ST}, \beta_{4ST}, \beta_{4ST}$ $\beta_{(zzx)}, \beta_{(zyy)}, \beta_{yyz}, \beta_{xyz}$	$m_{CT} = 1$, small t and $T < t$	$m_{CT} = -1$, large t or $T > t$
$E(m_{CT}, t, T) = E_{gf}^{-2}$	$\beta_{2ST}, \beta_{3ST}, \beta_{4ST}$ $\beta_{zzz}, \beta_{zzz}, \beta_{zzz}$	$m_{CT} = 0$, small t	$m_{CT} = \pm 1$, large t
$E(m_{CT}, t, T) = E_{ge}^{-1} E_{gf}^{-1}$	β_{3ST}, β_{4ST} $\beta_{(zzx)}, \beta_{(zyy)}$	$m_{CT} \in [0, 1/2]$, small t and $T < t$	$m_{CT} = \pm 1$, large t or $T > t$
$E(m_{CT}, t, T) = E_{ge}^{-2} + 2 E_{ge}^{-1} E_{gf}^{-1}$	β_{3ST}, β_{4ST} $\beta_{(zzx)}, \beta_{(zyy)}$	$m_{CT} > 0$, small t and $T < t$	$m_{CT} = \pm 1$, large t or $T > t$

Table 11.2: Location of remarkable points of $M(m_{CT})$ and $E(m_{CT}, t, T)$.

Comparison of the HRS quantities for the 4 systems

For the 2-state system, the classical expression of β_{HRS} is obtained from Eq. (11.24),

$$\beta_{HRS} = \sqrt{\frac{6}{35}} |\beta_{zzz}|. \quad (11.86)$$

Thus, a m_{CT} close (but not equal) to zero is ideal. For the C_{2v} system, the two invariants given in Eqs. (11.22) and (11.23) reduce to:

$$\langle \beta_{ZZZ}^2 \rangle = \frac{1}{7} \beta_{zzz}^2 + \frac{9}{35} \beta_{zxx}^2 + \frac{6}{35} \beta_{zzz} \beta_{zxx}, \quad (11.87)$$

$$\langle \beta_{ZXX}^2 \rangle = \frac{1}{35} \beta_{zzz}^2 + \frac{11}{105} \beta_{zxx}^2 - \frac{2}{105} \beta_{zzz} \beta_{zxx}, \quad (11.88)$$

which shows that in order to achieve large β_{HRS} , it would be interesting to favor $\beta_{(zxx)}$ over β_{zzz} (to some extent), since the coefficient in front of β_{zxx}^2 is smaller than the one in front of β_{zzz}^2 . This leads to prefer systems with positive m_{CT} , and θ values close to 60° . An illustration is given in Figure 11.3. This figure also shows the evolution of the DR, which can be separated between three areas : i) for the large θ values, the DR is dominated by $\beta_{(zxx)}$, so $DR \rightarrow \frac{27}{11} \approx 2.45$, and ii) in the low θ area, starting at $DR=5$ for small θ (dominated by β_{zzz}), the DR increases (gets dipolar) when $m_{CT} < 0$ and lowers (gets, and remains, octupolar) when $m_{CT} > 0$.

Similarly, for the C_{3v} system,

$$\langle \beta_{ZZZ}^2 \rangle = \frac{1}{7} \beta_{zzz}^2 + \frac{8}{35} \beta_{yyy}^2 + \frac{24}{35} \beta_{zyy}^2 + \frac{12}{35} \beta_{zzz} \beta_{zyy}, \quad (11.89)$$

$$\langle \beta_{ZXX}^2 \rangle = \frac{1}{35} \beta_{zzz}^2 + \frac{16}{105} \beta_{yyy}^2 + \frac{4}{21} \beta_{zyy}^2 - \frac{4}{105} \beta_{zzz} \beta_{zxx}, \quad (11.90)$$

the same analysis leads to favoring $\beta_{(zyy)}$ (and β_{yyy}) over β_{zzz} , which would lead to the same conclusion as for the C_{2v} system. Actually, as shown in Figure 11.4, the θ -dependence dominates: the D_{3h} structure (with m_{CT} close to 1 to get large β_{yyy}) is actually preferable. Concerning the DR, it can, again, be separated between three area : 1) for the large θ values, DR is dominated by $\beta_{(zyy)}$, so $DR \rightarrow \frac{3}{2}$, and 2) in the low θ areas, starting at $DR=5$ for small θ (dominated by β_{zzz}), the DR increases (gets dipolar) when $m_{CT} < 0$ and lowers (gets octupolar) when $m_{CT} > 0$. Compared to the C_{2v} system, there is more contrast in the map of the DR .

Then, for the T_d system,

$$\beta_{HRS} = \sqrt{\frac{4}{7}} |\beta_{(xyz)}|, \quad (11.91)$$

of which form is comparable to the expression to the 2-state system (it depends on one component), but is favored by m_{CT} close to 1.

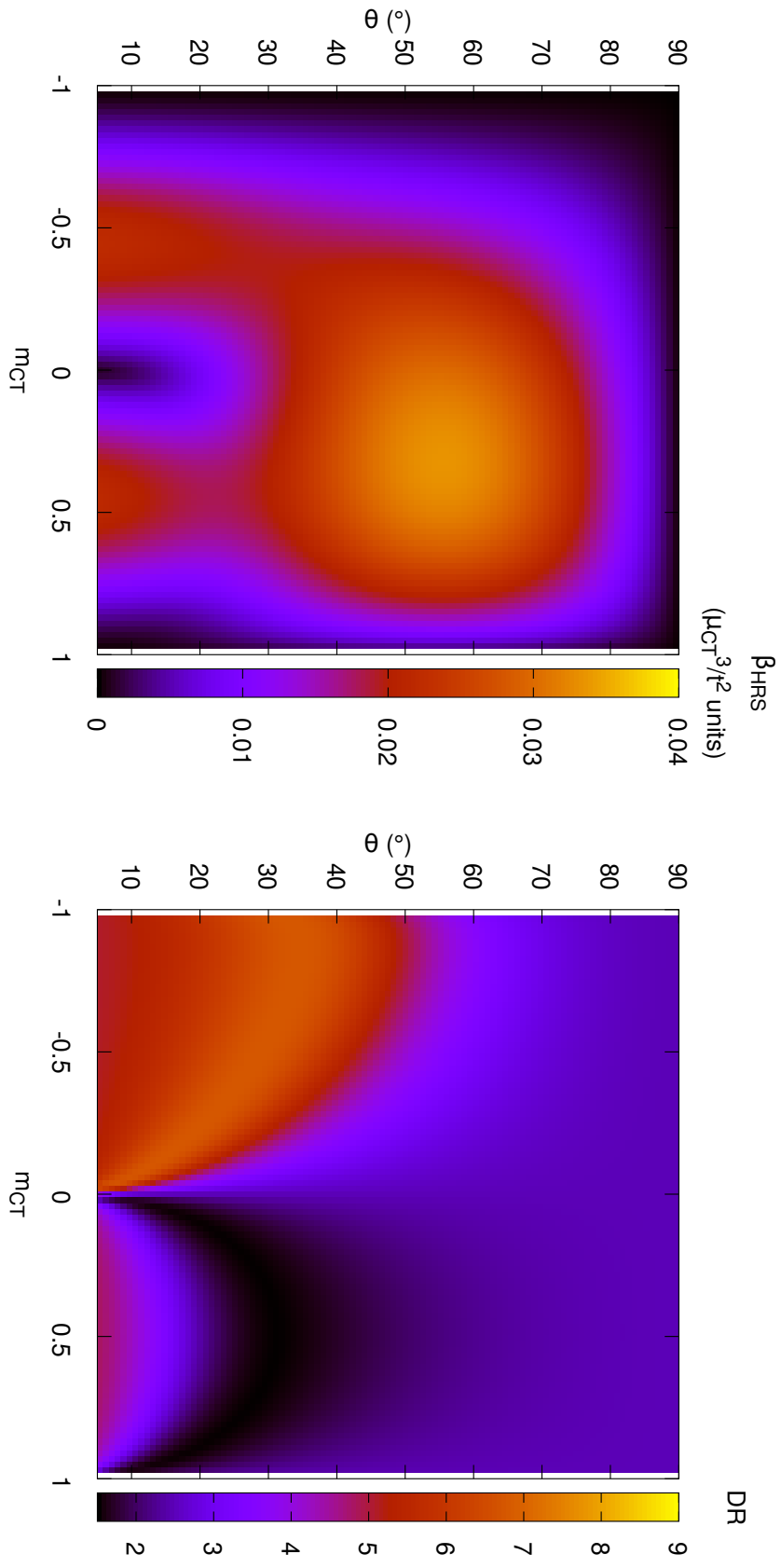


Figure 11.3: Evolution of β_{HRS} (left) and DR (right) as a function of m_{CT} and θ for a C_{2v} 3-state system (with $T = t$).

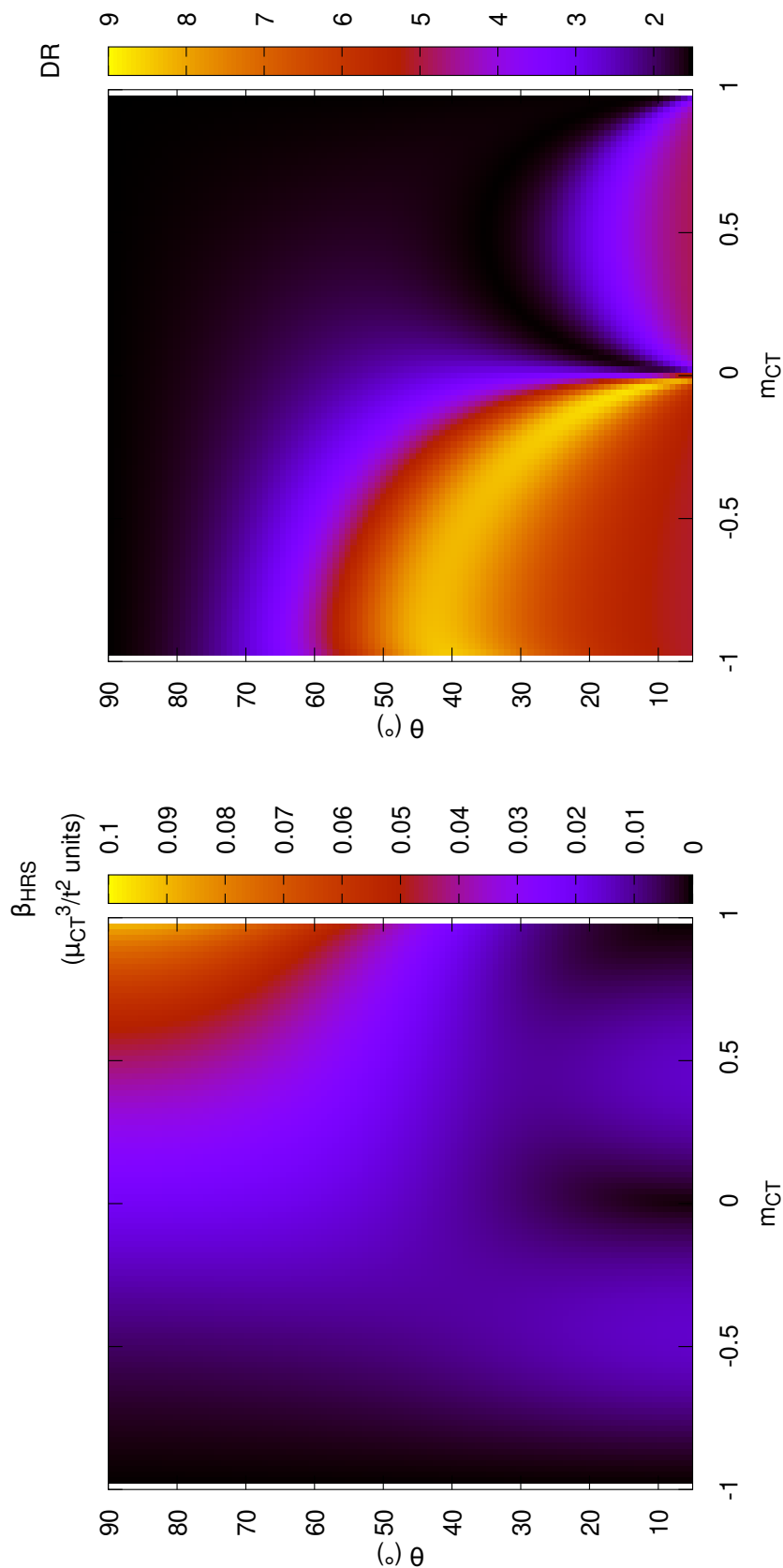


Figure 11.4: Evolution of β_{HRS} (left) and DR (right) as a function of m_{CT} and θ for a C_{3v} 4-state system (with $T = t$).

Finally, to comment on the influence of t and T and on the general performance of all models, a comparison of the β_{HRS} responses of representative 2-, 3- 4- and 5-state systems are given in Figure 11.5. It confirms, as expected from the analysis of $E(m_{CT}, t, T)$, that $T < t$ (exemplified by $T = t/2$) gives the largest β_{HRS} , and that small T are necessary to be competitive against the one-dimensional system (which does not depend on T). Furthermore, the VB- n CT models with $n > 1$ get interesting in the $m_{CT} > 0$ area, especially the D_{3h} and T_d systems near $m_{CT} = 1$. Using the 5-state model as a baseline, the ratios between the β_{HRS} of the latter and the other architecture are given in 11.6. It evidences that the T_d compounds, for all values of T , are never competitive against the D_{3h} one, which remains the most interesting near $m_{CT} = 1$. For lower mixing character ($m_{CT} \sim 0.5$ or below), either the one-dimensional, pyramidal (C_{3v}), or V-shaped (C_{2v}) molecules leads to good β_{HRS} , the two lasts of interest if $T < t$.

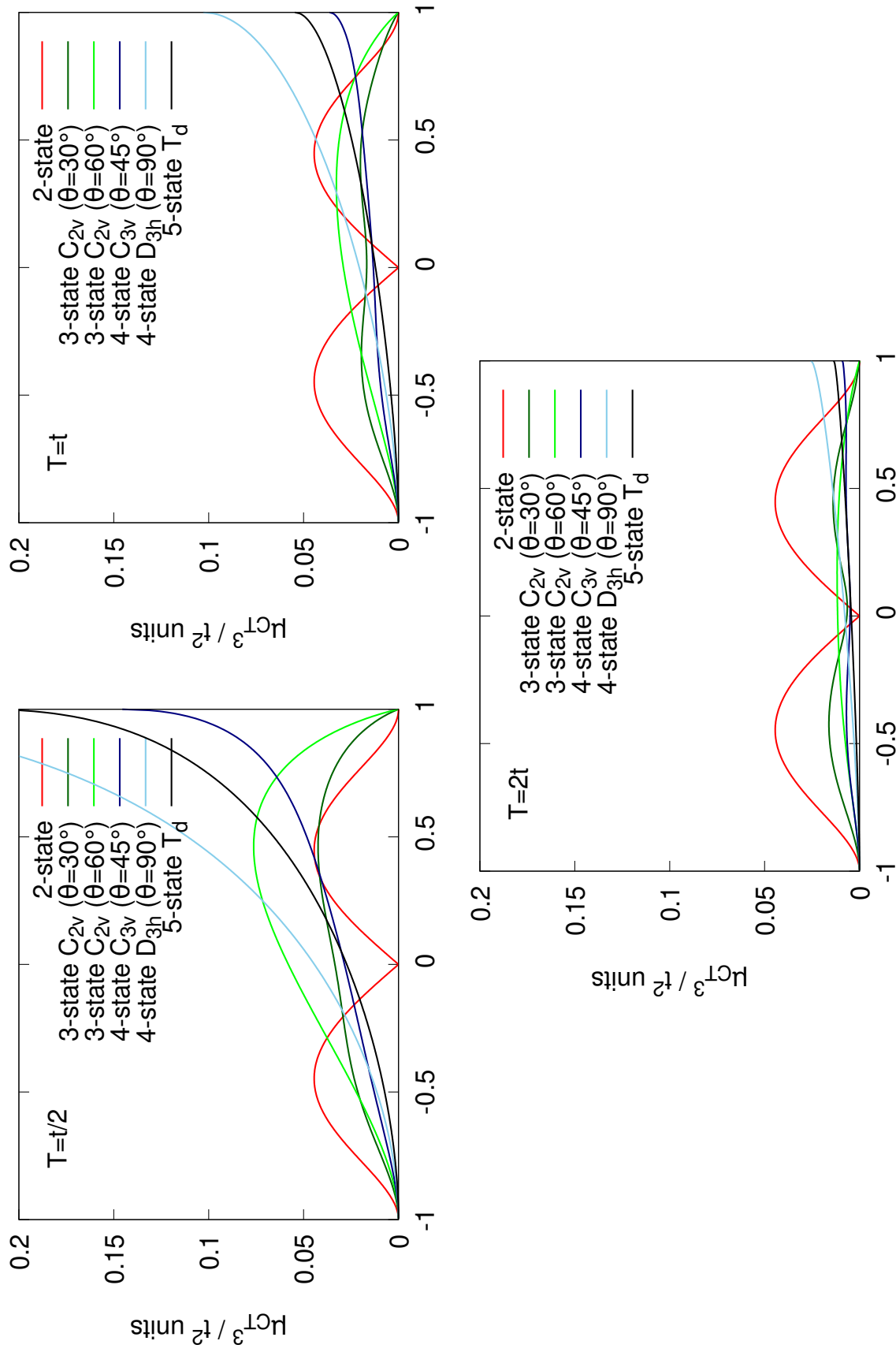
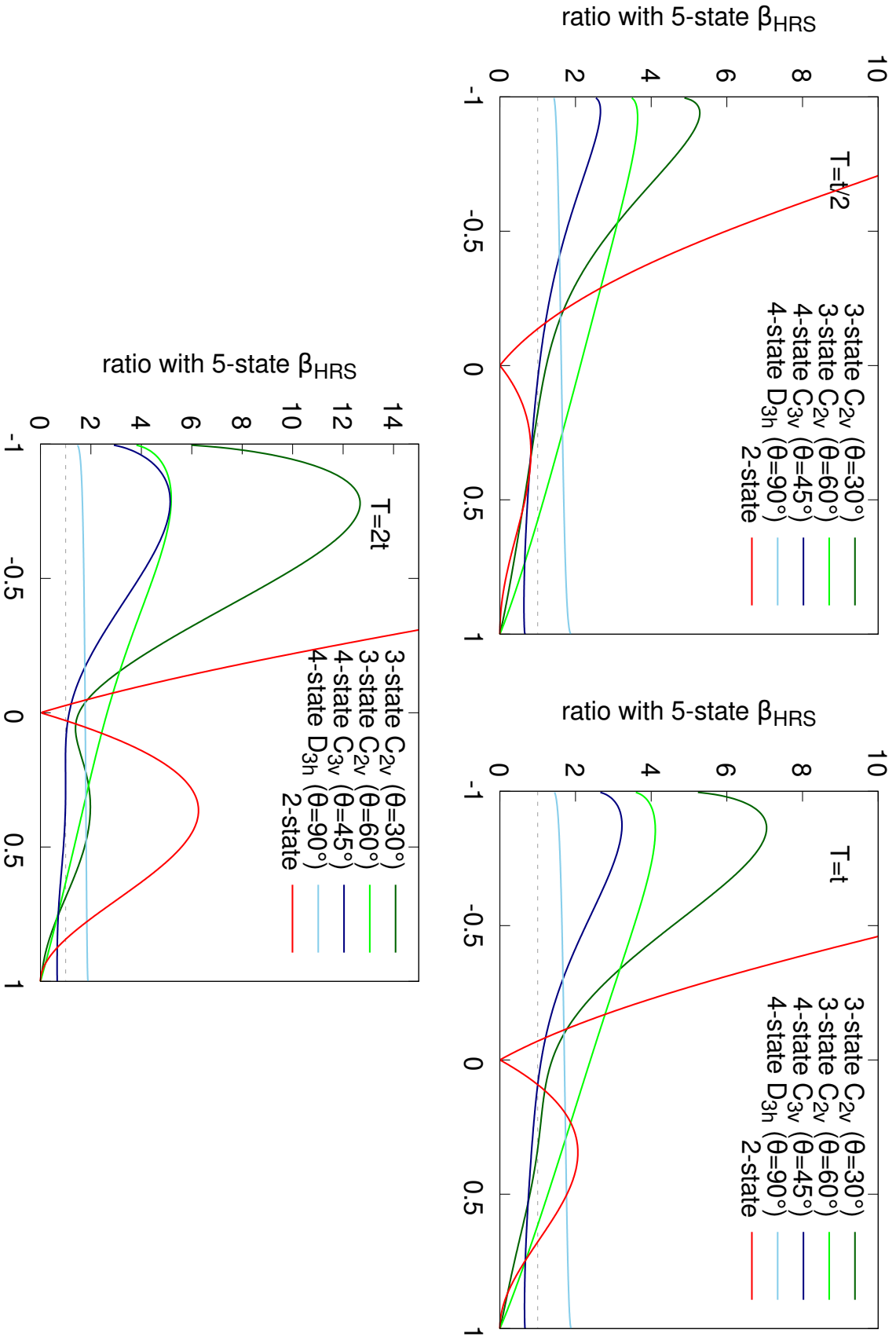


Figure 11.5: Evolution of β_{HRS} of VB- n CT (with $n = 1, 2, 3$, and 4) with m_{CT} [with $T = t/2$ (left), $T = t$ (right) and $T = 2t$ (bottom)].



Section 11.4

Conclusions and outlooks

In this paper, a comparative analysis of the VB- n CT models (with $n \in [1, 4]$) was performed in the context of the Hyper-Rayleigh Scattering (HRS) technique. The expression of the different components have been derived for 3 different parameterizations: $\delta \in [0, \pi/2]$, $\ell_{CT} \in [0, 1/n]$ and $m_{CT} \in [-1, 1]$, which all measure the CT character of the ground state: the lowest value of these parameters indicates that the ground state is dominated by the VB form, while the largest indicates the opposite situation, with the so-called *cyanine* limit at $\delta = \pi/4$ (or $m_{CT} = 0$). Together with t , T (transfer matrix elements), μ_{CT} (dipole moment of the CT states), and eventually θ (the angle between the CT dipoles), those 4 to 5 parameters are sufficient to describe a wide range of possible architectures belonging to the point groups $C_{\infty v}$ (2-state), T_d (5-state), D_{3h} , C_{3v} (4-state) or C_{2v} (3-state).

The performance of those respective architectures has been rationalized by looking at the expression of the different components, especially in terms of electronic excitation energies, followed by a comparison of their corresponding β_{HRS} . The main observations are: i) small t values are required to achieve large β , ii) to be competitive against the one-dimensional ($C_{\infty v}$) architectures, the others require $T < t$ and a large CT character (above the cyanine limit, $m_{CT} > 0$), iii) the octupolar D_{3h} architecture is the most interesting of all, if the CT character is very large ($m_{CT} \sim 1$), and iv) for intermediate CT character (e.g., $m_{CT} \sim 0.5$) the V-shaped (C_{2v}) and pyramidal (C_{3v}) architectures are interesting. This confirms the interest for more complex architectures than the classical one-dimensional dipolar NLO molecules, if one is able to control and increase the CT character of the compounds as well as decrease the value of the T integral.

Bibliography

- [1] Franken, P. A.; Hill, A. E.; Peters, C. W.; Weinreich, G. Generation of Optical Harmonics. *Phys. Rev. Lett.* **1961**, 7, 118–119.
- [2] Konotop, V. V.; Kuzmiak, V. Nonreciprocal Frequency Doubler of Electromagnetic Waves Based on a Photonic Crystal. *Phys. Rev. B* **2002**, 66, 235208.
- [3] Moreaux, L.; Sandre, O.; Blanchard-Desce, M.; Mertz, J. Membrane Imaging by Simultaneous Second-Harmonic Generation and Two-Photon Microscopy. *Opt. Lett.* **2000**, 25, 320–322.
- [4] Tran, R. J.; Sly, K. L.; Conboy, J. C. Applications of Surface Second Harmonic Generation in Biological Sensing. *Annu. Rev. Anal. Chem.* **2017**, 10, 387–414.
- [5] Campagnola, P. J.; Wei, M.-d.; Lewis, A.; Loew, L. M. High-Resolution Nonlinear Optical Imaging of Live Cells by Second Harmonic Generation. *Biophys. J.* **1999**, 77, 3341–3349.
- [6] Reeve, J. E.; Anderson, H. L.; Clays, K. Dyes for Biological Second Harmonic Generation Imaging. *Phys. Chem. Chem. Phys.* **2010**, 12, 13484–13498.
- [7] Papadopoulos, M. G., Sadlej, A. J., Leszczynski, J., Eds. *Non-Linear Optical Properties of Matter: From Molecules to Condensed Phases*; Challenges and Advances in Computational Chemistry and Physics 1; Springer: Dordrecht, 2006.
- [8] Kanis, D. R.; Ratner, M. A.; Marks, T. J. Design and Construction of Molecular Assemblies with Large Second-Order Optical Nonlinearities. Quantum Chemical Aspects. *Chem. Rev.* **1994**, 94, 195–242.
- [9] Bouas-Laurent, H.; Dürr, H. *Photochromism*; Elsevier, 2003; pp XXVII–LIII.
- [10] Castet, F.; Rodriguez, V.; Pozzo, J.-L.; Ducasse, L.; Plaquet, A.; Champagne, B. Design and Characterization of Molecular Nonlinear Optical Switches. *Acc. Chem. Res.* **2013**, 46, 2656–2665.
- [11] Beaujean, P.; Bondu, F.; Plaquet, A.; Garcia-Amorós, J.; Cusido, J.; Raymo, F. M.; Castet, F.; Rodriguez, V.; Champagne, B. Oxazines: A New Class of Second-Order Nonlinear Optical Switches. *J. Am. Chem. Soc.* **2016**, 138, 5052–5062.
- [12] Quertinmont, J.; Beaujean, P.; Stiennon, J.; Aidibi, Y.; Leriche, P.; Rodriguez, V.; Sanguinet, L.; Champagne, B. Combining Benzazolo-Oxazolidine Twins toward Multi-State Nonlinear Optical Switches. *J. Phys. Chem. B* **2021**, 125, 3918–3931.
- [13] Mulliken, R. S. Molecular Compounds and Their Spectra. II. *J. Am. Chem. Soc.* **1952**, 74, 811–824.
- [14] Bender, C. J. Theoretical Models of Charge-Transfer Complexes. *Chem. Soc. Rev.* **1986**,

15, 475.

- [15] Lu, D.; Chen, G.; Perry, J. W.; Goddard, W. A. Valence-Bond Charge-Transfer Model for Nonlinear Optical Properties of Charge-Transfer Organic Molecules. *J. Am. Chem. Soc.* **1994**, *116*, 10679–10685.
- [16] Meyers, F.; Marder, S. R.; Pierce, B. M.; Bredas, J. L. Electric Field Modulated Nonlinear Optical Properties of Donor-Acceptor Polyenes: Sum-Over-States Investigation of the Relationship between Molecular Polarizabilities (α , β and γ) and Bond Length Alternation. *J. Am. Chem. Soc.* **1994**, *116*, 10703–10714.
- [17] Barzoukas, M.; Fort, A.; Blanchard-Desce, M. A Two-Form Description of Push-Pull Molecules: Correlations Between Structure, Intramolecular Charge Transfer and (Hyper) Polarizabilities. *J. Nonlinear Opt. Phys. Mater.* **1996**, *05*, 757–765.
- [18] Barzoukas, M.; Runser, C.; Fort, A.; Blanchard-Desce, M. A Two-State Description of (Hyper) Polarizabilities of Push-Pull Molecules Based on a Two-Form Model. *Chem. Phys. Lett.* **1996**, *257*, 531–537.
- [19] Blanchard-Desce, M.; Barzoukas, M. Two-Form Two-State Analysis of Polarizabilities of Push Pull Molecules. *J. Opt. Soc. Am. B* **1998**, *15*, 302.
- [20] Hahn, S.; Kim, D.; Cho, M. Nonlinear Optical Properties of the Linear Quadrupolar Molecule: Structure-Function Relationship Based on a Three-State Model. *J. Phys. Chem. B* **1999**, *103*, 8221–8229.
- [21] Barzoukas, M.; Blanchard-Desce, M. Molecular Engineering of Push– Pull Dipolar and Quadrupolar Molecules for Two-Photon Absorption: A Multivalence-Bond States Approach. *J. Chem. Phys.* **2000**, *113*, 3951–3959.
- [22] Yang, M.; Champagne, B. Large Off-Diagonal Contribution to the Second-Order Optical Nonlinearities of Λ -Shaped Molecules. *J. Phys. Chem. A* **2003**, *107*, 3942–3951.
- [23] Cho, M.; Kim, H.-S.; Jeon, S.-J. An Elementary Description of Nonlinear Optical Properties of Octupolar Molecules: Four-State Model for Guanidinium-Type Molecules. *J. Chem. Phys.* **1998**, *108*, 7114–7120.
- [24] Cho, M.; An, S.-Y.; Lee, H.; Ledoux, I.; Zyss, J. Nonlinear Optical Properties of Tetrahedral Donor– Acceptor Octupolar Molecules: Effective Five-State Model Approach. *J. Chem. Phys.* **2002**, *116*, 9165–9173.
- [25] Clays, K.; Persoons, A. Hyper-Rayleigh Scattering in Solution. *Phys. Rev. Lett.* **1991**, *66*, 2980–2983.
- [26] Hendrickx, E.; Clays, K.; Persoons, A. Hyper-Rayleigh Scattering in Isotropic Solution. *Acc. Chem. Res.* **1998**, *31*, 675–683.
- [27] Verbiest, T.; Clays, K.; Rodriguez, V. *Second-Order Nonlinear Optical Characterization Techniques: An Introduction*; Taylor & Francis, 2009.

- [28] Shelton, D. P. Gas Phase Hyper-Rayleigh Scattering Measurements. *J. Chem. Phys.* **2012**, *137*, 044312.
- [29] Orr, B.; Ward, J. Perturbation Theory of the Non-Linear Optical Polarization of an Isolated System. *Mol. Phys.* **1971**, *20*, 513–526.
- [30] Beaujean, P.; Champagne, B. Coupled Cluster Evaluation of the Second and Third Harmonic Scattering Responses of Small Molecules. *Theor. Chem. Acc.* **2018**, *137*.
- [31] Andrews, D. L. Harmonic Generation in Free Molecules. *J. Phys. B* **1980**, *13*, 4091.
- [32] Verbiest, T.; Clays, K.; Rodriguez, V. *Second-Order Nonlinear Optical Characterization Techniques: An Introduction*; Taylor & Francis, 2009.
- [33] Castet, F.; Bogdan, E.; Plaquet, A.; Ducasse, L.; Champagne, B.; Rodriguez, V. Reference Molecules for Nonlinear Optics: A Joint Experimental and Theoretical Investigation. *J. Chem. Phys.* **2012**, *136*, 024506.

Part IV

Conclusions and perspectives

Chapter Twelve

Summary, conclusions and outlook

Abstract

The last chapter summarizes this thesis, highlights the main conclusions and achievements, and emphasizes on their respective importance in the goals presented in introduction. Finally, different perspectives are drawn for future research on the presented topics.

In this PhD thesis, different quantum chemistry (QC) methods have been implemented, tested and applied to the description and understanding of the NLO properties of molecules, to provide insight and to help towards their design. As demonstrated through the different chapters, this work was anchored into a multidisciplinary framework between theory and experiment, which helped each other to improve, one challenging the other at different occasions.

The results have been divided in two parts. The first (Chapters 4-6) has been devoted to provide a better understanding of the NLO responses of reference molecules in gas phase. To do so, a hierarchy of Coupled Cluster (CC) methods has been used to accurately describe the NLO response (first and second hyperpolarizabilities), with the quadratic (QRF) and cubic (CRF) response functions approaches and doubly-augmented correlation consistent basis sets. Substantial electron correlation effects have been evidenced, which has led to the choice of the CCSD/d-aug-cc-pVDZ level of approximation in all three studies, providing a good agreement with higher-level results in feasible cpu time. Chapter 4 paved the way by focusing on the agreement between the experimental and theoretical gas phase EFISHG first ($\beta_{||}$) and second ($\gamma_{||}$) hyperpolarizabilities results for water, methanol and dimethylether (DME). A good similarity (within the errors bars) is found and, in the case of DME, the experimental frequency dispersion is also well reproduced for both $\beta_{||}$ and $\gamma_{||}$. The variation in the dispersion factors for other NLO processes and all three compounds has also been explained, through the variation of their first excitation energy. Then, Chapter 5 concentrates on the second (SHS) and third (THS) harmonic scattering hyperpolarizabilities and their decomposition into spherical components. It considered other small molecules, generally used as external references: water, $\text{CH}_x\text{Cl}_{4-x}$ ($x \in [0, 3]$), and acetonitrile. The investigation revealed that for β_{SHS} , the dipolar contribution ($\beta_{J=1}$) increases from carbon tetrachloride to dichloromethane, chloroform, chloromethane and acetonitrile. On the other hand, the γ_{THS} response is dominated by its isotropic contribution ($\gamma_{J=0}$), which was further confirmed by comparison with liquid phase experimental results. The latter also suggested that the solvation effects are smaller for γ_{THS} than for β_{SHS} . Given the good agreement with experimental results, the impact of vibrational contributions on the NLO properties has been questioned. In Chapter 6, it was addressed for the water molecule, as a model system, using the perturbative theory of Bishop and Kirtman. A finite-field differentiation technique (in combination with the Romberg scheme) was implemented in a homemade code (nachos) in order to unravel the vibrational contribution to the average polarizability ($\bar{\alpha}$) as well as β_{SHS} and γ_{THS} and their corresponding depolarization ratio (DR). The results have highlighted that the vibrational contribution to the dynamic NLO properties are small but non-negligible (10 % or less), while much larger in the static limit. Insights on the roots of the different vibrational contributions (e.g., the stretching vibrational mode) have also been provided. Overall, this first part gave a better understanding of the NLO response of small molecules in order to provide accurate responses, which can be used as ref-

erence in experimental measurements. It pinpoints the importance of electron correlation and large basis sets to do so. Furthermore, and following two publications on their measurement, these were the first quantum chemistry investigations (to our knowledge) on i) γ_{THS} and its DR, ii) its decomposition in spherical tensor components, and iii) its vibrational contributions.

The second part (Chapters 11-10) is dedicated to the study of new NLO compounds and systems of increasing complexity. Due to the size of these systems, density functional theory (DFT) and smaller basis sets (*e.g.*, 6-311+G*) have been used for the calculations, while MP2 was the reference for the selection of the exchange-correlation (XC) functional.

Chapters 7 to 9 concentrate on molecular NLO switches, with a focus on the characterization of each state and the β contrast between them. On the one hand, in Chapter 7, an octupolar (type I) NLO switch, suggested by our collaborators, has been studied: it contains 6 Ruthenium centers triggered by redox. In order to further understand the NLO responses, its structure has been decomposed into its different fragments with the help of two tools (thanks to their symmetry): i) the few-states theory (which also importantly suggests design strategies), and ii) a radial charge difference to track the change of electron density upon excitations. Notwithstanding some computational difficulties intrinsic to those compounds (spin contamination and multireference character), the results are that the key to good contrasts is a combination of a low energy metal to ligand CT (MLCT) excited state for the reduced form and a reduction of π -conjugation upon oxidation (through a weakening of back bonding). To improve such octupolar compounds, a good equilibrium is required between the strength of the donor/acceptor and the length of the π -conjugated path.

On the other hand, multi-state and multi-addressable (type III) switches built from benzazoolooxaolidine (BOX) units have been investigated in the two following chapters. In these, BOX, itself, a two-state NLO switch (closed and open forms), is assembled with different π -conjugated linkers into diBOX (Chapter 8, 3 possible forms) and triBOX (Chapter 9, up to 8 possible forms). Despite their apparent chemical equivalence, the sequential and controllable opening of such systems has been experimentally observed for diBOX (with the addition of acid or oxidant) and further rationalized for both di- and triBOX by calculations. Then, the impact of the successive openings and of the linker on the linear and nonlinear optical properties have been unraveled. Concerning the latter, while the diBOXs feature three distinguishable β_{HRS} upon opening, the states of the triBOXs are better differentiated through their DR. One of the salient feature of this work, on the calculation side, is the sampling of the (main torsional angles) conformational space to better describe these compounds and to allow accessing experimental trends.

Then, Chapter 10 has focused on the β response of fluorescent proteins, which are biotags of choice for second-harmonic imaging microscopy. While their large size normally prevents full quantum chemistry calculation, a new (all-atom) methodology was enacted and optimized. It relies on the tight-binding GFN2-xTB method for the geometry optimization and

a simplified time-dependent DFT approach to get the corresponding β_{HRS} . Moreover, a new dual-threshold configuration selection approach has been introduced to further reduce the computational time. For the proof of concept, this methodology was tested on two proteins: iLOV and the bacteriorhodopsin. For the latter a good agreement with (low energy) experimental frequency dispersion of β_{HRS} has been achieved.

Finally, Chapter 11 reviews the VB-CT (valence bond-charge transfer) model that was successfully applied by others to β in order to unravel simple structure-activity relationships and design rules. Furthermore, this framework has been shown to be versatile enough to be extended to multiple donor/acceptor groups (of the same nature), leading to 3-, 4- and 5-state models. They provided a better understanding of the impact of molecular geometry and symmetry on the second-order NLO response. This last part substantiated the interest for more complex architectures (V-shaped, pyramidal, or octupolar molecules), already developed in Chapter 7, especially if the charge transfer character is large.

Altogether, this second part demonstrated the interplay between theory and experiment in a multidisciplinary framework, especially for the BOXs which constitutes a nice example of multidisciplinary collaboration.

In conclusion, this PhD thesis has addressed its goals of rationalization, insights and design rules at different occasions. Now, the challenges that need to be faced are multiple. One is the (neverending) quest for *accuracy*. It is incarnated in many forms, some of which are present in this work. An example is the inclusion of vibrational contributions, which could be extended at the CCSD level to other reference molecules. On this topic, the numerical differentiation scheme implemented in *nachos* (Chapter 6) currently requires the full $3N$ geometrical degrees of freedom, which could be reduced with the help of group theory for highly symmetrical systems. Another approach is to apply the recursive implementation of the response functions provided at the HF and DFT levels by K. Ruud and co-workers,¹ exemplified for vibrational contributions in Ref. 2. Sampling of the conformational space, as demonstrated in Chapters 8-9 is another way to grasp the complexity of a molecule in solution, either through a “manual” search of minima or with the help of (molecular and/or quantum) dynamics.^{3,4} Another realm of improvements is found in Chapter 7, which would require a different methodological approach⁵ to improve the accuracy on calculating first (and second) hyperpolarizability of Ruthenium (and other transition metals-containing) compounds. Nevertheless the most difficult and transverse area in this quest for improved multi-functional compound is certainly the inclusion of the *environment* in hyperpolarizability calculations. The best example in this thesis is found in Chapter 10, whose goal was to provide all-atom quantum mechanical description beyond the already used ONIOM one. Other methods, such as fluctuating charges,⁶ polarizable embedding,⁷ fragmentation⁸ ... exist, each with its advantages. Accounting for the environment is not only important if one wants to tackle complex surroundings like self-assembled monolayers,⁹ membrane systems,¹⁰ NLOphores embedded in a polymer matrix,^{11,12} etc, but

also for solvents like water¹³ or even carbon tetrachloride,^{14,15} it is a difficult task, which can call for further methodological developments.

To continue, other challenges are to be found in the *design* part. For example, the compounds in Chapters 7-9 could be improved based on the design rules derived in Chapter 11. It is especially interesting for octupolar compounds, since they were predicted to display an important first hyperpolarizability if well designed.¹⁶ Furthermore, and following Chapter 10, it is only but natural to extend this work to other (fluorescent) proteins¹⁷ as well as to propose improvements on existing ones, based on the design rules that would be extracted from this new set of calculations. Besides, it would be interesting to design new NLO compounds and switches with intermediate diradical characters and large γ_{THS} .¹⁸ Finally, the field would probably benefit from data mining/machine learning insights.¹⁹

Bibliography

- [1] Bast, R.; Frieze, D. H.; Gao, B.; Jonsson, D. J.; Ringholm, M.; Reine, S. S.; Ruud, K. OpenRSP: open-ended response theory. 2020; <https://doi.org/10.5281/zenodo.3923836>.
- [2] Gao, B.; Ringholm, M.; Bast, R.; Ruud, K.; Thorvaldsen, A. J.; Jaszuński, M. Analytic Density Functional Theory Calculations of Pure Vibrational Hyperpolarizabilities: The First Dipole Hyperpolarizability of Retinal and Related Molecules. *J. Phys. Chem. A* **2014**, *118*, 748–756.
- [3] Grimme, S. Exploration of Chemical Compound, Conformer, and Reaction Space with Meta-Dynamics Simulations Based on Tight-Binding Quantum Chemical Calculations. *J. Chem. Theory Comput.* **2019**, *15*, 2847–2862.
- [4] Pracht, P.; Bohle, F.; Grimme, S. Automated Exploration of the Low-Energy Chemical Space with Fast Quantum Chemical Methods. *Phys. Chem. Chem. Phys.* **2020**, *22*, 7169–7192.
- [5] Escudero, D.; Thiel, W.; Champagne, B. Spectroscopic and Second-Order Nonlinear Optical Properties of Ruthenium(II) Complexes: A DFT/MRCI and ADC(2) Study. *Phys. Chem. Chem. Phys.* **2015**, *17*, 18908–18912.
- [6] Giovannini, T.; Ambrosetti, M.; Cappelli, C. A Polarizable Embedding Approach to Second Harmonic Generation (SHG) of Molecular Systems in Aqueous Solutions. *Theor. Chem. Acc.* **2018**, *137*, 74.
- [7] Hršak, D.; Olsen, J. M. H.; Kongsted, J. Polarizable Density Embedding Coupled Cluster Method. *J. Chem. Theory Comput.* **2018**, *14*, 1351–1360.
- [8] Zahariev, F.; Gordon, M. S. Nonlinear Response Time-Dependent Density Functional Theory Combined with the Effective Fragment Potential Method. *J. Chem. Phys.* **2014**, *140*, 18A523.
- [9] Tonnelé, C.; Pielak, K.; Deviers, J.; Muccioli, L.; Champagne, B.; Castet, F. Nonlinear Optical Responses of Self-Assembled Monolayers Functionalized with Indolino–Oxazolidine Photoswitches. *Phys. Chem. Chem. Phys.* **2018**, *20*, 21590–21597.
- [10] Bouquiaux, C.; Tonnelé, C.; Castet, F.; Champagne, B. Second-Order Nonlinear Optical Properties of an Amphiphilic Dye Embedded in a Lipid Bilayer. A Combined Molecular Dynamics–Quantum Chemistry Study. *J. Phys. Chem. B* **2020**, *124*, 2101–2109.
- [11] Robinson, B. H.; Dalton, L. R. Monte Carlo Statistical Mechanical Simulations of the Competition of Intermolecular Electrostatic and Poling-Field Interactions in Defining Macroscopic Electro-Optic Activity for Organic Chromophore/Polymer Materials. *J. Phys.*

Chem. A **2000**, *104*, 4785–4795.

- [12] Sullivan, P. A.; Dalton, L. R. Theory-Inspired Development of Organic Electro-Optic Materials. *Acc. Chem. Res.* **2010**, *43*, 10–18.
- [13] Rodriguez, M. B.; Shelton, D. P. What Is Measured by Hyper-Rayleigh Scattering from a Liquid? *J. Chem. Phys.* **2018**, *148*, 134504.
- [14] Cardenuto, M. H.; Castet, F.; Champagne, B. Investigating the First Hyperpolarizability of Liquid Carbon Tetrachloride. *RSC Adv.* **2016**, *6*, 99558–99563.
- [15] de Wergifosse, M.; Castet, F.; Champagne, B. Frequency Dispersion of the First Hyperpolarizabilities of Reference Molecules for Nonlinear Optics. *J. Chem. Phys.* **2015**, *142*, 194102.
- [16] Zyss, J. Molecular Engineering Implications of Rotational Invariance in Quadratic Nonlinear Optics: From Dipolar to Octupolar Molecules and Materials. *J. Chem. Phys.* **1993**, *98*, 6583–6599.
- [17] De Meulenaere, E.; de Coene, Y.; Russier-Antoine, I.; Vanpraet, L.; Van den Haute, C.; Thevissen, K.; Baekelandt, V.; Bartic, C.; Hofkens, J.; Brevet, P.-F.; Clays, K. Fluorescence-Free First Hyperpolarizability Values of Fluorescent Proteins and Channel Rhodopsins. *J. Photochem. Photobiol. A* **2020**, *400*, 112658.
- [18] Nakano, M. Electronic Structure of Open-Shell Singlet Molecules: Diradical Character Viewpoint. *Top. Curr. Chem.* **2017**, *375*, 47.
- [19] Tuan-Anh, T.; Zaleśny, R. Predictions of High-Order Electric Properties of Molecules: Can We Benefit from Machine Learning? *ACS Omega* **2020**, *5*, 5318–5325.

List of publications

Included in this work:

- Beaujean, P; Champagne, B. Coupled Cluster Evaluation of the Frequency Dispersion of the First and Second Hyperpolarizabilities of Water, Methanol, and Dimethyl Ether. *J. Chem. Phys.* **2016**, *145*, 044311. DOI: 10.1063/1.4958736 (as Chapter 4).
- Beaujean, P; Champagne, B. Coupled Cluster Evaluation of the Second and Third Harmonic Scattering Responses of Small Molecules. *Theor. Chem. Acc.* **2018**, *4*, 137. DOI: 10.1007/s00214-018-2219-y (as Chapter 5).
- Beaujean, P; Champagne, B. Coupled Cluster Investigation of the Vibrational and Electronic Second and Third Harmonic Scattering Hyperpolarizabilities of the Water Molecule. *J. Chem. Phys.* **2019**, *151*, 064303. DOI: 10.1063/1.5110375 (as Chapter 6).
- Quertinmont, J.; Beaujean, P; Stiennon, J.; Aidibi, Y.; Leriche, P; Rodriguez, V; Sanguinet, L.; Champagne, B. Combining Benzazolo-Oxazolidine Twins toward Multi-State Nonlinear Optical Switches. *J. Phys. Chem. B* **2021**, *125*, 3918. DOI: 10.1021/acs.jpcc.1c01962 (as Chapter 8).

Not included in this work:

- Beaujean, P; Bondu, F; Plaquet, A.; Garcia-Amorós, J.; Cusido, J.; Raymo, F. M.; Castet, F.; Rodriguez, V; Champagne, B. Oxazines: A New Class of Second-Order Nonlinear Optical Switches. *J. Am. Chem. Soc.* **2016**, *138*, 5052. DOI: 10.1021/jacs.5b13243.
- Champagne, B.; Beaujean, P; de Wergifosse, M.; Cardenuto, M. H.; Liégeois, V.; Castet, F. *Quantum Chemical Methods for Predicting and Interpreting Second-Order Nonlinear Optical Properties: From Small to Extended -Conjugated Molecules*. In *Frontiers of Quantum Chemistry*; Wójcik, M. J., Nakatsuji, H., Kirtman, B., Ozaki, Y., Eds.; Springer Singapore: Singapore, 2018; pp 117138. DOI: 10.1007/978-981-10-5651-2_6.
- Lescos, L.; Sitkiewicz, S. P; Beaujean, P; Blanchard-Desce, M.; Champagne, B.; Matito, E.; Castet, F. Performance of DFT Functionals for Calculating the Second-Order Nonlinear Optical Properties of Dipolar Merocyanines. *Phys. Chem. Chem. Phys.* **2020**, *22*, 16579. DOI: 10.1039/D0CP02992K.

Part V

Appendices

Appendix A

Supporting information of Chapter 7

Abstract

This appendix (which refers to Chapter 7 in page 171) contains the i) basis set and XC functional impact on geometry of **2**, ii) basis set and XC functional impact on the static first hyperpolarizability of **2**, iii) analysis of additional excited states of **1b**, and iv) analysis of excited states of **3-5**.

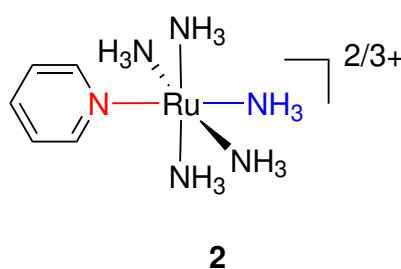
Section A.1

Benchmarks

The selection of appropriate levels of approximation for geometry optimizations and for the evaluation of the NLO properties is based on a moiety of compound **5** including the Ruthenium center. Thus, we selected compound **2**, for which two XRD structures are available in the CSD¹ and described in Ref. 2: NEFXUR for **2^{II}** and NEXYAY for **2^{III}**.

Geometry optimizations

Considering the XRD structures, the effect of oxidation leads to an increase of the Ru-N(py) bond length (red bond in Scheme A.1) of 0.02 Å (from 2.058 to 2.077 Å) and a decrease of the Ru-N(ax) bond length (blue bond in Figure A.1) of about −0.06 Å (from 2.158 to 2.100 Å). The geometry optimizations of both oxidation states of **2** were performed, using the B3LYP³, B3P86⁴, CAM-B3LYP⁵, and M06⁶ XC-functionals and the 6-31G(d), 6-311G(d), and cc-pVTZ basis sets together with LANL2DZ,⁷ LANL2TZ,^{7,8} and LANL2TZ(f)⁷⁻⁹ to model the Ru atom. The two bond lengths are reported in Tables A.1 (gas phase) and A.2 (acetonitrile, with IEF-PCM¹⁰⁻¹²).



Scheme A.1: Bonds that display the largest changes upon oxidation in compound **2**: Ru-N(py) (red) and Ru-N(ax) (blue).

For these two representative bonds with the Ru atoms, their lengths increase in the order B3P86 < M06 < CAM-B3LYP \approx B3LYP, while the variations between the different basis sets amount to about 0.01 Å. The effect of increasing the number of basis functions on the ECP is about 0.005 Å for **2^{II}** and 0.01 Å for **2^{III}**. Then, including an additional set of *f* polarization functions on the Ru also affects the bond length by a similar amount. Globally, the bond lengths are overestimated, especially for **2^{II}** and for Ru-N(ax) of **2^{III}**.

When considering the impact of a polarizable surroundings, as described by the IEF-PCM scheme, the Ru-N(ax) bond length of **2^{II}** and **2^{III}** are shrinking, improving the agreement with experiment. For the case of the Ru-N(py) bond, it is also shrunk in **2^{II}** but lengthened in **2^{III}**. As a consequence, in gas phase, the description of the oxidation effects is not consistent with the experimental results (in the best cases, the variations are too small; in other cases, their sign is incorrect). On the other hand, with a polarizable continuum, the Ru-N(py) bond

	Reduced (2^{II})				Oxidized (2^{III})				$\Delta(2^{\text{III}}-2^{\text{II}})$	
	6-31G(d)	6-311G(d)	cc-pVTZ		6-31G(d)	6-311G(d)	cc-pVTZ		6-31G(d)	6-311G(d)
LANL2DZ										
Ru-N(py)	B3LYP	2.145	2.146	2.120	2.090	2.097	2.088		-0.055	-0.049
	B3P86	2.105	2.105	2.098	2.114	2.073	2.109		0.009	-0.032
	CAM-B3LYP	2.142	2.144	2.136	2.077	2.084	2.080		-0.065	-0.060
	M06	2.122	2.121	2.113	2.124	2.086	2.116		0.002	-0.035
Ru-N(ax)	B3LYP	2.226	2.224	2.099	2.229	2.224	2.230		0.004	0.000
	B3P86	2.195	2.191	2.201	2.191	2.193	2.187		-0.004	0.002
	CAM-B3LYP	2.207	2.204	2.212	2.205	2.200	2.197		-0.001	-0.005
	M06	2.216	2.210	2.219	2.212	2.210	2.210		-0.004	0.000
LANL2TZ										
Ru-N(py)	B3LYP	2.146	2.113	2.142	2.096	2.103	2.099		-0.050	-0.010
	B3P86	2.105	2.142	2.104	2.075	2.079	2.075		-0.030	-0.063
	CAM-B3LYP	2.145	2.100	2.141	2.086	2.092	2.088		-0.059	-0.009
	M06	2.123	2.140	2.123	2.128	2.131	2.088		0.005	-0.010
Ru-N(ax)	B3LYP	2.226	2.226	2.233	2.240	2.224	2.227		0.014	-0.002
	B3P86	2.196	2.194	2.202	2.198	2.194	2.197		0.001	0.000
	CAM-B3LYP	2.208	2.207	2.214	2.202	2.200	2.202		-0.006	-0.007
	M06	2.217	2.211	2.220	2.210	2.205	2.213		-0.007	-0.007
LANL2TZ(f)										
Ru-N(py)	B3LYP	2.132	2.136	2.133	2.088	2.095	2.093		-0.043	-0.041
	B3P86	2.092	2.094	2.092	2.065	2.070	2.068		-0.027	-0.024
	CAM-B3LYP	2.131	2.135	2.132	2.119	2.083	2.081		-0.012	-0.052
	M06	2.111	2.113	2.107	2.120	2.086	2.082		0.008	-0.027
Ru-N(ax)	B3LYP	2.221	2.220	2.228	2.219	2.217	2.219		-0.002	-0.003
	B3P86	2.190	2.188	2.195	2.190	2.187	2.190		0.000	-0.001
	CAM-B3LYP	2.202	2.201	2.207	2.187	2.193	2.194		-0.015	-0.008
	M06	2.213	2.207	2.219	2.204	2.204	2.207		-0.009	-0.003

Table A.1: Geometrical parameters of 2^{II} and 2^{III} , as optimized with different XC-functionals, basis sets, and ECP's in the gas phase. When $\Delta(\text{III-II})$ goes in the same direction as "experiment", it is underlined.

	Reduced (2^{II})			Oxidized (2^{III})			$\Delta(2^{\text{III}}-2^{\text{II}})$		
	6-31G(d)	6-311G(d)	cc-pVTZ	6-31G(d)	6-311G(d)	cc-pVTZ	6-31G(d)	6-311G(d)	cc-pVTZ
LANL2DZ									
Ru-N(py)	B3LYP	2.127	2.129	2.121	2.113	2.121	2.111	-0.014	-0.008
	B3P86	2.086	2.085	2.077	2.087	2.092	2.084	<u>0.001</u>	<u>0.007</u>
	CAM-B3LYP	2.132	2.133	2.125	2.096	2.107	2.097	-0.036	-0.026
	M06	2.103	2.101	2.094	2.107	2.133	2.105	<u>0.004</u>	0.032
Ru-N(ax)	B3LYP	2.192	2.190	2.198	2.170	2.165	2.168	<u>-0.022</u>	<u>-0.025</u>
	B3P86	2.165	2.162	2.170	2.145	2.139	2.142	<u>-0.020</u>	<u>-0.022</u>
	CAM-B3LYP	2.175	2.174	2.180	2.150	2.145	2.146	<u>-0.025</u>	<u>-0.029</u>
	M06	2.186	2.181	2.189	2.162	2.145	2.160	<u>-0.024</u>	<u>-0.035</u>
LANL2TZ									
Ru-N(py)	B3LYP	2.123	2.127	2.122	2.119	2.127	2.122	-0.004	0.000
	B3P86	2.083	2.083	2.079	2.094	2.100	2.093	<u>0.011</u>	<u>0.016</u>
	CAM-B3LYP	2.129	2.133	2.128	2.109	2.115	2.100	-0.020	-0.018
	M06	2.102	2.102	2.097	2.113	2.136	2.128	<u>0.010</u>	<u>0.035</u>
Ru-N(ax)	B3LYP	2.194	2.193	2.200	2.169	2.166	2.168	<u>-0.025</u>	<u>-0.026</u>
	B3P86	2.167	2.165	2.172	2.146	2.142	2.145	<u>-0.022</u>	<u>-0.023</u>
	CAM-B3LYP	2.178	2.176	2.183	2.147	2.148	2.160	<u>-0.031</u>	<u>-0.028</u>
	M06	2.188	2.183	2.191	2.163	2.151	2.154	<u>-0.025</u>	<u>-0.033</u>
LANL2TZ(f)									
Ru-N(py)	B3LYP	2.111	2.116	2.112	—	2.117	2.115	—	0.001
	B3P86	2.070	2.071	2.069	2.085	2.090	2.086	<u>0.015</u>	<u>0.019</u>
	CAM-B3LYP	2.118	2.122	2.119	2.094	2.104	2.099	-0.024	-0.018
	M06	2.090	2.090	2.087	2.104	2.128	2.121	<u>0.014</u>	0.038
Ru-N(ax)	B3LYP	2.188	2.187	2.195	—	2.161	2.161	—	-0.026
	B3P86	2.162	2.159	2.166	2.136	2.135	2.138	<u>-0.025</u>	<u>-0.025</u>
	CAM-B3LYP	2.172	2.171	2.177	2.143	2.141	2.143	<u>-0.029</u>	<u>-0.030</u>
	M06	2.184	2.179	2.186	2.156	2.142	2.147	<u>-0.028</u>	<u>-0.037</u>

Table A.2: Geometrical parameters of 2^{II} and 2^{III} , as optimized with different XC-functionals, basis sets, and ECP's in acetonitrile (IEF-PCM). When $\Delta(\text{III-II})$ goes in the same direction as “experiment”, it is underlined.

lengths increase by about 0.025 Å, and the Ru-N(ax) bond length decreases by about the same amount, which is more consistent with experiment. On a quantitative point of view, the bonds remain too long compared to the X-ray diffraction results.

Globally, the B3P86 XC functional is confirmed to be reliable to describe the Ru-N bonds, while M06 is an alternative (B3LYP and CAM-B3LYP are less reliable). The LANL2TZ/6-311G(d) basis set [and 6-31G(d) for Zn] is chosen for the further geometry optimizations, because the modifications are modest when moving from LANL2TZ to LANL2TZ(f), and they are smaller between 6-311G(d) and cc-pVTZ.

First Hyperpolarizabilities

In order to get a β reference value, the MP2 method was used together with IEF-PCM (acetonitrile) and cc-pVTZ/LANL2TZ(f) on both oxidation states of **2**, as optimized at the B3P86/cc-pVTZ/LANL2TZ(f) level in acetonitrile (IEF-PCM). The computational procedure consisted in evaluating β from a finite field numerical differentiation of α . To do so, a Romberg procedure [with $|F_0| = 0.0004$ a.u., $a = 2$, $k_{max} = 5$ for **2^{II}**, $|F_0| = 0.0001$ a.u., $a = \sqrt{2}$, $k_{max} = 5$ for **2^{III}**] was employed. So, the β values accuracy is better than 1 a.u. The obtained static β_{HRS} (DR) values are 655 a.u. (4.54) for **2^{II}**, 34 a.u. (2.80) for **2^{III}**, thus resulting in a contrast of 19.

3 basis sets ([6-31G(d), 6-311G(d) and cc-pVTZ] and different XC-functionals (B3LYP, B3P86, M06 and M06-2X,⁶ CAM-B3LYP and LC-BLYP¹³) were tested on the same B3P86/cc-pVTZ/LANL2TZ(f) geometries [in acetonitrile (IEF-PCM)] used for MP2 calculations. Results are found in Tables A.3. For **2^{II}**, the order of the β_{HRS} amplitude is M06 > B3P86 > B3LYP > CAM-B3LYP > M06-2X > LC-BLYP, with the latter getting close to the MP2 β_{HRS} and DR values. Note that LC-BLYP and M06-2X were already highlighted by Zhang et al.¹⁴ to closely reproduce the experimental trends. Increasing the size of the basis set increases β_{HRS} . Concerning **2^{III}**, the ordering of the β_{HRS} amplitudes among the different XCFs depends much on the basis set. Then, improving the basis set usually decreases the values. Overall, the β_{HRS} of the reduced form are always overestimated with respect to MP2, even with the largest basis sets/ECPs.

On that account, the LC-BLYP/6-311G(d)/LANL2TZ level was selected. For the reduced form, the agreement with the MP2 value is excellent, while it predicts a strong decrease of β_{HRS} upon oxidation, though it is underestimated.

	Reduced (2^{II})			Oxidized (2^{III})			$2^{\text{II}}/2^{\text{III}}$ ratio	
	6-31G(d)	6-311G(d)	cc-pVTZ	6-31G(d)	6-311G(d)	cc-pVTZ	6-31G(d)	6-311G(d) cc-pVTZ
LANL2DZ								
B3LYP	1484 (4.64)	1697 (4.74)	1779 (4.83)	610 (4.51)	324 (3.87)	275 (3.62)	2.43	5.24 6.47
B3P86	1541 (4.71)	1744 (4.83)	1821 (4.92)	272 (3.72)	177 (2.78)	87 (1.60)	5.66	9.87 21.01
M06	1753 (4.78)	1967 (4.78)	2014 (4.89)	75 (3.01)	784 (4.61)	120 (6.05)	23.40	2.51 16.75
M06-2X	727 (4.49)	810 (4.74)	836 (4.88)	182 (3.58)	168 (3.27)	92 (1.91)	4.00	4.82 9.13
CAM-B3LYP	917 (4.56)	1059 (4.72)	1103 (4.84)	332 (4.27)	213 (3.59)	214 (6.92)	2.76	4.96 5.15
LC-BLYP	508 (4.37)	586 (4.64)	610 (4.81)	213 (3.85)	166 (3.25)	162 (3.16)	2.38	3.53 3.77
LANL2TZ								
B3LYP	1618 (4.64)	1822 (4.73)	1897 (4.82)	303 (4.29)	69 (1.62)	60 (1.83)	5.34	26.32 31.63
B3P86	1672 (4.70)	1868 (4.81)	1937 (4.90)	105 (2.34)	116 (2.26)	75 (2.42)	15.89	16.05 25.81
M06	1870 (4.76)	2077 (4.76)	2128 (4.87)	129 (4.20)	153 (4.77)	163 (5.81)	14.49	13.60 13.03
M06-2X	786 (4.52)	861 (4.76)	888 (4.88)	98 (2.91)	91 (2.56)	71 (1.80)	8.03	9.44 12.46
CAM-B3LYP	1029 (4.58)	1166 (4.72)	1203 (4.83)	219 (4.15)	103 (2.65)	529 (5.87)	4.71	11.29 2.27
LC-BLYP	579 (4.41)	652 (4.65)	670 (4.80)	171 (3.84)	128 (3.04)	126 (2.93)	3.38	5.08 5.31
LANL2TZ(f)								
B3LYP	1640 (4.63)	1848 (4.72)	1924 (4.81)	307 (4.40)	200 (5.62)	56 (1.72)	5.35	9.22 34.20
B3P86	1694 (4.69)	1894 (4.80)	1965 (4.89)	69 (1.58)	539 (5.69)	484 (5.74)	24.41	3.51 4.06
M06	1890 (4.76)	2100 (4.75)	2154 (4.86)	139 (4.27)	162 (4.77)	172 (5.75)	13.64	12.95 12.49
M06-2X	805 (4.52)	883 (4.76)	911 (4.88)	313 (4.42)	87 (2.68)	302 (4.01)	2.57	10.16 3.02
CAM-B3LYP	1050 (4.58)	1190 (4.72)	1228 (4.83)	56 (2.54)	57 (3.34)	72 (5.31)	18.66	20.91 16.98
LC-BLYP	595 (4.42)	671 (4.65)	690 (4.80)	180 (3.97)	146 (3.34)	144 (3.20)	3.30	4.59 4.80

Table A.3: Static first hyperpolarizability (β_{HRS} , a.u.) of the reduced (singlet) and oxidized (doublet) state of **2**, as computed with different XC-functionals, basis sets, and ECP's in acetonitrile (IEF-PCM). The depolarization ratio (DR) is given in parentheses.

Section A.2

Electronic transitions

Higher energy non-negligible electronic transitions of compound **1b** are detailed in Table A.4, while the radial density differences, $\rho_r(r)$, of the 8 excited states (with the one given in Table 2 of main text) are given Figure A.1. The first three were already discussed, while the next two (#4 and #5) and the last three (#6-#8) constitutes two separate families:

1. ES #1-#3 were already discussed in main text ;
2. The next family is constituted by two excitations (#4 and #5) located on one branch of the compound, resulting in large oscillator strengths, together with large q_{CT} , d_{CT} and r_{CT} . The radial density $\rho_r(r)$ shows that the density is moving from the C₃-C₄, C₄-C₅, C₇-C₈ and C₇-C₁₁ bonds (especially the last two), and goes into N₁ and the C₂-C₃, C₅-C₆ and C₄-C₇ bonds, confirmed by the large negative value of r_{CT} ;
3. The second family contains three excitations (#6-#8), with less important (but still appreciable) oscillator strengths and d_{CT} (q_{CT} remains around 0.4 e). A notable feature is the small r_{CT} . The radial density $\rho_r(r)$ is different from the previous one : density is moving from the C₂-C₃ and C₅-C₆ bonds (especially the last one) to the N₁-C₂, N₁-C₆ and the bonds implying C₄. Note that the similarity between the curves is explained by the fact that they have the same q_{CT} , even though ES #3 is located on one branch, while ES #4 and #5 delocalize on two branches.

The important electronic transitions of compounds **3-5** are given in Tables A.5-A.7 (for the full reduced forms **x^{II}**) and Tables A.8-A.10 (for the fully oxidized forms, **x^{III}**), while the radial density differences are summarized in Figs. 7.8-7.10. There are similarities between the $\rho_r(r)$ of all three compounds.

On the one hand, for the reduced fully forms,

1. ES #1 and #2 of all three compounds are clearly similar to the one of compound **2** (Figure 6 of main text), which involves displacement of the density from the Ru-donating moieties to the qpy ones, together with large charge transfer quantities (and important negative r_{CT}) ;
2. ES #3 of **5^{II}** seems different from the two previous ones, since it displays some positive density around the Ruthenium centers ;
3. ES #3 of **3^{II}** is also a displacement for the Ru-donating moieties, but the distribution over the qpy is different and centered around C₇, which results in smaller charge transfer distance and radius ;

4. ES #3 of **4^{II}** and ES #4 of **5^{II}** are ILCT states, which only involves the qpy moieties, like ES #1 and ES #2 of **1b** (Figure A.1), with comparable (and small) charge transfer quantities, even though the one of **5^{II}** extends more. Their excitation energies are also comparable ;
5. ES #4 of **3^{II}** and **4^{II}** and ES #5-#6 of **5^{II}** are similar to ES #4-#5 of compound **1b** for the qpy part (with a small contribution of the Ru-donating moieties), with moderate (with respect to the first two ES) charge transfer quantities ;
6. Finally ES #5 of **3^{II}** and **4^{II}** are similar to ES #6-#8 for the qpy part (with a small contribution of the Ru-donating moieties), which results, again, in moderate charge transfer quantities.

As expected, these excitations results of an interplay between the ones of **1b** (for the qpy part) and the ones of **2^{II}** (for the Ru-donating moieties). The clear MLCT character of the first ES drives the β_{HRS} response.

On the other hand, for the fully oxidized forms,

1. ES #1 of all three compounds (and ES #2 of **4^{III}**) are reminiscent of the first one of compound **1b** (Figure A.1), together with a small metal-to-metal charge transfer (MMCT) character.
2. ES #2 of compound **3^{III}** and ES #3 of compound **4^{III}** only involves the qpy moieties, thus they have the same characteristics as the corresponding ones in the reduced form (see above).
3. ES #3 of **3^{III}** and ES #4 of **4^{III}** are comparable to ES #4 and #5 of compound **1b**, together with a larger MMCT contribution than the first ES. This contribution is not comparable to the one of **2^{III}**.
4. Finally, ES #5 of **4^{III}** differs from the previous one in the area around the Ru atom, and is comparable to ES #2 of **2^{III}**.

The results are thus comparable to the one of **2^{III}**: the MLCT character is lost, together with an inversion of the displacement of the density upon excitation. Note that the spin contamination for these ES varies: it is generally low (<0.1), except for the last 2 ES of **4^{III}**, for which it is moderate (about 0.3), while the last one of **3^{III}** has a large contamination (0.7), and should probably be rejected.

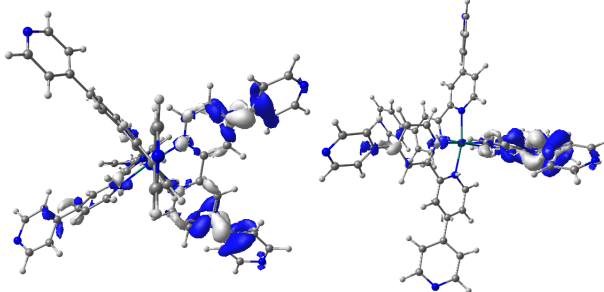
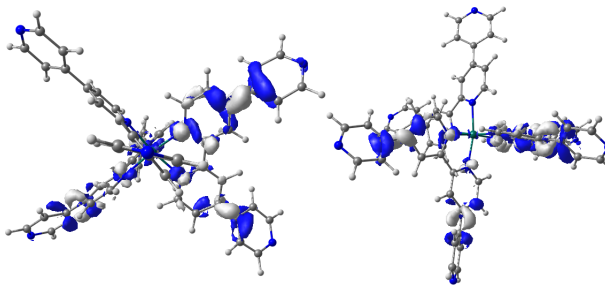
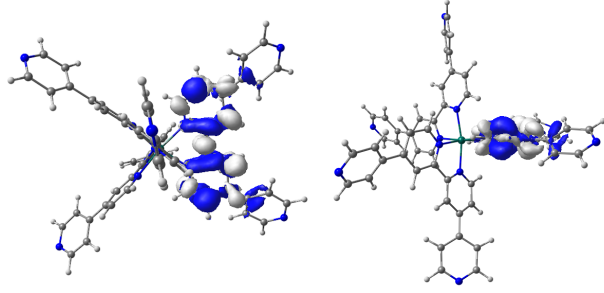
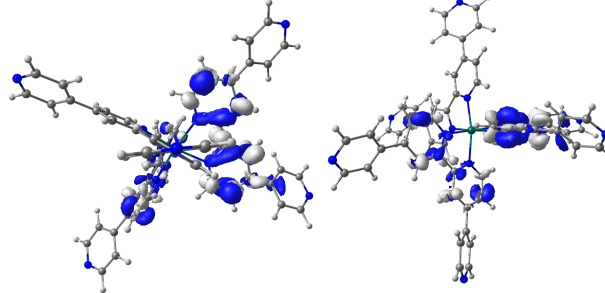
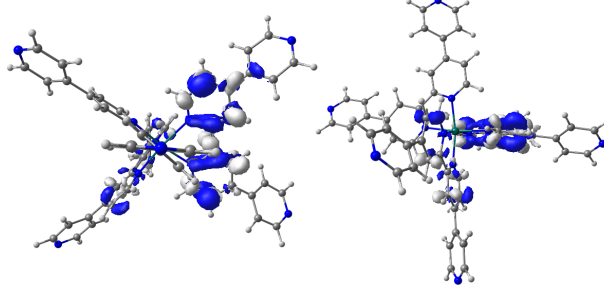
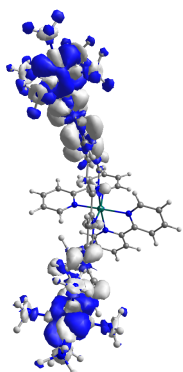
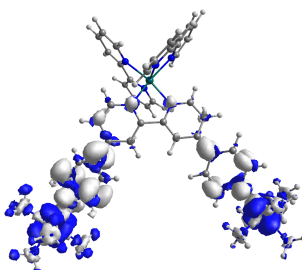
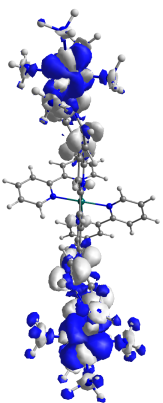
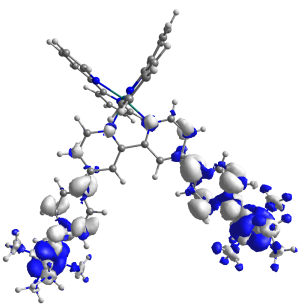
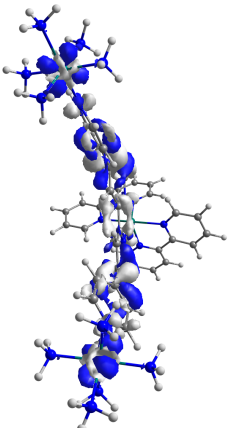
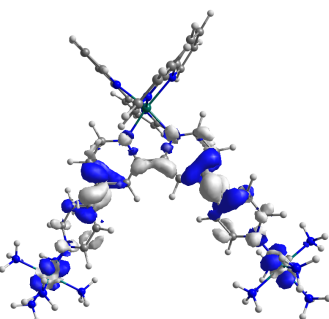
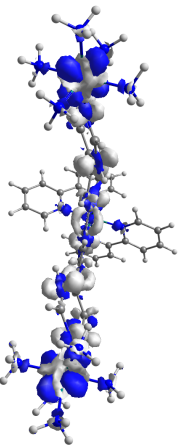
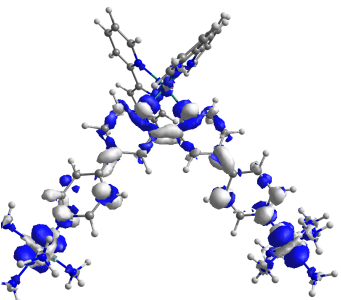
<p>ES #4, 228 nm (1.28)</p>  <p>$q_{CT} = 0.41 e$, $d_{CT} = 0.52 \text{ \AA}$ $r_{CT} = -0.88 \text{ \AA}$</p>	<p>ES #5, 222 nm (1.16)</p>  <p>$q_{CT} = 0.42 e$, $d_{CT} = 0.45 \text{ \AA}$ $r_{CT} = -0.97 \text{ \AA}$</p>
<p>ES #6, 216 nm (0.61)</p>  <p>$q_{CT} = 0.41 e$, $d_{CT} = 0.29 \text{ \AA}$ $r_{CT} = 0.10 \text{ \AA}$</p>	<p>ES #7, 216 nm (0.59)</p>  <p>$q_{CT} = 0.41 e$, $d_{CT} = 0.15 \text{ \AA}$ $r_{CT} = 0.02 \text{ \AA}$</p>
<p>ES #8, 215 nm (0.95)</p>  <p>$q_{CT} = 0.41 e$, $d_{CT} = 0.18 \text{ \AA}$ $r_{CT} = -0.01 \text{ \AA}$</p>	

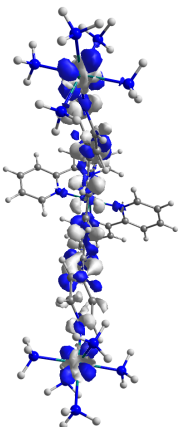
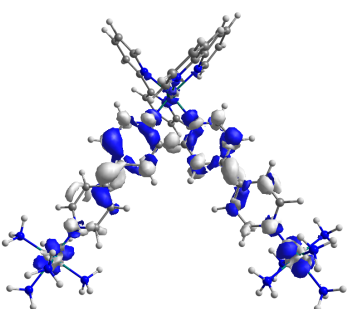
Table A.4: Higher energy electronic transitions natures (vertical excitation energy and oscillator strength in parentheses) and electron density difference (negative in blue, isovalue of 0.001 a.u., two orientations) together with the related quantities (charge transfer amplitude, q_{CT} , distance, d_{CT} , and radius, r_{CT}) of **1b** as computed at the LC-BLYP/6-311G(d)/LANL2TZ level in acetonitrile (IEF-PCM). Two molecular orientations are proposed for each transition state.



ES #1: 287 nm (0.48), $q_{CT} = 0.85 e$, $d_{CT} = 2.19 \text{ \AA}$, $r_{CT} = -2.89 \text{ \AA}$ ES #2: 284 nm (0.66), $q_{CT} = 0.91 e$, $d_{CT} = 2.25 \text{ \AA}$, $r_{CT} = -2.88 \text{ \AA}$



ES #3: 256 nm (0.64), $q_{CT} = 0.63 e$, $d_{CT} = 1.08 \text{ \AA}$, $r_{CT} = -1.76 \text{ \AA}$ ES #4: 215 nm (0.45), $q_{CT} = 0.46 e$, $d_{CT} = 1.44 \text{ \AA}$, $r_{CT} = -1.67 \text{ \AA}$



ES #5: 212 nm (0.42), $q_{CT} = 0.46 e$, $d_{CT} = 0.38 \text{ \AA}$, $r_{CT} = -0.78 \text{ \AA}$

Table A.5: Excitation energies (oscillator strength in parentheses) and their charge transfer quantities (charge transferred, q_{CT} , and distance of transfer, d_{CT} , and charge transfer radius r_{CT}) of the main ground to excited state transitions of **3^{II}**, as computed at the LC-BLYP/6-311-G(d)/LANL2TZ level in acetonitrile (IEF-PCM). Difference between excited and ground state densities are also plotted (with an isovalue of 0.001, negative in blue) with two different orientations.

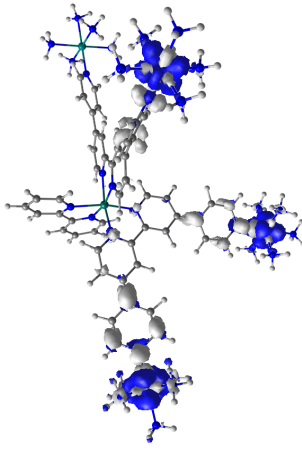
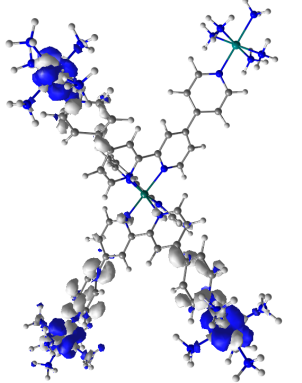
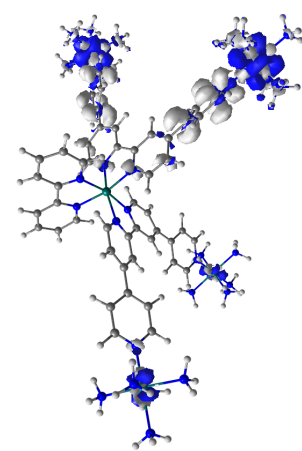
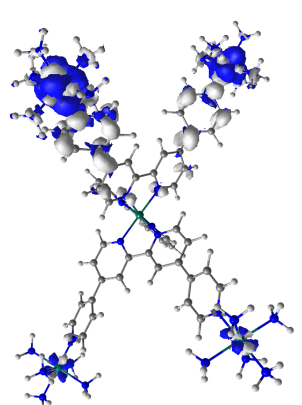
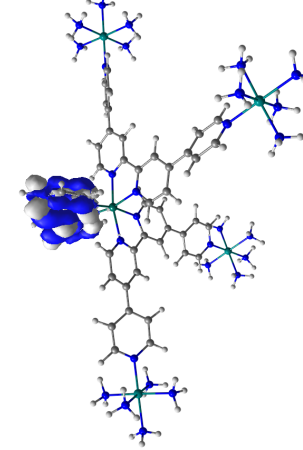
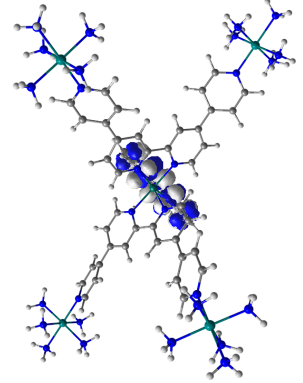
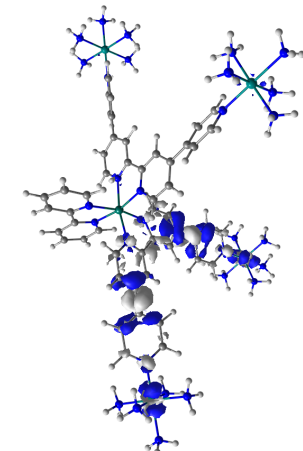
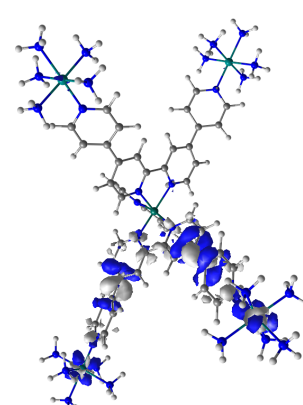
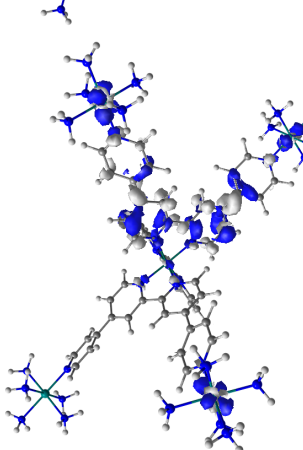
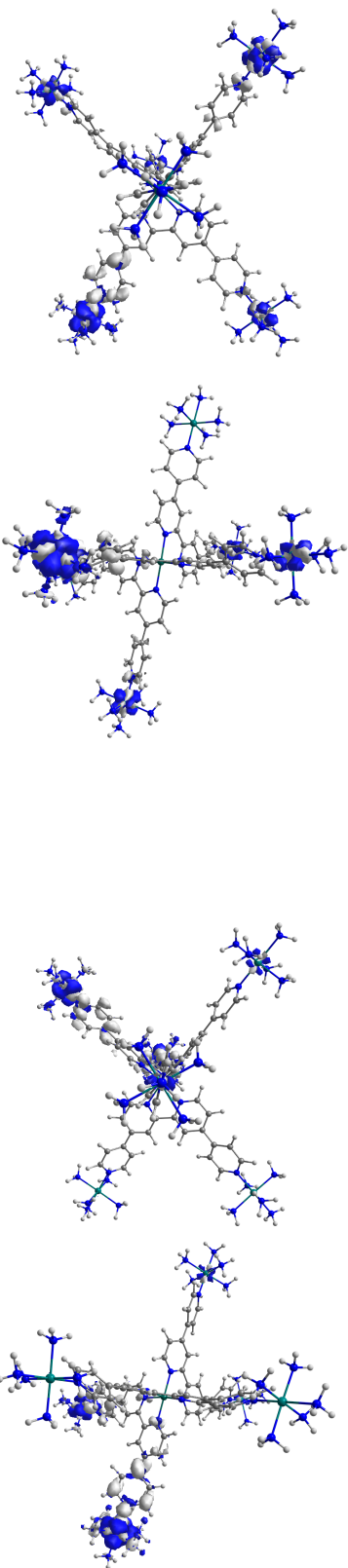
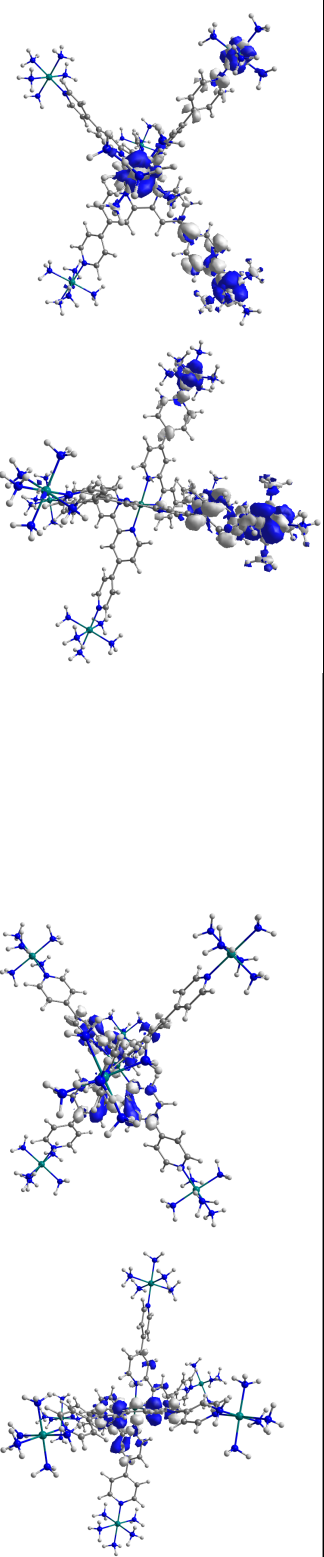
			
ES #1: 288 nm (0.71), $q_{CT} = 0.82e$, $d_{CT} = 1.68\text{\AA}$, $r_{CT} = -2.54\text{\AA}$	ES #2: 287 nm (0.66), $q_{CT} = 0.83e$, $d_{CT} = 1.73\text{\AA}$, $r_{CT} = -2.84\text{\AA}$		
			
ES #3: 258 nm (0.48), $q_{CT} = 0.43e$, $d_{CT} = 0.35\text{\AA}$, $r_{CT} = 0.01\text{\AA}$	ES #4: 218 nm (0.61), $q_{CT} = 0.46e$, $d_{CT} = 1.07\text{\AA}$, $r_{CT} = -1.40\text{\AA}$		
			
ES #5: 212 nm (0.54), $q_{CT} = 0.46e$, $d_{CT} = 0.51\text{\AA}$, $r_{CT} = -1.07\text{\AA}$			

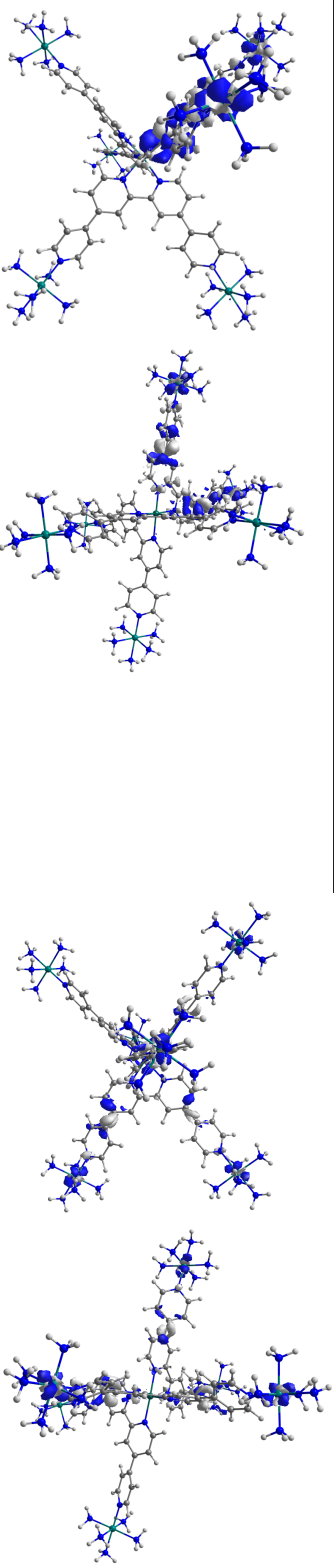
Table A.6: Excitation energies (oscillator strength in parentheses) and their charge transfer quantities (charge transferred, q_{CT} , and distance of transfer, d_{CT} , and charge transfer radius r_{CT}) of the main ground to excited state transitions of 4^{H} , as computed at the LC-BLYP/6-311-G(d)/LANL2TZ level in acetonitrile (IEF-PCM). Difference between excited and ground state densities are also plotted (with an isovalue of 0.001, negative in blue) with two different orientations.



ES #1: 289 nm (0.92), $q_{CT} = 0.81 e$, $d_{CT} = 0.67 \text{ \AA}$, $r_{CT} = -1.56 \text{ \AA}$ ES #2: 288 nm (0.59), $q_{CT} = 0.81 e$, $d_{CT} = 1.84 \text{ \AA}$, $r_{CT} = -2.04 \text{ \AA}$



ES #3: 287 nm (0.74), $q_{CT} = 0.84 e$, $d_{CT} = 1.71 \text{ \AA}$, $r_{CT} = -1.24 \text{ \AA}$ ES #4: 264 nm (0.55), $q_{CT} = 0.40 e$, $d_{CT} = 0.04 \text{ \AA}$, $r_{CT} = 0.40 \text{ \AA}$



ES #5: 218 nm (0.53), $q_{CT} = 0.46 e$, $d_{CT} = 1.23 \text{ \AA}$, $r_{CT} = -1.50 \text{ \AA}$ ES #6: 216 nm (0.63), $q_{CT} = 0.47 e$, $d_{CT} = 0.89 \text{ \AA}$, $r_{CT} = -1.28 \text{ \AA}$

Table A.7: Excitation energies (oscillator strength in parentheses) and their charge transfer quantities (charge transferred, q_{CT} , and distance of transfer, d_{CT} , and charge transfer radius r_{CT}) of the main ground to excited state transitions of **5^{II}**, as computed at the LC-BLYP/6-311-G(d)/LANL2TZ level in acetonitrile (IEF-PCM). Difference between excited and ground state densities are also plotted (with an isovalue of 0.001, negative in blue) with two different orientations.

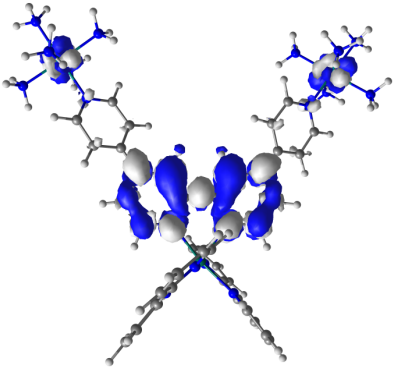
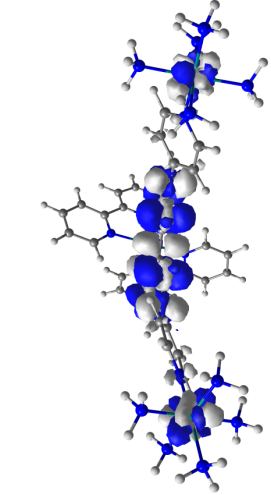
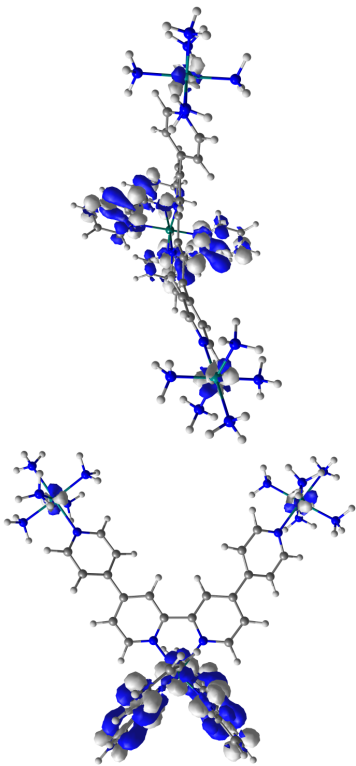
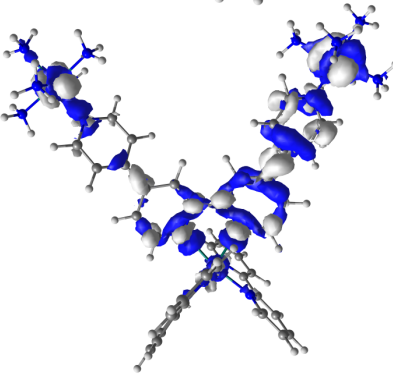
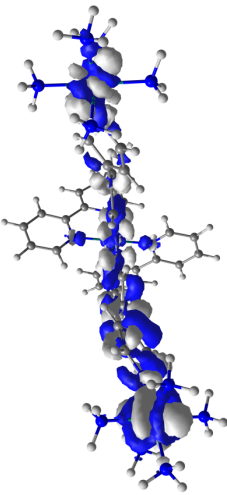
		
ES #1: 268 nm (0.40, $\Delta \langle S^2 \rangle = 0.03$) $q_{CT} = 0.59 e$, $d_{CT} = 0.49 \text{ \AA}$, $r_{CT} = 1.06 \text{ \AA}$		ES #2: 257 nm (0.61, $\Delta \langle S^2 \rangle = 0.18$) $q_{CT} = 0.43 e$, $d_{CT} = 0.28 \text{ \AA}$, $r_{CT} = 0.27 \text{ \AA}$
		
ES #3: 237 nm (0.34, $\Delta \langle S^2 \rangle = 0.71$) $q_{CT} = 0.67 e$, $d_{CT} = 1.38 \text{ \AA}$, $r_{CT} = 1.78 \text{ \AA}$		

Table A.8: Excitation energies (oscillator strength in parentheses) and their charge transfer quantities (charge transferred, q_{CT} , and distance of transfer, d_{CT} , and charge transfer radius r_{CT}) of the main ground to excited state transitions of **3^{III}**, as computed at the LC-BLYP/6-311-G(d)/LANL2TZ level in acetonitrile (IEF-PCM). Difference between excited and ground state densities are also plotted (with an isovalue of 0.001, negative in blue) with two different orientations.

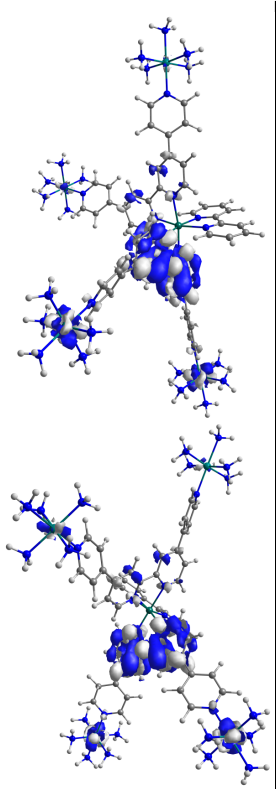
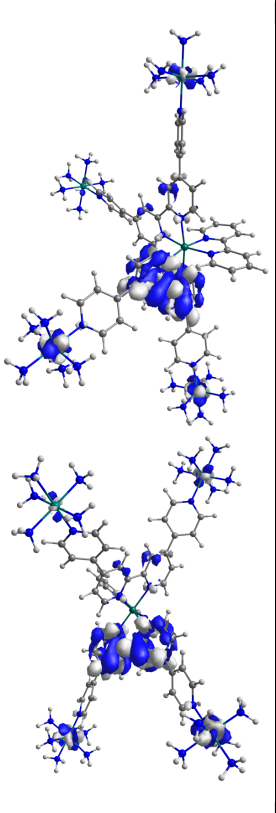
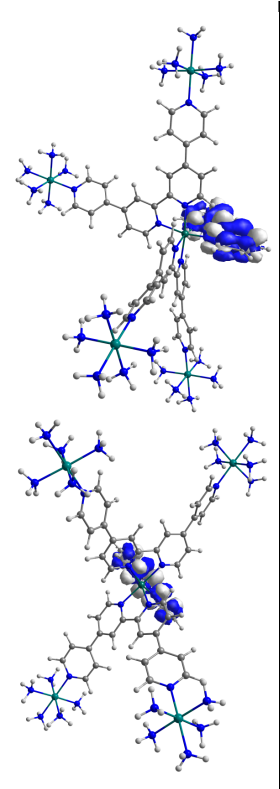
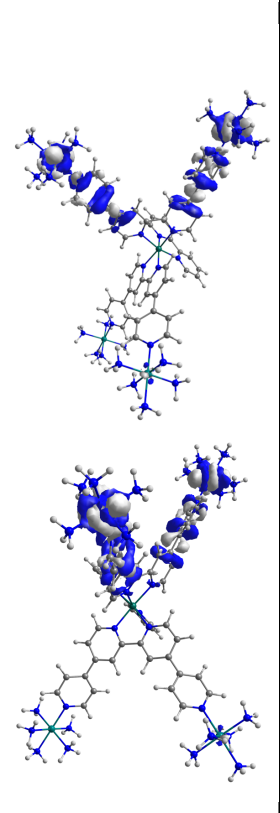
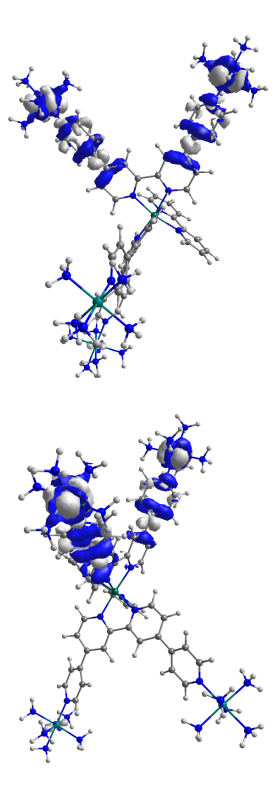
 <p>ES #1: 270 nm (0.33, $\Delta\langle S^2 \rangle = 0.03$) $q_{CT} = 0.60 e$, $d_{CT} = 0.27 \text{ \AA}$, $r_{CT} = 0.57 \text{ \AA}$</p>	 <p>ES #2: 268 nm (0.53, $\Delta\langle S^2 \rangle = 0.09$) $q_{CT} = 0.58 e$, $d_{CT} = 0.29 \text{ \AA}$, $r_{CT} = 0.90 \text{ \AA}$</p>
 <p>ES #3: 259 nm (0.51, $\Delta\langle S^2 \rangle = 0.03$) $q_{CT} = 0.45 e$, $d_{CT} = 0.37 \text{ \AA}$, $r_{CT} = 0.02 \text{ \AA}$</p>	 <p>ES #4: 237 nm (0.37, $\Delta\langle S^2 \rangle = 0.29$) $q_{CT} = 0.67 e$, $d_{CT} = 0.90 \text{ \AA}$, $r_{CT} = 1.39 \text{ \AA}$</p>
 <p>ES #5: 236 nm (0.42, $\Delta\langle S^2 \rangle = 0.28$) $q_{CT} = 0.67 e$, $d_{CT} = 0.90 \text{ \AA}$, $r_{CT} = 0.83 \text{ \AA}$</p>	

Table A.9: Excitation energies (oscillator strength in parentheses) and their charge transfer quantities (charge transferred, q_{CT} , and distance of transfer, d_{CT} , and charge transfer radius r_{CT}) of the main ground to excited state transitions of **4^{III}**, as computed at the LC-BLYP/6-311-G(d)/LANL2TZ level in acetonitrile (IEF-PCM). Difference between excited and ground state densities are also plotted (with an isovalue of 0.001, negative in blue) with two different orientations.

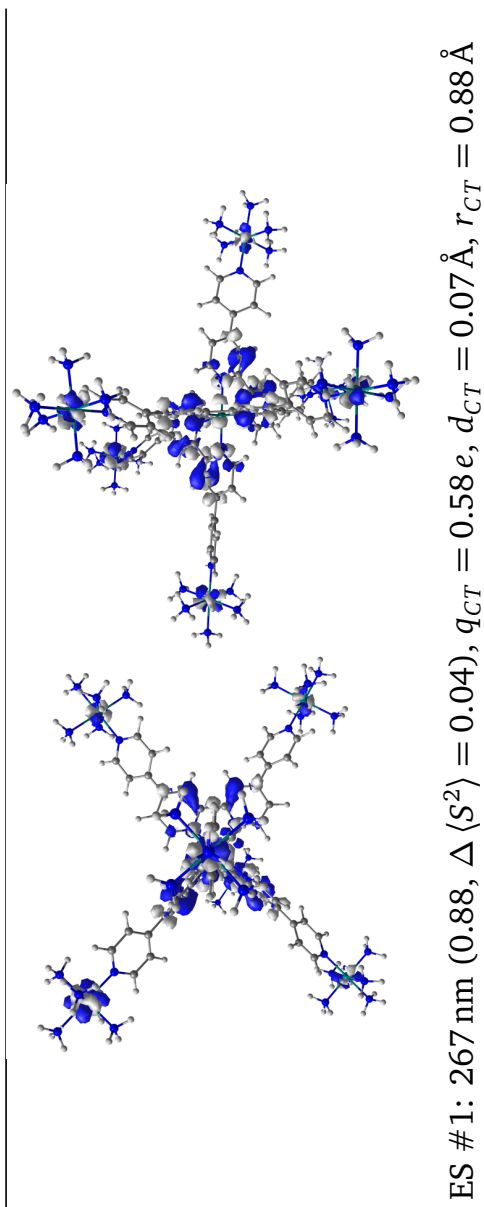


Table A.10: Excitation energies (oscillator strength in parentheses) and their charge transfer quantities (charge transferred, q_{CT} , and distance of transfer, d_{CT} , and charge transfer radius r_{CT}) of the main ground to excited state transitions of **5^{III}**, as computed at the LC-BLYP/6-311-G(d)/LANL2TZ level in acetonitrile (IEF-PCM). Difference between excited and ground state densities are also plotted (with an isovalue of 0.001, negative in blue) with two different orientations.

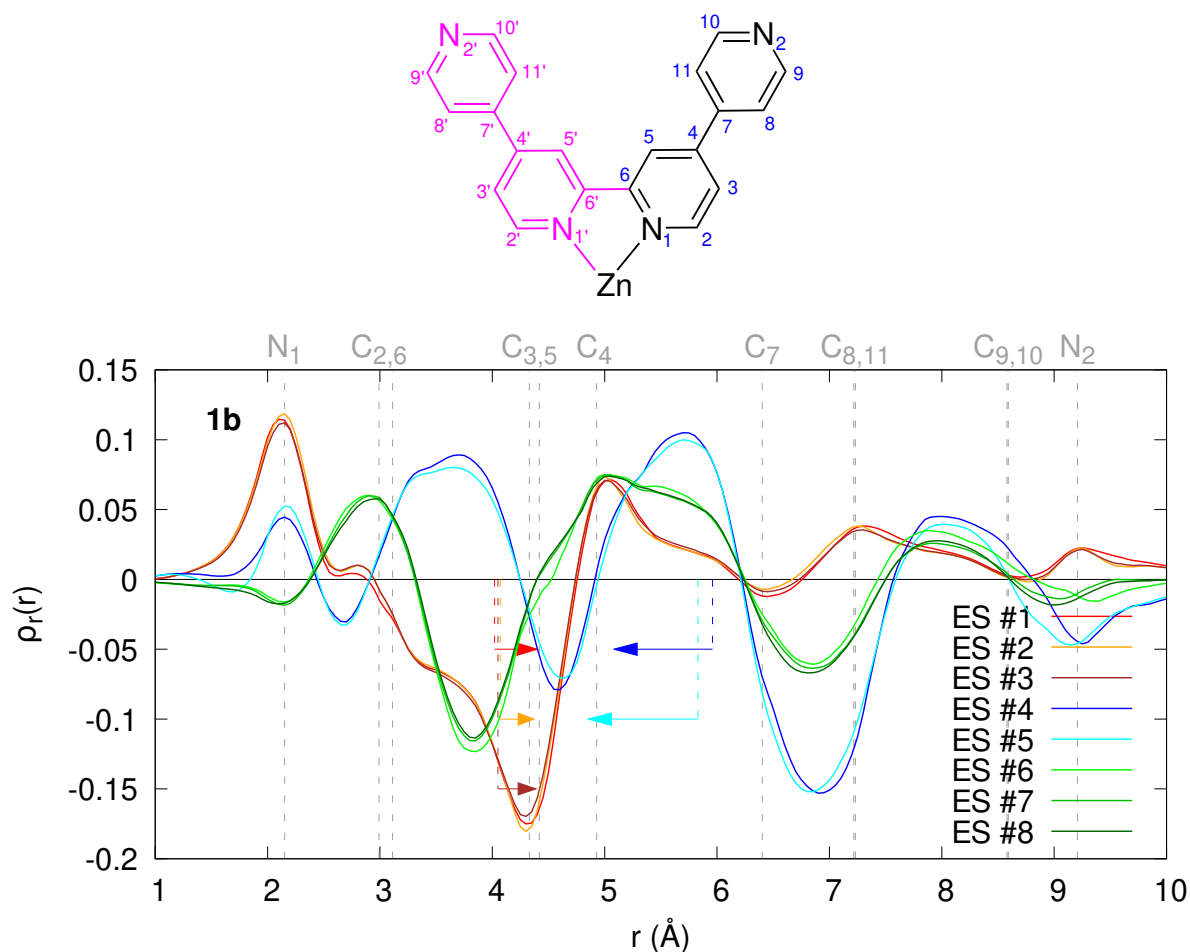


Figure A.1: Radial electron density distribution (centered on the Zn atom) of the excited states of **1b** as reported in Table 7.3 (bottom, numbering of the atoms on top, the atoms in purple are equivalent by symmetry) as computed at the LC-BLYP/6-311G(d)/LANL2TZ level in acetonitrile (IEF-PCM). Arrows indicate r_{CT} .

Bibliography

- [1] Groom, C. R.; Bruno, I. J.; Lightfoot, M. P.; Ward, S. C. The Cambridge Structural Database. *Acta Crystallogr. B* **2016**, *72*, 171–179.
- [2] Shin, Y.-g. K.; Szalda, D. J.; Brunschwig, B. S.; Creutz, C.; Sutin, N. Electronic and Molecular Structures of Pentaammineruthenium Pyridine and Benzonitrile Complexes as a Function of Oxidation State. *Inorg. Chem.* **1997**, *36*, 3190–3197.
- [3] Kim, K.; Jordan, K. D. Comparison of Density Functional and MP2 Calculations on the Water Monomer and Dimer. *J. Phys. Chem.* **1994**, *98*, 10089–10094.
- [4] Perdew, J. P.; Wang, Y. Accurate and Simple Analytic Representation of the Electron-Gas Correlation Energy. *Phys. Rev. B* **1992**, *45*, 13244–13249.
- [5] Yanai, T.; Tew, D. P.; Handy, N. C. A New Hybrid Exchange–Correlation Functional Using the Coulomb-Attenuating Method (CAM-B3LYP). *Chem. Phys. Lett.* **2004**, *393*, 51–57.
- [6] Zhao, Y.; Truhlar, D. G. The M06 Suite of Density Functionals for Main Group Thermochemistry, Thermochemical Kinetics, Noncovalent Interactions, Excited States, and Transition Elements: Two New Functionals and Systematic Testing of Four M06-Class Functionals and 12 Other Functionals. *Theor. Chem. Acc.* **2008**, *120*, 215–241.
- [7] Hay, P. J.; Wadt, W. R. Ab Initio Effective Core Potentials for Molecular Calculations. Potentials for K to Au Including the Outermost Core Orbitals. *J. Chem. Phys.* **1985**, *82*, 299–310.
- [8] Roy, L. E.; Hay, P. J.; Martin, R. L. Revised Basis Sets for the LANL Effective Core Potentials. *J. Chem. Theory Comput.* **2008**, *4*, 1029–1031.
- [9] Ehlers, A. W.; Böhme, M.; Dapprich, S.; Gobbi, A.; Höllwarth, A.; Jonas, V.; Köhler, K. F.; Stegmann, R.; Veldkamp, A.; Frenking, G. A Set of F-Polarization Functions for Pseudo-Potential Basis Sets of the Transition Metals ScCu, YAg and LaAu. *Chem. Phys. Lett.* **1993**, *208*, 111–114.
- [10] Cammi, R.; Cossi, M.; Mennucci, B.; Tomasi, J. Analytical Hartree–Fock Calculation of the Dynamical Polarizabilities α , β , and γ of Molecules in Solution. *J. Chem. Phys.* **1996**, *105*, 10556–10564.
- [11] Tomasi, J.; Mennucci, B.; Cancès, E. The IEF Version of the PCM Solvation Method: An Overview of a New Method Addressed to Study Molecular Solutes at the QM Ab Initio Level. *Comput. Theor. Chem.* **1999**, *464*, 211–226.
- [12] Corozzi, A.; Mennucci, B.; Cammi, R.; Tomasi, J. Structure versus Solvent Effects on Nonlinear Optical Properties of Push-Pull Systems: A Quantum-Mechanical Study Based

- on a Polarizable Continuum Model. *J. Phys. Chem. A* **2009**, *113*, 14774–14784.
- [13] Iikura, H.; Tsuneda, T.; Yanai, T.; Hirao, K. A Long-Range Correction Scheme for Generalized-Gradient-Approximation Exchange Functionals. *J. Chem. Phys.* **2001**, *115*, 3540–3544.
- [14] Zhang, Y.; Champagne, B. Understanding the Second-Order Nonlinear Optical Properties of One-Dimensional Ruthenium(II) Ammine Complexes. *J. Phys. Chem. C* **2013**, *117*, 1833–1848.

Supporting information of Chapter 10

Abstract

This appendix (which refers to Chapter 10 in page 257) contains a) details on the geometry optimizations (RMSD and MAD of the structures, probability density of important bonds and BLA of the chromophores), including justification of the ONIOM scheme, b) optimization of the parameters for the sTD-DFT-xTB calculations (y_J , y_K and $E_{thresh.}$), c) numerical results of Figure ??, d) dual-threshold results for iLOV when including Tyr and Trp amino acids, and e) description of the SVM model and its application to bR.

Section B.1

Geometry optimizations

For the geometry optimizations, the ONIOM scheme was used: the chromophore (C) and the near surrounding amino acids in a 4 Å radius (4A, Table B.1) were treated at the ω B97X-D/6-31G* level of theory, while remaining parts were optimized with the GFN2-xTB method^{1,2} (in water, implicitly accounted for by the GBSA (Generalized Born/Surface Area) model³). Direct cuts between both layers were done at the α -carbon (C_α) of amino acids included in the high layer, together with its side chain. If amino acids are connected together in the high layer (Table B.1, with a dash in between), their peptide bonds are also included in. The optimizations were carried out using criteria proposed by Schmitz et al.,⁴ e.g. until the maximum residual force is below $2 \times 10^{-3} E_h \text{ \AA}^{-1}$ and the change of energy below $5 \times 10^{-5} E_h$. It was performed with the Gaussian 16 A03 package⁵ together with the xtb 6.2.2 program.⁶ We also optimized geometries with the GFN2-xTB method alone to assess the improvement gained by using the ONIOM scheme.

	Content of 4A	Number of atoms		Charge	
		C-4A	P-EW	C-4A	P-EW
iLOV	V392-I393-T394, N401, F410, N425-A426-R427, L429-Q430, V439, I442-R443, I446, L456, N458, N468, L470, L472, F485, I486-G487, Q489, O1101, O1102, O1129, O1130, O1140	459	1987	+1	-1
bR	Y83, W86, T89-T90, L93, M118-I119, G122, W138, S141-T142, M145, W182, Y185-P186, W189, D212, A215- <u>K216</u> , O407, O446	380	3835	0	+1

Table B.1: List of amino acids (one-letter code) and water molecules (O) included in 4A (the amino acid directly linked to the bR (bacteriorhodopsin) chromophore is underlined), number of atoms and total charges in each part of the structure.

We used the same geometrical descriptors as in Reference 4 to compare the optimized geometries to their crystal structures. Figure B.2 reports the root mean square deviation (RMSD) of different parts of the structure and the mean average deviation (MAD) of the Ψ , Φ , ω , and χ_1 angles (Figure B.1). These quantities were determined with the Bio3d R package.⁷ For both proteins, RMSD for the ONIOM ω B97X-D:GFN2-xTB optimized geometries with respect to crystal structures are within the experimental uncertainty of 0.5 Å. Most of the differences come from displaced external water molecules (EW). The ONIOM scheme helps to reduce the RMSD with respect to GFN2-xTB only. Furthermore, heavy atoms (ha^P and ha^{P-EW}) and alpha

carbons (C_α) RMSDs show similar trends: the bR optimized geometry deviates less from the crystal structure than iLOV. This difference for iLOV comes mostly from the displacements of the ribityl side chain of the flavin mononucleotide (FMN) as well as the rotation of its terminal phosphate group and the rearrangement of surrounding amino acids located in 4A: Asn401, Asn425, Gln430 and Arg443. This observation is consistent with Reference 8, where the authors showed the relative mobility of the FMN inside the protein cavity. Considering the analysis of torsional angles, we observe a rather acceptable change of folding related to deviations of Φ and Ψ angles. Note that bR is more affected than iLOV in that respect while it is the reverse situation for the peptides planarity and orientation of the side chains (ω and χ_1). These kinds of geometrical changes were expected as Schmitz et al.⁴ already reported that GFN2-xTB reproduces well secondary features of proteins, but is less accurate for random coils. The use of the ONIOM scheme instead of the GFN2-xTB method alone slightly reduces these deviations with respect to experimental crystal structures.

Figure B.3 displays the length distributions of CC, CO, and CN bonds for both proteins. They are narrower after optimization, but remain in agreement with the experimental XRD values. These trends are similar to those reported by Schmitz et al.⁴ Since modifications of the π -conjugated pathway have usually large impacts on the first hyperpolarizability, Figure B.4 reports the alternance of single and double bonds (BLA) for both chromophores. The change of BLA with respect to the crystal structure is rather limited, especially for iLOV. Using the ONIOM scheme for the geometry optimization is particularly important to obtain the right BLA for the retinal Schiff base with respect to experiment while GFN2-xTB reduces it quite drastically.

In summary, the crystal structures are well preserved by the present optimizations. bR was less impacted by the optimization. The chromophore of iLOV undergoes some displacements of its side chain, but its π -conjugation is preserved. The ONIOM scheme reduces the gap between the GFN2-xTB optimized and crystal structures.

Section B.2

Fine-tuning of the parameters for the sTD-DFT-xTB method

For both chromophores (C) extracted from the ONIOM ω B97X-D:GFN2-xTB structures (for bR, Lys216 is substituted by a methyl), reference static β_{HRS} values in gas phase were computed at the MP2/6-31+G* level of theory with the Romberg differentiation procedure^{9,10} on α ($|F_0| = 0.0004$ a.u., $a=2$, $k_{max}=5$). Because it is not possible to compute the β_{HRS} frequency dispersion at the MP2 level, we employed the multiplicative scheme^{11,12} with frequency dispersions obtained by TD-DFT calculations with both M06-2X and ω B97X-D exchange-correlation functionals. To fine-tune y_J and y_K parameters, these results were compared to sTD-DFT-xTB ones considering a truncation threshold of 10.0 eV. Figure B.5 presents this comparison for

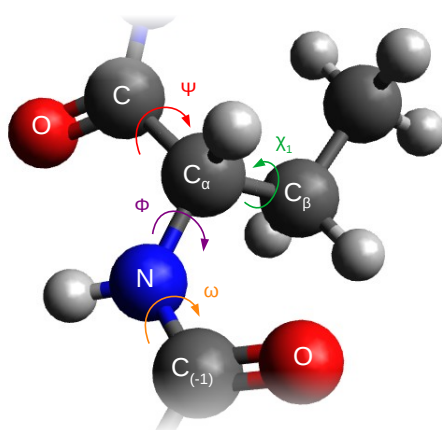


Figure B.1: Relevant torsional angles for the protein backbone.

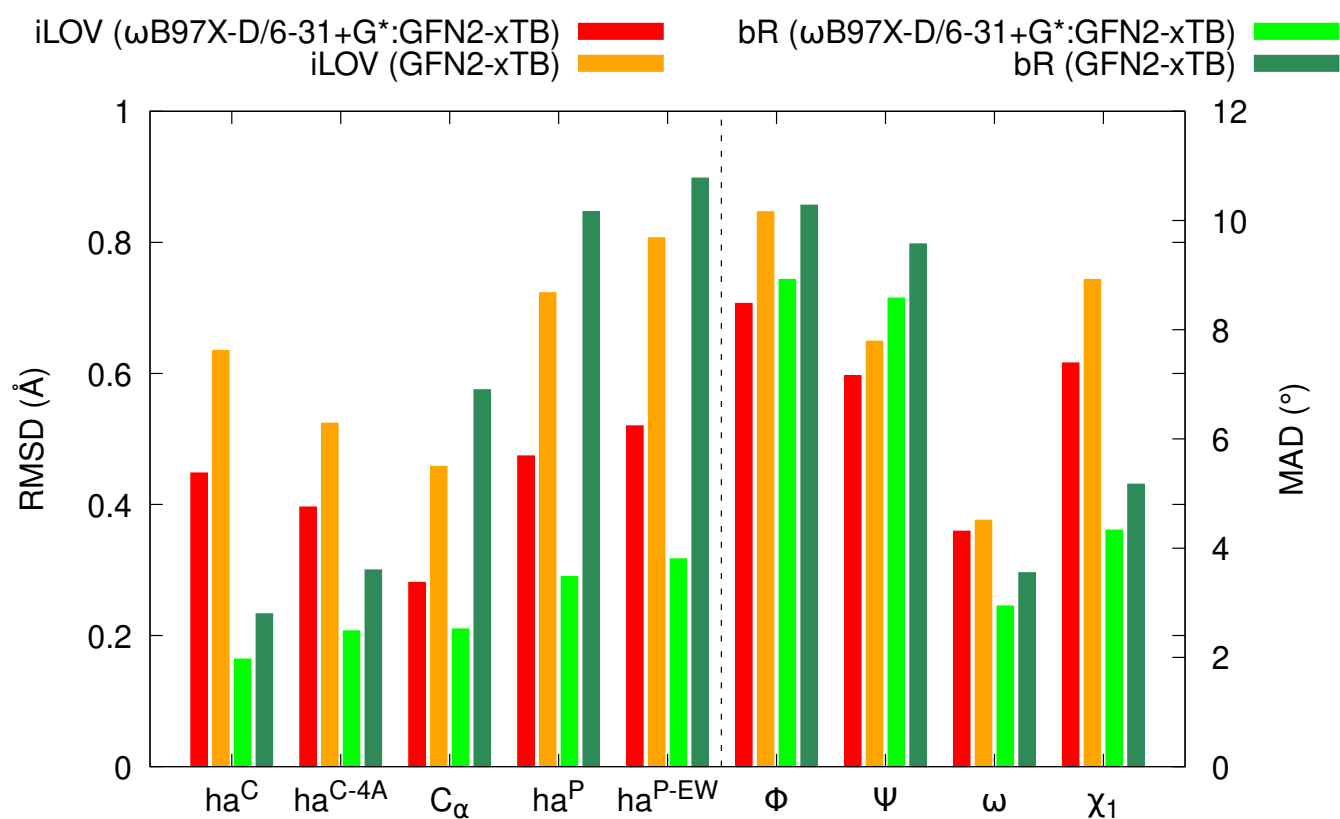


Figure B.2: Heavy atoms (ha, for different parts of the protein as defined in Scheme 2b) and alpha carbons (C_α) root-mean square deviations (RMSD), left panel and mean average deviations (MAD), right panel for the 4 angles defined in Figure B.1 for the optimized structures at both ONIOM ωB97X-D:GFN2-xTB and GFN2-xTB levels of theory with respect to XRD geometries.

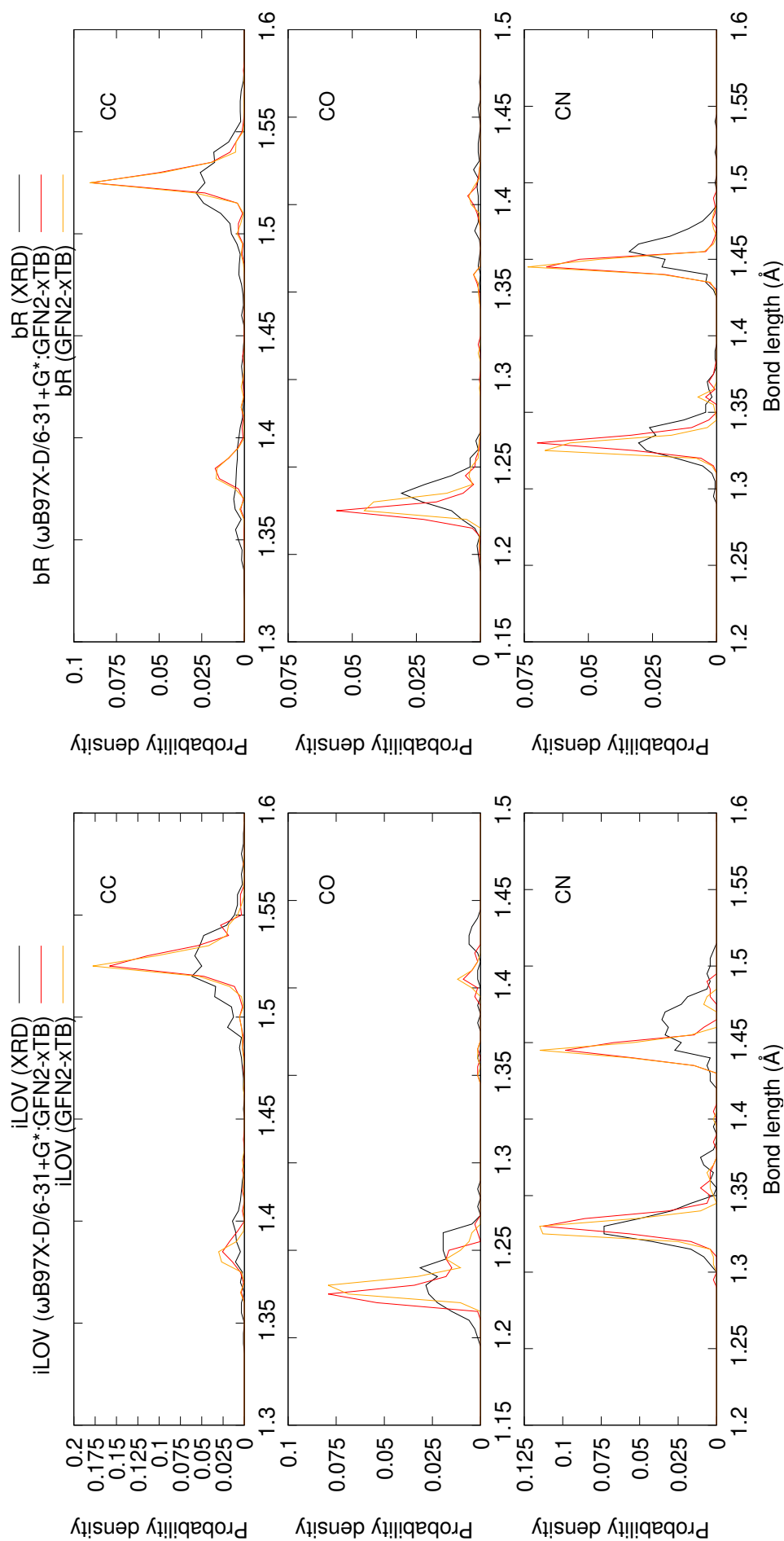


Figure B.3: Probability density for CC (top), CO (middle) and CN (bottom) bond lengths in the XRD and optimized structures (P-EW) of iLOV (left) and bR (right).

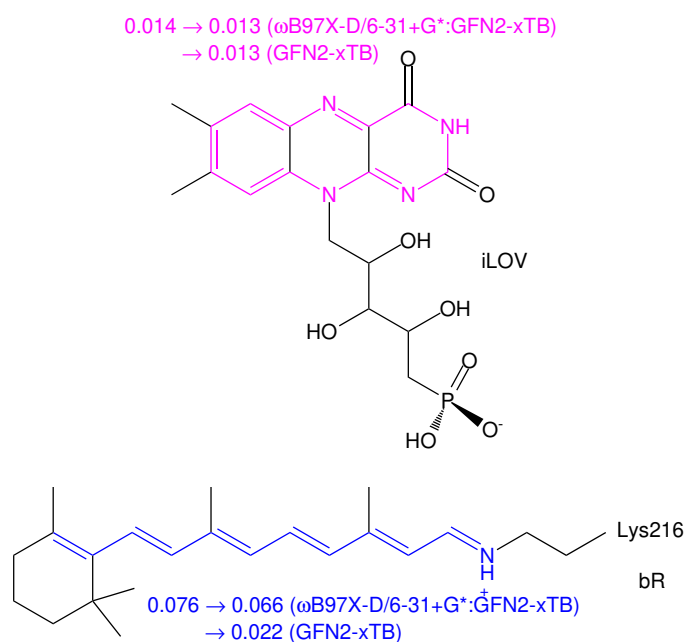


Figure B.4: Evolution of the bond length alternation (BLA, Å) before and after the optimization. The colors indicate the π -conjugated pathways considered to calculate the BLA.

$y_J = 2.0$ and $y_K = 0.15$ with an excellent agreement with respect to the reference MP2 values below 0.8 eV.

Figure B.6 shows the evolution of the static β_{HRS} relative error as a function of the truncation of the CI space represented by $E_{thresh.}$. The convergence is fast for bR, even for **C-4A**. A value of 9 eV is therefore chosen. iLOV requires a slightly larger energy threshold. We selected a value of 10 eV to balance the computational cost and accuracy.

Table B.2 reports β_{HRS} values computed at the sTD-DFT-xTB level of theory with these optimized parameters from the chromophore (**C**) to the full protein (**P-EW**).

Figure B.7 shows the influence of $E_{thresh.}$ on the static β_{HRS} values of iLOV, when including all tryptophan and tyrosine residues into the high layer using the dual threshold method.

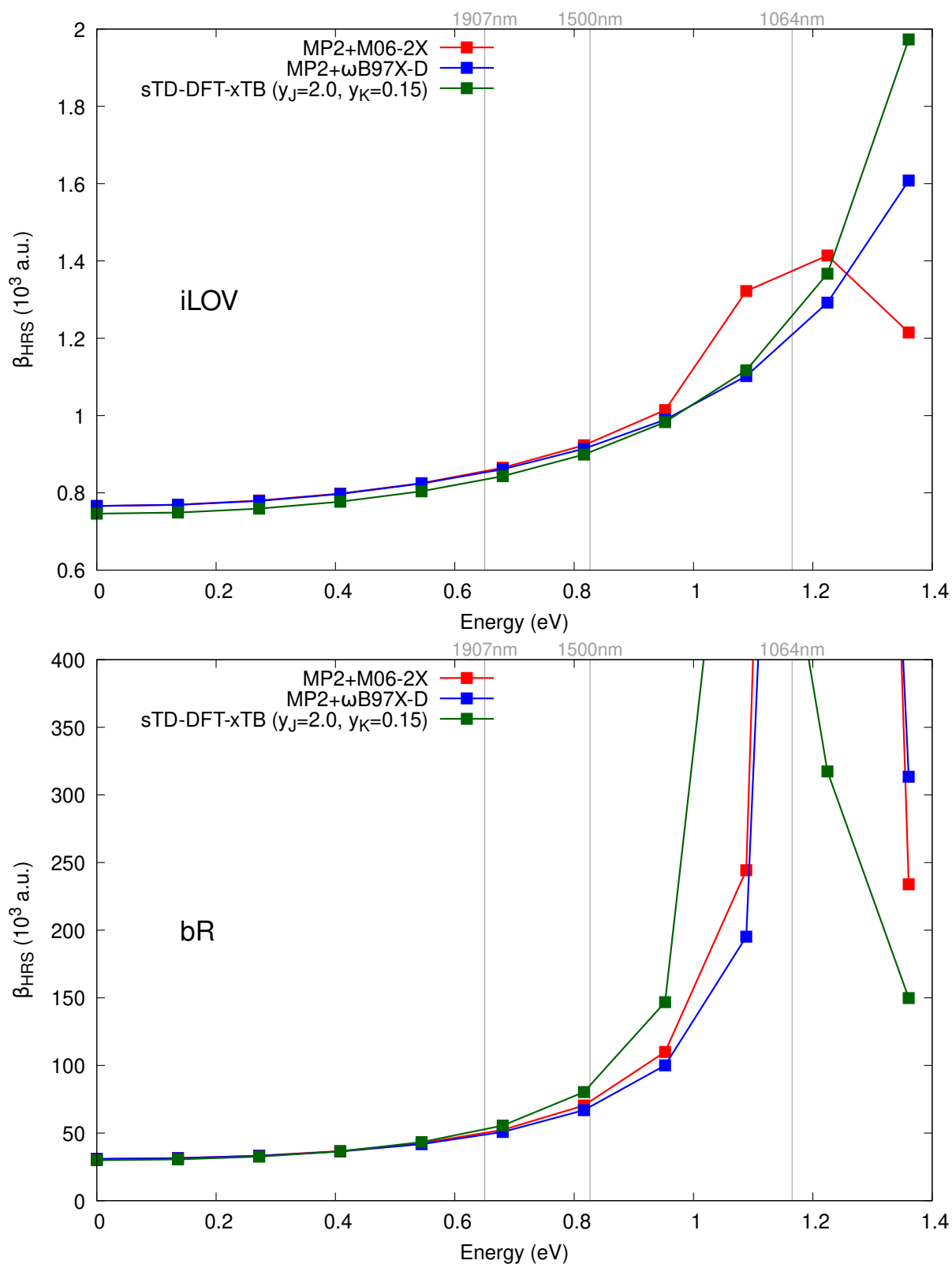


Figure B.5: Frequency dispersions of the β_{HRS} of the chromophore (C) of iLOV (top) and bR (bottom) in gas phase, at the MP2/6-31+G* level scaled with the ω B97X-D (blue) and M06-2X (red) frequency dispersions, in comparison with the sTD-DFT-XTB level (orange) method with the optimized parameters of $y_J = 2.0$ and $y_K = 0.15$ (and 10 eV for the threshold).

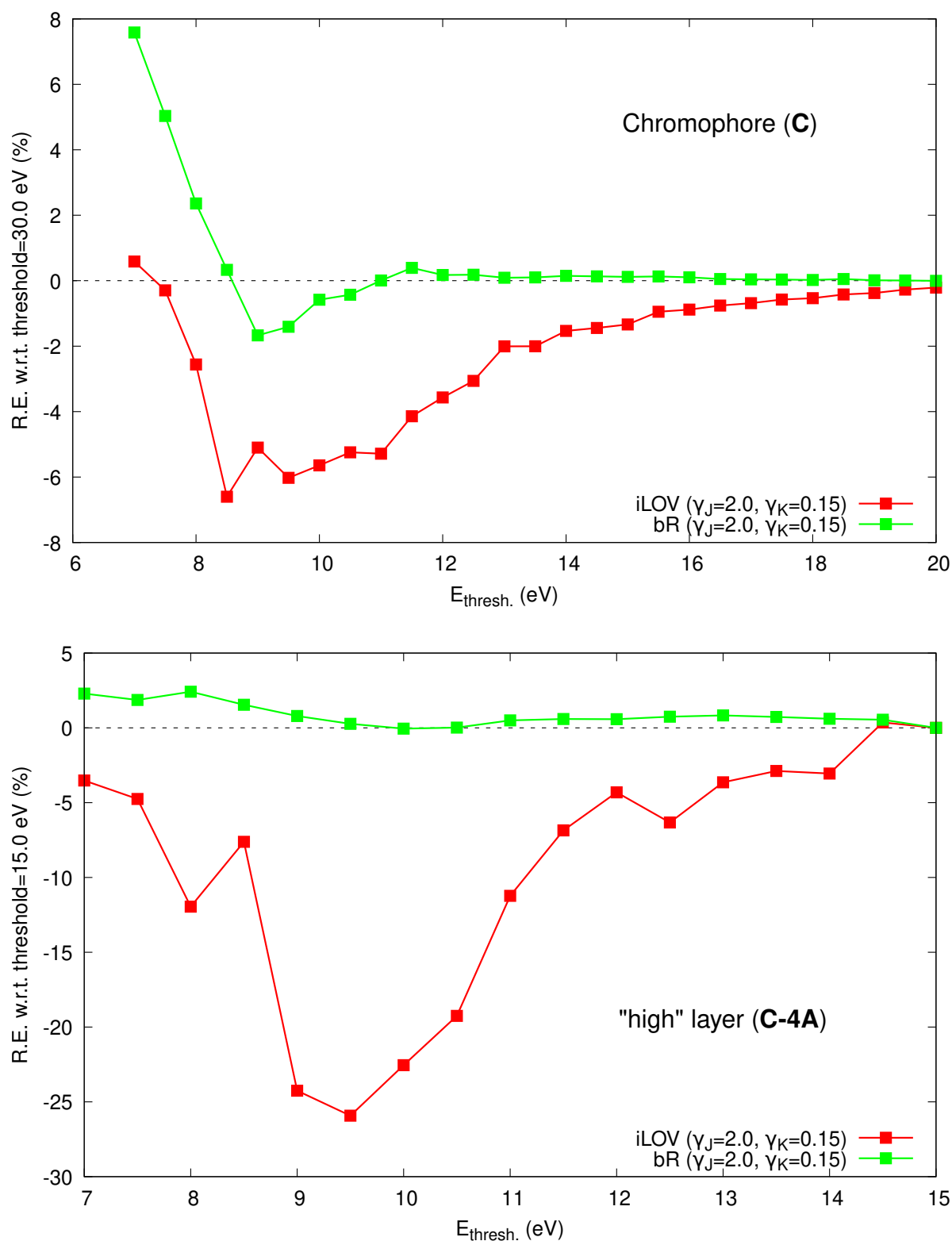


Figure B.6: Relative errors (R.E.) on the static β_{HRS} computed at the sTD-DFT-xTB level (with $y_J = 2.0$ and $y_K = 0.15$) for the chromophore (C, top) and the ONIOM "high" layer (C-4A, bottom) with different $E_{thresh.}$ value for the truncation of the CI space, with respect to the one obtained with the large threshold of 30 eV for C and 15 eV for C-4A.

Table B.2: Static and dynamic (laser energy in eV) β_{HRS} (in 10^3 a.u., DR in parentheses) of the chromophore (**C**), its surroundings (**4A**, with extra hydrogens to saturate bonds), **C-4A** (the ONIOM high layer, with extra hydrogens to saturate bonds) and the whole protein (**P-EW**), as computed at the sTD-DFT-xTB level (with $y_j = 2.0$, $y_K = 0.15$) in water (GBSA) with a threshold value of 10 eV for iLOV and 9 eV for bR.

	iLOV				bR			
	C	4A	C-4A	P-EW	C	4A	C-4A	P-EW
static	1.09 (4.8)	0.16 (2.3)	1.37 (6.2)	1.11 (3.6)	17.32 (4.7)	0.67 (6.0)	21.08 (4.9)	23.43 (5.0)
0.136	1.10 (4.8)	0.16 (2.3)	1.38 (6.2)	1.12 (3.6)	17.63 (4.7)	0.67 (6.0)	21.49 (4.9)	23.90 (5.0)
0.272	1.12 (4.8)	0.17 (2.3)	1.40 (6.3)	1.14 (3.6)	18.61 (4.8)	0.68 (5.9)	22.82 (4.9)	25.37 (5.0)
0.408	1.16 (4.9)	0.17 (2.3)	1.45 (6.3)	1.17 (3.7)	20.43 (4.8)	0.69 (5.9)	25.32 (4.9)	28.17 (5.0)
0.544	1.21 (4.9)	0.17 (2.3)	1.52 (6.3)	1.22 (3.8)	23.50 (4.8)	0.71 (5.9)	29.60 (4.9)	32.98 (5.0)
0.680	1.28 (5.0)	0.17 (2.3)	1.63 (6.3)	1.30 (3.9)	28.64 (4.8)	0.73 (5.9)	36.98 (4.9)	41.31 (5.0)
0.816	1.39 (5.1)	0.18 (2.3)	1.77 (6.3)	1.41 (4.0)	37.81 (4.8)	0.77 (5.9)	50.79 (4.9)	57.12 (5.0)
0.952	1.53 (5.1)	0.18 (2.3)	1.99 (6.2)	1.58 (4.2)	56.80 (4.8)	0.81 (5.8)	82.06 (4.9)	93.78 (5.0)
1.088	1.75 (5.1)	0.19 (2.3)	2.32 (5.9)	1.87 (4.3)	111.99 (4.8)	0.87 (5.8)	198.20 (4.9)	241.74 (4.9)
1.225	2.11 (4.9)	0.19 (2.3)	2.92 (5.4)	2.45 (4.2)	1045.16 (4.7)	0.94 (5.7)	808.01 (4.8)	621.09 (4.8)
1.361	2.82 (4.4)	0.20 (2.3)	4.31 (4.4)	4.19 (3.7)	173.34 (4.5)	1.04 (5.7)	161.58 (4.7)	162.63 (4.7)

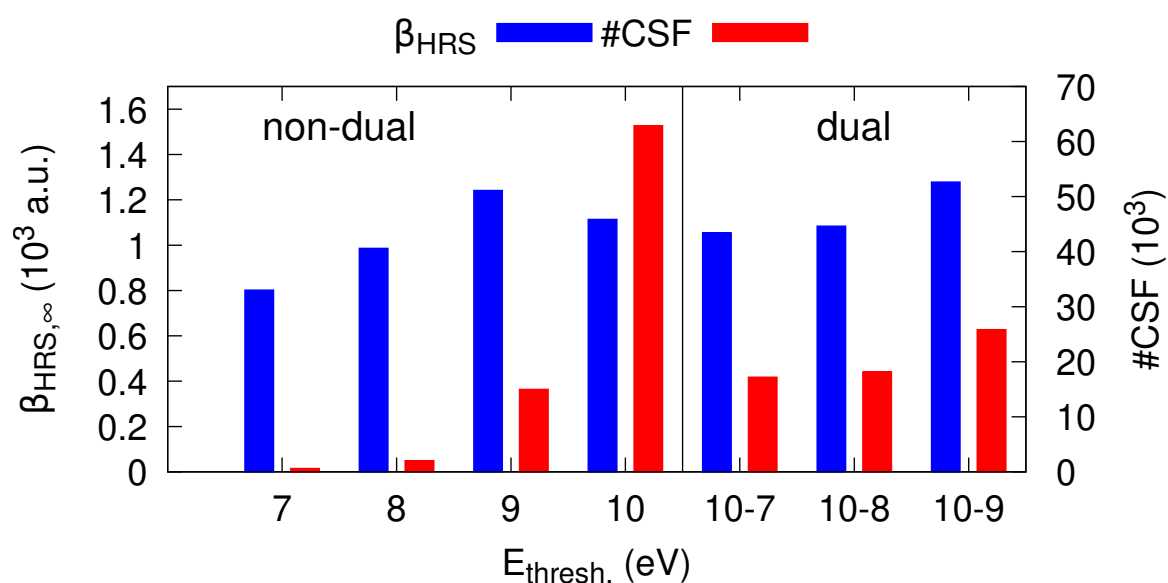


Figure B.7: For iLOV, the influence of $E_{\text{thresh.}}$ on the static β_{HRS} , as computed at the sTD-DFT-xTB level of theory (with $y_J = 2.0$ and $y_K = 0.15$) in water (GBSA), and corresponding CSFs. For the dual threshold scheme for which the high layer contains the chromophore and all tyrosine and tryptophan residues, the first number indicates E_{High} and the second E_{Low} .

Section B.3

Extrapolating the experimental β_{HRS} frequency dispersion to the static limit for the bacteriorhodopsin

The common way to extrapolate the static β_{HRS} from experimental dynamic values is to use the two-state approximation^{13,14} with an homogenous broadening. In that case, the UV-Vis absorption shape is represented by an homogenous Lorentzian distribution:

$$Abs(\omega) \propto \frac{1}{\pi} \frac{\omega_{eg} \gamma_h}{(\omega - \omega_{eg})^2 + \gamma_h^2}, \quad (B.1)$$

where γ_h represents the homogenous broadening and $\omega_{eg} = \omega_e - \omega_g$. The β_{HRS} frequency dispersion is obtained as:

$$\left| \frac{\beta_{HRS}(-2\omega; \omega, \omega)}{\beta_{HRS}(0; 0, 0)} \right| = \left| \frac{\omega_{ge}^2 (\omega_{ge} - i\gamma_h)^2}{[(\omega_{ge} - i\gamma_h)^2 - \omega^2][(\omega_{ge} - i\gamma_h)^2 - 4\omega^2]} \right|. \quad (B.2)$$

Following this, based on the seminal work of Otomo et al.,¹⁵ different schemes^{16–18} were proposed to account for the inhomogeneous broadening of the absorption spectra and its impact over the frequency dispersion. In this contribution, we propose a simpler approach that we called the simple vibronic model (SVM) where the absorption shape is modeled by a sum of vibronic contributions, each of them being described by a homogenous Lorentzian distribution:

$$Abs(\omega) \propto \sum_n^{vib} \frac{S^n e^{-S}}{n!} \frac{1}{\pi} \frac{\omega_n G}{(\omega - \omega_n)^2 + G^2}, \quad (B.3)$$

where G is the homogenous broadening for each vibrational (normal) mode, $\omega_n = \omega_{ge} + n\omega_{vib}$, and S is the Huang-Rhys factor (the coupling constant between the excited state and vibrational modes). Then, the SVM β_{HRS} frequency dispersion reads as:

$$\left| \frac{\beta_{HRS}(-2\omega; \omega, \omega)}{\beta_{HRS}(0; 0, 0)} \right| = \sqrt{\sum_n^{vib} \frac{S^n e^{-S}}{n!} \left| \frac{\omega_n^2 (\omega_n - iG)^2}{((\omega_n - iG)^2 - 4\omega^2)((\omega_n - iG)^2 - \omega^2)} \right|^2}. \quad (B.4)$$

The fluorescence-free β_{HRS} spectrum for the bacteriorhodopsin was recorded by Clays and coworkers.¹⁹ Note that the experimental β_{zzz} values were converted to β_{HRS} by multiplying by $\sqrt{6/35}$, after the conversion to a.u., and after correcting the data from the B to the T convention. To apply the SVM to extract the static β_{HRS} from the experimental value at 1300 nm, the experimental absorption spectrum was fitted by Equation (B.3) (Figure B.8) with $\omega_{ge} = 2.21$ eV, $G = 1400$ cm⁻¹, $S = 0.5$, and $\omega_{vib} = 0.15$ eV. From Equation (B.4), we obtained a static β_{HRS} value of 29.5×10^3 a.u. not so far from the computed sTD-DFT-xTB value of 23.4×10^3 a.u.. Note that the three lower energy β_{HRS} values as well as the two higher ones are particularly well reproduced by the SVM.

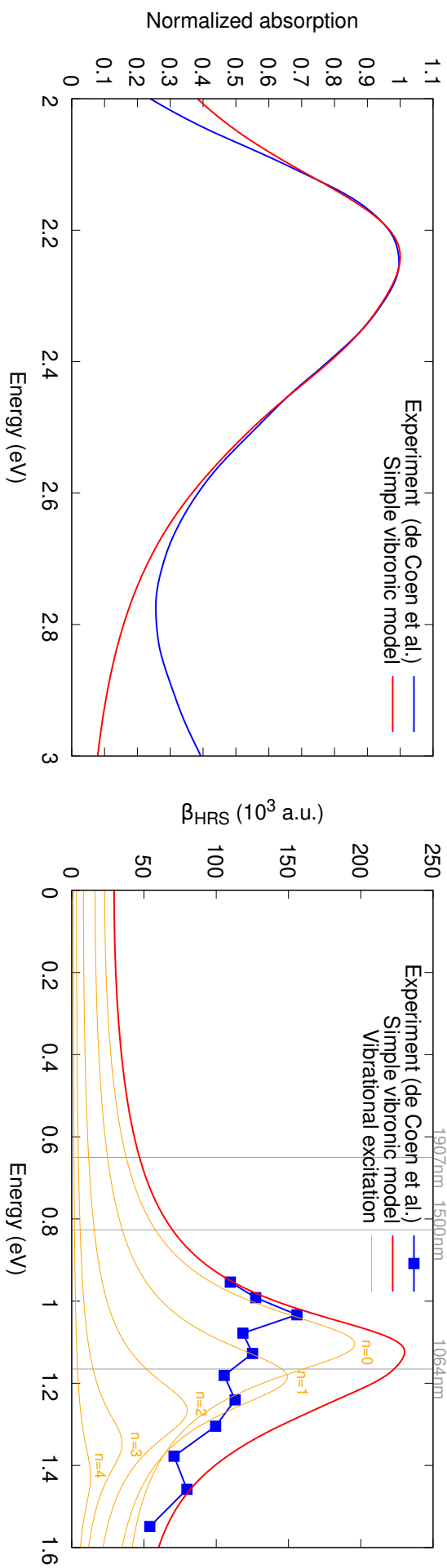


Figure B.8: For the bacteriorhodopsin, experimental normalized absorption fitted by the SVM (left) as well as β_{HRS} frequency dispersions obtained experimentally¹⁹ and extrapolated to the static limit by the SVM (right). Contributions from the 5 first successive vibrational excitations (orange curves) to the SVM are also displayed.

Bibliography

- [1] Bannwarth, C.; Ehlert, S.; Grimme, S. GFN2-xTB—An Accurate and Broadly Parametrized Self-Consistent Tight-Binding Quantum Chemical Method with Multipole Electrostatics and Density-Dependent Dispersion Contributions. *J. Chem. Theory Comput.* **2019**, *15*, 1652–1671.
- [2] Ehlert, S.; Bannwarth, C.; Grimme, S. Semiempirical Extended Tight-Binding Program Package xtb, version 6.2.2. <https://github.com/grimme-lab/xtb/>, Accessed: 2019-12-19. See also xTB documentation at <https://xtb-docs.readthedocs.io/en/latest/>.
- [3] Still, W. C.; Tempczyk, A.; Hawley, R. C.; Hendrickson, T. Semianalytical Treatment of Solvation for Molecular Mechanics and Dynamics. *J. Am. Chem. Soc.* **1990**, *112*, 6127–6129.
- [4] Schmitz, S.; Seibert, J.; Ostermeir, K.; Hansen, A.; Göller, A. H.; Grimme, S. Quantum Chemical Calculation of Molecular and Periodic Peptide and Protein Structures. *J. Phys. Chem. B* **2020**, *124*, 3636–3646.
- [5] Frisch, M. J. et al. Gaussian 16 Revision A.03. 2016; Gaussian Inc. Wallingford CT.
- [6] Bannwarth, C.; Caldeweyher, E.; Ehlert, S.; Hansen, A.; Pracht, P.; Seibert, J.; Spicher, S.; Grimme, S. Extended tightbinding quantum chemistry methods. *Wiley Interdiscip. Rev. Comput. Mol. Sci.* **2020**, *11*, e01493.
- [7] Grant, B.; Rodrigues, A.; ElSawy, K.; McCammon, J.; Caves, L. Bio3D: An R package for the comparative analysis of protein structures. *Bioinformatics* **2006**, *22*, 2695–2696.
- [8] Cardoso Ramos, F.; Cupellini, L.; Mennucci, B. Computational Investigation of Structural and Spectroscopic Properties of LOV-Based Proteins with Improved Fluorescence. *J. Phys. Chem. B* **2021**, *125*, 1768–1777.
- [9] Mohammed, A. A. K.; Limacher, P. A.; Champagne, B. Finding Optimal Finite Field Strengths Allowing for a Maximum of Precision in the Calculation of Polarizabilities and Hyperpolarizabilities. *J. Comp. Chem.* **2013**, *34*, 1497–1507.
- [10] de Wergifosse, M.; Liégeois, V.; Champagne, B. Evaluation of the Molecular Static and Dynamic First Hyperpolarizabilities. *Int. J. Quantum Chem.* **2014**, *114*, 900–910.
- [11] Sekino, H.; Bartlett, R. J. Hyperpolarizabilities of Molecules with Frequency Dependence and Electron Correlation. *J. Chem. Phys.* **1991**, *94*, 3665–3669.
- [12] Sekino, H.; Bartlett, R. J. Molecular Hyperpolarizabilities. *J. Chem. Phys.* **1993**, *98*, 3022–3037.

- [13] Orr, B.; Ward, J. Perturbation Theory of the Non-Linear Optical Polarization of an Isolated System. *Mol. Phys.* **1971**, *20*, 513–526.
- [14] Oudar, J. L.; Chemla, D. S. Hyperpolarizabilities of the Nitroanilines and Their Relations to the Excited State Dipole Moment. *J. Chem. Phys.* **1977**, *66*, 2664–2668.
- [15] Otomo, A.; Stegeman, G. I.; Flipse, M. C.; Diemeer, M. B. J.; Horsthuis, W. H. G.; Möhlmann, G. R. Nonlinear Contrawave Mixing Devices in Poled-Polymer Waveguides. *J. Opt. Soc. Am. B* **1998**, *15*, 759.
- [16] Berkovic, G.; Meshulam, G.; Kotler, Z. Measurement and Analysis of Molecular Hyperpolarizability in the Two-Photon Resonance Regime. *J. Chem. Phys.* **2000**, *112*, 3997–4003.
- [17] Campo, J.; Wenseleers, W.; Hales, J. M.; Makarov, N. S.; Perry, J. W. Practical Model for First Hyperpolarizability Dispersion Accounting for Both Homogeneous and Inhomogeneous Broadening Effects. *J. Phys. Chem. Lett.* **2012**, *3*, 2248–2252.
- [18] Campo, J.; Wenseleers, W.; Goovaerts, E.; Szablewski, M.; Cross, G. H. Accurate Determination and Modeling of the Dispersion of the First Hyperpolarizability of an Efficient Zwitterionic Nonlinear Optical Chromophore by Tunable Wavelength Hyper-Rayleigh Scattering. *J. Phys. Chem. C* **2008**, *112*, 287–296.
- [19] de Coene, Y.; Van Cleuvenbergen, S.; Van Steerteghem, N.; Baekelandt, V.; Verbiest, T.; Bartic, C.; Clays, K. Fluorescence-Free Spectral Dispersion of the Molecular First Hyperpolarizability of Bacteriorhodopsin. *J. Phys. Chem. C* **2017**, *121*, 6909–6915.

Supporting information of Chapter 11

Abstract

This appendix (which refers to Chapter 11 in page 273) contains i) the evolution of the different components with the CT mixing character (m_{CT}) for all models, ii) synoptic tables, which gather the expressions (for $n \in [1, 3]$) of the components for the different parameterizations of the CT character, and iii) the evolution of the $M(m_{CT})$ and $\Theta(\theta)$ parts of these components.

The evolution of the relevant quantities are plotted in the following Figures:

- for the 2-state model, in figures C.1-C.2,
- for the 3-state model, in Figures C.3-C.5,
- for the 4-state model, in Figures C.6-C.8, and
- for the 5-state model, in Figure C.9.

The expressions of the different energies and (transition or difference of) dipole moments are reported in Tables C.1-C.3 for the δ , ℓ_{CT} and m_{CT} parameterizations, respectively. Finally, Figures C.10 and C.11 report the evolution of $M(m_{CT})$ and $\Theta(\theta)$ to support the discussion.

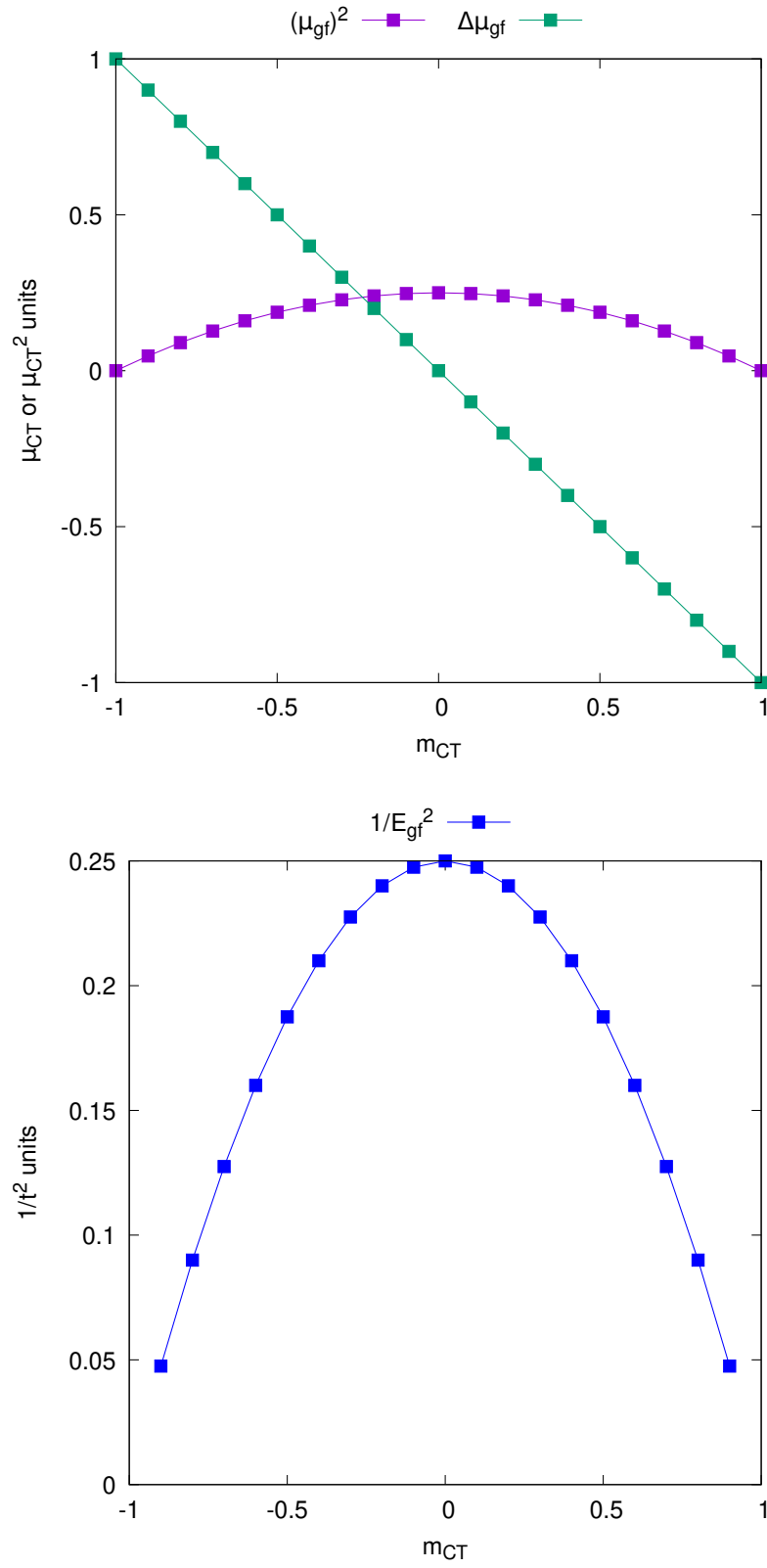


Figure C.1: Evolution of the different quantities involved in β of a 2-state model as a function of m_{CT} .

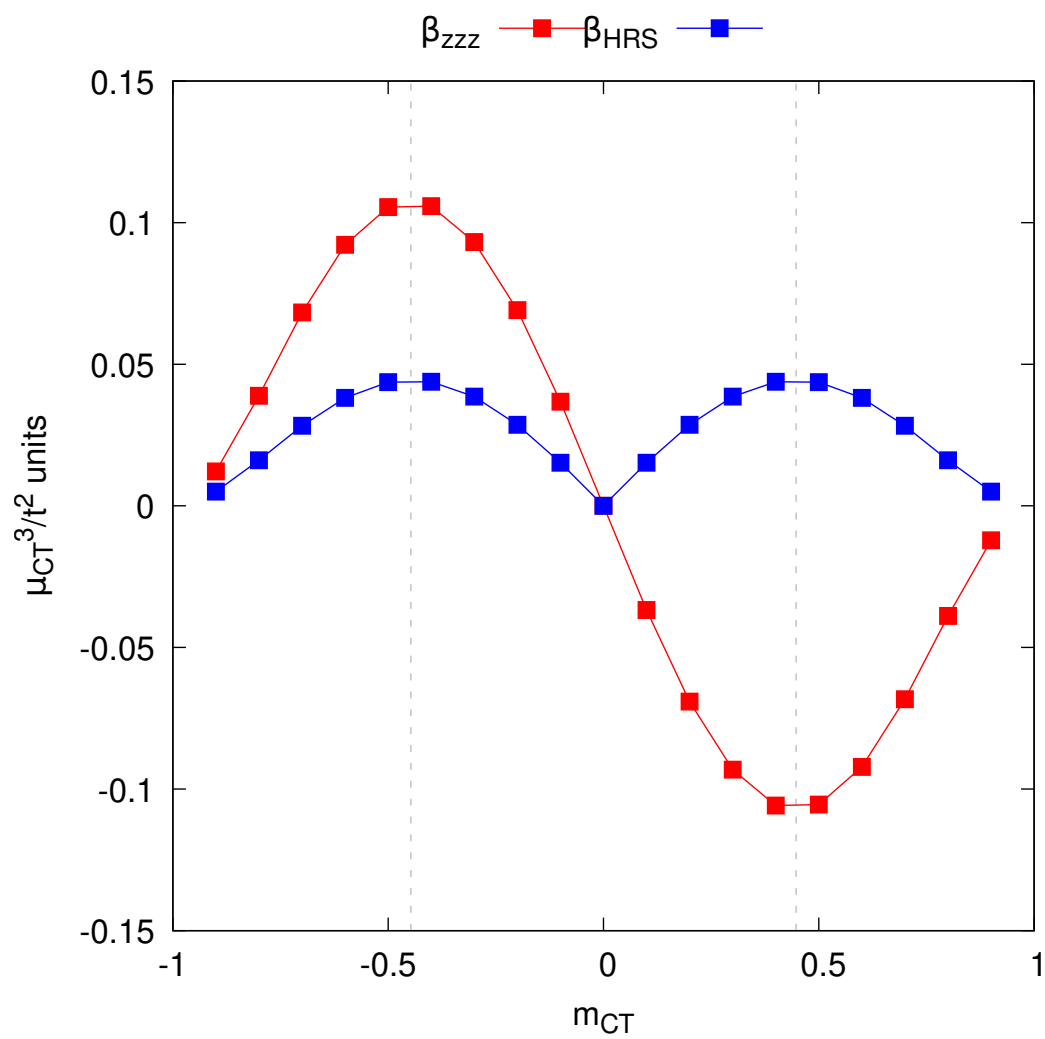


Figure C.2: Evolution of β as a function of m_{CT} for a 2-state model.

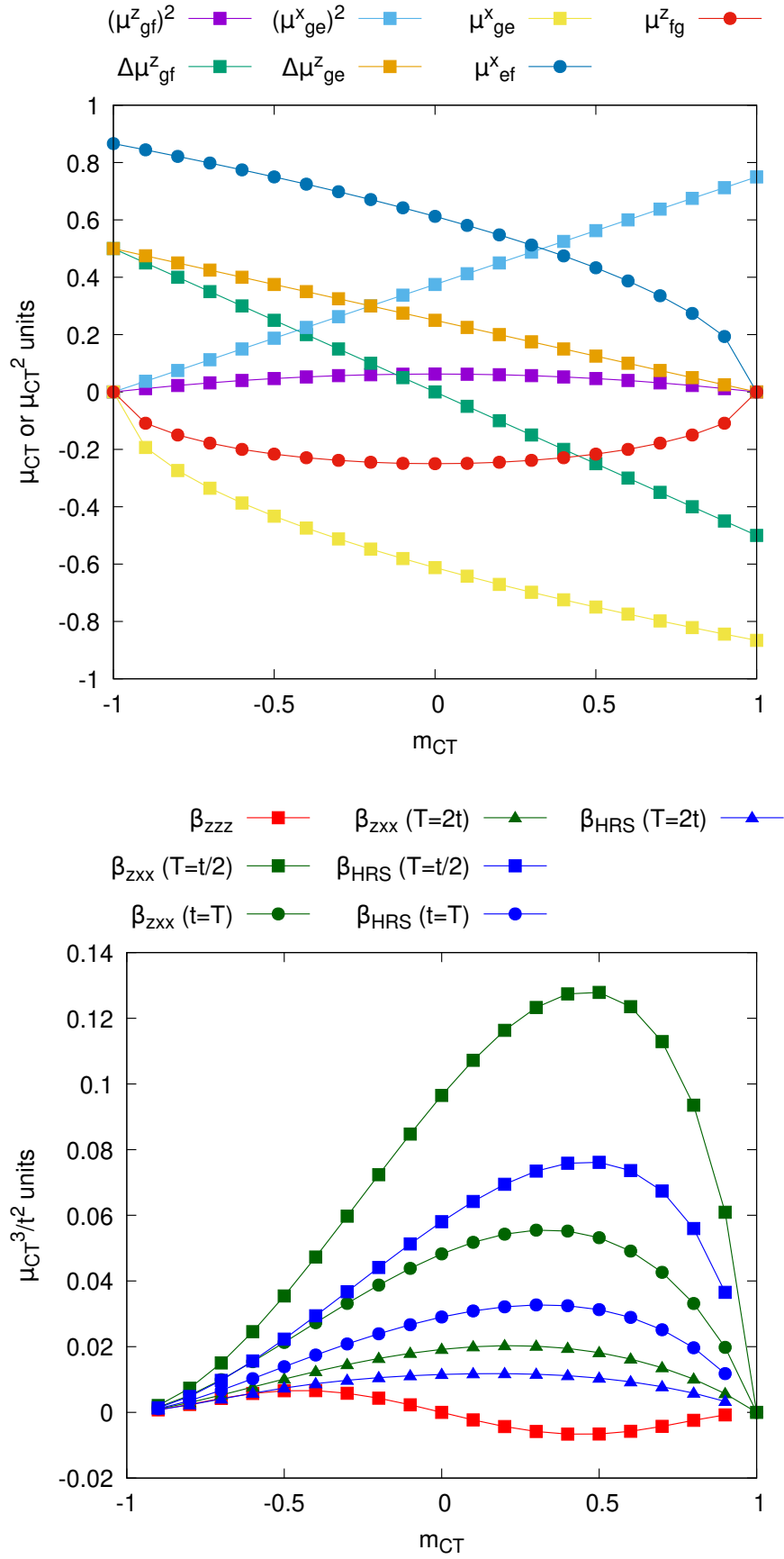


Figure C.3: Evolution of the different quantities as a function of m_{CT} for a 3-state model (with $\theta = 60^\circ$).

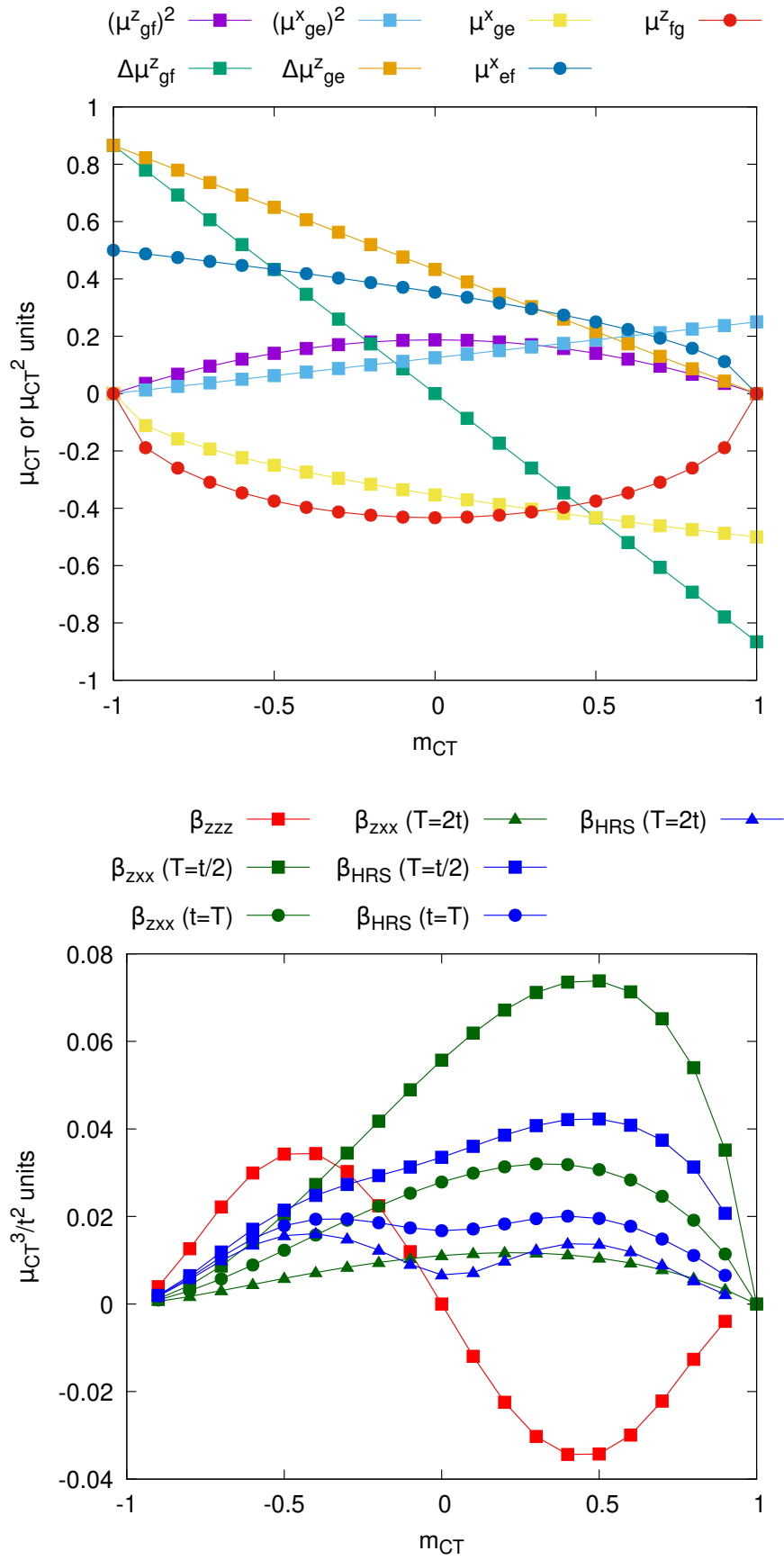


Figure C.4: Evolution of the different quantities as a function of m_{CT} for a 3-state model (with $\theta = 30^\circ$).

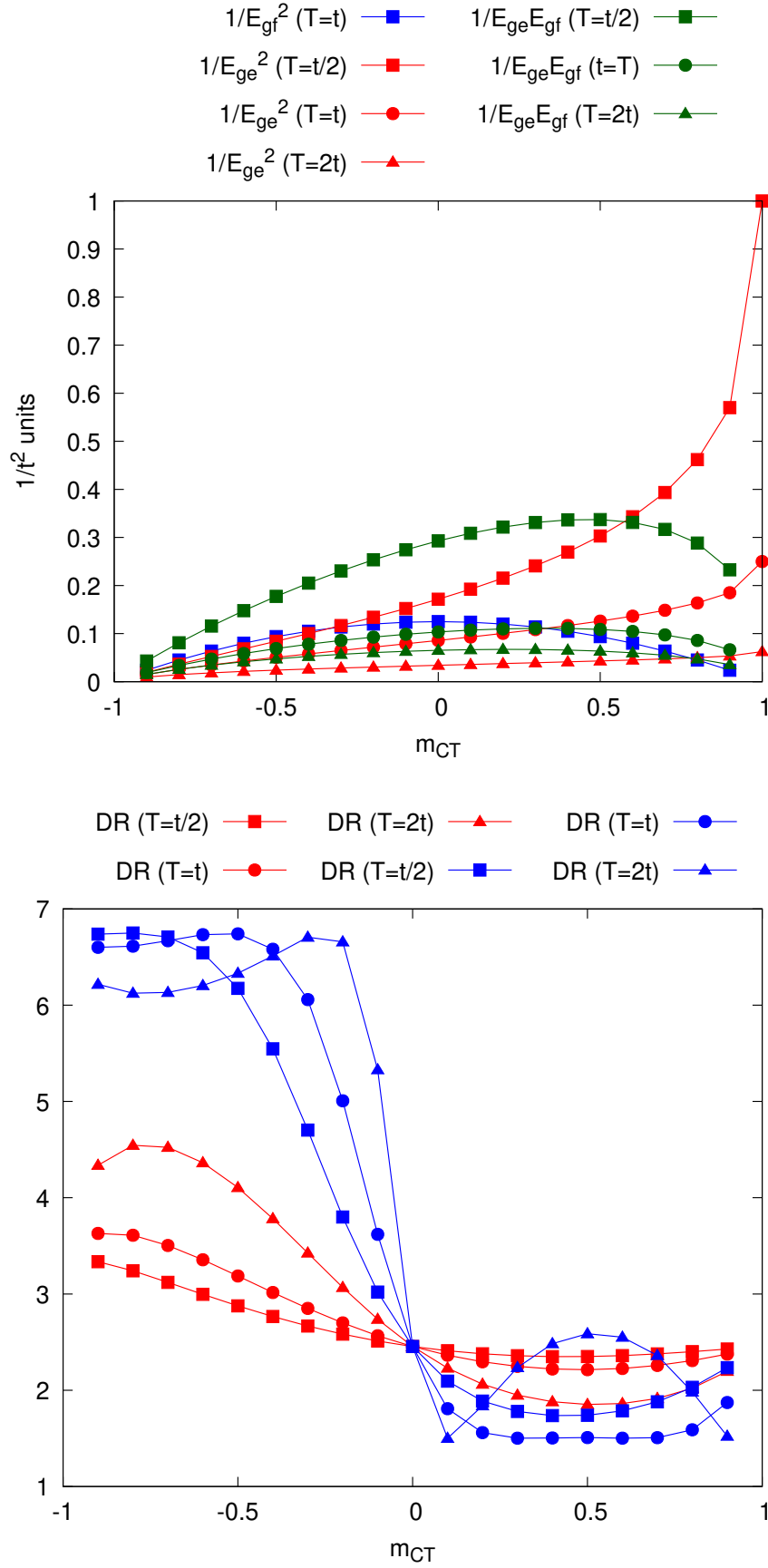


Figure C.5: Evolution of the inverse of the excitation energies (top) and of DR (bottom) as a function of m_{CT} for a 3-state model (with $\theta = 60^\circ$).

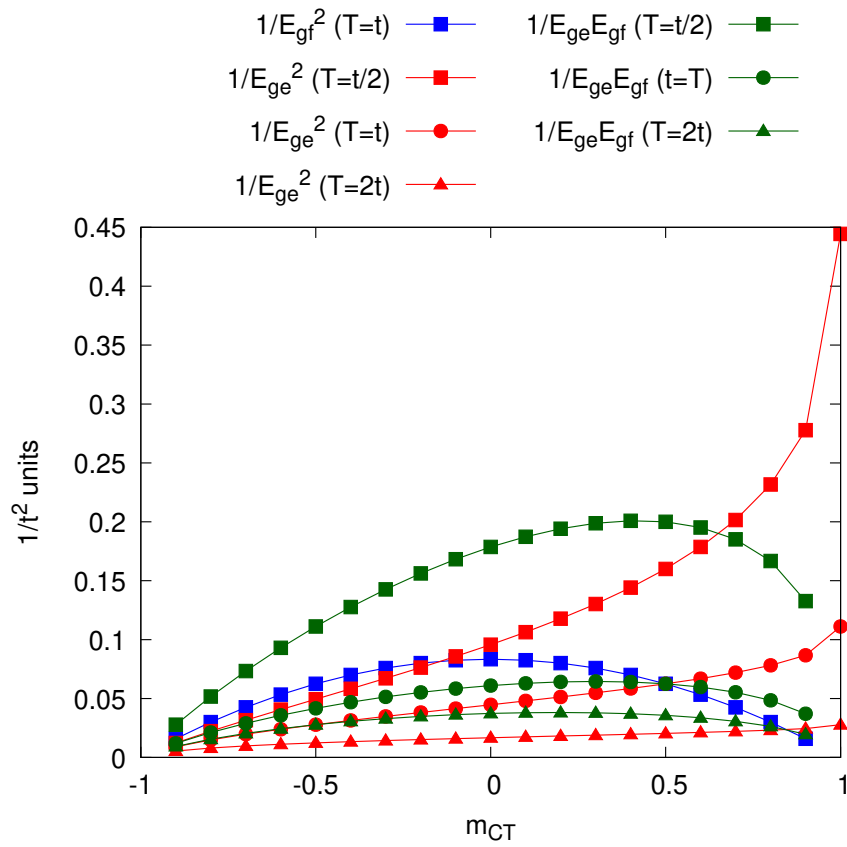


Figure C.6: Evolution of the inverse of the excitation energies as a function of m_{CT} for a 4-state model.

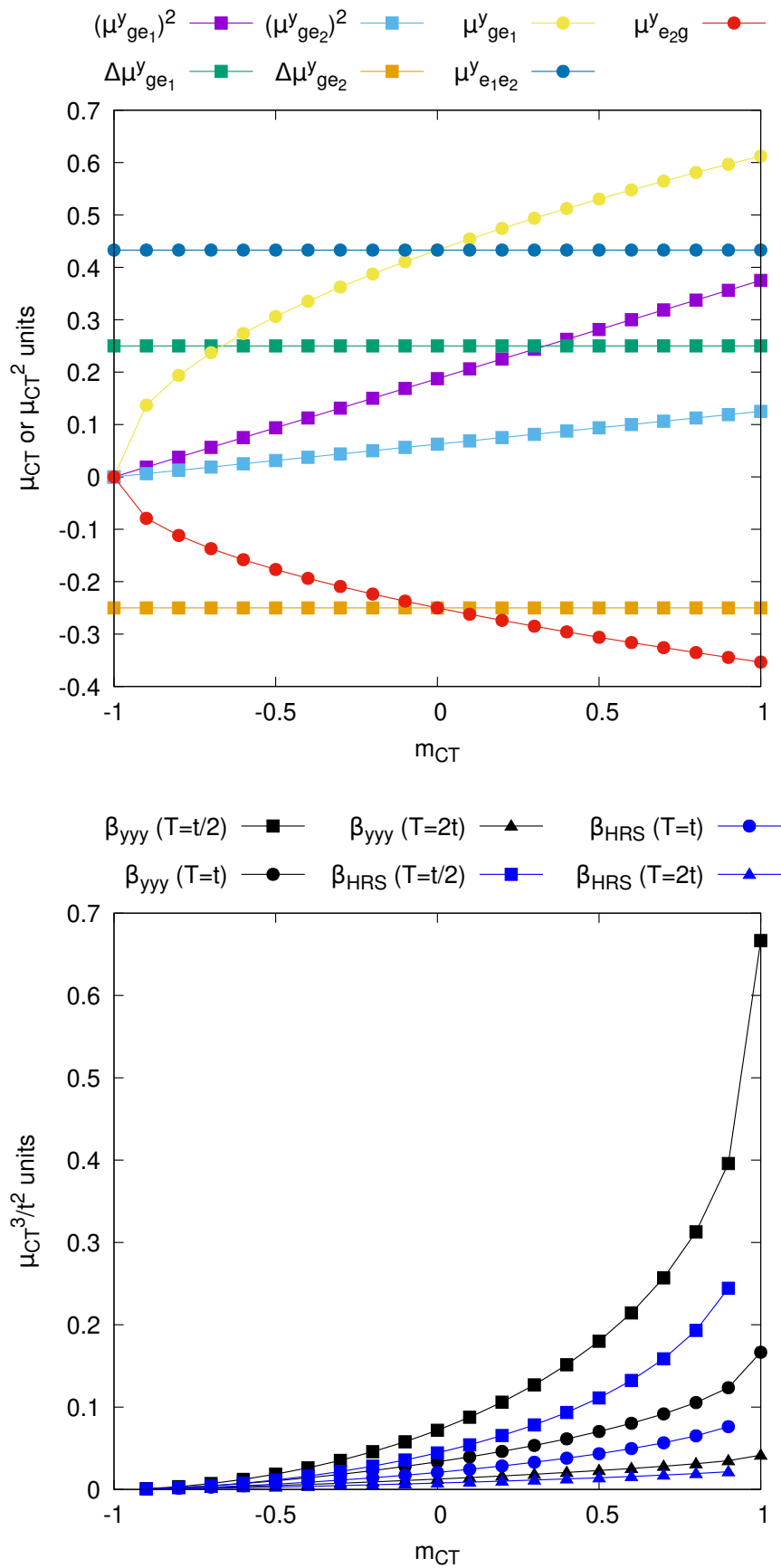


Figure C.7: Evolution of the transition dipole moments (top) and first hyperpolarizabilities (bottom) as a function of m_{CT} for a 4-state model ($\theta = 90^\circ$).

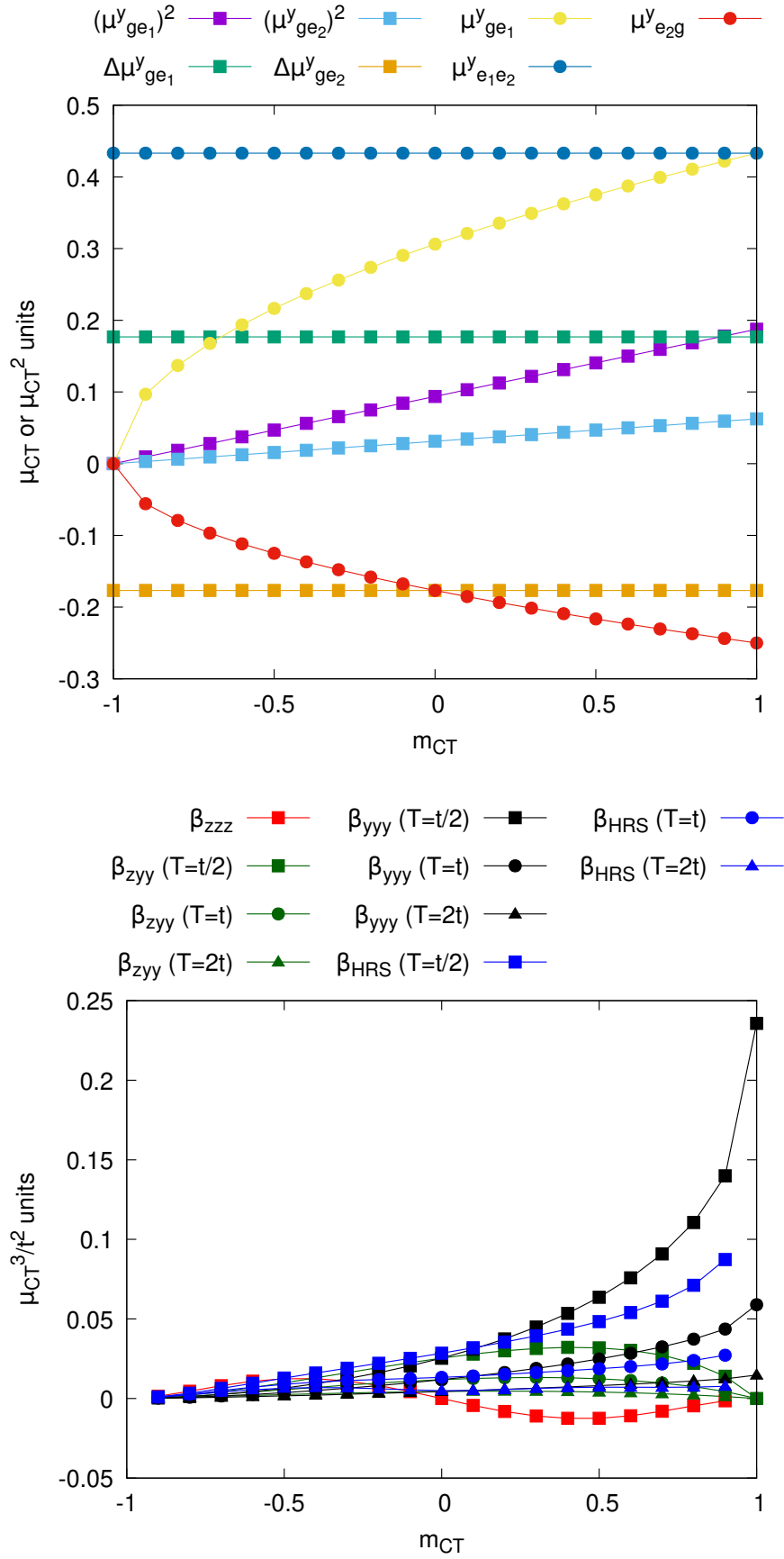


Figure C.8: Evolution of the transition dipole moments (top) and first hyperpolarizabilities (bottom) as a function of m_{CT} for a 4-state model ($\theta = 45^\circ$).

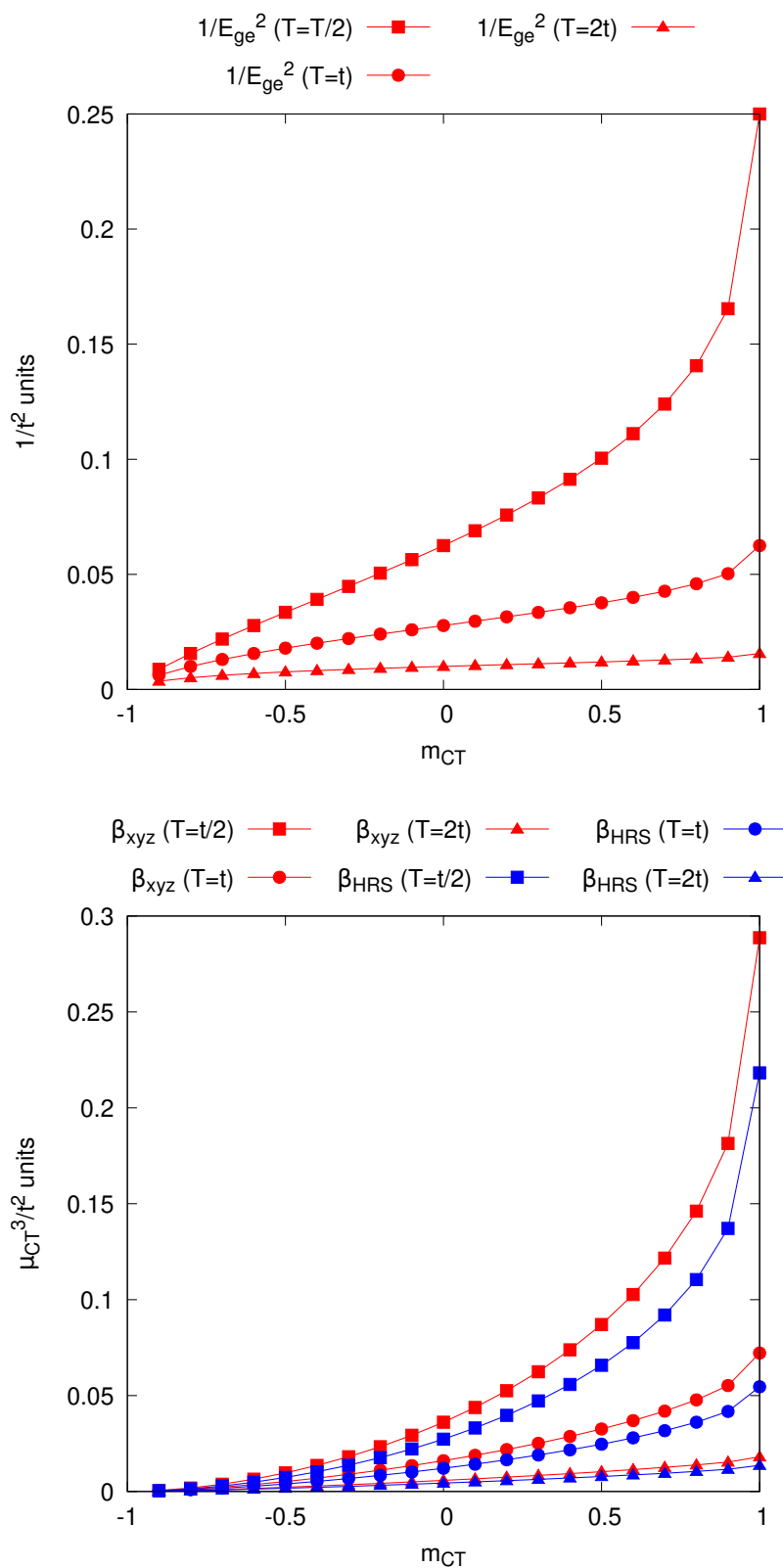


Figure C.9: Evolution of the inverse of the excitation energies (top) and first hyperpolarizabilities (bottom) with m_{CT} of the 5-state model.

	n=1	n=2	n=3
$ \Psi_g\rangle$	$\sqrt{\cos \delta} \psi_{VB}\rangle + \sin \delta \psi_{CT}\rangle$	$\cos \delta \psi_{VB}\rangle + \frac{\sin \delta}{\sqrt{2}} (\psi_{CT,1}\rangle + \psi_{CT,2}\rangle)$	$\cos \delta \psi_{VB}\rangle + \frac{\sin \delta}{\sqrt{3}} (\psi_{CT,1}\rangle + \psi_{CT,2}\rangle + \psi_{CT,3}\rangle)$
$ \Psi_{e_1}\rangle$	—	$\frac{1}{\sqrt{2}} (\psi_{CT,2}\rangle - \psi_{CT,1}\rangle)$	$\frac{1}{\sqrt{2}} (\psi_{CT,2}\rangle - \psi_{CT,1}\rangle)$
$ \Psi_{e_2}\rangle$	—	—	$\frac{1}{\sqrt{6}} (2 \psi_{CT,3}\rangle - \psi_{CT,2}\rangle - \psi_{CT,1}\rangle)$
$ \Psi_f\rangle$	$\sin \delta \psi_{VB}\rangle - \cos \delta \psi_{CT}\rangle$	$\sin \delta \psi_{VB}\rangle - \frac{\cos \delta}{\sqrt{2}} (\psi_{CT,1}\rangle + \psi_{CT,2}\rangle)$	$\sin \delta \psi_{VB}\rangle - \frac{\cos \delta}{\sqrt{3}} (\psi_{CT,1}\rangle + \psi_{CT,2}\rangle + \psi_{CT,3}\rangle)$
E_g	$-\frac{t}{\sin(2\delta)}$	$-\sqrt{2} \frac{t}{\sin(2\delta)}$	$-\sqrt{3} \frac{t}{\sin(2\delta)}$
E_e	—	$2T + t \sqrt{2} \cot(2\delta)$	$3T + t \sqrt{3} \cot(2\delta)$
E_f	$\frac{t}{\sin(2\delta)}$	$\sqrt{2} \frac{t}{\sin(2\delta)}$	$\sqrt{3} \frac{t}{\sin(2\delta)}$
E_{ge}	—	$t \sqrt{2} \cot(\delta) + 2T$	$t \sqrt{3} \cot(\delta) + 3T$
E_{gf}	$\frac{2t}{\sin(2\delta)}$	$\frac{2t\sqrt{2}}{\sin(2\delta)}$	$\frac{2t\sqrt{3}}{\sin(2\delta)}$
$\mu_{e_1} - \mu_g$	—	$\mu_{CT} \cos^2 \delta (0, 0, \cos \theta)$	$\mu_{CT} \left(\frac{\sqrt{3}}{4} \sin \theta, \frac{1}{4} \sin \theta, \cos^2 \delta \cos \theta \right)$
$\mu_{e_2} - \mu_g$	—	—	$\mu_{CT} \left(-\frac{\sqrt{3}}{4} \sin \theta, -\frac{1}{4} \sin \theta, \cos^2 \delta \cos \theta \right)$
$\mu_f - \mu_g$	$\mu_{CT} \cos(2\delta)$	$\mu_{CT} \cos(2\delta) (0, 0, \cos \theta)$	$\mu_{CT} \cos(2\delta) (0, 0, \cos \theta)$
μ_{ge_1}	—	$\mu_{CT} \sin \delta (-\sin \theta, 0, 0)$	$\frac{1}{4} \mu_{CT} \sin \delta (\sqrt{3} \sin \theta, -\sqrt{6} \sin \theta, 0)$
μ_{ge_2}	—	—	$\frac{\sqrt{2}}{4} \mu_{CT} \sin \delta (-\sqrt{3} \sin \theta, -\sin \theta, 0)$
μ_{gf}	$-\frac{1}{2} \mu_{CT} \sin(2\delta)$	$\frac{\mu_{CT}}{2} \sin(2\delta) (0, 0, -\cos \theta)$	$\frac{\mu_{CT}}{2} \sin(2\delta) (0, 0, -\cos \theta)$
$\mu_{e_1 e_2}$	—	—	$\frac{1}{4} \mu_{CT} (-\sin \theta, \sqrt{3} \sin \theta, 0)$
$\mu_{e_1 f}$	—	$\mu_{CT} \cos \delta (\sin \theta, 0, 0)$	$\frac{\sqrt{2}}{4} \mu_{CT} \cos \delta (-\sin \theta, \sqrt{3} \sin \theta, 0)$
$\mu_{e_2 f}$	—	—	$\frac{\sqrt{2}}{4} \mu_{CT} \cos \delta (\sqrt{3} \sin \theta, \sin \theta, 0)$

Table C.1: Synoptic table for the $n = 1, 2$ and 3 models with the δ parameterization.

	n=1	n=2	n=3
$ \Psi_g\rangle$	$\sqrt{1-\ell_{CT}} \psi_{VB}\rangle + \sqrt{\ell_{CT}} \psi_{CT}\rangle$	$\sqrt{1-2\ell_{CT}} \psi_{VB}\rangle + \sqrt{\ell_{CT}}(\psi_{CT,1}\rangle + \psi_{CT,2}\rangle)$	$\sqrt{1-3\ell_{CT}} \psi_{VB}\rangle$ $+ \sqrt{\ell_{CT}}(\psi_{CT,1}\rangle + \psi_{CT,2}\rangle + \psi_{CT,3}\rangle)$ $\frac{1}{\sqrt{2}}(\psi_{CT,2}\rangle - \psi_{CT,1}\rangle)$ $\frac{1}{\sqrt{6}}(2 \psi_{CT,3}\rangle - \psi_{CT,2}\rangle - \psi_{CT,1}\rangle)$
$ \Psi_{e_1}\rangle$	—	$\frac{1}{\sqrt{2}}(\psi_{CT,2}\rangle - \psi_{CT,1}\rangle)$	—
$ \Psi_{e_2}\rangle$	—	—	—
$ \Psi_f\rangle$	$\sqrt{\ell_{CT}} \psi_{VB}\rangle - \sqrt{1-\ell_{CT}} \psi_{CT}\rangle$	$\sqrt{1-2\ell_{CT}} \psi_{VB}\rangle - \sqrt{\frac{1}{2}-\ell_{CT}}(\psi_{CT,1}\rangle + \psi_{CT,2}\rangle)$	$\sqrt{1-3\ell_{CT}} \psi_{VB}\rangle$ $-\sqrt{\frac{1}{3}-\ell_{CT}}(\psi_{CT,1}\rangle + \psi_{CT,2}\rangle + \psi_{CT,3}\rangle)$
E_g	$-\frac{t}{2\sqrt{\ell_{CT}(1-\ell_{CT})}}$	$-\frac{t}{2\sqrt{\ell_{CT}(1-2\ell_{CT})}}$	$-\frac{t}{2\sqrt{\ell_{CT}(1-3\ell_{CT})}}$
E_e	—	$2T + \frac{t}{2\sqrt{\ell_{CT}(1-4\ell_{CT})}}$	$3T + \frac{t}{2\sqrt{\ell_{CT}(1-6\ell_{CT})}}$
E_f	$\frac{t}{2\sqrt{\ell_{CT}(1-\ell_{CT})}}$	$\frac{t}{2\sqrt{\ell_{CT}(1-2\ell_{CT})}}$	$\frac{t}{2\sqrt{\ell_{CT}(1-3\ell_{CT})}}$
E_{ge}	—	$2T + t\sqrt{\frac{1}{\ell_{CT}} - 2}$	$3T + t\sqrt{\frac{1}{\ell_{CT}} - 3}$
E_{gf}	$\frac{t}{\sqrt{\ell_{CT}(1-\ell_{CT})}}$	$\frac{t}{\sqrt{\ell_{CT}(1-2\ell_{CT})}}$	$\frac{t}{\sqrt{\ell_{CT}(1-3\ell_{CT})}}$
$\mu_{e_1} - \mu_g$	—	$(1-2\ell_{CT})\mu_{CT}(0, 0, \cos\theta)$	$\mu_{CT}\left(\frac{\sqrt{3}}{4}\sin\theta, \frac{1}{4}\sin\theta, (1-2\ell_{CT})\cos\theta\right)$
$\mu_{e_2} - \mu_g$	—	—	$\mu_{CT}\left(-\frac{\sqrt{3}}{4}\sin\theta, -\frac{1}{4}\sin\theta, (1-2\ell_{CT})\cos\theta\right)$
$\mu_f - \mu_g$	$(1-2\ell_{CT})\mu_{CT}$	$(1-4\ell_{CT})\mu_{CT}(0, 0, \cos\theta)$	$(1-6\ell_{CT})\mu_{CT}(0, 0, \cos\theta)$
μ_{ge_1}	—	$\sqrt{2\ell_{CT}}\mu_{CT}(-\sin\theta, 0, 0)$	$\frac{1}{4}\sqrt{3\ell_{CT}}\mu_{CT}(\sqrt{3}\sin\theta, -\sqrt{6}\sin\theta, 0)$
μ_{ge_2}	—	—	$\frac{\sqrt{2}}{4}\sqrt{3\ell_{CT}}\mu_{CT}(-\sqrt{3}\sin\theta, -\sin\theta, 0)$
μ_{gf}	$-\mu_{CT}\sqrt{\ell_{CT}(1-\ell_{CT})}$	$\sqrt{1-2\ell_{CT}}\mu_{CT}(\sin\theta, 0, 0)$	$\sqrt{3\ell_{CT}(1-3\ell_{CT})}\mu_{CT}(0, 0, -\cos\theta)$
$\mu_{e_1e_2}$	—	—	$\frac{1}{4}\mu_{CT}(-\sin\theta, \sqrt{3}\sin\theta, 0)$
μ_{e_1f}	—	$\sqrt{1-2\ell_{CT}}\mu_{CT}(\sin\theta, 0, 0)$	$\frac{\sqrt{2}}{4}\sqrt{1-3\ell_{CT}}\mu_{CT}(-\sin\theta, \sqrt{3}\sin\theta, 0)$
μ_{e_2f}	—	—	$\frac{\sqrt{2}}{4}\sqrt{1-3\ell_{CT}}\mu_{CT}(\sqrt{3}\sin\theta, \sin\theta, 0)$

Table C.2: Synoptic table for the $n = 1, 2$ and 3 models with the ℓ_{CT} parameterization.

	n=1	n=2	n=3
$ \Psi_g\rangle$	$\sqrt{\frac{1-m_{CT}}{2}} \psi_{VB}\rangle + \sqrt{\frac{1+m_{CT}}{2}} \psi_{CT}\rangle$	$\sqrt{\frac{1-m_{CT}}{2}} \psi_{VB}\rangle + \sqrt{\frac{1+m_{CT}}{4}} (\psi_{CT,1}\rangle + \psi_{CT,2}\rangle)$	$\sqrt{\frac{1-m_{CT}}{2}} \psi_{VB}\rangle$ $+ \sqrt{\frac{1+m_{CT}}{6}} (\psi_{CT,1}\rangle + \psi_{CT,2}\rangle + \psi_{CT,3}\rangle)$
$ \Psi_{e_1}\rangle$	—	$\frac{1}{\sqrt{2}} (\psi_{CT,2}\rangle - \psi_{CT,1}\rangle)$	$\frac{1}{\sqrt{2}} (\psi_{CT,2}\rangle - \psi_{CT,1}\rangle)$
$ \Psi_{e_2}\rangle$	—	—	$\frac{1}{\sqrt{6}} (2 \psi_{CT,3}\rangle - \psi_{CT,2}\rangle - \psi_{CT,1}\rangle)$
$ \Psi_f\rangle$	$\sqrt{\frac{1+m_{CT}}{2}} \psi_{VB}\rangle - \sqrt{\frac{1-m_{CT}}{2}} \psi_{CT}\rangle$	$\sqrt{\frac{1+m_{CT}}{2}} \psi_{VB}\rangle - \sqrt{\frac{1-m_{CT}}{4}} (\psi_{CT,1}\rangle + \psi_{CT,2}\rangle)$	$-\sqrt{\frac{1-m_{CT}}{6}} (\psi_{CT,1}\rangle + \psi_{CT,2}\rangle + \psi_{CT,3}\rangle)$
E_g	$-t \sqrt{\frac{1}{1-m_{CT}^2}}$	$-t \sqrt{\frac{2}{1-m_{CT}^2}}$	$-t \sqrt{\frac{3}{1-m_{CT}^2}}$
E_e	—	$2T - t \sqrt{2} \frac{m_{CT}}{\sqrt{1-m_{CT}^2}}$	$3T - t \sqrt{3} \frac{m_{CT}}{\sqrt{1-m_{CT}^2}}$
E_f	$t \sqrt{\frac{1}{1-m_{CT}^2}}$	$t \sqrt{\frac{2}{1-m_{CT}^2}}$	$t \sqrt{\frac{3}{1-m_{CT}^2}}$
E_{ge}	—	$2T + t \sqrt{2} \frac{1-m_{CT}}{1+m_{CT}}$	$3T + t \sqrt{3} \frac{1-m_{CT}}{1+m_{CT}}$
E_{gf}	$2t \sqrt{\frac{1}{1-m_{CT}^2}}$	$2t \sqrt{\frac{2}{1-m_{CT}^2}}$	$2t \sqrt{\frac{3}{1-m_{CT}^2}}$
$\mu_{e_1} - \mu_g$	—	$\frac{1-m_{CT}}{2} (0, 0, \cos \theta)$	$\mu_{CT} \left(\frac{\sqrt{3}}{4} \sin \theta, \frac{1}{4} \sin \theta, \frac{1-m_{CT}}{2} \cos \theta \right)$
$\mu_{e_2} - \mu_g$	—	—	$\mu_{CT} \left(-\frac{\sqrt{3}}{4} \sin \theta, -\frac{1}{4} \sin \theta, \frac{1-m_{CT}}{2} \cos \theta \right)$
$\mu_f - \mu_g$	$-m_{CT} \mu_{CT} \frac{\mu_{CT}}{2} \sqrt{1-m_{CT}^2} (0, 0, -\cos \theta)$	$-m_{CT} \mu_{CT} (0, 0, \cos \theta)$	$-m_{CT} \mu_{CT} (0, 0, \cos \theta)$
μ_{ge_1}	—	$\sqrt{\frac{1+m_{CT}}{2}} \mu_{CT} (-\sin \theta, 0, 0)$	$\frac{1}{4} \sqrt{\frac{1+m_{CT}}{2}} \mu_{CT} (\sqrt{3} \sin \theta, -\sqrt{6} \sin \theta, 0)$
μ_{ge_2}	—	—	$\frac{\sqrt{2}}{4} \sqrt{\frac{1+m_{CT}}{2}} \mu_{CT} (-\sqrt{3} \sin \theta, -\sin \theta, 0)$
μ_{gf}	$-\frac{\mu_{CT}}{2} \sqrt{1-m_{CT}^2}$	$\frac{\mu_{CT}}{2} \sqrt{1-m_{CT}^2} (0, 0, -\cos \theta)$	$\frac{\mu_{CT}}{2} \sqrt{1-m_{CT}^2} (0, 0, -\cos \theta)$
$\mu_{e_1 e_2}$	—	—	$\frac{1}{4} \mu_{CT} (-\sin \theta, \sqrt{3} \sin \theta, 0)$
$\mu_{e_1 f}$	—	$\mu_{CT} \sqrt{\frac{1-m_{CT}}{2}} (\sin \theta, 0, 0)$	$\frac{\sqrt{2}}{4} \sqrt{\frac{1-m_{CT}}{2}} \mu_{CT} (-\sin \theta, \sqrt{3} \sin \theta, 0)$
$\mu_{e_2 f}$	—	—	$\frac{\sqrt{2}}{4} \sqrt{\frac{1-m_{CT}}{2}} \mu_{CT} (\sqrt{3} \sin \theta, \sin \theta, 0)$

Table C.3: Synoptic table for the $n = 1, 2$ and 3 models with the m_{CT} parameterization.

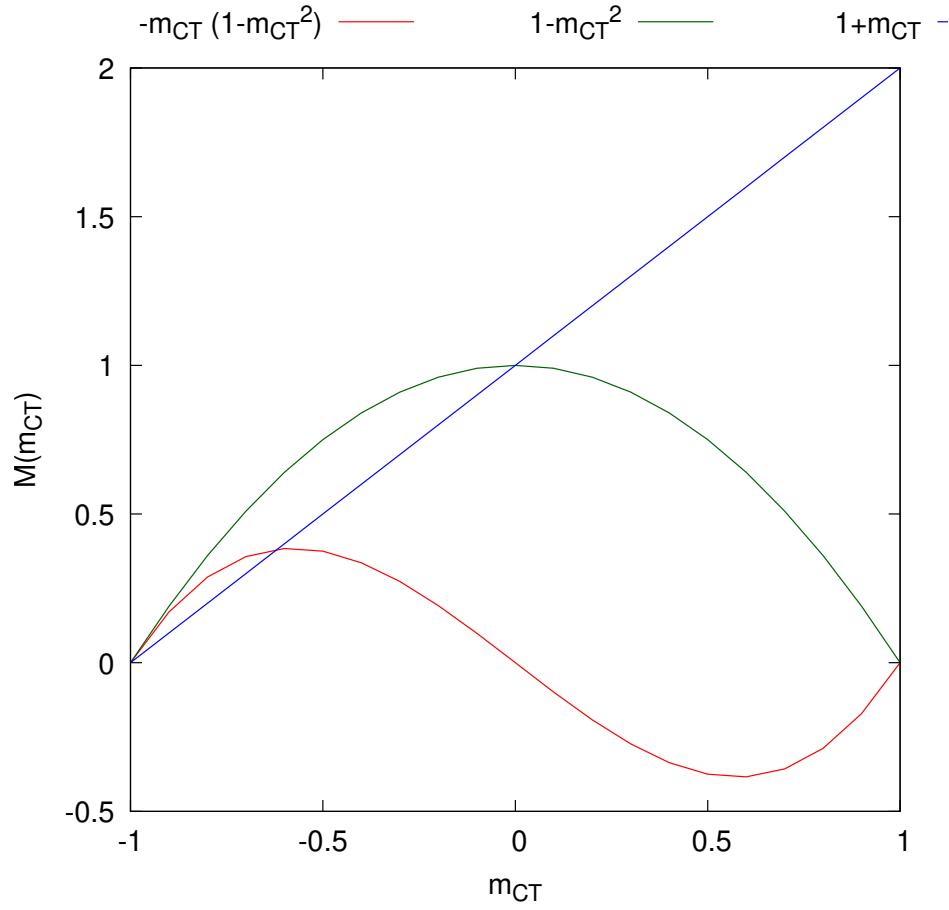


Figure C.10: Evolution of the different $M(m_{CT})$ parts (as detailed in Table 11.1) as a function of m_{CT} .

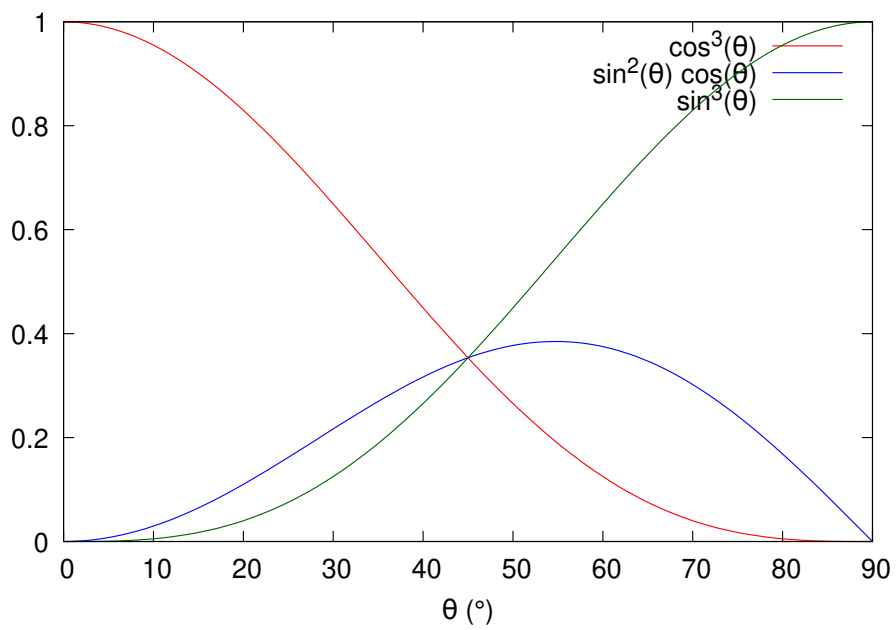


Figure C.11: Evolution of $\cos^3 \theta$, $\sin^3 \theta$ and $\sin^2 \theta \cos \theta$ with θ .